

**COUPLED FELDSPAR DISSOLUTION-CLAY PRECIPITATION
KINETICS AND LEAD SORPTION ONTO
FERRIHYDRITE NANO-PARTICLES**

Peng Lu

Submitted to the faculty of the University Graduate School
in partial fulfillment of the requirements
for the degree
Doctor of Philosophy
in the Department of Geological Sciences of
Indiana University
August, 2010

Accepted by the Graduate Faculty, Indiana University, in partial fulfillment of the requirements for the degree of Doctor of Philosophy

Chen Zhu, Ph.D., Committee Chair

Doctoral Committee:

Edward M. Ripley, Ph.D.

James G. Brophy, Ph.D.

Date of Oral Examination:

May 7th, 2010

Arndt Schimmelmann, Ph.D.

Jeff White, Ph.D., Minor Advisor

© Copyright, 2010

Peng Lu

ALL RIGHTS RESERVED

Acknowledgments

First I would like to thank my advisor, Dr. Chen Zhu, for mentoring me during my graduate studies and guiding the research that made this dissertation possible. It was through his leadership that I found the patience and persistence I needed to overcome the challenges of this research. You are not only an educator but a wonderfully compassionate human being. Thank you!

Secondly, I would like to acknowledge the financial support by the National Energy Technology Laboratory of Department of Energy (DE-FG26-04NT42125) as a Graduate Research Fellow at Indiana University. Material in this dissertation is based upon work supported by the U.S. Department of Energy under Award No. DE-FG26-04NT42125 to Dr. Chen Zhu and partially by the National Science Foundation under Award No.'s EAR0423971 and EAR0509775 to Dr. Chen Zhu. A National Science Foundation grant (#0318769) awarded to Department of Geological Sciences allowed for the purchase of the SEM at Indiana University.

I also thank the other members of my committee (Dr. James Brohpy, Dr. Edward Ripley, Dr. Arndt Schimmelmann, and Dr. Jeffrey R. White) in the realization of this dissertation. The author wishes to thank Qi Fu and Bill Seyfried at the University of Minnesota for hydrothermal feldspar dissolution experiments, Rick Haasch and John Baltrus for assistances with XPS analyses that were carried out in the Center for Microanalysis of Materials, University of Illinois and the National Energy Technology Laboratory. I thank Rick Knurr at University of Minnesota for chemical analyses of fluid samples, Hiromi Konishi and Huifang Xu at the University of Wisconsin for the TEM

analysis, and Kyle Jones at US EPA for BET surface analysis. I also thank Arndt Schimmelmann at Indiana University for the help with experiments.

I also appreciate the support and encouragement of the Indiana University Department of Geological Sciences, especially Claudia Johnson and Mary Iverson.

Finally I would like to thank my wife Xiaou and my parents for their continued support and encouragement that helped me a great deal in accomplishing this work and surviving the graduate school.

Peng Lu

**COUPLED FELDSPAR DISSOLUTION-CLAY PRECIPITATION KINETICS
AND LEAD SORPTION ONTO FERRIHYDRITE NANO-PARTICLES**

One of the fundamental problems in modern geochemistry is the significant discrepancy between laboratory-measured and field derived feldspar dissolution rates. Zhu et al. (2004) proposed a new hypothesis for explaining the laboratory–field discrepancy wherein the slow kinetics of secondary clay precipitation is the rate limiting step and thus controls the overall feldspar dissolution rate. We conducted new feldspar dissolution batch experiments and performed geochemical modeling to test this hypothesis. The experimental results show that partial equilibrium was not attained between secondary minerals and aqueous solutions for the feldspar hydrolysis batch systems. Modeling results show that a quasi-steady state was reached. At the quasi-steady state, dissolution reactions proceeded at rates that are orders of magnitude slower than the rates measured at far-from-equilibrium. Results reported in this dissertation lend support to Zhu et al. (2004) hypothesis and showed how the slow secondary mineral precipitation provides a regulator to explain why the systems are held close to equilibrium and show how the most often-quoted “near equilibrium” explanation for an apparent field-lab discrepancy can work quantitatively.

The second topic of this dissertation is Pb sorption onto ferrihydrite nano-particles. The differences of adsorption and coprecipitation of Pb with iron oxyhydroxide are studied with sorption edge measurements, High Resolution Transmission and Analytical Electron Microscopy (HR TEM-AEM), and geochemical modeling. Coprecipitation of Pb^{2+} with ferric oxyhydroxides occurred at ~ pH 4, about 0.5-1.0 pH

unit higher than Fe^{3+} precipitation. Coprecipitation is more efficient than adsorption in removing Pb^{2+} from aqueous solutions at similar sorbate/sorbent ratios. X-ray Diffraction and HRTEM shows Pb-Fe coprecipitates are 2-line ferrihydrite (2LFh) and lepidocrocite. Geochemical modeling shows that a surface complexation model can explain adsorption experimental data well. In contrast, a solid solution model or a model of combined solid solution formation and surface complexation can fit coprecipitation experimental data sets well. Hence, coprecipitation and adsorption experiments resulted in different Pb^{2+} incorporation mechanisms, which could result in different mobility, bioavailability, and long-term stability of Pb^{2+} in the environment.

TABLE OF CONTENTS

Title Page	i
Signature Page	ii
Copyright Notice	iii
Acknowledgements	iv
Abstract	vi
Table of Contents	viii
List of Tables	x
List of Figures	xii
Chapter 1: Introduction	1
1. Coupled Feldspar Dissolution-Clay Precipitation Kinetics	2
2. Navajo Sandstone-Brine-CO ₂ Interaction	6
3. Arsenic Eh-pH Diagrams at 25 °C and 1 bar (0.1 MPa)	7
4. Lead Sorption onto Ferrihydrite	8
5. Refereed Publications	11
References	12
Chapter 2: Alkali Feldspar Dissolution and Secondary Mineral Precipitation in Batch Systems: 1. New experiments at 200 °C and 300 bars (30 MPa)	20
1. Introduction	21
2. Experimental	23
3. Results	28
4. Conclusions	36
References	37
Chapter 3: Alkali Feldspar Dissolution and Secondary Mineral Precipitation in Batch Systems: 2. New Experiments with Supercritical CO₂ and Implications for Carbon Sequestration	41
1. Introduction	42
2. Experimental	44
3. Results	49
4. Discussion	71
5. Conclusions and Remarks	80
References	82
Chapter 4: Alkali Feldspar Dissolution and Secondary Mineral Precipitation in Batch Systems: 3. Saturation States of Product Minerals and Reaction Paths	93
1. Introduction	94
2. Background	97
3. Modeling Results	103
4. Discussion	130
5. Conclusions Remarks	137
Supplements for Chapter 2	140
References	152
Chapter 5: Alkali Feldspar Dissolution and Secondary Mineral Precipitation in Batch Systems: 4. Numerical Modeling of Kinetic Reaction Paths	161
1. Introduction	162

2. Conceptual Models and Assumptions	165
3. Modeling Results and Analyses	173
4. Discussions	202
5. Conclusions and Remarks	211
References	216
Chapter 6: Navajo Sandstone-Brine-CO₂ Interaction: Implications for Geological Carbon Sequestration	224
1. Introduction	225
2. Materials and Methods	227
3. Results and Discussion	232
4. Conclusions	258
References	260
Chapter 7: Arsenic Eh-pH Diagrams at 25 °C and 1 Bar (0.1 MPa)	266
1. Introduction	267
2. Internally Consistent Thermodynamic Properties for Arsenic	268
3. Eh-pH Diagrams	273
4. Concluding Remarks	278
References	284
Chapter 8: Lead Adsorption and Coprecipitation with Iron Oxyhydroxide Nano-Particles	289
1. Introduction	290
2. Materials and Methods	293
3. Experimental Results	298
4. Geochemical Modeling	316
5. Discussion and Conclusions	328
References	332
Chapter 9: Future Work	338
1. Introduction	339
2. Background and Rational	339
3. Project Description	348
4. Anticipated Results and Significance	370
References	371
Chapter 10: Conclusions	381
References	385
Vita	

LIST OF TABLES

Chapter 2

Table 1	Electron microprobe analysis (EMPA) results of alkali-feldspar grains ...	26
Table 2	Time-dependent changes in the composition of major dissolved constituents in aqueous fluid coexisting with alkali-feldspar	29
Table 3	XPS surface composition results of alkali-feldspar	35

Chapter 3

Table 1	Feldspar dissolution experiments with the presence of CO ₂ (batch reactor)	50
Table 2	Time-dependent changes in the composition of major dissolved constituents in aqueous fluid coexisting with alkali-feldspar	54
Table 3	Mineral saturation indices in experiments for the alkali feldspar dissolution	60

Chapter 4

Table 1	Equilibrium constants used in this study	101
Table 2	Summary of feldspar dissolution experiments used in this study	106
Table 3	Mineral saturation indices in experiments for the alkali feldspar dissolution	110
Table 4	Mineral saturation indices in experiments for the alkali feldspar dissolution (charged with CO ₂)	116
Table 5	Mineral saturation indices in the experiments for anorthite dissolution ...	117
Table 6	Mineral saturation indices for sanidine dissolution experiments	127
Table 7	Mineral saturation indices for albite dissolution experiments	128

Chapter 5

Table 1	List of Symbols	167
Table 2	Equilibrium constants used in this study	168

Chapter 6

Table 1	Time-dependent changes in the composition of major dissolved species (Experiment #1)	242
Table 2	Time-dependent changes in the composition of minor and trace dissolved species (Experiment #1)	242
Table 3	Thermodynamic data used in this report	244
Table 4	Saturation indices calculation for Experiment #1	245
Table 5	Comparison of batch experiments (#1 and #2)	249
Table 6	Time-dependent changes in the composition of major dissolved species (Experiment #2)	249
Table 7	Time-dependent changes in the composition of minor and trace dissolved species (Experiment #2)	250
Table 8	Saturation indices calculation for Experiment #2	250
Table 9	Time-dependent changes in the composition of major dissolved species (Experiment #3)	255
Table 10	Saturation indices calculation for Experiment #3	255
Table 11	Dissolution rates of Navajo Sandstone in the experiment with mixed flow reactor at 200 °C and 25 MPa	256

Chapter 7

Table 1	Equilibrium constants for As aqueous species from different sources	271
Table 2	Equilibrium constants for As solid dissolution reactions	271
Table 3	Gibbs free energy of formation for aqueous species and solids at 25 °C and	

1 bar (0.1 MPa)	272
Chapter 8	
Table 1 Titration experimental conditions	302
Table 2 Equilibrium constants used in modeling	327
Table 3 Surface properties for hydrous ferric oxides (HFO) used in this study	328

LIST OF FIGURES

Chapter 2

Figure 1	Changes in the dissolved concentrations of selected aqueous constituents with time for the perthitic alkali-feldspar dissolution experiments	30
Figure 2	SEM backscatter images of alkali-feldspar dissolution effects following reaction after 78 days (A, B) and 5 days (C, D)	31
Figure 3	X-ray diffraction patterns of mineral products following the 5-day experiment (A) and 78-day experiment (B)	32
Figure 4	TEM images and SAED patterns of mineral products from alkali-feldspar dissolution experiments	34

Chapter 3

Figure 1	Changes in the dissolved concentrations of selected aqueous constituents with time	55
Figure 2	SEM and TEM characterizations before and after reactions	58
Figure 3	XRD pattern of mineral products from Experiment S	61
Figure 4	Rates of alkali-feldspar dissolution in the Experiment S and a companion CO ₂ -free experiment (Fu et al., 2009)	62
Figure 5	SEM micrograph of products from Experiment E	65
Figure 6	Activity – activity diagrams showing the phase relations in the system Na ₂ O-(Al ₂ O ₃)-SiO ₂ -H ₂ O-HCl at 200 °C and 300 bars (30 MPa)	66
Figure 7	SEM micrographs of Experiment D	70
Figure 8	XRD diffraction pattern of mineral products following Experiment D ..	72
Figure 9	Experiment D TEM images	73
Figure 10	Activity – activity diagrams showing the phase relations in the system Na ₂ O-(Al ₂ O ₃)-SiO ₂ -H ₂ O-HCl at 200 °C and 300 bars (30 MPa)	74
Figure 11	Activity-activity diagram depicting mineral stability fields in the system Na ₂ O-Al ₂ O ₃ -SiO ₂ -CO ₂ -H ₂ O at 150 °C	75
Figure 12	Experimental <i>T-P</i> conditions compared with <i>T, P</i> ranges relevant to geological sequestration	78

Chapter 4

Figure 1	Reaction path of the dissolution of microcline in pure water at 25 °C ...	100
Figure 2	Activity–activity diagrams showing the phase relations in the system K ₂ O-(Al ₂ O ₃)-SiO ₂ -H ₂ O-HCl at 200 °C and 300 bars (30 MPa) (Fu et al., 2009)	108
Figure 3	Mineral saturation indices during the course of alkali feldspar dissolution at 200 °C and 300 bars (30 MPa) (Fu et al., 2009)	112
Figure 4	Activity–activity diagrams showing the phase relations in the system K ₂ O-(Al ₂ O ₃)-SiO ₂ -H ₂ O-HCl at 200 °C and 300 bars (30 MPa) (Experiment S)	114
Figure 5	Mineral saturation indices during the course of alkali feldspar dissolution (Experiment S)	115
Figure 6	Activity–activity diagrams showing the phase relations in the system Ca ₂ O-(Al ₂ O ₃)-SiO ₂ -H ₂ O (Murakami et al., 1998)	118
Figure 7	Calculated saturation indices for anorthite dissolution experiments (Murakami et al., 1998)	123

Figure 8	Activity–activity diagrams showing phase relations in the system Na_2O – (Al_2O_3) – SiO_2 – H_2O at 300 °C and 88 bars (8.8 MPa) (Alekseyev et al., 1997)	125
Figure 9	Calculated saturation indices (SI) from experimental data for sanidine dissolution (Alekseyev et al., 1997)	126
Figure 10	Activity–activity diagrams showing phase relations in the system K_2O – (Al_2O_3) – SiO_2 – H_2O at 300 °C and 88 bars (8.8 MPa) (Alekseyev et al., 1997)	129
Figure 11	Calculated saturation indices (SI) from experimental data for albite dissolution (Alekseyev et al., 1997)	130
Figure A1	Comparison of experimental (symbols) and calculated (lines) phase equilibrium involving boehmite	141
Figure A2	Fraction of Al aqueous species as a function of time for alkali feldspar dissolution and clay precipitation experiment	144
Figure A3	Fraction of Al species in the experiment of anorthite dissolution in 0.03 m NaAC solutions performed by Murakami et al. (1998)	145
Figure A4	Fraction of Al species in the experiments conducted by Alekseyev et al. (1997) at 300 °C and 88 bars (8.8 MPa)	147
Chapter 5		
Figure 1	Rates of albite dissolution in the first seven hours of experiments	177
Figure 2	Temporal evolution of dissolved constituent concentrations: (a) Na; (b) Al, and (c) Si	182
Figure 3	Ratios of albite dissolution rates vs. sanidine precipitation rates	183
Figure 4	Correlation between experimental effective rate constants and the amount of sanidine precipitated	183
Figure 5	Proportions of Al and Si concentrations over time	184
Figure 6	Proportions of Si and Na concentrations over time	185
Figure 7	Albite dissolution (a) and sanidine precipitation (b) rates over time	186
Figure 8	Saturation indices (SI) over time	187
Figure 9	Comparison of the mass of albite (a) and sanidine (b) in the reactor	188
Figure 10	Albite dissolution (a) and sanidine precipitation (b) rates (incongruent stage)	194
Figure 11	Rate of dissolution of albite as a function of dissolved Al concentrations	195
Figure 12	Activity diagram in the K_2O – Al_2O_3 – SiO_2 – H_2O – (CO_2) – HCl system at 300 °C and 88 bars (8.8 MPa) for albite dissolution	197
Figure 13	Predicted continued reactions in the batch reactor beyond experimental time of 1848 h following the reaction path model	198
Figure 14	Comparison of predicted solution chemistry from the reaction path model with experimental data	203
Figure 15	Calculated change in albite and boehmite saturation indices evolution compared with data from solubility calculations	204
Figure 16	Change of boehmite precipitation and albite dissolution rates over time	205
Figure 17	Activity diagram in the K_2O – Al_2O_3 – SiO_2 – H_2O – (CO_2) – HCl system	206
Figure 18	Calculated saturation indices for oligoclase at different time and space from coupled reactive transport model	212

Chapter 6

Figure 1	XRD patterns of the clay fraction in Navajo Sandstone before and after reaction	235
Figure 2	SEM images of Navajo Sandstone before reaction	236
Figure 3	SEM images of Navajo Sandstone after Experiment #1	238
Figure 4	Variation of Si, Na, Mg, Ca, and Al concentrations as a function of time	241
Figure 5	SEM images of Navajo Sandstone after Experiment #2	251
Figure 6	SEM images of Navajo Sandstone after Experiment #3	254

Chapter 7

Figure 1	Eh-pH diagram for the system As-O-H at 25 °C and 1 bar (0.1 MPa)	279
Figure 2	Eh-pH diagrams for the system As-O-H-S at 25 °C and 1 bar (0.1 MPa)	280
Figure 3	Eh-pH diagrams for the system As-O-H-S-Fe at 25 °C and 1 bar (0.1 MPa)	281
Figure 4	Eh-pH diagrams for the system As-O-H-Ba at 25 °C and 1 bar (0.1 MPa)	282
Figure 5	Eh-pH diagrams for the system As-O-H-S-Fe-Ba at 25 °C and 1 bar (0.1 MPa)	283

Chapter 8

Figure 1	Comparison of adsorption with coprecipitation experiments	303
Figure 2	Comparison of model calculations with coprecipitation experimental results	305
Figure 3	Comparison of model calculations with adsorption experimental results	306
Figure 4	Comparison of Fe ³⁺ solubility data with modeling calculations	307
Figure 5	Fraction of Pb extracted after ADS and CPT experiments as a function of different EDTA concentration	308
Figure 6	Fraction of Pb extracted as a function of fraction of Fe dissolved contacting with different concentration of EDTA for 1 h	308
Figure 7	Fraction of Fe dissolved vs. different extraction time of room temperature extraction experiments	310
Figure 8	XRD spectrum for precipitates after CPT experiments with precipitates after ADS experiments	313
Figure 9	Comparison of precipitates of ADS, CPT, and synthesized 2-line ferrihydrite	314
Figure 10	TEM image of Fe ³⁺ and Pb ²⁺ coprecipitates on holey carbon support ..	317
Figure 11	HRTEM image of Fe ³⁺ and Pb ²⁺ coprecipitates with spherical shape ..	318
Figure 12	HRTEM image of Fe ³⁺ and Pb ²⁺ coprecipitates with needle like shape ..	320
Figure 13	EDS Spectrum data show that Pb ²⁺ is associated in the freshly co-precipitated solids	324
Figure 14	Modeling coprecipitation experiments with surface complexation Models	326

Chapter 9

Figure 1	SEM images of wollastonite grain after 2 days of reaction in circum-neutral pH conditions	346
Figure 2	Experimental <i>T-P</i> conditions compared with <i>T, P</i> ranges relevant to geological sequestration	347
Figure 3	Schematic illustration of the flexible cell reaction system	350
Figure 4	SEM micrograph of K-feldspar grain enveloped by a clay rind in the	

Navajo sandstone	355
Figure 5 High resolution TEM image showing K^+ deficient amorphous layer	355
Figure 6 Activity – activity diagrams showing the phase relations in the system Na ₂ O-(Al ₂ O ₃)-SiO ₂ -H ₂ O-HCl at 200 °C and 300 bars (30 MPa)	359
Figure 7 Albite dissolution and sanidine precipitation are strongly coupled	362
Figure 8 Temporal evolution of dissolved constituent concentrations: (a) Na; (b) Al, and (c) Si	367
Figure 9 Albite dissolution (a) and sanidine precipitation (b) rates over time	386
Figure 10 Saturation indices (SI) over time	386
Figure 11 Comparison of the mass of albite (a) and sanidine (b) in the reactor ...	389
Figure 12 Activity diagram in the K ₂ O-Al ₂ O ₃ -SiO ₂ -H ₂ O-(CO ₂)-HCl system at 300 °C and 88 bars (8.8 MPa) for albite dissolution	197

CHAPTER 1

INTRODUCTION

1. COUPLED FELDSPAR DISSOLUTION-CLAY PRECIPITATION KINETICS

Feldspars are the most intensely-studied silicate minerals for their dissolution kinetics. This is partly because they are the most abundant minerals in the earth crust and they comprise as much as 60% (by weight) of the Earth's crust (Levin, 2005). Feldspar dissolution have important implications for many geologic, hydrologic and biologic processes that include the compositional changes in ground and surface water, long-term capacity of soils to neutralize anthropogenic acidic rainfall (e.g., Reuss and Johnson, 1986), formation of Karst, acid mine drainage, inorganic nutrients balance (Huntington et al., 2000), global elemental cycles (Lasaga et al., 1994), and global climate over geological timescales (Berner and Berner, 1997). In addition, there has been a great deal of recent concern over global climate change, and its link to growing atmospheric concentrations of carbon dioxide (CO_2). Geological carbon sequestration—the injection of carbon dioxide (CO_2) into deep geological formations—is presently the most promising method of sequestering CO_2 released from the burning of fossil fuels (IPCC, 2005; International Energy Agency, 2006). A key challenge to geological carbon sequestration involves the accurate prediction of kinetics of reactions among CO_2 , brine, and minerals in the geological formation, in which CO_2 is stored, and in the cap rocks (e.g., shale/mudstone), which prevent CO_2 seeping upward to the ground surface (IPCC, 2005).

Our ability to accurately quantify and model these processes would be greatly enhanced by an improved understanding of feldspar dissolution kinetics. However, one of the fundamental problems in modern geochemistry is the persistent two to five orders of magnitude discrepancy between laboratory-measured and field derived feldspar

dissolution rates (Paces, 1983; Velbel, 1990; Brantley, 1992; Blum and Stillings, 1995; Drever and Clow, 1995; White and Brantley, 2003; Zhu, 2005; and references therein). This discrepancy is huge and can lead to dramatically different modeling results. For example, the laboratory rates indicate that a 0.1 mm feldspar sphere should weather away in ~250 years, whereas the field rates predict a feldspar lifetime of millions of years (calculations followed Lasaga, 1998).

Numerous hypotheses have been proposed in the literature to explain the persistent huge gap between measured field and laboratory feldspar dissolution rates. These hypotheses include the possible armoring effects of the secondary minerals that coat the feldspar grain surfaces (Correns and Von Engelhardt, 1938; Correns, 1940; Helgeson, 1971, 1972; Luce et al., 1972; Paces, 1973; Busenberg and Clemency, 1976; Chou and Wollast, 1984; Nugent et al., 1998), the possible effects of the leached layer (Luce et al., 1972; Busenberg and Clemency, 1976; Chou and Wollast, 1984; Hellmann et al., 1990; Brantley and Stillings, 1996; Hellmann, 1997; Nesbitt and Skinner, 2001; Oelkers, 2001), the approach to saturation with respect to feldspars (Burch et al., 1993; Gautier et al., 1994; Oelkers et al., 1994; Oelkers, 2001; Beig and Lüttge, 2006; Hellmann and Tisserand, 2006), unknown biological effects, and inhibition by adsorbed Al^{3+} on feldspar surfaces (Chou and Wollast, 1985; Gautier et al., 1994; Oelkers et al., 1994; Oelkers, 2001).

Recognizing the close association between the secondary and primary minerals in the field, Zhu et al. (2004) proposed a new hypothesis focusing on the role of slow clay precipitation kinetics in coupled feldspar dissolution/clay precipitation reactions that are known to operate on a variety of spatial and temporal scales of interest. When modeling

feldspar dissolution reactions, it has long been assumed that a condition of partial equilibrium exist between mineral products (e.g., clay minerals) and aqueous solutions (Garrels, 1967; Garrels and Mackenzie, 1967). However, field observation (Zhu et al., 2004; Zhu et al., 2006), experimental investigations (Nagy and Lasaga, 1993; Price et al., 2005; Small, 1993), and numerical modeling (Lasaga, 1984; Lasaga, 1998; Lasaga et al., 1994; Steefel and van Cappellen, 1990) suggest that formation of secondary minerals does not reflect equilibrium conditions but may be influenced by a slow reaction kinetics. Clay precipitation promotes the dissolution of feldspar by removing solutes from the aqueous solution and maintaining a condition of feldspar undersaturation. Our preliminary study shows that the feldspar dissolution and clay precipitation are strongly coupled and sensitive to the rate of clay mineral precipitation (Ganor et al., 2007). Thus, the slow precipitation of secondary minerals can raise the saturation state of feldspar to close to equilibrium and thus imposes a strong control on overall reaction kinetics.

To test this hypothesis, we have conducted experiments of feldspar and secondary mineral precipitation in batch systems. As these reactions are too slow to be measured under ambient temperature and circumneutral pH conditions (Ganor et al., 2007), the experiments were conducted at 200 °C and 300 bars and acidic pH. Although the secondary minerals formed in these high temperature experiments may be different from clays formed under ambient, weathering temperatures, the failure to achieve partial equilibrium under hydrothermal conditions is highly likely an excellent indicator that partial equilibrium with secondary minerals is also not attained under weathering temperatures. Chapter 2 presents new experimental data of solution chemistry evolution and mineral characterizations of alkali-feldspar dissolution and secondary minerals

formation in acidic solution ($\text{pH} = 3.1$) with the duration of 1872 h. Reactions proceeded slowly and full equilibrium was not achieved, the relatively high temperature of the experiments notwithstanding. Thus, time series observations indicate continuous supersaturation with respect to boehmite and kaolinite, although the extent of this decreased with reaction progress as the driving force for albite dissolution decreased. Chapter 3 is on alkali-feldspar dissolution and clay precipitation in CO_2 -charged systems with the relevance to the geological carbon sequestration. The experimental results show that partial equilibrium was not attained between secondary minerals and aqueous solutions for the feldspar hydrolysis batch systems. Evidences came from both solution chemistry (supersaturation of the secondary minerals during the entire experimental duration) and metastable co-existence of secondary minerals. Chapter 4 conducted speciation-solubility modeling and described the saturation indices and reaction paths in terms of trajectories of aqueous chemical evolution on equilibrium activity-activity diagrams for experimental data in Chapter 2, Chapter 3, and Alekseyev et al. (1997). The modeling results demonstrated: (1) the experimental aqueous solutions were supersaturated with respect to product minerals for almost the entire duration of the experiments; (2) the aqueous solution chemistry did not evolve along the phase boundaries but crossed the phase boundaries at oblique angles; and (3) the earlier precipitated product minerals did not dissolve but continued to precipitate even after the solution chemistry had evolved into the stability fields of minerals lower in the paragenesis sequence. These three lines of evidence signify that product mineral precipitation is a slow kinetic process and partial equilibria between aqueous solution and product minerals were not held. Chapter 5 reports results of numerical reaction path

modeling that simulate the feldspar hydrolysis experiments by matching modeling results with experimental data. Modeling results show that a quasi-steady state was reached. At the quasi-steady state, dissolution reactions proceeded at rates that are orders of magnitude slower than the rates measured at far-from-equilibrium. The quasi-steady state is determined by the relative rate constants, and strongly influenced by the function of Gibbs free energy of reaction (ΔG_r) in the rate laws. To explore the potential effects of fluid flow rates on the coupling of reactions, a batch system (Ganor et al., 2007) was extrapolated to open systems and one-dimensional reactive mass transport was simulated for oligoclase dissolution and kaolinite precipitation in homogeneous porous media. Different steady states were achieved at different locations along the one-dimensional domain. However, the ratio between oligoclase dissolution rates and kaolinite precipitation rates remained 1.626, as in the batch system case (Ganor et al., 2007). Results reported in this dissertation lend support to our hypothesis that slow secondary mineral precipitation explains part of the well-known apparent discrepancy between lab measured and field estimated feldspar dissolution rates (Zhu et al., 2004).

2. NAVAJO SANDSTONE-BRINE-CO₂ INTERACTION

Chapter 6 presents experiments involving the reaction of Navajo Sandstone with acidic brine at 200 °C and 25 or 30 MPa to evaluate the extent of fluid-rock interactions. The first experiment examined sandstone interaction with CO₂ impregnated brine; the second experiment examined sandstone dissolution in CO₂-free acidic brine; the third one is carried out in a mixed flow reactor and designed to measure sandstone dissolution rates based on time-series Si concentrations. The solution chemistry data indicate that the

$\text{SiO}_2(\text{aq})$ increases gradually and pH increases slowly with reaction progress. Silicate minerals in the sandstone display textures (dissolution features, secondary mineralization), indicating that these phases are reacting strongly with the fluid. The chemical reactions likely increase the bulk porosity of the sandstone due to dissolution of silicate minerals. However, allophane and illite/smectite fill voids in sandstone grains and may affect the permeability and injectivity of the reservoir.

3. ARSENIC EH-PH DIAGRAMS AT 25 °C AND 1 BAR (0.1 MPA)

Currently, there is tremendous interest in arsenic geochemistry (Tamaki and Frankenberger, 1992; WHO, 2001; Nordstrom and Archer, 2002; Smedley and Kinniburgh, 2002; Oremland and Stolz, 2003; Swartz et al., 2004; Hollibaugh et al., 2005; Keimowitz et al., 2005; Amirbahman et al., 2006; Sverjensky and Fukushima, 2006; Fukushima and Sverjensky, 2007; Marini and Accornero, 2007). Eh-pH diagrams provide a useful guide for evaluating the predominance of dissolved species and stability of solids (Garrels and Christ, 1965; Pourbaix, 1966; Krauskopf and Bird, 1995). Since the last special publication of Eh-pH diagrams for arsenic was over ten years ago (Vink, 1996), new values of thermodynamic properties for arsenic species have become available through several re-evaluations, compilations, or estimations (Nordstrom and Archer, 2002; Pokrovski et al., 2002; Langmuir et al., 2006; Marini and Accornero, 2007). A new compilation that integrates data available for the As-O-H-S-Fe-Ba system is necessary. We compiled a thermodynamic dataset for arsenic species in As-O-H-S-Fe-Ba system from the literature. Using this dataset, Eh-pH diagrams for arsenic in the systems As-O-H, As-O-H-S, As-O-H-S-Fe, As-O-H-Ba, and As-O-H-S-Fe-Ba were constructed at 25

°C and 1 bar (0.1 MPa). The inclusion of thioarsenite species in the systems As-O-H-S and As-O-H-S-Fe results in substantial differences from previously published Eh-pH diagrams. There are considerable differences in the thermodynamic properties for orpiment, realgar, scorodite, arsenopyrite, barium arsenate, and barium hydrogen arsenate, which result in vastly different stability fields when different values are adopted. These diagrams provide a ready reference for practitioners working in the area of arsenic geochemistry.

4. LEAD SORPTION ONTO FERRIHYDRITE

The bioavailability, mobility, transport, distribution, and cycling of toxic metals in subsurface and surficial geological systems have long been of interest to geochemists. Unlike organic contaminants, toxic metals (e.g, Pb) are not biodegradable and can persist and accumulate in the environment and in living organisms, posing a serious threat to plants, animals, and humans (e.g., Sparks, 2005 and the reference therein). Iron oxyhydroxides occur widely in surficial and subsurface geological environments, and are efficient scavengers of trace metals and radionuclides (Jambor and Dutrizac, 1998). However, the mechanisms by which trace elements are sorbed onto iron oxyhydroxides in pristine and anthropogenically impacted water-rock systems are largely unknown. The present study focuses on sorption of Pb onto iron oxyhydroxides in order to understand the relevant sorption mechanisms. Controls on trace elements by iron oxyhydroxides have been attributed to a continuum that extends from specific adsorption to surface hydroxyl groups (surface complexation), solid solution, to surface precipitation as the discrete oxide or hydroxide (Martinez and McBride, 1998), possibly depending on

contact methods (e.g., precipitation, adsorption or coprecipitation), surface loading, and size difference of trace elements with host element (e.g., Fe). At low-surface coverages, surface complexation (e.g. outer- and inner-sphere adsorption) tends to dominate; as surface loadings increase, nucleation occurs and results in the formation of distinct entities or aggregates on the surface (solid solution); as surface loadings increase further, surface precipitation becomes the dominant mechanism (Farley et al., 1985; Zhu, 2002). Knowledge of sorption mechanisms is nevertheless central both to developing quantitative partitioning models that serve as a theoretical basis for the applications of trace elements as signatures of fluid flow, chemical reactions, and other geological and environmental processes and to predicting contaminant transport and stability in geological media.

Adsorption (ADS) and coprecipitation (CPT) contact methods attract more and more attentions in waste water treatment because they are free of voluminous sludge and producing extremely low soluble metal levels (Karthikeyan et al., 1997). In the ADS systems, for example, the Fe oxyhydroxides were formed and aged (typically for 24 h) first, and then Pb^{2+} was added; acid or base was used to adjust the solution to desired pH. Pb^{2+} sorption on pre-existing Fe oxyhydroxides is a common process, considering the case of Pb atmospheric fallouts (e.g., from car exhausts and smelters) onto soils and sediments. ADS onto ferrihydrite and other iron oxides has been shown to play an important role in the transportation of Pb from continental waters to the oceans (Erel and Morgan, 1992). In contrast, the CPT contact method for Pb^{2+} sorption by Fe oxyhydroxides is defined as a base titration with both the trace element (Pb^{2+}) and the host element (Fe^{3+}) in solution together (with low initial pH), while the pH is increased to

form a solid precipitate. CPT can occur in contaminated soils, sediments, and water systems. For example, when acid mine drainage or landfill leachate loaded with Fe^{3+} and trace metals (e.g., Pb, As, and Cu) is mixed with neutral surface water and groundwater or allowed to react with calcite in soils, sediments, and aquifers, the Fe^{3+} and trace metals (such as Pb^{2+}) are coprecipitated simultaneously. Numerous studies have been performed on Pb ADS (e.g., Gadde and Laitinen, 1974; Kinniburgh et al., 1976; Swallow et al., 1980; Balistrieri and Murray, 1982; Hayes and Leckie, 1986; Rose and Bianchi-Mosquera, 1993; Lützenkirchen, 1997; Trivedi et al., 2003) with sporadic mention of CPT (e.g., Ford et al., 1997; Martinez and McBride, 1998; Ford et al., 1999; Martinez and McBride, 2001) with iron oxyhydroxides, but direct comparison of Pb ADS and CPT are rare and comparison of desorption properties of precipitates prepared by ADS and CPT methods are even scarce. Schultz et al. (1987), as an exception, compared the forward and reverse (desorption) process of Pb with ADS and CPT methods. They found that a measurable fraction of the bound Pb is not easily desorbed and the retained (remaining sorbed) fraction of Pb after CPT process is larger than that after ADS process at time frame of their experiments (21.5 h). Thus, the main task of this study is to identify the difference of two sorption contact methods (adsorption and coprecipitation) and elucidate the sorption behavior and mechanisms.

This study focuses on the Pb sorption onto ferrihydrite and is being conducted in the following manner: (1) to compare the difference of two sorption contact methods (adsorption and coprecipitation), (2) to characterize the solids, (3) to elucidates the sorption behavior and mechanism, (4) to construct quantitative models to predict the fate of Pb, and (5) to study the effects of aging on the fate of Pb.

The mechanism of Pb^{2+} and Fe^{3+} coprecipitation is studied with sorption edge measurements, High Resolution Transmission and Analytical Electron Microscopy (HR TEM-AEM), and geochemical modeling. Coprecipitation of Pb^{2+} with ferric oxyhydroxides occurred at $\sim \text{pH } 4$, about 0.5-1.0 pH unit higher than Fe^{3+} precipitation. Coprecipitation is more efficient than adsorption in removing Pb^{2+} from aqueous solutions at similar sorbate/sorbent ratios. X-ray Diffraction (XRD) shows peaks of lepidocrocite and two additional broad peaks similar to fine particles of 2-line ferrihydrite (2LFh). HRTEM of the Pb-Fe coprecipitates shows a mixture of 2 to 6 nm diameter spheres and 8-20 by 200-300 nm needles, both uniformly distributed with Pb^{2+} . Geochemical modeling shows that solid solution model or combined solid solution formation and surface complexation can fit the experimental data sets well and explain the overlap between sorption edges with different Pb:Fe ratios, but surface complexation alone cannot account for all the Pb^{2+} bound to the solids.

Based on these results, we hypothesize that Pb^{2+} was first adsorbed onto the nanometer-sized, metastable, iron oxyhydroxide polymers of 2LFh. As the iron oxyhydroxides grew and transformed into more stable phases, Pb^{2+} was trapped in the iron oxyhydroxide structure. Hence, coprecipitation and adsorption experiments resulted in different Pb^{2+} incorporation mechanisms, which could result in different mobility, bioavailability, and long-term stability of Pb^{2+} in the environment.

5. REFEREED PUBLICATIONS

During the 6 years of my Ph.D. program, I have authored/co-authored the following refereed publications:

- **Lu, P.** and Zhu, C. Arsenic Eh-pH and solubility diagrams at 25 °C and 1 bar (0.1 MPa). *Environ. Earth Sci.* submitted.
- **Lu, P.**, Fu, Q., Seyfried, W. E., Hereford, A., and Zhu, C. (2010) Navajo sandstone-brine-CO₂ interaction: implications for geological carbon sequestration. *Environ. Earth Sci.* in press, DOI: 10.1007/s12665-010-0501-y.
- Zhu, C., **Lu, P.**, Zheng, Z., and Ganor, J. (2010) Alkali feldspar dissolution and secondary mineral precipitation in batch systems: 4. Numerical modeling of kinetic reaction paths. *Geochim. Cosmochim. Acta* in press.
- Zhu, C. and **Lu, P.** (2009) Alkali feldspar dissolution and secondary mineral precipitation in batch systems: 3. Saturation states of product minerals and reaction paths. *Geochim. Cosmochim. Acta* **73** (11): 3171-3200.
- Fu, Q., **Lu, P.**, Konishi, H., Dillmore, R., Xu, H., Seyfried, W. E. and Zhu, C. (2009) Coupled alkali-feldspar dissolution and secondary mineral precipitation in batch systems: 1. New experiments at 200 °C and 300 bars (30 MPa). *Chem. Geol.* **258** (3-4): 125-135.
- **Lu, P.**, Li, Q., and Zhai, J. (2008) Mineralogical characterizations and reaction path modeling of the pozzolanic reaction of fly ash-lime systems. *J. Am. Ceram. Soc.* **91**(3): 955-964.
- Huang, L., Zhai, j., **Lu, P.** Nutrient removal ability and resistance of five hydrophytes under low-temperature conditions. *Int. J. Environ. Pollut.* in press.
- Dillmore, R., **Lu, P.**, Allen, D., Soong, Y., Hedges, S., Fu, J.K., Dobbs, C.L., Degalbo, A., and Zhu, C. (2008) Sequestration of CO₂ in mixtures of bauxite residue and saline waste water. *Energ. Fuel.* **22**: 343-353.
- Kelly, S., **Lu, P.**, Bolin, T., Chattopadhyay, S., Newville, M. G., Shibata, T., and Zhu, C. (2008) Molecular structure of lead(II) coprecipitated with iron(III) oxyhydroxide, in: Barnett, M. and Kent D. (Eds.) *Adsorption of Metals by Geomedia II: Variables, Mechanisms, and Model Applications*, Elsevier Science, pp. 67-94.
- Ganor, J., **Lu, P.**, Zheng, Z., and Zhu, C. (2007) Bridging the gap between laboratory measurements and field estimations of silicate weathering using simple calculations. *Environ. Geol.* **53**(3): 599-610.

REFERENCES

- Alekseyev, V. A., Medvedeva, L. S., Prisyagina, N. I., Meshalkin, S. S., and Balabin, A. I., 1997. Change in the dissolution rates of alkali feldspars as a result of secondary mineral precipitation and approach to equilibrium. *Geochim. Cosmochim. Acta* **61**, 1125-1142.

- Amirbahman, A., Kent, D. B., Curtis, G. P., and Davis, J. A., 2006. Kinetics of sorption and abiotic oxidation of arsenic(III) by aquifer materials. *Geochim. Cosmochim. Acta* **70**, 533-547
- Balistrieri, L. S. and Murray, J. W., 1982. The adsorption of Cu, Pb, Zn, and Cd on goethite from major ion seawater. *Geochim. Cosmochim. Acta* **46**, 1253-1265.
- Beig, M. S. and Lüttge, A., 2006. Albite dissolution kinetics as a function of distance from equilibrium: Implications for natural feldspar weathering. *Geochim. Cosmochim. Acta* **70**, 1402-1420.
- Berner, R. A. and Berner, E. K., 1997. Silicate weathering and climate. In: Ruddiman, W. F. (Ed.), *Tectonic Uplift and Climate Change*. Plenum Press.
- Blum, A. and Stillings, L., 1995. Feldspar dissolution kinetics. In: Brantley, S. L. and White, A. R. (Eds.), *Chemical Weathering Rates of Silicate Minerals*. Mineralogical Society of America, Washington DC. v. 31, p. 291-351
- Busenberg, E., Clemency, C.V., 1976. The dissolution kinetics of feldspars at 25 °C and 1 atm CO₂ partial pressure. *Geochim. Cosmochim. Acta* **40**, 41-49.
- Brantley, S. L., 1992. Kinetics of dissolution and precipitation: experimental and field results. In *Proceedings of the Seventh International Conference on Water-Rock Interactions* (eds. Y. Kharaka and A. Maest). Rotterdam, Balkema, Park City, Utah.
- Brantley, S. L. and Stillings, L., 1996. Feldspar dissolution at 25 °C and low pH. *Am. J. Sci.* **296**, 101-127.
- Burch, T. E., Nagy, K. L., and Lasaga, A. C., 1993. Free energy dependence of albite dissolution kinetics at 80 °C and pH 8.8. *Chem. Geol.* **105**, 137-162.
- Chou, L. and Wollast, R., 1984. Study of the weathering of albite at room temperature and pressure with a fluidized bed reactor. *Geochim. Cosmochim. Acta* **48**, 2205-2217.
- Chou, L. and Wollast, R., 1985. Steady-state kinetics and dissolution mechanisms of albite. *Am. J. Sci.* **285**, 963-993.
- Correns, C.W., 1940. Die Chemische Verwitterung der Silikate, *Nature* **28**, 369-376.
- Correns, C.W. and von Engelhardt, W., 1938. Neue Untersuchungen über die Verwitterung des Kalifeldspates, *Chemie der Erde* **12**, 1-22.
- Drever, J. I. and Clow, D. W., 1995. Weathering rates in catchments. In: White, A. F. and Brantley, S. L. (Eds.), *Chemical Weathering Rates of Silicate Minerals*. Mineralogical Society of America. v. 31, p. 463-483.

- Erel, Y. and Morgan, J. J., 1992. The relationships between rock-derived lead and iron in natural waters. *Geochim. Cosmochim. Acta* **56**, 4157-4167.
- Farley, K. J., Dzombak, D. A., and Morel, F. M. M., 1985. A surface precipitation model for the sorption of cations on metal oxides. *J. Colloid. Interf. Sci.* **106**, 226-242.
- Ford, R. G., Bertsch, P. M., and Farley, K. J., 1997. Changes in transition and heavy metal partitioning during hydrous iron oxide aging. *Environ. Sci. Technol.* **31**, 2028-2033.
- Ford, R. G., Kemner, K. M., and Bertsch, P. M., 1999. Influence of sorbate-sorbent interactions on the crystallization kinetics of nickel- and lead-ferrihydrite coprecipitates. *Geochim. Cosmochim. Acta* **63**, 39-48.
- Fukushi, K. and Sverjensky, D. A., 2007. A predictive model (ETLM) for arsenate adsorption and surface speciation on oxides consistent with spectroscopic and theoretical molecular evidence. *Geochim. Cosmochim. Acta* **71**, 3717-3745.
- Gadde, R. R. and Laitinen, H. A., 1974. Study of heavy metal adsorption by hydrous iron and manganese oxides. *Anal. Chem.* **46**, 2022-2026.
- Ganor, J., Lu, P., Zheng, Z., and Zhu, C., 2007. Bridging the gap between laboratory measurements and field estimations of silicate weathering using simple calculations. *Environ. Geol.* **53**, 599-610.
- Garrels, R. M., 1967. Genesis of some ground waters from igneous rocks. In: Abelson, P. H. (Ed.), *Researches in Geochemistry*. John Wiley & Sons, New York.
- Garrels, R. M. and Christ, C. L., 1965. *Minerals, solutions, and equilibria*. Harper and Rowley, New York.
- Garrels, R. M. and Mackenzie, F. T., 1967. Origin of the chemical composition of some springs and systems. In: Stumm, W. (Ed.), *Equilibrium Concepts in Natural Water Systems*. American Chemical Society.
- Gautier, J.-M., Oelkers, E. H., and Schott, J., 1994. Experimental study of K-feldspar dissolution rates as a function of chemical affinity at 150° C and pH 9. *Geochim. Cosmochim. Acta* **58**, 4549-4560.
- Hayes, K. F. and Leckie, J. O., 1986. Mechanism of lead ion adsorption at the goethite-water interface. In: Davis, J. A., Hayes, K. F. (Eds.), *Geochemical Processes at Mineral Surfaces*. ACS Symposium Series 323. American Chemical Society: Washington, DC, pp 114-141.
- Helgeson, H. C., 1971. Kinetics of mass transfer among silicates and aqueous solutions. *Geochim. Cosmochim. Acta* **35**, 421-469.

- Helgeson, H.C., 1972. Kinetics of mass transfer among silicates and aqueous solutions: correction and clarification. *Geochim. Cosmochim. Acta* **36**, 1067–1070.
- Hellmann, R., 1997. The albite-water system: Part III, Characterization of leached and hydrogen-enriched layers formed at 300 °C using MeV ion beam techniques. *Geochim. Cosmochim. Acta* **61**, 1575-1594.
- Hellmann, R., Eggleston, C.R., Hochella, M.F., and Crerar, D.A., 1990. The formation of leached layers on albite surfaces during dissolution under hydrothermal conditions. *Geochim. Cosmochim. Acta* **54**, 1267–1281.
- Hellmann, R. and Tisserand, D., 2006. Dissolution kinetics as a function of the Gibbs free energy of reaction: An experimental study based on albite feldspar. *Geochim. Cosmochim. Acta* **70**, 364-383.
- Hollibaugh, J. T., Carini, S., Gürleyük, H., Jellison, R., Joye, S. B., Lecleir, G., Meile, C., Vasquez, L., and Wallschläger, D., 2005. Arsenic speciation in Mono Lake, California: Response to seasonal stratification and anoxia. *Geochim. Cosmochim. Acta* **69**, 1925-1937.
- Huntington, T. G., Hooper, R. P., Johnson, C. E., Aulenbach, B. T., Cappellato, R., and Blum, A. E., 2000. Calcium depletion in a Southeastern United States forest ecosystem. *Soil Sci. Soc. Am. J.* **64**, 1845-1858.
- International Energy Agency, 2006. *Greenhouse Gas R&D Programme Annual Review*. <http://www.ieaghg.org/index.php?/publications.html>
- IPCC (the Intergovernmental Panel on Climate Change), 2005. *Special Report on Carbon Dioxide Capture and Storage*, http://www.ipcc.ch/publications_and_data/publications_and_data_reports_carbon_dioxide.htm.
- Jambor, J. L. and Dutrizac, J. E., 1998. Occurrence and constitution of natural and synthetic ferrihydrite, a widespread iron oxyhydroxide. *Chem. Rev.* **98**, 2549-2586.
- Karthikeyan, K. G., Elliott, H. A., and Cannon, F. S., 1997. Adsorption and coprecipitation of copper with the hydrous oxides of iron and aluminum. *Environ. Sci. Technol.* **31**, 2721-2725.
- Keimowitz, A. R., Zheng, Y., Chillrud, S. N., Mailloux, B., Jung, H. B., Stute, M., and Simpson, H. J., 2005. Arsenic redistribution between sediments and water near a highly contaminated source. *Environ. Sci. Technol.* **39**, 8606-8613.

- Kinniburgh, D. G., Jackson, M. L., and Syers, J. K., 1976. Adsorption of alkaline earth, transition, and heavy metal cations by hydrous oxide gels of iron and aluminum. *Soil Sci. Soc. Am. J.* **40**, 796-800.
- Krauskopf, K. B. and Bird, D. K., 1995. *Introduction to Geochemistry*. McGraw-Hill, New York.
- Langmuir, D., Mahoney, J., and Rowson, J., 2006. Solubility products of amorphous ferric arsenate and crystalline scorodite ($\text{FeAsO}_4 \cdot 2\text{H}_2\text{O}$) and their application to arsenic behavior in buried mine tailings. *Geochim. Cosmochim. Acta* **70**, 2942-2956.
- Lasaga, A. C., 1984. Chemical kinetics of water-rock interactions. *J. Geophys. Res.* **89**, 4009-4025.
- Lasaga, A. C., 1998. *Kinetic Theory in the Earth Sciences*. Princeton University Press, New York.
- Lasaga, A. C., Soler, J. M., Ganor, J., Burch, T. E., and Nagy, K. L., 1994. Chemical weathering rate laws and global geochemical cycles. *Geochim. Cosmochim. Acta*
- Levin, H. L., 2005. *The Earth Through Time*, 8th Edition, Wiley, 616p.
- Luce, R. W., Bartlett, R. W., and Parks, G. A., 1972. Dissolution kinetics of magnesium silicates. *Geochim. Cosmochim. Acta* **36**, 35-50.
- Lützenkirchen, J., 1997. Ionic strength effects on cation sorption to oxides: Macroscopic observations and their significance in microscopic interpretation. *J. Colloid. Interf. Sci.* **195**, 149-155.
- Marini, L. and Accornero, M., 2007. Prediction of the thermodynamic properties of metal-arsenate and metal-arsenite aqueous complexes to high temperatures and pressures and some geological consequences. *Environ. Geol.* **52**, 1343-1363.
- Martinez, C. E. and McBride, M. B., 1998. Solubility of Cd^{2+} , Cu^{2+} , Pb^{2+} , and Zn^{2+} in aged coprecipitates with amorphous iron hydroxides. *Environ. Sci. Technol.* **32**, 743-748.
- Martinez, C. E. and McBride, M. B., 2001. Cd, Cu, Pb, and Zn coprecipitates in Fe oxide formed at different pH: Aging effects on metal solubility and extractability by citrate. *Environ. Toxicol. Chem.* **20**, 122-126.
- Nagy, K. L. and Lasaga, A. C., 1993. Simultaneous precipitation kinetics of kaolinite and gibbsite at 80 °C and pH 3. *Geochim. Cosmochim. Acta* **57**, 4329-4335.

- Nesbitt, H. W. and Skinner, W. M., 2001. Early development of Al, Ca, and Na compositional gradients in labradorite leached in pH 2 HCl solutions. *Geochim. Cosmochim. Acta* **65**, 715-727.
- Nordstrom, D. K. and Archer, D. G., 2002. Arsenic thermodynamic data and environmental geochemistry. In: Welch, A. H. and Stollenwerk, K. G. (Eds.), *Arsenic in Ground Water*. Springer.
- Nugent, M. A., Brantley, S. L., Pantano, C. G., and Maurice, P. A., 1998. The influence of natural mineral coatings on feldspar weathering. *Nature* **395**, 588-591.
- Oelkers, E. H., 2001. General kinetic description of multioxide silicate mineral and glass dissolution. *Geochim. Cosmochim. Acta* **65**, 3703-3719.
- Oelkers, E. H., Schott, J., and Devidal, J. L., 1994. The effect of aluminum, pH, and chemical affinity on the rates of aluminosilicate dissolution reactions. *Geochim. Cosmochim. Acta* **58**, 2011-2024.
- Oremland, R. S. and Stolz, J. F., 2003. The ecology of arsenic. *Science* **300**, 939-944.
- Pačes, T., 1973. Steady-state kinetics and equilibrium between ground water and granitic rocks. *Geochim. Cosmochim. Acta* **37**, 2641-2663.
- Pačes, T., 1983. Rate constants of dissolution derived from the measurements of mass balance in hydrological catchments. *Geochim. Cosmochim. Acta* **37**, 1855-1863.
- Pokrovski, G. S., Kara, S., and Roux, J., 2002. Stability and solubility of arsenopyrite, FeAsS, in crustal fluids. *Geochim. Cosmochim. Acta* **66**, 2361-2378.
- Pourbaix, M., 1966. *Atlas of Electrochemical Equilibria in Aqueous Solutions*. Pergamon Press, Oxford.
- Price, J. R., Velbel, M. A., and Patino, L. C., 2005. Rates and time scales of clay-mineral formation by weathering in saprolitic regoliths of the southern Appalachians from geochemical mass balance. *Geol. Soc. Am. Bull.* **117**, 783-794.
- Reuss, J.O. and Johnson, D.W., 1986. *Acid Deposition and the Acidification of Soils and Waters*. Springer Verlag, New York, 303p.
- Rose, A. W. and Bianchi-Mosquera, G. C., 1993. Adsorption of Cu, Pb, Zn, Co, Ni, and Ag on goethite and hematite; a control on metal mobilization from red beds into stratiform copper deposits. *Econ. Geol.* **88**, 1226-1236.
- Schultz, M. F., Benjamin, M. M., and Ferguson, J. F., 1987. Adsorption and desorption of metals on ferrihydrite: reversibility of the reaction and sorption properties of the regenerated solid. *Environ. Sci. Technol.* **21**, 863-869.

- Small, J. S., 1993. Experimental determination of the rates of precipitation of authigenic illite and kaolinite in the presence of aqueous oxalate and comparison to the K/Ar ages of authigenic illite in reservoir sandstones. *Clay. Clay. Miner.* **41**, 191-208.
- Smedley, P. L. and Kinniburgh, D. G., 2002. A review of the source, behaviour and distribution of arsenic in natural waters. *Appl. Geochem.* **17**, 517-568
- Sparks, D. L., 2005. Toxic metals in the environment: The role of surfaces. *Elements* **1**, 193-197.
- Steefel, C. I. and van Cappellen, P., 1990. A new kinetic approach to modeling water-rock interaction: The role of nucleation, precursors, and Ostwald ripening. *Geochim. Cosmochim. Acta* **54**, 2657-2677.
- Sverjensky, D. A. and Fukushi, K., 2006. A predictive model (ETLM) for As(III) adsorption and surface speciation on oxides consistent with spectroscopic data. *Geochim. Cosmochim. Acta* **70**, 3778-3802.
- Swallow, K. C., Hume, D. N., and Morel, F. M. M., 1980. Sorption of copper and lead by hydrous ferric oxide. *Environ. Sci. Technol.* **14**, 1326-1331.
- Swartz, C. H., Blute, N. K., Badruzzman, B., Ali, A., Brabander, D., Jay, J., Besancon, J., Islam, S., Hemond, H. F., and Harvey, C. F., 2004. Mobility of arsenic in a Bangladesh aquifer: Inferences from geochemical profiles, leaching data, and mineralogical characterization. *Geochim. Cosmochim. Acta* **68**, 4539-4557.
- Tamaki, S. and Frankenberger, W. T. J., 1992. Environmental biochemistry of arsenic. Reviews Environ. *Contam. Toxicol.* **124**, 79-110.
- Trivedi, P., Dyer, JA, and Sparks, DL, 2003. Lead sorption onto ferrihydrite. 1. A macroscopic and spectroscopic assessment. *Environ. Sci. Technol.* **37**, 908-914.
- Velbel, M.A., 1990. Influence of temperature and mineral surface characteristics on feldspar weathering rates in natural and artificial systems: a first approximation, *Water Resour. Res.* **26**, 3049–3053.
- Vink, B. W., 1996. Stability relations of antimony and arsenic compounds in the light of revised and extended Eh-pH diagrams. *Chem. Geol.* **130**, 21-30.
- White, A. F. and Brantley, S. L., 2003. The effect of time on the weathering of silicate minerals: why do weathering rates differ in the laboratory and field? *Chem. Geol.* **202**, 479-506.
- WHO, 2001. *Environmental Health Criteria 224: Arsenic and Arsenic Compounds*. World Health Organization, Geneva.

- Zhu, C., 2002. Estimation of surface precipitation constants for sorption of divalent metals onto hydrous ferric oxide and calcite. *Chem. Geol.* **188**, 23-32.
- Zhu, C., 2005. In situ feldspar dissolution rates in an aquifer. *Geochim. Cosmochim. Acta* **69**, 1435–1453.
- Zhu, C., Blum, A. E., and Veblen, D. R., 2004. Feldspar dissolution rates and clay precipitation in the Navajo aquifer at Black Mesa, Arizona, USA. In: Wanty, R. B. and Seal, R. R. I. (Eds.), *Water-Rock Interaction*. Vol. pp. 895-899, A.A. Balkema, Saratoga Springs, New York.
- Zhu, C., Veblen, D. R., Blum, A. E., and Chipera, S. J., 2006. Naturally weathered feldspar surfaces in the Navajo Sandstone aquifer, Black Mesa, Arizona: Electron microscopic characterization. *Geochim. Cosmochim. Acta* **70**, 4600-4616.

CHAPTER 2

ALKALI FELDSPAR DISSOLUTION AND SECONDARY MINERAL PRECIPITATION IN BATCH SYSTEMS: 1. NEW EXPERIMENTS AT 200 °C AND 300 BARS (30 MPa)¹

¹ The contents of this chapter has been published in Fu Q., Lu P., Konishi H., Dilmore R., Xu H., Seyfried, Jr., W. E. and Zhu C. (2009) Coupled alkali-feldspar dissolution and secondary mineral precipitation in batch systems: 1. New experiments at 200 °C and 300 bars (30 MPa). *Chem. Geol.* **258**, 125–135.

1. INTRODUCTION

Silicate mineral dissolution and secondary mineral precipitation are integrated processes in chemical weathering and hydrothermal alteration of rocks. Numerous experiments have been conducted for measuring silicate mineral dissolution rates (Busenburg and Clemency, 1976; Holdren and Berner, 1979; Chou and Wollast, 1985; Knauss and Wolery, 1986; Nagy et al., 1991; Nagy and Lasaga, 1992; Burch et al., 1993; Gautier et al., 1994; Hellmann, 1994; Oelkers et al., 1994; Hellmann, 1995; Nagy, 1995; Stillings and Brantley, 1995; Brantley and Stillings, 1996). The primary focus of many of these studies, however, was to derive mineral dissolution rates from steady state chemical conditions. In such experiments, silicate minerals, mostly feldspars, are dissolved far from equilibrium and secondary mineral precipitation is avoided by adjusting the chemistry and rate of recirculation of the fluid phase. Results of these experiments have been enormously successful, providing a wealth of data on the rate and mechanism of mineral dissolution processes under a wide range of chemical and physical conditions.

Batch reactor experiments of feldspar hydrolysis, on the other hand, provide a different set of data, which address the broader context of congruency and incongruency, phase relations, mineral metastability, and interconnections between dissolution and precipitation reactions. Tremendous progress in our understanding of feldspar hydrolysis in closed systems has come from the seminal work by Helgeson and co-workers (Helgeson, 1968; Helgeson et al., 1969, 1970; Helgeson, 1971, 1972, 1974, 1979; Helgeson et al., 1984). While the first feldspar hydrolysis experiments conducted in batch reactors provided valuable information on the mechanism of feldspar dissolution, as summarized in Helgeson (1971) and Petrovic (1976), technological development of

experimental design and apparatus has allowed the sampling of fluid co-existing with minerals at a wide range of temperatures and pressures (Seyfried et al., 1987).

Furthermore, electron microscopy and surface analytical techniques have advanced significantly, which allow more accurate identification of secondary minerals, even when such phases exist on the nanometer size scale (Penn et al., 2001; Zhu et al., 2006).

Here we report results of alkali-feldspar dissolution experiments in well-mixed batch reactors that were performed at 200 °C and 300 bars (30 MPa) in order to examine mineral dissolution and precipitation processes in moderately acidic fluids. Although dissolution reactions of single feldspars have been reported in the literature (Busenburg and Clemency, 1976; Holdren and Berner, 1979; Helgeson et al., 1984; Chou and Wollast, 1985; Knauss and Wolery, 1986; Wollast and Chou, 1992; Gautier et al., 1994; Hellmann, 1994; Oelkers et al., 1994; Hellmann, 1995; Stillings and Brantley, 1995; Brantley and Stillings, 1996; Hellmann and Tisserand, 2006), only a few experimental studies have been performed on feldspars with complex compositions (Morey and Fournier, 1961; Lagache, 1976; Rafal'skiy et al., 1990; Tsuchiya et al., 1995). The combination of time series monitoring of fluid chemistry and mineral analysis (scanning electron microscopy (SEM), high resolution transmission electron microscopy (HRTEM), X-ray diffraction (XRD), X-ray photoelectron spectroscopy (XPS), and electron microprobe analysis (EMPA)) at different reaction stages represents an insightful experimental strategy to assess geochemical controls on the temporal evolution of minerals and coexisting fluids. While this approach is relevant to mass transfer processes in a variety of natural and engineered hydrologic and hydrothermal rock–fluid systems, the experimental data are

important in that they form a basis for evaluating a number of theories and hypotheses on the kinetics of water–rock interactions.

2. EXPERIMENTS

Two batch experiments, with run times of 1872 h (78 days) and 120 h (5 days), involving perthitic alkali-feldspar dissolution in K-bearing (~ 0.20 KCl mol/kg) fluid at 200 °C, 300 bars (30 MPa) were conducted at the University of Minnesota and National Energy Technology Laboratory (NETL), respectively. 40 g KCl solution and 1.5 g alkali-feldspar were used for both experiments. Prior to the experiments, the starting fluid was acidified to pH=3.0 by addition of dilute HCl, so as to create initial conditions far from equilibrium.

“Orthoclase” crystals having an average size of ~ 0.5 cm were obtained from WARD'S Natural Sciences Establishment. The crystals were ground with an agate mortar and pestle, and subsequently dry sieved to retain the size fraction between 50 and 100 μm . For the freshly ground material, there were a large number of submicron-to-micron size particles that adhered to the surface of large grains. To remove these particles, the feldspar sample was first ultrasonically “cleaned” in analytical grade acetone, and then repeatedly rinsed with deionized water, prior to drying at 105 °C.

A Beckman Coulter SA-3100 was used for BET surface area analysis of alkali-feldspar samples before experiments. The instrument was calibrated before and after measurements, using NIST reference material 1900, a silicon nitrite powder with surface area of $2.85 \text{ m}^2/\text{g}$. Multipoint N_2 gas adsorption isotherms were measured to obtain the specific surface area of $0.13 \text{ m}^2/\text{g}$ ($\pm 5\%$) for the alkali-feldspar reactant.

The alkali-feldspar and acidified KCl solution were loaded into a flexible Au/Ti reaction cell and placed in a steel-alloy autoclave following procedures described in Seyfried et al. (1987). The reaction cell allows sampling of aqueous fluid from the ongoing reaction at constant temperature and pressure. Thus, internally filtered fluid samples could be recovered from the reaction cell any time during an experiment.

Fluid samples were analyzed for major dissolved components. Anion analyses were conducted on a Dionex ICS-2000 ion chromatography (IC) system composed of an AS 19 column (4 mm ID) and an ASRS self-regenerating suppressor (4 mm ID). KOH solution was used as the eluent at flow rate of 1 ml/min. Gradient eluent concentrations were programmed as follows: 4 mM for 30 min, 10 mM for 30 min and 25 mM for 15 min. The column temperature and cell temperature were constant at 30 °C. The injection volume of each sample was 50.0 μ l. Uncertainties in reported concentrations were estimated to be within $\pm 1\%$.

Major cation analyses were conducted on a Thermo Elemental PQ ExCell quadrupole inductively coupled plasma mass spectrometer (ICP-MS) with a simultaneous analog and pulse counting detector. System calibration was accomplished by using NIST traceable single or multi-element standard solutions. For each sample, standards and blanks were repeated 5 times to determine the mean and standard deviation for each selected elemental mass. All standards, blanks, and samples were atomized and introduced into a standard Meinhardt nebulizer by a free aspiration rate of approximately 1 ml/min. All elements were measured on the most appropriate mass by peak hopping with dwell times of approximately 35 μ s per mass and 25–50 mass sweeps per replicate. The clean matrix acid was used to flush the system for a minimum time of 65 s to prevent

carryover between samples. Uncertainties for all elements were estimated to be within $\pm 1\%$.

The pH of all fluid samples was measured at ambient laboratory conditions using a THERMO combination glass pH/reference electrode and Accumet AR-20 meter. Prior to measurement, the pH electrode was calibrated with NIST pH standard buffers, 4.0 and 7.0. Replicate measurements of fluid samples from the experiments indicate an uncertainty of the reported pH (25 °C) value of ± 0.02 units.

Mineral products were retrieved from both experiments when the runs were terminated after 78 days and 5 days. A variety of microscopic and analytical techniques were used to characterize solid reactants and experimental products, including XRD, EMPA, SEM, HRTEM, and XPS. Powder XRD analysis was carried out using a PANalytical X'Pert PRO Theta–Theta multipurpose diffractometer, equipped with a Cu anode operated at 45 kV and 40 mA, a divergent beam monochromator, and an X'Celerator detector. The scanning angle (2θ) ranged from 10.010 to 99.968°, with scan steps of 0.033°. Secondary minerals were analyzed on zero background quartz plate.

The chemical composition of alkali-feldspar lamellae (Table 1) was determined by wavelength dispersive EMPA using a CAMECA SX50. Operation accelerating voltage was 15 kV, while beam current and beam size were 15 nA and 1 μm , respectively. The structural formula for K-rich and Na-rich phases based on 8 oxygens is $\text{K}_{0.85}\text{Na}_{0.15}\text{Al}_{1.04}\text{Si}_{2.96}\text{O}_8$ and $\text{K}_{0.01}\text{Na}_{0.95}\text{Ca}_{0.04}\text{Al}_{1.04}\text{Si}_{2.96}\text{O}_8$, respectively.

SEM analysis was conducted with a Quanta 400 Field Emission Gun (FEG). The Energy Dispersive X-ray Spectrometer (EDS) system has an EDAX thin window and

CDU LEAP detector. The low energy X-ray detection with FEG provided high spatial resolution for microanalysis down to $\sim 0.1 \mu\text{m}^2$.

Table 1. Electron microprobe analysis (EMPA) results¹ of Na-rich laminae, K-rich laminae and whole alkali-feldspar grains

	Oxide	SiO ₂	Al ₂ O ₃	Na ₂ O	K ₂ O	FeO	CaO	Total
	wt%	68.20	20.45	10.49	0.18	0.09	0.83	100.22
Na-rich laminae	S. D. ²	0.03	0.05	0.18	0.06	0.03	0.04	
	N ³	2.96	1.04	0.95	0.01	0.00	0.04	5.00
	S. D.	0.00	0.00	0.02	0.00	0.00	0.00	
	wt%	63.69	18.95	1.66	13.82	0.05	0.00	98.16
K-rich laminae	S. D.	0.53	0.25	0.42	0.87	0.04	0.00	
	N	2.96	1.04	0.15	0.85	0.00	0.00	5.00
	S. D.	0.01	0.01	0.04	0.05	0.00	0.00	
	wt%	64.71	19.91	3.17	12.21			
Alkali-feldspar	N	2.95	1.07	0.28	0.71			

¹Each result reflects the average value of 5-10 measurements.

²S. D. = Standard deviation.

³N = the number of cations per 8 oxygen atoms.

A JEOL 1010 transmission electron microscope operated at 100 kV and a JEOL 2100F FEG Scanning Transmission Electron Microscope (STEM) with attached X-ray EDS and Gatan Imaging Filtering (GIF) system were used for analysis of reaction products. Thus, a fraction of the reaction products was immersed in ethanol and ultrasonically treated for several minutes. A small aliquot of the resulting suspension was mounted on a strip of holey-carbon film supported by a standard Cu TEM grid, prior to air-drying for approximately 10 min.

In addition to detailed examination of the fresh and reacted alkali-feldspar using microscopy, XPS was also used to determine the surface chemistry of the feldspar before and after hydrothermal reaction. XPS spectra of mineral reactant and products from the 78-day experiment were collected on a Physical Electronics 5400 instrument, with non-monochromatic Mg K α as the X-ray source, operated at 300 W. Similar analyses from

the 5-day experiment were collected on a PHI 5600ci instrument. This instrument made use of monochromatic Al K α as the X-ray source, operated at 400 W. In both cases, mineral samples were embedded on double-sided adhesive tape, which was then fixed to the sample holder of the respective instruments. The samples were degassed at 10⁻⁷ Torr, before achieving operating vacuum at 5 \times 10⁻⁸ Torr. The analysis area was 1 mm by 1.414 mm, while the photo electron take-off angle was 45°. Survey scans (0–1200 eV binding energy) were performed first to determine the near-surface composition of the samples, followed by multiple repetitive scans over the energy regions of interest: Si_{2p}, O_{1s}, K_{2p3/2} and Al_{2p}. Charge shifting of the analyzed photoelectrons was corrected by referencing a coexisting C_{1s} peak to 285.0 eV. Surface compositions of elements of interest were determined by analysis of peak areas taking explicit account of element specific atomic sensitivity factors.

Equilibrium constants for aqueous speciation calculations of fluid samples from experiments were calculated using a modified version of SUPCRT92 (Johnson et al., 1992). This code takes explicit account of recent revisions in keeping with the modified HKF equations of state for aqueous species (Shock and Helgeson, 1988; Shock et al., 1997; Sverjensky et al., 1997). Thermodynamic data for Al-bearing aqueous species, however, were from Tagirov and Schott (2001), while experimental data from Ho et al. (2001), Ho et al. (2000), and Ho et al. (1994) were used for HCl(aq)[°], KCl(aq)[°], and NaCl(aq)[°], respectively. In practice, calculations needed to assess mineral saturation states, pH_(in situ) (see below), and derive ion-activity diagrams were performed using the EQ3/6 computer code (Wolery and Daveler, 1992). Standard state thermodynamic properties for all Al-bearing minerals were from Holland and Powell (1998).

3. RESULTS

3.1. Cations, anions and dissolved SiO₂

Time series changes in fluid chemistry from both experiments are listed in Table 2 and illustrated in Fig. 1. As anticipated from the relative abundances of fluid and mineral components used for the experiments, dissolved Cl⁻ concentrations remained relatively constant. The concentration of dissolved K⁺, however, tended to decrease, although the extent of this represents a small fraction of that initially available in the fluid (200 mmol/kg).

Changes in dissolved concentrations of Na⁺, Ca²⁺, Al³⁺ and SiO₂ during the 78-day experiment were significant as alkali-feldspar dissolution proceeded. For example, dissolved SiO₂ increased slowly to approximately 1.70 mmol/kg after 456 h of reaction, then, surprisingly, decreased to 1.35 mmol/kg during the next 360 h of reaction, before again increasing to 4.18 mmol/kg at 1368 h. During the remaining 504 h of the experiment, dissolved SiO₂ decreased by 0.43 mmol/kg to a final value of 3.75 mmol/kg (Table 2). Dissolved concentrations of Na⁺ and Ca²⁺ generally tracked with SiO₂, suggesting the possible involvement of non-stoichiometric dissolution of minor accessory components in albite in the moderately acidic fluids. Al³⁺ concentration decreased sharply during the first 216 h, then increased to 0.08 mmol/kg by 456 h before decreasing gradually throughout the remainder of the experiment. Dissolved concentrations of Na⁺, Ca²⁺, Al³⁺ and SiO₂ from the 5-day experiment at 120 h were largely consistent with changes in fluid chemistry of the 78-day experiment at a similar time of reaction (Fig. 1).

3.2. pH

It is well known from results of numerous studies of reaction kinetics of silicate minerals in aqueous fluids that pH plays a particularly important role in the rate of mineral dissolution/ precipitation processes. This is the case during the present study as well. To examine pH effects, the pH value measured for the fluid sample at ambient conditions (25 °C, 0.1 MPa) (bench pH) was recalculated at experimental conditions (200 °C, 30 MPa) by taking account of the effect of temperature and pressure on the distribution of aqueous species. Accordingly, pH (in situ) was calculated for each sample taken during the course of experiments (Table 2). Owing to the relatively low experimental temperature, however, pH (in situ) was close to that measured, with an offset that ranged from approximately 0.1 to 0.4 units. During the 78-day experiment, pH values increased from 3.1 to 4.7 (Table 2).

Table 2. Time-dependent changes in the composition of major dissolved constituents in aqueous fluid coexisting with alkali-feldspar at 200°C and 300 bars (30 MPa)

Sample #	Time (Hours)	Cl ⁻	K ⁺	SiO ₂ (mmol/kg)	Na ⁺	Ca ²⁺	Al ³⁺	pH (25°C)	<i>In situ</i> pH (200°C)
<i>78-day experiment</i>									
	0	198.3	204.0	-	-	3.72	-	3.0	3.1
1	24	197.5	202.8	0.31	0.42	0.12	0.01	3.2	3.3
2	216	198.7	201.1	1.46	1.13	0.21	0.003	3.5	3.6
3	456	196.8	197.8	1.70	2.04	0.43	0.08	4.1	3.7
4	816	197.9	204.3	1.35	1.86	0.16	0.03	4.2	4.0
5	1368	199.5	197.0	4.18	3.72	0.30	0.01	4.9	4.5
6	1872	199.4	196.5	3.75	1.91	0.35	0.001	4.9	4.7
<i>5-day experiment</i>									
1	120	n.a. ¹	n.a.	1.31	0.88	0.35	0.005	n.a.	n.a.

¹n.a. = not available

3.3. Characterization of solid reactants and products

SEM photomicrographs of alkali-feldspar following the 78-day (Fig. 2A, B) and 5-day experiments (Fig. 2C, D) reveal channels and etch pits demonstrating dissolution heterogeneity, with albite lamellae preferentially dissolved. The presence of these mineral dissolution features was less obvious from results of the 5-day experiment.

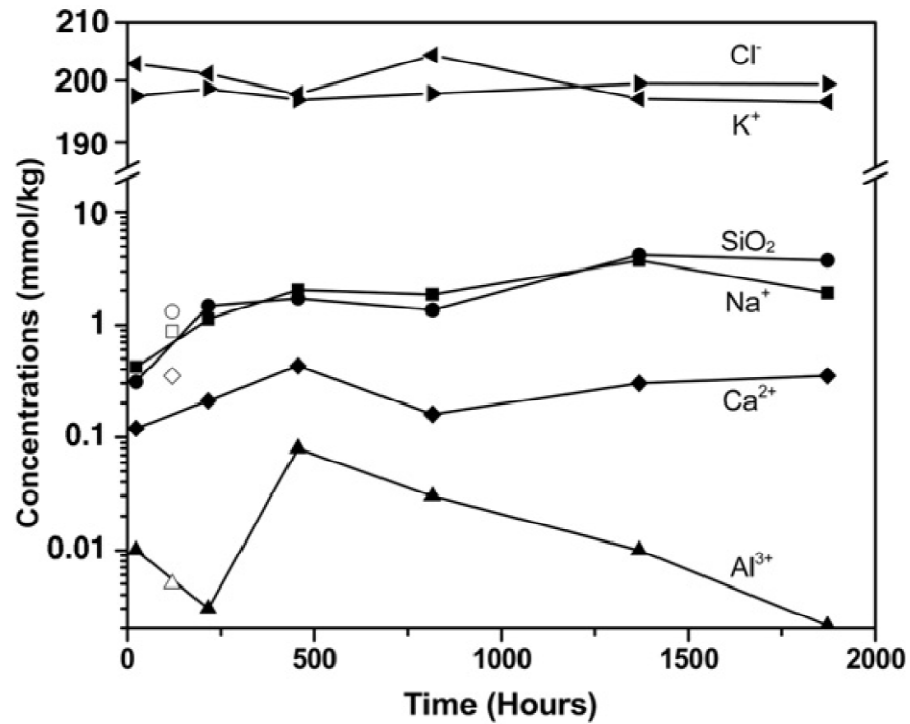


Fig. 1. Changes in the dissolved concentrations of selected aqueous constituents with time for the perthitic alkali-feldspar dissolution experiments at 200 °C and 300 bars (30 MPa). Dissolved concentrations of K^+ , Cl^- , Na^+ , Ca^{2+} , Al^{3+} and SiO_2 for the 78-day experiment (solid symbols) and Na^+ , Ca^{2+} , Al^{3+} and SiO_2 for the 5-day experiment (open symbols). Time series changes for K^+ , Cl^- concentrations for the 5-day experiment are not available beyond the start of the experiment (Table 2).

Secondary minerals, with cross sectional diameter (d) of less than 0.5 μm and height (h) of approximately 0.1 μm , covered approximately 20% of total alkali-feldspar surface from the 78-day experiment. Alteration products also exhibited hexagonal shape.

In the 5-day experiment, however, secondary minerals covered much less (~5%) of feldspar surface (Fig. 2). In both cases, secondary minerals were evenly distributed on the feldspar surface, suggesting no structural inheritance from the alkali-feldspar precursor. Feldspar dissolution and secondary mineral formation are likely coupled in the overall mass transfer process.

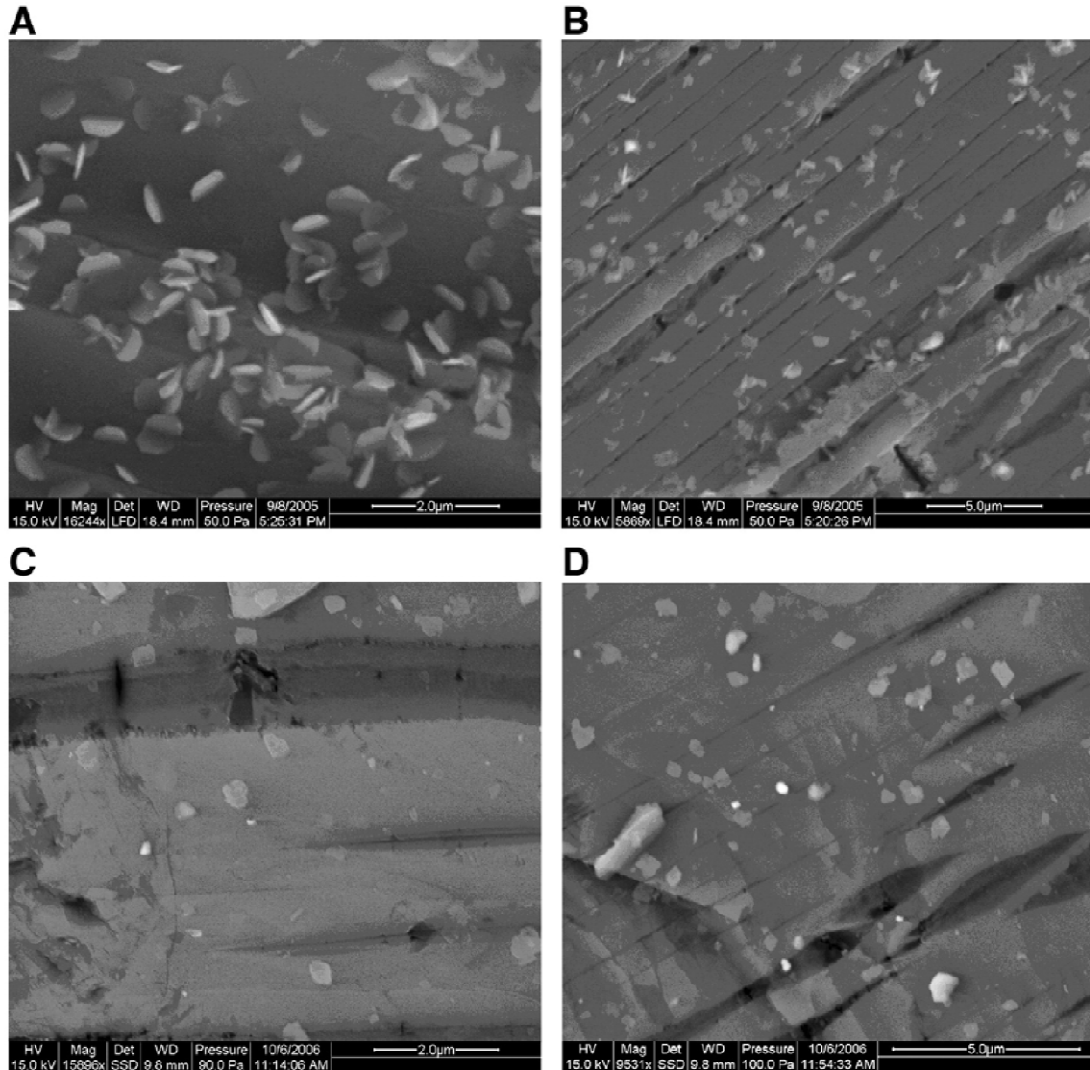


Fig. 2. SEM backscatter images of alkali-feldspar dissolution effects following reaction after 78 days (A, B) and 5 days (C, D). Reacted feldspar from the 78-day experiment reveal small (~0.5 μm) hexagon-shaped secondary minerals covering approximately 20% of the feldspar surface. In the 5-day experiment, secondary minerals cover only about 5% of the feldspar surface. The relative abundance of surface mineralization on the feldspars

from each experiment is consistent with observed distribution of mineral dissolution features, such as laminar channels and etch pits on Na-rich lamina.

XRD patterns of mineral products in both experiments showed the presence of kaolinite as well as boehmite (Fig. 3A, B). The high peak intensities of boehmite in the XRD patterns likely result from preferential orientation of boehmite, and are not directly proportional to abundance.

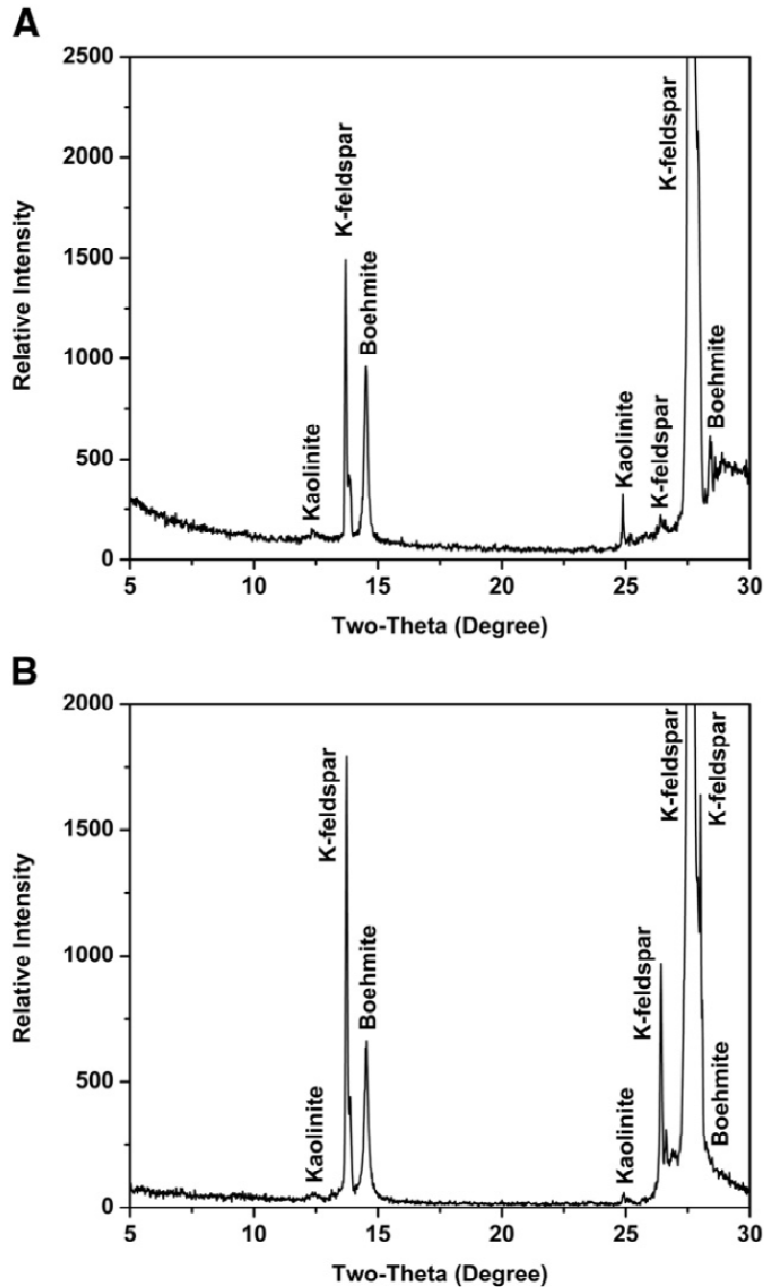


Fig. 3. X-ray diffraction patterns of mineral products following the 5-day experiment (A) and 78-day experiment (B). Kaolinite, boehmite, and K-feldspar were identified. The high peak intensity of boehmite is not a reflection of its abundance, but rather the result of preferential orientation.

Due to relatively low magnification of the JEOL 1010 operated at low voltage (100 kV), secondary mineral products (kaolinite and boehmite) from the 78-day experiment were manifest as a transparent phase with hexagonal shape and sizes of 200–300 nm (Fig. 4A). Selected area electron diffraction (SAED) patterns indicated that most alteration minerals are sheet silicates (Fig. 4B). The existence of boehmite crystals with rounded shapes, however, was confirmed by HRTEM observation with JEOL FEG 2100F (Fig. 4C). TEM images also showed “seesaw” edges of reacted alkali-feldspar from the experiment (Fig. 4D), suggesting preferential dissolution of Na lamellae, which is consistent with SEM observations. In the 5-day experiment, boehmite with distinctly sharp edges was observed on alkali-feldspar as the lone secondary mineral (Fig. 4E), which was confirmed by [010] SAED patterns, showing two dimensions for the Al octahedral structure (Fig. 4F). In contrast with boehmite from the 5-day experiment, boehmite following the 78-day experiment showed dissolution features characterized by more rounded grain boundaries (Fig. 4C).

Recently, Zhu et al. (2004a, 2006) observed an amorphous layer on naturally weathered feldspar, typically a few tens of nanometers thick. In the 78-day experiment, HRTEM observation also indicated that the alkali-feldspar grains were rimmed with an apparently amorphous layer (Fig. 4C). The amorphous nature of the edges was confirmed by the absence of electron diffraction pattern. It is still controversial whether an

amorphous layer is caused by leaching (Nugent et al., 1998; Nesbitt and Skinner, 2001) or is the result of silica reprecipitation effects (Hellmann et al., 2003, 2004).

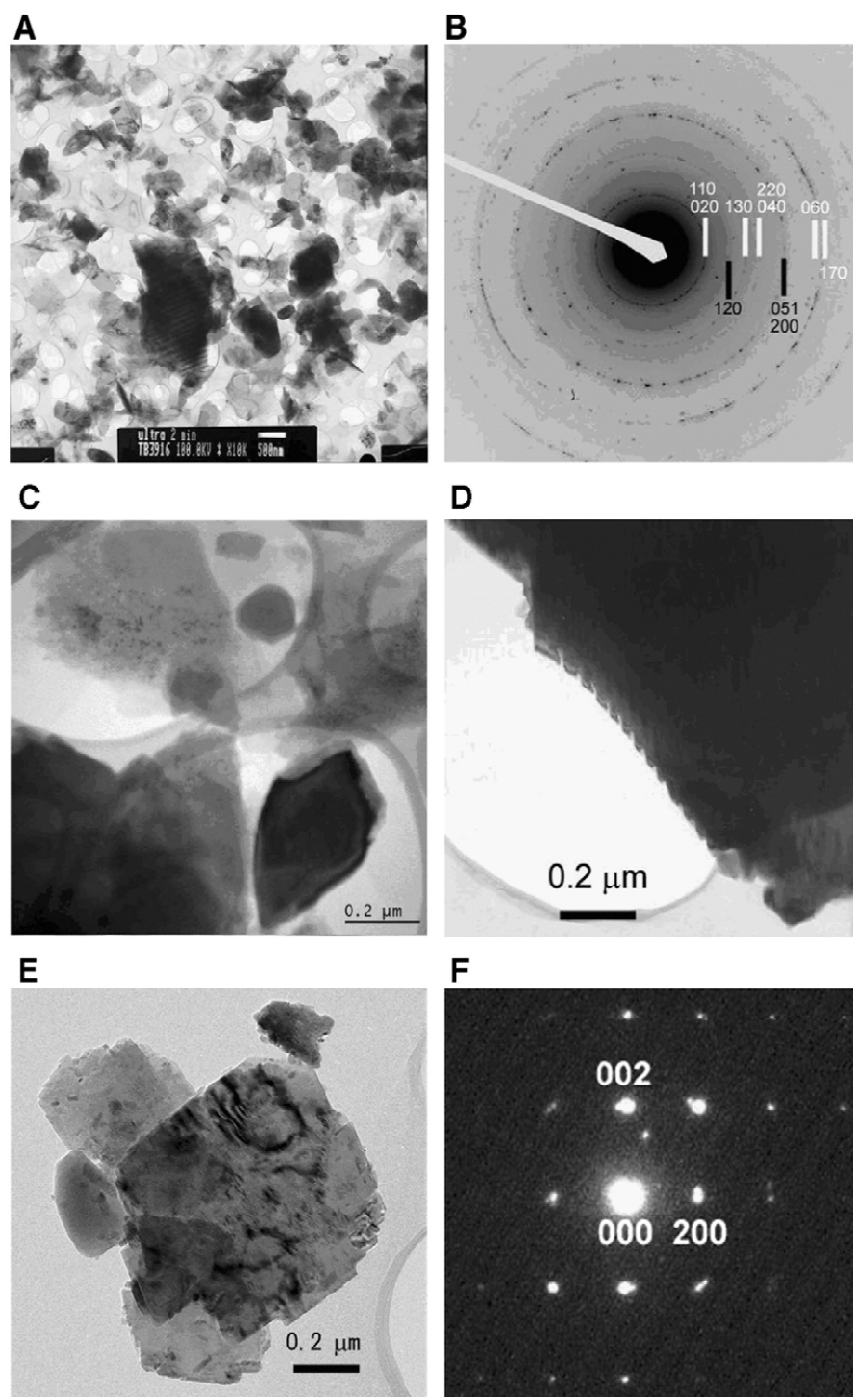


Fig. 4. TEM images and SAED patterns of mineral products from alkali-feldspar dissolution experiments at 200 °C and 300 bars (30 MPa). (A) Feldspar (large grains) and hexagonal secondary minerals (200–300 nm sized grains); (B) SAED pattern of mineral products labeled with Miller Indices for kaolinite (upper layer) and boehmite (lower layer); (C) Bright-field TEM image showing secondary minerals, with an alkali-feldspar grain at lower-right corner; (D) TEM image showing alkali-feldspar grain (dark color), seesaw edges indicate preferential dissolution of Na laminae; (E) TEM image showing alkali-feldspar grains with alteration mineral phases from the 5-day experiment; (F) [010] SAED pattern showing the octahedral structure of boehmite in the 5-day experiment. Unless otherwise noted, all samples were from the 78-day experiment. Image (A) was obtained by JEOL 1010 at 100 kV and (B)–(F) by JEOL 2100F at higher operating voltage.

XPS data for the alkali-feldspar before the 78-day experiment indicate K/Al and Al/Si mole ratios of 0.66 and 0.37, respectively. These data are in good agreement with the surface chemistry of the fresh feldspar used for the 5-day experiment in spite of the fact that two different instruments were utilized to acquire the data (Table 3). Following the 78-day experiment, however, the Al/Si mole ratio increased significantly to 0.57, while K/Al decreased to 0.37. These data confirm the existence of secondary mineral phases, such as kaolinite and boehmite, where Al has a greater compositional percentage than for K-feldspar or albite. Results from the 5-day experiment also indicate an increase of Al/Si mole ratio to 0.41, while the K/Al remained constant at 0.61, which can best be accounted for by formation of aluminous secondary minerals, but in less abundance than for the 78-day experiment.

Table 3. XPS surface composition results¹ of alkali-feldspar from both experiments in comparison with theoretical values for K-feldspar and kaolinite

	K	Al	O	Si	K/Al	Al/Si
	mole%				mole ratio	mole ratio
Starting alkali-feldspar ²	5.7	8.7	62.2	23.4	0.66	0.37
78-day experiment Product	4.3	11.6	63.6	20.4	0.37	0.57
Starting alkali-feldspar ³	4.8	7.9	63.2	24.1	0.61	0.33
5-day experiment Product	5.5	9.0	63.4	22.1	0.61	0.41

K-feldspar	7.7	7.7	61.5	23.1	1	0.33
Kaolinite	-	20.9	55.8	21.8	-	1

¹Each result reflects the average value of 4 measurements from different alkali-feldspar grains within the same sample.

²78-day experiment

³5-day experiment

4. CONCLUSIONS

Alkali-feldspar hydrolysis experiments using a well-mixed batch reactor allowed observations of time series in situ fluid chemistry at 200 °C and 300 bars (30 MPa) to be integrated with the mineralogy and composition of reaction products retrieved after 5 and 78 days. Hydrolysis of the albite component of alkali-feldspar resulted in the formation of boehmite, and then kaolinite. SEM, HRTEM and XPS analyses of the surface of alkali-feldspar provide clear evidence for the preferential reaction of albite and coexistence of secondary mineralization involving both boehmite and kaolinite.

Traditionally, feldspar hydrolysis is treated with the assumption of partial equilibria between the secondary minerals and the aqueous solution. If this partial equilibrium is not observed, the reaction paths are different in terms of both aqueous solution chemistry and secondary mineral paragenesis (Lasaga, 1998). Our detailed mineralogical analysis showed that boehmite and kaolinite persisted metastably during the entire 78 days experiment, which provides the first experimental evidence to support early modeling illustrations (Steefel and van Cappellen, 1990; Lasaga, 1998). The time series solution chemistry data and calculated saturation indices are also more consistent with Lasaga's (1998) cases with slow clay precipitation kinetics than the partial equilibrium case. Slow secondary mineral reaction kinetics means strong coupling between dissolution and precipitation reactions, which is important in interpretation of field derived rates (Zhu et al., 2004a,b).

REFERENCES

- Brantley, S.L., Stillings, L.L., 1996. Feldspar dissolution at 25 °C and low pH. *Am. J. Sci.* **296**, 101–127.
- Burch, T.E., Nagy, K.L., Lasaga, A.C., 1993. Free energy dependence of albite dissolution kinetics at 80 °C and pH 8.8. *Chem. Geol.* **105**, 137–162.
- Busenburg, E., Clemency, C.V., 1976. The dissolution kinetics of feldspars at 25 °C and 1 atm CO₂, partial pressure. *Geochim. Cosmochim. Acta* **40**, 41–49.
- Chou, L., Wollast, R., 1985. Steady-state kinetics and dissolution mechanisms of albite. *Am. J. Sci.* **285**, 963–993.
- Gautier, J.M., Oelkers, E.H., Schott, J., 1994. Experimental study of K-feldspar dissolution rates as a function of chemical affinity at 150 °C and pH 9. *Geochim. Cosmochim. Acta* **58**, 4549–4560.
- Helgeson, H.C., 1968. Evaluation of irreversible reactions in geochemical processes involving minerals and aqueous solutions — I. Thermodynamic relations. *Geochim. Cosmochim. Acta* **32**, 853–877.
- Helgeson, H.C., 1971. Kinetics of mass transfer among silicates and aqueous solutions. *Geochim. Cosmochim. Acta* **35**, 421–469.
- Helgeson, H.C., 1972. Kinetics of mass transfer among silicates and aqueous solutions: correction and clarification. *Geochim. Cosmochim. Acta* **36**, 1067–1070.
- Helgeson, H.C., 1974. Chemical interaction of feldspar and aqueous solutions. In: MacKenzie, W.S., Zussman, J. (Eds.), *The Feldspars*. Crane, Russak and Co. Inc., New York.
- Helgeson, H.C., 1979. Mass transfer among minerals and hydrothermal solutions. In: Barnes, H.L. (Ed.), *Geochemistry of Hydrothermal Ore Deposits*. John Wiley & Sons, New York.
- Helgeson, H.C., Garrels, R.M., Mackenzie, F.T., 1969. Evaluation of irreversible reactions in geochemical processing involving minerals and aqueous solutions — II. Applications. *Geochim. Cosmochim. Acta* **33**, 455–481.

- Helgeson, H.C., Brown, T.H., Nigrini, A., Jones, T.A., 1970. Calculation of mass transfer in geochemical processes involving aqueous solutions. *Geochim. Cosmochim. Acta* **34**, 569–592.
- Helgeson, H.C., Murphy, W.M., Aagaard, P., 1984. Thermodynamic and kinetic constraints on reaction rates among minerals and aqueous solutions: II. Rate constants, effective surface area, and the hydrolysis of feldspar. *Geochim. Cosmochim. Acta* **48**, 2405–2432.
- Hellmann, R., 1994. The albite–water system: Part I. The kinetics of dissolution as a function of pH at 100, 200, and 300 °C. *Geochim. Cosmochim. Acta* **58**, 595–611.
- Hellmann, R., 1995. The albite–water system: Part II. The time evolution of the stoichiometry of dissolution as a function of pH at 100, 200, and 300 °C. *Geochim. Cosmochim. Acta* **59**, 1669–1697.
- Hellmann, R., Tisserand, D., 2006. Dissolution kinetics as a function of the Gibbs free energy of reaction: an experimental study based on albite feldspar. *Geochim. Cosmochim. Acta* **70**, 364–383.
- Hellmann, R., Penisson, J.-M., Hervig, R.L., Thomassin, J.-H., Abrioux, M.-F., 2003. An EFTEM/HRTEM high-resolution study of the near surface of labradorite feldspar altered at acid pH: evidence for interfacial dissolution–reprecipitation. *Phys. Chem. Miner.* **30**, 192–197.
- Hellmann, R., Penisson, J.-M., Hervig, R.L., Thomassin, J.-H., Abrioux, M.-F., 2004. Chemical alteration of feldspar: a comparative study using SIMS and HRTEM/EFTEM. In: Wanty, R.B., Seal, R.R. (Eds.), *Proceedings of the 11th International Symposium on Water–Rock Interaction*, Saratoga Springs, New York.
- Ho, P.C., Palmer, D.A., Mesmer, R.E., 1994. Electrical conductivity measurements of aqueous sodium chloride solutions to 600 °C and 300 MPa. *J. Solution Chem.* **23**, 997–1018.
- Ho, P.C., Bianchi, H., Palmer, D.A., Wood, R.H., 2000. Conductivity of dilute aqueous electrolyte solutions at high temperatures and pressures using a flowcell. *J. Solution Chem.* **29**, 217–235.
- Ho, P.C., Palmer, D.A., Gruszkiewicz, M.S., 2001. Conductivity measurements of dilute aqueous HCl solutions to high temperatures and pressures using a flow-through cell. *J. Phys. Chem. B* **105**, 1260–1266.
- Holdren, G.R., Berner, R.A., 1979. Mechanism of feldspar weathering — I. Experimental studies. *Geochim. Cosmochim. Acta* **43**, 1161–1171.

- Holland, T.J.B., Powell, R., 1998. An internally consistent thermodynamic data set for phases of petrological interest. *J. Metamorph. Geol.* **16**, 309–343.
- Huang, W.L., Bishop, A.M., Brown, R.W., 1986. The effect of fluid/rock ratio on feldspar dissolution and illite formation under reservoir conditions. *Clay Miner.* **21**, 585–602.
- Knauss, K.G., Wolery, T.J., 1986. Dependence of albite dissolution kinetics on pH and time at 25 °C and 70 °C. *Geochim. Cosmochim. Acta* **50**, 2481–2497.
- Labotka, T.C., Cole, D.R., Fayek, M., Riciputi, L.R., Stadermann, F.J., 2004. Coupled cation and oxygen-isotope exchange between alkali feldspar and aqueous chloride solution. *Am. Mineral.* **89**, 1822–1825.
- Lagache, M., 1976. New data on the kinetics of the dissolution of alkali feldspars at 200 °C in CO₂ charged water. *Geochim. Cosmochim. Acta* **40**, 157–161.
- Lasaga, A.C., 1998. *Kinetic Theory in the Earth Sciences*. Princeton University Press, Princeton.
- Morey, G.W., Fournier, R.O., 1961. The decomposition of microcline, albite, and nepheline in hot water. *Am. Mineral.* **46**, 688–699.
- Nagy, K.L., 1995. Dissolution and precipitation kinetics of sheet silicates. In: White, A.F., Brantley, S.L. (Eds.), *Chemical Weathering Rates of Silicate Minerals*, vol. 31. Mineralogical Society of America, Washington, DC, pp. 173–225.
- Nagy, K.L., Lasaga, A.C., 1992. Dissolution and precipitation kinetics of gibbsite at 80 °C and pH 3: the dependence on solution saturation state. *Geochim. Cosmochim. Acta* **56**, 3093–3111.
- Nagy, K.L., Blum, A.E., Lasaga, A.C., 1991. Dissolution and precipitation kinetics of kaolinite at 80 °C and pH 3: the dependence on solution saturation state. *Am. J. Sci.* **291**, 649–686.
- Nesbitt, H.W., Skinner, W.M., 2001. Early development of Al, Ca, and Na compositional gradients in labradorite leached in pH 2 HCl solutions. *Geochim. Cosmochim. Acta* **65**, 715–727.
- Nugent, M.A., Brantley, S.L., Pantano, C.G., Maurice, P.A., 1998. The influence of natural mineral coatings on feldspar weathering. *Nature* **395**, 588–591.
- Oelkers, E.H., Schott, J., Devidal, J.-L., 1994. The effect of aluminum, pH, and chemical affinity on the rates of aluminosilicate dissolution reactions. *Geochim. Cosmochim. Acta* **58**, 2011–2024.

- Penn, R.L., Zhu, C., Xu, H., Veblen, D.R., 2001. Iron oxide coatings on sand grains from the Atlantic coastal plain: high-resolution transmission electron microscopy characterization. *Geology* **29**, 843–846.
- Petrovic, R., 1976. Rate control in feldspar dissolution — II: the protective effects of precipitates. *Geochim. Cosmochim. Acta* **40**, 1509–1522.
- Rafal'skiy, R.P., Prisyagina, N.I., Kondrushin, I.B., 1990. Reaction of microcline–perthite with aqueous solutions at 150 and 250 °C. *Geochem. Int.* **27**, 56–66.
- Seyfried Jr., W.E., Janecky, D.R., Berndt, M.E., 1987. Rocking autoclaves for hydrothermal experiments II: the flexible reaction cell system. In: Barnes, H.L., Ulmer, G.C. (Eds.), *Hydrothermal Experimental Techniques*. Wiley Interscience, pp. 216–240.
- Steefel, C. I. and van Cappellen, P., 1990. A new kinetic approach to modeling water-rock interaction: The role of nucleation, precursors, and Ostwald ripening. *Geochim. Cosmochim. Acta* **54**, 2657–2677.
- Stillings, L.L., Brantley, S.L., 1995. Feldspar dissolution at 25 °C and pH 3: reaction stoichiometry and the effect of cations. *Geochim. Cosmochim. Acta* **59**, 1483–1496.
- Tsuchiya, N., Nakatsuka, K., Yamagishi, Y., 1995. Kinetics and modeling of alkali-feldspar dissolution in a hydrothermal acid solution. In: Khraka, Y.K., Chudaev, O.V. (Eds.), *Proceedings of the 8th International Symposium on Water–Rock Interaction*. A. A. Balkema, Rotterdam, pp. 161–164.
- Wolery, T.J., Daveler, S.A., 1992. *EQ6, a Computer Program for Reaction Path Modeling of Aqueous Geochemical Systems: Theoretical Manual, User's Guide, and Related Documentation (version 7.0)* UCRL-MA-110662 PT IV, Lawrence Livermore National Laboratory, Livermore, CA. 337 pp.
- Wollast, R., Chou, L., 1992. Surface reactions during the early stages of weathering of albite. *Geochim. Cosmochim. Acta* **56**, 3113–3121.
- Zhu, C., Blum, A.E., Veblen, D.R., 2004a. Feldspar dissolution rates and clay precipitation in the Navajo aquifer at Black Mesa, Arizona, USA. In: Wanty, R.B., Seal, R.I. (Eds.), *Proceedings of the 11th International Symposium on Water–Rock Interaction*. A. A. Balkema, New York, pp. 895–899.
- Zhu, C., Blum, A.E., Veblen, D.R., 2004b. A new hypothesis for the slow feldspar dissolution in groundwater aquifers. *Geochim. Cosmochim. Acta* **68**, A148.
- Zhu, C., Veblen, D.R., Blum, A.E., Chipera, S.J., 2006. Naturally weathered feldspar surfaces in the Navajo Sandstone aquifer, Black Mesa, Arizona: electron microscopic characterization. *Geochim. Cosmochim. Acta* **70**, 4600–4616.

CHAPTER 3

ALKALI FELDSPAR DISSOLUTION AND SECONDARY MINERAL PRECIPITATION IN BATCH SYSTEMS: 2. NEW EXPERIMENTS WITH SUPERCRITICAL CO₂ AND IMPLICATIONS FOR CARBON SEQUESTRATION²

² This chapter is currently in preparation for publication: Lu, P., Zhu, C., Fu, Q., Seyfried, W. E., and Jones, K. Coupled Alkali Feldspar Dissolution and Secondary Mineral Precipitation in Batch Systems: 2. New Experiments with Supercritical CO₂ and Implications for Carbon Sequestration. *International Journal of Greenhouse Gas Control*, in preparation.

1. INTRODUCTION

Injection of CO₂ into deep geological formations is presently envisaged as one means of sequestering CO₂ released from the burning of fossil fuels in power generation facilities (IPCC, 2007a, b). Candidates for the suitable formations include deep saline aquifers in sedimentary basins, depleted oil and gas fields, and unmineable coal seams (IPCC, 2005). Deep saline aquifers currently receive a great deal of attention because of its common occurrence, large volume of pore space available, and potential for long-term hydrodynamic trapping of CO₂ (DOE-NETL, 2008). Injected CO₂ will dissolve into the native formation water, making the brine corrosive and therefore react aggressively with the native minerals.

Feldspars are abundant in both sandstone (reservoir rock) and shale (caprock). For example, the Mt. Simon Sandstone, a potential target for carbon sequestration in the Midwest of the U.S., contains about 22% feldspars (Eliasson et al., 1998). Eau Claire Shale, the caprock for Mt Simon Sandstone, contains an average of ~ 20 % feldspars (Becker et al., 1978). Although feldspar dissolution rates are usually slow (in the order of 10^{-8} to 10^{-12} mol m⁻² s⁻¹) in the temperature range relevant to geological carbon sequestration (Blum and Stillings, 1995), the extent of water-feldspar reaction will be significant because (1) the time scale for the safety of CO₂ storage site is in the orders of 1,000 to 100,000 years, and (2) feldspars are abundant. In general, the dissolution of alkali-feldspars is likely to increase porosity and thus enhance CO₂ mobility and accelerate further geochemical reactions, but the formation and mobility of clay minerals may inversely affect permeability (Emery and Robinson, 1993; Rogen and Fabricius, 2002; Strazisar et al., 2006; Worden and Morad, 2003).

Numerous experiments have been conducted for measuring silicate mineral dissolution rates in CO₂-charged systems (Amrhein and Suarez, 1988, 1992; Brady and Carroll, 1994; Busenberg and Clemency, 1976; Carroll and Knauss, 2005; Hangx and Spiers, 2009; Hellmann et al., 2007; Lagache, 1965, 1976; Sorai et al., 2007; Sorai et al., 2005; Tchoubar, 1965; Tchoubar and Oberlin, 1963; Utsunomiya et al., 1999; Wyart et al., 1963). The primary focus of many of these studies, however, was to derive the dissolution rates from steady state chemical conditions. In such experiments, silicate minerals, mostly feldspars, are dissolved far from equilibrium and secondary mineral precipitation is avoided by adjusting the chemistry or recirculation rate of the fluid phase. However, experimental data on how the feldspar dissolution and secondary mineral precipitation reactions are coupled are scarce.

In a series of papers, Zhu and co-workers have shown that feldspar dissolution and secondary mineral precipitation reactions are strongly coupled, and slow precipitation of secondary minerals provides a negative feedback to feldspar dissolution rate (Fu et al., 2009; Ganor et al., 2007; Hereford et al., 2007; Zhu, 2005, 2006; Zhu, 2009; Zhu et al., 2004; Zhu and Lu, 2009). In this study, we report results of three alkali-feldspar dissolution – secondary mineral precipitation batch reactor experiments at 150 - 200 °C and 300 bars (MPa) with the addition of CO₂. The experimental design permitted time series monitoring of fluid chemistry to constrain better mineral dissolution and precipitation processes of relevance to carbon sequestration. Previously, several experimental studies of interactions of CO₂-saturated brine with reservoir materials were conducted at relatively low temperatures and short durations. These experiments observed minimal aluminosilicate dissolution and undetectable concentrations of

secondary phases (e.g., Gunter et al., 2000; Gunter et al., 1997; Perkins and Gunter, 1995). We conducted experiments at higher temperatures, at which significant mineral alterations were observed (Hangx and Spiers, 2009; Kaszuba et al., 2003, 2005). Although experimental studies may be constrained by dissimilarities in system temperature, pressure, and ionic strength conditions, they can provide insightful information and understanding of the complex interplay of CO₂-brine-rock interactions.

The experimental work is supplemented with a critical review of literature regarding feldspar hydrolysis in CO₂-charged solution. The urgent needs from numerical geochemical models for evaluating and optimizing the injection program call for the establishment of a database at a wide spectrum of injection conditions.

2. EXPERIMENTAL

Three different alkali feldspars were used in the batch experiments. An alkali feldspar (“orthoclase”) and Amelia albite crystals were purchased from the WARD’S Natural Sciences Establishments, Inc. A potassium-rich alkali feldspar was obtained from the mineral collection at Indiana University. We shall term the three feldspars as “WardsAF”, “Amelia Albite”, and “IUB-KF”, respectively in the following discussion. The feldspar crystals were handpicked, ground with an agate mortar and pestle, and subsequently dry sieved to retain the fraction between 50 and 100 µm in size. For the freshly ground material, there were a large number of submicron-to-micron particles that adhered to the surface of large grains. Dissolution of these ultra-fine particles will result in initially non-linear rates of reaction or parabolic kinetics (Holdren and Berner, 1979). To remove these particles, the sample was first ultrasonically cleansed using analytical

grade acetone. This was performed eight times on each aliquot for about 20 min per treatment. The cleaned alkali-feldspar grains were finally rinsed with deionized water and then freeze-dried. Before experiments, alkali-feldspar sample was kept in an oven at 105 °C overnight to exclude possible organic contamination.

A Beckman Coulter SA-3100 surface area analyzer was used for BET surface area analysis of alkali-feldspar samples before experiments. The samples were degassed at 250 °C overnight prior to measurements. The instrument was calibrated before and during measurements periodically, using National Institute of Standards and Technology reference material 1900, a silicon nitrite powder with surface area of 2.85 m²/g. Multipoint N₂ gas adsorption isotherms were measured to obtain the specific surface area of 0.132 m²/g for WardsAF, 0.129 m²/g for IUB-KF, and 0.13 m²/g for Amelia albite, respectively.

The chemical compositions of alkali feldspar were determined by electron microprobe analysis using a CAMECA SX50 instrument. Operation accelerating voltage was 15 kV while beam current and beam size were 15 nA and ~1 μm, respectively. For “Wards-AF”, the average compositions of the two laminae were determined as K_{0.85}Na_{0.15}Al_{1.04}Si_{2.96}O₈ and K_{0.01}Na_{0.95}Ca_{0.04}Al_{1.04}Si_{2.96}O₈, respectively. X-ray diffraction (XRD) results show that the perthitic alkali feldspar contains 35% low albite, 60% orthoclase and 5% quartz. For “IUB-KF”, the chemical compositions were determined as K_{0.94}Na_{0.06}Al_{1.03}Si_{2.97}O₈ and NaAl_{1.04}Si_{2.96}O₈, respectively, for the two laminae. XRD characterized the K-rich laminae as microcline (70%) and the Na-rich laminae as low albite (30%). Amelia albite has been frequently used in experiments because it is a compositionally pure end-member albite (e.g., see Harlow and Brown, 1980; Harouiya

and Oelkers, 2004; Smith and Brown, 1988). The structure formula is



The alkali-feldspar and aqueous solutions were loaded into a flexible Au/Ti reaction cell, which was placed in a steel-alloy autoclave, following procedures described in Seyfried et al. (1987). The reaction cell allows on-line sampling of the aqueous phase at constant temperature and pressure simply by adding water under pressure to the autoclave surrounding the cell. Thus, internally filtered fluid samples could be recovered from the reaction cell contents any time during an experiment. The experimental matrix is shown in Table 1.

Fluid samples taken from the reactor were analyzed for major and some minor dissolved constituents. Dissolved cations were analyzed with inductively coupled plasma mass spectrometry (ICP-MS). Anions were analyzed by ion chromatography. Experimental run products were retrieved and characterized with a variety of microscopic and analytical techniques. Powder X-ray diffraction analyses were carried out using a Bruker D8 Advance diffractometers, equipped with a Cu anode at 20 kV and 5 mA, and with a SolX energy-dispersive detector. The scan parameters used were 2 to 70° 2 θ , with a step size of 0.02° 2 θ . Two different sample preparation methods were employed: “cavity mount” and “slurry mount”. For the cavity mount, starting samples were ground by hand in an agate mortar and pestle to get sufficient small particles. These particles were subsequently filled into the cavity of a titanium sample holder for XRD analysis. For the slurry mount, reaction products were immersed in 20 mL DI water in a plastic vessel (25 mL volume) and ultrasonicated three times for 15 min per treatment with 15 min interval. After the final ultrasonication, the samples were allowed to settle overnight.

Then, a pipette (0.5 mL volume) was used to carefully suck out the suspension and a syringe filter unit with silver filter membrane was employed to collect the clay minerals. The filter unit was aided with a vacuum system. After filtering, the silver membrane (with the slurry) was carefully removed from the filter unit. The slurry (clay with water) on the silver membrane was air-dried. Finally, the membrane with clays was mounted onto zero-background quartz plate for XRD characterization.

Scanning Electron Microscopy (SEM) was conducted with a Quanta 400 Field Emission Gun (FEG). The Energy Dispersive X-ray Spectrometer (EDS) system has an EDAX thin window and CDU LEAP detector. The low energy X-ray detection with FEG provided high spatial resolution for microanalysis down to $\sim 0.1 \text{ mm}^2$ under optimum conditions. SEM samples were prepared with double sided conductive tape and the reaction products were sprinkled on a glass slide. Transmission Electron Microscopy (TEM) observations were performed using a Philips CM 200UT microscope with a spherical aberration coefficient (Cs) of 0.5 mm and a point-to-point resolution of 0.19 nm. Data reduction was carried out using the standard Cliff-Lorimer method implemented in the DTSA.

The TEM samples were prepared with ultrasonic method. A fraction of the reaction products were immersed into absolute ethanol and ultrasonicated for several minutes to disengage the secondary minerals from feldspar surfaces. A drop of the resulting suspension (with grains of feldspar as well as secondary minerals) was mounted onto a holey-carbon film supported by a standard Cu TEM grid and air-dried for ~ 10 min. In this paper, saturation indices (SI) for relevant minerals were calculated from the measured temperatures, pressures, and chemical compositions of experimental aqueous

solutions. SI is defined as $\log(Q/K)$, where Q denotes the activity quotient and K the equilibrium constant (Zhu and Anderson, 2002, p. 45). Equilibrium activity-activity diagrams for mineral stability and phase relations were constructed to trace the evolution of the aqueous chemistry during the batch experiments. For all thermodynamic calculations, the standard states for the solids are defined as unit activity for pure end-member solids at the temperature and pressure of interest. The standard state for water is the unit activity of pure water. For aqueous species other than H_2O , the standard state is the unit activity of the species in a hypothetical one molal solution referenced to infinite dilution at the temperature and pressure of interest. Standard state thermodynamic properties for mineral end-members were taken from Holland and Powell (1998) except for boehmite, for water from Haar et al. (1984), for Al-bearing aqueous species from Tagirov and Schott (2001), $KCl^0_{(aq)}$ from Ho et al. (2000), and all other aqueous species from Shock and Helgeson (1988), Shock et al. (1989), Shock et al. (1997), and Sverjensky et al. (1997). The temperature and pressure dependences of thermodynamic properties for aqueous species, when applicable, were predicted using the parameters of the revised HKF equations of state for aqueous species (Helgeson et al., 1981; Shock et al., 1992; Tanger and Helgeson, 1988). Calculations of equilibrium constants were facilitated with a modified version of SUPCRT92 (Johnson et al., 1992) with the heat capacity function of Holland and Powell (1998) for minerals. Speciation and solubility calculations were aided with the computer code PHREEQC (Parkhurst and Appello, 1999) and EQ3/6 (Wolery, 1992) together with our own equilibrium constant databases for the programs with thermodynamic properties noted above. Activity coefficients for the charged aqueous species were calculated from the extended Debye-Hückel equation or B-

dot equation fitted to mean salt NaCl activity coefficients (Helgeson et al., 1978; Oelkers and Helgeson, 1990).

3. RESULTS

3.1. Results from the Experiment S with WardAF (St. Paul)

Time series changes in fluid chemistry from the experiments are listed in Table 2 and shown in Fig. 1a. The changes in dissolved concentrations of Na^+ , Al^{3+} , and $\text{SiO}_{2(\text{aq})}$ are consistent with albite dissolution. In evaluating the aqueous speciation and mineral saturation states at experimental conditions, we used the pH and total analytical concentrations of the constituents measured at ambient conditions (e.g., 22 °C and 0.1 MPa) as input into the modeling codes and then “re-heated” the solution to experimental T and P . This method calculates the *in situ* pH at the experimental conditions by taking account of the effects of T and P on the distribution of aqueous species (Reed and Spycher, 1984). Experimental data (Table 2) show degassing of $\text{CO}_{2(\text{g})}$ (difference between initial total CO_2 and dissolved CO_2 at each sampling point) was insignificant. Calculated *in situ* pH values increased from 4.5 to 5.7 from the beginning of the experiment to the end.

Table 1a. Feldspar dissolution experiments with the presence of CO₂ (batch reactor)

Mineral	T (°C)	pH	pCO ₂ (MPa)	Total pressure (MPa)	SA (m ² /g) ⁽²⁾	Time (d)	Initial solution	Rate Log (mol m ⁻² s ⁻¹)	Secondary minerals	Reference
Anorthite (Ca _{0.95} Na _{0.05} Al _{1.92} Si _{2.06} O ₈)	150	4.56 (4.97)	10 ^{-4.5}	0.48	0.28-0.32 cm ² ⁽³⁾	90	0.03 M NaAc	-7.23	Boehmite, modified boehmite, kaolinite by SEM-EDS and XRD	Utsunomiya et al. (1999)
Anorthite (Ca _{0.95} Na _{0.05} Al _{1.92} Si _{2.06} O ₈)	150	4.56 (4.97)	0.05	0.53	0.28-0.32 cm ² ⁽³⁾	10	0.03 M NaAc	-6.77	Boehmite, modified boehmite, by SEM-EDS and XRD	Utsunomiya et al. (1999)
Anorthite (Ca _{0.95} Na _{0.05} Al _{1.92} Si _{2.06} O ₈)	150	4.56 (4.97)	0.12	0.6	0.28-0.32 cm ² ⁽³⁾	81	0.03 M NaAc	-6.66	Boehmite, modified boehmite, kaolinite, by SEM-EDS and XRD	Utsunomiya et al. (1999)
Anorthite (Ca _{0.92} Na _{0.08} Al _{1.92} Fe _{0.01} Si _{2.07} O ₈)	300		0.4	6	Grain size 25± 10µm	7	Pure water		Hydrotalcite, boehmite and aragonite (?) by SEM, FEG-Microprobe confirmed hydrotalcite	Hangx and Spiers (2009)
Anorthite (Ca _{0.92} Na _{0.08} Al _{1.92} Fe _{0.01} Si _{2.07} O ₈)	300		0.4	6	Grain size 25± 10µm	21	Pure water		Hydrotalcite and boehmite by SEM and FTIR, Smectite/illite (?) by SEM	Hangx and Spiers (2009)
Anorthite (Ca _{0.92} Na _{0.08} Al _{1.92} Fe _{0.01} Si _{2.07} O ₈)	300		12	18	Grain size < 15 µm	11	Pure water		Hydrotalcite, boehmite and kaolinite by SEM and TGA	Hangx and Spiers (2009)
Anorthite (Ca _{0.92} Na _{0.08} Al _{1.92} Fe _{0.01} Si _{2.07} O ₈)	200		12	18	Grain size 25± 10µm	14	Pure water		Talc or semtite/illite-like, hydrotalcite-like phases by XRD	Hangx and Spiers (2009)
Anorthite (Ca _{0.92} Na _{0.08} Al _{1.92} Fe _{0.01} Si _{2.07} O ₈)	200		12	15	Grain size 25± 10µm	20	0.1 M NaCl		Not detected.	Hangx and Spiers (2009)
Anorthite (Ca _{0.92} Na _{0.08} Al _{1.92} Fe _{0.01} Si _{2.07} O ₈)	200		12	15	Grain size 25± 10µm	21	0.2 M MgCl ₂		Not detected.	Hangx and Spiers (2009)
Albite (Na _{0.99} K _{0.01} AlSi ₃ O ₈)	200		15	18	Grain size 40± 10µm	20	0.2 M MgCl ₂		Hydrotalcite by FTIR.	Hangx and Spiers (2009)
Albite (Na _{0.99} K _{0.01} AlSi ₃ O ₈)	200		15	18	Grain size 40± 10µm	21	0.2 M MgCl ₂		Not detected.	Hangx and Spiers (2009)
Alkali-feldspar (35% low albite 60% orthoclase and 5% quartz)	200	4.0 (4.5)	0.05 M ⁽¹⁾	30	0.132	27	0.20 m KCl	-8.89 ⁽⁴⁾	Boehmite, kaolinite, muscovite by SEM-EDS, XRD, and TEM	This study
Alkali-feldspar (30% low albite 70% microcline)	200	5.0 (5.7)	0.006 M ⁽¹⁾	30	0.129	140	0.05 m NaCl	-8.98 ⁽⁴⁾	Clay minerals (?) by SEM-EDS and XRD	This study
Albite (NaAlSi ₃ O ₈)	150	3.7 (3.8)	0.0133 M ⁽¹⁾	30	0.13	275	0.2 m NaCl	-9.62 ⁽⁴⁾	Boehmite, kaolinite, paragonite by SEM-EDS, XRD, and TEM	This study
Albite (NaAlSi ₃ O ₈)	100	3.99	0.58	0.68	0.04-0.2	20	Pure water	-9.43 ⁽⁵⁾	Not characterized.	Lagache (1965)
Albite (NaAlSi ₃ O ₈)	150	4.59	0.67	1.14	0.04-0.2	20	Pure water	-8.55 ⁽⁵⁾	Not characterized.	Lagache (1965)
Albite (NaAlSi ₃ O ₈)	200	7.27	10 ^{-4.5}	1.59	0.04-0.2	20	Pure water	-8.83 ⁽⁵⁾	Not characterized.	Lagache (1965)
Albite (NaAlSi ₃ O ₈)	200	5.44	0.263	1.853	0.04-0.2	20	Pure water	-8.83 ⁽⁵⁾	Not characterized.	Lagache (1965)
Albite (NaAlSi ₃ O ₈)	200	4.80	0.715	2.305	0.04-0.2	20	Pure water	-8.41 ⁽⁵⁾	Not characterized.	Lagache (1965)
Albite (NaAlSi ₃ O ₈)	200	4.70	2.62	4.21	0.04-0.2	20	Pure water	-8.56 ⁽⁵⁾	Not characterized.	Lagache (1965)
Adularia (K _{0.84} Na _{0.16} AlSi ₃ O ₈)	100	3.86	0.58	0.68	0.04-0.2	20	Pure water	-9.72 ⁽⁵⁾	Not characterized.	Lagache (1965)

Mineral	T (°C)	pH	pCO ₂ (MPa)	Total pressure (MPa)	SA (m ² /g) ⁽²⁾	Time (d)	Initial solution	Rate Log (mol m ⁻² s ⁻¹)	Secondary minerals	Reference
Adularia (K _{0.84} Na _{0.16} AlSi ₃ O ₈)	150	4.59	0.67	1.14	0.04-0.2	20	Pure water	-8.94 ⁽⁵⁾	Not characterized.	Lagache (1965)
Adularia (K _{0.84} Na _{0.16} AlSi ₃ O ₈)	200	4.70	0.71	2.3	0.04-0.2	20	Pure water	-8.43 ⁽⁵⁾	Not characterized.	Lagache (1965)
Labradorite (Ca _{0.54} Na _{0.43} Al _{1.59} Si _{2.43} O ₈)	200	4.88	0.71	2.3	0.04-0.2	20	Pure water	-8.48 ⁽⁵⁾	Not characterized.	Lagache (1965)
Sanidine (Na _{0.45} K _{0.55} AlSi ₃ O ₈)	200	5.35	0.71	2.3	0.03-0.25	20	Pure water	-8.28 ⁽⁵⁾	Not characterized.	Lagache (1976)
Albite (Or _{0.97} Ab _{98.93} An _{0.10})	25	4.55	0.1	0.2	0.83	20	Pure water	-11.36	Not characterized.	Busenberg and Clemency (1976)
Oligoclase (Or _{6.41} Ab _{69.62} An _{23.96})	25	4.55	0.1	0.2	1.01	22	Pure water	-11.59	Not characterized.	Busenberg and Clemency (1976)
Andesine (Or _{7.84} Ab _{49.50} An _{42.66})	25	4.55	0.1	0.2	1.49	17	Pure water	-11.86	Not characterized.	Busenberg and Clemency (1976)
Labradorite (Or _{2.55} Ab _{44.47} An _{52.98})	25	4.55	0.1	0.2	1.04	48	Pure water	-11.90	Not characterized.	Busenberg and Clemency (1976)
Bytownite (Or _{0.39} Ab _{22.19} An _{77.43})	25	4.55	0.1	0.2	1.14	46	Pure water	-11.97	Not characterized.	Busenberg and Clemency (1976)
Anorthite (Or _{0.22} Ab _{5.75} An _{94.02})	25	4.55	0.1	0.2	1.84	16	Pure water	-11.88	Not characterized.	Busenberg and Clemency (1976)
Orthoclase (Or _{79.46} Ab _{20.31} An _{0.23})	25	4.55	0.1	0.2	1.52	22	Pure water	-11.78	Not characterized.	Busenberg and Clemency (1976)
Microcline (Or _{75.15} Ab _{24.81} An _{0.04})	25	4.55	0.1	0.2	1.07	20	Pure water	-11.82	Not characterized.	Busenberg and Clemency (1976)
Plagioclase (An ₆₉ Ab ₃₀)	17	5.65	10 ^{-4.5}	0.1	Grain size 106-500 µm	70	Pure water		Not characterized.	Manley and Evans (1986)
Albite (An ₆ Ab ₉₄)	17	5.65	10 ^{-4.5}	0.1	Grain size 106-500 µm	70	Pure water		Not characterized.	Manley and Evans (1986)
Microcline (An ₂ Ab ₃₁ Or ₆₇)	17	5.65	10 ^{-4.5}	0.1	Grain size 106-500 µm	70	Pure water		Not characterized.	Manley and Evans (1986)
Anorthite (An ₉₃)	25	5.2	0.001	0.101	0.5	28	Pure water	-11.52	Not characterized.	Amrhein and Suarez (1988)
Anorthite (An ₉₃)	25	4.6	0.01	0.11	0.5	28	Pure water	-11.46	Not characterized.	Amrhein and Suarez (1988)
Anorthite (An ₉₃)	25	3.95	0.1	0.2	0.5	28	Pure water	-11.22	Not characterized.	Amrhein and Suarez (1988)
Anorthite	25	3.1	10	10.1		7	Pure water	-9.40 ⁽⁶⁾	Not characterized.	Sorai et al. (2005)
Anorthite	25	3.1	10	10.1		7	Pure water	-9.30 ⁽⁶⁾	Not characterized.	Sorai et al. (2005)
Anorthite	25	3.1	10	10.1		7	Pure water	-9.15 ⁽⁶⁾	Not characterized.	Sorai et al. (2005)

Mineral	T (°C)	pH	pCO ₂ (MPa)	Total pressure (MPa)	SA (m ² /g) ⁽²⁾	Time (d)	Initial solution	Rate Log (mol m ⁻² s ⁻¹)	Secondary minerals	Reference
Anorthite	25	3.1	10	10.1		7	Pure water	-9.05 ⁽⁶⁾	Not characterized.	Sorai et al. (2005)
Anorthite	50	3.1	10	10.1		7	Pure water	-9.70 ⁽⁶⁾	Not characterized.	Sorai et al. (2005)
Anorthite	50	3.1	10	10.1		7	Pure water	-9.52 ⁽⁶⁾	Not characterized.	Sorai et al. (2005)
Anorthite	50	3.1	10	10.1		7	Pure water	-8.82 ⁽⁶⁾	Not characterized.	Sorai et al. (2005)
Anorthite	50	3.1	10	10.1		7	Pure water	-8.80 ⁽⁶⁾	Not characterized.	Sorai et al. (2005)
Anorthite	65	3.1	10	10.1		7	Pure water	-8.84 ⁽⁶⁾	Not characterized.	Sorai et al. (2005)
Anorthite	65	3.1	10	10.1		7	Pure water	-8.78 ⁽⁶⁾	Not characterized.	Sorai et al. (2005)
Anorthite	80	3.1	10	10.1		7	Pure water	-8.57 ⁽⁶⁾	Not characterized.	Sorai et al. (2005)
Anorthite	80	3.1	10	10.1		7	Pure water	-8.52 ⁽⁶⁾	Not characterized.	Sorai et al. (2005)
Anorthite	25	3.1	10	10.1		7	Pure water	-10.52 ⁽⁷⁾	Not characterized.	Sorai et al. (2007)
Anorthite	50	3.1	10	10.1		7	Pure water	-8.00 ⁽⁷⁾	Not characterized.	Sorai et al. (2007)
Anorthite	80	3.1	10	10.1		7	Pure water	-8.52 ⁽⁷⁾	Not characterized.	Sorai et al. (2007)
Anorthite	80	3.1	10	10.1		7	Pure water	-10.00 ⁽⁸⁾	Not characterized.	Sorai et al. (2007)

⁽¹⁾ As total dissolved CO₂ (mol/kg). ⁽²⁾ SA stand for specific surface area. ⁽³⁾ Total surface area measured geometrically. ⁽⁴⁾ See text for rates calculation ⁽⁵⁾ Rates interpreted by Hellmann (1994) ⁽⁶⁾ Average rates during 7 days of dissolution. ⁽⁷⁾ Average rates during initial stage of dissolution. ⁽⁸⁾ Average rates during steady-state dissolution.

Table 1b. Feldspar dissolution experiments with the presence of CO₂ (mixed-flow reactor)

Mineral	T (°C)	pH	pCO ₂ (MPa)	Total pressure (MPa)	SA (m ² /g) ⁽²⁾	Time (d)	Initial solution	Rate Log (mol m ⁻² s ⁻¹)	Secondary minerals	Reference
Anorthite (An ₆₀)	21	4.02	10 ^{-4.5}	0.1			Pure water	1.00 ⁽³⁾	Not characterized.	Brady and Carroll (1994)
Anorthite (An ₆₀)	21	4.02	0.1	0.2			Pure water	1.10 ⁽³⁾	Not characterized.	Brady and Carroll (1994)
Anorthite (An ₆₀)	35	3.97	10 ^{-4.5}	0.1			Pure water	2.72 ⁽³⁾	Not characterized.	Brady and Carroll (1994)
Anorthite (An ₆₀)	35	3.97	0.1	0.2			Pure water	2.36 ⁽³⁾	Not characterized.	Brady and Carroll (1994)
Anorthite (An ₆₀)	60	3.92	10 ^{-4.5}	0.1			Pure water	9.87 ⁽³⁾	Not characterized.	Brady and Carroll (1994)
Anorthite (An ₆₀)	60	3.92	0.1	0.2			Pure water	10.59 ⁽³⁾	Not characterized.	Brady and Carroll (1994)
Anorthite (Ca _{1.2} Al _{1.94} Si _{2.0} O ₈)	25	5.65	0.01	0.11	0.43	40-50	0.05 m NaClO ₄ and NaHCO ₃	-11.85 ⁽⁴⁾	Not detected by SEM and XRD	Berg and Banwart (2000)
Anorthite (Ca _{1.2} Al _{1.94} Si _{2.0} O ₈)	25	6.12	0.01	0.11	0.43	40-50	0.05 m NaClO ₄ and NaHCO ₃	-11.72 ⁽⁴⁾	Not detected by SEM and XRD	Berg and Banwart (2000)
Anorthite (Ca _{1.2} Al _{1.94} Si _{2.0} O ₈)	25	6.32	0.01	0.11	0.43	40-50	0.05 m NaClO ₄ and NaHCO ₃	-11.54 ⁽⁴⁾	Not detected by SEM and XRD	Berg and Banwart (2000)
Anorthite (Ca _{1.2} Al _{1.94} Si _{2.0} O ₈)	25	7.10	0.01	0.11	0.43	40-50	0.05 m NaClO ₄ and NaHCO ₃	-11.36 ⁽⁴⁾	Not detected by SEM and XRD	Berg and Banwart (2000)
Anorthite (Ca _{1.2} Al _{1.94} Si _{2.0} O ₈)	25	7.33	0.01	0.11	0.43	40-50	0.05 m NaClO ₄ and NaHCO ₃	-11.38 ⁽⁴⁾	Not detected by SEM and XRD	Berg and Banwart (2000)
Anorthite (Ca _{1.2} Al _{1.94} Si _{2.0} O ₈)	25	6.67	0.001	0.101	0.43	40-50	0.05 m NaClO ₄ and NaHCO ₃	-11.63 ⁽⁴⁾	Not detected by SEM and XRD	Berg and Banwart (2000)
Anorthite (Ca _{1.2} Al _{1.94} Si _{2.0} O ₈)	25	7.20	0.001	0.101	0.43	40-50	0.05 m NaClO ₄ and NaHCO ₃	-11.44 ⁽⁴⁾	Not detected by SEM and XRD	Berg and Banwart (2000)
Anorthite (Ca _{1.2} Al _{1.94} Si _{2.0} O ₈)	25	7.33	0.001	0.101	0.43	40-50	0.05 m NaClO ₄ and NaHCO ₃	-11.41 ⁽⁴⁾	Not detected by SEM and XRD	Berg and Banwart (2000)
Anorthite (Ca _{1.2} Al _{1.94} Si _{2.0} O ₈)	25	8.05	0.001	0.101	0.43	40-50	0.05 m NaClO ₄ and NaHCO ₃	-11.26 ⁽⁴⁾	Not detected by SEM and XRD	Berg and Banwart (2000)
Anorthite (Ca _{1.2} Al _{1.94} Si _{2.0} O ₈)	25	8.30	0.001	0.101	0.43	40-50	0.05 m NaClO ₄ and NaHCO ₃	-11.27 ⁽⁴⁾	Not detected by SEM and XRD	Berg and Banwart (2000)
Labradorite (Ca _{0.6} Na _{0.4} Al _{1.69} Si _{2.4} O ₈)	31	3.2	0.61 m ⁽¹⁾		0.03	0.4-2.5	Pure water	-9.45	Probably Aluminum hydroxide by AFM	Carroll and Knauss (2005)
Labradorite (Ca _{0.6} Na _{0.4} Al _{1.69} Si _{2.4} O ₈)	60	3.2	0.61 m ⁽¹⁾		0.03	0.4-2.5	Pure water	-9.02	Probably Aluminum hydroxide by AFM	Carroll and Knauss (2005)
Labradorite (Ca _{0.6} Na _{0.4} Al _{1.69} Si _{2.4} O ₈)	100	3.19	0.61 m ⁽¹⁾		0.03	0.4-2.5	Pure water	-8.34	Probably Aluminum hydroxide by AFM	Carroll and Knauss (2005)

⁽¹⁾As total dissolved CO₂ (mol/kg). ⁽²⁾SA stand for specific surface area. ⁽³⁾Ratios of r_T/r_0 as reported in Brady and Carroll (1994). r_0 – dissolution rate at 21 °C. ⁽⁴⁾Rate based on [Al], converted from mol m⁻² h⁻¹.

Table 2. Time-dependent changes in the composition of major dissolved species in aqueous fluid coexisting with alkali-feldspar at 150 °C or 200 °C and 300 bars (30 MPa)

	Time (h)	Na ⁺	Mg ²⁺	K ⁺	SiO ₂	Al ³⁺ (mM/kg)	Ca ²⁺	Li ⁺	NH ₄ ⁺	Cl ⁻	CO ₂ (aq)	pH	
												25 °C	200 °C, 30 MPa
Exp. S	0	-		200.0	-	-				200.0	50.0	4.0	4.5
	24	0.26		196.31	0.40	0.01				199.22	47.90	4.3	4.9
	120*	1.89		200.0 [#]	1.96	0.006				200.0 [#]	50.0 [#]	N.A.	5.0
	144	0.45		194.30	1.88	0.01				196.51	44.47	4.5	5.1
	312	0.93		195.35	2.30	0.02				197.48	45.83	5.0	5.6
	480	1.41		196.19	2.42	0.06				199.40	45.35	5.1	5.7
	648*	0.97		195.40	2.49	0.09				198.77	45.17	5.1	5.7
Exp. E	0	50.22	0.01	0	0	0	0.03	0	0.01	48.18	6.0	5.0	5.7
	24	50.03	0.01	0.37	1.40	0.02	0.03	0.01	0.05	48.41	6.1	5.3	5.9
	408	49.87	0.01	0.87	2.80	0.03	0.03	0.01	0.05	49.53	6.2	5.4	6.0
	672	49.50	0.05	0.87	2.92	0.18	0.13	0.01	0.04	49.97	6.0	5.5	5.7
	1176	49.63	0.01	0.80	2.86	0.02	0.17	0.01	0.05	49.85	6.2	5.6	6.2
	1848	50.13	0.02	0.79	2.72	0.03	0.05	0.01	0.18	49.80	6.1	5.4	6.0
	3384	50.65	0.02	1.01	3.04	0.02	0.05	0.01	0.14	50.11	6.1	5.7	6.3
Exp. D												25°C,	150°C, 30 Mpa
	0	198.66	0	0	0	0	0			195.43	13.3	3.7	3.8
	24	199.78	0.13	0.11	0.47	0.047	0.20			194.89	13.1	4.1	4.0
	456	200.28	0	0	0.64	0.039	0.18			192.02	11.5	4.5	4.5
	960	197.14	0	0	0.85	0.019	0.17			190.74	10.3	4.8	4.8
	2472	198.98	0	0.12	0.99	0.052	0			189.57	9.7	4.9	4.8
	4392	196.50	0.15	0.24	1.00	0.045	0.21			191.43	9.3	5.0	4.9
	5568	194.03	0.12	0.16	0.91	0.066	0			191.50	9.2	5.0	4.9
	6600	205.01	0.27	0.15	0.85	0.071	0.29			194.72	9.2	5.1	5.0

Note: * Products were recovered for analysis. The overall analytical error for dissolved species is $\pm 5\%$. In-situ pH is calculated from distribution of aqueous species calculations at the temperature and pressure of the experiment using constraints imposed by major element concentrations and pH values measured at 25 °C.

SEM photomicrographs of the feldspar grains following experiments (Fig. 2) revealed laminar channels and etch pits, demonstrating dissolution heterogeneities, with albite laminae preferentially dissolved. Secondary minerals covered approximately 5% of total alkali-feldspar surface in the 5-day experiment. Secondary minerals were mostly evenly distributed on feldspar surface, but aggregates at kinks were also observed.

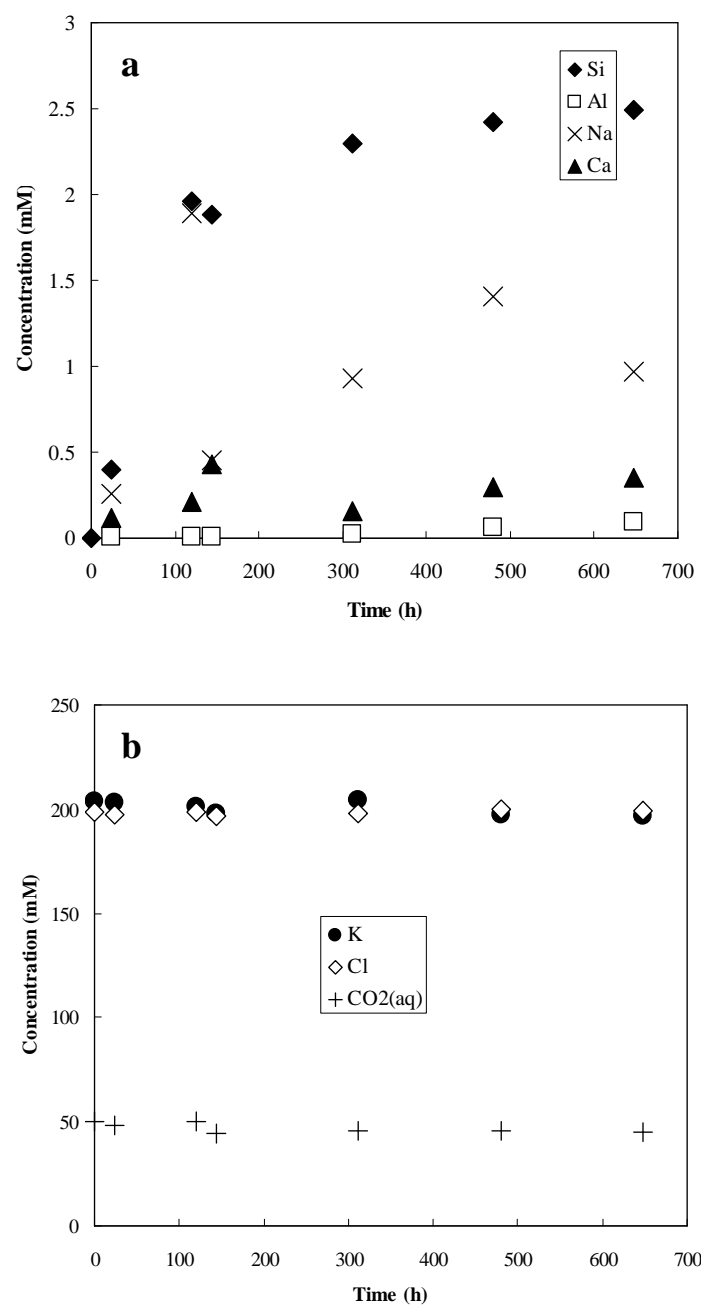


Fig. 1a. Changes in the dissolved concentrations of selected aqueous constituents with time for the perthitic alkali-feldspar dissolution experiments with the presence of CO₂ at 200 °C and 30 MPa (Experiment S).

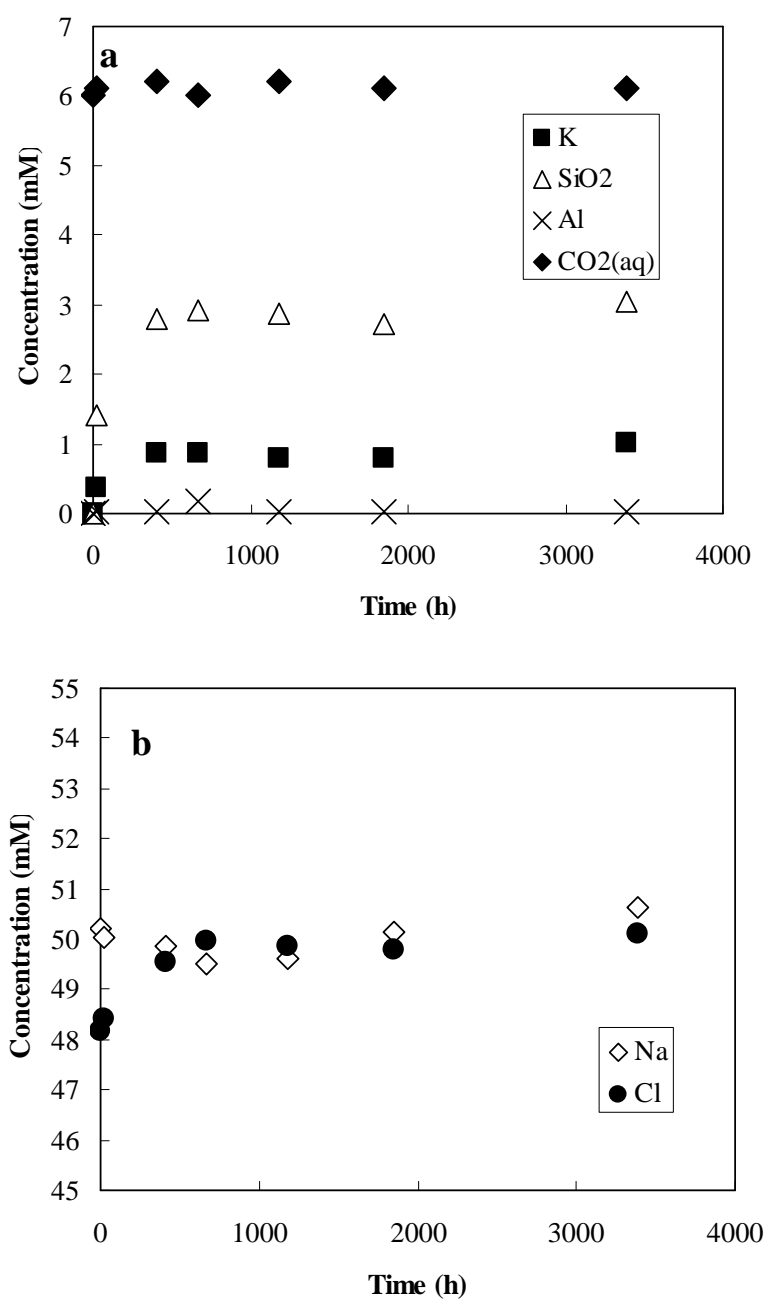


Fig. 1b. Changes in the dissolved concentrations of selected aqueous constituents with time for the alkali-feldspar dissolution experiments with the presence of CO₂ at 200 °C and 30 MPa (Experiment E).

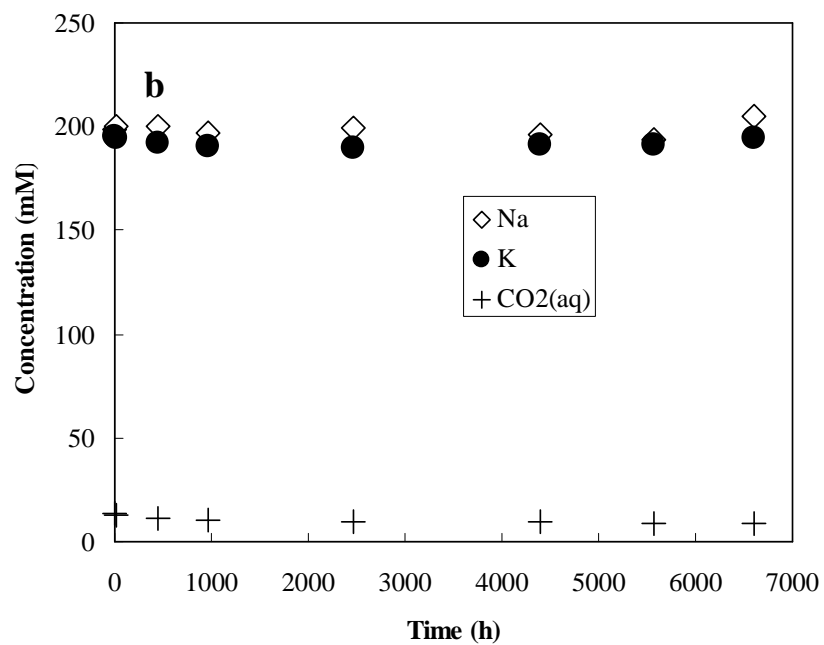
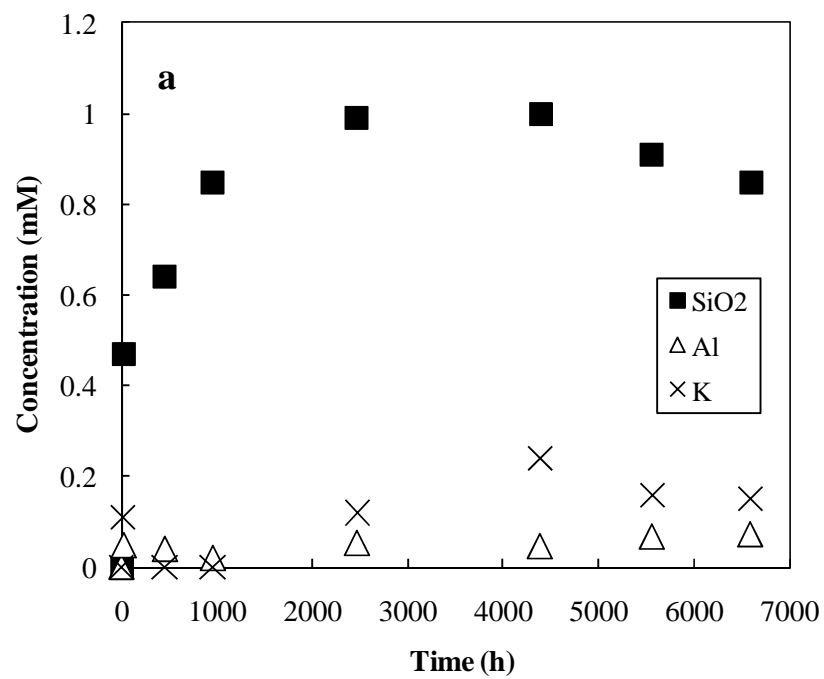


Fig. 1c. Changes in the dissolved concentrations of selected aqueous constituents with time for the albite dissolution experiments with the presence of CO₂ at 150 °C and 30 MPa (Experiment D).

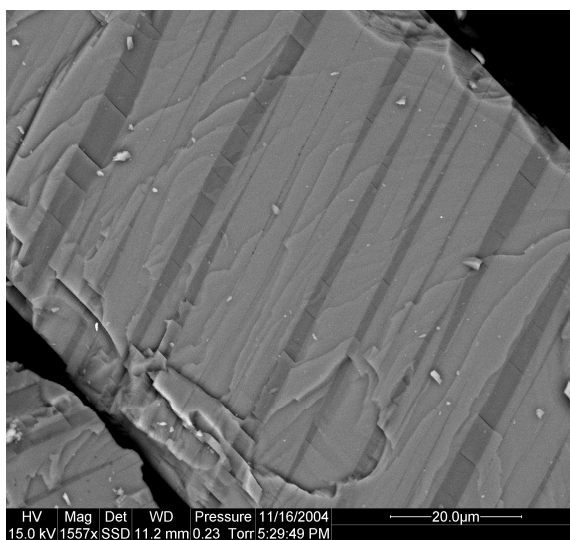


Figure 2a. Feldspar surface before the reactions (Experiment S).

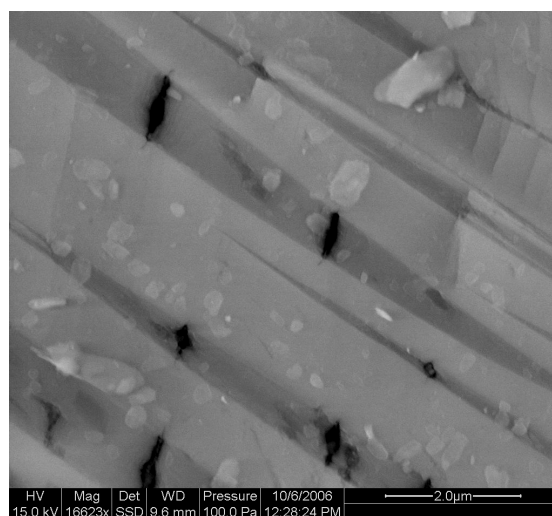


Fig. 2b. SEM backscatter image after 5 d reaction in Experiment S shows pitted surface of feldspar. The coverage of secondary minerals on feldspar surface is less than 5%.

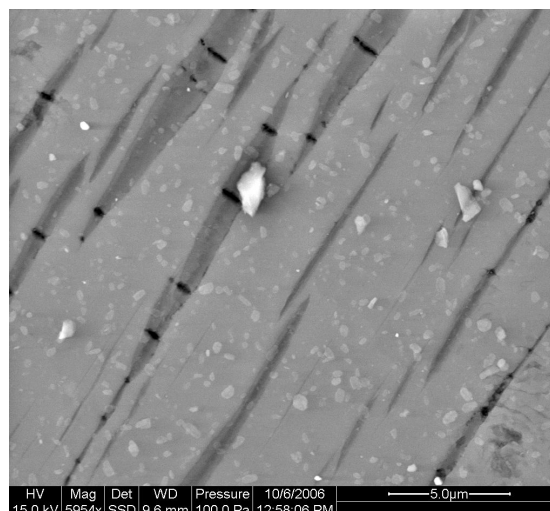


Fig. 2c. SEM backscatter image after 5 d reaction in Experiment S shows pitted surface of feldspar. The coverage of secondary minerals on feldspar surface is less than 5%.

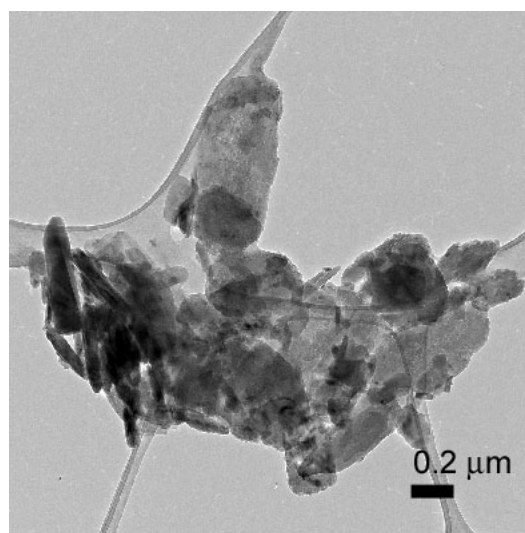


Fig. 2d. TEM images of alkali-feldspars after 120 h's dissolution experiment (Experiment S) with the presence of CO₂ using ultrasonication sample preparation method. Boehmite (plates) and un-identified phase (rod-like) were observed.

XRD pattern of the clay fraction of mineral products in the 5-day experiment showed the presence of boehmite and muscovite (Fig. 3). Geochemical modeling results show that the experimental solutions were undersaturated with respect to albite, but supersaturated with respect to microcline with the exception of the first sample, and supersaturated with respect to boehmite and muscovite (Table 3a). As shown by Zhu and

Lu (2009), the saturation indices clearly showed that the partial equilibrium assumption was not held during the experiments. The reaction path evolutions in activity-activity diagrams will be described in Chapter 4. Therefore, we will not repeat the discussion here.

Table 3a. Mineral saturation indices at each sampling time in experiments for the alkali feldspar dissolution in 0.2 M KCl and 0.05 M CO₂ solution at 200 °C and 30 MPa[†].

Time (h)	In situ pH	Albite	Boehmite	Diaspore	Kaolinite	Microcline	Muscovite	Paragonite	Pyrophyllite	Quartz
24	4.9	-5.13	1.18	1.40	1.43	-0.88	3.44	-1.04	-0.96	-0.96
(120)	5.0	-2.41	0.87	1.09	2.18	0.99	4.69	1.06	1.19	-0.27
144	5.1	-2.85	1.00	1.22	2.42	1.16	5.13	0.88	1.38	-0.29
312	5.6	-1.94	0.83	1.05	2.25	1.75	5.37	1.44	1.39	-0.20
480	5.7	-1.22	1.21	1.43	3.05	2.30	6.68	2.93	2.23	-0.18
(648)	5.7	-1.17	1.38	1.61	3.43	2.51	7.25	3.33	2.63	-0.16

[†]The parentheses on time in the first column on left denote to the time that the experiment was terminated and solids were recovered for characterization. In situ pH was calculated from the speciation modeling.

Table 3b. Mineral saturation indices (SI) at each sampling time of Experiment E[†].

Time (h)	In-situ pH	Albite	Boehmite	Diaspore	Kaolinite	Microcline	Muscovite	Paragonite	Pyrophyllite	Quartz
24	5.9	-0.83	0.52	0.74	1.18	-1.56	1.45	1.95	-0.14	-0.43
408	6.0	0.25	0.60	0.82	1.94	-0.11	3.06	3.18	1.22	-0.13
672	5.7	1.08	1.67	1.89	4.12	0.72	6.03	6.15	3.44	-0.11
1176	6.2	0.10	0.23	0.45	1.21	-0.30	2.12	2.28	0.50	-0.12
1848	6.0	0.22	0.60	0.82	1.91	-0.19	2.97	3.14	1.17	-0.14
3384	6.3	0.19	0.12	0.35	1.06	-0.12	2.10	2.16	0.41	-0.09

[†]For IUB-AF dissolution in 50 mM/kg NaCl solution and 6 mM/kg CO_{2(aq)} at 200 °C and 30 MPa

For a first approximation, we used the average rates of Na and Si release, r (mol L⁻¹ s⁻¹), as the albite dissolution rates, i.e., $r_{Ab} = \left(\frac{\Delta[Si]}{3\Delta t} + \frac{\Delta[Na]}{\Delta t} \right) / 2$, where $[Si]$ and $[Na]$ denote time series concentrations of Si and Na. For r_{Ab} corresponding to the fluid

samples at 24 h and 480 h, we used rates retrieved from Na release data or 1/3 Si release data only, respectively, because the Si and Na concentrations for 24 h and 480 h appear to be outliers, respectively. The method of using the average Na and Si values as r_{Ab} has also been used in previous studies (Alekseyev et al., 1997; Hellmann and Tisserand, 2006). Using the same method described above, we also calculated the dissolution rates from a companion experiment at 200 °C and 30 MPa but without the presence of CO₂ (Fu et al., 2009). Two sets of rates are presented in Fig. 4.

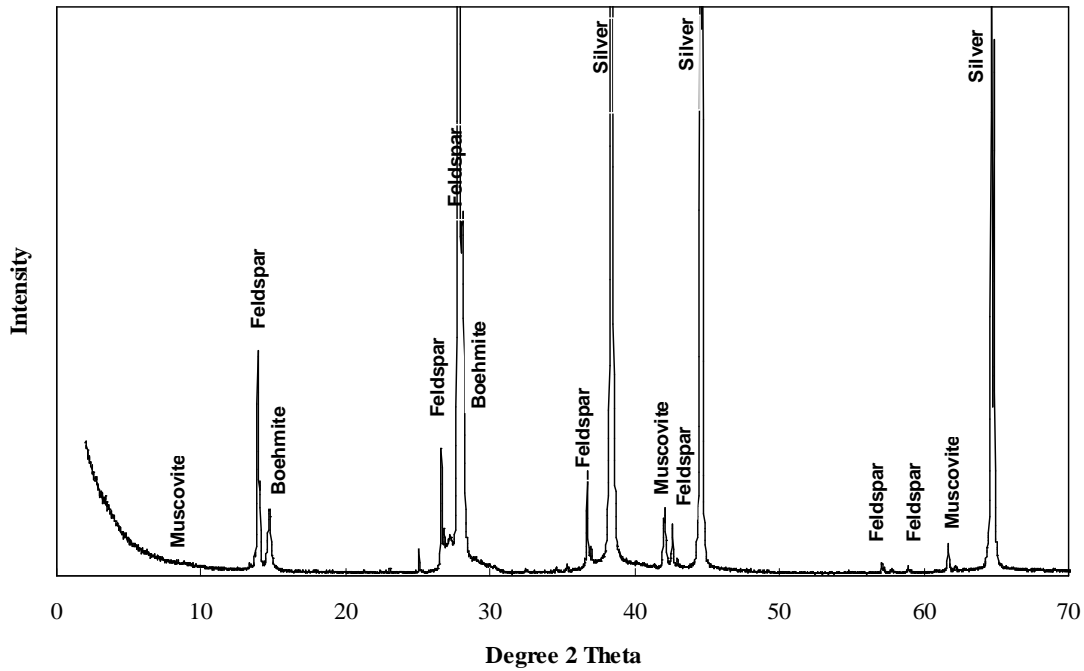


Fig. 3. X-ray diffraction pattern of mineral products recovered following 120-h experiment (Experiment S). Boehmite (ICDD card number: 21-1307), Muscovite (ICDD card number: 6-263), Kaolinite (ICDD card number: 14-164) and feldspar were identified.

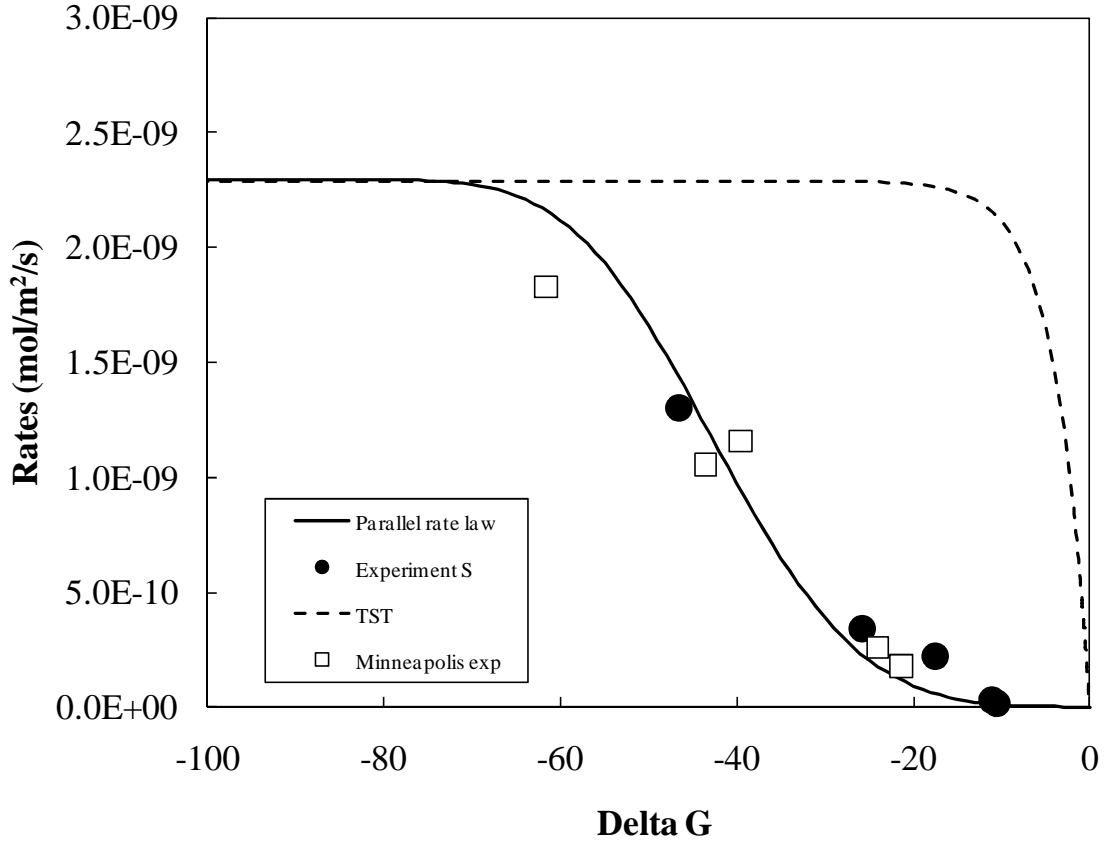


Fig. 4. Rates of alkali-feldspar dissolution in the Experiment S and a companion CO₂-free experiment (Fu et al., 2009) normalized to the initial BET surface areas (in mol m⁻² s⁻¹). Symbols denote experimental rates and lines indicate different rate law expressions. $\Delta G_{r,Ab}$ values were calculated in Zhu and Lu (2009) and this study. The solid line represents the Burch-type rate law (Eqn. 1) composed of two parallel rates. The dashed is based on linear rate law (TST).

The experimental $R = f(\Delta G_r)$ relationship is generally consistent with the empirical parallel rate law of Burch et al. (1993) in the form of,

$$R = k_1[1 - \exp(-ng^{m_1})] + k_2[1 - \exp(-g)]^{m_2} \quad (1)$$

where R is the dissolution rate of the mineral (mol s⁻¹ m⁻²), which already considers reactive surface area (S with the unit of m² L⁻¹), k_1 and k_2 denote the rate constants in

units of $\text{mol s}^{-1} \text{ m}^{-2}$, $g \equiv |\Delta G_r|/RT$, and n , m_1 , and m_2 are empirical parameters. We used k_1 of $2.29 \times 10^{-9} \text{ mol m}^{-2} \text{ s}^{-1}$ adopted from the mixed flow reactor experiment conducted by Hellmann et al. (1990). This albite dissolution experiment was performed at 225°C and pH 3.66, which is comparable to our experimental conditions (200°C and pH 4.0 at 25°C). The reported experimental rate ($5.25 \times 10^{-9} \text{ mol m}^{-2} \text{ s}^{-1}$) at 225°C was extrapolated to 200°C with the Arrhenius equation and an activation energy E_a of 65 kJ/mol. For parameters m_1 and n , we adopted the values from Hellmann and Tisserand (2006) (3.81 and 7.98×10^{-5} , respectively). The second term in Eqn. (3) is neither determined in our experiments nor in Hellmann and Tisserand (2006). The evolution of $\Delta G_{r,Ab}$ as a function of time was shown in Fig. 4.

To facilitate the comparison with other experiments (Table 1), we chose the rate from the first 24 h of hydrolysis of Experiment S as a representative for the dissolution rate. The choice of analyzing data at 24 h was made in order to limit the effects of both chemical affinity and the precipitation of secondary phases on rates of Si release (e.g., Hellmann, 1994).

3.2. Results from Experiment E.

The temporal evolution of the aqueous chemistry was shown in Table 2 and Fig. 1b. SEM micrographs show dissolution features and precipitation of secondary minerals on the feldspar surfaces (Fig. 5). K-feldspar dissolution was heterogeneous. Secondary minerals with no preferred orientation deposited either near dissolution kinks or evenly on the surface (Fig. 5). Geochemical modeling calculations show that the experimental solutions were supersaturated with respect to albite with the exception of the first sample,

undersaturated with respect to microcline, and supersaturated with respect to boehmite, kaolinite, and paragonite (Table 3b). Alkali-feldspar dissolution rate was calculated for 24 h only with the same method as for Experiment S, but using K release rates instead of Na. No attempt has been made to investigate the rate- ΔG_r function to derive parameters for the parallel rate law (Eqn. 1) because the range of the ΔG_r is narrow (from ~ -14 to -1 kJ/mol) and rates are all located in the near equilibrium region.

The time series evolution of aqueous chemistry of experiment E is traced on activity-activity diagrams of the $\text{Na}_2\text{O}-(\text{Al}_2\text{O}_3)\text{-SiO}_2\text{-H}_2\text{O-HCl}$ system (Figure 6). Because this experiment is a Na^+ -dominated system with respect to K^+ , we present the $\log a\text{SiO}_{2(\text{aq})}\text{-log}(a\text{Na}^+/a\text{H}^+)$ activity-activity diagrams, which approximately portray the phase relations pertaining to the experimental system. The solution chemistry fell within the paragonite stability field after 24 h for all samples except sample #3. The kaolinite field was skipped in this case because the experiment was started with a relatively high initial pH. At 672 h, the solution was supersaturated with respect to microcline (Table 3b).

The supersaturation of boehmite and kaolinite while the fluid chemistry was located in the paragonite fields indicates a departure from partial equilibria between the aqueous solution and the secondary phases, as discussed in Zhu and Lu (2009).

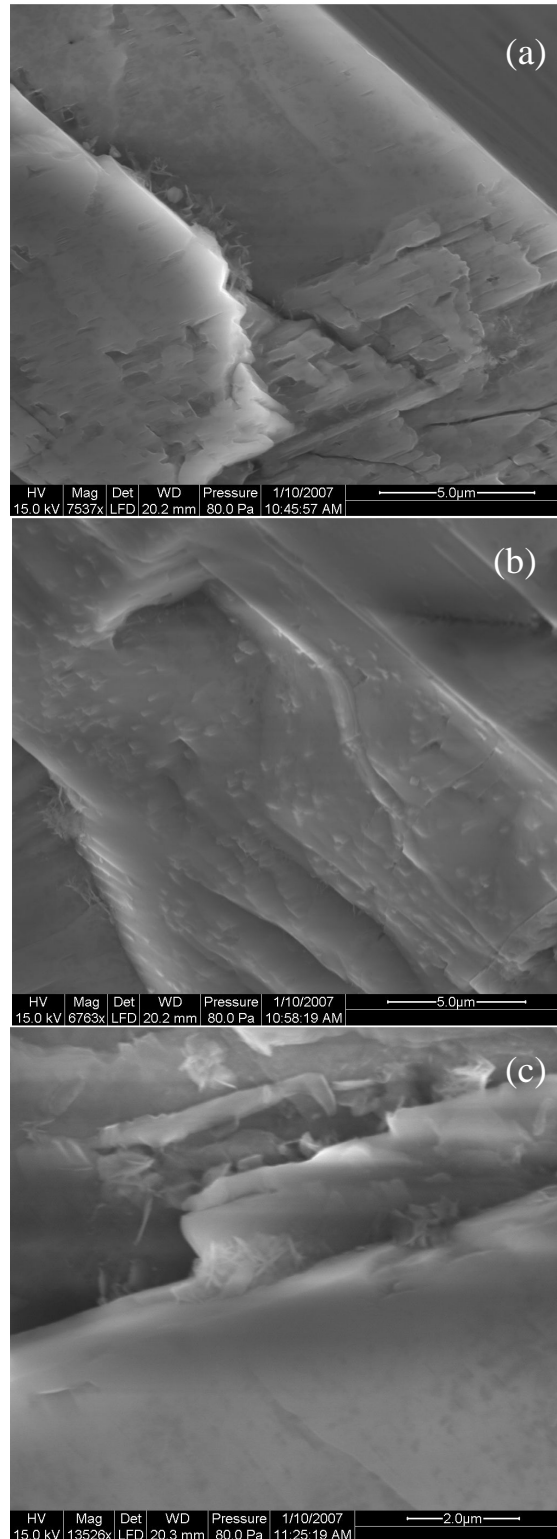


Fig. 5. SEM micrograph of products from Experiment E. (a) typical Alkali feldspar heterogeneous surface after dissolution experiment. Dissolution features of terraces, kinks, and steps are visible. Small amount of secondary minerals are deposited either near kinks (a,c) or evenly on the surface (b).

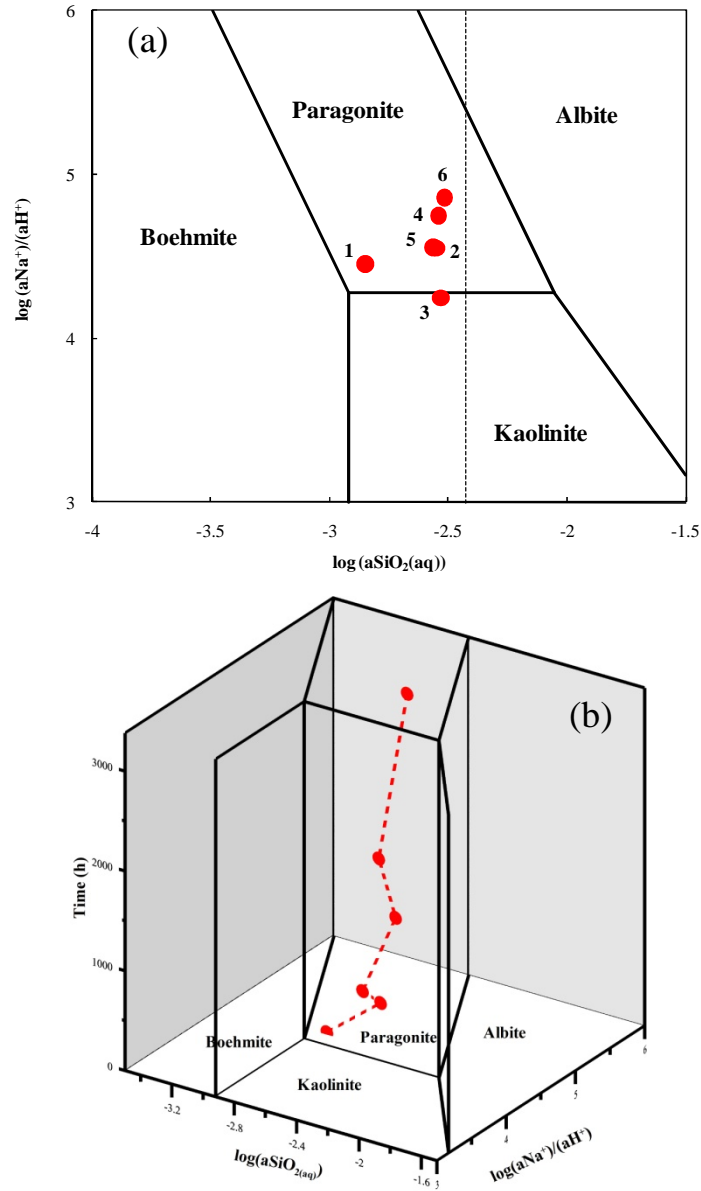


Fig. 6. Activity – activity diagrams showing the phase relations in the system $\text{Na}_2\text{O}-(\text{Al}_2\text{O}_3)\text{-SiO}_2\text{-H}_2\text{O-HCl}$ at 200 °C and 30 MPa. The dashed line in (a) denotes quartz saturation. Symbols represent experimental results of alkali feldspar dissolution in 50 mmol/kg KCl solution and 6 mmol/kg $\text{CO}_{2(\text{aq})}$ at 200 °C and 30 MPa. The activity and activity ratios were obtained from speciation modeling of the experimental system $\text{Na}_2\text{O-K}_2\text{O-Al}_2\text{O}_3\text{-SiO}_2\text{-H}_2\text{O-HCl}$, based on the experimental solution chemistry data in Table 2 and equilibrium constants listed in Zhu and Lu (2009). Points 1 through 6 represent experiment solutions at reaction time of 24, 408, 672, 1176, 1848, and 3384 h, respectively. The red dashed line in (b) connecting experimental data is for visualization of fluid chemical evolution.

3.3. Results from the Experiment D

The time series fluid chemistry from the dissolution of Amelia albite is listed in Table 2 and shown in Fig. 1c. Dissolved SiO₂ increased, reaching 0.85 mM after 960 h of reaction (Table 2). Solids were recovered at the end of the experiment (275 d or 6600 h). Typical dissolution features (e.g., terraces, kinks, steps) are visible on the surface of the albite particles (Fig. 7c, d, e), indicating that dissolution is heterogeneous. Secondary mineral precipitation is visible on the feldspar surface (Fig. 7d, f). XRD pattern shows that the secondary minerals are paragonite and minor kaolinite (Fig. 8). The presence of kaolinite was confirmed with TEM micrograph (Fig. 9a). TEM also shows the presence of an Al-bearing phase, probably boehmite (Fig. 9b,c). Albite dissolution rate was calculated with the same method as Experiment S from the 24 h data only. The calculated logarithm dissolution rate at 24 h is -9.62. We did not attempt to investigate the rate- ΔG_r function to derive parameters for the parallel rate law because albite dissolution was complicated by the secondary mineral precipitation as indicated by the persistence of solution chemistry in the kaolinite field after 960 h (Fig.10).

The concentrations of dissolved CO₂^o_(aq) decreased from 13.3 to 9.2 mM. The decrease of CO₂^o_(aq) concentrations with time suggests possible precipitation of a carbon-containing phase such as dawsonite [NaAlCO₃(OH)₂]. However, XRD pattern (Fig. 8) did not show discernable peaks of dawsonite. Geochemical modeling, using the solubility product for dawsonite, described by the reaction at 150 °C,



was calculated from equation 15 of Bénézech et al. (2007), which is based on their solubility measurement of dawsonite at 50 – 200 °C. The results showed that the experimental solutions were undersaturated with respect to dawsonite, which corroborates with the XRD results. Alternatively, the decrease of $\text{CO}_{2(\text{aq})}$ could have resulted from degassing of the samples. Figure 10 shows the dawsonite stability field under typical reservoir conditions of 150 °C and 300 bars. At 150 °C and 300 bars, CO_2 solubility in a 0.2 m NaCl solution is approximately 1.38 M (Duan et al., 2006). Dawsonite is not a stable phase even in CO_2 saturated solutions at 150 °C (Fig. 11). Our conclusion is thus in agreement with that of Hellevang et al. (2005) that dawsonite is not stable in typical formation waters.

The time series evolution of aqueous chemistry of Experiment D is traced on activity-activity diagrams of the $\text{Na}_2\text{O}-(\text{Al}_2\text{O}_3)\text{-SiO}_2\text{-H}_2\text{O-HCl}$ system (Fig.10). The solution chemistry fell within the kaolinite stability field after 24 h. During 24 – 960 h, the solution chemistry evolved progressively towards paragonite stability field. However, after 960 h the solution chemistry lingered within the kaolinite field until the end of the reaction. Albite dissolution seems to reach a steady state during this time, as indicated by the almost constant Si concentrations in the solution (Table 2).

Saturation indices calculations indicate that the solution was almost always supersaturated with respect to boehmite, kaolinite paragonite, pyrophyllite and smectite (beidellite and montmorillonite) when the fluid chemistry was located in kaolinite stability field. These facts confirmed that the partial equilibrium assumption does not hold (Zhu and Lu, 2009). The solution was undersaturated with respect to albite during 0-456 h, but slightly oversaturated during 960-6600 h. Considering the dissolution of

almost pure albite in this experiment, the activity of albite should be close to unity and the solution should be undersaturated or at equilibrium with respect to the albite. Therefore, the calculated SI (>0) indicates that the equilibrium constant of albite dissolution reaction has an error of at least 0.65 log units, which correspond to 5.3 kJ of the Gibbs free energy of formation of albite at 150 °C. This value is only 1.6 kJ higher than the propagated errors from 95% confidence interval from the reported standard deviation of enthalpy of formation at 25 °C alone (Holland and Powell, 1998). Holland and Powell(1998)'s data for albite are from Robie and Hemingway (1995), who also used Amelia albite to derive thermodynamic properties for albite from calorimetric measurements. Al-Si order/disorder has significant effect on feldspar solubility (Arnórsson and Stefánsson, 1999). Crystals of Amelia albite is partially disordered (e.g., Holm and Kleppa, 1968). Although both Robie and Hemingway (1995) and this study used Amelia albite, it is possible that the two specimens of Amelia albite may show slightly different Al-Si distributions. This leaves an uncertainty in calculating the degree of saturation of waters of specific composition with feldspars of a given composition.

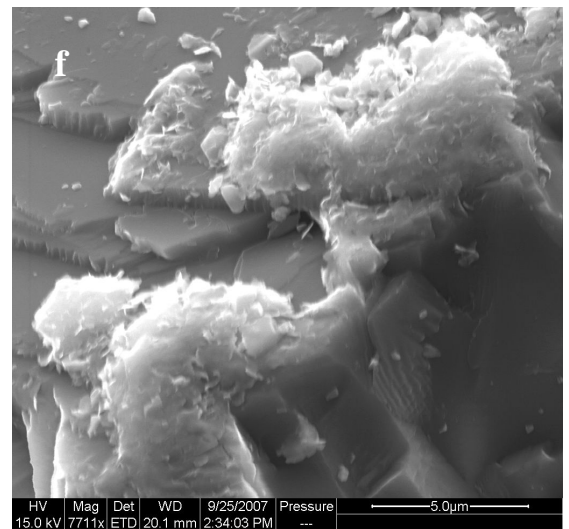
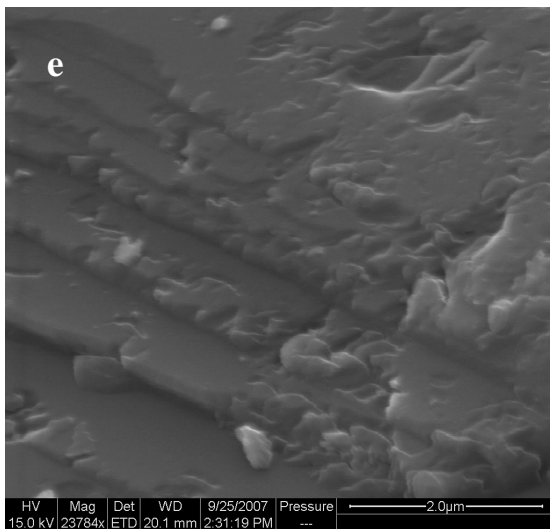
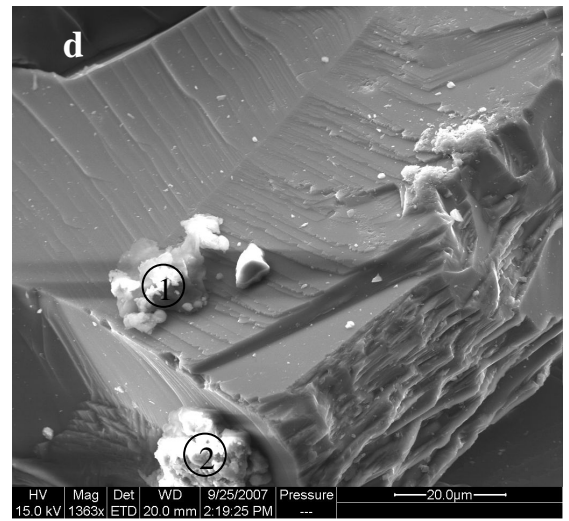
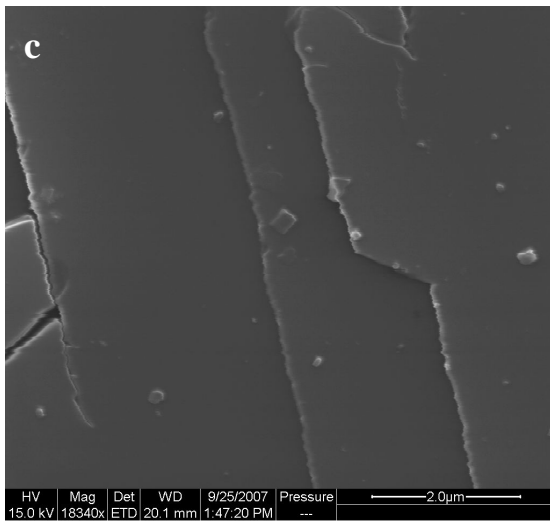
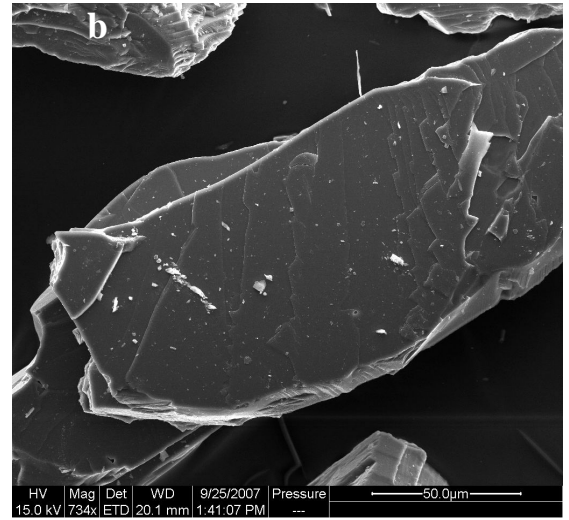
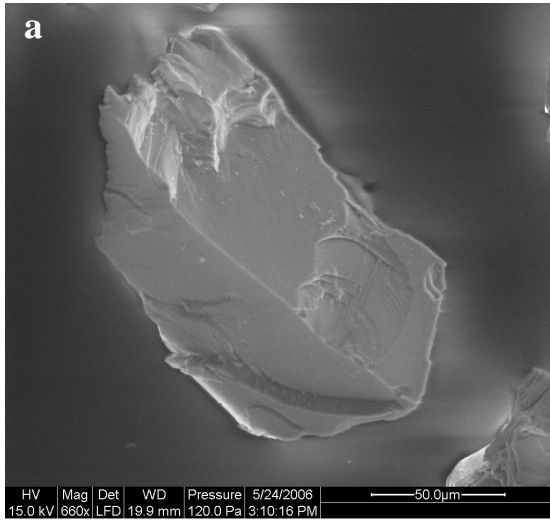


Fig. 7. SEM micrographs of Experiment D show (a) albite grains before the hydrothermal experiments, which are free from extra-fine particles and have angular shapes. This morphology is to be compared to reacted feldspars; (b) an albite particle after dissolution experiment. Surface topography consists of irregular, blocky terraces. The foreign objects are possibly debris of albite; (c) enlargement of (b). Seesaw edges of dissolution terraces. Terraces covered by barely visible surface precipitates ($<0.5\ \mu\text{m}$) in the form of platy crystals. The total coverage is about 1%; (d) surface of an albite particle after reaction showing dissolution stepwaves on twinned crystals. Precipitate is made of aggregates of secondary crystals; (e) an albite particle after dissolution experiment. Surface topography of dissolution terraces with irregular edges and irregular etch pits (with the size of $<0.1\ \mu\text{m}$ - $1\ \mu\text{m}$). The dissolution was intensive; (f) clusters of small secondary crystal aggregates and dissolution terraces with seesaw edges (about 6600 hours).

4. DISCUSSION

4.1. Partial equilibrium

Zhu and Lu (2009) examined the partial equilibrium assumption with speciation-solubility geochemical modeling and concluded that the partial equilibrium assumption does not hold. In this study, three additional experiments at CO_2 -charged conditions support Zhu and Lu's conclusion. Saturation indices calculations indicate that the experimental aqueous solutions were supersaturated with respect to secondary minerals for almost the entire durations of the experiments (Tables 3). In addition, for Experiment D, coexistence of kaolinite and an aluminum-bearing mineral (probably boehmite) was proved by TEM analysis (Fig. 6), indicating that the earlier precipitated secondary mineral (aluminum-bearing mineral) did not dissolve but persisted during the rest of the experiment. In other words, the sequential mineral dissolution and precipitation or mineral paragenesis as predicted by the partial equilibrium assumption was not observed in our experiments.

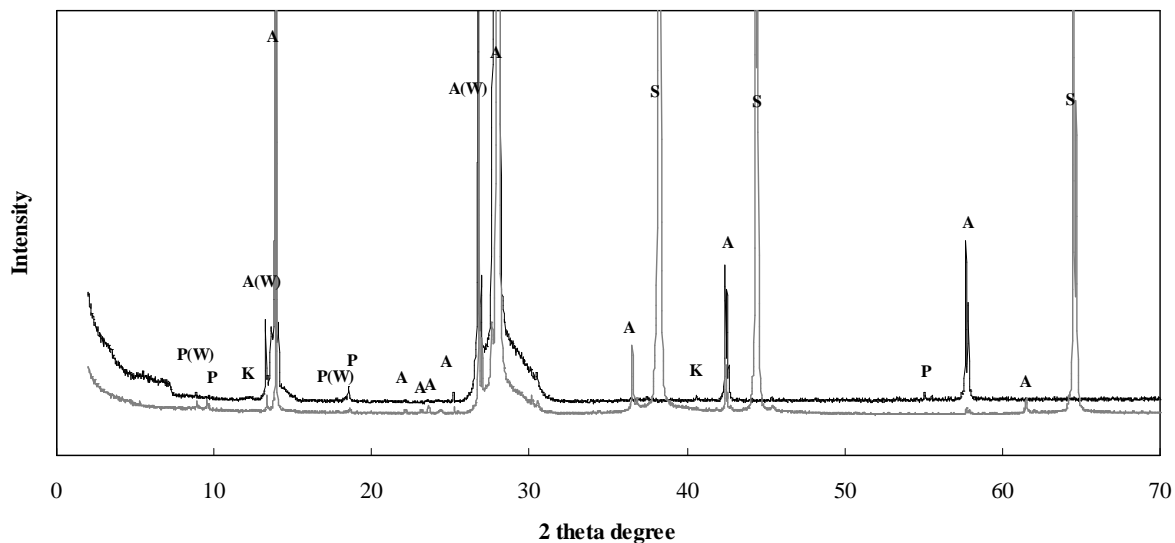


Fig. 8. X-ray diffraction pattern of mineral products following albite dissolution experiment (Experiment D dawsonite). A- Albite, ordered (ICDD: 9-466), P-Paragonite-1M (ICDD: 24-1047), K-Kaolinite (ICDD: 14-164), and S-silver (ICDD: 4-783) was from silver filter membrane. Note that A(W) and P(W) represent tungsten radiation (due to aged XRD tube) peaks of Albite and Paragonite, respectively. Grey line: “filtering-slurry mount” method. Black line: “slurry mount” method.

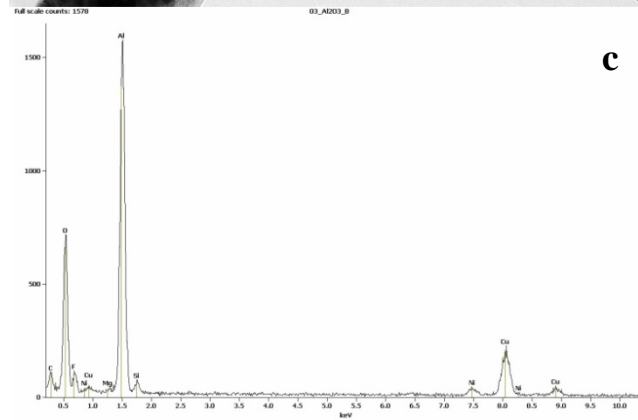
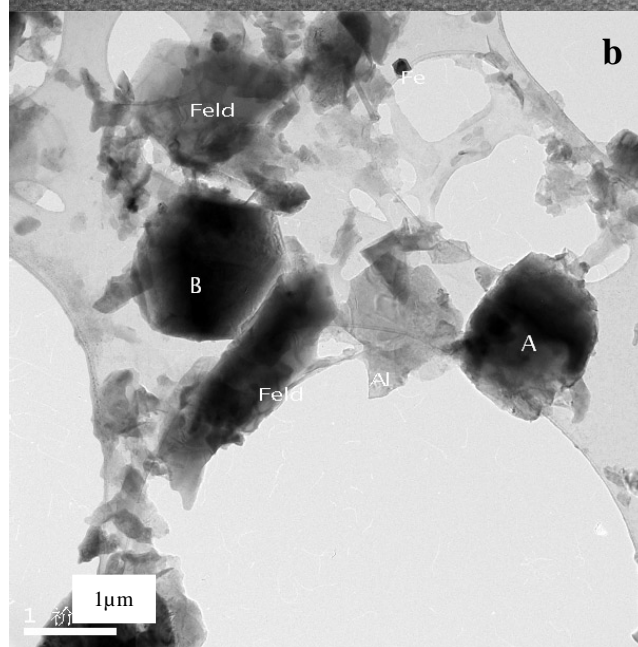
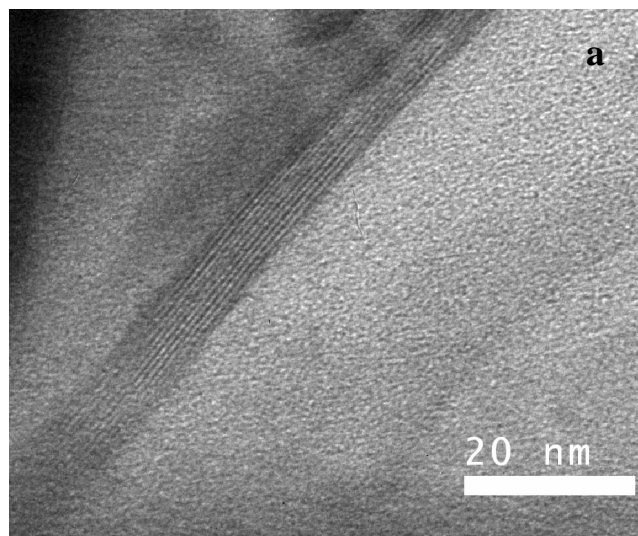


Fig. 9. Experiment D (dawsonite) TEM images (a) kaolinite like clay particle with a d-spacing ~ 0.7 nm; (b) A and B are Al-containing particles, probably boehmite; (c) EDS that shows A and B contain mainly Al.

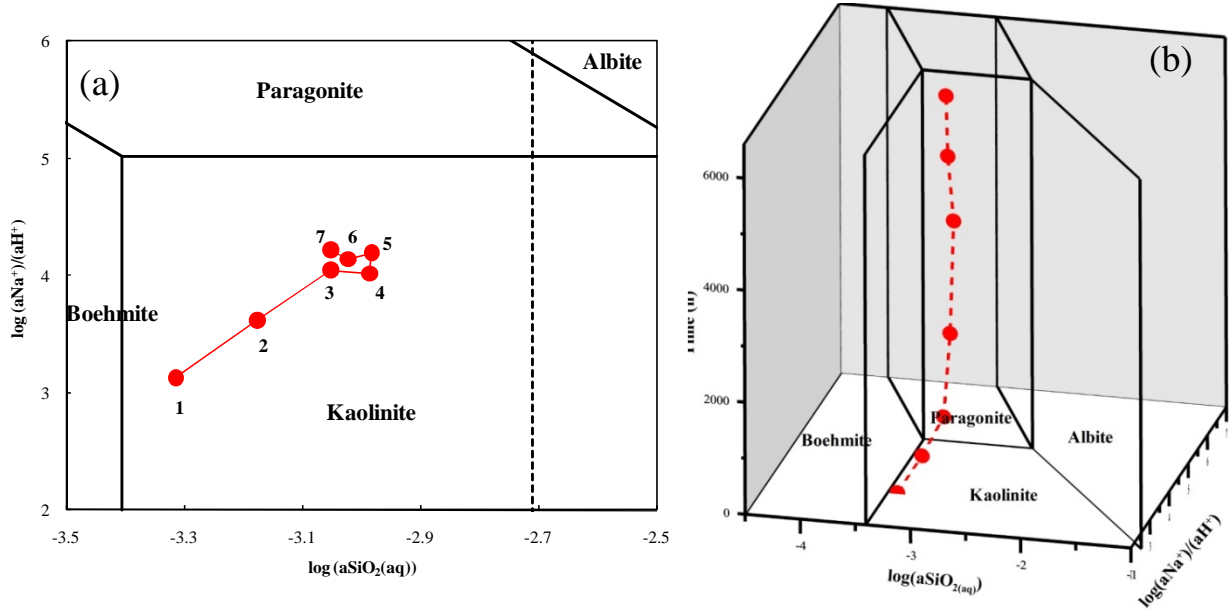


Fig. 10. Activity – activity diagrams showing the phase relations in the system $\text{Na}_2\text{O}-(\text{Al}_2\text{O}_3)-\text{SiO}_2-\text{H}_2\text{O}-\text{HCl}$ at 200°C and 30 MPa . The dashed line in (a) denotes quartz saturation. Symbols represent experimental results of albite dissolution in 200 mmol/kg KCl solution and 13.3 mmol/kg $\text{CO}_{2(\text{aq})}$ at 150°C and 30 MPa . The activity and activity ratios were obtained from speciation modeling of the experimental system $\text{Na}_2\text{O}-\text{K}_2\text{O}-\text{Al}_2\text{O}_3-\text{SiO}_2-\text{H}_2\text{O}-\text{HCl}$, based on the experimental solution chemistry data in Table 2. Points 1 through 7 represent experiment solutions at reaction time of 24, 456, 960, 2472, 4392, 5568, and 6600 h, respectively. The red line in (a) and red dashed line in (b) connecting experimental data is for visualization of fluid chemical evolution.

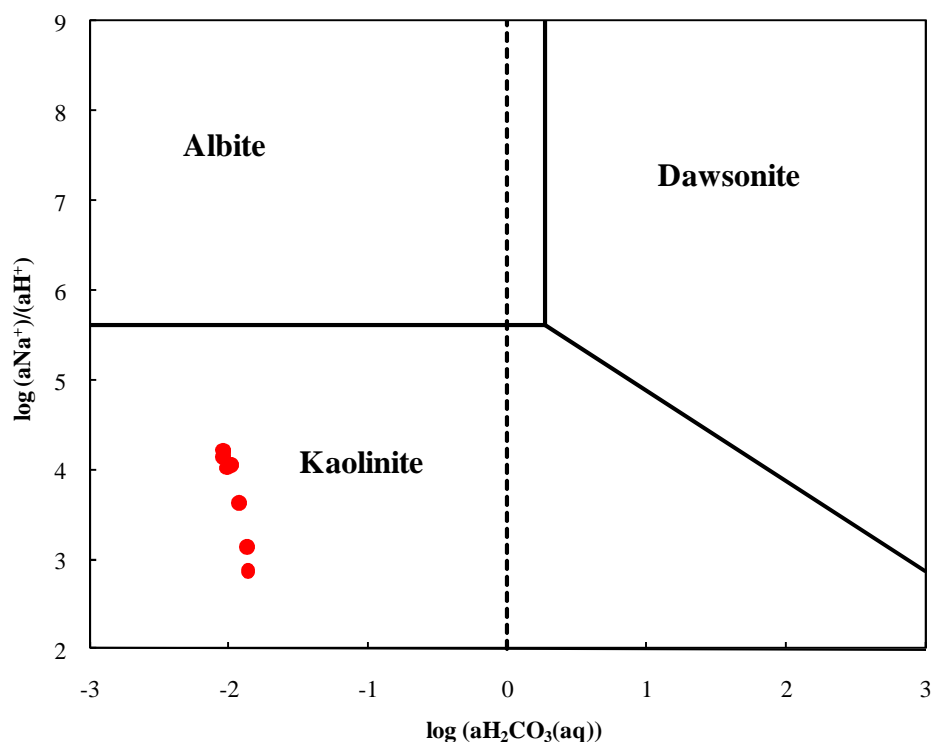


Fig.11. Activity-activity diagram depicting mineral stability fields in the system $\text{Na}_2\text{O}-\text{Al}_2\text{O}_3-\text{SiO}_2-\text{CO}_2-\text{H}_2\text{O}$ at 150 °C. SiO_2 activity is fixed by quartz saturation. Dots stand for experimental data from Experiment D. Dashed line is CO_2 equilibrium line (total CO_2 concentration of 1.38 M) at 150 °C.

4.2. Rate dependence on $p\text{CO}_2$

The effect of CO_2 on dissolution is of current interest because the storage of CO_2 in deep saline aquifer potentially promotes the mineral dissolution and carbonate precipitation reactions. Helgeson and co-workers (1971; 1984) interpreted the effect of carbon dioxide on the dissolution rate in the feldspar dissolution experiments of Lagache (1965, 1976) as a pure pH effect, amplifying the reaction with the hydrogen ion. However, Sverdrup (1990) indicated that the entropy change on formation of the activated surface complex for the hydrogen ion reaction is different from the entropy change determined for the reaction with CO_2 . He further modeled the effect of $p\text{CO}_2$ on

dissolution rates of several minerals. Carbonate surface complexes formation was also observed on goethite (Russell et al., 1975; Vangeen et al., 1994; Zeltner and Anderson, 1988), hematite (Bruno et al., 1992), and wollastonite (Xie and Walther, 1994). These interpretations and experimental observations can be summarized into two schools of opinions: (1) addition of CO₂ into the system does not change the mechanism and the effects of CO₂ are either on solution pH or negligible; (2) CO₂ changes the dissolution mechanism and forms surface complexes by adsorption onto the mineral surface.

Therefore, effects of pH on feldspar dissolution are still controversial. A recent experimental investigation (Carroll and Knauss, 2005) indicated that elevated CO₂ concentrations enhanced labradorite dissolution indirectly by acidifying solution pH at the temperature conditions (30-130 °C) relevant to carbon sequestration. We propose not to consider alteration of mechanism for modeling the effects of CO₂ on feldspar dissolution at the current stage. However, this is only a provisional choice. The role of dissolved CO₂ on feldspar dissolution rates calls for further studies.

4.3. Literature experiments involving feldspar hydrolysis in CO₂-charged solution

CO₂-charged feldspar dissolution experiments provide “ground truth” to assure the reliability of numerical models used for evaluating and optimizing injection programs. Table 1 summarizes experiments reported in the literature. Careful mineralogical characterization is the key to understanding the coupling of feldspar dissolution-secondary mineral precipitation reactions. However, most early batch experiments did not analyze reaction products (e.g., Amrhein and Suarez, 1988; Brady and Carroll, 1994; Busenberg and Clemency, 1976; Lagache, 1965, 1976; Manley and

Evans, 1986) even though secondary minerals are observed in some of the experiments listed above. The inferences of the secondary mineral identities from projected solution chemistry in the “stability fields” of activity-activity diagrams (Gardner, 1983) relies on the partial equilibrium assumption, which Zhu and Lu (2009) has demonstrated that it does not hold in feldspar hydrolysis experiments. Table 1a shows that only a limited number of experiments have characterized secondary minerals and can be used to study the coupling between dissolution and precipitation reactions.

Temperature and pressure conditions relevant to underground CO₂ storage vary widely, approximately 40-200 °C and 2-100 MPa (Bachu, 2000; Benson and Myer, 2000; Carter et al., 1998; Hitchon et al., 1999; Hurter and Pollack, 1996). However, most of the *T*, *P* conditions of literature studies are not in this range. Most studies provided *p*CO₂ values, although the values are relatively low with respect to injection conditions. Sorai et al. (2005) and Hangx and Spiers (2009) used higher *p*CO₂ values (up to 15 MPa), which are much closer to the injection conditions. The low *p*CO₂ conditions are still useful because *p*CO₂ may vary significantly away from the injection well. In addition, different *p*CO₂ conditions are also valuable to study effects of *p*CO₂ on feldspar dissolution rates. Figure 12 compares experimental *T*, *P* conditions with those relevant to geological sequestration superimposed on the CO₂ phase diagram.

Equilibrium constants for aqueous and mineral dissolution reactions at temperatures and pressures of interest are listed in Table 4. The choices of the thermodynamic properties for most aqueous species and minerals and the calculation methods have already been described in the Experimental Section. This compilation

features incorporation of an internally consistent, relatively new dataset from Holland and Powell (1998) and new data for Al-bearing aqueous species (Tagirov and Schott, 2001).

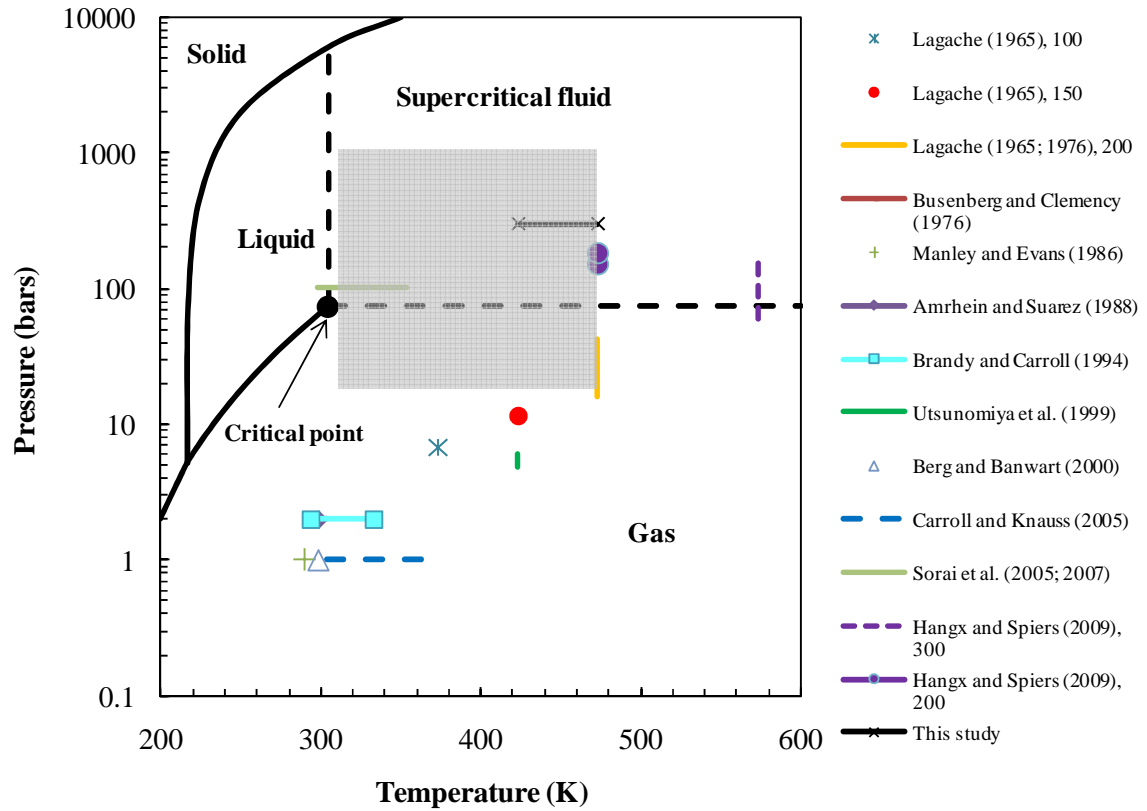


Fig. 12. Experimental T - P conditions compared with T , P ranges relevant to geological sequestration (40-200 °C, 20-1000 bars, or 2-100 MPa, gray shaded area) superimposed on carbon dioxide phase diagram (data from Brubacher, 2006). Total pressure in the system instead of $p\text{CO}_2$ is used for representing experimental data.

For feldspar dissolution rate laws, almost all published reactive transport modeling for CO_2 injection used the Transition State Theory (TST) (Lasaga, 1981a; Lasaga, 1981b) formulation for elementary reaction to model the overall feldspar dissolution reactions (Andre et al., 2007; Audigane et al., 2007; Gaus et al., 2005; Gherardi et al., 2007; Lagneau et al., 2005; Maher et al., 2009; Xu et al., 2004; Xu et al.,

2005; Xu et al., 2007; Zerai et al., 2006) either with or without considering the pH effect (e.g., acid, neutral, and basic mechanisms). The TST rate law features a plateau of constant rate at a solution chemistry condition far from equilibrium, but rates decrease exponentially near equilibrium. As a consequence, this law only starts to affect the rate at $\Delta G_r > -10$ kJ/mol at 200 °C (e.g., Fig. 4). However, a number of experiments near equilibrium have shown that actual relationships between r and ΔG_r deviated from the TST linear rate law (Alekseyev et al., 1997; Beig and Lüttge, 2006; Burch et al., 1993; Gautier et al., 1994; Hellmann and Tisserand, 2006; Nagy et al., 1991; Nagy and Lasaga, 1992; Nagy and Lasaga, 1993; Oelkers et al., 1994; Schramke et al., 1987; Taylor et al., 2000), instead they show a sigmoidal shape. As discussed in Zhu (2009), the empirical rate law of Burch et al. (1993) (Eqn. 1) is sufficient to fit the experimental data (as it is the case shown in this study) although it is by no means a mathematically unique expression. This empirical rate law affects the rate at the ΔG_r range of ~ -60 to -10 kJ/mol after a constant rate plateau at far from equilibrium condition (e.g., Fig. 4). However, the dependence of dissolution rate on ΔG_r and thus the reaction mechanism are still poorly understood (Beig and Lüttge, 2006; Brantley, 2008), especially when the solution chemistry is close to equilibrium. Nevertheless, we proposed a rate law formulation for albite dissolution

$$\frac{r}{S} = \{k_{acid}^{298.15k} \exp\left[\frac{-E_a^{acid}}{R}\left(\frac{1}{T} - \frac{1}{298.15}\right)\right] a_{H^+}^i + k_{neutral}^{298.15k} \exp\left[\frac{-E_a^{neutral}}{R}\left(\frac{1}{T} - \frac{1}{298.15}\right)\right]\} \{1 - \exp(-ng^{m1}) + \frac{1}{x} [1 - \exp(-g)]^{m2}\} \quad (3)$$

where $k_{acid}^{298.15k}$ and $k_{neutral}^{298.15k}$ denotes rate constant of acid and neutral mechanisms at 295.15 K, respectively. r is the feldspar dissolution rate in $\text{mol s}^{-1} \text{L}^{-1}$, S is the specific

reactive surface area per kg H₂O. $\exp \left[\frac{-E_a}{R} \left(\frac{1}{T} - \frac{1}{298.15} \right) \right]$ is a function using activation energy E_a to calculate the rate constant at the temperature of interest. The superscripts “acid” and “neutral” for E_a denote activation energy for acid and neutral mechanisms, respectively. r , g , n , m_1 , m_2 have been defined before, x is ratio of far from equilibrium and close to equilibrium rates, i is the empirical reaction order accounting for catalysis by H⁺ in solution. $k_{acid}^{298.15k}$, $k_{neutral}^{298.15k}$, E_a^{acid} , $E_a^{neutral}$ and i $10^{-10.16}$ mol m⁻² s⁻¹, $10^{-12.56}$ mol m⁻² s⁻¹, 65 kJ/mol, 69.8 kJ/mol, and 0.457, respectively (Palandri and Kharaka, 2004). For n , m_1 , m_2 , and x , we adopted values from Hellmann and Tisserand (2006), which are 7.98×10^{-5} , 3.81, 1.17, and 56.65, respectively.

5. CONCLUSIONS AND REMARKS

In order to evaluate the complex interplay of CO₂-brine-feldspar interactions relevant to geological carbon sequestration, we have investigated the reactions in feldspar-CO₂-brine systems under hydrothermal conditions (150-200 °C and 30 MPa). Our main findings can be summarized as follows:

(1) This study provided both solution chemistry evolution and secondary mineral data of three feldspar hydrolysis batch experiments at CO₂-charged conditions. Most previous studies either did not analyze the secondary minerals or the solution chemistry. The data of both are useful to decipher the coupling of dissolution and precipitation reactions in CO₂-charged systems.

(2) Speciation-solubility calculations indicate that the experimental aqueous solutions were undersaturated with respect to feldspar reactants and supersaturated with respect to clay minerals for almost the entire duration of the experiments. Extensive

dissolution features (etch pits, channels, kinks, and steps) were observed, indicating significant water-rock interactions. Boehmite, kaolinite, and paragonite were identified as secondary minerals. The presence of these secondary phases are observed in a wide range of experimental and field conditions (e.g., Apps et al., 1989; Bénézech et al., 2001, 2008; Bourcier et al., 1993; Burch et al., 1993; Carroll and Walther, 1990; Castet et al., 1993; Devidal et al., 1997; Ganor et al., 1995; Gautier et al., 2001; Hangx and Spiers, 2009; Hemingway et al., 1991; Nagy et al., 1999; Small, 1993; Wieland and Stumm, 1992; Yang and Steefel, 2008), and thus are likely to be formed under injection conditions.

A review of experiments reported in the literature indicates that the data available are insufficient and our understanding of CO₂-brine-feldspar interactions is still poor. New experiments are urgently needed to establish a database about feldspar dissolution mechanism, rates and rate laws, and secondary mineral information at reservoir conditions that can be used in performance and risk analysis modeling. We provided a thermodynamic dataset at 6 different temperature and pressure conditions and proposed a rate law formulation for albite dissolution which can be incorporated into reactive transport modeling.

REFERENCES

- Abdel-Rahman, A.F.M., 2001. Peraluminous plutonism: Nature and origin of the Moly May leucogranite and its coast plutonic complex granitic host-rocks, northwestern British Columbia. *Can. Mineral.* **39**, 1181-1196.
- Abramov, S.S., Kurdyukov, E.B., 1997. The origin of charnockite-enderbite complexes by magmatic replacement: Geochemical evidence. *Geokhimiya*, **3**, 260-268.
- Accornero, M., Marini, L., Ottonello, G., Zuccolini, M.V., 2005. The fate of major constituents and chromium and other trace elements when acid waters from the derelict Libiola mine (Italy) are mixed with stream waters. *Appl. Geochem.* **20**, 1368-1390.
- Aggett, J., Kriegman, M.R., 1988. The extent of formation of arsenic(III) in sediment interstitial waters and its release to hypolimnetic waters in lake Ohakuri. *Water Res.* **22**, 407-411.
- Ague, J.J., Brimhall, G.H., 1989. Geochemical modeling of steady state fluid flow and chemical reaction during supergene enrichment of porphyry copper deposits. *Econ. Geol.* **84**, 506-528.
- Alekseyev, V.A., Medvedeva, L.S., Prisyagina, N.I., Meshalkin, S.S., Balabin, A.I., 1997. Change in the dissolution rates of alkali feldspars as a result of secondary mineral precipitation and approach to equilibrium. *Geochim. Cosmochim. Acta* **61**, 1125-1142.
- Amrhein, C., Suarez, D.L., 1988. The use of a surface complexation model to describe the kinetics of ligand-promoted dissolution of anorthite. *Geochim. Cosmochim. Acta* **52**, 2785-2793.
- Amrhein, C., Suarez, D.L., 1992. Some factors affecting the dissolution kinetics of anorthite at 25° C. *Geochim. Cosmochim. Acta* **56**, 1815-1826.
- André, L., Audigane, P., Azaroual, M., Menjoz, A., 2007. Numerical modeling of fluid-rock chemical interactions at the supercritical CO₂-liquid interface during CO₂ injection into a carbonate reservoir, the Dogger aquifer (Paris Basin, France). *Energ. Convers. Manage.* **48**, 1782-1797.
- Apps, J.A., Neil, J.M., Jun, C.H., 1988. Thermochemical properties of gibbsite, bayerite, boehmite, diaspore, and the aluminate ion between 0 and 350 °C. Division of Waste Management, Office of Nuclear Material Safety and Safeguard, US NRC NUREG/CR-5271-LBL-21482.
- Arnórsson, S., Stefánsson, A., 1999. Assessment of feldspar solubility constants in water in the range of 0 to 350° C at vapor saturation pressures. *Am. J. Sci.* **299**, 173-209.

- Arvidson, R.S., Lüttge, A., 2010. Mineral dissolution kinetics as a function of distance from equilibrium – New experimental results. *Chem. Geol.* **269**, 79-88.
- Audigane, P., Gaus, I., Czernichowski-Lauriol, I., Pruess, K., Xu, T.F., 2007. Two-dimensional reactive transport modeling of CO₂ injection in a saline Aquifer at the Sleipner site, North Sea. *Am. J. Sci.* **307**, 974-1008.
- Bachu, S., 2000. Sequestration of CO₂ in geological media: criteria and approach for site selection in response to climate change. *Energ. Convers. Manage.* **41**, 953-970.
- Becker, L.E., Hreha, A.J., Dawson, T.A., 1978. Pre-knox (Cambrian) Stratigraphy in Indiana. Department of Natural Resources, *Geological Survey Bulletin* **57**.
- Beig, M.S., Lüttge, A., 2006. Albite dissolution kinetics as a function of distance from equilibrium: Implications for natural feldspar weathering. *Geochim. Cosmochim. Acta* **70**, 1402-1420.
- Bénézech, P., Palmer, D.A., Anovitz, L.M., Horita, J., 2007. Dawsonite synthesis and reevaluation of its thermodynamic properties from solubility measurements: Implications for mineral trapping of CO₂. *Geochim. Cosmochim. Acta* **71**, 4438-4455.
- Bénézech, P., Palmer, D.A., Wesolowski, D.J., 2001. Aqueous high-temperature solubility studies. II. The solubility of boehmite at 0.03 m ionic strength as a function of temperature and pH as determined by in situ measurements. *Geochim. Cosmochim. Acta* **65**, 2097-2111.
- Bénézech, P., Palmer, D.A., Wesolowski, D.J., 2008. Dissolution/precipitation kinetics of boehmite and gibbsite: Application of a pH-relaxation technique to study near-equilibrium rates. *Geochim. Cosmochim. Acta* **72**, 2429-2453.
- Benson, S.M., Myer, L., 2000. Advances in geologic sequestration: Identifying and addressing key issues. *Geological Society of America Abstracts with Programs* **32**, A200.
- Berg, A., Banwart, S.A., 2000. Carbon dioxide mediated dissolution of Ca-feldspar: Implications for silicate weathering. *Chem. Geol.* **163**, 25-42.
- Blum, A., Stillings, L., 1995. Feldspar dissolution kinetics, in: Brantley, S.L., White, A.F. (Eds.), *Chemical Weathering Rates of Silicate Minerals*. Mineralogical Society of America, Washington DC, pp. 291-351.
- Bourcier, W.L., Knauss, K.G., Jackson, K.J., 1993. Aluminum hydrolysis constants to 250 °C from boehmite solubility measurements. *Geochim. Cosmochim. Acta* **57**, 747-762.

- Brady, P.V., Carroll, S.A., 1994. Direct effects of CO₂ and temperature on silicate weathering - Possible implications for climate control. *Geochim. Cosmochim. Acta* **58**, 1853-1856.
- Brantley, S.L., 2008. Kinetics of Mineral Dissolution, in: Brantley, S.L., Kubicki, J.D., White, A.F. (Eds.), *Kinetics of Water-Rock Interaction*. Springer, New York, pp. 151-196.
- Brubacher, L., 2006. Obtaining reliable data online — Phase diagram for carbon dioxide. http://www.chem13news.uwaterloo.ca/issues/342/342_nov_06.html.
- Bruno, J., Stumm, W., Wersin, P., Brandberg, F., 1992. On the influence of carbonate in mineral dissolution: I. The thermodynamics and kinetics of hematite dissolution in bicarbonate solutions at T = 25 °C. *Geochim. Cosmochim. Acta* **56**, 1139-1147.
- Burch, T.E., Nagy, K.L., Lasaga, A.C., 1993. Free energy dependence of albite dissolution kinetics at 80° C and pH 8.8. *Chem. Geol.* **105**, 137-162.
- Busenberg, E., Clemency, C.V., 1976. The dissolution kinetics of feldspars at 25 °C and 1 atm CO₂ partial pressure. *Geochim. Cosmochim. Acta* **40**, 41-49.
- Carroll, S.A., Knauss, K.G., 2005. Dependence of labradorite dissolution kinetics on CO_{2(aq)}, Al_(aq), and temperature. *Chem. Geol.* **217**, 213-225.
- Carroll, S.A., Walther, J.V., 1990. Kaolinite dissolution at 25 °C, 60 °C, and 80 °C. *Am. J. Sci.* **290**, 797-810.
- Carter, L.S., Kelley, S.A., Blackwell, D.D., Naeser, N.D., 1998. Heat flow and thermal history of the Anadarko basin, Oklahoma. *AAPG Bull.* **82**, 291-316.
- Castet, S., Dandurand, J.L., Schott, J., Gout, R., 1993. Boehmite solubility and aqueous aluminum speciation in hydrothermal solutions (90–350 °C): Experimental study and modeling. *Geochim. Cosmochim. Acta* **57**, 4869-4884.
- Devidal, J.L., Schott, J., Dandurand, J.L., 1997. An experimental study of kaolinite dissolution and precipitation kinetics as a function of chemical affinity and solution composition at 150° C, 40 bars, and pH 2, 6.8, and 7.8. *Geochim. Cosmochim. Acta* **61**, 5165-5186.
- DOE-NETL, 2008. Carbon Sequestration Atlas of the United States and Canada, 2nd ed., U.S. Dept. of Energy, www.netl.doe.gov/technologies/carbonseq/refshelf/atlas/ATLAS.pdf.

- Duan, Z., Sun, R., Zhu, C., Chou, I., 2006. An improved model for the calculation of CO₂ solubility in aqueous solutions containing Na⁺, K⁺, Ca²⁺, Mg²⁺, Cl⁻, and SO₄²⁻. *Mar. Chem.* **98**, 131-139.
- Eliasson, B., Riemer, P., Wokaun, A., 1998. *Greenhouse Gas Control Technologies: Proceedings of the 4th International Conference on Greenhouse Gas Control Technologies*. Elsevier.
- Emery, D., Robinson, A.D., 1993. *Inorganic Geochemistry: Application to Petroleum Geology*. Blackwell Scientific Publication.
- Fu, Q., Lu, P., Konishi, H., Dillmore, R., Xu, H., Seyfried, W.E., Jr., Zhu, C., 2009. Coupled alkali-feldspar dissolution and secondary mineral precipitation in batch systems: 1. New experiments at 200° C and 300 bars. *Chem. Geol.* **285**, 125-135.
- Ganor, J., Lu, P., Zheng, Z., Zhu, C., 2007. Bridging the gap between laboratory measurements and field estimations of weathering using simple calculations. *Environ. Geol.* **53**, 599-610.
- Ganor, J., Mogollon, J.L., Lasaga, A.C., 1995. The effect of pH on kaolinite dissolution rates and on activation energy. *Geochim. Cosmochim. Acta* **59**, 1037-1052.
- Gardner, L.R., 1983. Mechanics and kinetics of incongruent feldspar dissolution. *Geology* **11**, 418-421.
- Gaus, I., Azaroual, M., Czernichowski-Lauriol, I., 2005. Reactive transport modelling of the impact of CO₂ injection on the clayey cap rock at Sleipner (North Sea). *Chem. Geol.* **217**, 319-337.
- Gautier, J.-M., Oelkers, E.H., Schott, J., 1994. Experimental study of K-feldspar dissolution rates as a function of chemical affinity at 150° C and pH 9. *Geochim. Cosmochim. Acta* **58**, 4549-4560.
- Gautier, J.M., Oelkers, E.H., Schott, J., 2001. Are quartz dissolution rates proportional to B.E.T. surface areas? *Geochim. Cosmochim. Acta* **65**, 1059-1070.
- Gherardi, F., Xu, T.F., Pruess, K., 2007. Numerical modeling of self-limiting and self-enhancing caprock alteration induced by CO₂ storage in a depleted gas reservoir. *Chem. Geol.* **244**, 103-129.
- Gunter, W.D., Perkins, E.H., Hutcheon, I., 2000. Aquifer disposal of acid gases: modelling of water-rock reactions for trapping of acid wastes. *Appl. Geochem.* **15**, 1085-1095.

- Gunter, W.D., Wiwchar, B., Perkins, E.H., 1997. Aquifer disposal of CO₂-rich greenhouse gases: Extension of the time scale of experiment for CO₂-sequestering reactions by geochemical modeling. *Miner. Petrol.* **59**, 121-140.
- Haar, L., Gallagher, J.S., Kell, G.S., 1984. *NBS/NRC steam tables: Thermodynamic and transport properties and computer programs for vapor and liquid states of water in SI units*. Hemisphere Publishing Corporation, New York, 320p.
- Hangx, S.J.T., Spiers, C.J., 2009. Reaction of plagioclase feldspars with CO₂ under hydrothermal conditions. *Chem. Geol.* **265**, 88-98.
- Harlow, G.E., Brown, G.E., 1980. Low albite: an X-ray and neutron diffraction study. *Am. Mineral.* **65**, 986-995.
- Harouiya, N., Oelkers, E.H., 2004. An experimental study of the effect of aqueous fluoride on quartz and alkali-feldspar dissolution rates. *Chem. Geol.* **205**, 155-167.
- Helgeson, H.C., 1971. Kinetics of mass transfer among silicates and aqueous solutions. *Geochim. Cosmochim. Acta* **35**, 421-469.
- Helgeson, H.C., Delany, J.M., Nesbitt, H.W., Bird, D.K., 1978. Summary and critique of the thermodynamic properties of rock-forming minerals. *Am. J. Sci.* **278A**, 1-229.
- Helgeson, H.C., Kirkham, D.H., Flowers, G.C., 1981. Theoretical prediction of the thermodynamic behavior of aqueous electrolytes by high pressures and temperatures. IV. Calculation of activity coefficients, osmotic coefficients, and apparent molal and standard and relative partial molal properties to 600° C and 5 kb. *Am. J. Sci.* **281**, 1249-1516.
- Helgeson, H.C., Murphy, W.M., Aagaard, P., 1984. Thermodynamic and kinetic constraints on reaction rates among minerals and aqueous solutions II. Rate constants, effective surface area, and the hydrolysis of feldspar. *Geochim. Cosmochim. Acta* **48**, 2405-2432.
- Hellmann, R., 1994. The albite-water system: Part I, The kinetics of dissolution as a function of pH at 100, 200, and 300° C. *Geochim. Cosmochim. Acta* **58**, 595-611.
- Hellmann, R., Daval, D., Tisserand, D., Renard, F., 2007. Albite feldspar dissolution kinetics as a function of the Gibbs free energy at high *p*CO₂, In *Water Rock Interaction* (T.D. Bullen, Y. Wang, eds.), Taylor & Francis, London, 591-595.
- Hellmann, R., Eggleston, C.R., Hochella, M.F., Crerar, D.A., 1990. The formation of leached layers on albite surfaces during dissolution under hydrothermal conditions. *Geochim. Cosmochim. Acta* **54**, 1267-1281.

- Hellmann, R., Tisserand, D., 2006. Dissolution kinetics as a function of the Gibbs free energy of reaction: An experimental study based on albite feldspar *Geochim. Cosmochim. Acta* **70**, 364-383.
- Hemingway, B.S., Robie, R.A., Apps, J.A., 1991. Revised values for the thermodynamic properties of boehmite, AlO(OH), and related species and phases in the system Al-H-O. *Am. Mineral.* **76**, 445-457.
- Hereford, A.G., Keating, E., Guthrie, G., Zhu, C., 2007. Reactions and reaction rates in the regional aquifer beneath the Pajarito Plateau, north-central New Mexico, USA. *Environ. Geol.* **52**, 965-977.
- Hitchon, B., Gunter, W.D., Gentzis, T., Bailey, R.T., 1999. Sedimentary basins and greenhouse gases: a serendipitous association. *Energ. Convers. Manage.* **40**, 825-843.
- Ho, P.C., Bianchi, H., Palmer, D.A., Wood, R.H., 2000. Conductivity of dilute aqueous electrolyte solutions at high temperatures and pressures using a flow cell. *J. Solution Chem.* **29**, 217-235.
- Holdren, G.R., Berner, R.A., 1979. Mechanism of feldspar weathering. I. Experimental studies. *Geochim. Cosmochim. Acta* **43**, 1161-1171.
- Holland, T.J.B., Powell, R., 1998. An internally consistent thermodynamic data set for phases of petrological interest. *J. Metamor. Geol.* **16**, 309-343.
- Holm, J.L., Kleppa, O.J., 1968. Thermodynamics of the disordering process in albite. *Am. Mineral.* **53**, 123-133.
- Hurter, S.J., Pollack, H.N., 1996. Terrestrial heat flow in the Parana Basin, southern Brazil. *J. Geophys. Res.-Sol. Ea.* **101**, 8659-8671.
- IPCC, 2005. Special Report on carbon Dioxide Capture and Storage. <http://www.unep.ch/ipcc/activity/srcs/>.
- IPCC, 2007a. Climate Change 2007: *Climate Changes Impacts, Adaptions, and Vulnerability*. www.ipcc-wg2.org/index.html.
- IPCC, 2007b. *Climate Change 2007: The Physical Science Basis*. Cambridge University Press.
- Johnson, J.W., Oelkers, E.H., Helgeson, H.C., 1992. SUPCRT92 - A software package for calculating the standard molal thermodynamic properties of minerals, gases, aqueous species, and reactions from 1-bar to 5000-bar and 0 °C to 1000 °C. *Comput. Geosci.* **18**, 899-947.

- Kaszuba, J.P., Janecky, D.R., Snow, M.G., 2003. Carbon dioxide reaction processes in a model brine aquifer at 200 °C and 200 bars: implications for geologic sequestration of carbon. *Appl. Geochem.* **18**, 1065-1080.
- Kaszuba, J.P., Janecky, D.R., Snow, M.G., 2005. Experimental evaluation of mixed fluid reactions between supercritical carbon dioxide and NaCl brine: Relevance to the integrity of a geologic carbon repository. *Chem. Geol.* **217**, 277-293.
- Lagache, M., 1965. Contribution a l'etude de l'alteration des feldspaths, dans l'eau, entre 100 et 200 Degr. C, sous diverses pressions de CO₂, et application a la synthese des mineraux argileux. *Bull. Soc. franc. Miner. Crist.* **88**, 223-253.
- Lagache, M., 1976. New data on the kinetics of the dissolution of alkali feldspars at 200 °C in CO₂ charged water. *Geochim. Cosmochim. Acta* **40**, 157-161.
- Lagneau, V., Pipart, A., Catalette, H., 2005. Reactive transport modelling and long term behaviour of CO₂ sequestration in saline aquifers. *Oil & Gas Science and Technology-Revue De L Institut Francais Du Petrole* **60**, 231-247.
- Lasaga, A.C., 1981a. Rate laws of chemical reactions. In: Lasaga, A.C., Kirkpatrick, R.J. (Eds.), *Kinetics of Geochemical Processes*. Mineralogical Society of America, Washington DC, pp. 1-68.
- Lasaga, A.C., 1981b. Transition State Theory, in: Lasaga, A.C., Kirkpatrick, R.J. (Eds.), *Kinetics of Geochemical Processes*. Mineralogical Society of America, Washington DC, pp. 135-169.
- Maher, K., Steefel, C.I., White, A.F., Stonestrom, D.A., 2009. The role of reaction affinity and secondary minerals in regulating chemical weathering rates at the Santa Cruz Soil Chronosequence, California. *Geochim. Cosmochim. Acta* **73**, 2804-2831.
- Manley, E.P., Evans, L.J., 1986. Dissolution of feldspar by low-molecular-weight aliphatic and aromatic acids. *Soil Sci.* **141**, 106-112.
- McCollom, T.M., Shock, E.L., 1997. Geochemical constraints on chemolithoautotrophic metabolism by microorganisms in seafloor hydrothermal systems. *Geochim. Cosmochim. Acta* **61**, 4375-4391.
- Nagy, K.L., Blum, A.E., Lasaga, A.C., 1991. Dissolution and precipitation kinetics of kaolinite at 80° C and pH 3: The dependence on solution saturation state. *Am. J. Sci.* **291**, 649-686.
- Nagy, K.L., Cygan, R.T., Hanchar, J.M., Sturchio, N.C., 1999. Gibbsite growth kinetics on gibbsite, kaolinite, and muscovite substrates: Atomic force microscopy evidence for epitaxy and an assessment of reactive surface area. *Geochim. Cosmochim. Acta* **63**, 2337-2351.

- Nagy, K.L., Lasaga, A.C., 1992. Dissolution and precipitation kinetics of gibbsite at 80°C and pH 3: The dependence on solution saturation state. *Geochim. Cosmochim. Acta* **56**, 3093-3111.
- Nagy, K.L., Lasaga, A.C., 1993. Simultaneous precipitation kinetics of kaolinite and gibbsite at 80°C and pH 3. *Geochim. Cosmochim. Acta* **57**, 4329-4335.
- Oelkers, E.H., Helgeson, H.C., 1990. Triple-ion anions and polynuclear complexing in supercritical electrolyte solutions. *Geochim. Cosmochim. Acta* **54**, 727-738.
- Oelkers, E.H., Schott, J., Devidal, J.L., 1994. The effect of aluminum, pH, and chemical affinity on the rates of aluminosilicate dissolution reactions. *Geochim. Cosmochim. Acta* **58**, 2011-2024.
- Palandri, J., Kharaka, Y.K., 2004. *A compilation of rate parameters of water–mineral interaction kinetics for application to geochemical modeling*. US Geol. Surv. Open File Report 2004-1068, 64 pp
- Parkhurst, D.L., Appello, A.A.J., 1999. *User's guide to PHREEQC (version 2)-a computer program for speciation, batch-reaction, one dimensional transport, and inverse geochemical Calculations*. Water-Resource Investigation Report. U.S. Geological Survey, p. 312.
- Perkins, E.H., Gunter, W.D., 1995. Aquifer disposal of CO₂-rich greenhouse gases: modelling of water–rock reaction paths in a siliciclastic aquifer. In: Kharaka, Y.K., Chudakov, O.V. (Eds.) *Proc. 8th Internat. Symp. Water-Rock Interaction*. A.A. Balkema, pp. 895–898.
- Reed, M.H., Spycher, N.F., 1984. Calculation of pH and mineral equilibria in hydrothermal waters with application to geothermometry and studies of boiling and dilution. *Geochim. Cosmochim. Acta*. **48**, 1479-1492.
- Robie, R.A., Hemingway, B.S., 1995. *Thermodynamic properties of minerals and related substances at 298.15 K and 1 bar (10⁵ pascals) pressure and at higher temperatures*. U.S. Geological Survey Bulletin 2131, 461p.
- Rogen, B., Fabricius, I.L., 2002. Influence of clay and silica on permeability and capillary entry pressure of chalk reservoirs in the North Sea. *Petrol. Geosci.* **8**, 287-293.
- Russell, J.D., Paterson, E., Fraser, A.R., Farmer, V.C., 1975. Adsorption of carbon dioxide on goethite (Alpha-FeOOH) surfaces, and its implications for anion adsorption. *J. Chem. Soc. Faraday Trans.* **71**, 1623-1630.

- Schramke, J.A., Kerrick, D.M., Lasaga, A.C., 1987. The reaction muscovite + quartz \rightleftharpoons andalusite + K-feldspar + water. Part I. Growth kinetics and mechanism. *Am. J. Sci.* **287**, 517-559.
- Shock, E.L., 1995. Organic acids in hydrothermal solutions: Standard molal thermodynamic properties of carboxylic acids and estimates of dissociation constants at high temperatures and pressures. *Am. J. Sci.* **295**, 496-580.
- Shock, E.L., Koretsky, C.M., 1993. Metal-organic complexes in geochemical processes: Calculation of standard partial molal thermodynamic properties of aqueous acetate complexes at high pressures and temperatures. *Geochim. Cosmochim. Acta* **57**, 4899-4922.
- Shock, E.L., Oelkers, E.H., Sverjensky, D.A., Johnson, J.W., Helgeson, H.C., 1992. Calculation of thermodynamic and transport properties of aqueous species at high pressures and temperatures. Effective electrostatic radii, dissociation constants and standard partial molal properties to 1000° C and 5 kb. *J. Chem. Soc. London, Faraday Transactions* **88**, 803-826.
- Small, J.S., 1993. Experimental determination of the rates of precipitation of authigenic illite and kaolinite in the presence of aqueous oxalate and comparison to the K/Ar ages of authigenic illite in reservoir sandstones. *Clay. Clay. Miner.* **41**, 191-208.
- Smith, J.V., Brown, W.L., 1988. *Feldspar minerals: Crystal structures, physical, chemical, and microtextural properties (2nd edition)*. 828p. Springer Verlag, Berlin.
- Sorai, A., Ohsumi, T., Ishikawa, A., Tsukamoto, K., 2007. Feldspar dissolution rates measured using phase-shift interferometry: Implications to CO₂ underground sequestration. *Appl. Geochem.* **22**, 2795-2809.
- Sorai, M., Ohsumi, T., Ishikawa, M., 2005. Nanoscale surface observation of feldspar dissolved under supercritical CO₂-water-mineral system. *Energy* **30**, 2334-2343.
- Strazisar, B.R., Zhu, C., Hedges, S.W., 2006. Preliminary modeling of the long-term fate of CO₂ following injection into deep geological formations. *Environ. Geosci.* **13**, 1-15.
- Sverdrup, H., 1990. *The Kinetics of Base Cation Release Due to Chemical Weathering*. Lund University Press, Lund.
- Sverjensky, D.A., 1987. Calculation of the thermodynamic properties of aqueous species and the solubilities of minerals in supercritical electrolyte solutions. *Reviews in Mineralogy and Geochemistry* **17**, 177-209.

- Sverjensky, D.A., Shock, E.L., Helgeson, H.C., 1997. Prediction of the thermodynamic properties of aqueous metal complexes to 1000 °C and 5 Kb. *Geochim. Cosmochim. Acta* **61**, 1359-1412.
- Tagirov, B., Schott, J., 2001. Aluminum speciation in crustal fluids revisited. *Geochim. Cosmochim. Acta* **65**, 3965-3992.
- Tanger, J.C., Helgeson, H.C., 1988. Calculations of the thermodynamic and transport properties of aqueous species at high pressures and temperatures: Revised equation of state for the standard partial molal properties of ions and electrolytes. *Am. J. Sci.* **288**, 19-98.
- Taylor, A.S., Blum, J.D., Lasaga, A.C., 2000. The dependence of labradorite dissolution and Sr isotope release rates on solution saturation state. *Geochim. Cosmochim. Acta* **64**, 2389-2400.
- Tchoubar, C., 1965. Formation de la kaolinite a partir d'albite alteree par i'eau a 200°C. Etude en microscopie et diffraction electroniques. *Soc. franc. mineralogie Cristallographie Bull* **88**, 483-518.
- Tchoubar, C., Oberlin, A., 1963. Alteration de i'albite par action de i'eau. Etude en microscopie et microdiffraction electroniques de la precipitation et de i'evolution des fibres de boehmite formee. *Jour. Microscopy* **2**, 415-432.
- Utsunomiya, S., Murakami, T., Kadohara, H., Tsukimura, K., 1999. The effect of partial pressure of carbon dioxide on anorthite dissolution. *Mineralogical Journal* **21**, 1-8.
- Van Geen, A., Robertson, A.P., Leckie, J.O., 1994. Complexation of carbonate species at the goethite surface: Implications for adsorption of metal ions in natural waters. *Geochim. Cosmochim. Acta* **58**, 2073-2086.
- Wieland, E., Stumm, W., 1992. Dissolution kinetics of kaolinite in acidic aqueous solutions at 25 °C. *Geochim. Cosmochim. Acta* **56**, 3339-3355.
- Wolery, T.J., 1992. *EQ3/6, A software package for geochemical modeling of aqueous systems: Package overview and installation guide (version 7.0)*. URCL-MA-110662-PT-I, Livermore, Calif., Univ. California, Lawrence Livermore Laboratory.
- Worden, R., Morad, S., 2003. *Clay Mineral Cements in Sandstones: Special Publication 34 of the IAS*. Wiley-Blackwell. 520 p, p. 520.
- Wyart, J., Oberlin, A., Tchoubar, C., 1963. Etude en microscopie et microdiffraction electroniques de la boehmite formee lors de i'alteration de i'albite. *Acad. Sci. Paris, Comptes Rendus* **256**, 554-555.

- Xie, Z.X., Walther, J.V., 1994. Dissolution stoichiometry and adsorption of alkali and alkaline-earth elements to the acid-reacted wollastonite surface at 25 °C. *Geochim. Cosmochim. Acta* **58**, 2587-2598.
- Xu, T., Apps, J.A., Pruess, K., 2004. Numerical simulation of CO₂ disposal by mineral trapping in deep aquifers. *Appl. Geochem.* **19**, 917-936.
- Xu, T., Apps, J.A., Pruess, K., 2005. Mineral sequestration of carbon dioxide in a sandstone-shale system. *Chem. Geol.* **217**, 295-318.
- Xu, T.F., Apps, J.A., Pruess, K., Yamamoto, H., 2007. Numerical modeling of injection and mineral trapping of CO₂ with H₂S and SO₂ in a sandstone formation. *Chem. Geol.* **242**, 319-346.
- Yang, L., Steefel, C.I., 2008. Kaolinite dissolution and precipitation kinetics at 22 °C and pH 4. *Geochim. Cosmochim. Acta* **72**, 99-116.
- Zeltner, W.A., Anderson, M.A., 1988. Surface charge development at the goethite/aqueous solution interface: effects of CO₂ adsorption. *Langmuir* **4**, 469-474.
- Zerai, B., Saylor, B.Z., Matisoff, G., 2006. Computer simulation of CO₂ trapped through mineral precipitation in the Rose Run Sandstone, Ohio. *Appl. Geochem.* **21**, 223-240.
- Zhu, C., 2005. In situ feldspar dissolution rates in an aquifer. *Geochim. Cosmochim. Acta* **69**, 1435-1453.
- Zhu, C., 2006. In situ silicate reaction rates in sandy aquifers. *Geochim. Cosmochim. Acta* **70**, A753.
- Zhu, C., 2009. Geochemical Modeling of Reaction Paths and Geochemical Reaction Networks, in: Oelkers, E.H., Schott, J. (Eds.), *Thermodynamics and kinetics of water-rock interaction*. Mineralogical Society of America, pp. 533-569.
- Zhu, C., Anderson, G.M., 2002. *Environmental Applications of Geochemical Modeling*. Cambridge University Press, London.
- Zhu, C., Blum, A.E., Veblen, D.R., 2004. Feldspar dissolution rates and clay precipitation in the Navajo aquifer at Black Mesa, Arizona, USA., in: Wanty, R.B., Seal, R.R.I. (Eds.), *Water-Rock Interaction*. A.A. Balkema, Saratoga Springs, New York, pp. 895-899.
- Zhu, C., Lu, P., 2009. Alkali feldspar dissolution and secondary mineral precipitation in batch systems: 3. Saturation indices of product minerals and reaction paths. *Geochim. Cosmochim. Acta* **73**, 3171-3200.

CHAPTER 4

ALKALI FELDSPAR DISSOLUTION AND SECONDARY MINERAL PRECIPITATION IN BATCH SYSTEMS: 3. SATURATION STATES OF PRODUCT MINERALS AND REACTION PATHS³

³ This chapter has been published as Zhu, C., Lu, P., 2009. Coupled alkali feldspar dissolution and secondary mineral precipitation in batch systems: 3. Saturation Indices of Product Minerals and Reaction Paths. *Geochimica et Cosmochimica Acta* **73**, 3171-3200.

1. INTRODUCTION

As pointed out by Drever (2004) in his foreword to the surficial geochemistry volume of the *Treatise on Geochemistry*, one fundamental assumption in geochemistry that has received relatively little attention since the initial proposal, is that partial equilibrium may exist among mineral products from the dissolution of the primary mineral (e.g., feldspar) and the aqueous solution (Garrels and Mackenzie, 1967; Helgeson, 1968, 1970, 1971, 1974; Helgeson et al., 1969, 1970; Helgeson and Murphy, 1983). The term “partial equilibrium” was used by Helgeson (1979) to describe the feldspar–water system as an example, in which all aqueous species are at equilibrium with each other and (selected) secondary minerals are at equilibrium with the aqueous solution but the aqueous solution is not at equilibrium with feldspar. As a consequence of partial equilibrium, mass transfer processes in silicate weathering systems is regarded as driven by irreversible dissolution of the primary mineral (Helgeson, 1979). A large body of literature on silicate weathering has focused on feldspar dissolution rates in soils and groundwater, with little references to the kinetics of product mineral precipitation (see reviews in Blum and Stillings, 1995; Drever and Clow, 1995; White and Brantley, 2003; Bricker et al., 2004). Over the years, it has been shown through numerical modeling of feldspar hydrolysis – secondary mineral precipitation reactions, that if the partial equilibrium assumption does not hold, aqueous chemistry evolution, mineral paragenesis, and reaction rates could deviate significantly from the Helgeson classic reaction path model (Steefel and Van Cappellen, 1990; Lasaga et al., 1994; Lasaga, 1998; Zhu et al., 2004a; Ganor et al., 2007). However, to date, the partial equilibrium hypothesis has yet to be systematically tested.

What has prompted us to re-examine this hypothesis proposed nearly half a century ago is its current relevance to the interpretation of the well known and extensively discussed apparent discrepancy between the field derived feldspar dissolution rates and those measured in the laboratory (Paces, 1983; Velbel, 1990; Brantley, 1992; Blum and Stillings, 1995; Drever and Clow, 1995; White and Brantley, 2003; Zhu, 2005; and references therein), which currently is under intense and active research. In general, field derived feldspar dissolution rates are two to five orders of magnitude slower than laboratory measured rates (*ibid*). Note, however, that when comparing field and laboratory derived rates, one must be careful that the former represent bulk and effective rates and the latter are usually measured at conditions far from equilibrium (Zhu, 2005). Nevertheless, such a large discrepancy underscores our poor understanding of some the fundamental chemical and physical processes which control silicate reaction kinetics in nature.

Numerous hypotheses have been proposed in the literature to explain the persistent discrepancy between field and laboratory feldspar dissolution rates. These hypotheses include the possible armoring effects of the secondary minerals that coat the feldspar grain surfaces (Correns and Von Engelhardt, 1938; Correns, 1940; Helgeson, 1971, 1972; Luce et al., 1972; Paces, 1973; Busenberg and Clemency, 1976; Chou and Wollast, 1984; Nugent et al., 1998), the possible effects of the leached layer (Luce et al., 1972; Busenberg and Clemency, 1976; Chou and Wollast, 1984; Hellmann et al., 1990; Brantley and Stillings, 1996; Hellmann, 1997; Nesbitt and Skinner, 2001; Oelkers, 2001), approach to saturation with respect to feldspars (Burch et al., 1993; Gautier et al., 1994; Oelkers et al., 1994; Oelkers, 2001; Beig and Luttge, 2006; Hellmann and Tisserand,

2006), biological effects, inhibition of adsorbed Al^{3+} on feldspar surfaces (Chou and Wollast, 1985; Gautier et al., 1994; Oelkers et al., 1994; Oelkers, 2001).

One distinction that differentiates the field and laboratory conditions is that weathering product minerals are often intimately associated with the primary minerals in nature (Banfield and Eggleton, 1990; Banfield et al., 1991; Banfield and Barker, 1994; Zhu et al., 2006; Hereford et al., 2007). Conversely, in laboratory experiments, the precipitation of product minerals was often avoided by adjusting the chemistry and rate of recirculation of the fluid phase. Recognizing the close association between the secondary minerals and primary mineral in the field, Zhu et al. (2004a) proposed a new hypothesis for explaining the laboratory–field discrepancy wherein the slow kinetics of secondary clay precipitation is the rate limiting step and thus controls the overall feldspar dissolution rate. Clay precipitation removes solutes from the aqueous solution, maintaining a condition of feldspar undersaturation, makes additional feldspar dissolution possible, but the slow clay precipitation (or smaller effective rate constants with respect to that for the dissolution reaction, see below) results in a steady state in which the aqueous solution is near equilibrium with feldspar. Therefore, slow clay precipitation could effectively reduce feldspar dissolution rates by orders of magnitude, in a fashion consistent with laboratory rates at conditions far from equilibrium, the control of dissolution rates by the Gibbs free energy of the reaction, and many field observations (Zhu et al., 2004a).

The potential control of slow clay precipitation on overall feldspar dissolution rates calls for rigorous testing of the above mentioned partial equilibrium hypothesis. Therefore, we have conducted a series of batch experiments of feldspar dissolution and

secondary mineral precipitation at elevated temperatures and pressures (Fu et al., 2009).

The new experiments are necessary because earlier studies, mostly conducted in the 1960s, typically did not (1) measure the aluminum concentrations that are necessary for saturation index evaluations; (2) analyze (or had the capacity to analyze with the techniques of the time) mineral products of nanometer size in great detail, or (3) take steps to ameliorate the influences of fine particles on the feldspar surfaces that were later found to produce parabolic rate law artifacts (Holdren and Berner, 1979).

This paper presents speciation–solubility modeling evaluating solid–fluid equilibria at discrete time points during physical experiments when fluid samples were analyzed. These calculations were then used to constrain fluid evolution paths in order to determine whether the partial equilibrium assumption provides a reasonable prediction for the reaction paths measured. This approach, while providing only “snapshots” and not a full “movie” of the reaction paths as could be computed using a forward reaction path modeling approach, assumptions involved in applying such a numerical model (e.g., reactive surface areas and the forms of rate laws) which would introduce such potential disadvantages that it is unlikely that we could reliably test the utility of the partial equilibrium model. It is important first to establish the evaluation of the partial equilibrium hypothesis without these assumptions.

2. BACKGROUND

To facilitate the discussions that follow, let us start with the classical reaction path model of feldspar hydrolysis (Helgeson, 1968, 1971, 1979; Helgeson et al., 1969), which

states that: (1) dissolution of primary feldspar is the rate limiting irreversible reaction and the driver of all processes in the system; (2) precipitation of all secondary minerals is instantaneous; (3) the aqueous solution is at equilibrium with or undersaturated with respect to all secondary minerals at all times; (4) fluid chemistry obeys the phase rule, such that on our two-dimensional activity–activity diagrams (abbreviated as *a–a* diagrams hereafter) at constant T and P, if three phases are present then the fluid must follow a linear phase boundary until one of the solid phases is no longer present; and (5) secondary minerals dissolve and precipitate in a paragenesis sequence as aqueous chemistry evolves. This model has been described in nearly all geochemistry textbooks (see Anderson and Crerar, 1993; Krauskopf and Bird, 1995; Drever, 1997; Faure, 1998).

Consider the classic example of K-feldspar (microcline) hydrolysis at 25 °C and 1 bar in a closed system (Fig. 1a). Because it is out of equilibrium, feldspar dissolves in pure water (with a little HCl) that initially contains essentially no Si, K, or Al. When the solution reaches point 1 on Fig. 1a, gibbsite forms and the solution is located in the gibbsite stability field. The aqueous solution has a saturation index (SI) of zero for gibbsite and is undersaturated with respect to kaolinite and muscovite. At point 2, kaolinite starts to precipitate. The coexistence of gibbsite and kaolinite buffers the activity of silica, and the fluid composition moves along the gibbsite–kaolinite boundary on the *a–a* diagram. As feldspar continues to dissolve, gibbsite is converted to kaolinite. Along 2 to 3, the saturation indices for both gibbsite and kaolinite are zero (at equilibrium) and for muscovite negative (undersaturated) (Fig. 1b). After all of the gibbsite is consumed, the fluid composition departs from the gibbsite–kaolinite boundary and traverses the kaolinite stability field toward microcline. Within the kaolinite stability field

(point 4), the solution is undersaturated with respect to gibbsite ($SI < 0$), saturated with respect to kaolinite ($SI = 0$), and undersaturated with respect to muscovite (Fig. 1b). Between points 4 and 5, as K and Si concentrations increase, the solution reaches saturation with respect to muscovite, and muscovite starts to precipitate. The coexistence of muscovite and kaolinite buffers the activity ratio (aK^+/aH^+), and the fluid composition moves horizontally along the muscovite–kaolinite boundary (points 5, 6). After all the kaolinite is consumed, the fluid composition departs from the kaolinite–muscovite boundary and evolves across the muscovite stability field towards K-feldspar. When the reaction path reaches point 7, quartz saturation is achieved. There are two different paths depending on whether quartz precipitates. If quartz precipitation is inhibited, the solution continues to evolve along the direction of point 6 → point 7, towards the K-feldspar field. If quartz precipitates, the solution would evolve along the direction of point 7 → point 8, i.e., along the quartz saturation line (dashed line). In the second case, muscovite and quartz both precipitate because the solution is supersaturated with both muscovite and quartz. It is also possible, depending on the starting point, that the reaction path would not encounter the muscovite stability but would reach the microcline field through the kaolinite field or directly from the gibbsite field into muscovite field (Helgeson, 1979; Steinmann et al., 1994). While the a – a diagrams depict the evolution of fluid chemistry (i.e., reaction path) in the feldspar–water system, the mineral abundance versus time diagram (Fig. 1c) depicts the sequential appearance and disappearance of gibbsite, kaolinite, muscovite, and quartz as the fluid moves from one stability field to another following the well known paragenesis sequence determined by thermodynamics.

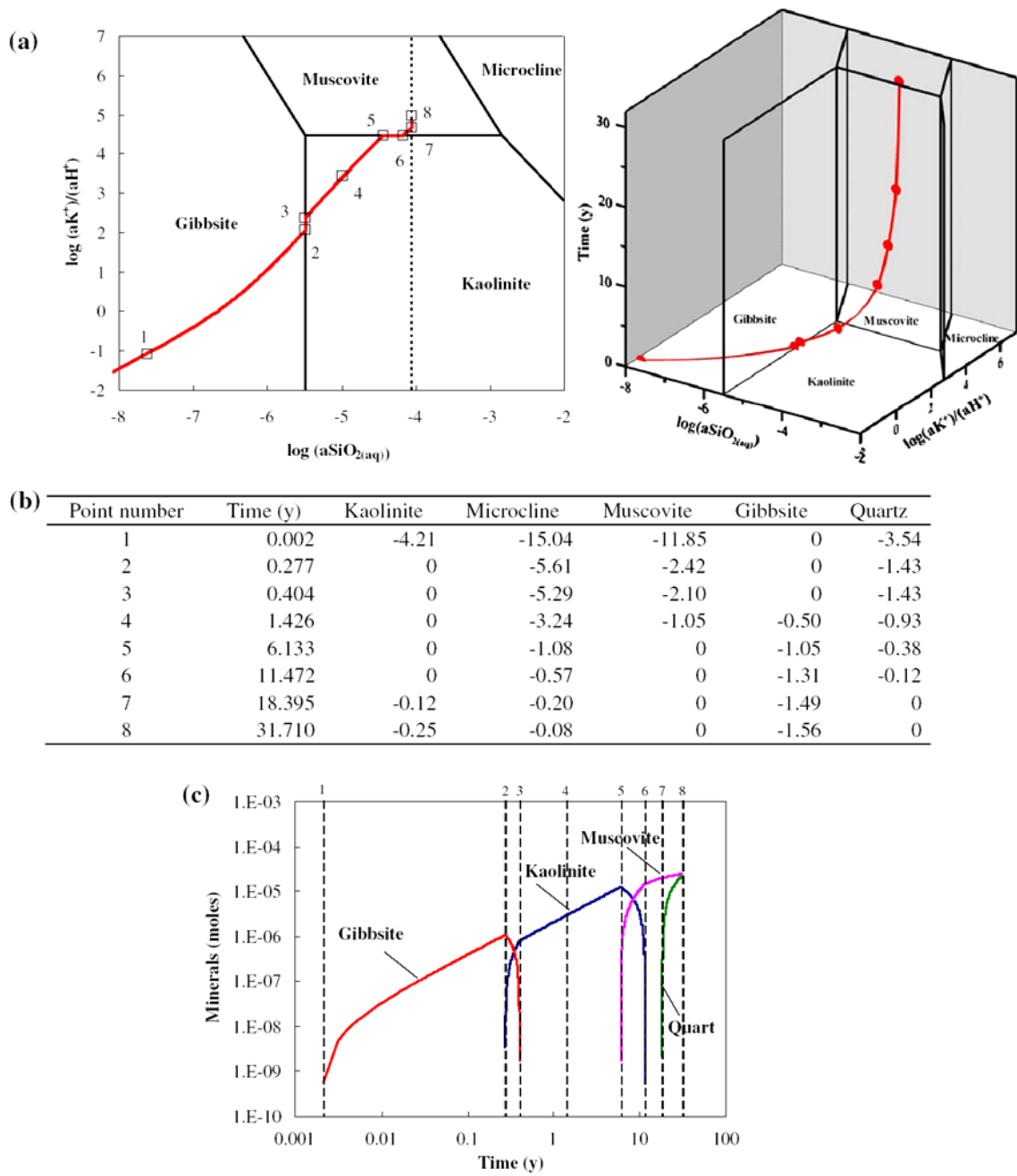


Fig. 1. Reaction path of the dissolution of microcline in pure water at 25 °C. (a) Equilibrium activity–activity diagram; (b) calculated mineral saturation indices; and (c) mineral abundance versus time. Thermodynamic data were from Table 1a, except for gibbsite (Robie and Hemingway, 1995). A linear rate law with a rate constant of $10^{-12} \text{ mol m}^{-2} \text{ s}^{-1}$ and a surface area of $0.13 \text{ m}^2/\text{g}$ (for total of 0.8 mol feldspar) for microcline was used.

Table 1a. Equilibrium constants used in this study (for the baseline case).

	25 °C 0.1 MPa	90°C, 0.1 MPa	150°C, Psat	210°C, Psat	200 °C, 30 MPa	300 °C, 8.8 MPa	Ref
Aqueous reactions							
$\text{H}_2\text{O} = \text{OH}^- + \text{H}^+$	-13.995	-12.422	-	-11.242	-11.163	-11.297	(1)
$\text{Al}^{3+} + \text{H}_2\text{O} = \text{Al}(\text{OH})^{2+} + \text{H}^+$	-4.964	-3.248	-2.129	-1.265	-1.446	-0.22	(2)
$\text{Al}^{3+} + 2\text{H}_2\text{O} = \text{Al}(\text{OH})_2^+ + 2\text{H}^+$	-10.921	-7.360	-5.045	-3.264	-3.63	-1.119	(2)
$\text{Al}^{3+} + 3\text{H}_2\text{O} = \text{Al}(\text{OH})_3^0 + 3\text{H}^+$	-17.044	-12.252	-9.168	-6.823	-7.301	-4.035	(2)
$\text{Al}^{3+} + 4\text{H}_2\text{O} = \text{Al}(\text{OH})_4^- + 4\text{H}^+$	-22.851	-17.299	13.747	-11.086	-11.572	-8.150	(2)
$\text{Al}^{3+} + \text{Na}^+ + 4\text{H}_2\text{O} = \text{NaAl}(\text{OH})_4^0 + 4\text{H}^+$	-22.90	-16.941	13.097	-10.153	-10.748	-6.63	(2)
$\text{Al}^{3+} + \text{SiO}_2^0 + 2\text{H}_2\text{O} = \text{AlH}_3\text{SiO}_4^{2+} + \text{H}^+$	-2.357	-0.276	1.026	2.001	1.86	3.188	(2)
$\text{Na}^+ + \text{H}_2\text{O} = \text{NaOH}^0 + \text{H}^+$	-14.205	-12.561	11.642	-11.047	-11.087	-10.480	(3)
$\text{SiO}_2^0 + \text{H}_2\text{O} = \text{HSiO}_3^- + \text{H}^+$	-9.585	-9.016	-8.802	-8.860	-8.707	-9.430	(3)
$\text{SiO}_2^0 + \text{Na}^+ + \text{H}_2\text{O} = \text{NaHSiO}_3^0 + \text{H}^+$	-7.754	-7.748	-7.753	-7.829	-7.767	-7.986	(3)
$\text{Ca}^{2+} + \text{H}_2\text{O} = \text{CaOH}^+ + \text{H}^+$	-12.833	-10.433	-8.903	-7.757	-7.961	-6.435	(3)
$\text{Acetate}^- + \text{H}^+ = \text{HAcetate}^0$	4.757	4.904	5.195	5.599		6.507	(4)
$\text{Acetate}^- + \text{Na}^+ = \text{NaAcetate}^0$	-0.103	0.089	0.428	0.863		1.798	(5)
$2\text{Acetate}^- + \text{Na}^+ = \text{Na}(\text{Acetate})_2^-$	-0.485	-0.361	0.246	1.078		2.736	(5)
$\text{Acetate}^- + \text{Ca}^{2+} = \text{CaAcetate}^+$	0.931	1.259	1.822	2.532		3.947	(5)
$2\text{Acetate}^- + \text{Ca}^{2+} = \text{Ca}(\text{Acetate})_2^0$	1.40	1.937	3.013	4.398		7.159	(5)
$\text{Acetate}^- + \text{Al}^{3+} = \text{Al}(\text{Acetate})_2^{2+}$	2.668	2.405	2.606	3.052		4.171	(5)
$2\text{Acetate}^- + \text{Al}^{3+} = \text{Al}(\text{Acetate})_3^+$	5.27	4.322	4.429	5.083		7.05	(5)
$3\text{Acetate}^- + \text{Al}^{3+} = \text{Al}(\text{Acetate})_3^0$	7.169	5.296	5.138	5.878		8.553	(5)
$\text{K}^+ + \text{H}_2\text{O} = \text{KOH}^0 + \text{H}^+$	-14.439	-12.584	11.551	-10.885	-10.939	-10.267	(3)
$\text{Cl}^- + \text{Ca}^{2+} = \text{CaCl}^+$	-0.292				1.146		(3)
$2\text{Cl}^- + \text{Ca}^{2+} = \text{CaCl}_2^0$	-0.644				0.672		(3)
$\text{H}^+ + \text{Cl}^- = \text{HCl}^0$	-0.710				-0.15		(6)
$\text{K}^+ + \text{Cl}^- = \text{KCl}^0$					0.456		(7)
$\text{Na}^+ + \text{Cl}^- = \text{NaCl}^0$	-0.777				0.019		(3)
$\text{HCO}_3^- + \text{H}^+ = \text{CO}_2 + \text{H}_2\text{O}$	6.345	6.343	6.724	7.305		8.525	(3)
$\text{HCO}_3^- = \text{CO}_3^{2-} + \text{H}^+$	-10.329	-10.082	-10.2	-10.534		-11.461	(3)
$\text{HCO}_3^- + \text{Na}^+ = \text{NaCO}_3^- + \text{H}^+$	-9.455					-8.468	(10)
$\text{HCO}_3^- + \text{Na}^+ = \text{NaHCO}_3^0$	-0.103					2.002	(10)
$\text{HCO}_3^- + \text{K}^+ = \text{KCO}_3^- + \text{H}^+$	-9.455					-8.468	(10)
$\text{HCO}_3^- + \text{K}^+ = \text{KHCO}_3^0$	-0.103					2.002	(10)
Mineral dissolution reactions							
$\text{NaAlSi}_3\text{O}_8 \text{ (Albite)} + 4\text{H}^+ = \text{Al}^{3+} + \text{Na}^+ + 3\text{SiO}_2^0 + 2\text{H}_2\text{O}$	2.065	-0.057	-1.713	-3.02	-2.508	-4.714	(8)
$\text{NaAlSi}_2\text{O}_7\text{H}_2 \text{ (Analcime)} + 4\text{H}^+ = \text{Al}^{3+} + \text{Na}^+ + 2\text{SiO}_2^0 + 3\text{H}_2\text{O}$	6.391	3.464	1.417	-0.155		-2.118	(8)
$\text{CaAl}_2\text{Si}_2\text{O}_8 \text{ (Anorthite)} + 8\text{H}^+ = 2\text{Al}^{3+} + \text{Ca}^{2+} + 4\text{H}_2\text{O} + 2\text{SiO}_2^0$	23.68	14.260	7.819	2.739	4.042	-3.606	(8)
$\text{AlO}_2\text{H (Boehmite)} + 3\text{H}^+ = \text{Al}^{3+} + 2\text{H}_2\text{O}$	7.610	4.023	1.660	-1.98	.242	-2.530	(9)
$\text{AlO}_2\text{H (Diaspore)} + 3\text{H}^+ = \text{Al}^{3+} + 2\text{H}_2\text{O}$	7.191	3.7	1.401	-0.407	0.02	-2.685	(8)
$\text{Al}_2\text{Si}_2\text{O}_5(\text{OH})_4 \text{ (Kaolinite)} + 6\text{H}^+ = 2\text{Al}^{3+} + 2\text{SiO}_2^0 + 5\text{H}_2\text{O}$	4.501	-0.254	-3.535	-6.119	-5.354	-9.443	(8)
$\text{KAlSi}_3\text{O}_8 \text{ (Microcline)} + 4\text{H}^+ = \text{Al}^{3+} + \text{K}^+ + 3\text{SiO}_2^0 + 2\text{H}_2\text{O}$	-1.05	-2.301	-3.434	-4.377	-3.923	-5.694	(8)
$\text{KAl}_3\text{Si}_3\text{O}_{10}(\text{OH})_2 \text{ (Muscovite)} + 10\text{H}^+ = \text{K}^+ + 3\text{Al}^{3+} + 3\text{SiO}_2^0 + 6\text{H}_2\text{O}$	11.22	3.297	-2.250	-6.687	-5.407	-12.445	(8)
$\text{NaAl}_3\text{Si}_3\text{O}_{10}(\text{OH})_2 \text{ (Paragonite)} + 10\text{H}^+ = \text{Na}^+ + 3\text{Al}^{3+} + 3\text{SiO}_2^0 + 6\text{H}_2\text{O}$	14.397	5.687	-0.328	-5.084	-3.753	-11.164	(8)
$\text{Al}_2\text{Si}_4\text{O}_{10}(\text{OH})_2 \text{ (Pyrophyllite)} + 6\text{H}^+ = 2\text{Al}^{3+} + 4\text{H}_2\text{O} + 4\text{SiO}_2^0$	-1.724	-5.394	-8.234	-10.549	-9.733	-13.647	(8)
$\text{SiO}_2 \text{ (Quartz)} = \text{SiO}_2^0$	-4.047	-3.204	-2.752	-2.414	-2.424	-2.033	(8)
$\text{KAlSi}_3\text{O}_8 \text{ (Sanidine)} + 4\text{H}^+ = \text{Al}^{3+} + \text{K}^+ + 3\text{SiO}_2^0 + 2\text{H}_2\text{O}$	-0.002	-1.571	-2.911	-4.009		-5.499	(8)
$\text{KAlSiO}_4 \text{ (Kalsilite)} + 4\text{H}^+ = \text{K}^+ + \text{Al}^{3+} + \text{SiO}_2^0 + 2\text{H}_2\text{O}$	12.543					1.187	(8)
$\text{NaAlSiO}_4 \text{ (Nepheline)} + 4\text{H}^+ = \text{Na}^+ + \text{Al}^{3+} + \text{SiO}_2^0 + 2\text{H}_2\text{O}$	13.423					1.185	(8)

(1) Haar et al. (1984); (2) Tagirov and Schott (2001); (3) Sverjensky et al. (1997); (4) Shock et al. (1995); (5) Shock and Koretsky (1993); (6) McCollom and Shock (1997); (7) Ho et al. (2000); (8) Holland and Powell (1998) for minerals and (1), (2), and (3) for aqueous species; (9) Hemingway et al. (1991) for boehmite; (10) Alekseyev et al. (1997).

Table 1b. Different sets of thermodynamic properties for aqueous and mineral species for used calculations of saturation indices[§]

Notation	A	B	C	BL=baseline case
Aqueous species	Al-bearing species and NaOH ^o from Pokrovskii and Helgeson (1995); All other species from Sverjensky et al. (1997) and those internally consistent to Sverjensky et al. (1997) in earlier Helgeson and co-workers' publications.	Al-bearing species, from Shock et al. (1997); All other species from Sverjensky et al. (1997) and those internally consistent to Sverjensky et al. (1997) in earlier Helgeson and co-workers' publications.	Al-bearing species, from Shock et al. (1997); All other species from Sverjensky et al. (1997) and those internally consistent to Sverjensky et al. (1997) in earlier Helgeson and co-workers' publications.	Al-bearing species from Tagirov and Schott (2001); KCl ^o from Ho et al. (2000); All other species from Sverjensky et al. (1997) and those internally consistent to Sverjensky et al. (1997) in earlier Helgeson and co-workers' publications.
Minerals	Al oxyhydroxides from Pokrovskii and Helgeson (1995); all others from Helgeson et al. (1978)	Helgeson et al. (1978)	Holland and Powell (1998)	Holland and Powell (1998); Boehmite from Hemingway et al. (1991)

[§]Equilibrium constants, corresponding to those listed in Table 1a for the baseline case, are listed in the Electronic Annex.

However, Lasaga (1998) used different ratios of rate constants k_i / k_{feld} , where i stands for clay minerals gibbsite, kaolinite, or muscovite, and showed that reaction paths could deviate from the classic reaction path model if the secondary minerals are not at equilibrium with the aqueous fluid. These calculations used a simplified rate law

$$R_i = k_i \frac{\Delta G_{r,i}}{RT} \text{ where } R_i \text{ stands for the rate of } i\text{th chemical reactions, } \Delta G_{r,i} \text{ the Gibbs free}$$

energy of i th reaction, R the gas constant, and T temperature in Kelvin. The rate dependence on the hydrogen ion (Helgeson et al., 1984), adsorbed aluminum (Oelkers et al., 1994), or other complicating factors were not considered in these illustrative calculations.

The deviations from partial equilibrium are manifested in two forms. First, the fluid chemistry no longer evolves along the mineral stability boundaries, but enters into another mineral stability field across the boundary at an oblique angle (hence, the

reaction path is different from the classic reaction path model in terms of fluid chemistry). Second, the secondary minerals precipitated earlier no longer dissolve completely as fluid moves into the stability field of another mineral lower in the paragenesis sequence, but persist for a duration determined by the rate constant ratios. For example, some gibbsite persists when the solution chemistry is in the stability field of kaolinite. There may be a region of coexistence of gibbsite and kaolinite, and even a region of coexisting gibbsite, kaolinite, and muscovite. These regions become larger as the ratios of k_i / k_{feld} become smaller. Zhu et al. (2004a,b) showed that when the k_i / k_{feld} ratios (or more precisely, the effective rate constants defined as $k^* = k \times \text{surface area}$) are in 10^{-2} to 10^{-4} , clay precipitation becomes the rate limiting step and a steady state persisted at which feldspar continues to dissolve near equilibrium at a much reduced rate due to the free energy effect. The term of “slow clay precipitation” in this communication refers to this scenario (i.e., $k_i^* / k_{feld}^* \ll 1$). However, these numerical predictions were intuitive and illustrative. The partial equilibrium hypothesis has not been hitherto tested systematically against experimental data.

3. MODELING RESULTS

In this paper, saturation indices (SI) for relevant minerals were calculated from the measured temperatures (T), pressures (P), and chemical compositions of experimental aqueous solutions. SI is defined as $\log(Q/K)$, where Q denotes the activity quotient and K the equilibrium constant (Zhu and Anderson, 2002, p. 45). Equilibrium activity–activity diagrams for mineral stability and phase relations were constructed to trace the evolution of the aqueous chemistry during the batch experiments. For all thermodynamic

calculations, the standard states for the solids are defined as unit activity for pure end-member solids at the T and P of interest. The standard state for water is the unit activity of pure water. For aqueous species other than H_2O , the standard state is the unit activity of the species in a hypothetical one molal solution referenced to infinite dilution at the T and P of interest. Standard state thermodynamic properties for mineral end-members were taken from Holland and Powell (1998) except for boehmite (see Supplement A), for water from Haar et al. (1984), for Al-bearing aqueous species from Tagirov and Schott (2001), $\text{KCl}^\circ(\text{aq})$ from Ho et al. (2000), and all other aqueous species from Shock and Helgeson (1988), Shock et al. (1989, 1997), and Sverjensky et al. (1997) (Table 1a). The T and P dependences of thermodynamic properties for aqueous species, when applicable, were predicted using the parameters of the revised HKF equations of state for aqueous species (Helgeson et al., 1981; Tanger and Helgeson, 1988; Shock et al., 1992).

Calculations of equilibrium constants were facilitated with a modified version of SUPCRT92 (Johnson et al., 1992) with the heat capacity function of Holland and Powell (1998) for minerals. Speciation and solubility calculations were aided with the computer codes PHREEQC (Parkhurst and Appello, 1999) and EQ3/6 (Wolery, 1992) together with our own equilibrium constant databases for the programs with thermodynamic properties noted above. Activity coefficients for the charged aqueous species were calculated from the extended Debye–Hückel equation or B-dot equation fitted to mean salt NaCl activity coefficients (Helgeson et al., 1978; Oelkers and Helgeson, 1990). Activity coefficients for neutral or uncharged aqueous species were either set to be unity (EQ3NR) or calculated from the Setchénow equation with a coefficient of 0.1 (PHREEQC). Activities coefficients for end-members of feldspar solid solutions as a

result from compositional impurities were first neglected, but the impacts on calculated SI were later assessed in Supplement A.

In evaluating the aqueous speciation and mineral saturation states at experimental conditions, we used the pH and total analytical concentrations of the constituents measured at ambient conditions (e.g., ~22 °C and 0.1 MPa) as input into the modeling codes and then “re-heated” the solution to experimental T and P . This method calculates the “in situ” pH at the experimental conditions by taking account of the effects of T and P on the distribution of aqueous species (Reed and Spycher, 1984). Owing to the relatively low experimental T , however, the calculated in situ pH values were close to those measured at ambient conditions in most cases, with an increase 0.1–0.4 units for Section 3.1, 0.1–0.4 for Section 3.2, and 0.1–0.8 for Section 3.3, and 0.1–0.2 for Section 3.4. The large differences between ambient and in situ pH values in Section 3.3 are due to the use of acetate and sodium acetate buffer, which has a large temperature variance. Note that the experimental design in Sections 3.1 and 3.2 allowed for sampling of aqueous fluids from the on-going reaction at constant T and P without quenching the reactor (Seyfried et al., 1987). Back reactions and precipitation of solids generally were not a concern.

In order to test whether the conclusions still stand when different sets of thermodynamic properties are used, SI values for primary minerals and product minerals were also calculated using three additional sets of thermodynamic properties for mineral end-members and aqueous species. These datasets are referred to A, B, and C in the following discussion, and their sources of thermodynamic properties are listed in Table 1b. The SI values calculated using these three datasets are presented as open symbols in

figures of temporal evolution of SI values, together with the baseline case (“BL” represented by solid symbols) described in the preceding paragraphs. Table 2 summarizes the batch experiments, for which geochemical modeling was carried out.

Table 2. Summary of feldspar dissolution experiments used in this study

Mineral Reactant	SA ⁽¹⁾ (m ² /g)	Initial pH	Solution Chemistry	T °C, P MPa ⁽²⁾	Reaction time (hrs)	secondary minerals	Reference
Alkali-feldspar (35% low albite; 60% orthoclase; 5% quartz)	0.132	3.1	0.20 m KCl	200, 30	1872	Boehmite + Kaolinite	Fu. et al. (2009)
Alkali-feldspar (35% low albite; 60% orthoclase; 5% quartz)	0.132	4.0	0.20 m KCl + 0.05 m CO ₂	200, 30	648	Boehmite + Kaolinite	Chapter 2, Experiment S
Anorthite	0.00333 (m ² /L)	4.69 4.97 5.4	0.3 m NaAc + HAc	90 150 210	8520 2160 3960	Bhm + Mod. Bhm ⁽³⁾ Bhm + Mod. Bhm ⁽³⁾ Bhm + Mod. Bhm ⁽³⁾ + Kaolinite	Murakami et al. (1998)
Low albite	0.12	9.0	0.1 m KHCO ₃	300, 8.8	1848	Sanidine	Alekseyev et al. (1997)
Sanidine	0.14		0.1 m NaHCO ₃			Analcime	

(1) SA stand for specific surface area except for anorthite, which is geometric SA measured by microscopic observations; (2) *T* °C, *P* bar refer temperature and pressure; (3) Bhm and Mod. Bhm refer to boehmite and modified boehmite, respectively, as reported in Murakami et al. (1998).

3.1. Alkali feldspar dissolution and clay precipitation

3.1.1. Experimental design and results

Two batch experiments for alkali feldspar dissolution in ~0.20 m KCl solution at an initial pH of 3.1 were conducted at 200 °C and 30 MPa in a flexible Au/Ti reaction cell, which was placed in a steel-alloy autoclave (Fu et al., 2009). “Orthoclase” crystals having an average size of ~0.5 cm were obtained from WARD’S Natural Sciences Establishment. X-ray diffraction (XRD) and electron microprobe analysis (EMPA) results show that the feldspar samples were perthitic alkali feldspars and were composed of 35% low albite (Ca_{0.04}Na_{0.95}K_{0.01}Al_{1.04}Si_{2.96}O₈), 60% orthoclase (K_{0.85}Na_{0.15}Al_{1.04}Si_{2.97}O₈), and 5% quartz. A time series of in situ aqueous samples was analyzed for Cl, Si, Al, K, Na, and Ca as well as trace elements. One experiment was

terminated at the end of 120 h, and the solids in the experiment were recovered for analysis. XRD and High Resolution Transmission Electron Microscopy (HRTEM) results showed boehmite and trace amount of kaolinite. Scanning Electron Microscopic (SEM) examination showed dissolution channels and the feldspar surfaces were covered with product minerals. The second experiment was terminated after 1872 h. XRD of the solids detected boehmite and kaolinite, but no detectable muscovite. SEM images of the reaction products after the batch experiments showed that hexagonally shaped secondary minerals were present on the grains of alkali feldspars, but with no clear orientation or preferential sites on the feldspar surfaces. Laminar channels and etch pits on the surface of alkali feldspars indicated dissolution heterogeneity. The surface coverage of the secondary minerals was approximately 20%.

3.1.2. Reaction paths and mineral saturation indices

The time evolution of aqueous chemistry in the system $\text{Na}_2\text{O}-\text{K}_2\text{O}-(\text{Al}_2\text{O}_3)-\text{SiO}_2-\text{H}_2\text{O}-\text{HCl}$ system is traced on $a-a$ diagrams (Fig. 2). The parentheses on Al_2O_3 indicate that Al_2O_3 is used as the balancing component in writing reversible reactions for this system. Although three-dimensional (3D) phase diagrams with axes of $\log a\text{SiO}_{2(\text{aq})}-\log(a\text{K}^+/a\text{H}^+)-\log(a\text{Na}^+/a\text{H}^+)$ represent the reaction paths more realistically, the 3D diagrams in publications are difficult to view without the ability to rotate the axes. Therefore, although we constructed the 3D $a-a$ diagrams and used them for data analysis, we present the $a-a$ diagrams in two-dimensions (2D), which can be viewed as the 2D projection of the three-dimensional diagrams on the plane that intersects zero on the third axis. Because this experiment is a K^+ -dominated system with respect to Na^+ , we present the 2D $\log a\text{SiO}_{2(\text{aq})}-\log(a\text{K}^+/a\text{H}^+)$ $a-a$ diagrams, which approximately portray the phase

relations pertaining to the experimental system. Microcline was used in place of orthoclase because thermodynamic properties for orthoclase are not available in the database of Holland and Powell (1998) or any other databases known to us. To illustrate the temporal evolution of the system, we added time as the vertical axis in Fig. 2b.

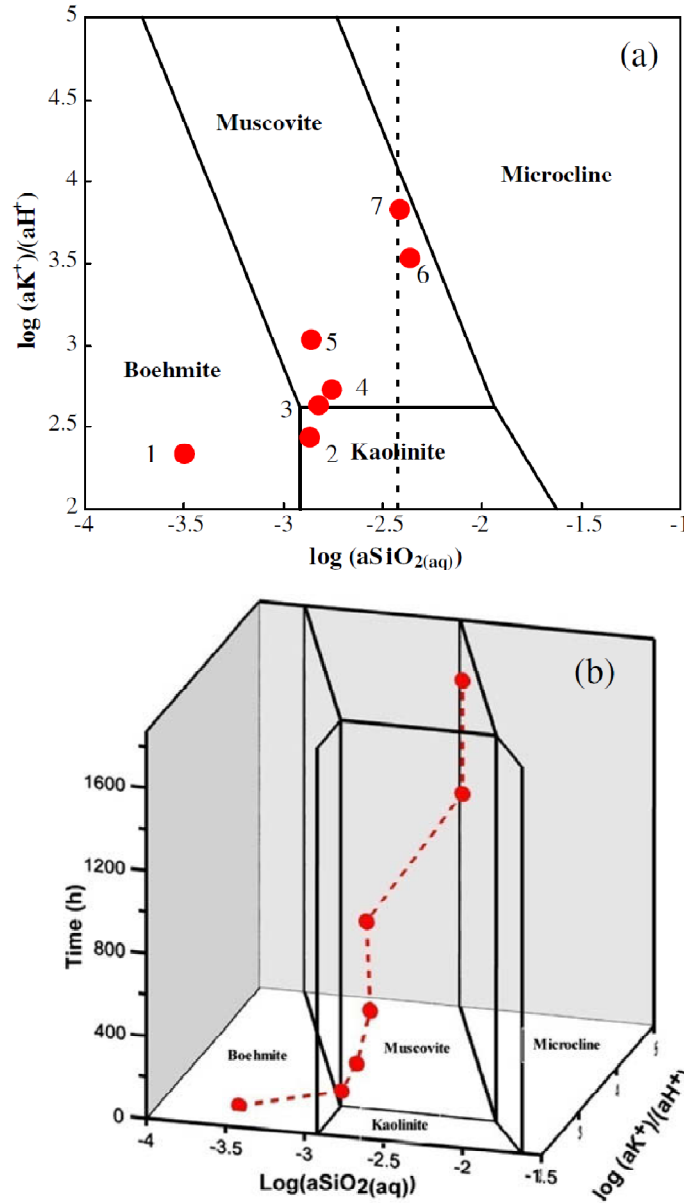


Fig. 2. Activity–activity diagrams showing the phase relations in the system $K_2O-(Al_2O_3)-SiO_2-H_2O-HCl$ at 200 °C and 30 MPa. The dashed line in (a) denotes quartz saturation. Symbols represent experimental results of alkali feldspar dissolution in 0.2 m KCl solution at 200 °C and 30 MPa (Fu et al., 2009, see Section 3.1). The activity and

activity ratios were obtained from speciation modeling of the experimental system $\text{Na}_2\text{O}-\text{K}_2\text{O}-(\text{Al}_2\text{O}_3)-\text{SiO}_2-\text{H}_2\text{O}-\text{HCl}$, based on the experimental solution chemistry data of Fu et al. (2009) and equilibrium constants listed in Table 1a. Points 1–7 represent experiment solutions at reaction time of 24, 120, 216, 456, 816, 1368, and 1872 h, respectively. The red dashed line in (b) connecting experimental data is for visualization of fluid chemical evolution.

The solution chemistry fell within the boehmite stability field after 24 h. The 120 h sample showed that the aqueous fluid crossed the boehmite–kaolinite boundary and entered into the kaolinite stability field. Fluid chemistry fell in the muscovite stability field from 216 to 1872 h, but muscovite was not detected in the products (Fu et al., 2009). Dissolution of the microcline should have stopped at 456 h because the microcline was supersaturated at this point (see below), but the fluid chemistry did not reach the microcline stability field even at the end of the experiment. It should be noted that the conventional “stability fields” represent equilibrium phase relationships, but the saturation indices were determined by speciation-solubility calculations with a numerical code.

Although albite continued to dissolve in the experiment (Fu et al., 2009), the 2D $\log a\text{SiO}_{2(\text{aq})}-\log(a\text{Na}^+/a\text{H}^+)$ diagram is omitted here because it gives misleading projection that samples 3–7 fell within the kaolinite stability. In the 3D $a-a$ diagram (not shown), it is clear that these samples fell within the muscovite stability field in this K^+ -dominated system.

SI values of the minerals of interest were calculated at each sampling time (Table 3). All sampled solutions were undersaturated with respect to albite (i.e., the major reactant), but the experimental solution changed from undersaturation with respect to microcline from 24 to 216 h to supersaturation at 456 h. The solutions reached

supersaturation with respect to boehmite, kaolinite, and muscovite at the earliest sampling time of 24 h, and these phases continued to be supersaturated during the entire experiment (Fig. 3 and Table 3). Boehmite SI decreased slightly from 24 to 216 h coinciding with the fluid chemistry entries into the kaolinite field, increased to a maximum of 2.4 at 456 h, and then decreased toward the end of the experiment. Kaolinite SI showed a maximum at 456 h, and then decreased toward the end of the experiment.

Table 3. Mineral saturation indices at each sampling time in experiments for the alkali feldspar dissolution in 0.2 m KCl solution at 200 °C and 30MPa[†].

Time (h)	In situ pH	Albite	Boehmite	Diaspore	Kaolinite	Microcline	Muscovite	Paragonite	Pyrophyllite	Quartz
24	3.3	-6.80	1.23	1.45	1.30	-2.75	1.67	-2.62	-1.30	-1.07
(120)	3.4	-4.80	0.93	1.15	1.96	-1.08	2.75	-1.22	0.61	-0.44
216	3.6	-4.37	0.90	1.13	2.01	-0.75	3.02	-0.83	0.75	-0.39
456	3.7	-2.33	2.40	2.62	5.13	1.02	7.79	4.20	3.99	-0.33
816	4.0	-2.66	2.11	2.33	4.34	0.75	6.93	3.28	3.02	-0.43
1368	4.5	-1.02	1.47	1.69	4.05	2.07	6.98	3.65	3.71	0.06
(1872)	4.8	-2.36	0.26	0.48	1.53	1.02	3.50	-0.12	1.09	0.01

[†]Solution chemistry data are from (Fu et al., 2008). The parentheses on time in the first column on left denote to the time that the experiment was terminated and solids were recovered for characterization. In situ pH was calculated from the speciation modeling.

The supersaturation of kaolinite and muscovite while the fluid chemistry is located in the boehmite stability field, and the supersaturation of boehmite while the fluid chemistry is located in the kaolinite and muscovite fields, indicate a departure from partial equilibria between the aqueous solution and the secondary phases. Lasaga (1998) found muscovite supersaturation while the fluid is in the kaolinite field in the reaction path simulations that incorporated kinetics of secondary mineral dissolution and precipitation.

The solution was undersaturated with respect to paragonite from 24 h to 216 h, but supersaturated from 456 h to 1872 h (Table 3) while the solution was located in the muscovite stability field. The sampled solutions were undersaturated with respect to quartz up to 816 h, but close to equilibrium with quartz after 1368 h (Table 3).

The conclusion of supersaturation of product minerals for the baseline case (with solid symbols and connecting lines in Fig. 3) seems to sustain when different sets of thermodynamic properties are used (Fig. 3, open symbols and labeled as “A”, “B”, “C”, see Table 1b). In other words, the uncertainties of the thermodynamic properties for mineral end-members and aqueous species are not large enough to result in indications of opposite reaction directions for the experiments examined. To evaluate the baseline case further, the propagated errors in SI values were calculated for 95% confidence interval from the reported standard deviation of enthalpy of formation at 25 °C alone (Hemingway et al., 1991; Holland and Powell, 1998).

The reaction path from sample at 816 h to samples at 1368 h and 1872 h requires the total consumption of boehmite in the partial equilibrium case. However, as noted earlier, the prolonged experiment did not show the disappearance of boehmite even though the solution chemistry had drastically departed from the boehmite field (Fig. 2b). In other words, the experimental data did not show sequential mineral dissolution and precipitation or paragenesis from boehmite to kaolinite to muscovite, as predicted by theoretical calculations assuming partial equilibrium between the product minerals and the aqueous solution with evolving chemistry. It should also be noted that the solution reached boehmite supersaturation very quickly after the experiment commenced (the earliest sampling time was 24 h after the experiment started).

3.2. Alkali feldspar dissolution and clay precipitation in CO₂ Charged systems

3.2.1. Experimental design and results

These two batch experiments for alkali feldspar dissolution were similar in design to those presented in the preceding section. However, the experiments differed by adding 50 mM CO₂ into the experimental charge. One experiment was terminated at the end of 120 h, and a second experiment was terminated after 648 h. SEM images of the reaction products showed extensive dissolution features and secondary mineral coverage on feldspar grain surfaces. TEM study detected boehmite in samples after 120 h reaction, and XRD patterns indicated boehmite and possibly muscovite in the 648 h sample. The fluid chemistry data are presented in Chapter 2 (experiment S).

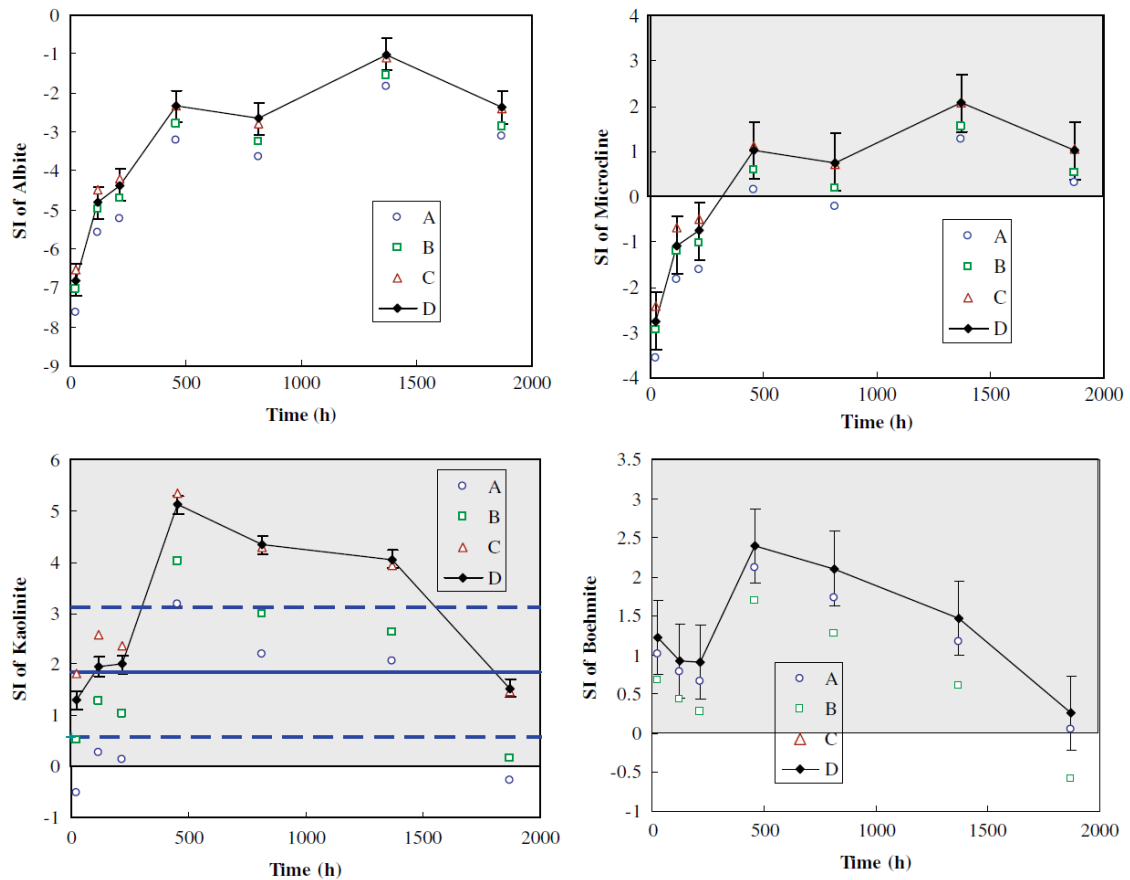


Fig. 3. Mineral saturation indices during the course of alkali feldspar dissolution in 0.2 m KCl solution at 200 °C and 30 MPa (Fu et al., 2009, see Section 3.1). “BL” (baseline case, Table 1a), and “A”, “B”, and “C” stand for calculated SI using thermodynamic datasets as described in Table 1b. Vertical errors bars represent the uncertainty from the ΔH_f° at 25 °C alone. The gray shaded areas highlight mineral supersaturation. For the kaolinite graph, the solid line stands for zero SI of halloysite and dashed lines variations of SI values resulting from the 2σ of ΔG_f° of halloysite.

3.2.2. Reaction paths and mineral saturation indices

The reaction paths from these two batch experiments (Fig. 4) are different from those in the counterpart experiments without CO₂ (cf. Fig. 2) because they started with a higher initial pH so that the kaolinite field was skipped. SI values of the minerals of interest are listed in Table 4. All sampled solutions were undersaturated with respect to albite, but the experimental solution changed from undersaturation with respect to microcline to supersaturation after 24 h. As in the experiments without CO₂, the solutions attained supersaturation with respect to boehmite, pyrophyllite, kaolinite, and muscovite at the earliest sampling time of 24 h, and these phases were supersaturated during the entire experiment (Fig. 5 and Table 4). The supersaturation of muscovite while the fluid chemistry has located in the boehmite stability field, and the supersaturation of boehmite while the fluid chemistry was located in the muscovite stability field are, again, indicative of a departure from partial equilibria between the aqueous solution and secondary phases (Lasaga, 1998).

Similar to what Steinmann et al. (1994) illustrated in classroom exercises at room temperature, the fluid chemistry would be fixed at a point on the boehmite–muscovite boundary for the partial equilibrium case because the reaction



does not change aqueous compositions of the system. However, the experimental data show that the aqueous fluid departed from the boehmite–muscovite boundary while boehmite was still observed at the end of the experiment. Apparently, partial equilibria were not observed.

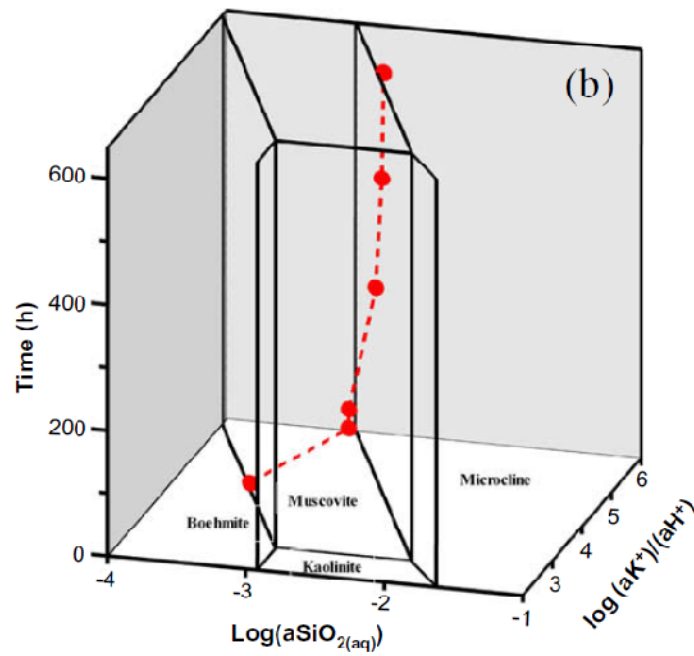
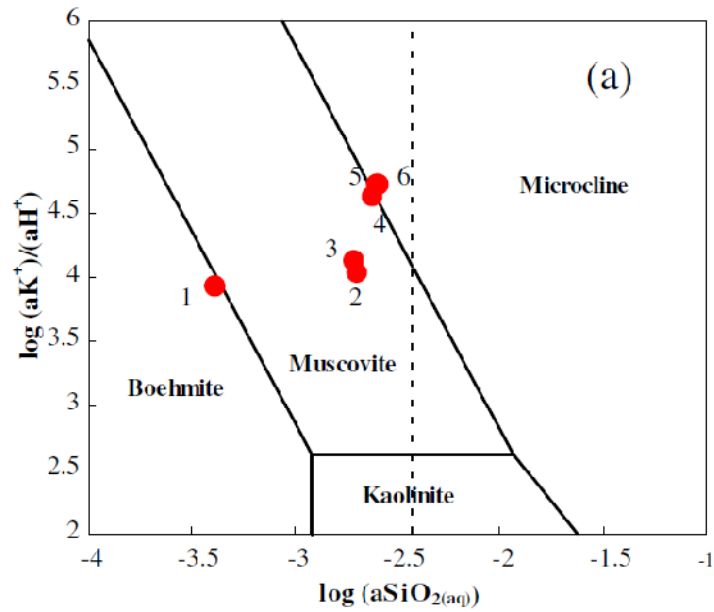


Fig. 4. Activity–activity diagrams showing the phase relations in the system K_2O – (Al_2O_3) – SiO_2 – H_2O – HCl at 200 °C and 30 MPa. The dashed line in (a) denotes quartz saturation. Solid dots represent experimental results of alkali feldspar dissolution in 0.2 m KCl and 0.05 m CO_2 solution at 200 °C and 30 MPa (cf. Section 3.2 and Chapter 2). The activity and activity ratios were obtained from speciation modeling of the experimental system Na_2O – K_2O – Al_2O_3 – SiO_2 – H_2O – HCl – CO_2 , based on the experimental solution chemistry data in Chapter 2 (Experiment S) and equilibrium constants listed in Table 1a. The red dashed line in (b) connecting experimental data is for visualization of fluid chemical evolution.

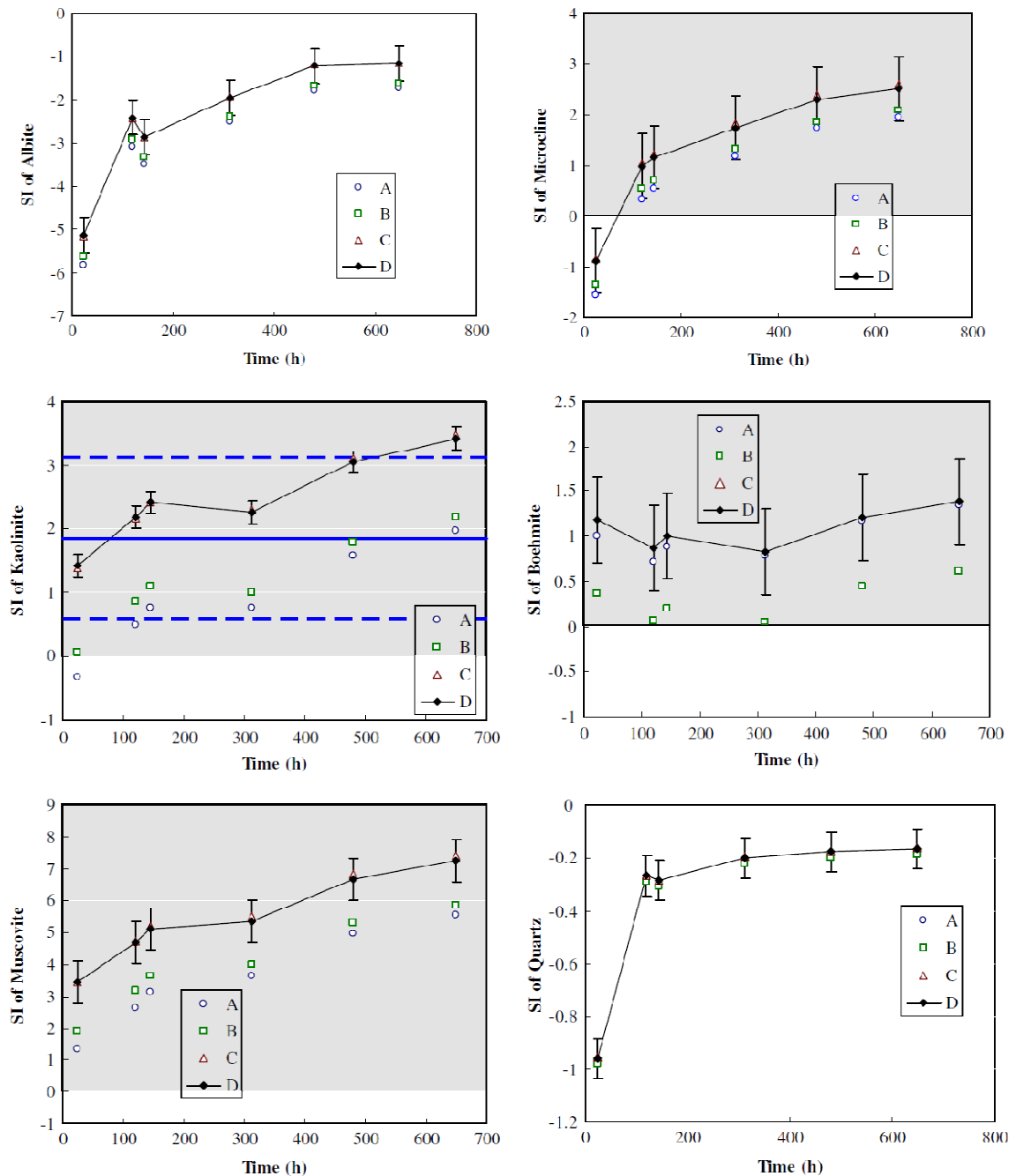


Fig. 5. Mineral saturation indices during the course of alkali feldspar dissolution in 0.2 m KCl and 0.05 m CO₂ solution at 200 °C and 30 MPa (cf. Section 3.2 and Chapter 2). See the caption for Fig. 3 for notations.

Table 4. Mineral saturation indices at each sampling time in experiments for the alkali feldspar dissolution in 0.2 m KCl and 0.05 m CO₂ solution at 200 °C and 30 MPa[†].

Time (h)	In situ pH	Albite	Boehmite	Diaspore	Kaolinite	Microcline	Muscovite	Paragonite	Pyrophyllite	Quartz
24	4.9	-5.13	1.18	1.40	1.43	-0.88	3.44	-1.04	-0.96	-0.96
(120)	5.0	-2.41	0.87	1.09	2.18	0.99	4.69	1.06	1.19	-0.27
144	5.1	-2.85	1.00	1.22	2.42	1.16	5.13	0.88	1.38	-0.29
312	5.6	-1.94	0.83	1.05	2.25	1.75	5.37	1.44	1.39	-0.20
480	5.7	-1.22	1.21	1.43	3.05	2.30	6.68	2.93	2.23	-0.18
(648)	5.7	-1.17	1.38	1.61	3.43	2.51	7.25	3.33	2.63	-0.16

[†]See solution analytical data in Chapter 2 (Experiment S). The parentheses on time in the first column on left denote to the time that the experiment was terminated and solids were recovered for characterization. In situ pH was calculated from the speciation modeling.

3.3. Anorthite dissolution batch experiments

3.3.1. Experimental design and results

Murakami et al. (1998) performed three series of batch experiments for anorthite (An₉₅Ab₅) dissolution in 0.03M sodium acetate at 90, 150, and 210 °C with a room temperature initial pH of 4.56. Single crystals of anorthite were prepared by crushing and pieces with fresh surfaces approximately 1 x 1 x 1 mm in size were selected. The geometric surface areas of the single crystals were estimated under a light microscope (Table 2). The crystals were washed ultrasonically in acetone in an attempt to remove fine particles from the surface. Experimental runs were from 72 h to 8520 h. After the run, the reaction vessel was cooled to room temperature within 30 min, and the aqueous solution was filtered with 0.22 µm filters. Secondary minerals formed during the experiments were identified with XRD, SEM, and HRTEM. A sequence of secondary minerals, including boehmite, “modified boehmite” with silica, and kaolinite, was formed with increasing reaction time. Table 5 summarizes their reported experimental times when the different product minerals were observed.

Table 5. Mineral saturation indices in the experiments for anorthite dissolution in 0.03 M NaAc and HAc solutions[†]

	T (h)	Product minerals [‡]	pH (in situ)	albite	anorthite	boehmite	kaolinite	paragonite	pyrophyllite	quartz
90°C	72	b	4.71	-4.88	-7.02	2.54	3.68	2.55	-0.88	-1.65
	240	b	4.63	-1.86	-4.27	3.52	6.94	7.36	3.67	-1.00
	720	b	4.67	-0.11	-1.33	3.61	8.25	9.37	6.13	-0.43
	2160	mb	4.65	-0.48	-3.26	2.08	5.95	5.89	4.59	-0.05
	3816	mb	4.69	0.49	-1.24	2.98	7.84	8.76	6.55	-0.01
	8520	mb	4.72	0.59	-1.30	2.73	7.58	8.40	6.54	0.12
150°C	72	b	4.98	-2.73	-3.78	1.23	2.20	1.67	-0.21	-0.80
	240	b	4.92	0.25	0.83	2.91	6.45	7.98	4.93	-0.36
	720	mb	4.93	1.02	1.72	3.02	7.11	8.98	6.02	-0.14
	2160	mb	4.99	0.48	0.13	1.88	5.21	6.19	4.50	0.05
210°C	72	b?	5.31	-1.94	-1.86	0.72	1.09	1.17	-0.55	-0.62
	240	mb	5.30	-0.71	-0.19	1.19	2.54	3.33	1.41	-0.37
	816	mb	5.36	-0.39	0.23	1.21	2.74	3.69	1.77	-0.29
	2328	mb k	5.36	-0.14	0.37	1.08	2.73	3.67	2.02	-0.16
	3960	mb k	5.47	0.15	0.71	0.99	2.74	3.80	2.21	-0.07

[†]Solution chemistry experimental data from Murakami et al. (1998); [‡]Product minerals observed by Murakami et al. (1998) “b” stands for boehmite; “mb” for modified boehmite; “k” for kaolinite. In situ pH was calculated from the speciation modeling performed in this study.

3.3.2. Reaction path and mineral saturation indices

The time evolution of Murakami et al.’s (1998) aqueous solution chemistry in the system CaO–Na₂O–(Al₂O₃)–SiO₂–H₂O–HCl–acetate was traced on the *a–a* diagrams (Fig. 6). In all experiments, the solution chemistry quickly evolved from the boehmite stability field to the kaolinite stability field after 240, 72, and 72 h, at 90, 150 and 210 °C, respectively. The solution chemistry stayed within the kaolinite field with little change for thousands more hours. This results in an almost vertical trend on the 3D *a–a–t* diagrams (Fig. 6b). Murakami et al. (1998) found that boehmite and “modified boehmite” are the main product minerals from anorthite dissolution at 90, 150, and 210 °C. Kaolinite was found after 2328 h of experiment at 210 °C, long after the solution chemistry had entered into the kaolinite stability field.

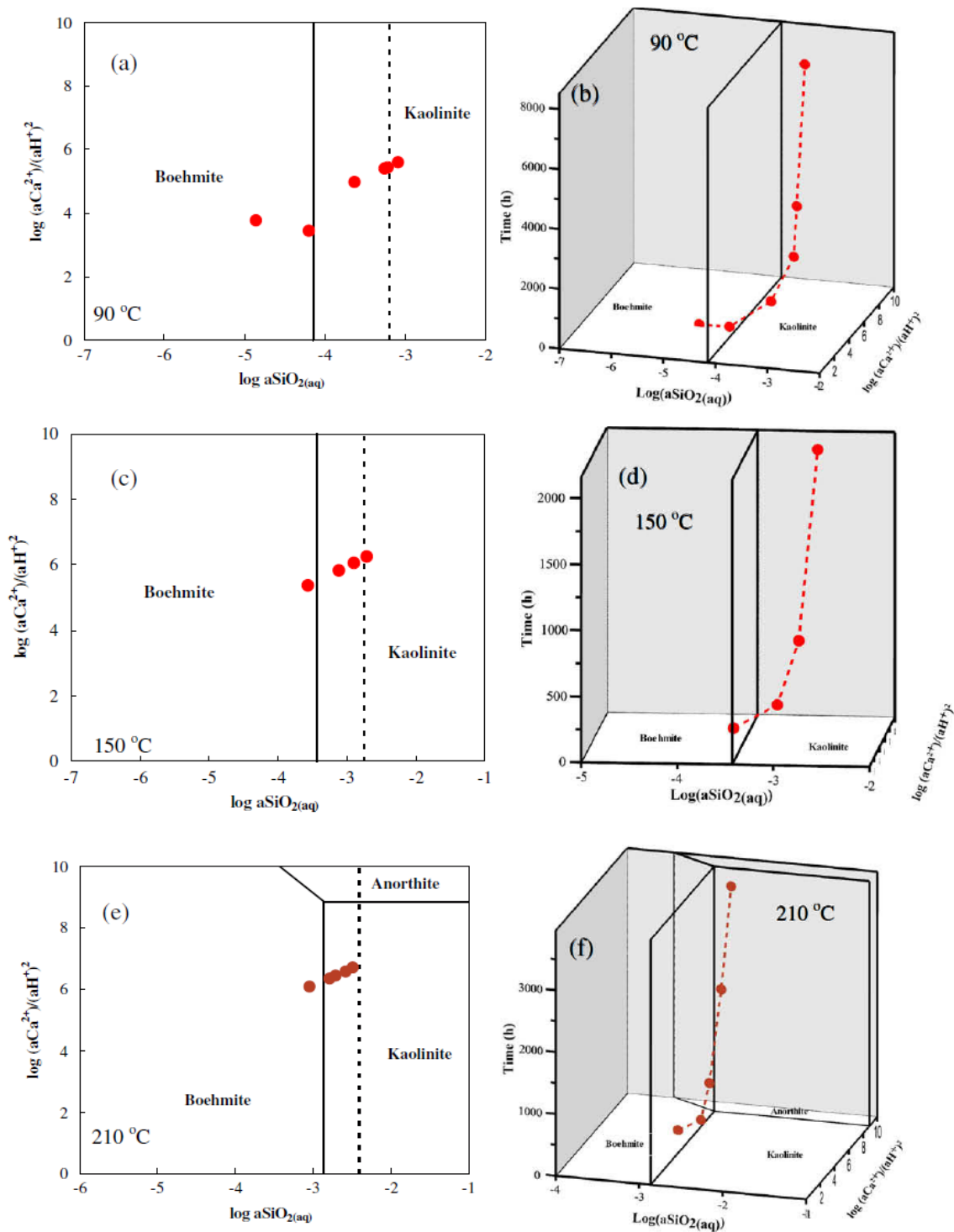


Fig. 6. Activity–activity diagrams showing the phase relations in the system $\text{Ca}_2\text{O}-(\text{Al}_2\text{O}_3)\text{-SiO}_2\text{-H}_2\text{O}$ at 90 °C (a and b), 150 °C (c and d), and 210 °C (e and f) and pressures of vapor saturation. The dashed lines in (a, c and e) denote quartz saturation. Solid dots represent experimental results of anorthite dissolution in 0.03 m NaAc solutions, which were published in Murakami et al. (1998). The activity and activity

ratios were obtained from speciation modeling of the experimental system $\text{Ca}_2\text{O}-\text{Al}_2\text{O}_3-\text{SiO}_2-\text{H}_2\text{O}-\text{HAc}-\text{NaAc}$, based on the experimental solution chemistry data from Murakami et al. (1998) and equilibrium constants listed in Table 1a. The red dashed lines in (b, d and f) connecting experimental data are for visualization of fluid chemical evolution.

The solutions were supersaturated with respect to boehmite and kaolinite during the entire experiments at 90, 150, and 210 °C (Fig. 7 and Table 5). Kaolinite supersaturation occurred when the fluid chemistry was still located in the boehmite field. The solutions were undersaturated with respect to anorthite during the 90 °C experiment, but changed from undersaturation to supersaturation at 150 °C after 240 h, and 210 °C after 816 h (Fig. 7 and Table 5). At 90 and 150 °C, anorthite SI did not vary monotonically. There was an increase, and then a decrease with time, probably coincident with precipitation of product mineral(s). Murakami et al. (1998) believed that anorthite dissolution continued during the entire experiment as evidenced by the continued increase of Ca^{2+} concentrations. Therefore, the calculated SI (>0) of anorthite in the experiments could result from uncertainties of thermodynamic properties for anorthite, which show an unusually large range in the literature (Arnórsson and Stefánsson, 1999). The experimental solutions were also supersaturated with respect to paragonite. The experimental solutions were close to quartz saturation at the end of the experiments.

3.4. Sanidine and albite dissolution experiments

Alekseyev et al. (1997) conducted two series of batch experiments. The first one was for sanidine ($\text{KNa}_{0.03}\text{Al}_{0.99}\text{Si}_3\text{O}_8$) dissolution in 0.1 m NaHCO_3 solution and the second series for low albite ($\text{Na}_{0.97}\text{K}_{0.02}\text{AlSi}_3\text{O}_8$) dissolution in 0.1 m KHCO_3 solution, both at 300 °C and 88 bars and with duration as long as 1848 h (Alekseyev

et al., 1997). The pH was buffered by the dissolved carbonate and bicarbonate to near 9. XRD and SEM results indicate that the secondary minerals formed for sanidine and albite dissolution were analcime ($\text{NaAlSi}_2\text{O}_6 \cdot \text{H}_2\text{O}$) (after ~7 h) and sanidine (after ~16 h), respectively. Alekseyev et al. (1997) carried out speciation–solubility modeling to evaluate the saturation states for the primary and secondary minerals in their experimental solutions. They also performed mathematical calculations to show that the partial equilibrium assumption would not be consistent with their temporal solute concentration data. Here, we conducted speciation–solubility modeling using their experimental data, but with four different sets of thermodynamic properties for minerals and aqueous species (see Table 1b), which is different from the thermodynamic data set that they used. We also traced the solution chemistry evolution on phase *a–a* diagrams.

3.4.1. Sanidine dissolution in NaHCO_3 solution

The evolution of the aqueous solution chemistry during Alekseyev et al.’s (1997) experiments is depicted in the *a–a* diagrams for the $\text{Na}_2\text{O–K}_2\text{O–(Al}_2\text{O}_3\text{)–SiO}_2\text{–H}_2\text{O–CO}_2$ system, projected for the zero $\log(a\text{K}^+/a\text{H}^+)$ for the Na dominated experimental system (Fig. 8). The solution chemistry evolved from the paragonite stability field to the analcime stability field after 0.25 h. The solution stayed in the analcime stability field from 0.25 to 7 h, and entered into the albite stability field and stayed there until the end of the experiment (16–1848 h) (Fig. 8b). Even though the solution chemistry fell in the albite stability field, albite was not detected with either XRD or SEM and was undersaturated (see below). Alekseyev et al. (1997) observed analcime precipitation from

16 to 1848 h. Because both the pH of the solution was buffered around 9 and Na^+ was predominant, the $a\text{Na}^+/a\text{H}^+$ ratios stayed nearly constant.

Saturation indices for minerals of interest were calculated for each experiment (Fig. 9 and Table 6). The solutions were undersaturated with respect to sanidine during the entire experiment (Fig. 9 and Table 6). The solutions were supersaturated with respect to analcime and albite during 7 to 72 h and 16 to 72 h reaction time, respectively. During the other time intervals, the solutions were undersaturated with respect to analcime and albite. The apparent conflict between calculated $\text{SI} < 0$ values and the observation of continued analcime precipitation (Alekseyev et al., 1997) is puzzling, but could be related to uncertainties in the thermodynamic properties for analcime. As a member of the zeolite group, analcime may have a range of chemical compositions and structural details. Our calculated analcime SI values are within 0.2 units of those calculated by Alekseyev et al. (1997) who used different thermodynamic properties but also showed negative SI while reporting analcime precipitation. However, it is clear from the experimental data that, although the experiments had progressed into the albite stability field, analcime is the mineral that was detected.

3.4.2. Albite dissolution in KHCO_3 solution

Activity–activity diagrams projected for the zero $\log(a\text{Na}^+/a\text{H}^+)$ for this K-dominated experimental system in the $\text{K}_2\text{O}\text{--}\text{Na}_2\text{O}\text{--}(\text{Al}_2\text{O}_3)\text{--}\text{SiO}_2\text{--}\text{H}_2\text{O}\text{--}\text{CO}_2$ system are shown in Fig. 10. The solution chemistry evolved from the muscovite stability field to the sanidine stability field after only 0.5 h. For the next 16 h, fluid chemistry moved horizontally in the sanidine field as the $a\text{K}^+/a\text{H}^+$ ratios were buffered and silica activity increased with time. Thereafter, the fluid chemistry changed little from 16 to 1848 h

within the sanidine field, which is manifested on overlapping data points on the 2D diagram (Fig. 10a) and a straight vertical line on the 3D diagram (Fig. 10b). Alekseyev et al. (1997) observed that sanidine precipitated during this period of time.

The solutions were undersaturated with respect to albite during the entire experiment and supersaturated with respect to sanidine after 1.25 h (Table 7 and Fig. 11), shortly after the solution chemistry entered into the sanidine field at 0.5 h. Alekseyev et al. (1997) observed no sanidine precipitation during this time period, and their analysis of solution chemistry stoichiometry showed that albite dissolution was congruent. The solution was undersaturated with respect to muscovite during the time (0–0.5 h) while the fluid composition was located in the muscovite stability field. After that, for the duration of the experiment, muscovite was either supersaturated (7–48 h) or undersaturated (all other times).

Alekseyev et al. (1997) concluded that slow precipitation of secondary minerals dominated the overall reactions in these two experimental series. The relatively higher temperature (300 °C) in the experiments resulted in fast chemical evolution into the field of more stable phases, but a steady state was reached for the coupled dissolution–precipitation reactions (Figs. 8b and 10b), which prevailed during the majority of the experiments. Zhu et al. (2004a,b) used reaction path modeling to show that such a steady state could be reached when the effective precipitation rate constants are lower than the dissolution effective rate constants.

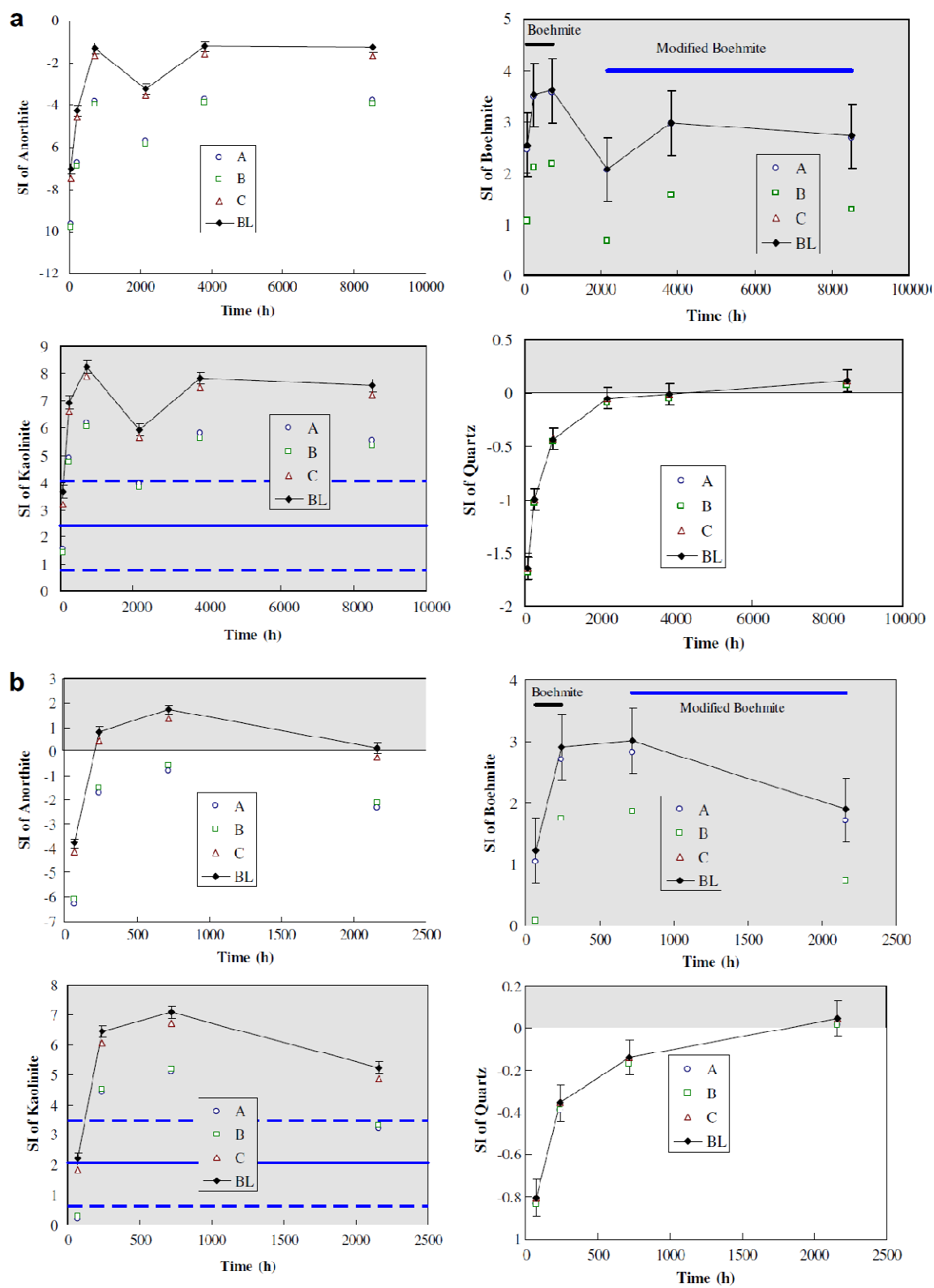


Fig. 7. To be continued.

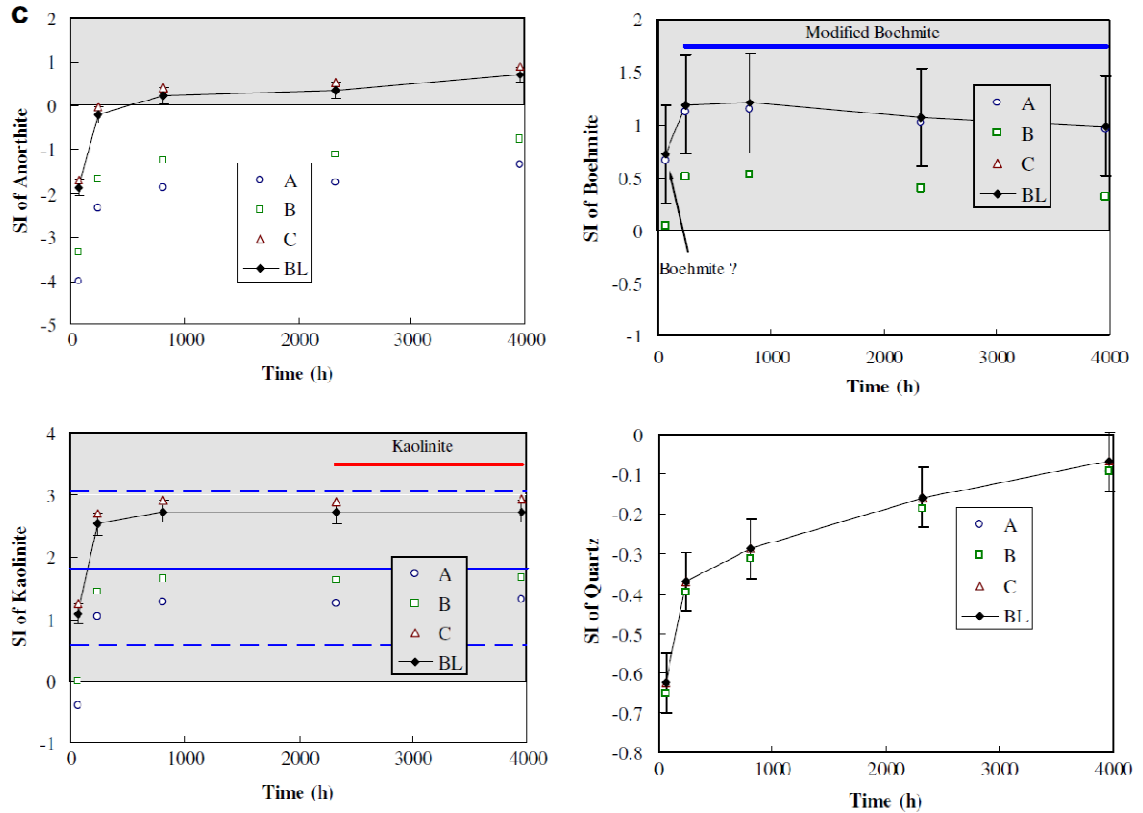


Fig. 7. (a) Calculated saturation indices for anorthite dissolution experiments (Murakami et al., 1998) at 90 °C. See the caption for Fig. 3 for notations. The bars in the boehmite graph indicate the time scale when the respective phases were observed in the mineralogical analysis. (b) Calculated saturation indices for anorthite dissolution experiments (Murakami et al., 1998) at 150 °C. See the caption for Fig. 3 for notations. The bars in the boehmite graph indicate the time scale when the respective phases were observed in the mineralogical analysis. (c) Calculated saturation indices for anorthite dissolution experiments (Murakami et al., 1998) at 210 °C. See the caption for Fig. 3 for notations. The bars in the boehmite and kaolinite graphs indicate the time scale when the respective phases were observed in the mineralogical analysis.

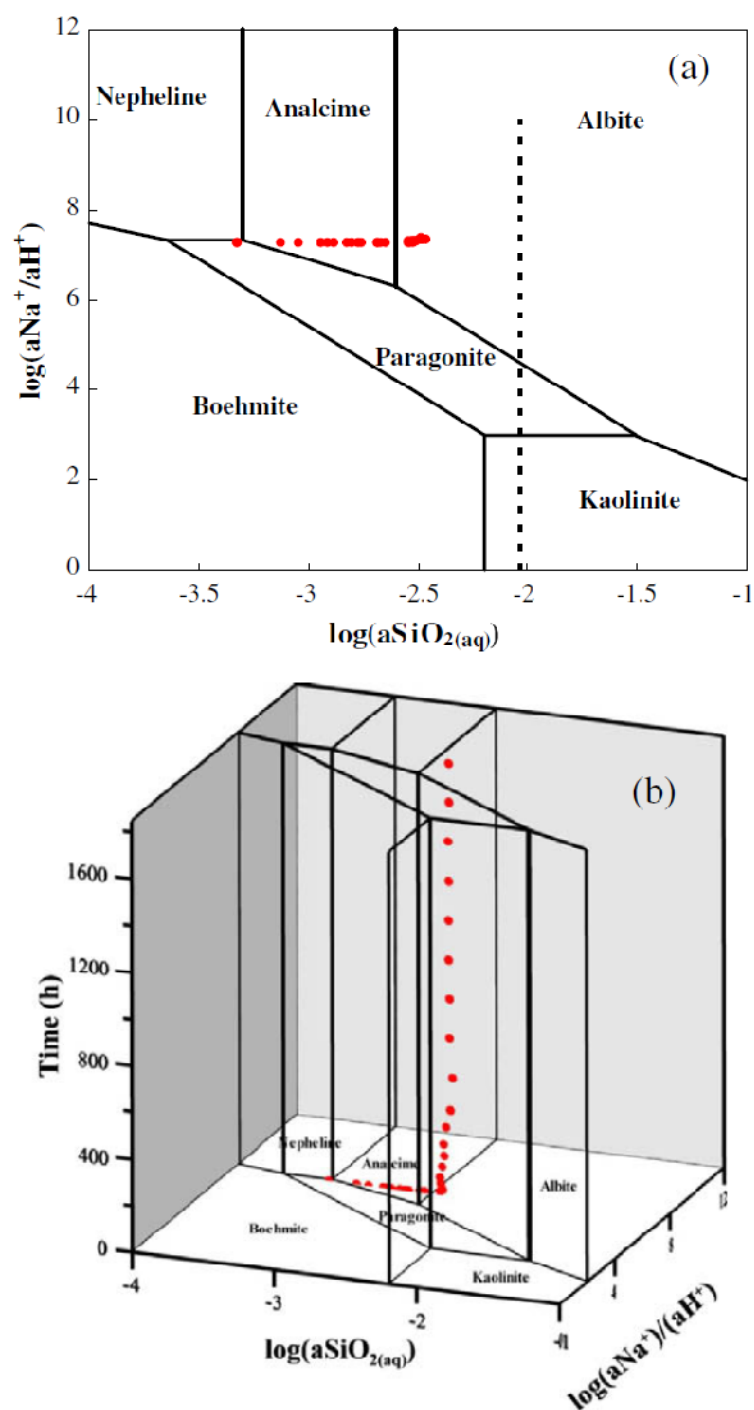


Fig. 8. Activity–activity diagrams showing phase relations in the system $\text{Na}_2\text{O}-(\text{Al}_2\text{O}_3)-\text{SiO}_2-\text{H}_2\text{O}$ at 300 °C and 8.8 MPa. Symbols represent results from experiments conducted by Alekseyev et al. (1997) for sanidine dissolution in 0.1 m NaHCO_3 solutions. The dashed line in (a) denotes quartz saturation. Activity and activity ratios were obtained from speciation modeling in the system $\text{K}_2\text{O}-\text{Na}_2\text{O}-(\text{Al}_2\text{O}_3)-\text{SiO}_2-\text{H}_2\text{O}-\text{CO}_2$ based on solution chemistry data from Alekseyev et al. (1997) and values of $\log K$ listed in Table 1a.

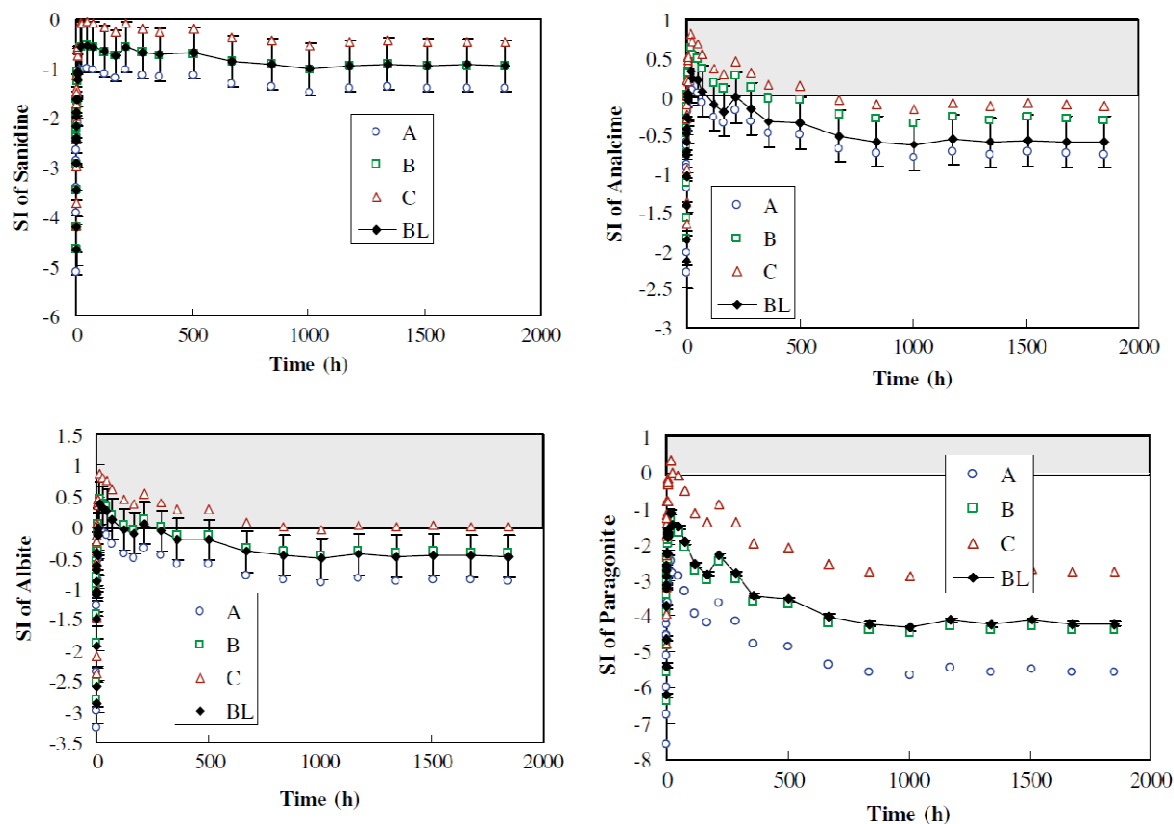


Fig. 9. Calculated saturation indices (SI) from experimental data for sanidine dissolution in 0.1 m NaHCO_3 solutions at 300 °C and 8.8 MPa. Experimental data from Alekseyev et al. (1997). See the caption for Fig. 3 for notations.

Table 6. Mineral saturation indices in each batch experiment for sanidine dissolution in 0.1 m NaHCO₃ solution at 300 °C and 8.8 MPa[†]

t, h	Sanidine	Analcime	Albite	Quartz	Boehmite	Kaolinite	Muscovite	Paragonite	Pyrophyllite	Kalsilite	Nepheline
0	-4.66	-2.14	-2.86	-1.29	-2.37	-7.01	-7.52	-6.22	-9.44	-4.71	-2.12
0.25	-4.19	-1.86	-2.59	-1.29	-2.10	-6.46	-6.51	-5.40	-8.89	-4.24	-1.85
0.5	-3.45	-1.42	-1.95	-1.09	-2.04	-5.95	-5.66	-4.64	-8.00	-3.89	-1.60
0.75	-2.92	-1.04	-1.48	-1.01	-1.82	-5.34	-4.68	-3.73	-7.22	-3.53	-1.30
1	-2.41	-0.72	-1.04	-0.88	-1.76	-4.96	-4.04	-3.16	-6.58	-3.27	-1.11
1.25	-2.46	-0.76	-1.11	-0.90	-1.75	-5.00	-4.08	-3.22	-6.67	-3.27	-1.13
1.5	-2.18	-0.59	-0.88	-0.85	-1.70	-4.77	-3.69	-2.88	-6.32	-3.11	-1.02
2	-1.88	-0.42	-0.62	-0.76	-1.69	-4.59	-3.38	-2.62	-5.98	-2.98	-0.93
2.5	-1.97	-0.48	-0.7	-0.79	-1.70	-4.66	-3.48	-2.71	-6.09	-3.01	-0.96
3	-1.63	-0.27	-0.43	-0.72	-1.61	-4.35	-2.97	-2.26	-5.66	-2.80	-0.81
3.5	-1.64	-0.28	-0.45	-0.74	-1.60	-4.36	-2.96	-2.26	-5.69	-2.79	-0.81
4	-1.24	-0.04	-0.13	-0.65	-1.54	-4.05	-2.42	-1.81	-5.21	-2.56	-0.66
5	-1.09	0.04	-0.02	-0.63	-1.49	-3.92	-2.18	-1.61	-5.04	-2.45	-0.60
6	-1.12	-0.00	-0.09	-0.65	-1.49	-3.97	-2.22	-1.69	-5.13	-2.44	-0.62
7	-1.05	0.02	-0.03	-0.61	-1.54	-3.99	-2.25	-1.72	-5.08	-2.45	-0.63
Analcm started to precipitate											
16	-0.57	0.33	0.38	-0.51	-1.44	-3.58	-1.58	-1.11	-4.46	-2.18	-0.44
24	-0.56	0.24	0.32	-0.49	-1.58	-3.82	-1.83	-1.46	-4.66	-2.20	-0.54
48	-0.53	0.21	0.27	-0.50	-1.59	-3.87	-1.83	-1.52	-4.73	-2.15	-0.56
72	-0.57	0.07	0.13	-0.51	-1.73	-4.17	-2.14	-1.94	-5.05	-2.17	-0.69
120	-0.66	-0.11	-0.04	-0.50	-1.96	-4.59	-2.69	-2.57	-5.45	-2.29	-0.88
168	-0.75	-0.19	-0.11	-0.48	-2.06	-4.78	-2.99	-2.85	-5.60	-2.4	-0.98
216	-0.57	-0.02	0.06	-0.49	-1.88	-4.42	-2.45	-2.31	-5.25	-2.22	-0.80
288	-0.68	-0.16	-0.07	-0.47	-2.07	-4.76	-2.93	-2.81	-5.55	-2.36	-0.96
360	-0.73	-0.33	-0.20	-0.44	-2.31	-5.18	-3.45	-3.42	-5.91	-2.47	-1.16
504	-0.69	-0.34	-0.20	-0.42	-2.36	-5.25	-3.52	-3.53	-5.96	-2.46	-1.19
672	-0.86	-0.52	-0.40	-0.45	-2.50	-5.58	-3.97	-4.01	-6.33	-2.59	-1.34
840	-0.91	-0.58	-0.47	-0.45	-2.57	-5.72	-4.17	-4.22	-6.47	-2.64	-1.41
1008	-1.01	-0.63	-0.52	-0.45	-2.60	-5.78	-4.32	-4.32	-6.54	-2.73	-1.45
1176	-0.94	-0.56	-0.45	-0.45	-2.53	-5.64	-4.10	-4.11	-6.40	-2.65	-1.38
1344	-0.91	-0.59	-0.48	-0.45	-2.58	-5.74	-4.17	-4.25	-6.50	-2.62	-1.41
1512	-0.93	-0.57	-0.46	-0.45	-2.53	-5.65	-4.11	-4.13	-6.42	-2.64	-1.38
1680	-0.93	-0.59	-0.47	-0.45	-2.57	-5.72	-4.18	-4.22	-6.47	-2.65	-1.41
1848	-0.94	-0.59	-0.48	-0.45	-2.57	-5.72	-4.19	-4.22	-6.48	-2.66	-1.41

[†]Experiments conducted by Alekseyev et al. (1997). SI values were calculated in this study using their solution chemistry data.

Table 7. Mineral saturation Indices in each batch experiment for albite dissolution in 0.1 m KHCO₃ solution at 300 °C and 8.8 MPa[†]

t, h	Albite	Sanidine	Microcline	Boehmite	Kaolinite	Muscovite	Paragonite	Pyrophyllite	Quartz	Kalsilite	Nepheline
0	-7.50	-4.08	-3.89	-2.49	-8.49	-7.17	-11.1	-12.2	-1.92	-2.87	-5.50
0.25	-5.18	-1.99	-1.79	-2.13	-6.62	-4.37	-8.05	-9.15	-1.34	-1.93	-4.34
0.5	-4.09	-0.99	-0.79	-1.86	-5.59	-2.83	-6.43	-7.64	-1.09	-1.43	-3.74
0.75	-3.20	-0.24	-0.05	-1.63	-4.78	-1.62	-5.07	-6.48	-0.92	-1.02	-3.19
1	-3.15	-0.21	-0.02	-1.64	-4.78	-1.60	-5.03	-6.45	-0.91	-1.02	-3.17
1.25	-3.14	-0.22	-0.03	-1.64	-4.78	-1.61	-5.03	-6.46	-0.91	-1.02	-3.15
1.5	-2.61	0.23	0.43	-1.51	-4.30	-0.9	-4.24	-5.76	-0.8	-0.79	-2.85
2	-2.33	0.47	0.67	-1.46	-4.08	-0.56	-3.86	-5.41	-0.74	-0.68	-2.69
2.5	-2.37	0.45	0.64	-1.48	-4.12	-0.63	-3.95	-5.45	-0.74	-0.7	-2.73
3	-2.23	0.56	0.75	-1.41	-3.96	-0.38	-3.67	-5.26	-0.72	-0.62	-2.62
3.5	-2.19	0.55	0.75	-1.45	-4.00	-0.45	-3.69	-5.29	-0.71	-0.64	-2.60
4	-2.20	0.56	0.76	-1.46	-4.01	-0.46	-3.72	-5.28	-0.71	-0.64	-2.62
5	-1.88	0.84	1.03	-1.36	-3.70	0.00	-3.21	-4.85	-0.65	-0.49	-2.42
6	-2.02	0.69	0.89	-1.40	-3.85	-0.22	-3.43	-5.07	-0.68	-0.56	-2.49
7	-1.81	0.88	1.08	-1.36	-3.67	0.04	-3.14	-4.8	-0.63	-0.48	-2.38
16	-1.70	0.99	1.19	-1.37	-3.60	0.148	-3.04	-4.65	-0.59	-0.44	-2.35
Sanidine started to precipitate											
24	-1.63	1.06	1.25	-1.35	-3.54	0.24	-2.94	-4.55	-0.58	-0.41	-2.31
48	-1.83	0.87	1.06	-1.37	-3.69	0.019	-3.17	-4.82	-0.63	-0.48	-2.39
72	-1.93	0.77	0.96	-1.40	-3.80	-0.15	-3.34	-4.98	-0.66	-0.54	-2.44
120	-1.87	0.76	0.96	-1.42	-3.83	-0.18	-3.31	-5	-0.66	-0.55	-2.39
168	-1.79	0.86	1.05	-1.42	-3.76	-0.09	-3.23	-4.87	-0.62	-0.52	-2.37
216	-1.78	0.83	1.02	-1.37	-3.72	-0.02	-3.13	-4.88	-0.65	-0.49	-2.32
288	-1.69	0.84	1.03	-1.39	-3.75	-0.06	-3.09	-4.89	-0.64	-0.5	-2.25
360	-1.72	0.76	0.95	-1.42	-3.85	-0.2	-3.17	-5.03	-0.66	-0.54	-2.23
504	-1.55	0.72	0.92	-1.45	-3.93	-0.3	-3.07	-5.13	-0.67	-0.56	-2.05
672	-1.44	0.74	0.94	-1.46	-3.93	-0.29	-2.96	-5.13	-0.67	-0.55	-1.94
840	-1.40	0.67	0.86	-1.51	-4.07	-0.48	-3.04	-5.29	-0.68	-0.59	-1.88
1008	-1.51	0.50	0.69	-1.52	-4.20	-0.65	-3.15	-5.55	-0.74	-0.64	-1.86
1176	-1.44	0.55	0.74	-1.50	-4.15	-0.57	-3.06	-5.47	-0.73	-0.61	-1.81
1344	-1.44	0.49	0.68	-1.56	-4.28	-0.74	-3.17	-5.62	-0.74	-0.65	-1.79
1512	-1.43	0.50	0.70	-1.54	-4.24	-0.69	-3.13	-5.58	-0.74	-0.64	-1.79
1680	-1.46	0.43	0.62	-1.57	-4.35	-0.83	-3.22	-5.72	-0.76	-0.68	-1.78
1848	-1.43	0.47	0.67	-1.56	-4.30	-0.76	-3.16	-5.65	-0.75	-0.65	-1.77

[†]Experimental data from by Alekseyev et al. (1997). SI values were calculated in this study using their solution chemistry data.

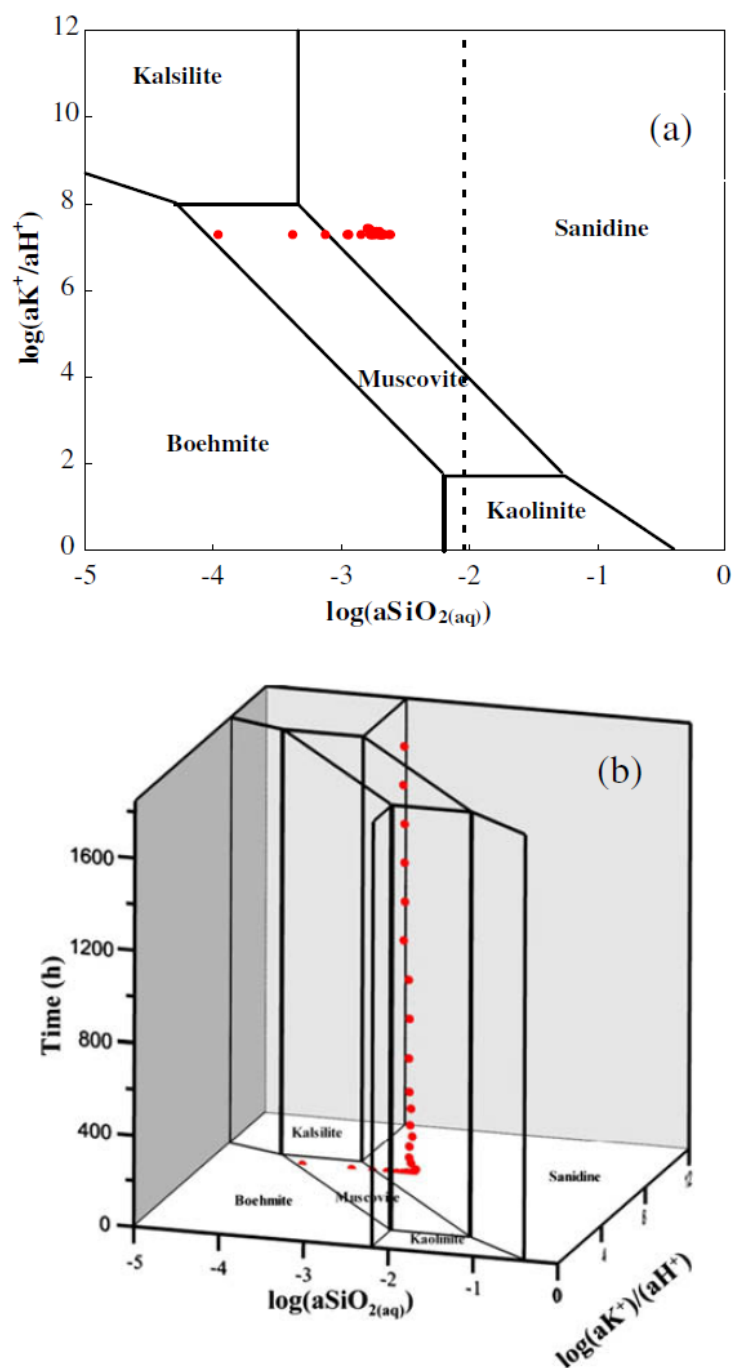


Fig. 10. Activity–activity diagrams showing phase relations in the system $\text{K}_2\text{O}-(\text{Al}_2\text{O}_3)-\text{SiO}_2-\text{H}_2\text{O}$ at 300 °C and 8.8 MPa. Symbols represent results from experiments conducted by Alekseyev et al. (1997) for albite dissolution in 0.1 m KHCO_3 solutions. The dashed line in (a) denotes quartz saturation. Activity and activity ratios were obtained from speciation modeling in the system $\text{K}_2\text{O}-\text{Na}_2\text{O}-\text{Al}_2\text{O}_3-\text{SiO}_2-\text{H}_2\text{O}-\text{CO}_2$ based on solution chemistry data from Alekseyev et al. (1997) and $\log K$ listed in Table 1a.

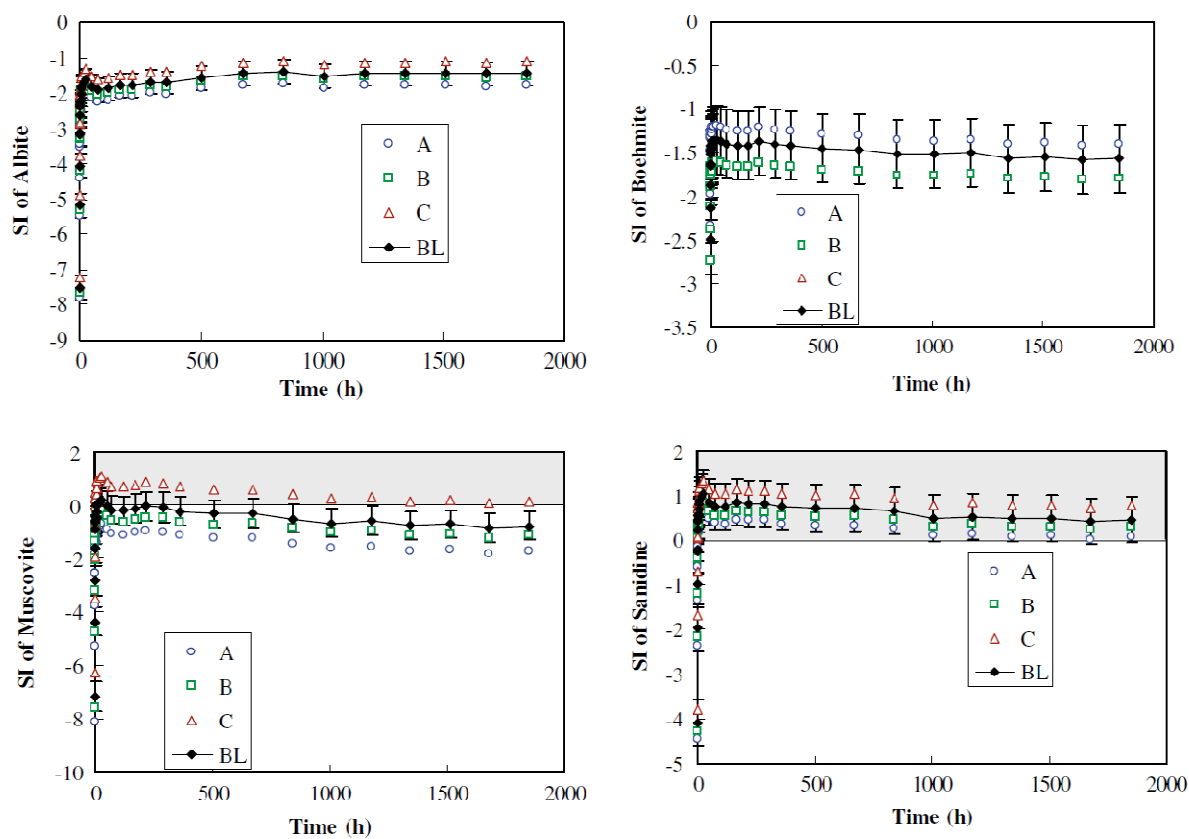


Fig. 11. Calculated saturation indices (SI) from experimental data for albite dissolution in 0.1 m KHCO_3 solutions at 300 °C and 8.8 MPa. Experimental data from Alekseyev et al. (1997). See the caption for Fig. 3 for notations.

4. DISCUSSION

4.1. Uncertainties of thermodynamic properties on calculated saturation indices

The calculated saturation states depend on the values of the standard state thermodynamic properties of both the minerals and aqueous species. Various internally consistent databases for thermodynamic properties for mineral species have been compiled (Helgeson et al., 1978; Berman, 1988, 1990; Robie and Hemingway, 1995; Holland and Powell, 1998). However, controversies and discrepancies still exist, particularly for the alumino-silicate minerals that are the primary focus of this study (see Pokrovskii and Helgeson, 1995; Arno´rsson and Stefa´nsson, 1999). We chose to use the

thermodynamic properties for mineral species from Holland and Powell (1998) as the base case because this database is internally consistent and it has incorporated recent experimental data as compared to other databases. Thermodynamic properties for boehmite are not available from the Holland and Powell (1998) database, and are discussed in Supplement A.

It is known that thermodynamic properties of minerals derived from calorimetric and phase equilibrium experiments rarely can predict experimental solubility results accurately (Sverjensky et al., 1991). The Holland and Powell thermodynamic properties for feldspars, kaolinite, and muscovite were derived from calorimetric and phase equilibrium measurements. However, Holland and Powell (1998) showed (their Fig. 2) that although the solubility data in the $\text{K}_2\text{O}\text{--}\text{Al}_2\text{O}_3\text{--}\text{SiO}_2\text{--}\text{H}_2\text{O}\text{--}\text{HCl}$ system reported by Sverjensky et al. (1991) were not used simultaneously together with phase equilibrium and calorimetric data in regressing thermodynamic properties for alumino-silicates, the off-sets of calculated phase stability fields from experimental data are small. This adds confidence to our calculated saturation indices for the $\text{K}_2\text{O}\text{--}\text{Al}_2\text{O}_3\text{--}\text{SiO}_2\text{--}\text{H}_2\text{O}\text{--}\text{HCl}$ system.

The boundaries of mineral stability fields are sensitive to the free energies used in the construction of a–a diagrams (Zhu and Anderson, 2002). For example, an increase of 1.2 kJ/mol of the ΔG_f° for boehmite would move the boehmite–kaolinite phase boundary to the right about 0.13 unit of $\log a\text{SiO}_{2(\text{aq})}$ in Fig 2a. The adjusted ΔG_f° value of -919.6 kJ/mol is still within the uncertainties of the ΔG_f° values given by Hemingway et al. (1991) and McHale et al. (1997), and would fit to the kaolinite–boehmite phase equilibrium experiments by Hemley et al. (1980) better but fit the boehmite–andalusite

phase equilibrium less well (see Supplement A). Likewise, the adjustment of 1.2 kJ/mol to ΔG_f° for boehmite would lead to an adjustment of 0.13 SI units for boehmite, which, however, is insufficient to change the nature of boehmite supersaturation, as boehmite was one to two SI unit supersaturated in these sampled solutions (cf. Table 3). In other words, it would require an adjustment of 21.7 kJ/mol to ΔG_f° for boehmite to be at equilibrium with the aqueous solution at 456 h in Fu et al.'s (2009) experiments. This conclusion also applies to the alkali feldspar experiments with CO₂ (Table 4) and experiments by Murakami et al. (1998), which show boehmite supersaturation from one to two SI units (cf. Table 5).

As discussed briefly earlier, to further test the validity of the conclusion that experimental solutions were supersaturated with respect to product minerals in the batch experiments that we have examined, we calculated saturation indices using different sets of thermodynamic properties for aqueous species and minerals, and different combinations of the two. The conclusion of supersaturation of product minerals still holds for the batch experiments examined in this study. In other words, the calculated saturation states are valid with the known uncertainties of thermodynamic properties.

Another layer of uncertainties may arise that amorphous or poorly crystalline metastable phases may be present in addition to the crystalline phases during the feldspar hydrolysis experiments (Helgeson, 1971, 1972; Petrovic, 1976). Further, metastable or poorly crystalline phases may transform during the experiments (e.g., Murakami et al., 1998). Supplement B shows that partial equilibrium between possible amorphous phases and aqueous solutions may explain the initial stage of the experiments, but not the entire experiments.

4.2. The coupling of dissolution and precipitation reaction kinetics

Lasaga (1998) showed, analytically, how the precipitation kinetics of secondary minerals could be coupled to the rate of feldspar dissolution reaction. The kinetics of secondary mineral formation comes into play in the mass balance equations. Starting with the mass balance on Al and assuming the metastable coexistence of kaolinite and boehmite, we have,

$$R_{feld} = \frac{-R_{bhm} - 2R_{kln}}{\left[\sum_j \frac{dn_{Al_{j,aq}}}{d\xi} - 1 \right]} \quad (1)$$

where R_i is the net rate ($d\xi/dt$) of dissolution of feldspar, boehmite, and kaolinite ($R_i < 0$ means precipitation). n denotes the moles of j th Al aqueous species and ξ the overall progress variable (Helgeson, 1968). Eq. (1) is equivalent to Lasaga's (1998) Eq. (1.235).

If we expand the net rate expression and divide the right hand side by k_{feld} , we have,

$$R_{feld} = \frac{-k_{bhm}/k_{feld} S_{bhm} f(\Delta G_{bhm}) - 2k_{kln}/k_{feld} S_{kln} f(\Delta G_{kln})}{\left[\sum_j \frac{dn_{Al_{j,aq}}}{d\xi} - 1 \right] / k_{feld}} \quad (2)$$

where k_i denotes the rate constant, S_i the surface area, and ΔG_i the Gibbs free energy of the i th reactions. $f(\Delta G_i)$ stands for the relationship between rate and Gibbs free energy of reaction.

Eq. (2) shows the inter-dependence between the rate constants of feldspar dissolution and those of boehmite and kaolinite precipitation. The net feldspar dissolution rate is a function of k_i/k_{feld} ratios. The smaller the k_i/k_{feld} ratio, the slower feldspar

dissolves, provided that all other quantities are kept the same. In fact, the experiments discussed in Section 3 showed that secondary minerals were several SI units supersaturated. Zhu et al. (2004a, 2004b) explored the inter-connections numerically via reaction path modeling. When the effective rate constant ratios k_i^*/k_{feld}^* (defined as $k \times S$) are between 10^{-2} to 10^{-4} , slow clay precipitation became the limiting step, and the net feldspar dissolution rates are orders of magnitude slower than that at conditions at far from equilibrium.

Note that the above discussion following Lasaga (1998) is a necessary over simplification as a starting point and the rate law expression in Eq. (2) only means to facilitate further discussions. Obviously, the expression neglects other terms such as those accounting for the well known effects of hydrogen and Al on the rates (Aagaard and Helgeson, 1982; Helgeson et al., 1984; Oelkers et al., 1994; Oelkers, 2001). In a sense, the rate constant k_i is only a nominal; the relationship between dissolution and precipitation kinetics still stands when other factors also play a role in the rate laws (e.g., H, Al). One could just replace k_i^* with k_i , with k_i^* lumping all other factors except the $f(\Delta G_r)$ term. This statement is necessary because while k_i is meant to represent the intrinsic kinetics properties, in reality it is a value derived after subtraction of all “known” environmental factors from experimental data. In other words, the coupled relationship between dissolution and precipitation reactions originates from the principle of mass balance and the sharing of same aqueous components in the $f(\Delta G_r)$ term (Lasaga, 1998). It is broader than what Eq. (2) represents.

It follows then it is difficult to extrapolate experimental results from elevated temperatures and pressures, as examined here, to ambient conditions where silicate

weathering occurs. The precipitation rates of clay minerals as a function of temperatures have not been completely understood. If the temperature dependence of k_i for feldspar dissolution, or more broadly, all the terms in the rate law, is significantly higher than those for secondary mineral formation, the k_i/k_{feld} ratio or the inter-dependence of dissolution–precipitation reaction kinetics may possibly change at ambient temperature and pressure. However, coupled reactions under ambient conditions are too slow to be measured in laboratory experiments. The temperature dependence remains to be an unknown factor at the present time.

In summary, through systematic analysis of a broad range of experimental data, we confirm early conjecture that secondary minerals might not be at equilibrium with the fluid (Steefel and Van Cappellen, 1990; Lasaga, 1998). This conjecture was previously supported by specific experiments and limited modeling analysis (Alekseyev et al., 1997). Here, we have conducted a comprehensive modeling study and have shown that the slow kinetics nature of secondary mineral precipitation was evident from both the fluid chemistry, which crossed the phase boundaries on the a – a diagrams, and from mineral product analysis, which show persistent boehmite presence even after the fluid chemistry had evolved into the kaolinite and muscovite stability fields.

4.3. Extrapolation to natural systems

Natural systems differ from the laboratory experiments examined here mainly in two aspects. First, experimental results from batch systems cannot be applied directly to systems where advective and dispersive fluxes are significant. However, even in the case of fluid flow in a hydrological system flushed with fresh dilute water, the downstream

water receives the solute fluxes from upstream, and the effects of supersaturation with respect to secondary minerals must be similar if the flow system has persisted for a while. These scenarios can be tested in a coupled reactive mass transport model in the future.

Second, laboratory experiments are brief on the scale of geological time. It is therefore necessary to examine samples from geological systems. Assessments of SI in the field are difficult, however, because of the absence or difficulty of aluminum analyses, the complex chemistry and structures of clay minerals, and the lack of internally consistent thermodynamic properties for clay minerals with such complex chemistry and structures. Nevertheless, Kwicklis (2004) calculated SI values of aluminosilicate minerals in the volcanic tuff aquifer in southern Nevada in the vicinity of Yucca Mountain. While the groundwaters there are undersaturated with respect to albite, they are supersaturated with respect to smectite and Ca-clinoptilolite. The more meaningful aspect of his findings is probably the areal distribution of the SI values – the SI values increase four to five fold southward along the groundwater flow from the Yucca Mountain and Fortymile Wash area to the Amargosa desert. These solubility- speciation modeling exercises are marred by the general problems with Al analysis and clay mineral properties discussed above, and specifically by the assumption of equilibrium between kaolinite and groundwaters. Nevertheless, the southward increase of SI for smectite and Ca-clinoptilolite along the flow path appears to support Kwicklis's (2004) assertion that "silicate weathering reactions are providing ions to the groundwater faster than they can be removed by smectite precipitation."

5. CONCLUDING REMARKS

Feldspars comprise over 50% of the volume of the earth's crust. Establishing reliable rates for low-temperature feldspar dissolution is essential to quantify many basic geological and environmental processes. Among these are the functional relationship between silicate weathering and the global climate over geologic time (Berner and Berner, 1997), controls on surface and groundwater quality, global elemental cycling (Lasaga et al., 1994), the availability of inorganic nutrients in soils (Federer et al., 1989; Likens et al., 1998), impacts of acid mine drainage, neutralization of acid precipitation in watersheds (Drever and Clow, 1995), safety of nuclear waste repositories (Spycher et al., 2003), and geological carbon sequestration (White et al., 2003).

The pioneering work by Helgeson and co-workers (Garrels and Mackenzie, 1967; Helgeson, 1968; Helgeson et al., 1969, 1984; Aagaard and Helgeson, 1982; Helgeson and Murphy, 1983) to model feldspar hydrolysis as a process of coupled dissolution and precipitation reactions transformed the study of water-rock interactions into a quantitative science and opened up vast new fields of geochemistry in the following decades. The early model, however, assumed partial equilibria between the aqueous solution and the secondary phases. Although the assumption of partial equilibrium has been questioned in the intervening years (Steefel and Van Cappellen, 1990; Nagy and Lasaga, 1993; Small, 1993; Lasaga et al., 1994; Alekseyev et al., 1997; Lasaga, 1998; Zhu et al., 2004a; Price et al., 2005; Zhu, 2006; Ganor et al., 2007), until now there has never been a rigorous examination of this hypothesis. Here, we systematically analyzed our own feldspar hydrolysis batch experiments (Fu et al., 2009) and those in the literature. We find three lines of experimental evidence that contradicts the partial equilibrium hypothesis in the experimental feldspar-water system: saturation indices, reaction paths,

and secondary mineral paragenesis. However, we must emphasize that the partial equilibrium assumption between secondary minerals and aqueous solutions often produces a useful approximation of geochemical processes. Partial equilibrium may well exist for systems that involve rapidly precipitating secondary minerals (e.g., pyrite oxidation and precipitation of amorphous iron oxyhydroxides and in the case of evaporation and the resultant deposition of salt minerals as modeled by Garrels and Mackenzie (1967) or even for the feldspar–water system at higher temperatures and pressures.

In the feldspar–water system, the slow kinetics of secondary mineral precipitation results in close inter-dependence of the dissolution and precipitation reaction rates (Steefel and Van Cappellen, 1990; Lasaga et al., 1994; Alekseyev et al., 1997; Lasaga, 1998), which, if clay precipitation k^* are sufficiently slower than feldspar dissolution k^* , could rationalize the well-known discrepancy between field feldspar dissolution (bulk, effective) rates and rates measured in laboratory dissolution experiments at conditions far from equilibrium (Zhu et al., 2004a). Field studies often focused on the dissolution rates only. However, as seen in the batch experiments examined by this study, the congruent dissolution stage in the closed systems is short, probably a matter of hours at 90–300 °C. A steady state or near steady state of aqueous chemistry for some constituents persisted as a consequence of the coupled dissolution and precipitation reactions. Zhu et al. (2004a) used a numerical reaction path model to show that such a steady state can result if the effective rate constants of clay precipitation are orders of magnitude smaller than those of feldspar. Note that although the reaction Gibbs free energy effect on dissolution rates is a widely cited reason to explain the field–laboratory rate discrepancy, there is a need of a

control that such a state of proximity to equilibrium can be maintained in natural systems for prolonged time and over long distance. Slow clay precipitation may serve this role.

Clearly, interpretation of field based reaction rates needs to consider dissolution reactions within a network of dissolution–precipitation reactions. Future work should employ numerical modeling of reaction paths to match the experimental data and hence to quantitatively evaluate the inter-dependence of dissolution–precipitation reactions. However, the challenge is to measure precipitation rates and derive proper rate laws to describe precipitation processes. While the details may evolve over time (e.g., Al adsorption on feldspar surface as a retardation mechanism (Oelkers et al., 1994) and slow clay precipitation kinetics discussed here), the framework of modeling mass transfer in geological systems developed by Helgeson and co-workers will continue to serve as the foundation for rigorous and quantitative geochemical predictions.

SUPPLEMENTS FOR CHAPTER 2

SUPPLEMENT A. DISCUSSION OF THERMODYNAMIC PROPERTIES

A.1. Thermodynamic properties for Boehmite

The only aluminum oxyhydroxide mineral listed in the Holland and Powell (1998) database is diaspore. However, boehmite was detected in the experiments that we examined in this study (Murakami et al., 1998; Fu et al., 2009). Here, we adopted the heat capacity, entropy, and enthalpy of formation for boehmite from Hemingway et al. (1991). The experimental heat capacity values were fitted to the Holland and Powell heat capacity function. Hemingway et al. (1991) derived their ΔH_f of 996.4 ± 2.2 kJ/mol from their third-law entropy measurements and solubility data in alkaline solutions taken from the literature. Hemingway et al.'s (1991) ΔH_f was used by Tagirov and Schott (2001) in their derivation of Al hydrolysis constants (see below). Later, McHale et al. (1997) measured calorimetrically a ΔH_f of 995.4 ± 1.6 kJ/mol. These two values are within each other's experimental errors. Note that the solubility based ΔG_f proposed by Hemingway et al. (1991) is only half to 1 kJ/mol different from those of Boucier et al. (1993) and Pokrovskii and Helgeson (1995), who also derived ΔG_f for boehmite from solubility data.

To examine the consistency of these adopted thermodynamic properties for boehmite with the rest of the Holland and Powell (1998) database, we compared the calculated phase boundary against the kaolinite–boehmite experimental data of Hemley et al. (1980) and Hemley's andalusite–boehmite experiment reported by Helgeson et al. (1978, p. 114) (Fig. A1). Hemley et al. (1980) warned that the scattering of the kaolinite–boehmite at low temperatures might have resulted from boehmite being metastable and being re-crystallized to diaspore. For this reason, we also calculated the diaspore–

kaolinite boundary (the dashed line). The comparison shows that most experimental data match more closely to the diaspore–kaolinite equilibrium curve than to the boehmite–kaolinite equilibrium curve although experiments with lower SiO_2 concentrations match with the boehmite–kaolinite equilibrium curve. The maximum discrepancies between the experimental and calculated boehmite–kaolinite boundary are about 0.25–0.3 log unit of $a\text{SiO}_{2(\text{aq})}$.

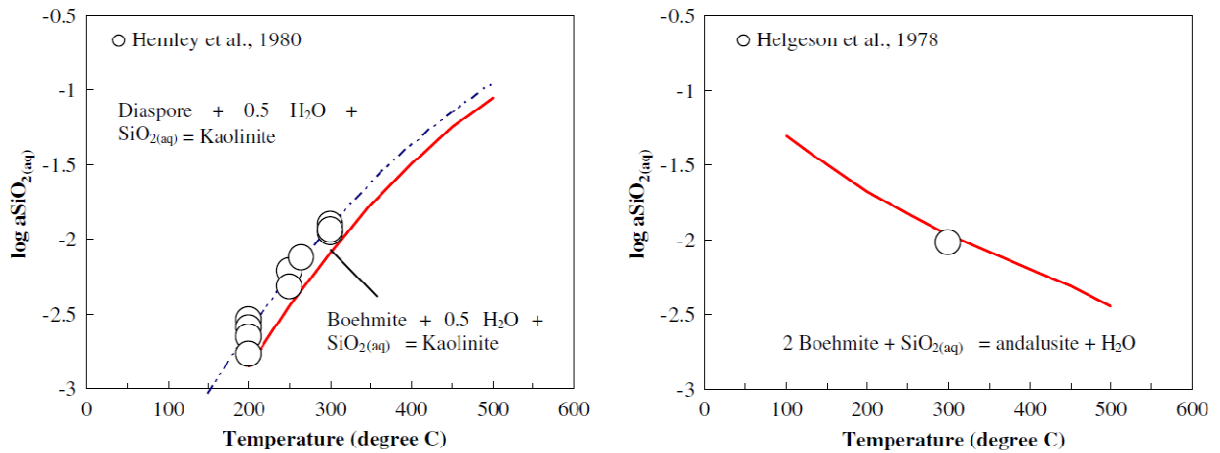


Fig. A1. Comparison of experimental (symbols) and calculated (lines) phase equilibrium involving boehmite. Thermodynamic properties for kaolinite and andalusite are from Holland and Powell (1998), for $\text{SiO}_{2(\text{aq})}$ from Shock et al. (1989), and for boehmite from Hemingway et al. (1991). As in Hemley et al. (1980), the only aqueous silica species is assumed to be $\text{SiO}_{2(\text{aq})}$ and the activity coefficient for this neutral species is assumed to be unity. The andalusite–boehmite experiment was conducted by Hemley, but as cited in Helgeson et al. (1978).

No detailed description of the boehmite–andalusite experiment was given, but the one experimental datum matches the calculation. These comparisons demonstrate that the adopted boehmite thermodynamic properties are approximately consistent with other Al-bearing minerals in Holland and Powell (1998) in the temperature and pressure range of our interest. Note that Holland and Powell (1998) have included other phase equilibrium

experiment data of Hemley et al. (1980) in their derivation of ΔH_f values for diaspore, kaolinite, andalusite, and pyrophyllite.

A.2. Thermodynamic properties for aqueous Al species

Various competing Al hydrolysis constants and Al-metal complexes were proposed at the temperatures and pressures of our interest (among them: Apps and Neil, 1990; Bourcier et al., 1993; Pokrovskii and Helgeson, 1995; Shock et al., 1997; Tagirov and Schott, 2001). We adopted the species and equilibrium constants from Tagirov and Schott (2001) because their constants are consistent with the latest boehmite solubility measurements (Bénézeth et al., 1997, 2001; Palmer et al., 2001) and at the same time, they adopted the Hemingway et al. (1991) thermodynamic properties for boehmite, which we also adopted. Thus, the calculated saturation indices for boehmite should be consistent with the knowledge of boehmite solubilities in the temperature and pressure range of our interest.

As suspected, our calculations show that Al speciation is dependent on pH, solution chemistry, and temperature (Figs. A2–A4). For the experiments of alkali feldspar dissolution in KCl solution at 200 °C and 30 MPa (Section 3.1), the dominant Al species are $\text{Al}(\text{OH})_2^+$, $\text{Al}(\text{OH})^{2+}$, $\text{Al}(\text{OH})_3^0_{(\text{aq})}$, and $\text{AlH}_3\text{SiO}_4^{2+}$ at pH 3.3–4.0, and $\text{Al}(\text{OH})_4^-$ and $\text{Al}(\text{OH})_3^0_{(\text{aq})}$ at pH 4.5–4.8 (Fig. A2a). Thus, the Al aqueous complex $\text{AlH}_3\text{SiO}_4^{2+}$ proposed by Tagirov and Schott (2001) is an important Al species at the early stage of the experiment when pH was below 4.0. The omission of this species would result in higher calculated SI values for boehmite, kaolinite, muscovite, and feldspars. For the experiment of alkali feldspar dissolution in 0.2 m KCl and 0.05 m CO_2 solution at 200 °C and 30

MPa (Section 3.2), the pH varied from 4.9 at the start of the experiment to 5.7 at the end of the experiment. The dominant species is $\text{Al}(\text{OH})_4^-$, with less than 10% as $\text{Al}(\text{OH})_3^0_{(\text{aq})}$ at the early stage of the experiment (Fig. A2b). Arnórsson and Stefánsson (1999) argue that the thermodynamic properties for $\text{Al}(\text{OH})_4^-$ is well known.

For the anorthite dissolution experiments published by Murakami et al. (1998) (Section 3.3), the dominant species are $\text{Al}(\text{OH})_2^+$, $\text{Al}(\text{OH})^{2+}$, $\text{Al}(\text{OH})_3^0_{(\text{aq})}$, $\text{Al}(\text{OH})_4^-$ but $\text{AlH}_3\text{SiO}_4^{2+}$ comprises of about 10% of the Al species at 90 °C. The Al–acetate complexes, although included in the speciation model, only make up <5% of the total. The calculated in situ pH was about 4.7 at 90 °C. The experiments at 150 °C had pH around 5.0, and the dominant Al species are $\text{Al}(\text{OH})_3^0_{(\text{aq})}$ and $\text{Al}(\text{OH})_4^-$. The Na–Al complex proposed by Tagirov and Schott (2001) comprises about 5% of total Al species, which does not significantly affect the calculated SI values. The experiments at 210 °C had pH around 5.4 and the dominant species is $\text{Al}(\text{OH})_4^-$. Neither Al–Na complex or Al–acetate complexes are significant. As mentioned earlier, calculated SI values for anorthite are >0 for the baseline thermodynamic dataset (Fig. 7) while Murakami et al. (1998) demonstrated continued anorthite dissolution. Using the thermodynamic properties from Helgeson et al. (1978) would result in anorthite undersaturation (Fig. 7). There is a difference of >16 kJ/mol for the standard enthalpy of formation at 25 °C and 0.1 MPa between those values chosen by Helgeson et al. (1978) and by Holland and Powell (1998). Arnórsson and Stefánsson (1999) also showed that the temperature variation of the anorthite solubility can also differ significantly when different sets of thermodynamic properties are used. These problems, however, seem to rest with the anorthite properties and should not affect our conclusions of secondary mineral supersaturation.

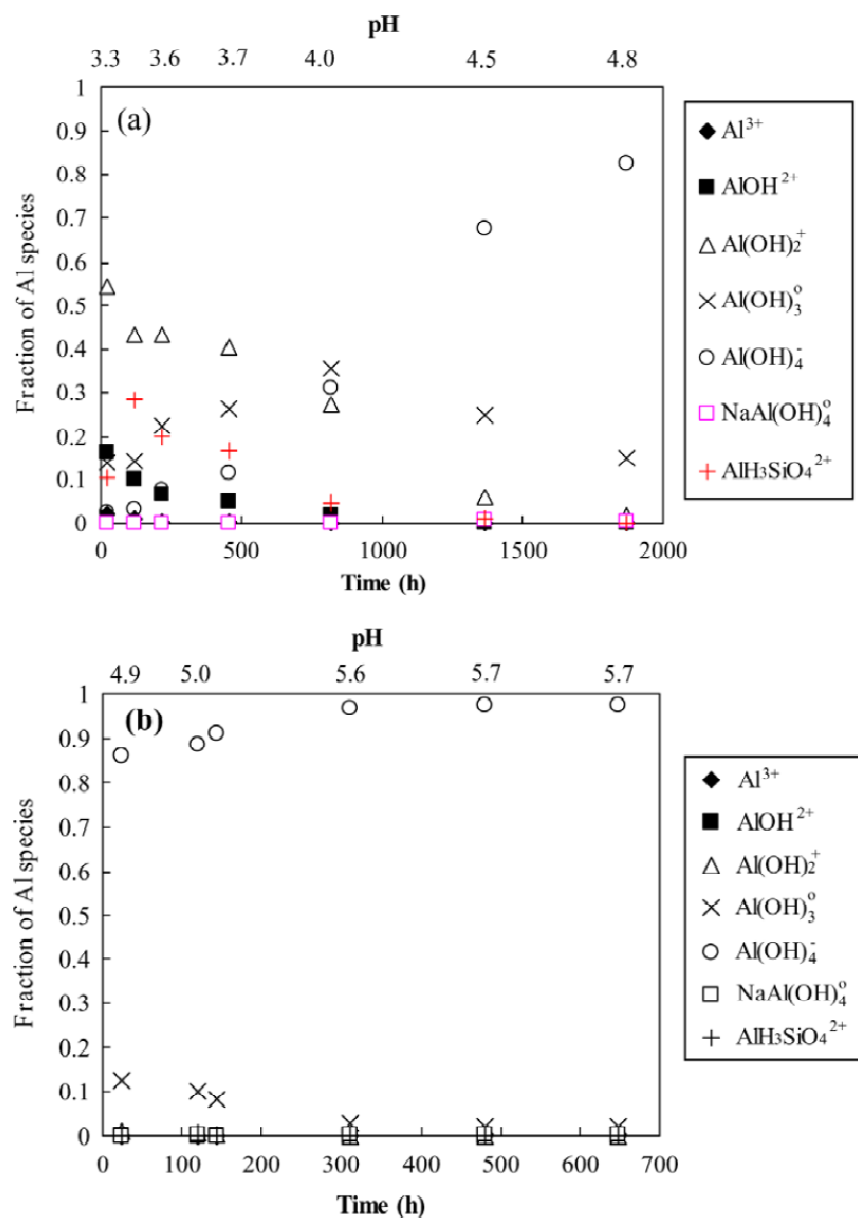


Fig. A2. Fraction of Al aqueous species as a function of time for alkali feldspar dissolution and clay precipitation experiment at 200 °C and 30 MPa. (a) Alkali feldspar + 0.2 m KCl (described in Section 3.1) and (b) alkali feldspar + 0.2 m KCl + 0.05 m CO_2 (described in Section 3.2). Al aqueous speciation was calculated with the thermodynamic properties from Table 1a. Solution pH increased from the start of the experiment to end from 3.3 to 4.8 for (a) and from 4.9 to 5.7 for (b).

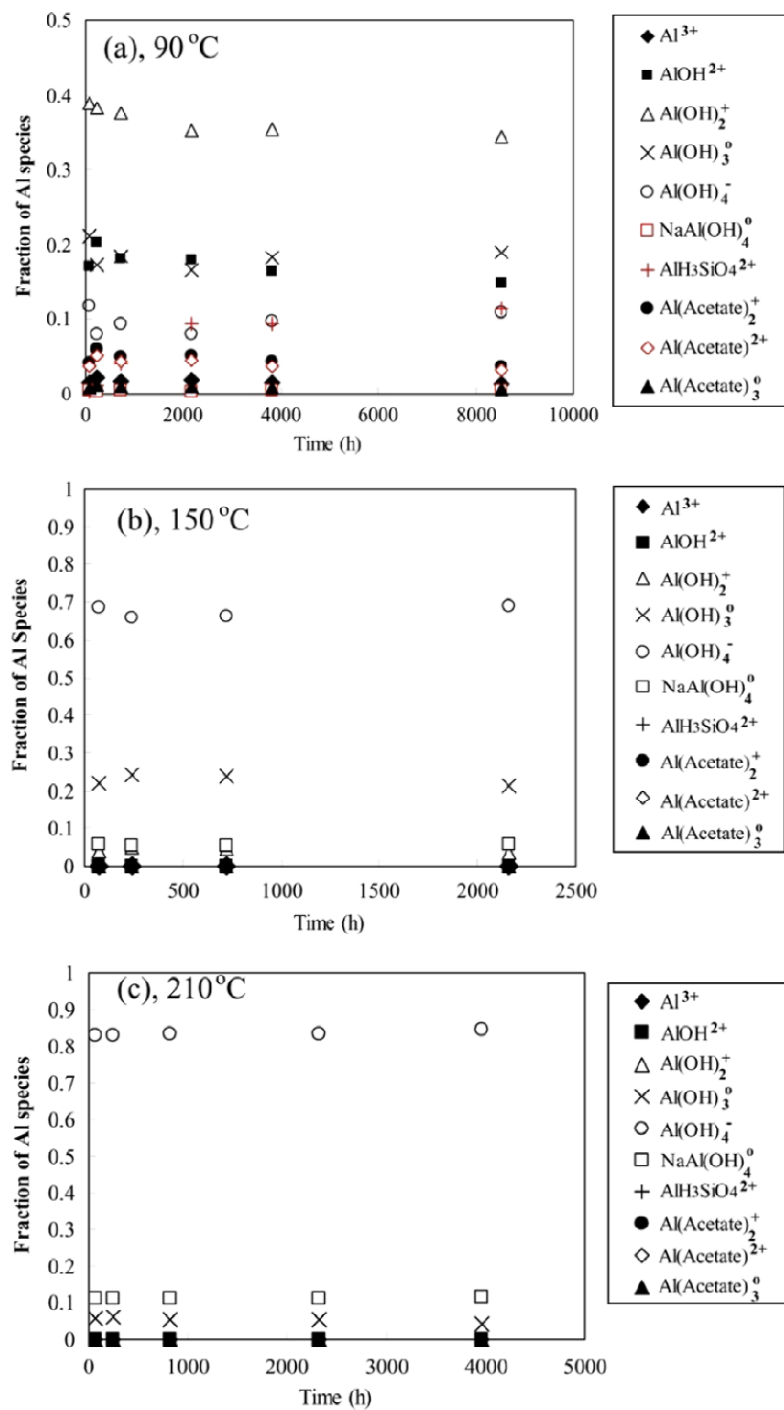


Fig. A3. Fraction of Al species in the experiment of anorthite dissolution in 0.03 m NaAC solutions performed by Murakami et al. (1998) and described in Section 3.3. At 90 °C (a), 150 °C (b), and 210 °C (c). Al speciation was calculated with the thermodynamic properties from Table 1a. Solution pH was buffered around 4.7 for (a), 5.0 for (b), and 5.4 for (c).

For the sanidine dissolution in 0.1 m NaHCO₃ solution at 300 °C and 8.8 MPa, experiments conducted by Alekseyev et al. (1997) (Section 3.4), Al(OH)₄⁻ (65%) and NaAl(OH)₄⁰_(aq) (35%) are the dominant species. The solution pH was around 9. Whether or not to include the species NaAl(OH)₄⁰_(aq) could contribute significantly to the calculated SI values (Fig. 7). However, even with this uncertainty of Al speciation, the calculated SI values do not reverse the signs. For the albite dissolution in 0.1 m KHCO₃ solution at 300 °C and 8.8 MPa conducted by Alekseyev et al. (1997), the calculated in situ pH are also around 9, and the dominant Al species is Al(OH)₄⁻ (>95%) (Fig. A4b).

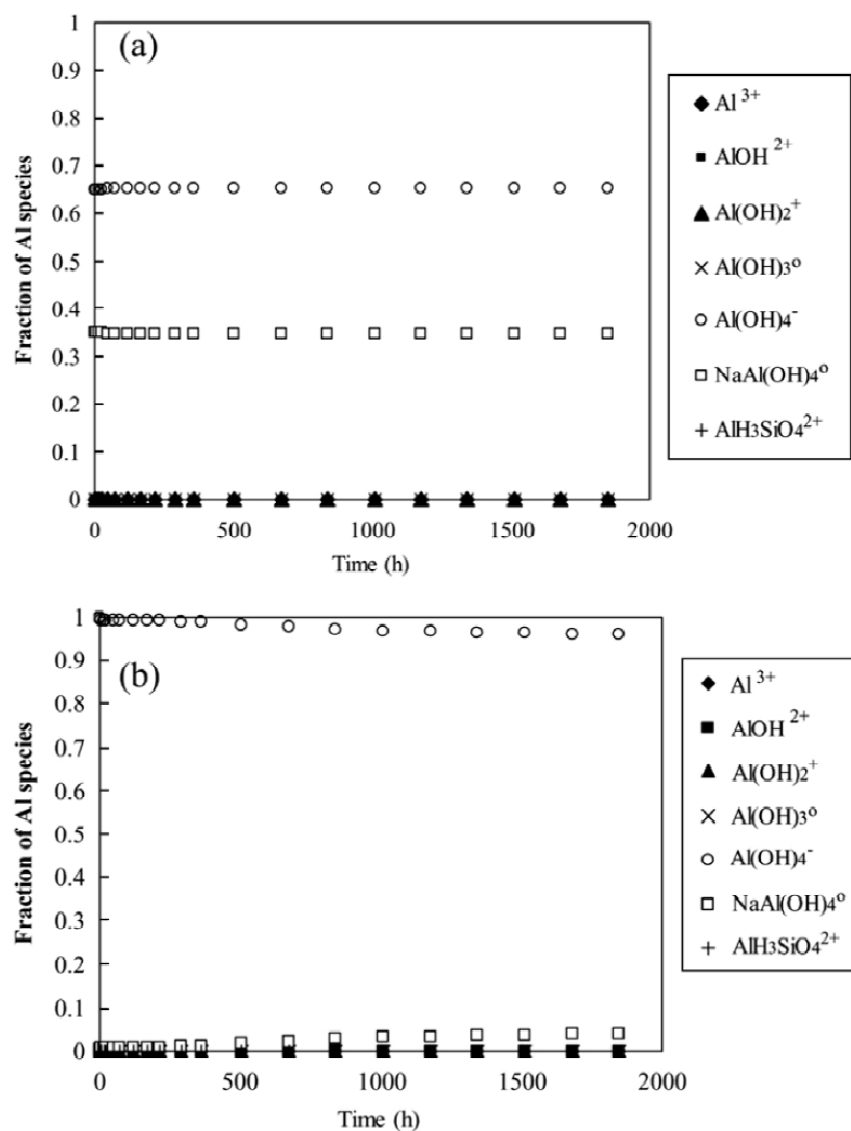


Fig. A4. Fraction of Al species in the experiments conducted by Alekseyev et al. (1997) at 300 °C and 8.8 MPa (described in Section 3.4). (a) Sanidine dissolution in 0.1 m NaHCO₃ solution; (b) albite dissolution in 0.1 m KHCO₃ solution Al speciation was calculated with the thermodynamic properties from Table 1a. Solution pH was buffered around 9 for both (a) and (b).

A.3. Chemical impurities and crystallinity

Another source of error is that the standard thermodynamic properties used for calculations are derived from pure end-members (typically measured from gem quality crystals) while the primary minerals (feldspars) and secondary mineral products in the experiments may not be chemically pure or may have different crystallinity from those used to derive thermodynamic properties. While Murakami et al. (1998) used an $\text{An}_{95}\text{Ab}_{0.5}$ anorthite, Fu et al. (2009) used a perthitic feldspar with a K-feldspar laminae with 15% Na component. According to Arnórsson and Stefánsson (1999), the ΔG_{mix} of alkali feldspar is positive, indicating that alkali–feldspar solid solutions are more soluble than the respective pure endmembers. However, they showed that the ΔG_{mix} is less than 1 kJ/mol for composition of 10% Na low albite in the low albite–microcline series, which translates to about 0.1–0.2 in $\log K$ at 200 °C. Therefore, taking into account of the solid solution effects, the calculated albite SI values reported in Sections 3.1 and 3.2 would be 0.2 unit lower. The Na component in the anorthite will reduce the solubility of anorthite. At 90–210 °C, the 5% Na will most likely introduce about 0.25 in $\log K$.

Murakami et al. (1998) noted that the boehmite in their experiments contained high concentrations of Si. The effect of this on thermodynamic properties is unknown. Kaolin mineral occur with varying degrees of structural order and hence free energy (Drever, 2004). The errors on the SI are not assessed.

SUPPLEMENT B. POSSIBLE AMORPHOUS PHASES AND PHASE TRANSITION

Incongruent hydrolysis of feldspars is known to produce reaction products that are disordered, amorphous, or cryptocrystalline metastable phases (Helgeson, 1971, 1972; Petrovic, 1976). Here, we examined a working hypothesis that the solution chemistry in the experiments discussed in Section 3 was controlled by partial equilibrium with metastable amorphous phases that were not detected by XRD, SEM, or TEM. These amorphous phases have higher solubility and the partial equilibrium between these phases and aqueous solution resulted in persistent supersaturation with crystalline boehmite and kaolinite as discussed in Sections 3 and 4.1.

Let's assume that there was an amorphous boehmite in the experiments of Fu et al. (2009) discussed in Section 3.1. The amorphous boehmite has the same chemical stoichiometry as crystalline boehmite but a ΔG_f value 9 kJ/mol higher than that of the crystalline boehmite used in previous calculations. The calculated SI for this amorphous phase is one unit higher than that of the crystalline boehmite. The first three experimental samples (after 24, 120, and 216 h) would be consistent with partial equilibrium between this phase and aqueous solutions. However, the SI of the stoichiometric boehmite (whatever it is, amorphous or crystalline) increased with time from 0.90 to 2.4 at 456 h (Fig. 3). If partial equilibrium between the amorphous boehmite and aqueous solution dominated solution chemistry during the entire experimental run, the SI values of the amorphous phase should decrease with time (see Section 2, the phase at partial equilibrium with the solution chemistry can only have SI 6 0).

Now, let's further assume that there was a phase transition during the 1872 h experiment. The first precipitated phase was an amorphous boehmite and it completely disappeared after 216 h. A crystalline or more crystalline boehmite took control of the solution chemistry from 456 h. The $SI > 0$ values for this crystalline or more crystalline phases for the rest of the experiments still indicate that partial equilibrium was not held between this crystalline phase and aqueous solutions or between any phase and aqueous solution throughout the experiments. Furthermore, XRD and SEM analyses of reaction products demonstrated crystalline boehmite after 120 h and 1872 h (Fu et al., 2009).

We can further test the working hypothesis that a halloysite with the same chemical stoichiometry as kaolinite but a ΔG_f 16.8 kJ/mol high than that of kaolinite (Robie and Hemingway, 1995) were present in the experiments discussed in Section 3.1. The calculated SI values for this halloysite is 1.85 SI units higher than that of kaolinite at 200 °C and is represented by a solid line in Fig. 3 at SI of 1.85. Robie and Hemingway (1995) gave a two standard deviation of 10 kJ/mol, which were represented as two dashed lines bracketing the solid line in Fig. 3. We can see that it would be consistent with the two experimental data points at 120 and 216 h. However, the SI values for the stoichiometric kaolin jumped to 5.13 at 456 h. The calculated SI values are outside of the halloysite SI range. This could be explained by the complete disappearance of the amorphous halloysite, and the high SI values represent the control of a more crystalline phase. For the same reasons discussed in the previous paragraph, the experimental data could not be consistent with partial equilibrium with the amorphous phase throughout the experiments or at partial equilibrium with the crystalline or more crystalline kaolinite.

Note that XRD and SEM analyses of reaction products demonstrated crystalline boehmite after 120 h and 1872 h (Fu et al., 2009).

In the case of experiments in Section 3.2, one could argue that partial equilibrium with an amorphous boehmite persisted throughout the experiment run within thermodynamic and analytical data uncertainties (Fig. 5). However, kaolinite and muscovite SI increase with time. Regardless of crystallinity, they cannot be at partial equilibrium with the aqueous solutions. Crystalline boehmite were detected with XRD and SEM. Only traces of muscovite were detected.

The experiments conducted by Murakami et al. (1998) discussed in Section 3.3 could be alternatively explained by partial equilibrium between an amorphous boehmite and aqueous solutions at 90, 150, and 210 °C except for the first points in the experiments. At 90 °C, it could be that the second and third points were at partial equilibrium with this amorphous boehmite with a ΔG_f value 24 kJ/mol higher than that of crystalline boehmite. Later, the Al concentrations in the aqueous solutions were controlled by an even more soluble “modified boehmite”. At 150 °C, a similar case cannot be made. SI of boehmite increased and changed with time. Apparently, this is not a case of partial equilibrium. The SI for kaolinite or halloysite changed with time except 90 and 150 °C. The calculated SI values for kaolinite at 210 °C could be argued to stay almost constant, but modified boehmite did not disappear, but persisted the whole time.

Therefore, while the presence of amorphous phases could not be ruled out, despite the deliberate efforts by Murakami et al. (1998) and Fu et al. (2009), and amorphous phases would introduce more complexity into the interpretations of the feldspar hydrolysis experiments, their presences, however, would not change our

conclusions that partial equilibrium was generally not held in these laboratory experimental systems.

REFERENCES

- Aagaard P. and Helgeson H. C. (1982) Thermodynamic and kinetic constraints on reaction rates among minerals and aqueous solutions. I. Theoretical considerations. *Am. J. Sci.* **282**, 237–285.
- Alekseyev V. A., Medvedeva L. S., Prisyagina N. I., Meshalkin S. S. and Balabin A. I. (1997) Change in the dissolution rates of alkali feldspars as a result of secondary mineral precipitation and approach to equilibrium. *Geochim. Cosmochim. Acta* **61**, 1125–1142.
- Anderson G. M. and Crerar D. A. (1993) *Thermodynamics in Geochemistry: The Equilibrium Model*. Oxford University Press, New York.
- Apps J. A. and Neil J. M. (1990) Solubilities of aluminum hydroxides and oxyhydroxides in alkaline solutions. In *Chemical Modeling of Aqueous Solutions II* (eds. D. A. Melchior and R. L. Bassett). ACS Symposium Series 416, Washington, DC.
- Arnórsson, S. and Stefánsson, A. (1999) Assessment of feldspar solubility constants in water in the range of 0 to 350 °C at vapor saturation pressures. *Am. J. Sci.* **299**, 173–209.
- Banfield J. F. and Barker W. W. (1994) Direct observation of reactant–product interfaces formed in natural weathering of exsolved, defective amphibole to smectite – evidence for episodic, isovolumetric reactions involving structural inheritance. *Geochim. Cosmochim. Acta* **58**, 1419–1429.
- Banfield J. F. and Eggleton R. A. (1990) Analytical transmission electron-microscope studies of plagioclase, muscovite, and K-feldspar weathering. *Clays Clay Miner.* **38**, 77–89.
- Banfield J. F., Jones B. F. and Veblen D. R. (1991) An AEM–TEM study of weathering and diagenesis, Albert Lake, Oregon. I. Weathering reactions in the volcanics. *Geochim. Cosmochim. Acta* **55**, 2781–2793.
- Beig M. S. and Luttge A. (2006) Albite dissolution kinetics as a function of distance from equilibrium: implications for natural feldspar weathering. *Geochim. Cosmochim. Acta* **70**, 1402–1420.
- Bénézeth P., Palmer D. A. and Wesolowski D. J. (1997) The aqueous chemistry of aluminum. A new approach to hightemperature solubility measurements. *Geothermics* **26**, 465–481.

- Bénezeth P., Palmer D. A. and Wesolowski D. J. (2001) Aqueous high-temperature solubility studies. II. The solubility of boehmite at 0.03 m ionic strength as a function of temperature and pH as determined by in situ measurements. *Geochim. Cosmochim. Acta* **65**, 2097–2111.
- Berman R. G. (1988) Internally-consistent thermodynamic data for minerals in the system $\text{Na}_2\text{O}-\text{K}_2\text{O}-\text{CaO}-\text{MgO}-\text{FeO}-\text{Fe}_2\text{O}_3-\text{Al}_2\text{O}_3-\text{SiO}_2-\text{TiO}_2-\text{H}_2\text{O}-\text{CO}_2$. *J. Petrol.* **29**, 445–522.
- Berman R. G. (1990) Mixing properties of Ca–Mg–Fe–Mn garnets. *Am. Mineral.* **75**, 328–344.
- Berner R. A. and Berner E. K. (1997) Silicate weathering and climate. In *Tectonic Uplift and Climate Change* (ed. W. F. Ruddiman). Plenum Press, pp. 353–364.
- Blum A. and Stillings L. (1995) Feldspar dissolution kinetics. In *Chemical Weathering Rates of Silicate Minerals* (eds. S. L. Brantley and A. R. White). Mineralogical Society of America, Washington DC (vol. 31, pp. 291–346).
- Bourcier W. L., Knauss K. G. and Jackson K. J. (1993) Aluminum hydrolysis constants to 250 °C from boehmite solubility measurements. *Geochim. Cosmochim. Acta* **57**, 747–762.
- Brantley S. L. (1992) Kinetics of dissolution and precipitation experimental and field results. In *Proceedings of the Seventh International Conference on Water–Rock Interactions* (eds. Y. Kharaka and A. Maest). Rotterdam, Balkema, Park City, Utah.
- Brantley S. L. and Stillings L. (1996) Feldspar dissolution at 25 °C and low pH. *Am. J. Sci.* **296**, 101–127.
- Bricker O. P., Jones B. and Bowser C. J. (2004) Mass-balance approach to interpreting weathering reactions in watershed systems. In *Surface and Ground Water* (ed. J. I. Drever). Elsevier, Oxford (vol. 5, pp. 119–132).
- Burch T. E., Nagy K. L. and Lasaga A. C. (1993) Free energy dependence of albite dissolution kinetics at 80 °C and pH 8.8. *Chem. Geol.* **105**, 137–162.
- Busenberg E. and Clemency C. V. (1976) The dissolution kinetics of feldspars at 25 °C and 1 atm CO_2 partial pressure. *Geochim. Cosmochim. Acta* **40**, 41–49.
- Chou L. and Wollast R. (1984) Study of the weathering of albite at room temperature and pressure with a fluidized bed reactor. *Geochim. Cosmochim. Acta* **48**, 2205–2217.
- Chou L. and Wollast R. (1985) Steady-state kinetics and dissolution mechanisms of albite. *Am. J. Sci.* **285**, 963–993.

- Correns C. W. (1940) Die Chemische Verwitterung der Silikate. *Nature* **28**, 369–376.
- Correns C. W. and von Engelhardt W. (1938) Neue Untersuchungen über die Verwitterung des Kalifeldspates. *Chemie der Erde* **12**, 1–22.
- Drever J. (2004) Volume editor's introduction. In *Treatise on Geochemistry*, vol. 5 (eds. H. D. Holland and K. K. Turekian). Elsevier, pp. xv–xvii.
- Drever J. I. (1997) *The Geochemistry of Natural Waters: Surface and Groundwater Environment*, second ed. Prentice-Hall, Englewood Cliffs, NJ.
- Drever J. I. and Clow D. W. (1995) Weathering rates in catchments. In *Chemical Weathering Rates of Silicate Minerals*, vol. 31 (eds. A. F. White and S. L. Brantley). Mineralogical Society of America, pp. 463–481.
- Faure G. (1998) *Principles and Applications of Inorganic Geochemistry*. Prentice Hall, New York.
- Federer C. A., Hornbeck J. W., Tritton L. M., Martin R. S., Pierce R. S. and Smith C. T. (1989) Long-term depletion of calcium and other nutrients in eastern US forests. *Environ. Manag.* **13**, 593–601.
- Fu Q., Lu P., Konishi H., Dillmore R., Xu H., Seyfried, Jr., W. E. and Zhu C. (2009) Coupled alkali–feldspar dissolution and secondary mineral precipitation in batch systems: 1. New experiment data at 200 °C and 30 MPa. *Chem. Geol.* **91**, 955–964.
- Ganor J., Lu P., Zheng Z. and Zhu C. (2007) Bridging the gap between laboratory measurements and field estimations of weathering using simple calculations. *Environ. Geol.* **53**, 599–610.
- Garrels R. M. and Mackenzie F. T. (1967) Origin of the chemical composition of some springs and lakes. In *Equilibrium Concepts in Natural Water Systems*, vol. 67 (ed. R. F. Gould). American Chemical Society, Washington, DC, pp. 222–242.
- Gautier J.-M., Oelkers E. H. and Schott J. (1994) Experimental study of K-feldspar dissolution rates as a function of chemical affinity at 150 °C and pH 9. *Geochim. Cosmochim. Acta* **58**, 4549–4560.
- Haar L., Gallagher J. S. and Kell G. S. (1984) *NBS/NRC steam tables: thermodynamic and transport properties and computer programs for vapor and liquid states of water in SI units*. Hemisphere Publishing Corporation, New York, p. 320.
- Helgeson H. C. (1968) Evaluation of irreversible reactions in geochemical processes involving minerals and aqueous solutions-1. Thermodynamic relations. *Geochim. Cosmochim. Acta* **32**, 853–877.

- Helgeson H. C. (1970) A chemical and thermodynamic model of ore deposition in hydrothermal systems. In *Fiftieth Anniversary Symposia*, vol. 3 (ed. B. A. Morgan). Min. Soc. Amer., pp. 155–186 (Special Paper).
- Helgeson H. C. (1971) Kinetics of mass transfer among silicates and aqueous solutions. *Geochim. Cosmochim. Acta* **35**, 421–469.
- Helgeson H. C. (1972) Kinetics of mass transfer among silicates and aqueous solutions: correction and clarification. *Geochim. Cosmochim. Acta* **36**, 1067–1070.
- Helgeson H. C. (1974) Chemical interaction of feldspar and aqueous solutions. In *The Feldspars* (eds. W. S. MacKenzie and J. Zussman). Crane, Russak and Co., Inc., New York, pp. 184–217.
- Helgeson H. C. (1979) Mass transfer among minerals and hydrothermal solutions. In *Geochemistry of Hydrothermal Ore Deposits* (ed. H. L. Barnes). John Wiley & Sons, New York, pp. 568–610.
- Helgeson H. C., Brown T. H., Nigrini A. and Jones T. A. (1970) Calculation of mass transfer in geochemical processes involving aqueous solutions. *Geochim. Cosmochim. Acta* **34**, 569–592.
- Helgeson H. C., Delany J. M., Nesbitt H. W. and Bird D. K. (1978) Summary and critique of the thermodynamic properties of rock forming minerals. *Am. J. Sci.* **278A**, 569–592.
- Helgeson H. C., Garrels R. M. and Mackenzie F. T. (1969) Evaluation of irreversible reactions in geochemical processing involving minerals and aqueous solutions-II. Applications. *Geochim. Cosmochim. Acta* **33**, 455–481.
- Helgeson H. C., Kirkham D. H. and Flowers G. C. (1981) Theoretical prediction of the thermodynamic behavior of aqueous electrolytes at high pressures and temperatures. IV. Calculation of activity coefficients, osmotic coefficients, and apparent molal and standard and relative partial molal properties to 600 °C and 5 kb. *Am. J. Sci.* **281**, 1249–1516.
- Helgeson H. C. and Murphy W. M. (1983) Calculation of mass transfer among minerals and aqueous solutions as a function of times and surface area in geochemical processes, I. Computational approach. *Math. Geol.* **15**, 109–130.
- Helgeson H. C., Murphy W. M. and Aagaard P. (1984) Thermodynamic and kinetic constraints on reaction rates among minerals and aqueous solutions II. Rate constants, effective surface area, and the hydrolysis of feldspar. *Geochim. Cosmochim. Acta* **48**, 2405–2432.

- Hellmann R. (1997) The albite-water system; part IV, diffusion modeling of leached and hydrogen-enriched layers. *Geochim. Cosmochim. Acta* **61**, 1595–1611.
- Hellmann R., Eggleston C. R., Hochella M. F. and Crerar D. A. (1990) The formation of leached layers on albite surfaces during dissolution under hydrothermal conditions. *Geochim. Cosmochim. Acta* **54**, 1267–1281.
- Hellmann R. and Tisserand D. (2006) Dissolution kinetics as a function of the Gibbs free energy of reaction: an experimental study based on albite feldspar. *Geochim. Cosmochim. Acta* **70**, 364–383.
- Hemingway B. S., Robie R. A. and Apps J. A. (1991) Revised values for the thermodynamic properties of boehmite, $\text{AlO}(\text{OH})$, and related species and phases in the system $\text{Al}-\text{H}-\text{O}$. *Am. Mineral.* **445**, 457.
- Hemley J. J., Montoya J. W., Marinenko J. W. and Luce R. W. (1980) Equilibria in the System $\text{Al}_2\text{O}_3-\text{SiO}_2-\text{H}_2\text{O}$ and some general implications for alteration–mineralization processes. *Econ. Geol.* **75**, 210–228.
- Hereford A. G., Keating E., Guthrie G. and Zhu C. (2007) Reactions and reaction rates in the aquifer beneath Pajarito Plateau, north-central New Mexico. *Environ. Geol.* **52**, 965–977.
- Ho P. C., Bianchi H., Palmer D. A. and Wood R. H. (2000) Conductivity of dilute aqueous electrolyte solutions at high temperatures and pressures using a flow cell. *J. Solut. Chem.* **29**, 217–235.
- Holdren G. R. and Berner R. A. (1979) Mechanism of feldspar weathering. I. Experimental studies. *Geochim. Cosmochim. Acta* **43**, 1161–1171.
- Holland T. J. B. and Powell R. (1998) An internally consistent thermodynamic data set for phases of petrological interest. *J. Metamorph. Geol.* **16**, 309–343.
- Johnson J. W., Oelkers E. H. and Helgeson H. C. (1992) SUPCRT92 – a software package for calculating the standard molal thermodynamic properties of minerals, gases, aqueous species, and reactions from 1-bar to 5000-bar and 0 °C to 1000 °C. *Comput. Geosci.* **18**, 899–947.
- Krauskopf K. B. and Bird D. K. (1995) *Introduction to Geochemistry*. WCB McGraw-Hill, Boston.
- Kwicklis E. (2004) *Geochemical and isotopic constraints on groundwater flow directions, mixing, and recharge at Yucca Mountain, Nevada*. Office of Civilian Radi, Waste anagement.

- Lasaga A. C. (1998) *Kinetic Theory in the Earth Sciences*. Princeton University Press, New York.
- Lasaga A. C., Soler J. M., Ganor J., Burch T. E. and Nagy K. L. (1994) Chemical weathering rate laws and global geochemical cycles. *Geochim. Cosmochim. Acta* **58**, 2361–2386.
- Likens G. E., Driscoll C. T., Buso D. C., Siccama T. G., Johnson C. E., Lovett G. M., Fahey T. J., Reiners W. A., Ryan D. F., Maring C. W. and Bailey S. W. (1998) The biogeochemistry of calcium at Hubbard Brook. *Biogeochemistry* **41**, 89–173.
- Luce R. W., Bartlett R. W. and Parks G. A. (1972) Dissolution kinetics of magnesium silicates. *Geochim. Cosmochim. Acta* **36**, 35–50.
- McCollom T. M. and Shock E. L. (1997) Geochemical constraints on chemolithoautotrophic metabolism by microorganisms in seafloor hydrothermal systems. *Geochim. Cosmochim. Acta* **61**, 4375–4391.
- McHale J. M., Yurekli K., Dabbs D. M., Navrotsky A., Sundaresan S. and Aksay I. A. (1997) Metastability of spinel-type solid solutions in the $\text{SiO}_2\text{--Al}_2\text{O}_3$ system. *Chem. Mater.* **9**, 3096–3100.
- Murakami T., Kogure T., Kadohara H. and Ohnuki T. (1998) Formation of secondary minerals and its effects on anorthite dissolution. *Am. Mineral.* **83**, 1209–1219.
- Nagy K. L. and Lasaga A. C. (1993) Kinetics of simultaneous kaolinite and gibbsite precipitation. *Geochim. Cosmochim. Acta* **57**, 4329–4337.
- Nesbitt H. W. and Skinner W. M. (2001) Early development of Al, Ca, and Na compositional gradients in labradorite leached in pH 2 HCl solutions. *Geochim. Cosmochim. Acta* **65**, 715–727.
- Nugent M. A., Brantley S. L., Pantano C. G. and Maurice P. A. (1998) The influence of natural mineral coatings on feldspar weathering. *Nature* **395**, 588–591.
- Oelkers E. H. (2001) General kinetic description of multioxide silicate mineral and glass dissolution. *Geochim. Cosmochim. Acta* **65**, 3703–3719.
- Oelkers E. H. and Helgeson H. C. (1990) Triple-ion anions and polynuclear complexing in supercritical electrolyte-solutions. *Geochim. Cosmochim. Acta* **54**, 727–738.
- Oelkers E. H., Schott J. and Devidal J. L. (1994) The effect of aluminum, pH, and chemical affinity on the rates of aluminosilicate dissolution reactions. *Geochim. Cosmochim. Acta* **58**, 2011–2024.

- Paces T. (1973) Steady-state kinetics and equilibrium between ground water and granitic rocks. *Geochim. Cosmochim. Acta* **37**, 2641–2663.
- Paces T. (1983) Rate constants of dissolution derived from the measurements of mass balance in hydrological catchments. *Geochim. Cosmochim. Acta* **37**, 1855–1863.
- Palmer D. A., Be´ne´zeth P. and Wesolowski D. J. (2001) Aqueous high-temperature solubility studies. I. The solubility of boehmite as functions of ionic strength (to 5 molal, NaCl), temperature (100–290 °C), and pH as determined by in situ measurements. *Geochim. Cosmochim. Acta* **65**, 2081–2095.
- Parkhurst D. L. and Appello A. A. J. (1999) *User's guide to PHREEQC (version 2)-a computer program for speciation, batch-reaction, one dimensional transport, and inverse geochemical modeling*. Water-Resource Investigation Report. U.S. Geological Survey.
- Petrovic R. (1976) Rate control in feldspar dissolution II. The protective effects of precipitates. *Geochim. Cosmochim. Acta* **40**, 1509–1521.
- Pokrovskii V. A. and Helgeson H. C. (1995) Thermodynamic properties of aqueous species and the solubilities of minerals at high pressures and temperatures: the system Al₂O₃–H₂O–NaCl. *Am. J. Sci.* **295**, 1255–1342.
- Price J. R., Velbel M. A. and Patino L. C. (2005) Rates and time scales of clay-mineral formation by weathering in saprolitic regoliths of the southern Appalachians from geochemical mass balance. *Geol. Soc. Am. Bull.* **117**, 783–794.
- Reed M. H. and Spycher N. F. (1984) Calculation of pH and mineral equilibria in hydrothermal waters with application to geothermometry and studies of boiling and dilution. *Geochim. Cosmochim. Acta*. **48**, 1479–1492.
- Robie R. A. and Hemingway B. S. (1995) *Thermodynamic properties of minerals and related substances at 298.15 K and 1 bar (105 pascals) pressure and at higher temperatures*. U.S. Geological Survey Bulletin 2131, 456.
- Seyfried, Jr., W. E., Janecky D. R. and Berndt M. E. (1987) Rocking autoclaves for hydrothermal experiments: II. The flexible reaction-cell system. In *Hydrothermal Experimental Techniques* (ed. H. L. Barnes). Wiley-Interscience, pp. 216–239.
- Shock E. L. (1995) Organic acids in hydrothermal solutions: standard molal thermodynamic properties of carboxylic acids and estimates of dissociation constants at high temperatures and pressures. *Am. J. Sci.* **295**, 496–580.
- Shock E. L. and Helgeson H. C. (1988) Calculation of the thermodynamic and transport properties of aqueous species at high pressures and temperatures: correlation

- algorithms for ionic species and equation of state predictions to 5 kb and 1000 °C. *Geochim. Cosmochim. Acta* **52**, 2009–2036.
- Shock E. L., Helgeson H. C. and Sverjensky D. A. (1989) Calculations of the thermodynamic and transport properties of aqueous species at high pressures and temperatures: standard partial molal properties of inorganic neutral species. *Geochim. Cosmochim. Acta* **53**, 2157–2183.
- Shock E. L. and Koretsky C. M. (1993) Metal-organic complexes in geochemical processes: calculation of standard partial molal thermodynamic properties of aqueous acetate complexes at high pressures and temperatures. *Geochim. Cosmochim. Acta* **57**, 4899–4922.
- Shock E. L., Oelkers E. H., Sverjensky D. A., Johnson J. W. and Helgeson H. C. (1992) Calculation of thermodynamic and transport properties of aqueous species at high pressures, temperatures. Effective electrostatic radii, dissociation constants, standard partial molal properties to 1000 °C and 5 kb. *J. Chem. Soc. Lond. Faraday Trans.* **88**, 803–826.
- Shock E. L., Sassani D. C., Willis M. and Sverjensky D. A. (1997) Inorganic species in geologic fluids: correlations among standard molal thermodynamic properties of aqueous ions and hydroxide complexes. *Geochim. Cosmochim. Acta* **61**, 907–950.
- Small J. S. (1993) Experimental determination of the rates of precipitation of authigenic illite and kaolinite in the presence of aqueous oxalate and comparison to the K/Ar ages of authigenic illite in reservoir sandstones. *Clays Clay Miner.* **41**, 191–208.
- Spycher N. F., Sonnenthal E. L. and Apps J. A. (2003) Fluid flow and reactive transport around potential nuclear waste emplacement tunnels at Yucca Mountain, Nevada. *J. Contam. Hydrol.* **62–63**, 653–673.
- Steefel, C. I. and van Cappellen, P., 1990. A new kinetic approach to modeling water-rock interaction: The role of nucleation, precursors, and Ostwald ripening. *Geochim. Cosmochim. Acta* **54**, 2657–2677.
- Steinmann P., Lichtner P. C. and Shotyk W. (1994) Reaction-path approach to mineral weathering reactions. *Clays Clay Miner.* **42**, 197–206.
- Sverjensky D. A., Hemley J. J. and D'Angelo W. M. (1991) Thermodynamic assessment of hydrothermal alkali feldspar–mica–aluminosilicate equilibria. *Geochim. Cosmochim. Acta* **55**, 989–1004.
- Sverjensky D. A., Shock E. L. and Helgeson H. C. (1997) Prediction of the thermodynamic properties of aqueous metal complexes to 5 kb and 1000 °C. *Geochim. Cosmochim. Acta* **61**, 1359–1412.

- Tagirov B. and Schott J. (2001) Aluminum speciation in crustal fluids revisited. *Geochim. Cosmochim. Acta* **65**, 3965–3992.
- Tanger J. C. and Helgeson H. C. (1988) Calculations of the thermodynamic and transport properties of aqueous species at high pressures and temperatures: revised equation of state for the standard partial molal properties of ions and electrolytes. *Am. J. Sci.* **288**, 19–98.
- Velbel M. A. (1990) Influence of temperature and mineral surface characteristics on feldspar weathering rates in natural and artificial systems: a first approximation. *Water Resour. Res.* **26**, 3049–3053.
- White A. F. and Brantley S. L. (2003) The effect of time on the weathering of silicate minerals: why do weathering rates in the laboratory and field? *Chem. Geol.* **202**, 479–506.
- White C., Strasizar B. R., Granite E. J., Hoffman J. S. and Pennline H. W. (2003) Separation and capture of CO₂ from large stationary sources and sequestration in geological formations –coalbeds and deep saline aquifers. *J. Air Waste Manag. Assoc.* **53**, 645–715.
- Wolery T. J. (1992) *EQ3/6, a software package for geochemical modeling of aqueous systems: package overview and installation guide (version 7.0)*. URCL-MA-110662-PT-I, Livermore. California University, Lawrence Livermore Laboratory, California.
- Zhu C. (2005) In situ feldspar dissolution rates in an aquifer. *Geochim. Cosmochim. Acta* **69**, 1435–1453.
- Zhu C. (2006) In situ silicate reaction rates in sandy aquifers. *Geochim. Cosmochim. Acta* **70**, A753.
- Zhu C. and Anderson G. M. (2002) *Environmental Applications of Geochemical Modeling*. Cambridge University Press, London.
- Zhu C., Blum A. E. and Veblen D. R. (2004a) Feldspar dissolution rates and clay precipitation in the Navajo aquifer at Black Mesa, Arizona, USA. In *Water–Rock Interaction* (eds. R. B. Wanty and R. R. I. Seal). A.A. Balkema, Saratoga Springs, New York, pp. 895–899.
- Zhu C., Blum A. E. and Veblen D. R. D. (2004b) A new hypothesis for the slow feldspar dissolution in groundwater aquifers. *Geochim. Cosmochim. Acta* **68**, A148.
- Zhu C., Veblen D. R., Blum A. E. and Chipera S. J. (2006) Naturally weathered feldspar surfaces in the Navajo Sandstone aquifer, Black Mesa, Arizona: electron microscopic characterization. *Geochim. Cosmochim. Acta* **70**, 4600–4616.

CHAPTER 5

ALKALI FELDSPAR DISSOLUTION AND SECONDARY MINERAL PRECIPITATION IN BATCH SYSTEMS: 4. NUMERICAL MODELING OF KINETIC REACTION PATHS⁴

⁴ This chapter is currently in press: Zhu, C., Lu, P., Zheng, Z., and Ganor, J. (2010) Alkali feldspar dissolution and secondary mineral precipitation in batch systems: 4. Numerical modeling of kinetic reaction paths. *Geochimica et Cosmochimica Acta*, In Press.

1. INTRODUCTION

Numerous hypotheses have been proposed in the literature to explain the persistent apparent discrepancy between measured field and laboratory feldspar dissolution rates (for the discrepancy, see Paces, 1973; Siegel and Pfannkuch, 1984; Velbel, 1990; Brantley, 1992; Blum and Stillings, 1995; Drever and Clow, 1995). These hypotheses include the possible armoring effects of the secondary minerals that coat the feldspar grain surfaces (Correns and Von Engelhardt, 1938; Correns, 1940; Helgeson, 1971, 1972; Luce et al., 1972; Paces, 1973; Busenberg and Clemency, 1976; Chou and Wollast, 1984; Nugent et al., 1998), the possible effects of the leached layer (Luce et al., 1972; Busenberg and Clemency, 1976; Chou and Wollast, 1984; Hellmann et al., 1990; Brantley and Stillings, 1996; Hellmann, 1997; Nesbitt and Skinner, 2001; Oelkers, 2001), the approach to saturation with respect to feldspars (Burch et al., 1993; Gautier et al., 1994; Oelkers et al., 1994; Oelkers, 2001; Beig and Lüttge, 2006; Hellmann and Tisserand, 2006), unknown biological effects, and inhibition by adsorbed Al^{3+} on feldspar surfaces (Chou and Wollast, 1985; Gautier et al., 1994; Oelkers et al., 1994; Oelkers, 2001).

One distinction that differentiates field from laboratory conditions is that weathering product minerals are often intimately associated with the primary minerals in nature (Banfield and Eggleton, 1990; Banfield et al., 1991; Banfield and Barker, 1994; Nugent et al., 1998; Zhu et al., 2006; Hereford et al., 2007). Conversely, in laboratory experiments, the precipitation of product minerals was often avoided by adjusting the chemistry and recirculation rate of the fluid phase. Recognizing the close association between the secondary and primary minerals in the field, Zhu et al. (2004) proposed a

new hypothesis (Zhu-Blum-Veblen or ZBV hypothesis) for explaining the laboratory-field discrepancy wherein the slow kinetics of secondary clay precipitation is the rate limiting step and thus controls the overall feldspar dissolution rate. Clay precipitation removes solutes from the aqueous solution, maintaining a condition of feldspar undersaturation. This makes additional feldspar dissolution possible, but the slow clay precipitation (or smaller effective rate constants with respect to that for the dissolution reaction, see below) results in a quasi-steady state in which the aqueous solution is near equilibrium with feldspar. Therefore, slow clay precipitation could effectively reduce feldspar dissolution rates by orders of magnitude, in a fashion consistent with laboratory rates at conditions far from equilibrium, the control of dissolution rates by the Gibbs free energy of the reaction, and many field observations (Zhu et al., 2004).

To test this hypothesis, we have conducted experiments of feldspar dissolution and secondary mineral precipitation in batch systems. As these reactions are too slow to be measured under ambient temperature and circumneutral pH conditions (Ganor et al., 2007), the experiments were conducted at 200 °C and 30 MPa. Although the secondary minerals formed in these high temperature experiments are different from clays formed under ambient, weathering temperatures, the failure to achieve partial equilibrium under hydrothermal conditions is highly likely an excellent indicator that partial equilibrium with secondary minerals is also not attained under weathering temperatures. In the first of this series of articles, we presented new experimental data, which documented the temporal evolution of aqueous chemistry and secondary minerals (Fu et al., 2009). The second paper is on CO₂ effects on feldspar hydrolysis and it is still in preparation. The third paper described the saturation indices and reaction paths in terms of trajectories of

aqueous chemical evolution on equilibrium activity-activity diagrams (Zhu and Lu, 2009). These articles document that secondary minerals were not at equilibrium with the aqueous solutions, but their precipitation was likely controlled by kinetic processes that are slower than the dissolution rates. Partial equilibrium between secondary minerals and aqueous solutions was not observed (Zhu and Lu, 2009).

In the present communication, we report results of numerical reaction path modeling that simulate the feldspar hydrolysis experiments by matching modeling results with experimental data. The reaction path modeling reported here is different from the speciation and solubility modeling in Paper 3 (Zhu and Lu, 2009). Speciation and solubility modeling simulates a snapshot of a chemical system while the reaction path modeling simulates processes. To simulate the experimental processes, reaction path models use the initial experimental solutions as a starting point. The course of the chemical evolution in the system is set by the rate laws for primary mineral dissolution and secondary mineral precipitation. In reaction path modeling, it is therefore necessary to make assumptions regarding reactive surface areas and the appropriate forms that the rate laws should take. Both topics are controversial and are presently undergoing intense research.

However, the reaction path models, reported here, give rich quantitative information of the reaction processes during these experiments. For example, the speciation – solubility modeling did not tell how the dissolution and precipitation reactions are coupled quantitatively, but reaction path modeling does, as shown in this paper. We should emphasize that the batch systems are simple model systems to test ideas of reaction kinetics before kinetic theories can be applied to complex natural

systems, e.g., without further assumptions of flow and transport properties (Zhu, 2009). It is a necessary step in the process of going from laboratory dissolution rate experiments at far-from-equilibrium (e.g., mixed flow reactor with fixed solution chemistry) to natural systems. However, simulation of reactive mass transport in idealized model systems allows us to explore the potential effects of fluid flow rates on the coupling of dissolution and precipitation reactions.

2. CONCEPTUAL MODELS AND ASSUMPTIONS

The mathematical formulation of reaction path modeling has been extensively described before (Helgeson, 1968; Helgeson et al., 1969; Helgeson, 1979; Wolery, 1992). Essentially, for a geochemical system that has n species, the following ordinary differential equations completely define the geochemical reaction network in a well-mixed reactor (Helgeson et al., 1970),

$$\frac{dm_i}{dt} = \sum_j \nu_{i,j} r_{i,j}, i \in n \quad (1)$$

where m_i denotes the concentrations of i th species, t the time, $\nu_{i,j}$ the stoichiometric coefficient for the i th species in the j th reaction, and $r_{i,j}$ the production or consumption rate of the i th species in the j th reaction. See Table 1 for symbols and notations.

The numerical techniques for solving this set of equations are well established (Wolery, 1992) and several computer codes are now available for performing the computation task. In our study, we used the computer code PHREEQC (Parkhurst and Appello, 1999), but with our own database for equilibrium constants at appropriate

temperatures, pressures, and customized rate laws. In the reaction path models, we assumed that all homogenous reactions are instantaneous i.e., that all aqueous species are at equilibrium with each other. Aqueous speciation was modeled for all fluid samples taking explicit account of mass balance, mass action, and charge balance constraints. Activity coefficients for the charged aqueous species were calculated from the extended Debye-Hückel equation or B-dot equation fitted to mean salt NaCl activity coefficients (Helgeson et al., 1978; Oelkers and Helgeson, 1990). Activity coefficients for neutral or uncharged aqueous species were calculated from the Setchénow equation with a coefficient of 0.1. Deviation from unity for activity coefficients for end-members of feldspar or clay solid solutions that result from compositional impurities was neglected. The rates of mass transfer between solid and aqueous phases are prescribed by the rate laws described below.

2.1. Standard State Thermodynamic Data

In all calculations, the standard states for solids are defined as unit activity for pure end-member solids at the temperature and pressure of interest. The standard state for water is the unit activity of pure water. For aqueous species other than H₂O, the standard state is the unit activity of the species in a hypothetical one molal solution referenced to infinite dilution at the temperature and pressure of interest. Equilibrium constants ($\log K$) for reactions were calculated from the standard state thermodynamic properties for mineral end-members and aqueous species. The values of $\log K$ and the sources of thermodynamic properties that were used are listed in Table 2. In all cases, internally consistent thermodynamic properties were used when possible. See Zhu and Lu (2009) for a detailed discussion of the choices regarding standard thermodynamic properties.

Table 1. List of Symbols

symbols	Explanations
aq	Subscript: aqueous species
E_a	Activation energy (J/mol)
g	$g \equiv \Delta G_r / RT$
$\Delta G_{r,j}$	Gibbs free energy of reaction for the j th mineral (J mol^{-1})
$f(\Delta G_r)$	Reaction rates as a function of Gibbs free energy of reaction in the rate law
k^*	Effective rate constant
k_1	Rate constant for the first term of the empirical parallel rate law of Burch et al. (1993) ($\text{mol m}^{-2} \text{s}^{-1}$)
k_2	Rate constant for the second term of the empirical parallel rate law of Burch et al. (1993) ($\text{mol m}^{-2} \text{s}^{-1}$)
k_j	Rate constant of j th mineral reaction ($\text{mol s}^{-1} \text{m}^{-2}$)
K	Equilibrium constant
$m_{t,i}$	Total concentrations of the i th aqueous constituent in molality
m_i	Molality of the i th aqueous species
m_1	Empirical parameters fitted from experimental data for the first term of the empirical parallel rate law of Burch et al. (1993)
m_2	Empirical parameters fitted from experimental data for the first term of the empirical parallel rate law of Burch et al. (1993)
n_1	Empirical parameters fitted from experimental data for the first term of the empirical parallel rate law of Burch et al. (1993)
N_j	Moles of mineral j , per kg of water
Q	Activity quotient
r_j	Rate of dissolution or precipitation of the j th mineral in $\text{mol kgw}^{-1} \text{s}^{-1}$ (kgw=kg water)
SI	Saturation Index
S_j	Surface area of the j th mineral
σ	Temkin coefficient in the rate law
\in	Include
Mineral abbreviations	Albite, Ab; sanidine, San; quartz, Qtz

Table 2. Equilibrium constants used in this study

	25 °C 0.1 MPa	200 °C, 30 MPa	300 °C, 8.8 MPa	Ref
Aqueous reactions				
$\text{H}_2\text{O} = \text{OH}^- + \text{H}^+$	-13.995	-11.163	-11.297	(1)
$\text{Al}^{3+} + \text{H}_2\text{O} = \text{Al}(\text{OH})_2^{2+} + \text{H}^+$	-4.964	-1.446	-0.22	(2)
$\text{Al}^{3+} + 2\text{H}_2\text{O} = \text{Al}(\text{OH})_3^+ + 2\text{H}^+$	-10.921	-3.63	-1.119	(2)
$\text{Al}^{3+} + 3\text{H}_2\text{O} = \text{Al}(\text{OH})_4^0 + 3\text{H}^+$	-17.044	-7.301	-4.035	(2)
$\text{Al}^{3+} + 4\text{H}_2\text{O} = \text{Al}(\text{OH})_5^- + 4\text{H}^+$	-22.851	-11.572	-8.150	(2)
$\text{Al}^{3+} + \text{Na}^+ + 4\text{H}_2\text{O} = \text{NaAl}(\text{OH})_4^0 + 4\text{H}^+$	-22.90	-10.748	-6.63	(2)
$\text{Al}^{3+} + \text{SiO}_2^0 + 2\text{H}_2\text{O} = \text{AlH}_3\text{SiO}_4^{2+} + \text{H}^+$	-2.357	1.86	3.188	(2)
$\text{Na}^+ + \text{H}_2\text{O} = \text{NaOH}^0 + \text{H}^+$	-14.205	-11.087	-10.480	(3)
$\text{SiO}_2^0 + \text{H}_2\text{O} = \text{HSiO}_3^- + \text{H}^+$	-9.585	-8.707	-9.430	(3)
$\text{SiO}_2^0 + \text{Na}^+ + \text{H}_2\text{O} = \text{NaHSiO}_3^0 + \text{H}^+$	-7.754	-7.767	-7.986	(3)
$\text{Ca}^{2+} + \text{H}_2\text{O} = \text{CaOH}^+ + \text{H}^+$	-12.833	-7.961	-6.435	(3)
$\text{K}^+ + \text{H}_2\text{O} = \text{KOH}^0 + \text{H}^+$	-14.439	-10.939	-10.267	(3)
$\text{Cl}^- + \text{Ca}^{2+} = \text{CaCl}^+$	-0.292	1.146		(3)
$2\text{Cl}^- + \text{Ca}^{2+} = \text{CaCl}_2^0$	-0.644	0.672		(3)
$\text{H}^+ + \text{Cl}^- = \text{HCl}^0$	-0.710	-0.15		(4)
$\text{K}^+ + \text{Cl}^- = \text{KCl}^0$		0.456		(5)
$\text{Na}^+ + \text{Cl}^- = \text{NaCl}^0$	-0.777	0.019		(3)
$\text{HCO}_3^- + \text{H}^+ = \text{CO}_2 + \text{H}_2\text{O}$	6.345		8.525	(3)
$\text{HCO}_3^- = \text{CO}_3^{2-} + \text{H}^+$	-10.329		-11.461	(3)
$\text{HCO}_3^- + \text{Na}^+ = \text{NaCO}_3^- + \text{H}^+$	-9.455		-8.468	(8)
$\text{HCO}_3^- + \text{Na}^+ = \text{NaHCO}_3^0$	-0.103		2.002	(8)
$\text{HCO}_3^- + \text{K}^+ = \text{KCO}_3^- + \text{H}^+$	-9.455		-8.468	(8)
$\text{HCO}_3^- + \text{K}^+ = \text{KHCO}_3^0$	-0.103		2.002	(8)
Mineral dissolution reactions				
$\text{NaAlSi}_3\text{O}_8 \text{ (Albite)} + 4\text{H}^+ = \text{Al}^{3+} + \text{Na}^+ + 3\text{SiO}_2^0 + 2\text{H}_2\text{O}$	2.065	-2.508	-4.714	(6)
$\text{AlO}_2\text{H (Boehmite)} + 3\text{H}^+ = \text{Al}^{3+} + 2\text{H}_2\text{O}$	7.610	.242	-2.530	(7)
$\text{AlO}_2\text{H (Diaspore)} + 3\text{H}^+ = \text{Al}^{3+} + 2\text{H}_2\text{O}$	7.191	0.02	-2.685	(6)
$\text{Al}_2\text{Si}_2\text{O}_5(\text{OH})_4 \text{ (Kaolinite)} + 6\text{H}^+ = 2\text{Al}^{3+} + 2\text{SiO}_2^0 + 5\text{H}_2\text{O}$	4.501	-5.354	-9.443	(6)
$\text{KAlSi}_3\text{O}_8 \text{ (Microcline)} + 4\text{H}^+ = \text{Al}^{3+} + \text{K}^+ + 3\text{SiO}_2^0 + 2\text{H}_2\text{O}$	-1.05	-3.923	-5.694	(6)
$\text{KAl}_3\text{Si}_3\text{O}_{10}(\text{OH})_2 \text{ (Muscovite)} + 10\text{H}^+ = \text{K}^+ + 3\text{Al}^{3+} + 3\text{SiO}_2^0 + 6\text{H}_2\text{O}$	11.22	-5.407	-12.445	(6)
$\text{NaAl}_3\text{Si}_3\text{O}_{10}(\text{OH})_2 \text{ (Paragonite)} + 10\text{H}^+ = \text{Na}^+ + 3\text{Al}^{3+} + 3\text{SiO}_2^0 + 6\text{H}_2\text{O}$	14.397	-3.753	-11.164	(6)
$\text{Al}_2\text{Si}_4\text{O}_{10}(\text{OH})_2 \text{ (Pyrophyllite)} + 6\text{H}^+ = 2\text{Al}^{3+} + 4\text{H}_2\text{O} + 4\text{SiO}_2^0$	-1.724	-9.733	-13.647	(6)
$\text{SiO}_2 \text{ (Quartz)} = \text{SiO}_2^0$	-4.047	-2.424	-2.033	(6)
$\text{KAlSi}_3\text{O}_8 \text{ (Sanidine)} + 4\text{H}^+ = \text{Al}^{3+} + \text{K}^+ + 3\text{SiO}_2^0 + 2\text{H}_2\text{O}$	-0.002		-5.499	(6)
$\text{KAlSiO}_4 \text{ (Kalsilite)} + 4\text{H}^+ = \text{K}^+ + \text{Al}^{3+} + \text{SiO}_2^0 + 2\text{H}_2\text{O}$	12.543		1.187	(6)
$\text{NaAlSiO}_4 \text{ (Nepheline)} + 4\text{H}^+ = \text{Na}^+ + \text{Al}^{3+} + \text{SiO}_2^0 + 2\text{H}_2\text{O}$	13.423		1.185	(6)

(1) Haar et al. (1984); (2) Tagirov and Schott (2001); (3) Sverjensky et al. (1997); (4) McCollom and Shock (1997); (5) Ho et al. (2000); (6) Holland and Powell (1998) for minerals and (1), (2), and (3) for aqueous species; (7) Hemingway et al. (1991) for boehmite; (8) Alekseyev et al. (1997).

2.2. Rate Laws

A general form of rate laws for heterogeneous reactions may be written as

(Lasaga et al., 1994)

$$r_j = \frac{dN_j}{dt} = k_j S_j a_{\text{H}^+}^{n_{\text{H}^+}} g(I) \prod_a a_i^{n_i} f(\Delta G_r) \quad (2)$$

where r_j is the dissolution rate of the j th mineral ($\text{mol s}^{-1} \text{ kgw}^{-1}$; $\text{kgw}=\text{kg water}$), N_j

denotes the moles of mineral j per kg of water (mol kgw^{-1}), k_j is the respective rate

constant ($\text{mol m}^{-2} \text{s}^{-1}$), and S_j is the reactive surface area of the j th mineral ($\text{m}^2 \text{kgw}^{-1}$). a_{H}^+ stands for the activity of hydrogen in the aqueous solution, and hence this term accounts for the well-noted pH dependence of dissolution rates. The term $g(I)$ accounts for possible ionic strength dependence of the rates. The term $\prod_a a_i^{n_i}$ incorporates possible catalytic and inhibitory effects of aqueous species. ΔG_r (J/mol) denotes the Gibbs free energy of reaction.

The term $f(\Delta G_r)$ describes the effect of deviation from equilibrium on the rate and represents the thermodynamic driving force for chemical reactions (Prigogine and Defay, 1965; Aagaard and Helgeson, 1982). A simple form for the r_j - ΔG_r relationship is proposed based on the Transition State Theory (TST) (Lasaga, 1981a; Lasaga, 1981b; Aagaard and Helgeson, 1982),

$$f(\Delta G_r) = \left(1 - \exp\left(\frac{\Delta G_r}{RT}\right) \right) \quad (3)$$

This formulation of the free energy term has also been termed the “linear TST rate law” because the relationship between r_j and ΔG_r becomes linear near equilibrium.

However, a number of experiments near equilibrium have shown that the actual relationship between r_j and ΔG_r deviates from this so-called linear kinetics (Schramke et al., 1987; Nagy et al., 1991; Nagy and Lasaga, 1992; Burch et al., 1993; Nagy and Lasaga, 1993; Gautier et al., 1994; Alekseyev et al., 1997; Cama et al., 2000; Taylor et al., 2000; Beig and Lüttge, 2006; Hellmann and Tisserand, 2006). As shown below, the linear TST rate law also cannot fit the experimental data of Zhu and Lu (2009).

Different non-linear rate laws were proposed for feldspar dissolution. For example, Alekseyev et al. (1997) introduced a non-linear rate law in the form of

$$f(\Delta G_r) = \left| 1 - \left(\frac{Q}{K} \right)^p \right|^q \quad (4)$$

where Q is the activity quotient, K is the equilibrium constant, p and q are fitting parameters. Burch et al. (1993) proposed an empirical parallel rate law in the form of,

$$r / S = k_1 [1 - \exp(-ng^{m_1})] + k_2 [1 - \exp(-g)]^{m_2} \quad (5)$$

where k_1 and k_2 denote the rate constants in units of $\text{mol s}^{-1} \text{m}^{-2}$, $g \equiv |\Delta G_r| / RT$, and n_1 , m_1 , and m_2 are empirical parameters fitted from experimental data. Note that the first term is equivalent to Eqn (4) if $n_1 = p$, $m_1 = 1$, and $q = 1$. The second term is also equivalent to Eqn (4) if $p = 1$ and $m_2 = q$. In the reaction path modeling of the present study, the rate law of Eq. (5) is used for albite and oligoclase dissolution. Rate laws for other mineral dissolution and precipitation reactions will be discussed below as they appear.

2.3. Reactive Surface Area

The concept of “reactive surface area (RSA)” (Helgeson et al., 1984) is rooted in the theories of surface controlled reaction kinetics. The rates of heterogeneous reactions are proportional to the “concentrations” of reactive surface sites. The RSA thus substitutes for site concentrations in lieu of reactant concentrations in a first order rate law (Zhu and Anderson, 2002). Apparently, RSA represents the key scaling parameter for extrapolating from atomic to laboratory and field scales. However, this concept is

difficult to implement in practice. Different crystal faces have different types of surface sites and site concentrations. Surface topography (e.g., kinks, edges, and adatoms) and types and densities of defects on mineral surfaces are difficult to quantify. The “reactive site concentrations” would also depend on whether and how deep a “leached layer” is developed near the mineral surfaces (Stillings et al., 1995; Oelkers, 2001).

The common practice in geochemistry is to use the Brunauer-Emmett-Teller (BET) surface area (Braunauer et al., 1938) of the dry powder as a proxy for the RSA. However, there are several challenges in substituting BET surface area for RSA in Eqn (2). From a theoretical point of view, we are using a single parameter to represent a variety of surface sites with different reactivity and concentrations. The BET SA is more physically based (gas adsorption and surface roughness) than chemical in nature. From a practical point of view, it is difficult to measure BET SA for a mineral within a mixture and for secondary minerals with miniature quantities. Often, the reactive surface areas are significantly less than the BET surface area (Helgeson et al., 1984).

In an experiment, reactive surface area may vary due to the growth or reduction of crystal sizes. In such cases, S during dissolution or precipitation may be empirically related to the initial total surface area (S^0) by (Christoffersen and Christoffersen, 1976; Witkamp et al., 1990; Zhang and Nancollas, 1992; He et al., 1994)

$$S / S^0 = (N^t / N^0)^P \quad (6)$$

where P is a coefficient that depends on the shape of the crystal and the relative rates of dissolution (or growth) on different surfaces. P equals to 2/3 if the shape of the crystals

remains unchanged and rates on all faces are equal. P values of 0.5 indicate that dissolution or growth occur predominantly in two directions while P values of 0 indicate one direction (e.g., Witkamp et al., 1990).

The reactive surface areas may also vary during experiments as a result of the extinction of highly reactive fine particles (Helgeson et al., 1984), change of the ratios of reactive and nonreactive sites (Gautier et al., 2001), mechanical disaggregation of particles (Nagy and Lasaga, 1992; Ganor et al., 1999), and formation of surface coating (Ganor et al., 1995; Nugent et al., 1998; Cubillas et al., 2005; Metz et al., 2005).

It is even more difficult to estimate the reactive surface areas for precipitating secondary phases. Precipitation of a new mineral phase requires nucleation and crystal growth. Currently, the lack of parameters prevents the application of nucleation theories to the experiments that we examined in this study (see review by Fritz and Noguera, 2009). For modeling, it also presents a dilemma: precipitation cannot proceed without surface area first; and without precipitates at first, there are no surface areas for the secondary phases. Although the size of stable nuclei can be calculated using classical nucleation theory (Nielsen, 1964), there are no strict ways to assess the reactivity of such nuclei.

In this study, we followed common practice in geochemistry and used the BET surface areas for starting reactants in the reaction path modeling as the initial conditions. Then, we assessed the possible temporal variation of reactive surface areas from experimental data. When it was difficult to separate the effects of rate constant and reactive surface areas from batch reactor data, we introduced an effective rate constant, k^*

$$k^* = k \times S \quad (7)$$

where S stands for reactive surface area. k^* has a unit of $\text{mol kgw}^{-1} \text{ s}^{-1}$ if S has units of $\text{m}^2 \text{ kgw}^{-1}$. Note that k^* , as a fitting parameter, in effect, could represent all terms in the empirical rate law (Eqn. 5), except for the Gibbs free energy term and other effects explicitly noted.

3. MODELING RESULTS AND ANALYSES

3.1. Albite Dissolution - Sanidine Precipitation Experiments

Alekseyev et al. (1997) conducted a series of batch experiments for low albite ($\text{Na}_{0.97}\text{K}_{0.02}\text{AlSi}_{3.01}\text{O}_8$) dissolution in 0.1 m KHCO_3 fluid. The experiments were conducted at 300 °C and 88 bars and pH ~9.0 (buffered by bicarbonate). The measured initial BET specific surface areas are $0.12 \text{ m}^2/\text{g}$ for albite reactants. XRD and SEM results show that the only secondary mineral formed was sanidine.

Alekseyev et al. (1997, shortened to Alek97) calculated albite dissolution rates at the congruent stage (the first 7 hours, cf. their Fig 2) on the basis of molal concentrations of Na, Al, and Si in the solutions, which are almost stoichiometric. At the incongruent stages (7 – 1848 h), they used a mass balance approach that accounts for primary mineral dissolution and secondary mineral precipitation to calculate reaction rates, which is essentially numerical inverse mass balance modeling but with statistical rigor. For convenience, we will reference the original values of rates, rate constants, mineral abundances etc. reported by Alek97 as “experimental data” although many of these values were derived and not directly measured.

3.1.1. Congruent Dissolution Stage (0-7 h)

The first seven (7) hours of the 1848 h experiments, according to Alek97, showed essentially congruent dissolution of albite. That was based on the stoichiometric ratios of Na, Al, and Si released into the solution (see below) and on the lack of detectable sanidine in the reaction products. The experiments started far from equilibrium, and congruent dissolution of albite was recorded in the $\Delta G_{r,Ab}$ range from -59 to ca. -20 kJ/mol (Fig. 1a). The initial mass/volume ratio in the experiment was 2.5 g albite kgw⁻¹ (9.52×10^{-3} mol kgw⁻¹) and the initial specific BET surface area was 0.12 m²/g. During the first 7 hours, about 8% of the albite was dissolved. The amounts of remaining albite N (mol kgw⁻¹) at the time of interest were roughly estimated from the mass balance,

$$N^i \approx N^{i-1} - [r^i \times (t^i - t^{i-1})] \quad (8)$$

where i stands for the i th sample in the batch series, t for time (s) and r for the rate of dissolution in units of mol s⁻¹ kgw⁻¹ as reported by Alek97. The amount of albite was reduced to $\sim 8.8 \times 10^{-3}$ mol at 7 h according to Eqn (8). It must be emphasized that Eqn (8) only gives rough estimates of the albite mass in the reactor. For simplicity, we assumed that the total surface area of albite S_{Ab} remained constant during the first 7 hours. This assumption resulted in an underestimation of the dissolution rate towards the end of 7 h.

The experimental data allowed the fitting of k_1 , m_1 and n_1 in Eqn (5). The fitted k_1 value (4.35×10^{-7} mol s⁻¹ m⁻²) at far from equilibrium condition (i.e., at $\Delta G_{r,Ab} = -59$

kJ/mol) is consistent with the independent data of Hellmann (1994) for Amelia albite (log $k = -6.2$ or $k = 6.3 \times 10^{-7} \text{ mol s}^{-1} \text{ m}^{-2}$ at pH 8.6 and 300 °C). To fit the shape of the $r - \Delta G_{r,Ab}$ curve, we used $m_1 = 6$ and $n_1 = 5 \times 10^{-6}$. Because all experimental data were in the range $\Delta G_{r,Ab} < -16 \text{ kJ/mol}$, the second term of Eqn (5) could not be determined with the Alek97 data. Figure 1a compares the predicted change in albite dissolution rate (r) vs. deviation from equilibrium ($\Delta G_{r,Ab}$) to the experimental observations and to the rate laws of Alek97 and TST.

Note that the $r - \Delta G_{r,Ab}$ curve (dotted curve in Fig. 1a) calculated with Alek97's rate law (Eq. (4)), slightly over-predicted the experimental data while it matched well with their Fig. 7. This is because we re-calculated the $\Delta G_{r,Ab}$ values with a different thermodynamic database (Zhu and Lu, 2009), which shifted the data points $\sim 4.34 \text{ kJ/mol}$ towards lower $\Delta G_{r,Ab}$. The parameters we used for the first term (k_1 , m_1 and n) yielded a slightly better fitting of the albite rates as a function of $\Delta G_{r,Ab}$ than the rate law of Alek97 re-calculated with our thermodynamic database (Fig. 1a). Although both Eqns (4) and (5) fit the experimental $r = f(\Delta G_r)$ data well and both show asymptotical behavior, the predicted rates closer to equilibrium are quite different, with Eqn (4) predicting impossibly slow rates toward equilibrium as a result of its mathematical form. These slow rates do not agree with experimental data of Burch et al. (1993), Taylor et al. (2000) and Beig and Lüttge (2006) (Fig. 6 of Zhu, 2009). The TST linear rate law (i.e., Eqn 3), fitted to the initial rate constant far from equilibrium, led to serious over-estimation of dissolution rates at near equilibrium (dashed line in Fig. 1a).

The experimental data described a sigmoidal shape for the $r = f(\Delta G_r)$ function. Burch et al. (1993) showed a steep slope for albite dissolution at 80 °C and pH 8.8 while

Hellmann and Tisserand (2006) proposed a gentler slope for albite dissolution at 150 °C and pH 9.2. Neither of their m_1 and n_1 pairs would fit the experimental $r - \Delta G_{r,Ab}$ data (Fig. 1b).

In short, the experimental data of congruent dissolution of albite in the first seven hours have adequately defined k , and, to some extent, a sigmoidal $r = f(\Delta G_r)$. It is clear that the experimental data cannot be represented by a linear TST rate law. It is also clear that the rate law proposed by Alek97 (Eqn 4) and regressed from the 0 – 7 h experimental data predicts unrealistically slow rates close to equilibrium. We will demonstrate, below, that the sigmoidal $r - \Delta G_{r,Ab}$ plays a significant role in defining how the reactions are coupled and how the ZBV hypothesis can be applied to field data. However, we must remember Eqn (5) is an empirical expression. In §3.2, we will add the parameters of the second term in Eqn (5), which only affects the later (and closer to equilibrium) period of the experiment.

Note that the well known rapid ion-exchange reactions with fresh albite surfaces at the onset of the experiments (e.g., Garrels and Howard, 1957) were also observed in the abovementioned experiments. We have taken into account of these reactions following Alek97 in the calculations of albite dissolution rates and in the reaction path simulation described below. Also note that the term “ion-exchange” in the literature sometimes also refers to replacement reactions (see Section 3.1.2).

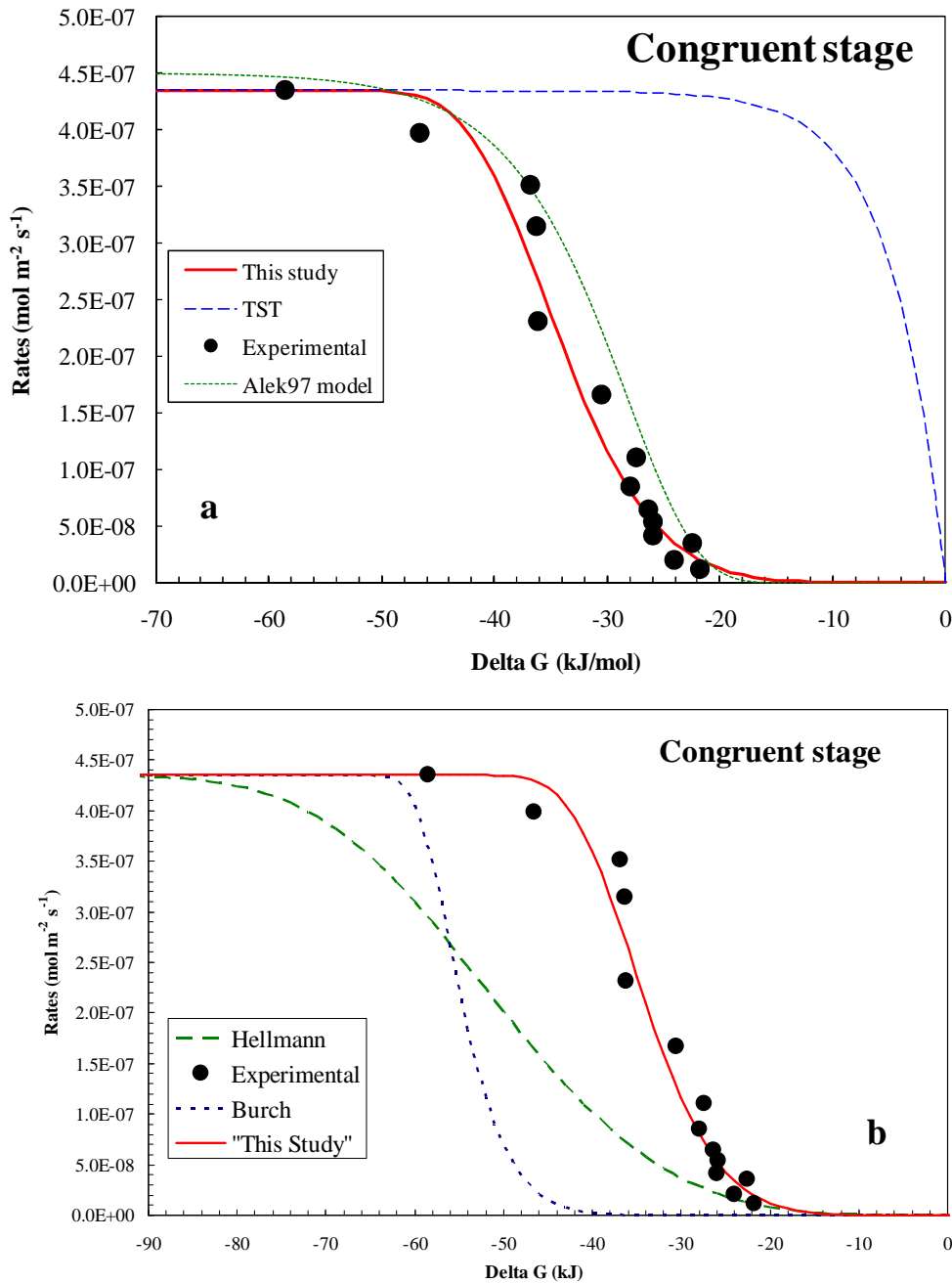


Figure 1. Rates of albite dissolution in the first seven hours of experiments normalized to the initial BET surface areas (in $\text{mol m}^{-2} \text{s}^{-1}$). Symbols denote experimental rates (Table 3 of Alekseyev et al., 1997) and lines indicate different rate law expressions. $\Delta G_{r,Ab}$ values were calculated in Zhu and Lu (2009). (a) The solid line represents rate law used in this study (Eqn. 5) with customized parameters. The dashed and dotted lines are based on linear rate law (TST) and rate expressions from Alekseyev et al. (1997), respectively. (b) The dotted and dashed lines denote calculated rates based on parameters from Burch et al (1993) and Hellmann and Tisserand (2006), respectively.

3.1.2. Steady State Dissolution of Albite and Precipitation of Sanidine (~672 - 1848 h)

During the second stage of the experiment (7-672 h), sanidine nucleation occurred, which was followed by its precipitation. As geochemical models are currently limited in dealing with nucleation, we will first discuss here the last stage of the experiment (672 – 1848 h). During this stage, the system was in a quasi-steady state, during which concentrations of some elements (e.g., Al and Si) but not all (e.g., Na) were almost constant (Fig. 2). The rates of albite dissolution r_{Ab} approximately, although not exactly (see below), were equal to the rates of sanidine precipitation r_{San} on a mol kgw⁻¹ s⁻¹ basis (Fig. 3),

$$|r_{Ab}| \approx |r_{San}| \quad (9)$$

Note that discrete sanidine crystals were formed on albite surfaces or dissolution cavities in the experiments (Alekseyev et al., 1997). Therefore, the dissolution-precipitation process 300 °C is fundamentally different from that at higher temperature (e.g., 600 °C), during which isomorphous replacement or “ion exchange” reactions occurred (Putnis, 2002; Labotka et al., 2004)

Significant amounts of albite were dissolved from 672 h to 1848 (~5.8 × 10⁻³ mol kgw⁻¹ at 672 h, and 65% of that was dissolved at 1848 h) so that we must account for the variation of reactive surface areas associated with the change of albite mass. The parameters in Eqn (5) k_1 , m_1 , and n_1 for albite had already been fitted from the congruent dissolution data (0 – 7 h). However, the parameters for the second term in Eqn (5), m_2 and k_2 , could not be determined using the Alek97 data at the congruent stage, in which

dissolution occurred relatively far from equilibrium and therefore the first term of Eqn (5) dominated dissolution rates. The dissolution rates during 672 -1848 h were mainly affected by reactive surface areas and also slightly by the second term of Eqn (5). We included the second term by assuming that the ratio of $k_1 / k_2 = 56.67$ and $m_2 = 1.17$ are the same as those of Hellmann and Tisserand (2006). However, the effects of including the second term in Eqn (5) are small in our study and the conclusions below are not affected by this assumption. With these parameters, we can calculate the ratio between the experimental rates r_{Ab}^{exp} and the rates computed from Eqn (5):

$$r_{Ab}^{exp} / r^* \quad (10)$$

where

$$r^* = S_{Ab}^o \{k_1 [1 - \exp(-ng^{m_1})] + k_2 [1 - \exp(-g)]^{m_2}\} \quad (11)$$

and S_{Ab}^o ($m^2 \text{ kgw}^{-1}$) is the initial surface area in the reactor for the time period of interest.

The ratios so calculated from Eqn (10) represent changes of reactive surface areas if all the fitting parameters are constant throughout the experiment and all additional factors not accounted in Eqn (11) are negligible for the period 672 – 1848 h (e.g., Al inhibition). Apparently, the calculated values of r^* depend on the k_2 and m_2 values that are used. Use of Burch's k_1 / k_2 and m_2 , for example, would produce a different set of r^* values. However, for the Alek97 experiments, the first term in Eqn (11) is dominant, even during 672 -1848 h.

It turned out that a decrease of reactive surface area by a factor of 2.4 from 672 to 1828 h was necessary and the temporal evolution of the reactive surface areas can be approximated by an expression of $(N^t / N_{672h}^o)^{2/3}$ for $t = 672\text{--}1848$ h, which is not the best fit, but suits the principle of parsimony. The best fit was obtained with $(N^t / N_{672}^o)^{0.8}$. As indicated previously, this P value of $\sim 2/3$ may indicate that albite dissolution rates were approximately equal on all faces, and the shape of albite grains did not change during the dissolution.

To fit the sanidine precipitation rate data, we used the classic Burton-Cabrera-Frank (BCF) theory for crystal growth (Burton et al., 1951),

$$r_{San} / S_{San} = -k_- \left(e^{\frac{\Delta G_r}{RT}} - 1 \right)^2 \quad (12)$$

where all symbols are as presented before. The negative sign ensures proper accounting during the simulation.

As mentioned in §2, the reactive surface areas for the precipitating solids are difficult to estimate and the experimental data really defined the effective rate constant k_-^* . The temporal evolution of k_-^* can be evaluated from the equation,

$$k_-^* = k_- \times S_{San} = -r_{San} / \left(e^{\frac{\Delta G_r}{RT}} - 1 \right)^2 \quad (13)$$

where $\Delta G_{r,San}$ was calculated according to Zhu and Lu (2009). The calculated k_-^* values correlate linearly with $(N_{San}^t)^{0.5}$ (Fig. 4). This correlation cannot be used to derive the

reactive surface area of sanidine, but numerically, is sufficient to model the change in dissolution rate using the rate law,

$$r_{San} = -k'_- \left(N_{San}^t \right)^{0.5} \left(e^{\frac{\Delta G_r}{RT}} - 1 \right)^2 \quad (14)$$

with a k'_- value of $3 \times 10^{-9} \text{ mol m}^{-2} \text{ s}^{-1}$.

In the simulation, the starting point was the experimental concentrations of Na, Si, Al and the estimated N_{San} at 672 h (these were batch experiments and each batch was not connected). The simulation results matched well with the experimental data. The good fit is demonstrated by the Si, Al, Na concentrations (Fig. 2), the Si:Al and Si:Na ratios (Figs. 5, 6), albite dissolution and sanidine precipitation rates (Fig. 7a, b), the saturation indices (Figs. 8), ratios of r_{Ab} / r_{San} (Fig. 3), and the mass of albite and sanidine remaining in the batch reactors at the end of the experimental runs (Fig. 9).

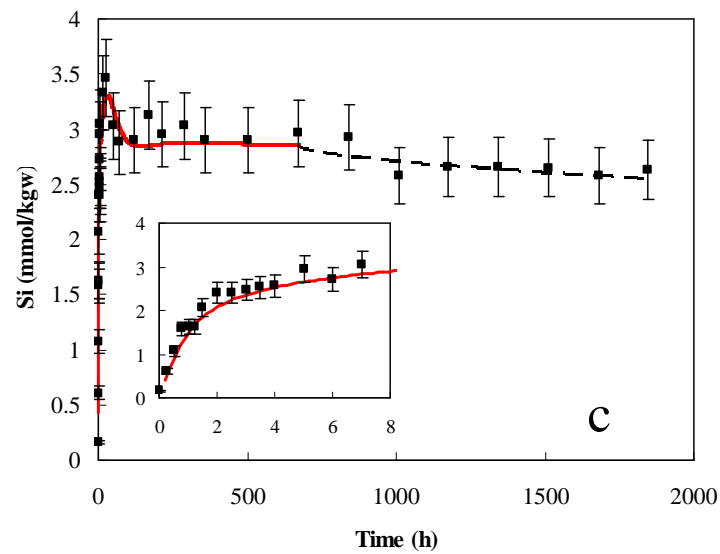
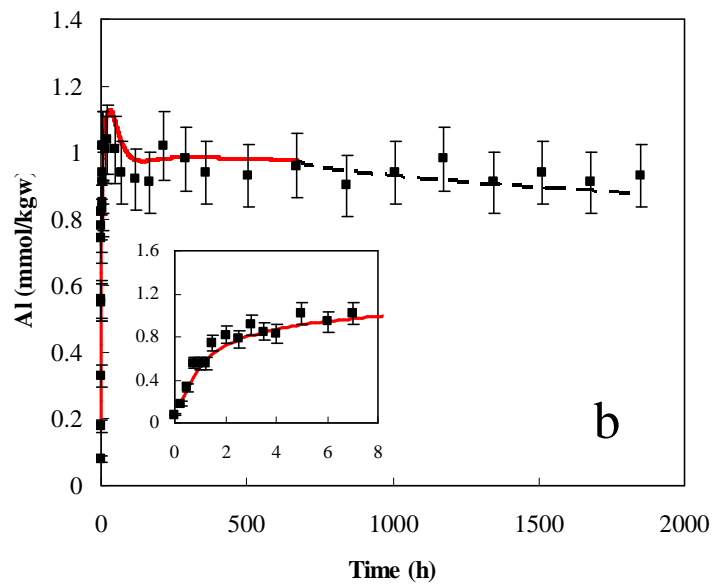
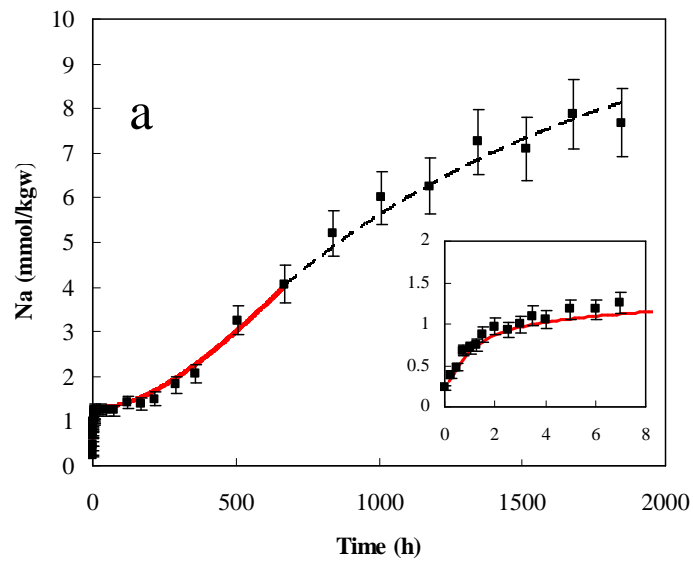


Figure 2. Temporal evolution of dissolved constituent concentrations: (a) Na; (b) Al, and (c) Si. Symbols denote experimental data; lines results from numerical reaction path model simulation. The portion of dotted line shows the simulation results during 672-1848 h. Error bars indicate 10% uncertainty in analytical measurements (the same hereafter).

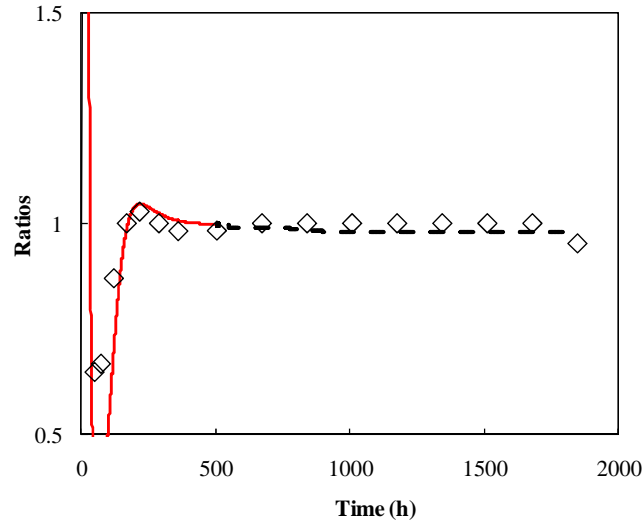


Figure 3. Ratios of albite dissolution rates vs. sanidine precipitation rates when expressed in unit of $\text{mol s}^{-1} \text{kgw}^{-1}$. Symbols denote experimental data; lines denote the results of numerical reaction path model simulation. Here and thereafter, the dotted line shows portion of 672-1848 h.

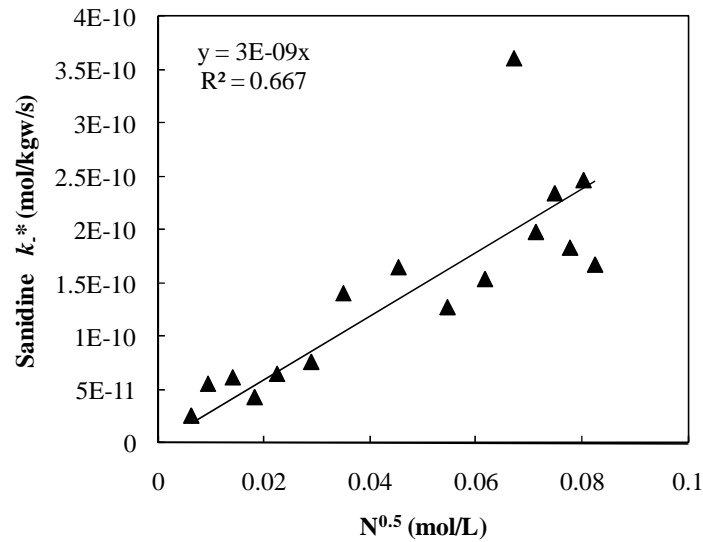


Figure 4. Correlation between experimental effective rate constants ($k_{-}^{*} = k \times S$) and the amount of sanidine precipitated. Both quantities were estimated.

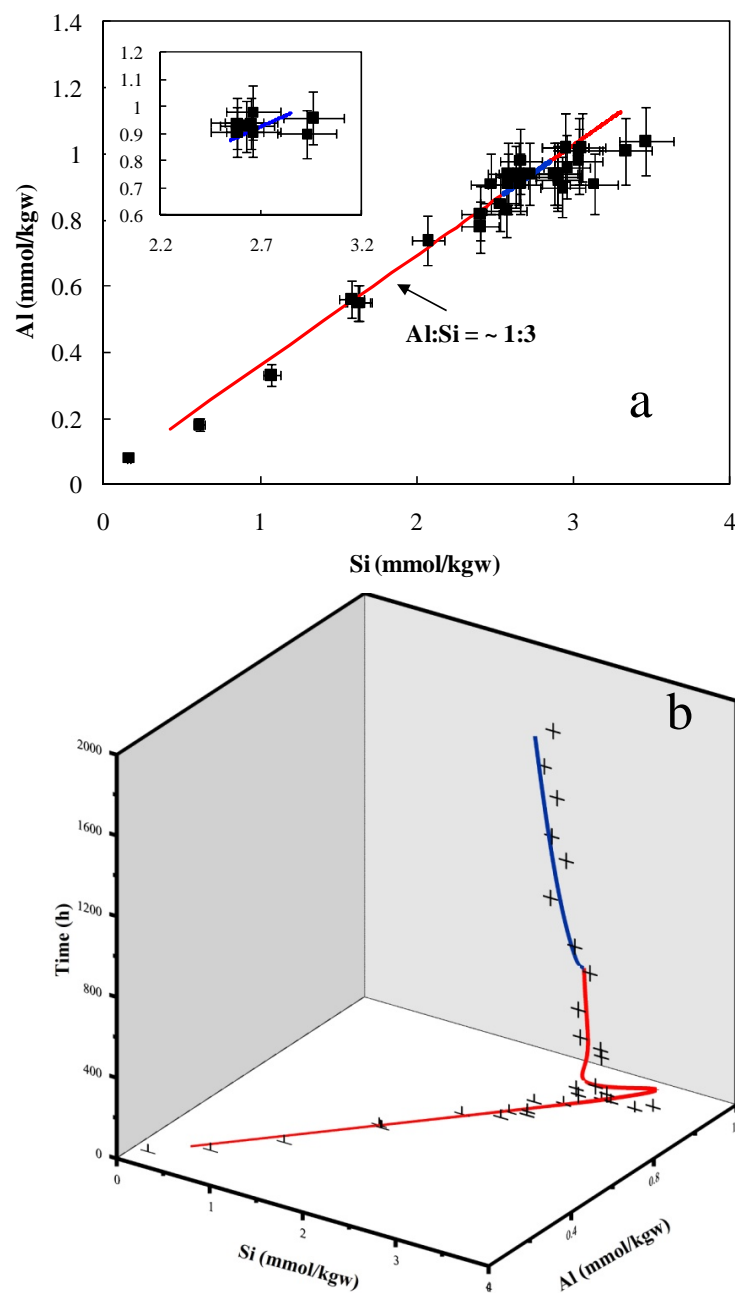


Figure 5. Proportions of Al and Si concentrations over time. Symbols denote experimental data (Ale97); lines results from numerical reaction path model simulation. (a) Inset shows the simulation results during 672-1848 h. (b) 3D diagram with time as the third axis to illustrate the temporal evolution. Stoichiometric dissolution of albite and sanidine precipitation would result in Al:Si \approx 1:3, which coincide with the model simulation line.

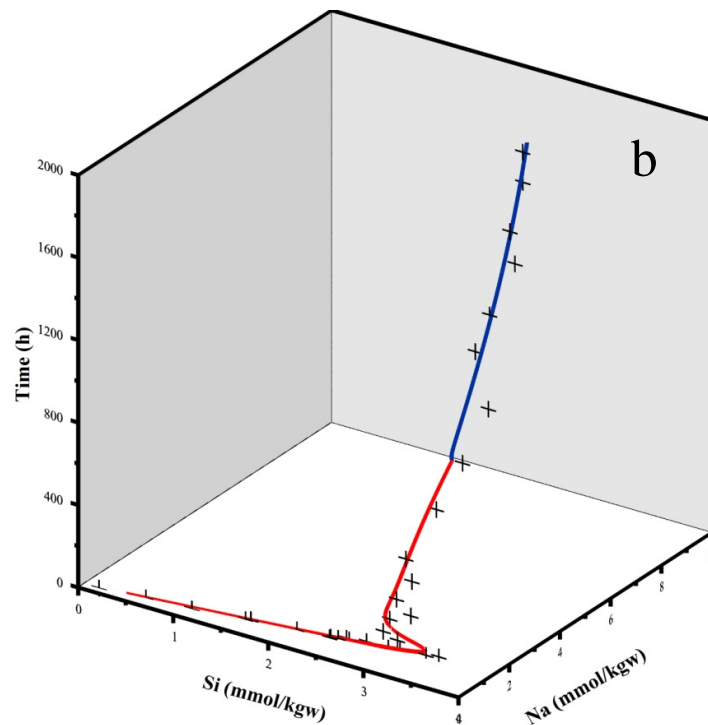
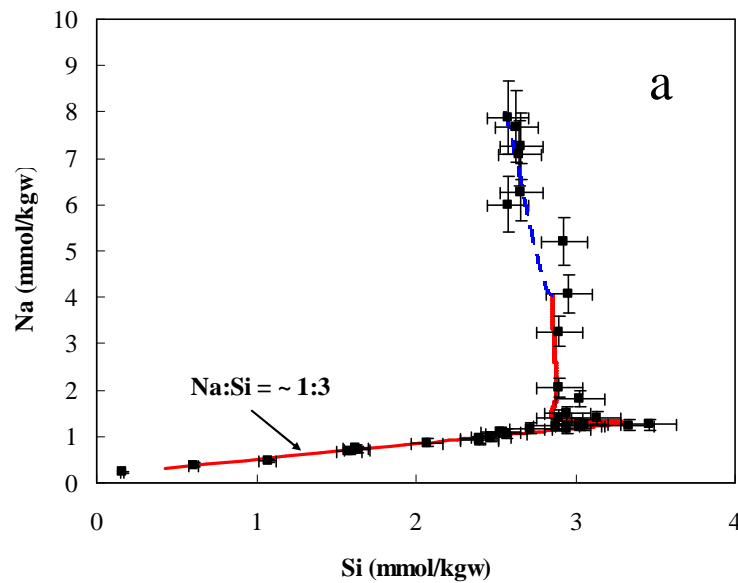


Figure 6. Proportions of Si and Na concentrations over time. Symbols denote experimental data (Alek97); lines result from numerical reaction path model simulation. Stoichiometric and congruent dissolution of albite would result in Na:Si = 1:3. The experimental Na/Si ratios fall on the Na:Si = 1:3 line for the first 7 h, then significantly deviated from 1:3 when sanidine started to precipitate.

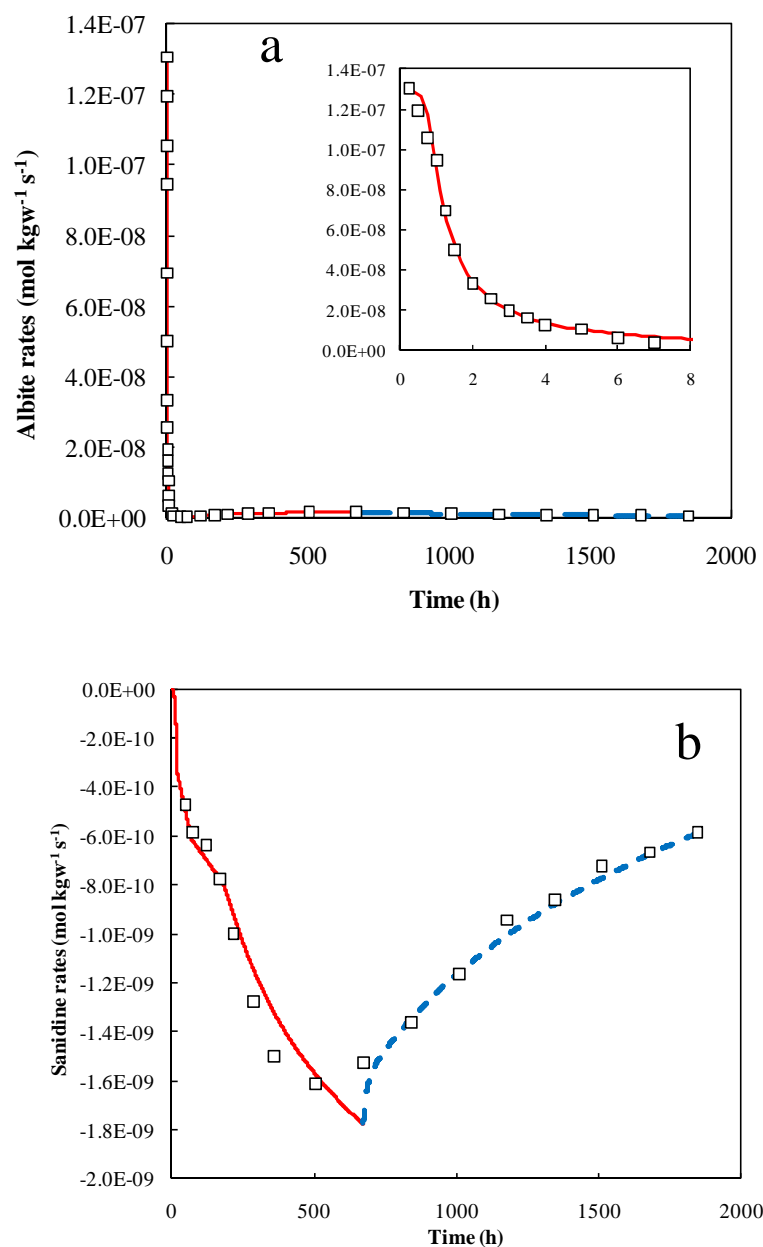


Figure 7. Albite dissolution (a) and sanidine precipitation (b) rates over time. Symbols denote experimental data (AleK97); lines result from numerical reaction path model simulation. Note that the unit of the rates is expressed in mol kgw⁻¹ s⁻¹. An empirical function was used in order to take into account changes in surface reactivity with time (see text). Rates are a function of both S and ΔG_r .

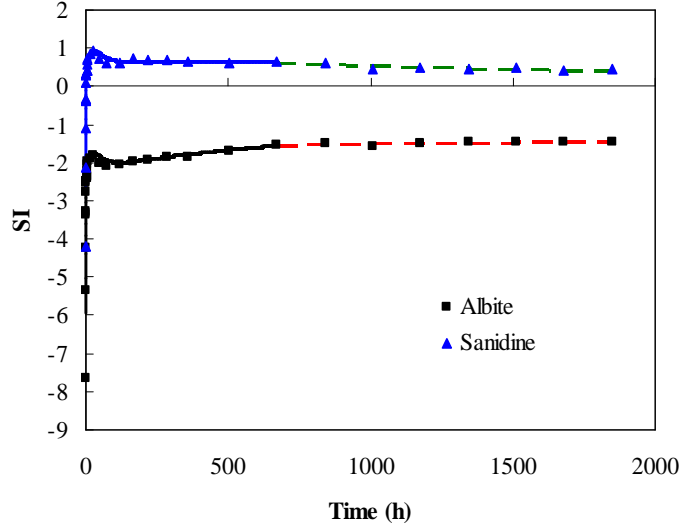
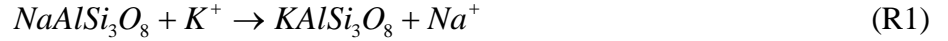


Figure 8. Saturation indices (SI) over time. Symbols represent SI calculated from speciation – solubility modeling for samples independently from each other (as snapshots) (Zhu and Lu, 2009). Lines from reaction path modeling that simulate the processes.

The overall dissolution – precipitation reaction is,



As albite is dissolved, Na^+ concentrations increased while the Al^{3+} and Si concentrations remained to be almost constant (Fig. 2) and the Al:Si ratios are almost 1:3 (Fig. 5).

Because Na^+ increased, Saturation index (SI) for albite increased with time (Fig. 8) and hence the slight decrease of r_{Ab} with time (Fig. 7a). Sanidine rates also decreased with time (Fig. 7b).

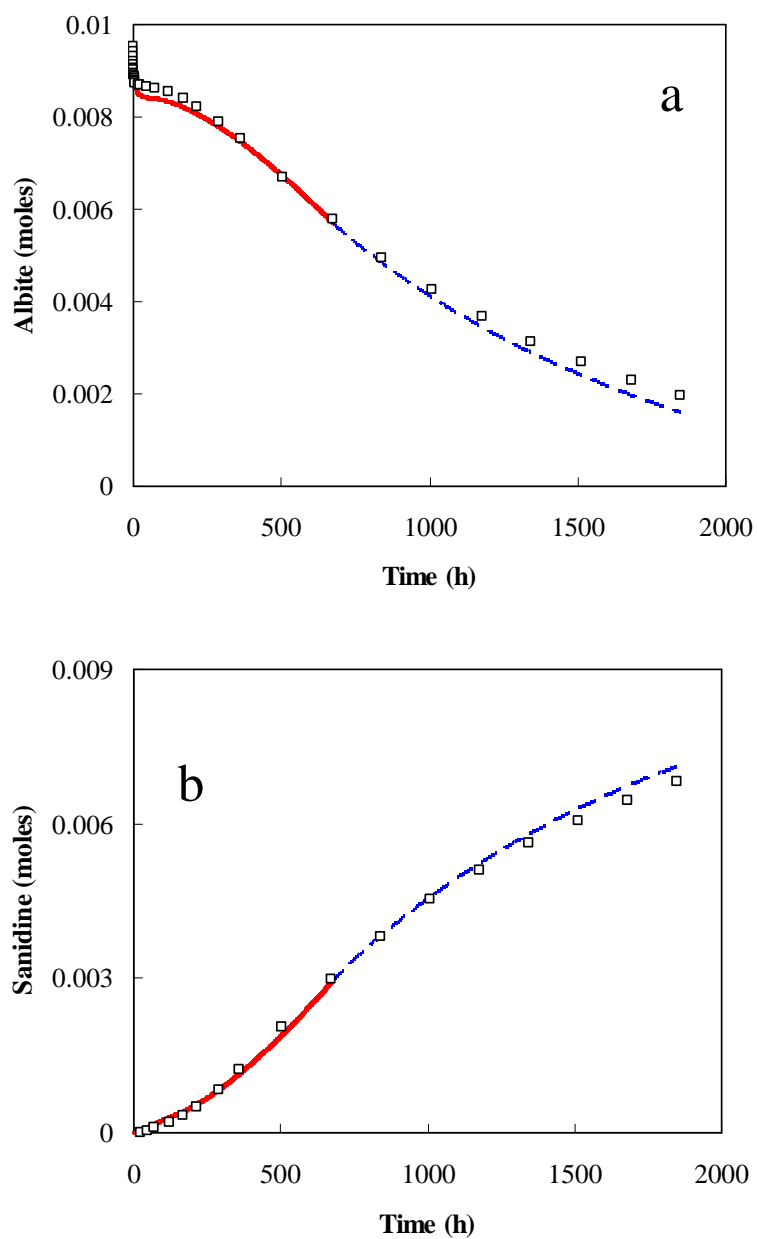


Figure 9. Comparison of the mass of albite (a) and sanidine (b) in the reactor (mol kgw^{-1}) predicted from the reaction path simulation (line) with rough estimation from rates and reaction intervals (symbols).

Of particular note is the simulated $r - \Delta G_r$. Alekseyev et al. (1997) discussed the peculiar experimental data of the incongruent stage for both albite and sanidine. We will discuss them later in more detail, but here we focus on the reactions that occurred between 672 and 1848 h. The simulated $r - \Delta G_r$ matched well with experimental data between 672 to 1848 h (Fig. 10a). The decrease of r_{Ab} was due to both a slight increase of $\Delta G_{r,Ab}$ and a decrease of S_{Ab} . For sanidine, the simulation also matched well with experimental sanidine rates (Fig. 7b). Note that these two diagrams are different from Fig. 1a,b because the rates are expressed as $\text{mol kgw}^{-1} \text{s}^{-1}$ so that the rate changes are a function of both ΔG_r and S_j . The agreement, therefore, indicates that the formulae for $S(t)$ as a function of moles of albite and sanidine and the BCF model of sanidine precipitation generated acceptable approximations.

The simulations based on these assumptions generated results that match the experimental data for the period 672 – 1848 h. The most important result is a quasi-steady state in terms of r_{Ab} / r_{San} ratios that are almost unity. This important conclusion is not related to more assumptions below, which are needed to simulate experimental period 7 – 504 h.

3.1.3. Albite Incongruent Dissolution with Initiation of Sanidine Precipitation (7 – 504 h)

The Alek97 experiments started with an aqueous solution that was undersaturated with respect to sanidine. The sanidine SI rose rapidly, becoming supersaturated at 1.5 h and reaching a maximum of ~1.0 at 24 h (Fig. 8). From that point on, the sanidine SI

decreased linearly, approaching but not reaching zero. This SI temporary evolution is typical result of competition of continued primary mineral dissolution and secondary mineral nucleation and growth (Fritz and Noguera, 2009).

The beginning of sanidine nucleation was marked by a perturbation of Al and Si concentrations (Figs. 2b, c) and also SI of albite, which first increased rapidly until reaching a maximum at 24 h, then decreased from 24 to 72 h, and finally increased linearly from 72 to 1848 h (Fig. 8). Because of the similarity of the albite and sanidine structures, sanidine nucleation is expected to be on albite surface sites. It is apparent that nucleation of sanidine on albite surfaces caused a dramatic decrease of albite dissolution rate (Fig. 7a). r_{Ab} decreased monotonically during the first 48 h, even though there is an albite maximum in SI during this period (7 – 48 h, Fig. 8). This observation indicates that the r_{Ab} decrease was not merely a function of $\Delta G_{r,Ab}$. It appears that changes of reactive surface area must also have contributed.

Such reduction of the “reactive surface area” cannot be accounted for by the reduction in the physical surface areas (be geometric or BET), but only by the blocking of the reactive surface sites on albite, due to the presence of an inhibitor or due to surface coating. It has been shown in several studies that dissolution rates of feldspar are retarded in the presence of Al (Gautier et al., 1994; Oelkers et al., 1994; Oelkers, 2001). However, the experimental data of Alek97 show that Al concentrations are 1.02, 1.01, 1.04, and 1.01 mM at 7, 16, 24, and 48 h, respectively. As the drastic reduction of r_{Ab} coincided with almost constant Al concentrations for 7- 48 h (Fig. 11), Al inhibition alone cannot explain the reduction in albite dissolution rate here. We suggest that the reduction in r_{Ab} was due to the nucleation of sanidine on the albite surface. From 7 to 48

hours, the amount of sanidine increased from 0 to 0.04 mmol kgw⁻¹. As the amount of albite (8.7 mmol kgw⁻¹) was much higher, one can argue that the amount of growing sanidine is not sufficient to fully cover the surface of albite. However, mineral dissolution (as well as crystal growth) mainly occurs on the reactive surface sites that are provided by kinks, and a full blockage of these sites can still be attained with relatively small amounts of coating. For example, it has been reported that only a few percent of the crystal surface needs to be covered with an inhibitor to achieve total blockage of the crystal growth process (Liu and Nancollas, 1975; Weijnen and Van Rosmalen, 1986; Hoch et al., 2000). It is expected that sanidine nucleation would mainly occur at or near the sites where albite dissolution occurred, as (1) these sites may provide a template for nucleation; and (2) the oversaturation may be somewhat higher near the dissolving sites due to the local supply of Al and Si. Indeed, Alek97 observed that crystals of sanidine were nucleated mainly on the walls of dissolution cavities in albite (see Fig. 4c of Alek97).

However, even though the experimental evidence pointed out nucleation on albite surface as the probable cause for the reduction of albite reactivity, modeling this process quantitatively is still impossible at the present time (see review by Fritz and Noguera, 2009). An ad hoc approach must be used instead. If we assume that the first term in Eqn (5) has adequately accounted for the $r - \Delta G_r$ effects (in fact the second term as described in the previous section has little effect here because of the distance from equilibrium), we can compute the ratios between rates predicted from Eqn (5) with a constant S_j^o and the experimental rates. The ratios can be regarded as the correction factors Y ($Y = S_j^o k_1 [1 - \exp(-ng^{m1})] / r^{\text{exp}}$), accounting for the evolution of r_{Ab} as reaction progressed,

where r_{ab}^o denotes the rates normalized to initial surface area (S_j^o). Y needs to be 4×, 6×, 20× smaller at 16, 24 and 48 h, respectively. Apparently, during this period of sanidine nucleation, the change in the reactivity of the albite cannot be described by the formula $(N/N^o)^{0.67}$ that was used for 672 – 1848 h in §3.2, which here can only provide a correction factor of 1.05. It seems that the decrease in albite reactivity from 7 to 48 h is independent of the change in albite amount. To describe this change in reactivity, we used a time dependent Y function. The regression of Y generated $Y = e^{0.0661t}$ where Y appears in the denominator in Eqn (5) and t is the reaction time in hours. With this empirical fitting, the experimental data of the first 48 h were approximately reproduced.

Alek97 noted that, for the incongruent dissolution stage, the $r_{Ab} - \Delta G_{r,Ab}$ relationships were erratic, in a horse shoe shape, as shown in Fig. 10a. At first glance, this experimental observation defies the TST, but these rates are not normalized to the reactive surface area. This horse shoe shape could be explained by the coalescence of sanidine nucleus and particles. At this stage (48 – 504 h), the degree of oversaturation with respect to sanidine is much lower than that during the peak of the nucleation stage (around 16 h). Numerical modeling of simple precipitation and growth of clay particles in model system show that the small particles initially created are subsequently destabilized and resorbed. Only some classes of particles survive and grow (Fritz and Noguera, 2009). This process appears to explain the increase of reactive surface areas and albite dissolution rates from 48 h to ~500 h (Fig. 7a) while r_{Ab} apparently correlates positively with the increase of $\Delta G_{r,Ab}$ (Fig. 10a). Currently, we cannot predict the increase in albite reactive surface area, and therefore we need to employ empirical functions that would describe it. The Y function $Y = 4600.5t^{-1.202}$ for 48 – 504 h helped the match between

simulated and experimental values. The simulation also matched well with the non trivial $r_{Ab} - \Delta G_{r,Ab}$ relationship (Fig. 10a).

3.1.4. Sanidine Precipitation (7 – 672 h)

The precipitation of sanidine 7- 672 h was constrained by experimental data r_{San} , and Na:Si ratios (Figs. 6, 7b). r_{San} increased with time until about 504 h (Fig. 7b). This monotonic increase coincided with an increase, a decrease, and an increase again of sanidine SI (Fig. 8). The sanidine $r - \Delta G_r$ relationship is also erratic, with an increase of r_{San} coinciding with a decrease of $\Delta G_{r,San}$ during 7 – 504 h and forming a horse shoe shape for the entire experimental period (Fig. 10b). However, close inspection shows that $r - \Delta G_r$ is not randomly distributed, but follows a strict chronological order of increasing rates with increasing time from 48 to 504 h (Fig. 10b).

The BCF theory-based approach, combined with an empirical formula for reactive surface area increase (Eqn. 14), appears to account well for the competing effects of ΔG_r and S_{San} . Rates increased to 504 h due to the rapid increase of reactive surface areas despite a slight decrease of $\Delta G_{r,San}$. After 504 h, the decrease of $\Delta G_{r,San}$ offset the small increase of S_{San} and the overall precipitation rates declined. The decrease of $\Delta G_{r,San}$ was caused by the slowdown of albite dissolution. The reaction path model was able to simulate the horse shoe shaped $r - \Delta G_r$ without excess fitting. Note that the wiggles around 24 h and 120 h in Fig. 10b are due to changes of SI. The simulation was able to catch all these variations.

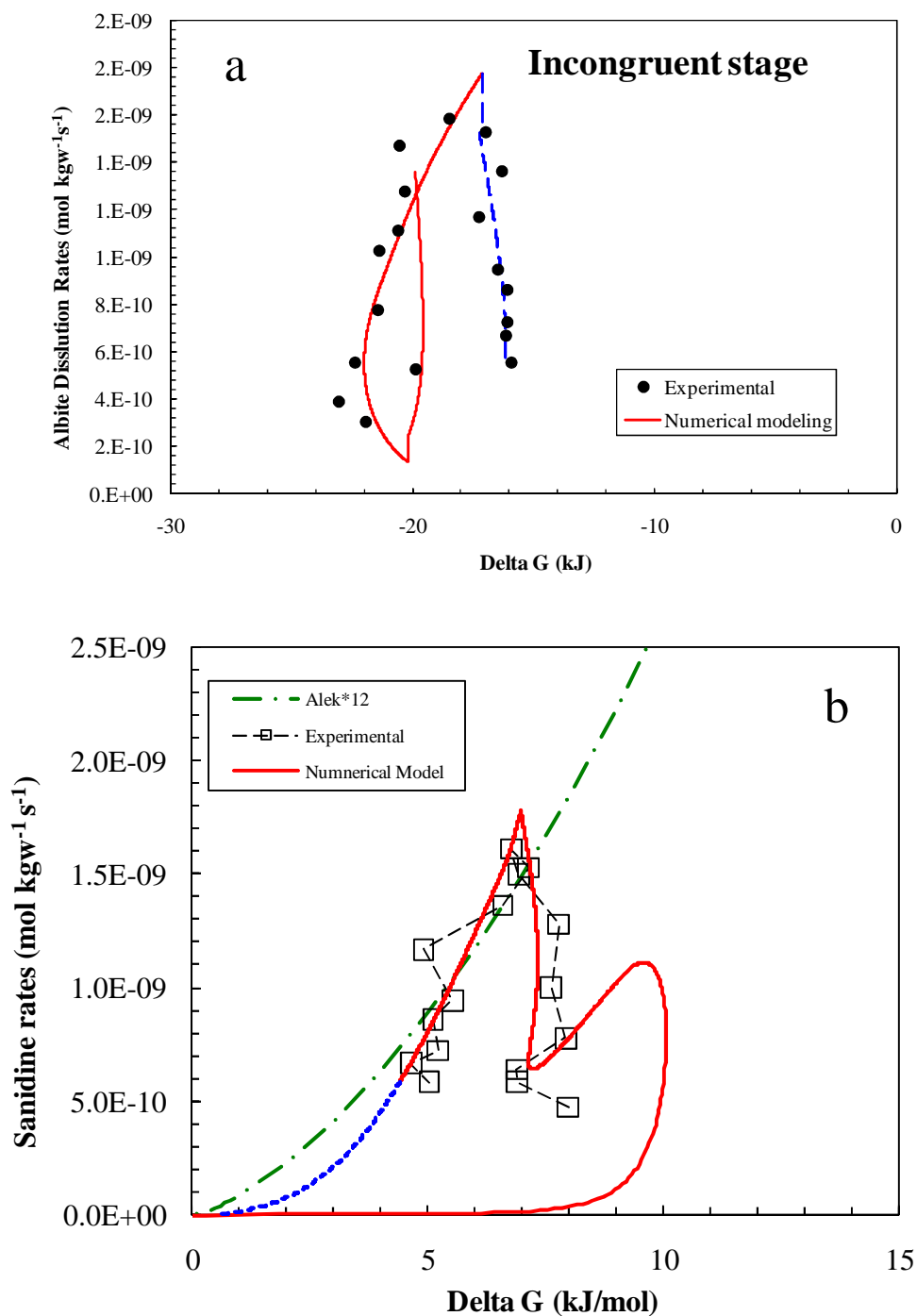


Figure 10. Albite dissolution (a) and sanidine precipitation (b) rates (in moles $\text{kgw}^{-1} \text{s}^{-1}$). Symbols denote experimental data (Alek97) and lines represent reaction path simulation. An empirical function was used in order to take into account changes in surface reactivity with time (see text). Labels besides symbols indicate hours of reaction. Dotted line shows simulation extended to 4445 h.

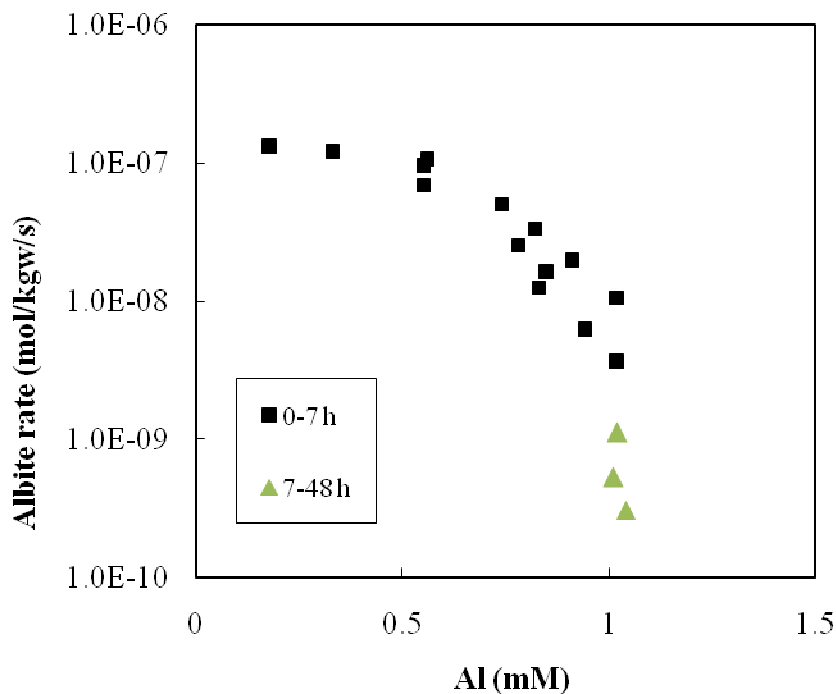


Figure 11. Rate of dissolution of albite as a function of dissolved Al concentrations. Rates are expressed in $\text{mol s}^{-1} \text{kgw}^{-1}$.

3.1.5. Simulation of the Entire Experiment Period (0 – 1848 h) and Beyond

When all the time segments discussed above were put together in a model and the entire period of the experiment was simulated at once, the results matched well with the experimental data (Fig. 2, 3, 5-10, 12). It should be noted that $\Delta G_{r,Ab}$ never reached values $> -16 \text{ kJ/mol}$ (Fig. 10a). The experiments experienced a period when sanidine precipitation proceeded faster than albite dissolution as sanidine was nucleated (Fig. 3). After ~ 200 hours, a quasi-steady state was reached where $|r_{Ab}|/|r_{San}|$ is close to unity (Fig. 3). The simulation shows that the ratio was stabilized at ~ 0.98 . It should be pointed out that a poor match for sanidine simulations in the early stage in our trial and error

simulations would not grossly upset the simulated $|r_{Ab}|/|r_{San}|$ in a later time. The system appears to revert to a quasi-steady state regardless.

We also performed predictive simulations, extending to 4445 h, beyond the experimental duration of 1848 h. All albite is dissolved at ca. 3650 h. Sanidine continued to precipitate until equilibrium was reached at ca. 4170 h (Fig. 13a). The ratios of $|r_{Ab}|/|r_{San}|$ remain at 0.98 (Fig. 13b). Note that due to the coupling between albite dissolution and sanidine precipitation, albite never reached equilibrium with the aqueous solution, but continued to dissolve at the same degree of undersaturation (

$$\Delta G_{r,Ab} \approx -16 \text{ kJ/mol}).$$

3.2. Feldspar Hydrolysis Batch Experiments at 200 °C and 300 bars

The two feldspar hydrolysis batch experiments were described in detail in Zhu and Lu (2009). The batch experiments dissolved alkali feldspar ($\text{Na}_{0.95}\text{Ca}_{0.04}\text{K}_{0.01}\text{Al}_{1.04}\text{Si}_{2.96}\text{O}_8$ and $\text{K}_{0.85}\text{Na}_{0.15}\text{Al}_{1.04}\text{Si}_{2.97}\text{O}_8$ laminae) in ~0.20 M KCl – HCl solution with 50 mM CO_2 for 5 and 27 days. The experiments were conducted at 200 °C and 30 MPa. The precipitates were identified as mainly boehmite and possibly trace of muscovite after five days. The retrieved solids from the 27 days show much more coverage of secondary minerals on feldspar grains than those after 5 days, but XRD analysis was not successful. The approximately 1:3 Na:Si ratios in the aqueous solution indicate stoichiometric dissolution of albite. The amount of muscovite or microcline precipitation must be negligible.

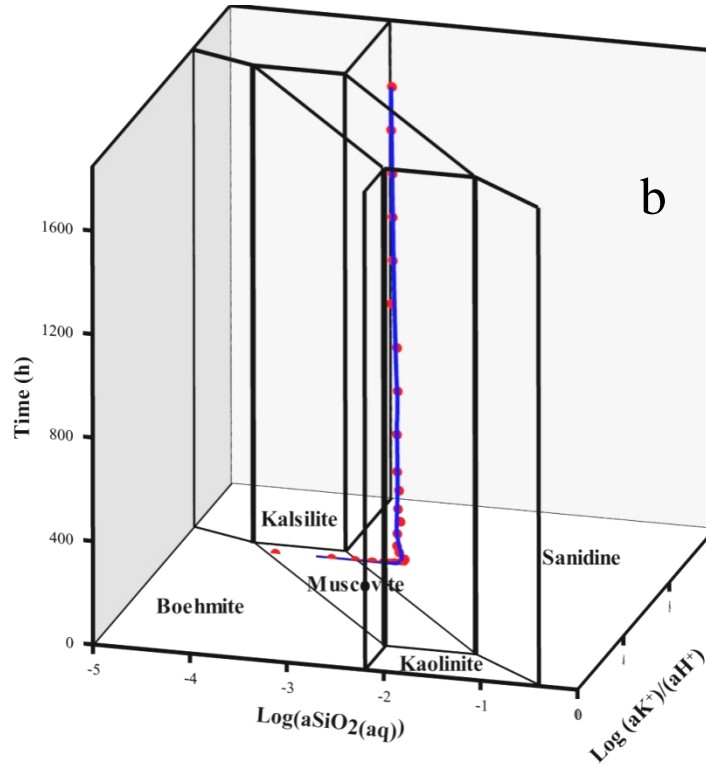
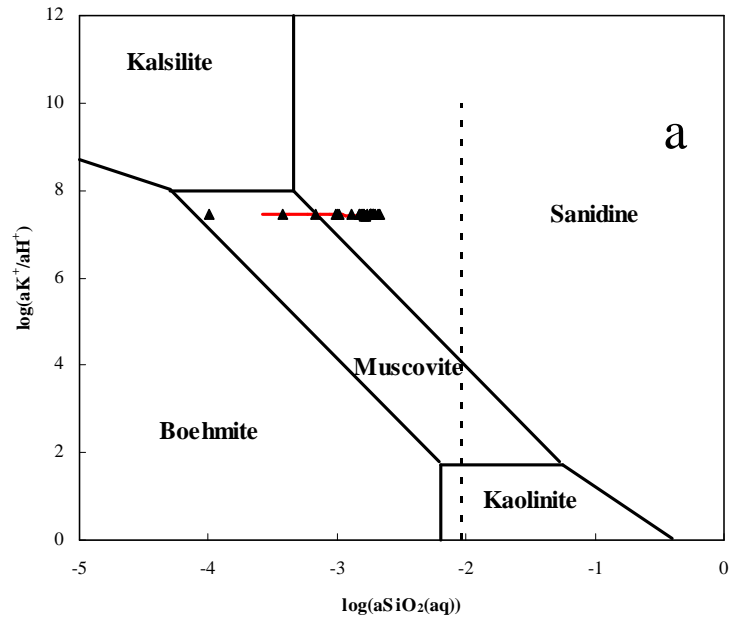


Figure 12. Activity diagram in the $\text{K}_2\text{O}-\text{Al}_2\text{O}_3-\text{SiO}_2-\text{H}_2\text{O}-(\text{CO}_2)-\text{HCl}$ system at 300 °C and 8.8 MPa for albite dissolution. The dashed line is quartz saturation. Symbols denote experimental results, and the solid line the reaction path simulation results. (b) shows the evolution of reaction path as a function of time.

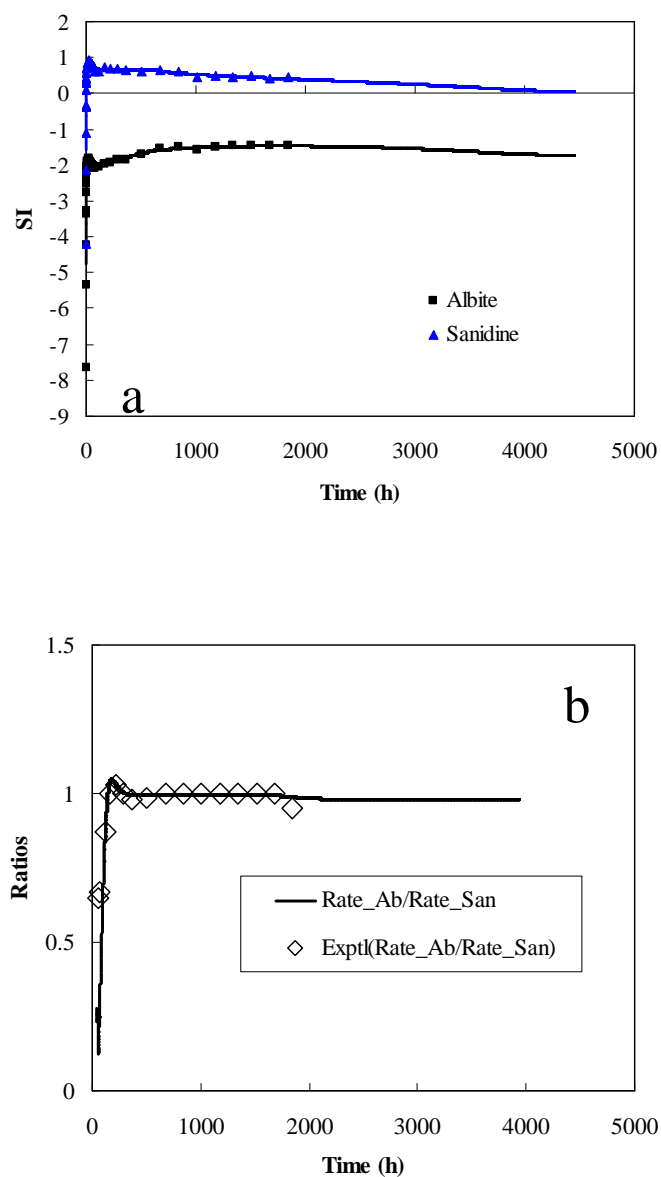


Figure 13. Predicted continued reactions in the batch reactor beyond experimental time of 1848 h following the reaction path model. (a) saturation indices over time; (b) ratios of albite dissolution rates vs. sanidine precipitation rates. Albite was dissolved at ca. 3650 h. Sanidine continued to precipitate until reaching equilibrium at ca. 4170 h.

To model albite dissolution, we used Eqn (5) and a far from equilibrium k_1 derived from Hellmann et al. (1990)'s albite dissolution experiment at 225 °C (pH 3.66) with an activation energy E_a of 50 kJ/mol. For the exponent parameters and k_1/k_2 ratio in Eqn (5), we adopted the values from Hellmann and Tisserand (2006). Only a small percentage of albite was dissolved in the experiment so that we assumed that the reactive surface areas of albite remained to be constant during the experiments. The measured BET SA 0.132 m²/g was used for the reactive surface area.

For boehmite precipitation, we essentially followed Bénézeth et al. (2008) and used the rate law,

$$r_{Bhm} = -k_{-}^{*} (H^{+})^{1.7} \left(e^{\frac{\Delta G_r}{RT}} - 1 \right) \quad (15)$$

Bénézeth et al. (2008) conducted boehmite precipitation experiments for pH 6 – 9 at 100.3 °C. They found that the TST $f(\Delta G_r)$ function fit to their data and the precipitation rate is a function of pH. Boehmite precipitation in our experiments occurred in the pH range of 4.5 to 5.1, slightly more acidic than the experimental condition of Bénézeth et al. (2008). Nagy (1995) documented V-shaped pH dependence of aluminum oxyhydroxides dissolution rates and proposed an exponent of 1.7 for hydrogen concentrations for acidic solutions, which we adopted.

In the reaction path model, the only fitted term in Eqn (15) was the effective rate constant k_{Bhm}^{*} , which was assumed to be constant here because the reactive surface areas for boehmite could not be assessed independently. The first aqueous sample was taken

after 24 h. Therefore, the experimental data probably represent the stage where the initial nucleation of boehmite was already passed.

Such a simplistic model matched well the solution chemistry evolution in the first 312 h of the experiments (Fig. 14). Si and Na concentrations increased rapidly (0-312 h) as albite dissolved first starting from the condition of far from equilibrium, but the increase decelerated due to the $f(\Delta G_r)$ term in the rate law. The Al concentrations appear to reach a quasi-steady state as a result from the competition between albite dissolution and boehmite precipitation. The pH increased because boehmite precipitation consumes H^+ . Note that the dominant Al species is $Al(OH)_4^-$ in this experiment (Zhu and Lu, 2009). The predicted SI over time matched well with speciation – solubility calculations for both primary mineral (albite) and secondary mineral (boehmite) (Fig. 15).

Essentially, the reaction path model simulated albite dissolution,



and boehmite precipitation,



The albite dissolution and boehmite precipitation reactions are closely coupled. Change of k_{Bhm}^* and hence the boehmite precipitation rate resulted in changes of albite dissolution rate and predicted Si and Na concentrations. In other words, the k_{Bhm}^* was constrained by both Al and Si-Na-H concentrations. The ratios of albite dissolution and boehmite precipitation rates are unity on $mol\ kgw^{-1}\ s^{-1}$ basis although the individual rates decreased

rapidly as solutes accumulate in the solution (Fig. 16). The stoichiometric rate ratio is 1:1, reflecting the overall reaction,



This result is significant and consistent with the conclusions in §3.1 and Ganor et al. (2007). Note that the above modeling results are largely predictive. No fitting parameters were used for albite. The only fitting parameter was k_{Bhm}^* , which was constrained by the Si, Na, Al, and H data. The assumption of a constant reactive surface area cannot be true as no boehmite seeds were used in the experiments and boehmite reactive surface areas have certainly grown. Another assumption was that the albite dissolution rate is independent of pH, which was not a large factor for the first 312 h, but will artificially over-predict the albite dissolution rates for the late stage.

However, the above simple reaction path model can only match the 312 – 648 h experimental data by ad hoc adjustment of the pH in the model to experimental values. Here the in situ pH values in the reactor were calculated from pH measured at room temperature and recalculated to the experimental temperature via speciation – solubility modeling (Reed and Spycher, 1984; Zhu and Lu, 2009). While the values were calculated from modeling and these values cannot be verified independently, the model was applied consistently and hence the trend is probably reliable. We noted that measured $\text{CO}_{2(\text{aq})}$ concentrations decreased to 44 mM from the starting concentrations of 50 mM around 300 h. However, modeling calculations show that possible degassing cannot account for the large increase of pH as observed.

We should mention that, with exception of pH after 312 h, the experimental data constrain the rate laws. A change of the form of rate law or parameters would result in mismatch with the experimental data. For example, if we had used a BCF rate law for boehmite precipitation instead but kept all other parameters the same in Eqn (15), the predicted Al concentrations after 312 h would be too low. The order of H^+ concentration in Eqn (15) was constrained by the Al concentration increase after 312 h. A higher order would be a better fit. Different sets of exponents in Eqn (5) for albite dissolution would result in mismatch with the experimental data as the curvature of Si and Na increase over time define the $f(\Delta G_r)$ dependence of albite dissolution. Therefore, while the batch experimental data did not define a unique reaction path model, it at least narrow down to a limited sets of plausible models.

4. DISCUSSIONS

4.1. The Influence of $f(\Delta G_r)$ and S_j on the Coupling of Reactions

Although the inter-dependence between dissolution and precipitation reactions has been discussed before in the literature (e.g., Alek97), the development of a numerical model allows us more freedom to explore this relationship quantitatively. Let's look at the simulation of Alek97 experiments discussed in § 3. On the basis of $\text{mol kgw}^{-1} \text{s}^{-1}$, we have $|r_{Ab}| \approx |r_{San}|$ after a hiatus of sanidine nucleation and coalescence. In the period of 672 – 1848 h when the issue of sanidine nucleation and coalescence has passed and speculative assumptions of reactive surface areas for albite were no longer necessary,

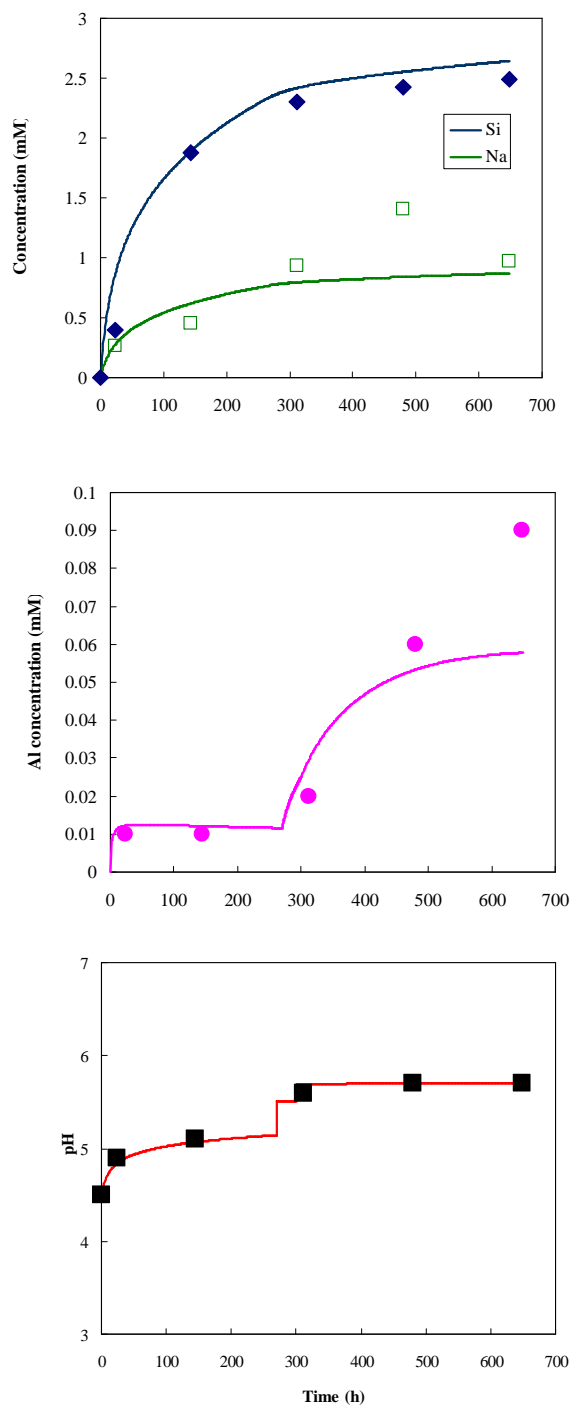


Figure 14. Comparison of predicted solution chemistry from the reaction path model (lines) with experimental data (symbols) during the course of alkali-feldspar dissolution batch experiments at 200 °C and 30 MPa. The pH values in the simulation were adjusted to fit the experimental data.

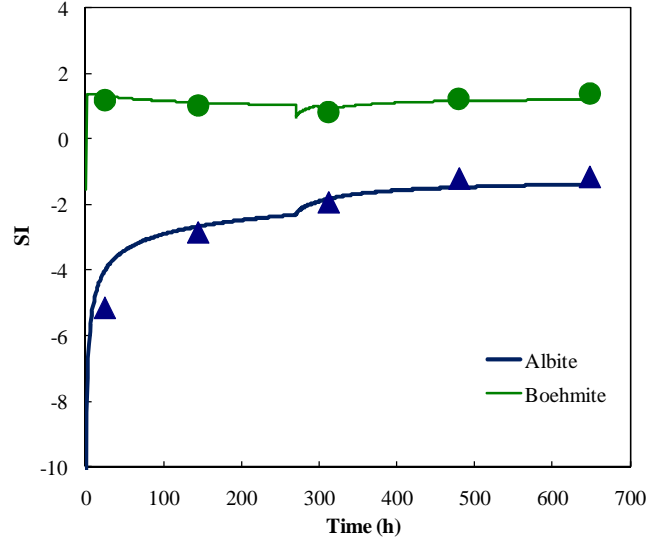


Figure 15. Calculated change in albite and boehmite saturation indices evolution compared with data from solubility calculations (Zhu and Lu, 2009).

we have,

$$\left\{ k_1 / k_{San} \left(1 - e^{-n \left| \frac{\Delta G_r}{RT} \right|^{m1}} \right) + k_2 / k_{San} \left(1 - e^{-\left| \frac{\Delta G_r}{RT} \right|^{m2}} \right) \right\}_{Ab} / \left(e^{\frac{\Delta G_r}{RT}} - 1 \right)_{San}^2 = S_{San} / S_{Ab} \quad (16)$$

Since the k_j are constant, as well as all other empirical exponent parameters, S_j and ΔG_r are the only temporal variables in the equation and they co-evolved. In our simulation for 672 – 1848 h, S_{Ab} decreased and S_{San} increased so that S_{Ab} / S_{San} decreased with time.

The $\Delta G_{r,San} / \Delta G_{r,Ab}$ decreased correspondingly by decreasing $\Delta G_{r,San}$ while maintaining an almost constant $\Delta G_{r,Ab}$.

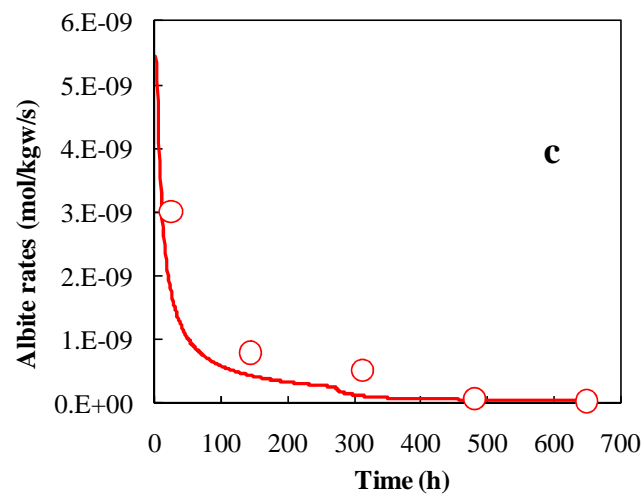
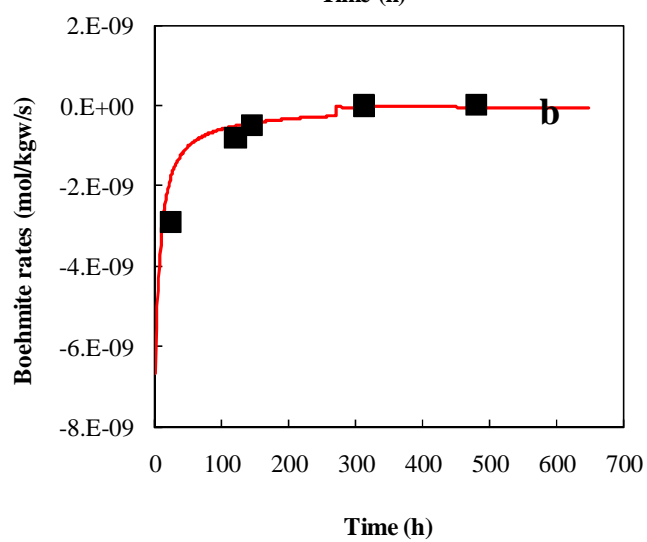
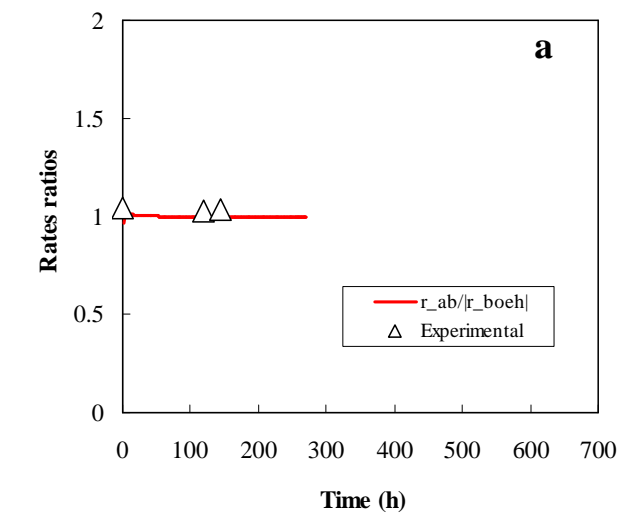


Figure 16. (a) Simulated ratios of albite dissolution rates versus boehmite precipitation rates when expressed in unit of $\text{mol kgw}^{-1} \text{s}^{-1}$ for the first 312 h. (b) boehmite precipitation rates over time. (c) albite dissolution rates over time. Bulk albite dissolution rates in unit of $\text{mol kgw}^{-1} \text{s}^{-1}$ were estimated from the average release rates of Na and Si and boehmite precipitation rates from the balance on Al.

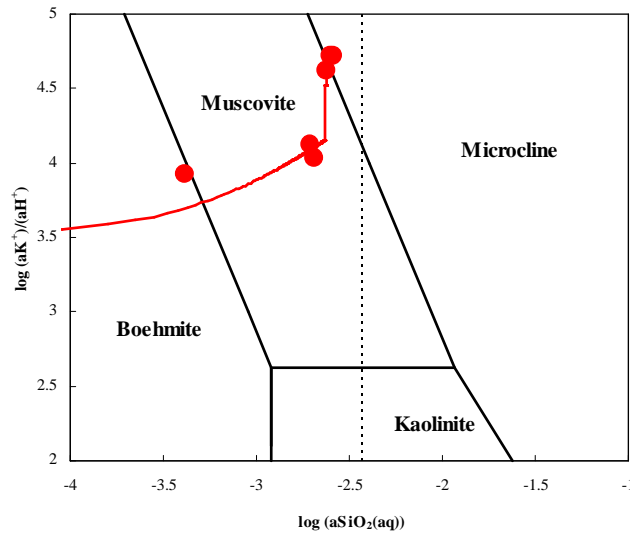


Figure 17. Activity diagram in the $\text{K}_2\text{O}-\text{Al}_2\text{O}_3-\text{SiO}_2-\text{H}_2\text{O}-(\text{CO}_2)-\text{HCl}$ system at 200°C and 30 MPa . The symbols represent values calculated by Zhu and Lu (2009) from experimental data via speciation – solubility modeling. The line denotes to reaction path modeling prediction from this study.

These relationships quantitatively demonstrate the closely coupled or mutual dependence nature of precipitation and dissolution reactions. In fact, these two reactions are inter-locked. They reached a quasi-steady state at $\Delta G_{r,Ab} \approx -16$ kJ/mol with a reduction of two orders of magnitude of r_{Ab} (or a r_{Ab}/r_{Ab}^o of 0.01) due to the $f(\Delta G_r)$ effects. r_{Ab} , on the other hand, decreased as S_{Ab} decreased. However, the system did not move closer to albite equilibrium; albite continued to dissolve at $\Delta G_{r,Ab} \approx -16$ kJ/mol until all albite was dissolved after ca. 3650 h (Fig. 13). Thus, the system is “arrested”, in terms of preventing albite from reaching equilibrium.

The interpretations of the Alek97 experimental data are non-unique. This is particularly true as reactive surface areas and $f(\Delta G_r)$ co-evolved during these batch reactor experiments. The “experimental” reactive surface areas were deducted from the residues of the $f(\Delta G_r)$ effects. However, the rate laws for dissolution and precipitation, while affecting the deduced S_j , do not alter the fact of the coupling. During the trials and errors of developing a reaction path model in order to match the experimental data, we had used the first term in Eqn (5) only for albite dissolution and used Alek97’s rate law of sanidine dissolution for sanidine precipitation. The omission of the second term resulted in requirements of higher S_{Ab} for 672 – 1848 h. In other words, the second term of Eqn (5) only started to affect the results after 360 h. The relationship $|r_{Ab}| \approx |r_{San}|$ still held and the system was “arrested” at the same quasi-steady state at $\Delta G_{r,Ab} \approx -16$ kJ/mol.

As we pointed out before, there is no experimental basis for the second term from the Alek97 or the Hellmann and Tisserand (2006) experimental data. The use of the

Burch et al. (1993) parameters for the second term, for example, would result in significant revisions of the reactive surface areas in order to match experimental data. However, this is not going to change the outcome of coupling. Likewise, the use of Alek97's rate law for sanidine precipitation had resulted in different fittings of the reactive surface areas for sanidine. The same coupling outcome was obtained ($|r_{Ab}| \approx |r_{San}|$) and the system “arrested” at the same quasi-steady state at $\Delta G_{r,Ab} \approx -16$ kJ/mol).

Such a quasi-steady state is important for us to interpret field and laboratory experimental data. First, field samples are difficult to interpret as many coupled reactions in a network could go on simultaneously. Indeed, an interlocked reaction network is the most likely case for any given field site. Second, on the other hand, observed close coupling of reactions helps us to understand why in some field sites feldspar dissolution rates are orders of magnitude slower than far-from-equilibrium lab dissolution rates, but by all measured saturation indices of feldspars are still far from equilibrium (White et al., 2001; Georg et al., 2009). This kind of observation was difficult to explain with the TST linear rate law, which requires near equilibrium to achieve significant reduction of rates due to the $f(\Delta G_r)$ effects.

4.2. Influences from Fluid Flow Rates

As pointed out by Zhu and Anderson (2002) and numerous others, most geochemical reaction problems are reactive mass transport problems. It is the fluid flow that brings about mass and heat fluxes that disrupt the equilibria and drive the reactions. For the subject we have discussed in this paper, we contend that the steady state rates under which chemical reactions proceed in a geological system are the results of

competition among the three rates in the simplest case: the rate of dissolution of the primary phase, the rate of precipitation of a secondary phase, and rates of material fluxes associated with fluid flow in a system. The coupling of these three rates is best explored with a reactive mass transport model. However, geological systems are notoriously heterogeneous, with the hydraulic conductivity varying up to 13 orders of magnitude (Freeze and Cherry, 1979). To add uncertainties of hydraulic and geochemical heterogeneities and boundary conditions of a geologic body on top of the uncertainties associated with reactive surface areas and rate laws does not provide much more insight (Zhu, 2009). Instead, we will conduct reactive mass transport in a model system as below.

We took the geochemical reaction path model of oligoclase dissolution and kaolinite precipitation from Ganor et al. (2007) and simulated coupled reaction, advection, and dispersion in a one-dimensional (1D) porous media. The model system is represented by a 100 meter strip discretized into 100 cells, each being one meter in length. As a first approximation, a uniform and constant average velocity along the entire cross-section was used. A longitudinal dispersivity of 1 m was assigned to the model. It was assumed in the study that molecular diffusion is negligible compared to advection and dispersion. Cauchy flux boundary conditions were used for both ends of the 1D strip. Initial pore fluid was taken as the chemistry of the fluid at the end of the reaction path simulation in Ganor et al. (2007), and inflow water into the column was taken as the chemistry of initial fluid from Ganor et al. (2007). All geochemical parameters used were the same as those in Ganor et al. (2007), with exception that the k_1 , k_2 in Eqn (5), which were scaled two orders of magnitude higher. The advection, dispersion, and reaction of

aqueous components under the initial and boundary conditions (described above) were simulated by using PHREEQC Version 2.3, a one-dimensional finite-difference model (Parkhurst and Appello, 1999).

Three different average linear velocities were used for the three scenarios. Figure 18 shows the results of coupling among the dissolution, precipitation, and flow rates in terms of SI for oligoclase at different time and space. For the base case of 0.1 m/y, different levels of steady state SI were established at different locations along the 1D strip after some time, with lower SI near the entrance (flushed by a dilute solution). These SI values were fed back to $f(\Delta G_r)$ in the rate laws for oligoclase and kaolinite, which, in turn, determined the reaction rates, resulting in steady state concentrations of aqueous constituents at specific spatial locations.

For a slower flow rate (0.01 m/y), steady state was generally not achieved within 1000 years of the simulation period. Here we see that the steady state was at a higher SI for oligoclase as compared to the base case. In other words, the smaller solute fluxes from upstream brought about less dilution of the pore fluids in the domain as compared to the base case, resulting in less influence from transport. For a faster flow rate (1 m/y), we see the transport effects are stronger.

In all three scenarios, steady states were established at different levels of SI, resulting in different rates of dissolution and precipitation reactions in the time-space domain. However, the ratios of oligoclase dissolution rate and kaolinite precipitation remained to be 1.626, as in the batch system case (Ganor et al., 2007). Therefore, the simulation results demonstrated the coupling among dissolution, precipitation, and flow rates. Instead of reaching a single steady state that was determined by the ratios of

effective rate constants, surface areas, and rate laws, a series of steady state rates were established at different locations of the domain, even in this initially geochemically homogeneous media. The time to achieve the steady state and the SI and reaction rates of the steady state was a function of the flow rates, assuming the geochemical parameters are the same in all scenarios.

5. CONCLUSIONS AND REMARKS

The geochemical modeling results in the preceding sections lend support to the Zhu-Blum-Veblen hypothesis for explaining the apparent field – lab discrepancy (Zhu et al., 2004). In the literature, the majority laboratory studies have focused on measuring dissolution rates under which secondary mineral precipitation were suppressed while the majority of field weathering studies have attempted to derive dissolution rates only, without information of the precipitation rates and as if the dissolution rates were independent from other reactions in the reaction network. Not surprisingly, the derived field rates are orders of magnitude slower than the far from equilibrium lab rates. The ZBV hypothesis has now been developed in more detail:

(a) Experiments show that the congruent dissolution stage for feldspar dissolution is short because of the low solubility of aluminum silicate minerals. Secondary mineral(s) started to precipitate after only a small amount of primary minerals are dissolved. The same is expected in the field. In fact, it would be difficult to find field situations that secondary mineral precipitation is not present. Therefore, we must always look at the primary mineral dissolution as part of the reaction network;

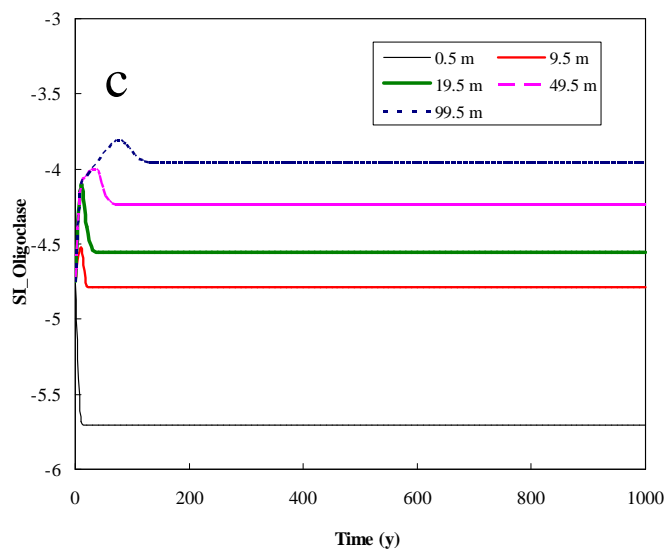
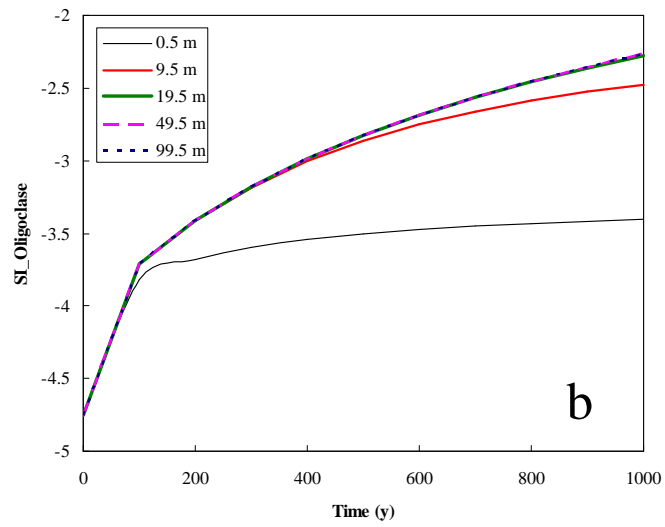
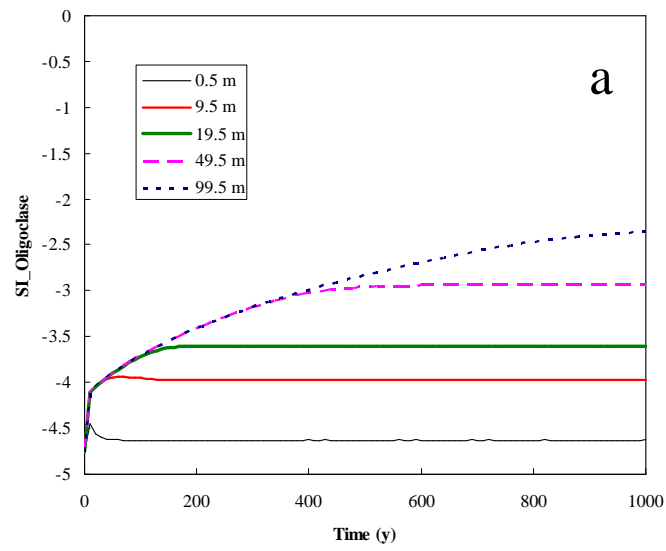


Figure 18. Calculated saturation indices for oligoclase at different time and space from coupled reactive transport model. (a) average linear velocity of 0.1 m/y, (b) 0.01 m/y, and (c) 1 m/y.

(b) Previously, we have shown qualitatively that the partial equilibrium assumption does not hold in these experimental systems (Zhu and Lu, 2009). The numerical reaction path modeling results in this study provided more quantitative evidence. Although many simplifications were made in the reaction path model, and the reaction path models presented above are by no means unique representations of the experimental data, the basic conclusion on the lack of partial equilibrium stands. In a partial equilibrium system, the irreversible dissolution of feldspar is the driving force. We show that when partial equilibrium between secondary minerals and aqueous solution does not hold, the precipitation of secondary minerals is the limiting step, which caps the dissolution rate of the primary mineral. The lack of achieving partial equilibrium under hydrothermal conditions (200 – 300 °C) are indicators that partial equilibrium is also not attained at ambient weathering conditions even though the secondary minerals are different;

(c) A quasi-steady state is reached when $k_1^* / k_2^* > q$, where q is a threshold value. At the quasi-steady state, the ratios for dissolution and precipitation rates are fixed when the rates are expressed in unit of $\text{mol s}^{-1} \text{kgw}^{-1}$, and dissolution reaction proceeds at a fixed ΔG_r . The values of this ratio are a function of the overall reaction stoichiometry, e.g., almost unity in the albite dissolution – sanidine precipitation experiments of Alekseyev et al. (1997) and 1.626 for oligoclase dissolution – kaolinite precipitation in the simulation of Ganor et al. (2007). The steady state dissolution rate, r^{ss} , expressed as $\text{mol s}^{-1} \text{kgw}^{-1}$, may be orders of magnitude slower than the far from equilibrium rate, r^o .

For the experiments by Alekseyev et al. (1997) and Fu et al. (2009), $r^{ss}/r^o \approx 0.01$ at 300 °C and 200 °C. With increasing k_1^* / k_2^* (increasingly slower initial precipitation with respect to dissolution), the steady state dissolution rates of the primary mineral also decrease (Fig. 3 of Zhu, 2009);

(d) Under which conditions the system reaches a steady state with regard to coupled dissolution – precipitation reactions is also determined by the $r - \Delta G_r$ relationships for the dissolution and precipitation reactions. With the experimentally defined sigmoidal shape relationships for albite, the influence range of the ΔG_r term take place in solutions of more undersaturation with respect to the dissolving primary mineral than previously thought, i.e., using the $f(\Delta G_r)$ function of Transition State Theory, and it now does not require to be very close to equilibrium to reduce orders of magnitude of dissolution rates due to the coupling effects. In the case of albite dissolution – sanidine precipitation at 300 °C (Alekseyev et al., 1997), the ΔG_r for albite dissolution – sanidine precipitation reactions were locked at $\Delta G_{r,Ab} \sim -16$ kJ/mol. In contrast, the TST linear rate law would require near equilibrium conditions with respect to the primary minerals to reach orders of magnitude reduction of dissolution rate due to the ΔG_r effects. Field data show that field rates are orders of magnitude slower than the far-from-equilibrium lab rates, whereas the groundwater is not very close to saturation with feldspar (White et al., 2001; Georg et al., 2009).

(e) The potential effects of fluid flow on the coupling of reactions were demonstrated with reactive mass transport modeling in a system resembling that described by Ganor et al. (2007). The results of solute fluxes generated a series of steady states (i.e., SI, aqueous concentrations, and reaction rates) at different locations in the

computational domain, even though the media was assumed to be geochemically homogeneous. The time-space distribution and levels of quasi-steady states are determined by the flow rates for a given kinetics model. A range of rates can be sampled in a field system for samples with close spatial proximity, as well as transient chemical states in a system. Therefore, slow clay precipitation effectively reduces feldspar dissolution rates by orders of magnitude, in a fashion consistent with laboratory rates, transition state theory, and field observations. Furthermore, “close to equilibrium” is probably the most quoted explanation for the apparent discrepancy. However, how this explanation can work quantitatively was not explained before. Our hypothesis provides a quantitative explanation.

The control of feldspar dissolution by the precipitation kinetics of the secondary minerals reconciles many of the apparent discrepancies between laboratory experimental rates and field measurements, and explains field observations that previously appeared inconsistent. It explains slow but persistent feldspar dissolution in sandstone aquifers (Zhu, 2005 for the Navajo sandstone aquifer in northeastern Arizona); why smectite coatings occur on all sediment grains, not only on feldspars (Zhu et al., 2006); why kaolinite is preserved and co-exists with smectite in natural systems over hundreds of thousands to millions years (Zhu et al., 2006). Our hypothesis shifts the paradigm from debate about feldspar dissolution kinetics to the formation kinetics of secondary phases, and opens up new possibilities for laboratory and field experiments to unravel the rates of overall aluminosilicate weathering reactions.

So far, our work has only focused on the coupling of one dissolution reaction with one precipitation reaction. In field situations, several dissolution and precipitation

reactions may operate simultaneously. The coupling effects in the reaction network can become extremely complex. The experimental data at elevated temperatures 200 °C and 300 °C showed a maximum two orders of magnitude reduction due to the coupled reaction effects. Our modeling study has clearly identified the research needs of the rate laws in the near equilibrium regions, rate law for precipitation reactions, and more studies of reactive surface areas.

Another source of retardation of dissolution rates in the field can come from surface passivation. Zhu et al. (2006) found a thin 10 – 50 nanometer amorphous layer on the K-feldspar surfaces in the Jurassic Navajo sandstone in Arizona. Whether such a layer is widespread for minerals that have been in contact with water for thousands to million years and what the role this layer plays is currently unclear.

REFERENCES

- Aagaard, P. and Helgeson, H. C., 1982. Thermodynamic and kinetic constraints on reaction rates among minerals and aqueous solutions. I. Theoretical considerations. *Am. J. Sci.* **282**, 237-285.
- Alekseyev, V. A., Medvedeva, L. S., Prisyagina, N. I., Meshalkin, S. S., and Balabin, A. I., 1997. Change in the dissolution rates of alkali feldspars as a result of secondary mineral precipitation and approach to equilibrium. *Geochim. Cosmochim. Acta* **61**, 1125-1142.
- Banfield, J. F. and Barker, W. W., 1994. Direct observation of reactant-product interfaces formed in natural weathering of exsolved, defective amphibole to smectite - evidence for episodic, isovolumetric reactions involving structural inheritance. *Geochim. Cosmochim. Acta* **58**, 1419-1429.
- Banfield, J. F. and Eggleton, R. A., 1990. Analytical Transmission Electron-Microscope Studies of Plagioclase, Muscovite, and K-Feldspar Weathering. *Clay. Clay. Miner.* **38**, 77-89.
- Banfield, J. F., Jones, B. F., and Veblen, D. R., 1991. An AEM-TEM study of weathering and diagenesis, Albert Lake, Oregon. I. Weathering reactions in the volcanics. *Geochim. Cosmochim. Acta* **55**, 2781-2793.

- Beig, M. S. and Lüttge, A., 2006. Albite dissolution kinetics as a function of distance from equilibrium: Implications for natural feldspar weathering. *Geochim. Cosmochim. Acta* **70**, 1402-1420.
- Bénézech, P., Palmer, D. A., and Wesolowski, D. J., 2008. Dissolution/precipitation kinetics of boehmite and gibbsite: Application of a pH-relaxation technique to study near-equilibrium rates. *Geochim. Cosmochim. Acta* **72**, 2429-2453.
- Blum, A. and Stillings, L., 1995. Feldspar dissolution kinetics. In: Brantley, S. L. and White, A. R. (Eds.), *Chemical Weathering Rates of Silicate Minerals*. Vol. 31, pp.291-351, Mineralogical Society of America, Washington DC.
- Brantley, S. L., 1992. Kinetics of dissolution and precipitation: experimental and field results. In: Kharaka, Y. and Maest, A. (Eds.) *Proceedings of the Seventh International Conference on Water-Rock Interactions*, Park City, Utah: Rotterdam, Balkema.
- Brantley, S. L. and Stillings, L., 1996. Feldspar dissolution at 25° C and low pH. *Am. J. Sci.* **296**, 101-127.
- Braunauer, S., Emmett, P. H., and Teller, E., 1938. Adsorption of gases in multimolecular layers. *Journal of the American Chemical Society* **60**, 309-319.
- Burch, T. E., Nagy, K. L., and Lasaga, A. C., 1993. Free energy dependence of albite dissolution kinetics at 80° C and pH 8.8. *Chem. Geol.* **105**, 137-162.
- Burton, W. K., Cabrera, N., and Frank, F. C., 1951. The growth of crystals and the equilibrium structure of their surfaces. *Royal Soc. London Philos. Trans.* **243**, 299-358.
- Busenberg, E. and Clemency, C. V., 1976. The dissolution kinetics of feldspars at 25° C and 1 atm CO₂ partial pressure. *Geochim. Cosmochim. Acta* **40**, 41-49.
- Cama, J., Ganor, J., Ayora, C., and Lasaga, C. A., 2000. Smetite dissolution kinetics at 80 °C and pH 8.8. *Geochim. Cosmochim. Acta* **64**, 2701-2717.
- Chou, L. and Wollast, R., 1984. Study of the weathering of albite at room temperature and pressure with a fluidized bed reactor. *Geochim. Cosmochim. Acta* **48**, 2205-2217.
- Chou, L. and Wollast, R., 1985. Steady-state kinetics and dissolution mechanisms of albite. *Am. J. Sci.* **285**, 963-993.
- Christoffersen, J. and Christoffersen, M. R., 1976. The kinetics of dissolution of calcium sulphate dihydrate in water. *Journal of Crystal Growth* **35**, 79-88.
- Correns, C. W., 1940. Die Chemische Verwitterung der Silikate. *Nature* **28**, 369-376.

- Correns, C. W. and von Engelhardt, W., 1938. Neue Untersuchungen über die Verwitterung des Kalifeldspates. *Chemie der Erde* **12**, 1-22.
- Cubillas, P., Kohler, S., Prieto, M., Causserand, C., and Oelkers, E. H., 2005. How do mineral coating affect dissolution rates? An experimental study of coupled CdCO_3 dissolution -- CdCO_3 precipitation. *Geochim. Cosmochim. Acta* **69**, 5459-5476.
- Drever, J. I. and Clow, D. W., 1995. Weathering rates in catchments. In: White, A. F. and Brantley, S. L. (Eds.), *Chemical Weathering Rates of Silicate Minerals*. Vol. 31, pp.463-483, Mineralogical Society of America.
- Freeze, R. A. and Cherry, J. A., 1979. *Groundwater*. Prentice-Hall, New York.
- Fritz, B. and Noguera, C., 2009. Mineral precipitation kinetics. In: Oelkers, E. H. and Schott, J. (Eds.), *Thermodynamics and kinetics of water-rock interaction*. Vol. 70, pp.371-409, Mineralogical Society of America.
- Fu, Q., Lu, P., Konishi, H., Dillmore, R., Xu, H., Seyfried, W. E., Jr., and Zhu, C., 2009. Coupled alkali-feldspar dissolution and secondary mineral precipitation in batch systems: 1. New experiment data at 200° C and 300 bars. *Chem. Geol.* **91**, 955-964.
- Ganor, J., Lu, P., Zheng, Z., and Zhu, C., 2007. Bridging the gap between laboratory measurements and field estimations of silicate weathering using simple calculations. *Environ. Geol.* **53**, 599-610.
- Ganor, J., Mogollon, J. L., and Lasaga, A. C., 1995. The effect of pH on kaolinite dissolution rates and on activation energy. *Geochim. Cosmochim. Acta* **59**, 1037-1052.
- Ganor, J., Mogollon, J. L., and Lasaga, A. C., 1999. Kinetics of gibbsite dissolution under low ionic strength conditions. *Geochim. Cosmochim. Acta* **63**, 1635-1651.
- Garrels, R. M. and Howard, D. F., 1957. Reactions of feldspar and mica with water at low temperatures and pressures, *The Sixth National Conference on Clays and Glau Minerals*. Vol. 67, pp.68-88, New York, Pergamon Press, Berkeley, California.
- Gautier, J.-M., Oelkers, E. H., and Schott, J., 1994. Experimental study of K-feldspar dissolution rates as a function of chemical affinity at 150° C and pH 9. *Geochim. Cosmochim. Acta* **58**, 4549-4560.
- Gautier, J. M., Oelkers, E. H., and Schott, J., 2001. Are quartz dissolution rates proportional to B.E.T. surface areas? *Geochim. Cosmochim. Acta* **65**, 1059-1070.

- Georg, R. B., Zhu, C., Reynolds, R. C., and Halliday, A. N., 2009. Stable silicon isotopes of groundwater, feldspars, and clay coatings in the Navajo Sandstone aquifer, Black Mesa, Arizona, USA. *Geochim. Cosmochim. Acta* **73**, 2229-2241.
- Haar, L., Gallagher, J. S., and Kell, G. S., 1984. *NBS/NRC Steam Tables: Thermodynamic and Transport Properties and Computer Programs for Vapor and Liquid States of Water in SI Units*. Hemisphere Publishing Corporation, New York, 320p.
- He, S., Oddo, J. E., and Tomson, M. B., 1994. The Seeded Growth of Calcium Sulfate Dihydrate Crystals in NaCl Solutions up to 6 m and 90°C. *J. Colloid. Interf. Sci.* **163**, 372-378.
- Helgeson, H. C., 1968. Evaluation of irreversible reactions in geochemical processes involving minerals and aqueous solutions-1. Thermodynamic relations. *Geochim. Cosmochim. Acta* **32**, 853-877.
- Helgeson, H. C., 1971. Kinetics of mass transfer among silicates and aqueous solutions. *Geochim. Cosmochim. Acta* **35**, 421-469.
- Helgeson, H. C., 1972. Kinetics of mass transfer among silicates and aqueous solutions: Correction and clarification. *Geochim. Cosmochim. Acta* **36**, 1067-1070.
- Helgeson, H. C., 1979. Mass transfer among minerals and hydrothermal solutions. In: Barnes, H. L. (Ed.), *Geochemistry of Hydrothermal Ore Deposits*. Vol. pp.568-610, John Wiley & Sons, New York.
- Helgeson, H. C., Brown, T. H., Nigrini, A., and Jones, T. A., 1970. Calculation of mass transfer in geochemical processes involving aqueous solutions. *Geochim. Cosmochim. Acta* **34**, 569-592.
- Helgeson, H. C., Delany, J. M., Nesbitt, H. W., and Bird, D. K., 1978. Summary and critique of the thermodynamic properties of rock forming minerals. *Am. J. Sci.* **278A**, 1-229.
- Helgeson, H. C., Garrels, R. M., and Mackenzie, F. T., 1969. Evaluation of irreversible reactions in geochemical processing involving minerals and aqueous solutions- II. Applications. *Geochim. Cosmochim. Acta* **33**, 455-481.
- Helgeson, H. C., Murphy, W. M., and Aagaard, P., 1984. Thermodynamic and kinetic constraints on reaction rates among minerals and aqueous solutions II. Rate constants, effective surface area, and the hydrolysis of feldspar. *Geochim. Cosmochim. Acta* **48**, 2405-2432.
- Hellmann, R., 1994. The albite-water system; Part I, The kinetics of dissolution as a function of pH at 100, 200, and 300° C. *Geochim. Cosmochim. Acta* **58**, 595-611.

- Hellmann, R., 1997. The albite-water system; Part III, Characterization of leached and hydrogen-enriched layers formed at 300° C using MeV ion beam techniques. *Geochim. Cosmochim. Acta* **61**, 1575-1594.
- Hellmann, R., Eggleston, C. R., Hochella, M. F., and Crerar, D. A., 1990. The formation of leached layers on albite surfaces during dissolution under hydrothermal conditions. *Geochim. Cosmochim. Acta* **54**, 1267-1281.
- Hellmann, R. and Tisserand, D., 2006. Dissolution kinetics as a function of the Gibbs free energy of reaction: An experimental study based on albite feldspar. *Geochim. Cosmochim. Acta* **70**, 364-383.
- Hemingway, B. S., Robie, R. A., and Apps, J. A., 1991. Revised values for the thermodynamic properties of boehmite, AlO(OH), and related species and phases in the system Al-H-O. *Am. Mineral.*, **76**, 445-457.
- Hereford, A. G., Keating, E., Guthrie, G., and Zhu, C., 2007. Reactions and reaction rates in the aquifer beneath Pajarito Plateau, north-central New Mexico. *Environ. Geol.* **52**, 965-977.
- Ho, P. C., Bianchi, H., Palmer, D. A., and Wood, R. H., 2000. Conductivity of dilute aqueous electrolyte solutions at high temperatures and pressures using a flow cell. *J. Solution Chem.* **29**, 217-235.
- Hoch, A. R., Reddy, M. M., and Aiken, G. R., 2000. Calcite crystal growth inhibition by humic substances with emphasis on hydrophobic acids from the Florida Everglades. . *Geochim. Cosmochim. Acta* **64**, 61-72.
- Holland, T. J. B. and Powell, R., 1998. An internally consistent thermodynamic data set for phases of petrological interest. *J. Metamorph. Geol.* **16**, 309-343.
- Labotka, T. C., Cole, D. R., Fayek, M., Riciputi, L. R., and Stadermann, F. J., 2004. Coupled cation and oxygen-isotope exchange between alkali feldspar and aqueous chloride solution. *Am. Mineral.* **89**, 1822-1825.
- Lasaga, A. C., 1981a. Rate laws of chemical reactions. In: Lasaga, A. C., Kirkpatrick, R.J. (Ed.), *Kinetics of Geochemical Processes*. Vol. 8, pp.1-68, Mineralogical Society of America, Washington DC.
- Lasaga, A. C., 1981b. Transition State Theory. In: Lasaga, A. C. and Kirkpatrick, R. J. (Eds.), *Kinetics of Geochemical Processes*. Vol. 8, pp.135-169, Mineralogical Society of America, Washington DC.

- Lasaga, A. C., Soler, J. M., Ganor, J., Burch, T. E., and Nagy, K. L., 1994. Chemical weathering rate laws and global geochemical cycles. *Geochim. Cosmochim. Acta* **58**, 2361-2386.
- Liu, S. T. and Nancollas, G. H., 1975. A kinetic and morphological study of the seeded growth of calcium sulfate dihydrate in the presence of additives. *J. Colloid. Interf. Sci.* **52**, 593-601.
- Luce, R. W., Bartlett, R. W., and Parks, G. A., 1972. Dissolution kinetics of magnesium silicates. *Geochim. Cosmochim. Acta* **36**, 35-50.
- McCollom, T. M. and Shock, E. L., 1997. Geochemical constraints on chemolithoautotrophic metabolism by microorganisms in seafloor hydrothermal systems. *Geochim. Cosmochim. Acta* **61**, 4375-4391.
- Metz, V., Raanan, H., Pieper, H., Bosbach, D., and Ganor, J., 2005. Towards the establishment of a reliable proxy for the reactive surface area of smectite. *Geochim. Cosmochim. Acta* **69**, 2581-2591.
- Nagy, K. L., 1995. Dissolution and precipitation kinetics of sheet silicates. In: White, A. F. and Brantley, S. L. (Eds.), *Chemical Weathering Rates of Silicate Minerals*. Vol. 31, pp.173-225, Mineralogical Society of America.
- Nagy, K. L., Blum, A. E., and Lasaga, A. C., 1991. Dissolution and precipitation kinetics of kaolinite at 80° C and pH 3: the effect of deviation from equilibrium. *Am. J. Sci.* **291**, 649-686.
- Nagy, K. L. and Lasaga, A. C., 1992. Dissolution and precipitation kinetics of gibbsite at 80°C and pH-3 - The dependence on solution saturation state. *Geochim. Cosmochim. Acta* **56**, 3093-3111.
- Nagy, K. L. and Lasaga, A. C., 1993. Kinetics of simultaneous kaolinite and gibbsite precipitation. *Geochim. Cosmochim. Acta* **57**, 4329-4337.
- Nesbitt, H. W. and Skinner, W. M., 2001. Early development of Al, Ca, and Na compositional gradients in labradorite leached in pH 2 HCl solutions. *Geochim. Cosmochim. Acta* **65**, 715-727.
- Nielsen, A. E., 1964. *Kinetics of Precipitation*. Pergamon, Oxford.
- Nugent, M. A., Brantley, S. L., Pantano, C. G., and Maurice, P. A., 1998. The influence of natural mineral coatings on feldspar weathering. *Nature* **395**, 588-591.
- Oelkers, E. H., 2001. General kinetic description of multioxide silicate mineral and glass dissolution. *Geochim. Cosmochim. Acta* **65**, 3703-3719.

- Oelkers, E. H. and Helgeson, H. C., 1990. Triple-ion anions and polynuclear complexing in supercritical electrolyte-solutions. *Geochim. Cosmochim. Acta* **54**, 727-738.
- Oelkers, E. H., Schott, J., and Devidal, J. L., 1994. The effect of aluminum, pH, and chemical affinity on the rates of aluminosilicate dissolution reactions. *Geochim. Cosmochim. Acta* **58**, 2011-2024.
- Paces, T., 1973. Steady-state kinetics and equilibrium between ground water and granitic rocks. *Geochim. Cosmochim. Acta* **37**, 2641-2663.
- Parkhurst, D. L. and Appello, A. A. J., 1999. *User's guide to PHREEQC (version 2)-a computer program for speciation, batch-reaction, one dimensional transport, and inverse geochemical modeling*. U.S. Geological Survey. Water-Resource Investigation Report 99-4259 pp. 312
- Prigogine, I. and Defay, R., 1965. *Chemical Thermodynamics*. Longmans Green, London.
- Putnis, A., 2002. Mineral replacement reactions: from macroscopic observations to microscopic mechanisms. *Mineralogical Magazine* **66**, 689-708.
- Reed, M. H. and Spycher, N. F., 1984. Calculation of pH and mineral equilibria in hydrothermal waters with application to geothermometry and studies of boiling and dilution. *Geochim. Cosmochim. Acta* **48**, 1479-1492.
- Schramke, J. A., Kerrick, D. M., and Lasaga, A. C., 1987. The reaction muscovite + quartz \rightleftharpoons andalusite + K-feldspar + water. Part I. Growth kinetics and mechanism. *Am. J. Sci.* **287**, 517-559.
- Siegel, D. I. and Pfannkuch, H. O., 1984. Silicate dissolution influence on Filson Creek chemistry, northeastern Minnesota. *Geol. Soc. Am. Bull.* **95**, 1446-1453.
- Stillings, L. L., Brantley, S. L., and Machesky, M. L., 1995. Proton adsorption at an adularia feldspar surface. *Geochim. Cosmochim. Acta* **59**, 1473-1482.
- Sverjensky, D. A., Shock, E. L., and Helgeson, H. C., 1997. Prediction of the thermodynamic properties of aqueous metal complexes to 5 Kb and 1000 oC. *Geochim. Cosmochim. Acta* **61**, 1359-1412.
- Tagirov, B. and Schott, J., 2001. Aluminum speciation in crustal fluids revisited. *Geochim. Cosmochim. Acta* **65**, 3965-3992.
- Taylor, A. S., Blum, J. D., and Lasaga, A. C., 2000. The dependence of labradorite dissolution and Sr isotope release rates on solution saturation state. *Geochim. Cosmochim. Acta* **64**, 2389-2400.

- Velbel, M. A., 1990. Influence of temperature and mineral surface characteristics on feldspar weathering rates in natural and artificial systems: A first approximation. *Water Resources Research* **26**, 3049-3053.
- Weijnen, M. P. C. and Van Rosmalen, G. M., 1986. Adsorption of phosphonates on gypsum crystals. *J. Cryst. Growth* **79**, 157-168.
- White, A. F., Bullen, T. D., Schulz, M. S., Blum, A. E., Huntington, T. G., and Peters, N. E., 2001. Differential rates of feldspar weathering in granitic regoliths. *Geochim. Cosmochim. Acta* **65**, 847-869.
- Witkamp, G. J., Van der Eerden, J. P., and Van Rosmalen, G. M., 1990. Growth of gypsum : I. Kinetics. *J. Cryst. Growth* **102**, 281-289.
- Wolery, T. J., 1992. *EQ3/6, A software package for geochemical modeling of aqueous systems: Package overview and installation guide (version 7.0)*: URCL-MA-110662-PT-I, Livermore, Calif., Univ. California, Lawrence Livermore Laboratory.
- Zhang, J. and Nancollas, G. H., 1992. Influence of calcium/sulfate molar ratio on the growth rate of calcium sulfate dihydrate at constant supersaturation. *J. Cryst. Growth* **118**, 287-294.
- Zhu, C., 2005. In situ feldspar dissolution rates in an aquifer. *Geochim. Cosmochim. Acta* **69**, 1435-1453.
- Zhu, C., 2009. Geochemical Modeling of Reaction Paths and Geochemical Reaction Networks. In: Oelkers, E. H. and Schott, J. (Eds.), *Thermodynamics and kinetics of water-rock interaction*. Vol. 70, pp.533-569, Mineralogical Society of America.
- Zhu, C. and Anderson, G. M., 2002. *Environmental Applications of Geochemical Modeling*. Cambridge University Press, London.
- Zhu, C., Blum, A. E., and Veblen, D. R., 2004. Feldspar dissolution rates and clay precipitation in the Navajo aquifer at Black Mesa, Arizona, USA. In: Wanty, R. B. and Seal, R. R. I. (Eds.), *Water-Rock Interaction*. Vol. pp. 895-899, A.A. Balkema, Saratoga Springs, New York.
- Zhu, C. and Lu, P., 2009. Coupled alkali feldspar dissolution and secondary mineral precipitation in batch systems: 3. Saturation Indices of Product Minerals and Reaction Paths. *Geochim. Cosmochim. Acta* **73**, 3171-3200.
- Zhu, C., Veblen, D. R., Blum, A. E., and Chipera, S. J., 2006. Naturally weathered feldspar surfaces in the Navajo Sandstone aquifer, Black Mesa, Arizona: Electron microscopic characterization. *Geochim. Cosmochim. Acta* **70**, 4600-4616.

CHAPTER 6

NAVAJO SANDSTONE-BRINE-CO₂ INTERACTION: IMPLICATIONS FOR GEOLOGICAL CARBON SEQUESTRATION⁵

⁵ This chapter is will be published as: Lu, P., Hereford, A., Fu, Q., Seyfried, W. E, and Zhu, C. (2010) Navajo sandstone-brine-CO₂ interaction: implications for geological carbon sequestration. Environmental Earth Sciences, in press, DOI: 10.1007/s12665-010-0501-y.

1. INTRODUCTION

An ever-increasing amount of scientific evidence suggests that anthropogenic release of CO₂ has led to a rise in global temperatures since the Industrial Revolution (Crowley, 2000). The injection of CO₂ into deep saline aquifers is presently being evaluated as an option for greenhouse gas reduction (Gale, 2002). Currently, the U.S. Department of Energy (DOE) is conducting pilot CO₂ injection tests to evaluate the feasibility of storing millions of tons of carbon dioxide in deep saline aquifers around the U.S. The Navajo Sandstone and its geological equivalent, the Nugget Sandstone, are two of the target aquifers in the western United States; the Nugget Sandstone saline formation was selected as the target for one of the large-volume injection tests by the Big Sky Carbon Sequestration Partnership (Spangler, 2007). The Jurassic Navajo/Nugget Sandstone has been identified as regionally extensive in the western U.S. (Loope and Rowe, 2003), and is thus potentially significant with respect to carbon sequestration in these regions.

While from a capacity perspective, deep saline aquifers offer significant potential (DOE, 2007; Gale, 2002), considerable uncertainties remain because CO₂ is reactive, particularly when dissolved in water. CO₂ is likely to react with the sandstone, causing precipitation and dissolution of minerals, and changing the porosity, permeability, and injectivity of the aquifer (e.g., Xu et al., 2004). To date, the published literature has focused mainly on carbonate precipitation without regard to the reactivity of the host rock. CO₂-fluid- rock interactions within saline aquifers have received less attention. Dissolution of silicate minerals in a brine and precipitation of carbonate are reported in limited numerical modeling studies that involve reaction kinetics (Gunter et al., 2000;

Gunter et al., 1997; Parry et al., 2007; Perkins and Gunter, 1995) and experimental studies (Gunter et al., 1997; Kaszuba et al., 2003; Kaszuba et al., 2005). A month-long batch experiment at 105 °C and 9 MPa yielded a large increase in alkalinity and minor water-mineral reactions (Gunter et al., 1997). In contrast, 32- to 77- d experiments at 200 °C and 20 MPa resulted in texturization of silicate minerals (quartz, plagioclase, microcline and biotite) in the aquifer and the aquitard (an artificial analog) indicative of more significant reactions (Kaszuba et al., 2003; 2005). However, the following questions remained unanswered: What is the response of an aquifer system far away from an injection well to the injected CO₂? Are there any new clay minerals formed and what is the stability of indigenous clay minerals — do they disappear by dissolution, transform into new minerals, or become free and mobile and tend to clog the pore throats? The answer to latter question has implications for permeability and may pose a concern on reservoir quality and injectivity. In addition, it is not at all clear from available data whether high CO₂ concentrations in fluids (due to CO₂ injection) act to catalyze or inhibit silicate mineral dissolution and secondary mineral precipitation. In this study, we conducted a series of CO₂- sandstone-brine interaction experiments to investigate the response of the Navajo Sandstone to the injection of CO₂. Detailed SEM and XRD work was performed to characterize the product minerals. Sandstone from a drill core was used in the experiments to facilitate the investigation of indigenous clay mineral stability. This study provides critical constraints that can serve as a basis to refine numerical performance modeling of CO₂ sequestration in saline aquifers.

2. MATERIALS AND METHODS

Experimental approach. A total of three hydrothermal experiments have been conducted to assess primary mineral dissolution and secondary mineral precipitation. The first batch experiment exposed the Navajo Sandstone to CO₂- impregnated brine and assessed the mineral reactivity as it affected permeability, porosity, and permanent sequestration via precipitation of carbonates and dissolution/precipitation of silicates and clays. These data will provide input for further simulation studies. The second batch experiment dissolved the Navajo Sandstone in acidic brine without CO₂ and with a lower pH, for comparison against experiment #1. Finally, a mixed flow experiment (experiment #3) was performed to measure the sandstone dissolution rates based on variations of Si concentration as a function of time. Our experimental pressures (25-30 MPa) are similar to the pressure of the target formation studied by the Big Sky Carbon Sequestration Partnership (~26 MPa), but the experimental temperature is higher (200° C) than that of the Big Sky study (~98 °C). Our pressure and temperature conditions are comparable with those in Kuszuba et al. (2003; 2005) (20 MPa and 200° C). Gunter et al. (1997) also used higher temperature (105° C) than that of the corresponding aquifer (54° C) because reaction rates at 54 °C were apparently insufficient to produce observable reactions. Indeed, the higher temperature is justifiable because (1) it accelerates the reactions to measurable rates in and (2) it expedites the sluggish kinetic processes to the controllable time scales in the laboratory, considering the time scales of performance assessments are usually on the order of thousands of years or longer (Wildenborg and van der Meer, 2002).

The use of KCl solutions in our experiments does not represent realistic reservoir conditions, but accelerates possible smectite to illite conversion, which could have severe effects on permeability (see below). In using KCl, instead of NaCl or Na-Ca-Cl solutions, we also assume that reaction mechanisms for silicate dissolution and precipitation reactions are unaffected by variations in background solutions. However, KCl may result in faster plagioclase dissolution and slower K-feldspar dissolution than the use of NaCl. The effects of solution chemistry on saturation indices were taken into account in the speciation-solubility modeling.

Experimental apparatus for batch experiments. The prepared sandstone particles were placed in a flexible Au reaction cell with detachable Ti closure, which was placed in a steel-alloy autoclave (Seyfried et al., 1987). This arrangement allows easy access to the reactants at the end of the experiment. More importantly, the flexible cell permits on-line sampling of the aqueous phase at constant temperature and pressure simply by adding water, in an amount equivalent to the sampled fluid, to the region surrounding the reaction cell. These experimental data are generally superior to those derived from samples collected after the reactors are cooled down because backward reactions may occur during cooling. The experiments using the flexible cell system were conducted at 200 °C and 30 MPa.

Experimental apparatus for mixed flow experiment. The mixed flow dissolution experiment of the Navajo Sandstone was performed using a hydrothermal flow system. A fixed volume (~100 ml) Ti reactor is the central unit of the flow system. It connects to a high-pressure fluid delivery system (Shimadzu 10A HPLC pump) that keeps the rate of fluid flow at pre-selected values. The outlet side of the reactor is

connected to a computer-controlled regulating valve that serves to maintain the total pressure at fixed values. Temperature control is provided by a series of Watlow band heaters external to the Ti reactor. The reactor is also equipped with a magnetic stirrer (Parr Instrument, A1120HC), which allows reactants to remain suspended in the fluid during the experiment.

Experimental methods. Reddish Navajo Sandstones were collected from Black Mesa, Arizona. The major mineral component of Navajo Sandstone is quartz, with ~2% feldspars (Dulaney, 1989; Harshbarger et al., 1957; Zhu, 2005). A sandstone sample (MSE 136.5-137) was gently crushed with an agate mortar and pestle, and then dry-sieved. The fraction between 50 and 100 μm was used directly for hydrothermal experiments. To test the stability of clay coatings under disturbance by mechanized force, the sonication method was employed. Ten g of the sandstone fractions and 150 ml deionized water were placed into a 200-ml polyethylene bottle and ultrasonic-cleaned with a sonic probe 5 times, for 10 min per treatment. The bottle was cooled in a water bath to during ultrasonication. The supernatant was disposed of and the remaining solid was freeze-dried.

KCl solutions were made from analytical grade chemicals purchased from Fisher Scientific. Initial pH was adjusted through titration of HCl solutions.

Analytical methods. Fluid samples were taken from the reactor at regular intervals and analyzed for all major and some minor dissolved constituents. Dissolved cations were analyzed by inductively coupled plasma mass spectrometry (ICP-MS) while anions were analyzed by ion chromatography (IC). Reactants and products were

characterized with X-ray diffraction (XRD, for phase identification) and SEM (for phase relationships and surface morphology).

Samples were analyzed on a ThermoElemental PQ ExCell argon ICP quadrupole mass spectrometer with a simultaneous analog and pulse counting detector. All elements were measured on the most appropriate mass by peak hopping with dwell times of approximately 35 ms per mass and 25-50 mass sweeps per replicate. For each sample, standard, and blank, this set of sweeps was replicated 5 times to determine a mean and standard deviation for each selected elemental mass. Calibration was accomplished by comparing a NIST traceable single- or multi-element standard solution to the unknowns. All blanks, standards, and samples are acid-matrix matched to reduce matrix and polyatomic overlap effects and are diluted such that element concentrations are in the linear working range of the standard and detector combination. Calibration blocks consist of a blank, standard, and up to 5 unknown samples. An external drift correction is applied between calibration blocks to compensate for instrument signal drift. Internal standard elements (Sc, Rh, In) are added on occasion to diluted samples to further compensate for drift and for matrix effects when widely varying major element concentrations are expected. On each day, before acquiring data, a detector cross calibration is performed between the analog and pulse counting detectors to provide a working linear range of >6 orders of magnitude if the appropriate solution standards are used. All blanks, standards, and samples must be in aqueous solution and are atomized and introduced to the instrument by a free aspiration rate of approximately 1 ml/min into a standard Meinhardt nebulizer. The probe and all sample introduction tubing are made of Teflon and are

flushed for a minimum of 65 s with clean matrix acid to prevent carryover between samples.

Ion chromatography analysis was performed with a Dionex IC25 Ion chromatograph with an LC25 Chromatography oven and an AS14H column and Atlas suppressor supplied by Dionex. The samples were analyzed within 7 d after sampling, and were kept refrigerated to 4 °C until analysis. A seven-ion standard was used to calibrate the instrument and was run intermittently to monitor the instrument throughout the analysis. Standard deviations are reported for the seven-ion standard data.

XRD analyses were carried out using a Bruker D8 Advance diffractometer, equipped with a Cu anode at 20 kV and 5 mA, and with a SolX energy-dispersive detector. The scan parameters used were 2 to 70° 2 θ , with a step size of 0.02° 2 θ . The sample preparation method is called “slurry mount”. Reaction products were immersed in a 20 ml deionized water in a plastic vessel (25 ml volume) and ultrasonicated three times for 15 min per treatment with 15-min breaks. After the final ultrasonication, the samples were allowed to settle overnight. Then, the suspension (clay with water) was carefully pipetted out, mounted onto a zero background quartz plate and air-dried. The mount-dry cycle was repeated to ensure enough material for XRD analysis.

SEM is conducted with a Quanta 400 Field Emission Gun (FEG). The equipped Energy Dispersive X-ray Spectrometer (EDS) system has an EDAX thin window and CDU LEAP detector. The low-energy X-ray detection with FEG provided high spatial resolution for microanalysis down to ~0.1 mm³ under optimum conditions.

3. RESULTS AND DISCUSSION

Navajo Sandstone before hydrothermal reactions. Detailed studies of untreated Navajo Sandstone were described in Zhu et al. (2006). XRD analysis of the bulk Navajo Sandstone showed ~ 90% by weight quartz, with minor amounts of K-feldspar and smectite, and trace amounts of kaolinite and illite/mica (Zhu et al., 2006). Feldspar grains are covered with an inner layer of kaolinite and an outer layer of smectite (Zhu et al., 2006). Smectite coatings occur not only on feldspar grains but also on quartz and Fe-Ti oxides (Zhu et al., 2006). X-ray diffraction results confirmed Zhu et al.'s (2006) findings that the clay coating on the Navajo Sandstone is mainly composed of smectite and kaolinite (Fig. 1).

Figure 2 shows SEM microphotographs of the Navajo Sandstone after ultrasonication. The smectite coating is largely removed (Fig. 2). However, the kaolinite coating persists on K-feldspar surfaces (Figs. 2b and 2c). The easy removal of smectite from its original place presents an important concern on reservoir quality and injectivity: whether chemical reactions induced by CO₂ injection will mobilize the smectite and cause pore throat clogging.

Batch experiment 1: Navajo Sandstone dissolution in CO₂-impregnated brine. The first Navajo Sandstone dissolution experiment is a batch experiment at 200 °C, 30 MPa, and pH 4.1 (measured at 25 °C). Four g of Navajo Sandstone were reacted with 40 g 200 mmol/kg KCl solution in the presence of 20 mmol/kg CO₂ (aq). X-ray diffraction results (Fig. 1) indicate that our experiment produced secondary clay minerals after 552 h of reaction. Hydrothermal reactions led to the illitization of smectite minerals (Fig. 1). The peak at 1.1-1.2 nm is illite/smectite. Illitization of smectite has been widely

documented by XRD studies and continues to draw the attention of researchers all over the world. From the time of the pioneering study of Hower et al. (1976), there has been general agreement that illitization of smectite involves interstratified intermediates, with the proportion of illite in mixed-layer illite/smectite increasing as a function of increasing temperature, time and burial depth of basin sediments (Bauluz et al., 2002; Cuadros and Linares, 1996). Kaolinite and allophane were also identified (Fig. 1). While kaolinite was present before the experiment, allophane was newly precipitated as a reaction product in the experiment. Allophane ($\text{Al}_2\text{Si}_2\text{O}_5 \cdot 3\text{H}_2\text{O}$) is a poorly crystallized hydrous aluminum silicate clay mineral and has a composition similar to kaolinite ($\text{Al}_2\text{Si}_2\text{O}_5(\text{OH})_4$). Rhombohedra-shaped carbonate grains were occasionally found on quartz particles (Fig. 3f). However, there are not sufficient quantities of carbonate minerals to be successfully identified with XRD.

SEM images show the morphology change of the sandstone during the course of the experiment. The reacted sandstone displays evidence of fluid-rock interactions, similar to that observed in Kaszuba et al. (2003; 2005). Increased Si concentrations through time suggest silicate dissolution (Table 1 and Fig. 4a), although dissolution features on sandstones are not evident. Abundant clay minerals adhered to quartz and K-feldspars after the reaction and commonly filled or bridged the pores. Product minerals observed with SEM were consistent with XRD results. Newly formed allophane aggregates filled the voids in sandstone grains (Fig. 3a and 3c). These allophanes were poorly crystallized. XRD (Fig. 1) and SEM with X-ray microanalysis (SEM/EDS) analysis (Fig. 3d) confirm the identity of allophane. SEM observations confirmed the illitization of smectite. The morphologies ranged from the typical "corn-flake," "maple

leaf," or "honeycomb" habit of smectite to the typical platy or scalloped (with curled points) habit of illite, as described by Keller et al. (1986). The elongated fabric of the platy or ribbon-like illite/smectite is shown in Figs. 3a-3g. This morphology of illite/smectite has also been observed in Keller et al. (1986), Nadeau (1998), Nadeau et al. (2002), and Celik et al. (1999). Illite, as interwoven ribbons, is intimately associated with the smectite (Fig. 3g). The smectite and kaolinite coatings persisted on the K-feldspar grains, indicating that the chemical reactions did not remove the coatings (Fig. 3 h-j).

The solution chemistry results are presented in Tables 1 and 2 and Fig. 4a. During the experiment run, dissolved K^+ and Cl^- concentrations remained relatively constant (Table 1). Dissolved SiO_2 increased, reaching 2.20 mmol/kg by the end of experiment. The smectite-to-illite conversion generally consumes K^+ and releases SiO_2 (Cuadros and Linares, 1996). This conversion is likely to be a source of increased SiO_2 . Another source of SiO_2 is dissolution of feldspars. Saturation index calculations indicate that the solution was undersaturated with respect to albite and anorthite during the entire course of the reaction (see below), suggesting the dissolution of plagioclase. The dissolved concentrations of Mg^{2+} and Ca^{2+} also increased with time (Fig. 4a). There was only a slight decrease in dissolved CO_2 concentration during the experiment (which suggests the formation of carbonates) while pH values increased slowly with reaction progress (Fig. 4a). Generally, the dissolved concentrations of most minor and trace elements approached steady-state values within the first 48 h (Table 2). Trace element analysis shows that toxic metals (Cu, Zn, and Ba) were released. Kaszuba et al. (2005) also noted the mobilization of trace elements in their CO_2 -bearing hydrothermal experiments.

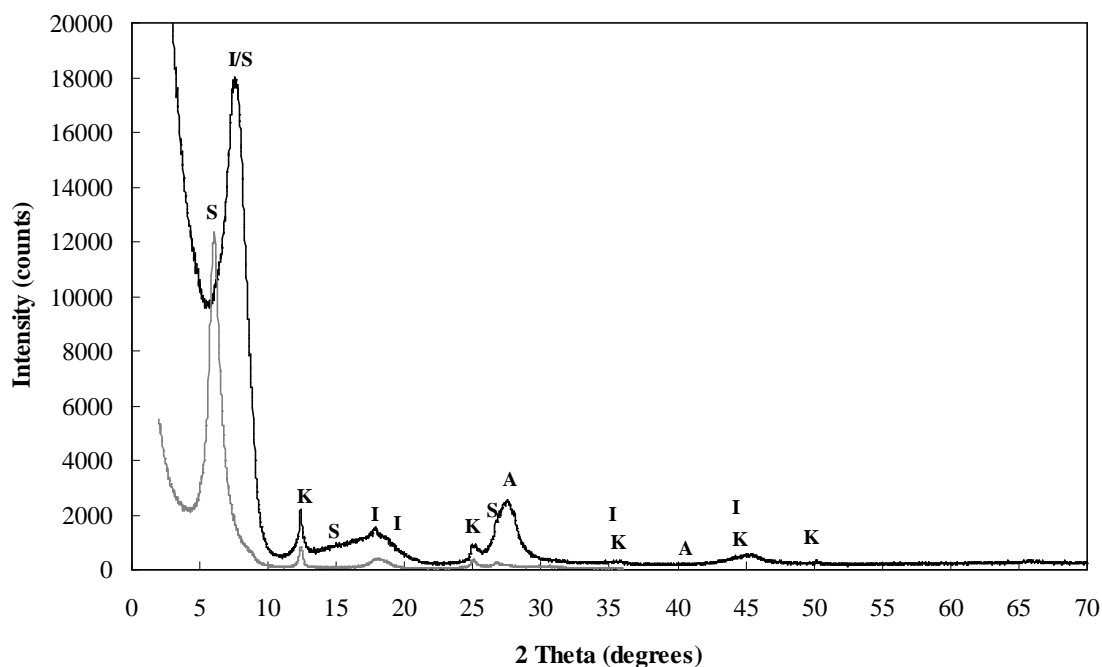


Fig. 1. X-ray diffraction patterns of the clay fraction in Navajo Sandstone before (grey line) and after reaction with CO₂-impregnated brine (black line). Before reaction the clay fraction is mainly composed of smectite (with the (001) reflection between 1.4-1.5 nm) and kaolinite (K, ICDD: 14-164). The clays of the reacted sandstone show an (001) reflection of 1.1-1.2 nm (illite/smectite), suggesting illitization of smectite due to hydrothermal reactions. Kaolinite and allophane were also identified. "I" Illite (ICDD: 29-1496), "A" Allophane (ICDD: 38-499), "I/S" Illite/Smectite.

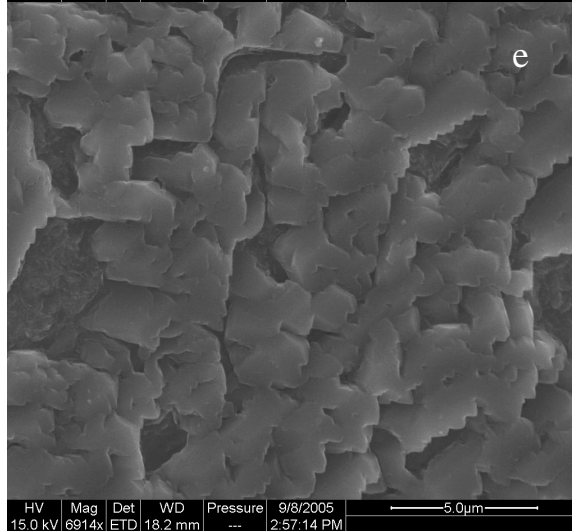
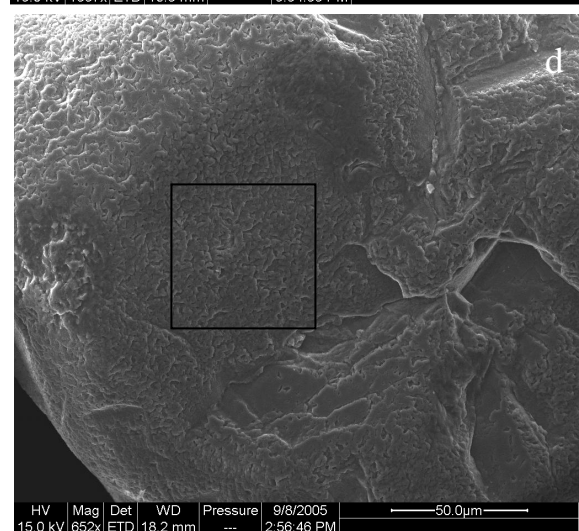
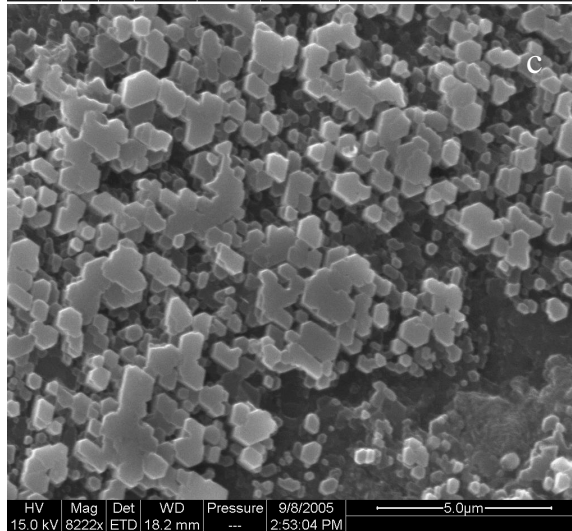
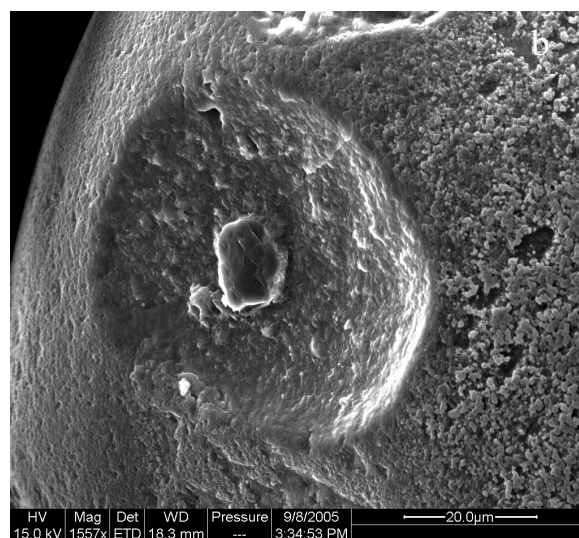
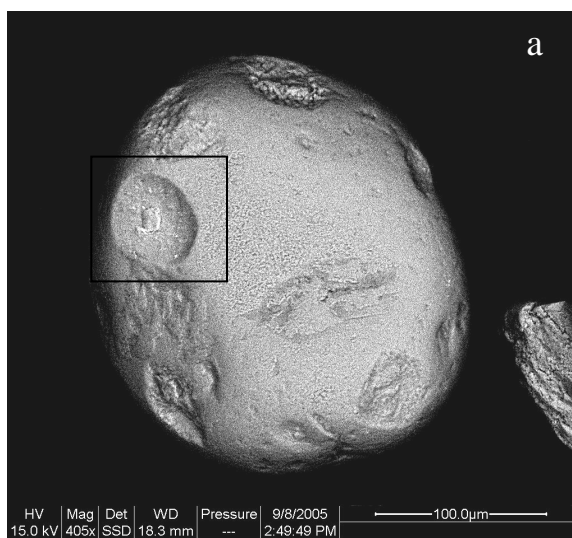
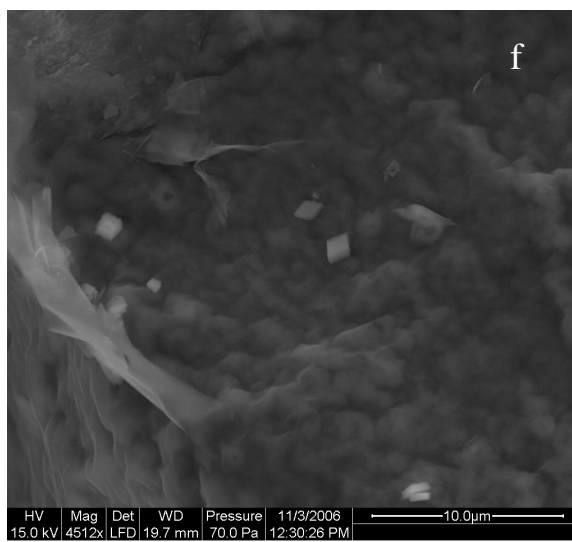
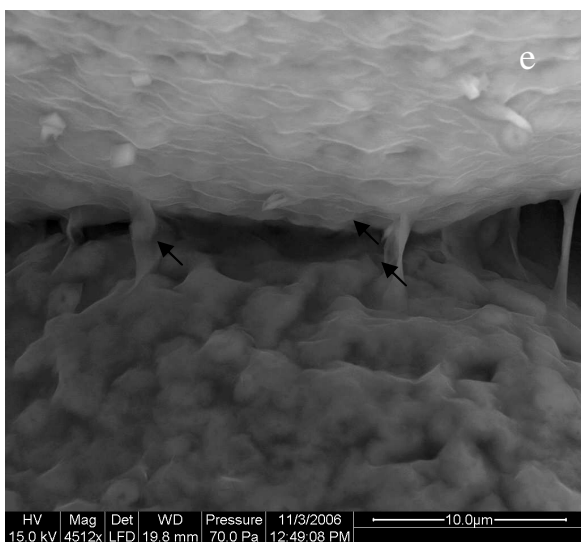
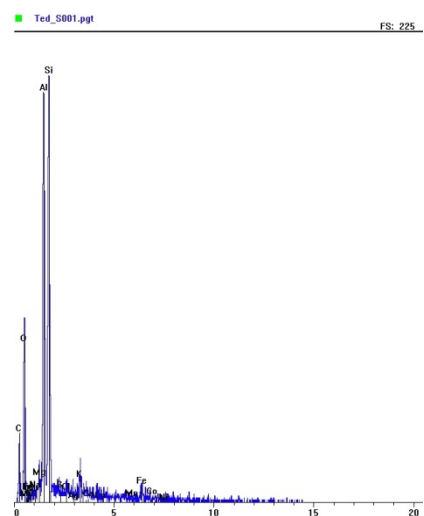
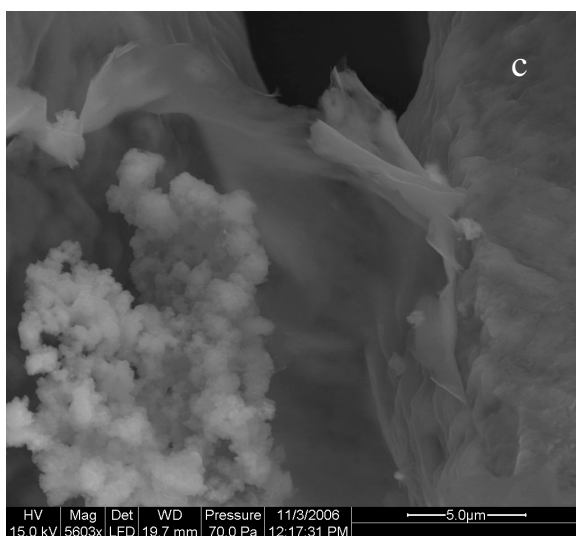
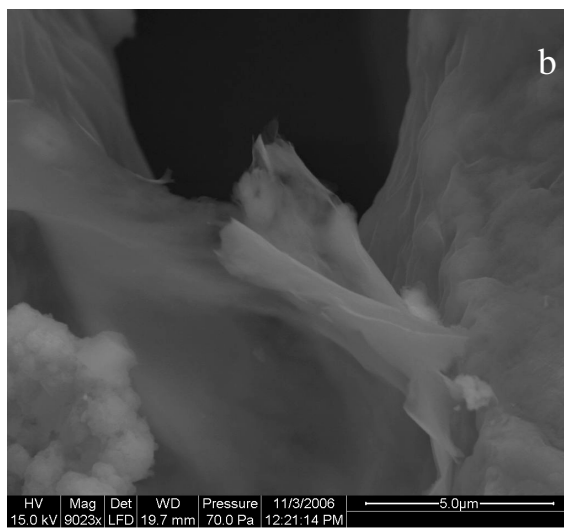
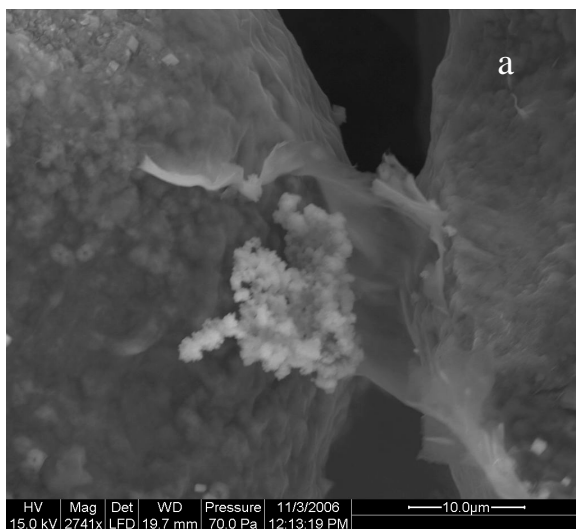


Fig.2. (a) A K-feldspar particle image after ultrasonication with a sonic probe. The K-feldspar is rounded with pitted surface topography. The identification of K-feldspar was confirmed by EDS; (b) Enlargement of one of the etch-pits outlined by the black box in (a), showing dissolution features. A kaolinite coating is visible to the right of the etch-pit; (c) Enlarged view of the kaolinite coating. The kaolinite is euhedral to semi-euhedral hexagonal platelets, with a size of $\sim 0.5 \mu\text{m}$. These platelets are aggregated and well-oriented, but do not form a continuous cover. The basal plane always faces the feldspar surface; (d) A typical quartz particle after the ultrasonication treatment and before the dissolution experiment. The surface of the quartz is coated with incipient quartz overgrowth; (e) High resolution view of an area outlined by the black box in (d), showing incipient quartz overgrowth.



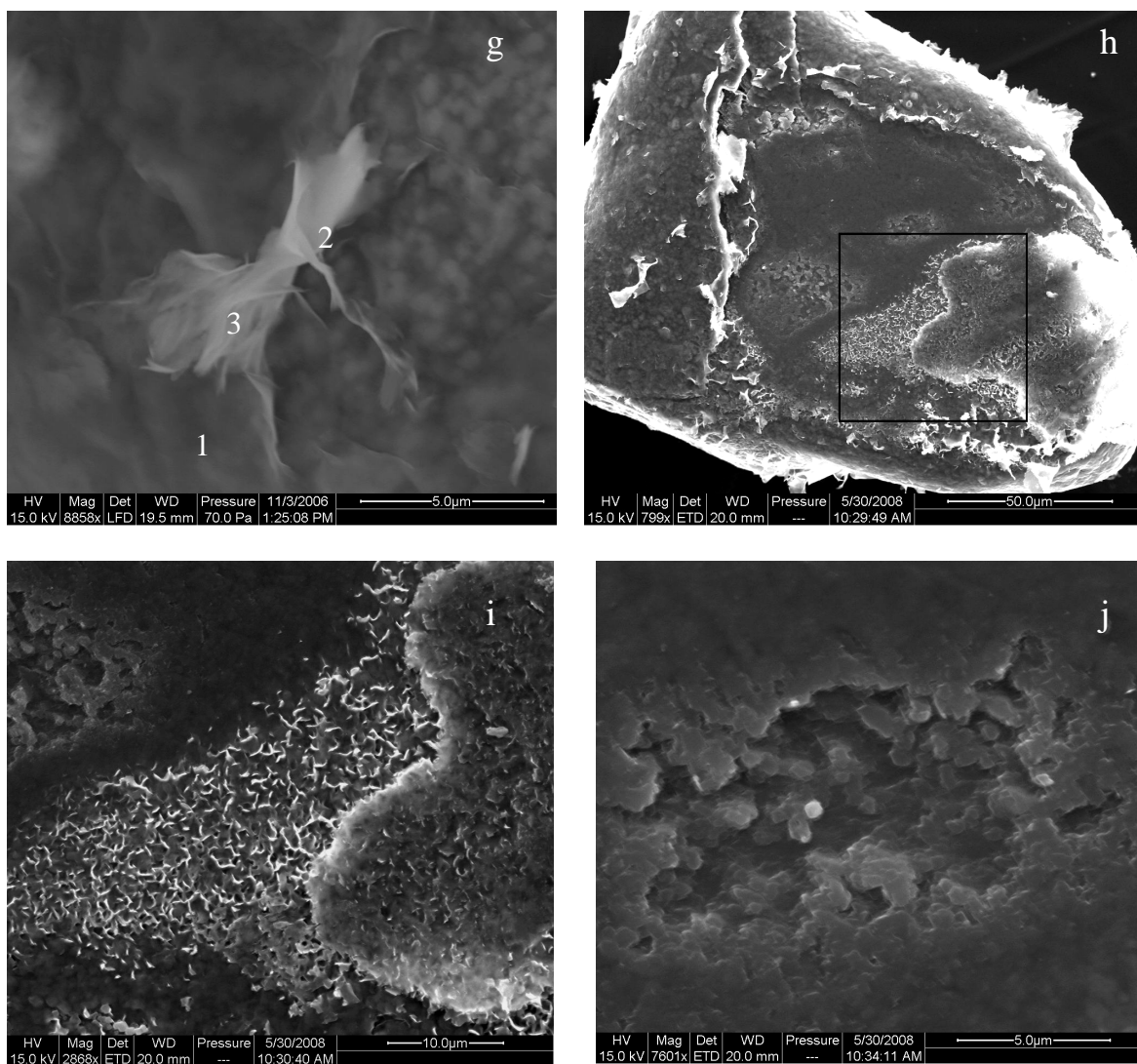


Fig.3. (a) SEM microphotograph shows a ribbon-like secondary mineral bridging two quartz particles and aggregated secondary minerals filling the pore between the quartz particles; (b) Enlarged view of the platy, flaky secondary mineral (approximately 8 μm wide) shown in (a) with slightly scalloped, curled edges. This morphology looks similar to the reference illite shown in Keller et al. (1986). It is likely to be illite/smectite, with the chemical composition close to the illite end member; (c) Enlarged view of the aggregated secondary mineral. Poorly-crystallized allophane partly fills pores. Allophane has not been observed in the sandstone reactant and thus is newly formed; (d) EDS analysis yielding nearly equal peak heights of Si and Al suggests the minerals are probably allophane. The weak signal of C is likely from carbon coating; (e) SEM microphotograph shows the smooth, flaky secondary mineral filling the pore and bridging two quartz particles. Similar morphology of illite/smectite was also shown in Keller et al. (1986), Nadeau (1998), Nadeau et al. (2002), and Celik et al. (1999); (f) SEM microphotograph shows rhombohedra-shaped secondary minerals (indicated by black arrows), approximately 1 μm in size. These minerals are likely to be carbonates. However, it was difficult to confirm with EDS due to their small size. The flaky

secondary mineral (approximately 3 μm wide) to the left is illite/smectite; (g) SEM microphotograph shows secondary minerals on a quartz surface. The smooth, flaky secondary minerals (marked as “1” and “2”) are illite/smectite. The interwoven ribbons feature is a typical morphology of illite (marked as “3”). The length of a single ribbon is about 2 μm . The existence of illite was confirmed by XRD (Figure 1); (h) SEM microphotograph shows a K-feldspar particle after reaction. A massive, webby smectite aggregate covers the right-hand part of the K-feldspar; (i) Enlarged view of an area outlined by the box in (h). Well-developed, highly crenulated smectite formed a thin, webby crust. The webby morphology is a common crystal habit of smectite. The morphology of the webby smectite is similar to that shown in Zhu et al. (2006), but it is much denser; (j) SEM microphotograph shows pore-filling kaolinite on a K-feldspar particle. The kaolinite particles are semi-euhedral platelets. These platelets are aggregated and well-oriented, but do not form a continuous cover. The basal plane always faces the feldspar surface.

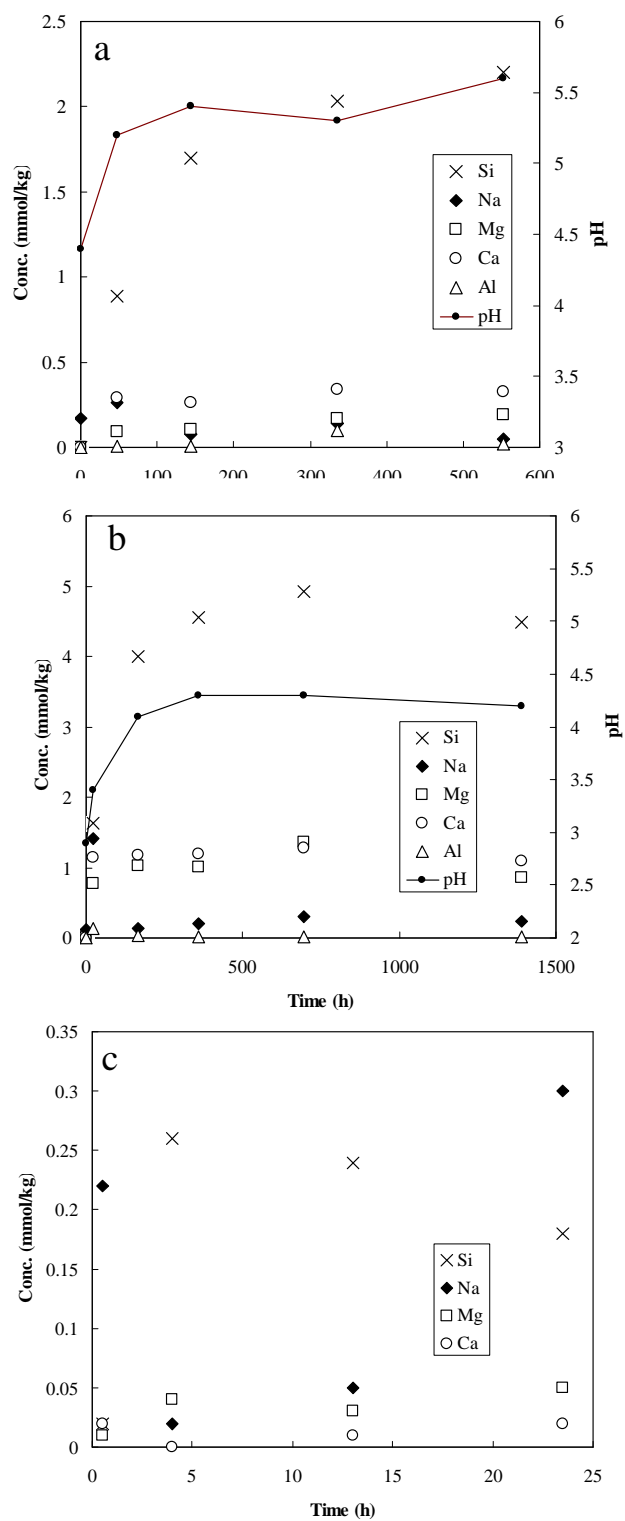


Fig. 4. Variation of Si, Na, Mg, Ca, and Al concentrations as a function of time. (a) Experiment #1; (b) Experiment #2; (c) Experiment #3.

Table 1. Time-dependent changes in the composition of major dissolved species in CO₂-bearing aqueous fluid coexisting with Navajo Sandstone at 200 °C and 30 MPa from Experiment#1. The overall analytical error for dissolved species is $\pm 5\%$.

Sample	Time (h)	K ⁺	SiO ₂	Al ³⁺	Na ⁺	Mg ²⁺	Ca ²⁺	Cl ⁻	SO ₄ ²⁻	CO ₂ (aq)	pH	
					(mmol/kg)						25°C	In-situ*
starting	0	197	-	-	0.17	-	-	201	0.04	20.3	4.1	4.4
#1	48	195	0.89	0.01	0.26	0.09	0.29	193	0.16	19.2	4.7	5.2
#2	144	190	1.70	0.01	0.08	0.11	0.26	198	0.05	19.7	4.8	5.4
#3	336	193	2.03	0.10	0.14	0.17	0.34	192	-	19.5	4.9	5.3
#4	552	200	2.20	0.02	0.05	0.19	0.33	194	0.18	19.6	4.9	5.6

In-situ pH is calculated from distribution of aqueous species calculations at the temperature and pressure of the experiment using constraints imposed by major element concentrations and pH values measured at 25°C.

Table 2. Time-dependent changes in the composition of minor and trace dissolved species in CO₂-bearing aqueous fluid coexisting with Navajo Sandstone at 200 °C and 30 MPa from Experiment#1. The overall analytical error for concentration measurements is $\pm 5\%$.

Sample	Time (h)	Li	Cr	Fe	Mn	Co	Ni	Cu	Zn	Rb	Sr	Cs	Ba
								(ppm)					
Starting	0	-	-	-	-	-	-	0.10	0.24	0.29	0.01	0.01	0.01
#1	48	-	-	1.70	0.09	0.01	-	0.06	0.32	0.27	0.36	0.01	0.22
#2	144	-	-	-	0.08	-	-	0.13	0.20	0.27	0.36	0.01	0.30
#3	336	0.04	0.01	6.63	0.13	0.01	0.25	0.27	0.38	0.43	0.36	0.08	0.25
#4	552	0.05	-	0.67	0.12	-	0.18	0.09	0.17	0.32	0.35	0.02	0.24

The measured fluid chemistry and pH, when considered alongside aqueous speciation distribution, and taking explicit account of mass balance, mass action and charge balance constraints, together with constraints imposed by the revised HKF equation of state (Johnson et al., 1992; Shock, 1995; Shock and Helgeson, 1988; Shock et al., 1989; Shock et al., 1992; Shock et al., 1997), permit calculation of ion activities of dissolved species. Speciation-solubility calculations were facilitated with the geochemical modeling code PHREEQC (Parkhurst and Appello, 1999). Thermodynamic data used in the speciation-solubility calculations are listed in Table 3.

Mineral saturation index (SI) calculations (Table 4) show that the solution was supersaturated with respect to microcline and undersaturated with respect to albite during the entire course of the reaction; the solution changed from undersaturated (144 h) to supersaturated (336 h) back to undersaturated (552 h) with respect to anorthite; the solution was supersaturated with respect to calcite and magnesite and slightly undersaturated with respect to quartz. SI calculations indicate that the formation of carbonate minerals (e.g., calcite and magnesite) was thermodynamically favored. As for the clay minerals, the solution was supersaturated with respect to kaolinite and illite during the entire course of the reaction and changed from undersaturated to supersaturated with respect to beidellite-K (another type of smectite) and montmorillonite-K (a type of smectite) at 144 h and 336 h, respectively.

Table 3. Thermodynamic data used in this report, calculated with the computer code of SUPCRT92 (Johnson et al., 1992).

Aqueous reactions	logK 25°C, 0.1 MPa	logK 200°C, 30 MPa	logK 200°C, 25 MPa	Ref
$\text{H}_2\text{O} = \text{OH}^- + \text{H}^+$	-13.995	-11.163	-11.183	(1)
$\text{H}_2\text{O} + \text{Al}^{+3} = \text{AlOH}^{+2} + \text{H}^+$	-4.964	-1.446	-1.438	(2)
$2\text{H}_2\text{O} + \text{Al}^{+3} = \text{Al}(\text{OH})_2^+ + 2\text{H}^+$	-10.921	-3.630	-3.614	(2)
$3\text{H}_2\text{O} + \text{Al}^{+3} = \text{Al}(\text{OH})_3^0 + 3\text{H}^+$	-17.044	-7.301	-7.281	(2)
$4\text{H}_2\text{O} + \text{Al}^{+3} = \text{Al}(\text{OH})_4^- + 4\text{H}^+$	-22.851	-11.572	-11.557	(2)
$\text{Na}^+ + 4\text{H}_2\text{O} + \text{Al}^{+3} = \text{NaAl}(\text{OH})_4^0 + 4\text{H}^+$	-22.9	-10.748	-10.724	(2)
$\text{SiO}_2 + 2\text{H}_2\text{O} + \text{Al}^{+3} = \text{AlH}_3\text{SiO}_4^{+2} + \text{H}^+$	-2.357	1.86	1.858	(2)
$\text{Na}^+ + \text{H}_2\text{O} = \text{NaOH}^0 + \text{H}^+$	-14.205	-11.087	-11.095	(3)
$\text{Na}^+ + \text{Cl}^- = \text{NaCl}^0$	-0.777	0.019	.031	(4)
$\text{K}^+ + \text{Cl}^- = \text{KCl}^0$		0.456	0.464	(5)
$\text{H}^+ + \text{Cl}^- = \text{HCl}^0$	-0.710	-0.15	-0.15	(6)
$\text{K}^+ + \text{H}_2\text{O} = \text{KOH}^0 + \text{H}^+$	-14.439	-10.939	-10.946	(3)
$\text{Na}^+ + \text{HCO}_3^- = \text{NaHCO}_3$	0.1541	-1.213		(7)
$\text{Na}^+ + \text{HCO}_3^- = \text{NaCO}_3^- + \text{H}^+$	-9.8144	-12.632		(7)
$\text{K}^+ + \text{HCO}_3^- = \text{KHCO}_3$	0.1541	-1.213		(8)
$\text{K}^+ + \text{HCO}_3^- = \text{KCO}_3^- + \text{H}^+$	-9.8144	-12.632		(8)
$\text{Cl}^- + \text{Ca}^{+2} = \text{CaCl}^+$	-0.292	1.146	1.159	(4)
$2\text{Cl}^- + \text{Ca}^{+2} = \text{CaCl}_2^0$	-0.644	0.672	0.700	(4)
$\text{H}_2\text{O} + \text{Ca}^{+2} = \text{CaOH}^+ + \text{H}^+$	-12.833	-7.961	-7.956	(3)
$\text{Ca}^{+2} + \text{HCO}_3^- = \text{CaCO}_3^0 + \text{H}^+$	-7.002	-5.05		(3)
$\text{Ca}^{+2} + \text{HCO}_3^- = \text{Ca}(\text{HCO}_3)^+$	1.047	2.305		(4)
$\text{HCO}_3^- + \text{H}^+ = \text{CO}_2^0 + \text{H}_2\text{O}$	6.345	7.067		(3)
$\text{CO}_3^{-2} + \text{H}^+ = \text{HCO}_3^-$	10.329	10.298		(3)
$\text{NH}_3^0 + \text{H}^+ = \text{NH}_4^+$	9.241	5.825		(3)
$\text{Mg}^{+2} + \text{HCO}_3^- = \text{MgHCO}_3^+$	1.036	2.288		(9)
$\text{Mg}^{+2} + \text{HCO}_3^- = \text{MgCO}_3 + \text{H}^+$	-7.35	-5.92		(4)
$\text{Ca}^{+2} + \text{SO}_4^{-2} = \text{CaSO}_4$	2.111	3.291	3.313	(3)
$\text{Mg}^{+2} + \text{Cl}^- = \text{MgCl}^+$	-0.135	0.911	.924	(4)
$\text{Mg}^{+2} + \text{H}_2\text{O} = \text{Mg}(\text{OH})^+ + \text{H}^+$	-11.682	-7.424	-7.419	(4)
$\text{H}^+ + \text{SO}_4^{-2} = \text{HSO}_4^-$	1.979	4.350	4.369	(4)
$\text{K}^+ + \text{SO}_4^{-2} = \text{KSO}_4^-$	0.88	1.854	1.864	(4)
$\text{K}^+ + \text{HSO}_4^- = \text{KHSO}_4$	-3.474	-1.366	-1.355	(4)
$\text{Mg}^{+2} + \text{SO}_4^{-2} = \text{MgSO}_4$	2.23	3.383	3.408	(4)
$\text{Na}^+ + \text{SO}_4^{-2} = \text{NaSO}_4^-$	0.7	1.666	1.683	(4)
$\text{SiO}_2 + \text{H}_2\text{O} = \text{HSiO}_3^- + \text{H}^+$	-9.585	-8.707	-8.728	(4)
$\text{SiO}_2 + \text{H}_2\text{O} + \text{Na}^+ = \text{NaHSiO}_3^0 + \text{H}^+$	-7.754	-7.767	-7.775	(4)
Mineral reactions				
$\text{KAlSi}_3\text{O}_8 \text{ (microcline)} + 4\text{H}^+ = \text{Al}^{+3} + \text{K}^+ + 2\text{H}_2\text{O} + 3\text{SiO}_2(\text{aq})$	-1.050	-3.923	-3.975	(10)
$\text{NaAlSi}_3\text{O}_8 \text{ (albite)} + 4\text{H}^+ = \text{Al}^{+3} + \text{Na}^+ + 2\text{H}_2\text{O} + 3\text{SiO}_2(\text{aq})$	2.065	-2.508	-2.561	(10)
$\text{CaAl}_2\text{Si}_2\text{O}_8 \text{ (anorthite)} + 8\text{H}^+ = \text{Ca}^{+2} + 2\text{Al}^{+3} + 2\text{SiO}_2(\text{aq}) + 4\text{H}_2\text{O}$	23.68	4.042	3.954	(10)
$\text{AlO}_2\text{H (diaspore)} + 3\text{H}^+ = \text{Al}^{+3} + 2\text{H}_2\text{O}$	7.191	0.02	-0.005	(10)
$\text{AlO}_2\text{H (boehmite)} + 3\text{H}^+ = \text{Al}^{+3} + 2\text{H}_2\text{O}$	7.595	0.242	0.217	(11)
$\text{CaCO}_3 \text{ (calcite)} + \text{H}^+ = \text{Ca}^{+2} + \text{HCO}_3^-$	1.816	-0.438		(10)
$\text{MgCO}_3 \text{ (magnesite)} + \text{H}^+ = \text{Mg}^{+2} + \text{HCO}_3^-$	2.29	-1.066		(10)
$\text{NaAlCO}_3(\text{OH})_2 \text{ (dawsonite)} + 3\text{H}^+ = \text{Al}^{+3} + \text{HCO}_3^- + \text{Na}^+ + 2\text{H}_2\text{O}$	4.3464	-0.4756	-0.4756	(12)
$\text{CaMg}(\text{CO}_3)_2 \text{ (dolomite)} + 2\text{H}^+ = \text{Ca}^{+2} + \text{Mg}^{+2} + 2\text{HCO}_3^-$	3.240	-2.018		(10)
$\text{SiO}_2 \text{ (quartz)} = \text{SiO}_2(\text{aq})$	-4.047	-2.424	-2.431	(10)
$\text{CO}_2(\text{g}) = \text{CO}_2^0$	-1.473	-2.132		(10)
$\text{Al}_2\text{Si}_2\text{O}_5(\text{OH})_4 \text{ (kaolinite)} + 6\text{H}^+ = 2\text{Al}^{+3} + 2\text{SiO}_2(\text{aq}) + 5\text{H}_2\text{O}$	4.501	-5.354	-5.415	(10)
$\text{KAl}_3\text{Si}_3\text{O}_{10}(\text{OH})_2 \text{ (muscovite)} + 10\text{H}^+ = \text{K}^+ + 3\text{Al}^{+3} + 3\text{SiO}_2(\text{aq}) + 6\text{H}_2\text{O}$	11.22	-5.407	-5.506	(10)
$\text{NaAl}_3\text{Si}_3\text{O}_{10}(\text{OH})_2 \text{ (paragonite)} + 10\text{H}^+ = \text{Na}^+ + 3\text{Al}^{+3} + 3\text{SiO}_2(\text{aq}) + 6\text{H}_2\text{O}$	14.397	-3.753	-3.852	(10)
$\text{Al}_2\text{Si}_4\text{O}_{10}(\text{OH})_2 \text{ (pyrophyllite)} + 6\text{H}^+ = 2\text{Al}^{+3} + 4\text{H}_2\text{O} + 4\text{SiO}_2(\text{aq})$	-1.724	-9.733	-9.809	(10)
$\text{K}_{0.6}\text{Mg}_{0.25}\text{Al}_{2.3}\text{Si}_{3.5}\text{O}_{10}(\text{OH})_2 \text{ (illite)} + 8\text{H}^+ = 0.25\text{Mg}^{+2} + 0.6\text{K}^+ + 2.3\text{Al}^{+3} + 3.5\text{SiO}_2(\text{aq}) + 5\text{H}_2\text{O}$	9.0260	-4.6120	-4.6120	(13)
$\text{K}_{0.33}\text{Al}_{2.33}\text{Si}_{3.67}\text{O}_{10}(\text{OH})_2 \text{ (beidellite-K)} + 7.32\text{H}^+ = 0.33\text{K}^+ + 2.33\text{Al}^{+3} + 3.67\text{SiO}_2(\text{aq}) + 4.66\text{H}_2\text{O}$	5.252	-6.559	-6.644	(10)
$\text{K}_{0.33}\text{Mg}_{0.33}\text{Al}_{1.67}\text{Si}_4\text{O}_{10}(\text{OH})_2 \text{ (montmorillonite-K)} + 6\text{H}^+ = 0.33\text{Mg}^{+2} + 0.33\text{K}^+ + 1.67\text{Al}^{+3} + 4\text{H}_2\text{O} + 4\text{SiO}_2(\text{aq})$	2.102	-5.766	-5.839	(10)

(1) Haar et al. (1984); (2) Tagirov and Schott (2001); (3) Shock et al. (1997); (4) Sverjensky et al. (1997); (5) Ho et al., (2000); (6) McCollom and Shock (1997); (7) Wagman et al. (1982), 200 °C, P_{sat} ; (8) Assumed log K as same as Na species; (9) Shock and Koretsky (1995); (10) Holland and Powell (1998); (11)

Hemingway et al. (1991) for boehmite; (12) Robie and Hemingway (1995), 200 °C, P_{sat} ; (13) Wolery (1978), 200 °C, P_{sat} .

Table 4. Saturation indices calculation for experiment #1.

Minerals	48 (h)	144 (h)	336 (h)	552 (h)
Quartz	-0.61	-0.33	-0.25	-0.22
Microcline	0.19	1.04	2.27	1.70
Albite	-4.05	-3.71	-2.24	-3.27
Diaspore	1.13	0.94	2.04	1.05
Boehmite	0.91	0.72	1.82	0.83
Kaolinite	1.58	1.77	4.11	2.21
Muscovite	3.98	4.45	7.87	5.33
Paragonite	-0.51	-0.54	3.12	0.12
Pyrophyllite	-0.10	0.65	3.14	1.31
Calcite	7.78	8.14	8.05	8.62
Anorthite	-1.87	-1.33	0.93	-0.40
Magnesite	7.95	8.45	8.43	9.06
Illite	0.54	1.33	4.06	2.26
Beidellite-K	-0.50	0.15	2.96	0.89
Montmorillonite-K	-1.25	-0.21	1.89	0.69

The calculated SIs discussed above are sensitive to the uncertainties of standard state thermodynamic properties used in the calculations. Zhu and Lu (2009) used different sets of thermodynamic property databases to evaluate the uncertainties on calculated SI values for silicate minerals from the feldspar-water batch experiments. They found a discrepancy of a few SI units. The thermodynamic properties for aluminosilicate minerals used in this study are from Holland and Powell (1998). The calculated SI values are relatively higher than those calculated from other thermodynamic datasets (Zhu and Lu, 2009).

Batch experiment 2: Navajo Sandstone dissolution in acidic brine. The second Navajo Sandstone dissolution experiment is a batch experiment at 200 °C and 30 MPa without the presence of CO₂ (aq). Four g of Navajo Sandstone are reacted with 40 g 200 mmol/kg KCl solution at pH 2.8 (25 °C). The pH values of the CO₂-saturated brines under injection conditions (salinity, temperature, and pressure) are likely in the 2-3 range (Schaefer and McGrail, 2004). Therefore, the lower pH (2.8 at 25 °C) used in this experiment is appropriate to simulate the extent of reactions in the field. Dissolved CO₂ likely acts to acidify the brine and provide a carbon source for carbonate minerals (Brady and Carroll, 1994; Brantley, 2008; Giammar et al., 2005; Knauss et al., 1993; Stephens and Hering, 2004). Considering this, experiment #2 can be regarded as an analog for an aquifer system with substantial CO₂ injection and can be compared with the system of experiment #1 (an analog of an aquifer system with lower injection levels). The comparison of experiment #1 and #2 is shown in Table 5.

The solution chemistry results are presented in Tables 6 and 7 and Fig. 4b. During the experiment, dissolved K⁺ and Cl⁻ concentrations remained relatively constant (Table 5). Dissolved SiO₂ continuously increased, reaching 4.93 mmol/kg at 696 h and then approaching steady-state. The sandstone dissolved much faster in this experiment than in Experiment #1 because the initial pH of experiment #2 (2.8 at 25 °C) is much lower than that of experiment #1 (4.1 at 25 °C). The release of SiO₂ was possibly due both to dissolution of feldspars (albite, plagioclase, and anorthite; see SI calculations below) and to the conversion of smectite to illite. Dissolved Al³⁺ reached a maximum value of 0.14 mmol/kg at 24 h and decreased thereafter. The dissolved concentrations of Mg²⁺ and Ca²⁺ also increased with time (Fig. 4b). pH values increased rapidly with reaction progress

during the first 360 h and remained almost constant during the rest of the experiment (Fig. 4b). Generally, the dissolved concentrations of most minor and trace elements approached steady-state values within the first 24 h (Table 6).

SEM images show that after reaction with acidic brine, the dissolution features are much more intensive than in experiment #1, owing to the lower pH and longer experiment duration (Table 7). Although the surface of K-feldspar grains used as starting material have some rounded and angular pits (Fig. 2a), those observed on K-feldspar after reaction were more numerous and deep (Fig. 5h and 5i), sometimes with dissolution features in the pits (Fig. 5i). The development of dissolution features (pits, steps and channels) shows that the dissolution was heterogeneous (e.g., Fig. 5e-i). The smectite coatings remained, indicating that the chemical reactions did not remove coatings (Fig. 5a). Abundant clay minerals adhered to quartz and K-feldspars after the reaction and stretched across pores and open fractures. The smooth, flaky illite/smectite filled the pore and bridged particles (e.g., Figs. 5c and 5d). Illite, as interwoven ribbons, displayed intergrowth with the smectite (Fig. 5b).

Mineral SI calculations (Table 8) show that the solution was supersaturated with respect to microcline after 24 h (the first sample), and saturation increased greatly from 168 h to the end of the experiment. The solution was undersaturated with respect to albite during the entire course of the reaction; the solution changed from undersaturated (24 h) to slightly supersaturated (168 h) with respect to anorthite; the solution was supersaturated with respect to boehmite, muscovite, paragonite and pyrophyllite; and slightly undersaturated (before 24 h) to supersaturated with respect to quartz (168 h). As

for the clay minerals, the solution was supersaturated with respect to kaolinite, illite, beidellite-K and montmorillonite-K during the entire course of the reaction.

When integrating the solution chemistry data, SI calculations, and SEM observations, it appears that the dissolution features on K-feldspar were associated with dissolution produced before the first sample at 24 h. The starting solution had KCl and HCl, but no Si or Al. Therefore, the starting solution must have been undersaturated with respect to K-feldspar and K-feldspar must have first been dissolved. With accumulation of Si and Al in the solution, K-feldspar became supersaturated later. The solution chemistry data (Table 6) showed a large increase of SiO₂ from ~0.0 mmol/L at 0 h to 1.63 mmol/L at 24 h. The solution chemistry also shows a large increase of SiO₂ from 24 to 168 h. One could argue that the SI value of 0.59 for microcline at 24 h was a calculational artifact as microcline was used as a proxy for K-feldspar in modeling (no thermodynamic data are available for K-feldspar in the Holland and Powell database). The 0.59 SI value could also be an artifact of the uncertainties of thermodynamic properties discussed earlier in this paper and in Zhu and Lu (2009).

Table 5. Comparison of batch experiments (#1 and #2)

Experiments	Conditions	Solution chemistry	Morphology
# 1	200 °C, 30 MPa, pH 4.1 (at 25 °C), 0.2 mol/kg KCl, 0.02 mol/kg CO ₂ (aq), duration 552 h	Si: 0-2.2 mmol/kg. pH (in-situ): 4.4-5.6. CO ₂ (aq): 20.3-19.6 mmol/kg.	Dissolution features not evident; abundant clay minerals (e.g., pore-filing allophane, flaky illite/semctite); illitization of semectite; small amount of carbonate minerals under SEM
# 2	200 °C, 30 MPa, pH 2.8 (at 25 °C), 0.2 mol/kg KCl, duration 1392 h	Si: 0-4.49 mmol/kg. pH (in-situ): 2.9-4.2.	Intensive dissolution features (e.g. etch pits on K- feldspar); clay minerals (e.g., flaky illite/semctite); illitization of semectite; no carbonate minerals observed.

Table 6. Time-dependent changes in the composition of major dissolved species in aqueous fluid coexisting with Navajo Sandstone at 200 °C and 30 MPa from Experiment#2. The overall analytical error for dissolved species is $\pm 5\%$.

Sample	Time	K ⁺	SiO ₂	Al ⁺³	Na ⁺	Mg ²⁺	Ca ²⁺	Cl ⁻	pH	
	(h)								25 °C	In-situ*
starting	0	204	-	-	0.11	-	-	188	2.8	2.9
#1	24	197	1.63	0.14	1.42	0.77	1.15	185	3.6	3.4
#2	168	200	4.00	0.03	0.14	1.03	1.17	183	4.6	4.1
#3	360	193	4.55	0.02	0.21	1.01	1.20	202	4.9	4.3
#4	696	209	4.93	0.02	0.30	1.36	1.28	201	5.0	4.3
#5	1392	199	4.49	0.02	0.24	0.86	1.09	199	5.1	4.2

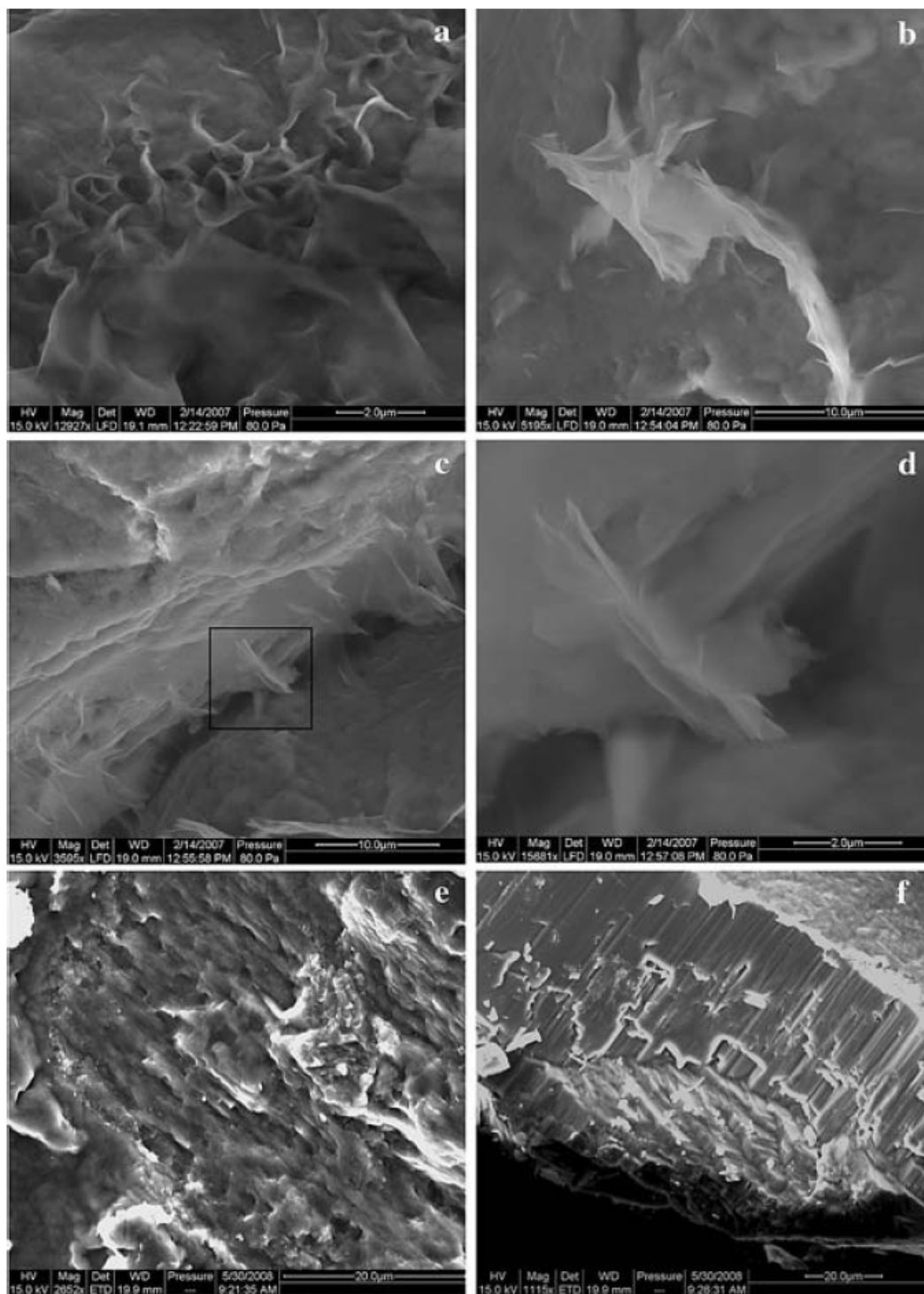
*In-situ pH is calculated from distribution of aqueous species calculations at the temperature and pressure of the experiment using constraints imposed by major element concentrations and pH values measured at 25°C.

Table 7. Time-dependent changes in the composition of minor and trace dissolved species in aqueous fluid coexisting with Navajo Sandstone at 200 °C and 30 MPa from Experiment#2. The overall analytical error for concentration measurements is $\pm 5\%$.

Sample	Li	Cr	Fe	Mn	Co	Ni	Cu	Zn	Rb	Sr	Cs	Ba
	(ppm)											
Starting	-	-	-	-	-	-	-	0.04	0.12	0.01	0.01	0.04
#1	-	-	1.57	0.94	-	-	6.07	0.52	0.12	0.54	0.01	0.41
#2	-	-	0.10	0.75	-	0.09	0.10	0.20	0.13	0.54	0.01	0.30
#3	0.10	-	0.12	0.37	0.02	0.21	0.14	0.06	0.14	0.53	0.01	0.30
#4	-	-	0.34	0.28	-	-	0.11	0.05	0.18	0.56	0.02	0.45
#5	0.24	-	0.27	0.28	-	-	0.2	0.32	0.15	0.55	0.01	0.35

Table 8. Saturation indices calculation for experiment #2.

Minerals	24 (h)	168 (h)	360 (h)	696 (h)	1392 (h)
Quartz	-0.36	0.04	0.10	0.14	0.09
Microcline	0.59	2.24	2.38	2.51	2.30
Albite	-2.92	-2.29	-1.96	-1.70	-1.99
Diaspore	2.57	2.30	2.09	2.09	2.12
Boehmite	2.35	2.08	1.87	1.87	1.89
Kaolinite	4.97	5.24	4.92	4.99	4.96
Muscovite	7.25	8.37	8.08	8.21	8.05
Paragonite	3.50	3.60	3.51	3.76	3.53
Pyrophyllite	3.78	4.86	4.65	4.79	4.68
Anorthite	-1.49	0.18	0.29	0.36	0.08
Illite	2.99	4.59	4.50	4.67	4.42
Beidellite-K	3.18	4.27	4.04	4.17	4.05
Montmorillonite-K	0.69	2.59	2.65	2.83	2.55



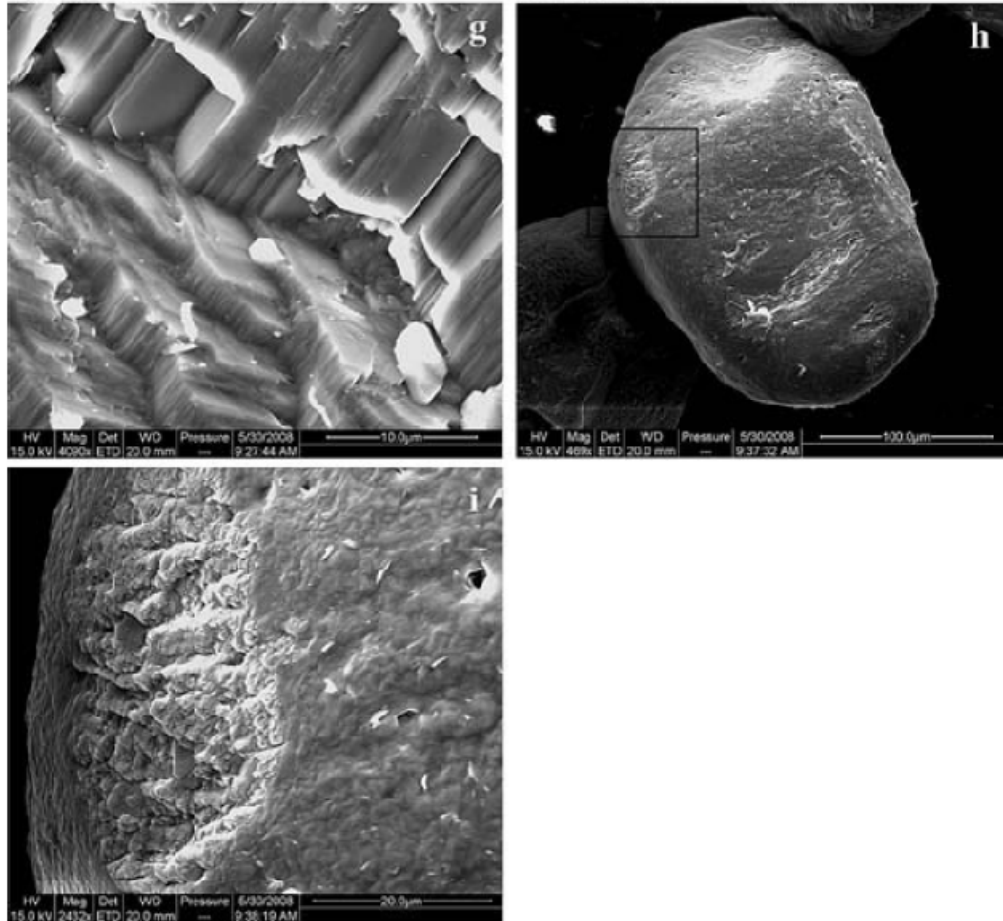


Fig. 5. (a) SEM microphotograph shows secondary minerals on a quartz surface after experiment #2. The cornflake-shaped smectites at the upper part have a similar morphology to those in Zhu et al. (2006). These smectites possibly existed before the dissolution experiment. However, the smooth, flaky illite/smectite at the lower part is much larger and is possibly formed during the dissolution experiment. (b) SEM microphotograph shows secondary minerals on another quartz surface. The secondary minerals are likely to be illite (ribbons) intergrown with smectite, which suggests the progressive illitization of smectite; (c) SEM microphotograph shows secondary minerals (illite/smectite) filling the pore and bridging two quartz particles. Some smooth, flaky illite/smectite minerals are visible (indicated by arrows). These minerals are also likely to be newly formed; (d) Enlarged view of an area outlined by the black box in (c), showing one of the particle-bridging secondary minerals. The smooth, flaky mineral (~5 μm) is illite/smectite; (e) SEM microphotograph shows dissolution features on a K-feldspar particle; (f) SEM microphotograph shows dissolution features on a K-feldspar particle; (g) Close-up of dissolution features on the K-feldspar particle showed in (f). The feldspar has angular and prismatic features at the micron scale. Dissolution steps are visible along the c-axis of the cleavages and dissolution channels along the b-axis of the cleavages; (h) SEM microphotograph shows the surface morphology of a K-feldspar particle after reaction; (i) Enlarged view of an area outlined by the black box in Fig. 5h, showing an etch pit.

Mixed flow experiment: Navajo Sandstone dissolution in acidic brine. The third Navajo Sandstone dissolution experiment was a mixed flow experiment at 200 °C and 25 MPa. Five g of Navajo Sandstone were reacted with 200 mmol/kg KCl fluid. The KCl fluid was acidified to pH 3.9 before the experiment at ambient temperature and pressure by addition of dilute HCl. The rate of fluid input was kept at 0.82 ml/min for the whole experiment of 23.5 h. The results are presented in Table 9. During the experiment, dissolved K^+ and Cl^- concentrations remained relatively constant (Table 9 and Fig. 4c). The dissolved concentrations of Si and Mg approached steady-state values within the first 4 h (Fig. 4c). pH values remained essentially the same with reaction progress (Fig. 4c).

SEM images show that after dissolution in a flow-through reactor, the dissolution features were less intensive than those in experiment #1 and #2. The K-feldspar grains partially preserved the “three layer onion” structure of unreacted sandstones (see Fig. 6). Newly formed smectite/illite, observed in the products of experiment #1 and #2 are also found (e.g., Figs. 6b, 6c, 6e, and 6f).

The Al concentrations are under the detection limit. Saturation states for aluminosilicates are thus unknown. The solution is also undersaturated with respect to quartz (Table 10).

Dissolution rates of Navajo Sandstone per mole of Si were calculated according to the following formula based on time-series Si concentrations:

$$r = \frac{(C_{out})(\vartheta_0)(10^{-6})}{\delta A}$$

where C_{out} is the output concentration of Si in mg/L, ϑ_0 is the input flow rate in ml/s, δ is the stoichiometric coefficient of Si (set to 1), and A is the total surface area in m^2 . The average dissolution rate is $6.85 \times 10^{-10} \text{ mol } m^{-2} s^{-1}$ as per mole of Si (Table 11).

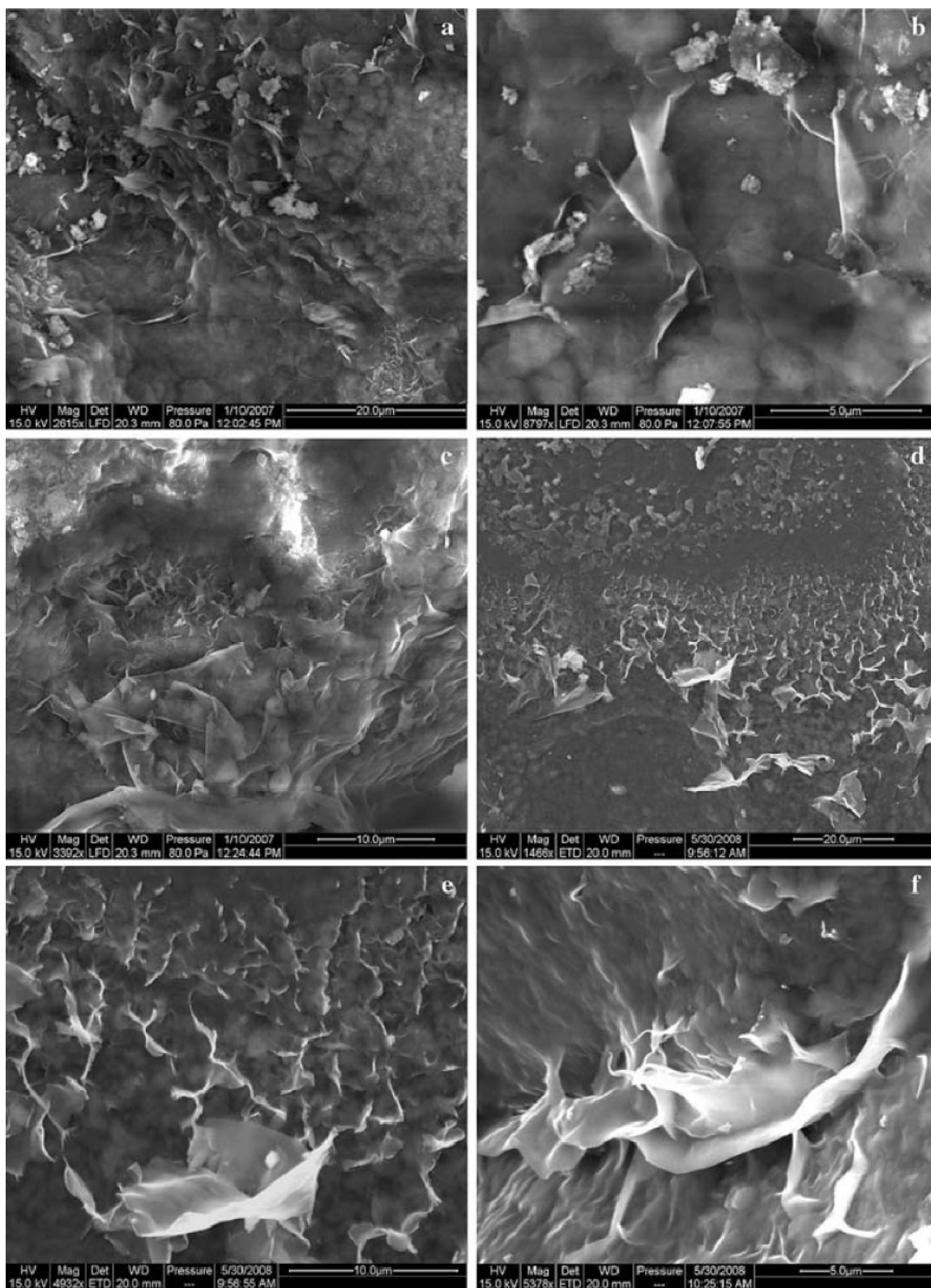


Fig. 6. (a) SEM microphotograph shows the quartz surface after reaction. Secondary minerals (possibly illite) are visible; (b) Enlarged view of upper right corner of (a). The large smooth, flaky smectite/illite is possibly formed during the dissolution experiment; (c) SEM microphotograph shows the quartz surface after the hydrothermal experiment. Similar to Fig. 4a, the corn-flake-shaped smectites in the upper part have a similar morphology to those in Zhu et al. (2006). These smectites possibly existed before the hydrothermal reaction. However, the smooth, flaky smectite/illite at the lower part is much larger than authigenic smectite in the center of the image and possibly formed during the dissolution experiment; (d) SEM microphotograph shows the “three layer onion” described in Zhu et al. (2006). The grain is K-feldspar, coated with a layer of kaolinite. Smectite in turn covers kaolinite; (e) Close-up of the smectite shown in (d). The smooth, flaky, slightly crenulated smectite/illite at the lower part is much larger than authigenic smectite shown in this image and is possibly formed during the dissolution experiment; (f) The smooth, flaky illite/smectite with scalloped, curled edges is much larger than the authigenic smectite shown in this image and is possibly formed during the dissolution experiment.

Table 9. Time-dependent changes in the composition of major dissolved species in aqueous fluid coexisting with Navajo sandstone at 200 °C and 25 MPa from Experiment#3. The overall analytical error for dissolved species is $\pm 5\%$.

Sample	Time (h)	K ⁺	SiO ₂	Al ³⁺	Na ⁺	Mg ²⁺	Ca ²⁺	Cl ⁻	pH 25°C In-situ*	
					(mmol/kg)					
#1	0.5	196	0.02	-	0.22	0.01	0.02	201	5.2	5.2
#2	4	209	0.26	-	0.02	0.04	-	199	5.3	5.2
#3	13	207	0.24	-	0.05	0.03	0.01	197	5.3	5.2
#4	23.5	205	0.18	-	0.30	0.05	0.02	197	5.5	5.3

*In-situ pH is calculated from distribution of aqueous species calculations at the temperature and pressure of the experiment using constraints imposed by major element concentrations and pH values measured at 25 °C.

Table 10. Saturation indices calculation for experiment #3.

Minerals	0.5 (h)	4 (h)	13 (h)	23.5 (h)
Quartz	-2.25	-1.14	-1.17	-1.30

Table 11. Dissolution rates of Navajo Sandstone in the experiment with mixed flow reactor at 200 °C and 25 MPa. The total surface area of 5 gram Navajo sandstone is assumed to be 3.5 m². The input flow rate is 0.82 ml/min.

Sample	Dissolution Rate (mol m ⁻² s ⁻¹)*
#1	7.81×10 ⁻¹¹
#2	1.02×10 ⁻⁹
#3	9.37×10 ⁻¹⁰
#4	7.03×10 ⁻¹⁰
Average	6.85×10 ⁻¹⁰

* As per mole of Si

Fate of CO₂ and sandstone responses to CO₂ injection. In experiment #1, the CO₂ is mainly trapped in aqueous solution as carbonate species. Carbonate mineral precipitation is observed with SEM, and supported by calculated SI values, but the amount precipitated is small judging from the decrease of CO₂ in solution chemistry data and absence of CO₂ indicators in XRD patterns. This result is consistent with the modeling results of Perry et al. (2007), which suggests that CO₂ is trapped mainly by solubility and that storage as free CO₂ in pore space for Navajo Sandstone and mineral trapping is not significant. Gilfillan et al. (2009) studied nine natural gas fields in North America, China and Europe, using noble gas and carbon isotope tracers. They found solubility trapping in formation water is the dominant CO₂ sink in natural gas fields.

The dissolution of silicates is likely to increase porosity, but permeability is probably inversely affected by the formation of clay minerals in pore throats. Open, interconnected pores lined with ribbons of illite/smectite, coating grain surfaces and bridging the pores between grains will create permeability barriers to fluid flow (e.g., Figs. 3a, 3b, 3c, 3e, 5c, 5d, and 6f). Neasham (1977) demonstrated that this clay texture severely reduces permeability without significantly affecting porosity. The potential

reduction in reservoir permeability due to the introduction of clay fines in near well-bore region is a serious concern in the oil industry and can lead to a significant decline in productivity (Emery and Robinson, 1993; McDowell-Boyer et al., 1986; Poesio and Ooms, 2007).

Changes in ionic strength (salinity, pH, etc) may modify the balance between the forces at the particle-grain interface and result in particle detachment (Cerdeña, 1987; Khilar and Fogler, 1998; Kretzschmar et al., 1999; Vaidya and Fogler, 1990). This phenomenon is called “water sensitivity” and the resulting decrease in hydraulic conductivity is called “formation damage” (Baudracco, 1990; Khilar and Fogler, 1984; Khilar et al., 1983; Kia et al., 1987; Mohan et al., 1999; Ochi and Vernoux, 1998; Vaidya and Fogler, 1990). During geological carbon sequestration, the injection of CO₂ may cause abrupt changes in solution chemistry (pH decrease and carbonation), possibly resulting in the detachment of clay coatings. However, in this study, there is no evidence of clay coating detachment due to the addition of CO₂.

Clay fines may also be released by mechanical force (agitation, hydrodynamic, high pressure, etc.). Once released the particles can either redeposit on the matrix, be transported with flow, or get entrapped at pore constrictions, clogging pore throats (Blume et al., 2002). During CO₂ injection, the highly pressurized CO₂ will increase the fluid velocity significantly near the well-bore region. Ramachandran and Fogler (1999) found that with increasing fluid velocity, the rate of particle-bridge formation increases. Zhu et al. (2006) and this study found that the smectite coating in the Navajo Sandstone is easily removed by sonification in the laboratory. Based on these findings, some clay minerals are suspected to be mobile in the Navajo Sandstone. In addition, the newly

formed allophane is loosely aggregated (Fig. 3a and 3c). It is uncertain whether mechanical forces near the injection well would mobilize the smectite and allophane and cause pore clogging. A study by Beresnev and Johnson (1994) indicates that ultrasonic irradiation of the near well-bore region can have a negative effect on the permeability. Thus, the mobility of smectite and allophane is an important concern for injection operations.

4. CONCLUSIONS

The experimental system in this paper mimics long term CO₂ interaction with a sandstone aquifer. CO₂ injection into deep saline aquifers in sedimentary basins represents a huge potential for both CO₂ storage and sequestration. The large volume of pore space available and long-term hydrodynamic trapping of CO₂ (Bachu et al., 1994) are optimal conditions for storage; with the formation of carbonate minerals (Kaszuba et al., 2003; 2005), the CO₂ will be permanently trapped in the subsurface (Hitchon et al., 1999). However, water-rock interactions bring uncertainty to this potential option as they may either enhance (increase the porosity/permeability) or reduce (decrease the permeability and injectivity) the potential of the reservoir by the dissolution of primary minerals, precipitation of secondary clay, and progressive evolution of clay. The following conclusion can be made:

(1) Our experimental data show that the Navajo Sandstone will react strongly with CO₂-impregnated brine during CO₂ injection and storage. The lower the pH, the more severe the reactions are in our experiments, regardless the CO₂ concentrations. Thus, dissolved CO₂ likely acts to acidify the brine and provide a carbon source for carbonate

minerals. With respect to CO₂ solubility, the extent of reactions in the field would likely resemble our experiment with the most acidic brine (Experiment #2). Although our experiments were conducted at a higher temperature than that in some field injection projects in order to expedite observable changes in the laboratory (Gunter et al., 1997), the longer time frame that CO₂-impregnated brine interacts with sandstone in the actual injection case justifies the conclusions that the reactions will be significant and possibly affect injectivity.

(2) Increase of dissolved SiO₂ and gradual increase of pH indicate that silicate mineral dissolutions are dominant reactions. Another likely source of SiO₂ release is the conversion of smectite to illite.

(3) The observed progressive illitization of smectite minerals in our experiments was due to the high temperatures of our experiments (200 °C) and high K⁺ concentrations, and will likely not occur in CO₂ injection projects because of much lower temperatures in the reservoirs (e.g., 100 °C). KCl may result in faster plagioclase dissolution and slower K-feldspar dissolution than the use of NaCl. However, the observed allophane precipitation in our experiments can occur at the reservoir temperatures. SEM images show that newly formed, aggregated, allophane-like phases fill the pores, which is a concern for injection operations.

(4) The chemical reactions likely increase the porosity of the sandstone due to silicate dissolution. However, permeability might be reduced by the precipitation of pore-filling allophane. The smectite coatings remain on the sediment grains after the experiments, indicating that chemical reactions did not remove coatings. It is uncertain whether the mechanical forces near the injection well would mobilize the smectite and

allophane and cause pore clogging. This mobility of smectite and allophane is an important concern for injection operations.

(5) Trace amounts of toxic metals (e.g., Cu, Zn, and Ba) are mobilized, but at low concentrations.

REFERENCES

- Bachu, S., Gunter, W.D. and Perkins, E.H., 1994. Aquifer Disposal of CO₂ - Hydrodynamic and Mineral Trapping. *Energ. Convers. Manage.*, **35**(4): 269-279.
- Baudracco, J., 1990. Variations in permeability and fine particle migrations in unconsolidated sandstones. *Geothermics*, **19**(2): 213-221.
- Bauluz, B., Peacor, D.R. and Ylagan, R.F., 2002. Transmission electron microscopy study of smectite illitization during hydrothermal alteration of a rhyolitic hyaloclastite from Ponza, Italy. *Clay. Clay. Miner.*, **50**(2): 157-173.
- Beresnev, I.A. and Johnson, P.A., 1994. Elastic-wave stimulation of oil production : a review of methods and results. *Geophysics*, **59**(6): 1000-1017.
- Blume, T., Weisbrod, N. and Selker, J.S., 2002. Permeability changes in layered sediments: impact of particle release. *Ground Water*, **40**(5): 466-474.
- Brady, P.V. and Carroll, S.A., 1994. Direct Effects of CO₂ and Temperature on Silicate Weathering - Possible Implications for Climate Control. *Geochim. Cosmochim. Acta*, **58**(7): 1853-1856.
- Brantley, S.L., 2008. Kinetics of Mineral Dissolution. In: S.L. Brantley, J.D. Kubicki and A.F. White (Editors), *Kinetics of Water-Rock Interaction*. Springer, New York, pp. 151-196.
- Celik, M., Karakaya, N. and Temel, A., 1999. Clay minerals in hydrothermally altered volcanic rocks, Eastern Pontides, Turkey. *Clay. Clay. Miner.*, **47**(6): 708-717.
- Cerda, C.M., 1987. Mobilization of kaolinite fines in porous-media. *Colloid. Surface.*, **27**(1-3): 219-241.
- Crowley, T.J., 2000. Causes of climate change over the past 1000 years. *Science*, **289**(5477): 270-277.
- Cuadros, J. and Linares, J., 1996. Experimental kinetic study of the smectite-to-illite transformation. *Geochim. Cosmochim. Acta*, **60**(3): 439-453.

- DOE, 2007. *Carbon Sequestration Atlas of the United States and Canada*, National Energy Technology Laboratory, U.S. Department of Energy.
- Dulaney, A.R., 1989. *The geochemistry of the N-aquifer system, Navajo and Hopi Indian Reservations, Northeastern Arizona*. Master thesis, 209p Thesis, Northern Arizona University, Flagstaff, Arizona.
- Emery, D. and Robinson, A.D., 1993. *Inorganic Geochemistry: Application to Petroleum Geology*. Blackwell Scientific Publication.
- Gale, J., 2002. *Overview of CO₂ emission sources, potential, transport and geographical distribution of storage possibilities.*, Intergovernmental Panel on Climate Change, Working Group III: Mitigation of Climate Change, Workshop on Carbon Dioxide Capture and Storage, Regina, Canada, pp.15-30.
- Giammar, D.E., Bruant, R.G.J. and Peters, C.A., 2005. Forsterite dissolution and magnesite precipitation at conditions relevant for deep saline aquifer storage and sequestration of carbon dioxide. *Chem. Geol.*, **217**: 257-276.
- Gilfillan, S.M.V. et al., 2009. Solubility trapping in formation water as dominant CO₂ sink in natural gas fields. *Nature*, **458**(7238): 614-618.
- Gunter, W.D., Perkins, E.H. and Hutcheon, I., 2000. Aquifer disposal of acid gases: modeling of water-rock reactions for trapping of acid wastes. *Appl. Geochem.*, **15**(8): 1085-1095.
- Gunter, W.D., Wiwchar, B. and Perkins, E.H., 1997. Aquifer disposal of CO₂-rich greenhouse gases: extension of the time scale of experiment for CO₂-sequestering reactions by geochemical modeling. *Miner. Petrol.*, **59**: 121-140.
- Haar, L., Gallagher, J.S. and Kell, G.S., 1984. *NBS/NRC Steam Tables: Thermodynamic and Transport Properties and Computer Programs for Vapor and Liquid States of Water in SI Units*. Hemisphere Publishing Corporation, New York, 320p.
- Harshbarger, J.W., Repenning, C.A. and Irwin, J.H., 1957. *Stratigraphy of the Uppermost Triassic and the Jurassic Rocks of the Navajo Country*. U.S. Geological Survey Professional Paper 291, 71p, 71 pp.
- Hemingway, B.S., Robie, R.A. and Apps, J.A., 1991. Revised values for the thermodynamic properties of boehmite, AlO(OH), and related species and phases in the system Al-H-O. *Am. Mineral.*, **76**(3-4): 445-457.
- Hitchon, B., Gunter, W.D., Gentzis, T. and Bailey, R.T., 1999. Sedimentary basins and greenhouse gases: a serendipitous association. *Energ. Convers. Manage.*, **40**(8): 825-843.

- Ho, P.C., Bianchi, H., Palmer, D.A. and Wood, R.H., 2000. Conductivity of dilute aqueous electrolyte solutions at high temperatures and pressures using a flow cell. *J. Solution Chem.*, **29**(3): 217-235.
- Holland, T.J.B. and Powell, R., 1998. An internally consistent thermodynamic data set for phases of petrological interest. *J. Metamorph. Geol.*, **16**: 309-343.
- Hower, J., Eslinger, E.V., Hower, M.E. and Perry, E.A., 1976. Mechanism of burial metamorphism of argillaceous sediments: Mineralogical and chemical evidence. *Geol. Soc. Am. Bull.*, **87**: 725 -737.
- Johnson, J.W., Oelkers, E.H. and Helgeson, H.C., 1992. SUPCRT92 - A software package for calculating the standard molal thermodynamic properties of minerals, gases, aqueous species, and reactions from 1-bar to 5000-bar and 0°C to 1000°C. *Comput. Geosci.*, **18**(7): 899-947.
- Kaszuba, J.P., Janecky, D.R. and Snow, M.G., 2003. Carbon dioxide reaction processes in a model brine aquifer at 200o C and 200 bars: implications for geologic sequestration of carbon. *Appl. Geochem.*, **18**(7): 1065-1080.
- Kaszuba, J.P., Janecky, D.R. and Snow, M.G., 2005. Experimental evaluation of mixed fluid reactions between supercritical carbon dioxide and NaCl brine: Relevance to the integrity of a geologic carbon repository. *Chem. Geol.*, **217**(3-4): 277-293.
- Keller, W.D., Reynolds, R.C. and Inoue, A., 1986. Morphology of clay minerals in the smectite-to-illite conversion series by scanning electron microscopy. *Clay. Clay. Miner.*, **34**(2): 187-197.
- Khilar, K.C. and Fogler, H.S., 1984. The existence of a critical salt concentration for particle release. *J. Colloid. Interf. Sci.*, **10**(1): 214-224.
- Khilar, K.C. and Fogler, H.S., 1998. *Theory and Applications of Transport in Porous Media, Volumn 12: Migration of Fines in Porous Media*, Dordrecht: Kluwer Academic Publishers.
- Khilar, K.C., Fogler, H.S. and Ahluwalia, J.S., 1983. Sandstone water sensitivity: Existence of a critical rate of salinity decrease for particle capture. *Chem. Eng. Sci.*, **38**(5): 789-800.
- Kia, S.F., Fogler, H.S. and Reed, M.G., 1987. Effect of pH on colloiddally induced fines migration. *J. Colloid. Interf. Sci.*, **118**(1): 158-168.
- Knauss, K.G., Nguyen, S.N. and Weed, H.C., 1993. Diopside dissolution kinetics as a function of pH, CO₂, temperature, and time. *Geochim. Cosmochim. Acta*, **57**(2): 285-294.

- Kretzschmar, R., Borkovec, M., Grolimund, D. and Elimelech, M., 1999. Mobile subsurface colloids and their role in contaminant transport. *Adv. Agron.*, **66**: 121-193.
- Loope, D.B. and Rowe, C.M., 2003. Long-Lived Pluvial Episodes during Deposition of the Navajo Sandstone. *J. Geol.*, **111**: 223–232.
- McCollom, T.M. and Shock, E.L., 1997. Geochemical constraints on chemolithoautotrophic metabolism by microorganisms in seafloor hydrothermal systems. *Geochim. Cosmochim. Acta*, **61**(20): 4375-4391.
- McDowell-Boyer, L.M., Hunt, J.R. and Sitar, N., 1986. Particle Transport Through Porous Media. *Water Resour. Res.*, **22**(13): 1901–1921.
- Mohan, K.K., Reed, M.G. and Fogler, H.S., 1999. Formation damage in smectitic sandstones by high ionic strength brines. *Colloid. Surfaces A*, **154**(3): 249-257
- Nadeau, P.H., 1998. An experimental study of the effects of diagenetic clay minerals on reservoir sands. *Clay. Clay. Miner.*, **46**(1): 18-26.
- Nadeau, P.H., Peacor, D.R., Yan, J. and Hillier, S., 2002. I-S precipitation in pore space as the cause of geopressuring in Mesozoic mudstones, Egersund Basin, Norwegian Continental Shelf. *Am. Mineral.*, **87**(11-12): 1580-1589.
- Neasham, J.W., 1977. Applications of scanning electron microscopy to the characterization of hydrocarbon-bearing rocks, v. 1, 1-8. In: R.P. Becker (Editor), *Scanning Electron Microscopy, Proceedings of the 10th Annual SEM Symposium*, Chicago, pp. 1-8.
- Ochi, J. and Vernoux, J.-F., 1998. Permeability decrease in sandstone reservoirs by fluid injection: Hydrodynamic and chemical effects. *J. Hydrol.*, **208**(3-4): 237-248
- Parkhurst, D.L. and Appello, A.A.J., 1999. *User's guide to PHREEQC (version 2)-a computer program for speciation, batch-reaction, one dimensional transport, and inverse geochemical modeling*. 99-4259, U.S. Geological Survey.
- Parry, W.T., Forster, C.B., Evans, J.P., Bowen, B.B. and Chan, M.A., 2007. Geochemistry of CO₂ sequestration in the Jurassic Navajo Sandstone, Colorado Plateau, Utah. *Environ. Geosci.*, **14**(2): 91-109.
- Perkins, E.H. and Gunter, W.D., 1995. Aquifer disposal of CO₂-rich greenhouse gasses: modelling of water–rock reaction paths in a siliciclastic aquifer. Proceedings of the 8th international symposium on water–rock interaction, A.A. Balkema, Vladivostok, Russia, pp. 895–898.

- Poesio, P. and Ooms, G., 2007. Removal of particle bridges from a porous material by ultrasonic irradiation. *Transport Porous Med.*, **66**(3): 235-257.
- Ramachandran, V. and Fogler, H.S., 1999. Plugging by hydrodynamic bridging during flow of stable colloidal particles within cylindrical pores. *J. Fluid Mech.*, **385**: 129-156.
- Robie, R.A. and Hemingway, B.S., 1995. *Thermodynamic Properties of Minerals and Related Substances at 298.15 K and 1Bar (105 Pascals) Pressures and at Higher Temperatures*. U.S. Geological Survey Bulletin 2131, 461p.
- Schaef, H.T. and McGrail, B.P., 2004. Direct measurements of pH and dissolved CO₂ in H₂O–CO₂ brine mixtures to supercritical conditions, AAPG Annual Meeting, Dallas, Texas.
- Seyfried, W.E., Jr., Janecky, D.R. and Berndt, M.E., 1987. Rocking autoclaves for hydrothermal experiments; II, The flexible reaction-cell system. In: H.L. Barnes (Editor), *Hydrothermal Experimental Techniques*. Wiley-Interscience, 216-239, pp. 216-239.
- Shock, E.L., 1995. Organic acids in hydrothermal solutions: Standard molal thermodynamic properties of carboxylic acids and estimates of dissociation constants at high temperatures and pressures. *Am. J. Sci.*, **295**: 496-580.
- Shock, E.L. and Helgeson, H.C., 1988. Calculation of the thermodynamic and transport properties of aqueous species at high pressures and temperatures: Correlation algorithms for ionic species and equation of state predictions to 5 kb and 1000° C. *Geochim. Cosmochim. Acta*, **52**: 2009-2036.
- Shock, E.L., Helgeson, H.C. and Sverjensky, D.A., 1989. Calculations of the thermodynamic and transport properties of aqueous species at high pressures and temperatures: Standard partial molal properties of inorganic neutral species. *Geochim. Cosmochim. Acta*, **53**: 2157-2183.
- Shock, E.L. and Koretsky, C.M., 1995. Metal-Organic Complexes in Geochemical Processes - Estimation of Standard Partial Molal Thermodynamic Properties of Aqueous Complexes between Metal-Cations and Monovalent Organic-Acid Ligands at High-Pressures and Temperatures. *Geochim. Cosmochim. Acta*, **59**(8): 1497-1532.
- Shock, E.L., Oelkers, E.H., Sverjensky, D.A., Johnson, J.W. and Helgeson, H.C., 1992. Calculation of thermodynamic and transport properties of aqueous species at high pressures and temperatures. Effective electrostatic radii, dissociation constants and standard partial molal properties to 1000° C and 5 kb. *J. Chem. Soc. London, Faraday Transactions*, **88**: 803-826.

- Shock, E.L., Sassani, D.C., Willis, M. and Sverjensky, D.A., 1997. Inorganic species in geologic fluids: Correlations among standard molal thermodynamic properties of aqueous ions and hydroxide complexes. *Geochim. Cosmochim. Acta*, **61**(5): 907-950.
- Spangler, L., 2007. Regional Characterization Activities and Large Volume Injection Test -Nugget Sandstone formation. Regional Carbon Sequestration Partnerships Initiative Review Meeting, Pittsburgh, Pennsylvania.
- Stephens, J.C. and Hering, J.G., 2004. Factors affecting the dissolution kinetics of volcanic ash soils: Dependencies on pH, CO₂, and oxalate. *Appl. Geochem.*, **19**: 1217-1232.
- Tagirov, B. and Schott, J., 2001. Aluminum speciation in crustal fluids revisited. *Geochim. Cosmochim. Acta*, **65**(21): 3965-3992.
- Vaidya, R.N. and Fogler, H.S., 1990. Formation damage due to colloidally induced fines migration. *Colloid. Surface.*, **50**: 215-229.
- Wagman, D.D. et al., 1982. The NBS tables of chemical thermodynamic properties, selected values for inorganic and c1 and c2 organic substances in SI units. *J. Phys. Chem. Ref. Data*, 11, supp. 2: 392p.
- Wildenborg, A.F.B. and van der Meer, L.G.H., 2002. *The use of oil, gas and coal fields as CO₂ sinks*. Intergovernmental Panel on Climate Change, Working Group III: Mitigation of Climate Change, Workshop on Carbon Dioxide Capture and Storage, Regina, Canada, pp. 61-78.
- Wolery, T.J., 1978. *Some chemical aspects of hydrothermal processes at mid-oceanic ridges -- A theoretical study. I. Basalt-sea water reaction and chemical cycling between the oceanic crust and the oceans. II. Calculation of chemical equilibrium between aqueous solutions and minerals*, Northwestern University, 263p, Evanston, IL.
- Xu, T., Apps, J.A. and Pruess, K., 2004. Numerical simulation to study mineral trapping for CO₂ disposal in deep aquifers. *Appl. Geochem.*, **19**: 917-936
- Zhu, C., 2005. In situ Feldspar Dissolution Rates in an Aquifer. *Geochim. Cosmochim. Acta*, **69**(6): 1435-1453.
- Zhu, C. and Lu, P., 2009. Coupled alkali feldspar dissolution and secondary mineral precipitation in batch systems: 3. Saturation Indices of Product Minerals and Reaction Paths. *Geochim. Cosmochim. Acta*, **73**: 3171-3200.
- Zhu, C., Veblen, D.R., Blum, A.E. and Chipera, S.J., 2006. Naturally weathered feldspar surfaces in the Navajo Sandstone aquifer, Black Mesa, Arizona: Electron microscopic characterization. *Geochim. Cosmochim. Acta*, **70**(18): 4600-4616.

CHAPTER 7

ARSENIC EH-PH DIAGRAMS AT 25 °C AND 1 BAR (0.1 MPa)⁶

⁶ This chapter is currently under review: Lu, P. and Zhu, C. Arsenic Eh-pH and Solubility Diagrams at 25 °C and 1 bar (0.1 MPa). *Environmental Earth Sciences*, submitted.

1. INTRODUCTION

Currently, there is tremendous interest in arsenic geochemistry (Tamaki and Frankenberger, 1992; WHO, 2001; Nordstrom and Archer, 2002; Smedley and Kinniburgh, 2002; Oremland and Stolz, 2003; Swartz et al., 2004; Hollibaugh et al., 2005; Keimowitz et al., 2005; Amirbahman et al., 2006; Sverjensky and Fukushima, 2006; Fukushima and Sverjensky, 2007; Marini and Accornero, 2007). Eh-pH diagrams provide a useful guide for evaluating the predominance of dissolved species and stability of solids (Garrels and Christ, 1965; Pourbaix, 1966; Krauskopf and Bird, 1995). Various versions of Eh-pH diagrams for inorganic arsenic have been previously constructed (Ferguson and Gavis, 1972; Brookins, 1986; 1988; Vink, 1996; Takeno, 2005). These Eh-pH diagrams differ because: (1) different thermodynamic properties for aqueous species and solids are used for construction of Eh-pH diagrams by different authors; (2) inclusion or exclusion of certain arsenic species (e.g., thio-arsenic species and ferric arsenate); and (3) different chemical systems of interest. Since the last special publication of Eh-pH diagrams for arsenic was over ten years ago (Vink, 1996), new values of thermodynamic properties for arsenic species have become available through several re-evaluations, compilations, or estimations (Nordstrom and Archer, 2002; Pokrovski et al., 2002; Langmuir et al., 2006; Marini and Accornero, 2007). Several previous compilations focused on particular systems of interest. For example, Nordstrom and Archer (2002) focused on the As-O-H-S system; Langmuir et al. (2006) concentrated on the As-O-H-Fe system; Marini and Accornero (2007) focused on thermodynamic properties of metal-arsenate and metal-arsenite aqueous complexes; Root et al. (2009) focused on arsenic surface complexation with Fe. In addition, new experimental data for barium arsenate and barium hydrogen

arsenate data (Zhu et al., 2005) are available. Thus, a new compilation that integrates data available for the As-O-H-S-Fe-Ba system is necessary.

In this contribution, we compiled a thermodynamic database for arsenic species and constructed Eh-pH diagrams at 25 °C and 1 bar (0.1 MPa) for a number of chemical systems relevant to the environment. These diagrams provide a ready reference for practitioners working in the area of arsenic geochemistry. The thermodynamic properties used in the construction of Eh-pH diagrams in this study are listed in Tables 1 and 2. Construction of the Eh-pH diagrams were facilitated with the computer code Geochemist's Workbench (GWBTM) version 5.0 (Bethke, 2004).

The range of As concentrations found in natural waters is large, ranging from less than 0.5 µg L⁻¹ (6.7×10^{-9} M) to more than 5000 µg L⁻¹ (6.7×10^{-5} M) (Smedley and Kinniburgh, 2002). A relatively wider range of arsenic concentration (10^{-3} to 10^{-8} M) was chosen in this study for general purpose, e.g., contaminated waters. Eh-pH diagrams in this study considered pH dependence of species distribution for sulfur, iron, and barium species. Moreover, activities (instead of molalities) considering the influence of ionic strength and ion association phenomena were calculated with the aid of geochemical modeling code.

2. INTERNALLY CONSISTENT THERMODYNAMIC PROPERTIES FOR ARSENIC

To construct Eh-pH diagrams, we first derived a set of internally consistent thermodynamic properties for arsenic aqueous species and complexes, and arsenic-containing oxides, sulfides, and ferric arsenate minerals.

Nordstrom and Archer (2002) critically reviewed available thermodynamic data for some arsenic species and pointed out the unreliability of most previous compilations. They further provided an internally consistent thermodynamic data set by simultaneous weighted least-squares multiple regressions on thermochemical measurements. However, thermodynamic data for ferric and ferrous arsenate complexes and ferric arsenate minerals are unavailable in their compilation. Ferric arsenate minerals are important because, for example, scorodite is the least soluble arsenate phase in many mine tailings systems and it controls arsenic releases to tailings pore water and to the environment (e.g., Langmuir et al., 2006). Langmuir et al. (2006) critically reviewed solubility data of arsenate minerals and provided equilibrium constants for Fe-bearing aqueous arsenic species, amorphous ferric arsenate and crystalline scorodite which are computed using equilibrium constants for arsenic acid species and complexes based on Nordstrom and Archer (2002). Langmuir et al. (2006) used equilibrium constants obtained by Whiting (1992). Marini and Accornero (2007) independently estimated thermodynamic properties of Fe-bearing arsenate and arsenite aqueous complexes.

In this study, we adopted the thermodynamic properties of Fe-As complexes from Marini and Accornero (2007). The estimates from Marini and Accornero (2007) are in a good agreement with those of Whiting (1992), except $FeAsO_4^0$ (Table 3). To ensure the consistency, we recalculated the equilibrium constants of reactions (at 25 °C) involving Fe-bearing arsenate and arsenite aqueous complexes (Table 1) from Marini and Accornero (2007) using thermodynamic properties of arsenic acid species and complexes from Nordstrom and Archer (2002). We also recalculated Langmuir et al.'s (2006) solubility products of amorphous ferric arsenate and crystalline scorodite considering Fe-

As complexes from Marini and Accornero (2007) following the procedure of Langmuir et al. (2006) (Table 2). Marini and Accornero (2007) noticed a large discrepancy with Whiting (1992) for $FeAsO_4^o$. They argued that the discrepancy may be due to the fact that Whiting's evaluations are influenced by the stability constants of $FePO_4^o$ complexes derived by Langmuir (1979) which appears to be too high (Marini and Accornero, 2007). Note that Marini and Accornero (2007) provided a species $FeH_2AsO_3^{2+}$ which is not used in Langmuir et al. (2006) (Table 1 and 3).

Barium arsenate has been thought to control arsenic concentrations in fresh water and in solid waste leachates (Wagemann, 1978; Turner, 1981; Essington, 1988). However, as pointed out by Zhu et al. (2005), the solubilities of barium arsenate are inconsistent in the literature. Zhu and co-workers conducted new dissolution and precipitation experiments to measure the solubility of barium arsenate and barium hydrogen arsenate. However, when they calculated the solubility values, they used equilibrium constants from the MINTEQ database (Allison et al., 1991). In this study, we recalculated the solubility products of Zhu et al. (2005)'s experimental data for barium arsenate and barium hydrogen arsenate using log K values listed in Table 1. These recalculated values are thus internally consistent with other adopted log K s for arsenic species listed in Table 1.

Therefore, we derived a set of internally consistent thermodynamic properties for arsenic as the basis for Eh-pH diagrams. These thermodynamic properties consist of those from Nordstorm and Archer (2002), metal arsenic complexes recalculated for Marini and Accornero (2007), amorphous ferric arsenate and scorodite recalculated for

Langmuir et al. (2006), and barium arsenate and barium hydrogen arsenate recalculated for Zhu et al. (2005).

Table 1. Equilibrium constants for As aqueous species from different sources

Aqueous reactions	WATEQ 4F ¹	MINTE QA2 ²	LLNL ³	Nordstrom & Archer (2003)	Langmuir et al. (2006)	Marini and Accornero (2007)	Adopted values
$\text{H}_3\text{AsO}_3^0 = \text{H}_2\text{AsO}_3^- + \text{H}^+$	-9.15	-9.23	-9.21	-9.17		-9.234	-9.17
$\text{H}_3\text{AsO}_3^0 = \text{HAsO}_3^{2-} + 2\text{H}^+$	-23.85	-21.33	-20.22	-23.27			-23.27
$\text{H}_3\text{AsO}_3^0 = \text{AsO}_3^{3-} + 3\text{H}^+$	-39.55	-34.74		-38.27			-38.27
$\text{H}_3\text{AsO}_3^0 + \text{H}^+ = \text{H}_4\text{AsO}_3^+$	-0.305	-0.31					
$3\text{H}_3\text{AsO}_3^0 + 6\text{HS}^- + 5\text{H}^+ = \text{As}_3\text{S}_4(\text{HS})_2^- + 9\text{H}_2\text{O}$	72.314			72.23			72.23
$\text{H}_3\text{AsO}_3^0 + 2\text{HS}^- + \text{H}^+ = \text{AsS}(\text{OH})(\text{HS})^- + 2\text{H}_2\text{O}$	18.038			18.008			18.008
$\text{H}_3\text{AsO}_4^0 = \text{H}_2\text{AsO}_4^- + \text{H}^+$	-2.3	-2.24	-2.25	-2.3		-2.265	-2.3
$\text{H}_3\text{AsO}_4^0 = \text{HAsO}_4^{2-} + 2\text{H}^+$	-9.46	-9.00	-9.01	-9.29		-9.23	-9.29
$\text{H}_3\text{AsO}_4^0 = \text{AsO}_4^{3-} + 3\text{H}^+$	-21.11	-20.6	-20.61	-21.08		-20.619	-21.08
$\text{H}_3\text{AsO}_4^0 + 2\text{H}^+ + 2\text{e}^- = \text{H}_3\text{AsO}_3^0 + \text{H}_2\text{O}$	19.35		19.35	19.35			19.35
$\text{Fe}^{3+} + \text{H}_3\text{AsO}_4^0 = \text{FeAsO}_4^0 + 3\text{H}^+$					-2.19	-6.86 (-6.97)	-6.97
$\text{Fe}^{3+} + \text{H}_3\text{AsO}_4^0 = \text{FeHAsO}_4^+ + 2\text{H}^+$					0.57	0.71 (0.59)	0.59
$\text{Fe}^{3+} + \text{H}_3\text{AsO}_4^0 = \text{FeH}_2\text{AsO}_4^{2+} + \text{H}^+$					1.74	2.00 (1.88)	1.88
$\text{Fe}^{2+} + \text{H}_3\text{AsO}_4^0 = \text{FeH}_2\text{AsO}_4^+ + \text{H}^+$					0.38	0.53 (0.41)	0.41
$\text{Fe}^{2+} + \text{H}_3\text{AsO}_4^0 = \text{FeHAsO}_4^0 + 2\text{H}^+$					-5.75	-5.87 (-5.99)	-5.99
$\text{Fe}^{2+} + \text{H}_3\text{AsO}_4^0 = \text{FeAsO}_4^- + 3\text{H}^+$					-14.03	-13.41 (-13.53)	-13.53
$\text{Fe}^{3+} + \text{H}_3\text{AsO}_3^0 = \text{FeH}_2\text{AsO}_3^{2+} + \text{H}^+$						-1.95 (-1.98)	-1.98
$\text{Ba}^{2+} + \text{H}_3\text{AsO}_3^0 = \text{BaH}_2\text{AsO}_3^+ + \text{H}^+$						-7.81 (-7.83)	-7.83

Parenthetic values for metal arsenic and arsenate complexes have been computed using the As thermodynamic properties from Nordstrom and Archer (2003). (1) Ball and Nordstrom (1991); (2) Allison et al. (1991); (3) Wolery et al. (1992)

Table 2. Equilibrium constants for As solid dissolution reactions

Reactions	WATEQ 4F ⁽¹⁾	MINTE QA2 ⁽²⁾	LLNL ⁽³⁾	Nordstrom & Archer (2003)	Langmuir et al.(2006)	Adopted values
$\text{As} (\alpha, \text{cr}) + 3\text{H}_2\text{O} = \text{H}_3\text{AsO}_3^0 + 3\text{H}^+ + 3\text{e}^-$	-12.17 ⁽⁴⁾		-12.5836	-12.525		-12.525
$\text{As}_2\text{O}_5 (\text{cr}) + 3\text{H}_2\text{O} = 2\text{H}_3\text{AsO}_4^0$	6.699 ⁽⁵⁾	6.699	6.6585	8.26		8.26
$\text{FeAsO}_4 \cdot 2\text{H}_2\text{O} (\text{scorodite}) = \text{Fe}^{3+} + \text{AsO}_4^{3-} + 2\text{H}_2\text{O}$	-20.249 ⁽⁶⁾	-20.197			-26.12	-26.08 ⁽⁸⁾
$\text{FeAsO}_4 \cdot 2\text{H}_2\text{O} (\text{am}) = \text{Fe}^{3+} + \text{AsO}_4^{3-} + 2\text{H}_2\text{O}$					-23.3	-23.29 ⁽⁸⁾
$\text{As}_2\text{O}_3 (\text{arsenolite}) + 3\text{H}_2\text{O} = 2\text{H}_3\text{AsO}_3^0$	-1.4 ⁽⁵⁾		-1.4269	-1.38		-1.38
$\text{As}_2\text{O}_3 (\text{claudetite}) + 3\text{H}_2\text{O} = 2\text{H}_3\text{AsO}_3^0$	-1.53 ⁽⁵⁾		-1.3551	-1.34		-1.34
$\text{As}_2\text{S}_3 (\text{orpiment}) + 6\text{H}_2\text{O} = 2\text{H}_3\text{AsO}_3^0 + 3\text{HS}^- + 3\text{H}^+$	-60.971 ⁽⁵⁾	-60.971	-61.0063	-46.3		-46.3
$\text{As}_2\text{S}_3 (\text{am}) + 6\text{H}_2\text{O} = 2\text{H}_3\text{AsO}_3^0 + 3\text{H}_2\text{S}$				-23.9		-23.9
$\text{AsS} (\text{realgar}) + 3\text{H}_2\text{O} = \text{H}_3\text{AsO}_3^0 + \text{HS}^- + 2\text{H}^+ + \text{e}^-$	-19.747 ⁽⁶⁾	-19.747	-27.0028	-20.11		-20.11
$\text{AsS} (\beta, \text{realgar}) + 3\text{H}_2\text{O} = \text{H}_3\text{AsO}_3^0 + \text{HS}^- + 2\text{H}^+ + \text{e}^-$				-20.05		-20.05
$\text{FeAsS} (\text{arsenopyrite}) + 3\text{H}_2\text{O} = \text{H}_2\text{AsO}_3^- + \text{Fe}^{2+} + \text{HS}^- + 3\text{H}^+ + 3\text{e}^-$			-16.6137	-34.799 ⁽⁷⁾		-34.799
$\text{Ba}_3(\text{AsO}_4)_2 (\text{c}) + 6\text{H}^+ = 2\text{H}_3\text{AsO}_4^0 + 3\text{Ba}^{2+}$	-7.89	-8.91				18.3 ⁽⁸⁾
$\text{BaHAsO}_4 \cdot \text{H}_2\text{O} = \text{AsO}_4^{3-} + \text{H}_2\text{O} + \text{H}^+ + \text{Ba}^{2+}$						3.62 ⁽⁸⁾

(1) Ball and Nordstrom (1991); (2) Allison et al. (1991); (3) Wolery et al. (1992); (4) Christensen et al. (1975); (5) Wagman et al. (1982); (6) Naumov et al. (1974); (7) Pokrovski et al. (2002); (8) Recalculated values in this study based on Langmuir et al. (2006) and solubility experiments of Zhu et al. (2005).

Table 3. Gibbs free energy of formation for aqueous species and solids at 25 °C and 0.1 MPa (kJ/mol)

Aqueous Species	Ferguson & Gavis (1972)	Brookins (1986, 1988)	Vink (1996)	Craw et al. (2003)	Nordstrom & Archer (2002)	Langmuir et al. (2006)	Zhu et al. (2005)	Marini and Accornero (2007)	Adopted values
H ₃ AsO ₄ ⁰	-769.856 ⁽¹⁾	-766.007 ⁽⁴⁾	-766.09 ⁽⁴⁾	-766.09 ⁽⁴⁾	-766.75			-766.09 ⁽¹⁰⁾	-766.75
H ₂ AsO ₄ ⁻	-757.304 ⁽¹⁾	-753.162 ⁽⁴⁾	-753.12 ⁽⁴⁾	-753.12 ⁽⁴⁾	-753.65			-753.162 ⁽¹⁰⁾	-753.65
HAsO ₄ ²⁻	-717.556 ⁽¹⁾	-714.167 ⁽⁴⁾	-714.627 ⁽⁴⁾	-714.627 ⁽⁴⁾	-713.73			-714.585 ⁽¹⁰⁾	-713.73
AsO ₄ ³⁻	-651.867 ⁽¹⁾	-648.394 ⁽⁴⁾	-648.52 ⁽⁴⁾	-648.52 ⁽⁴⁾	-646.36			-648.394 ⁽¹⁰⁾	-646.36
H ₃ AsO ₃ ⁰	-646.01 ⁽¹⁾	-639.817 ⁽⁴⁾	-639.734 ⁽⁴⁾	-639.8 ⁽⁹⁾	-640.03			-639.851 ⁽¹⁰⁾	-640.03
H ₂ AsO ₃ ⁻	-593.291 ⁽¹⁾	-587.141 ⁽⁴⁾	-587.015 ⁽⁴⁾	-587.1 ⁽¹⁰⁾	-587.66			-587.141 ⁽¹⁰⁾	-587.66
HAsO ₃ ²⁻	-524.255 ⁽¹⁾	-524.297 ⁽⁵⁾	-524.255 ⁽⁵⁾		-507.4				-507.4
AsO ₃ ³⁻		-447.688 ⁽⁵⁾	-447.688 ⁽⁵⁾		-421.8				-421.8
HAsS ₂ ⁰	-48.5762 ⁽²⁾								
AsS ₂ ⁻	-27.447 ⁽²⁾								
As ₃ S ₄ (HS) ₂ ⁻					-125.6				-125.6
AsS(OH)SH ⁻					-244.4				-244.4
Fe ²⁺			-79.0776 ⁽⁴⁾	-91.5 ⁽¹⁰⁾				-91.5 ⁽¹⁰⁾	-91.5
Fe ³⁺			-4.6024 ⁽⁴⁾					-17.24 ⁽¹⁰⁾	-17.24
SO ₄ ²⁻		-744.54 ⁽⁴⁾	-744.334 ⁽⁴⁾	-744.5 ⁽¹⁰⁾	-744.5 ⁽¹¹⁾			-744.46 ⁽¹³⁾	-744.5
H ₂ S		-27.82 ⁽⁴⁾	-27.6144 ⁽⁴⁾	-27.6 ⁽⁴⁾	-27.87			-27.92 ⁽¹³⁾	-27.87
HS ⁻		12.09 ⁽⁴⁾	12.1336 ⁽⁴⁾	12 ⁽¹⁰⁾	12.05			11.97 ⁽¹³⁾	12.05
Ba ²⁺								-560.78 ⁽¹³⁾	-560.78
BaOH ⁺								-720.9 ⁽¹³⁾	-720.9
FeAsO ₄ ⁰						-771.49		-744.17	-744.17
FeHAsO ₄ ⁺						-787.24		-787.38	-787.38
FeH ₂ AsO ₄ ²⁺						-793.92		-794.75	-794.75
FeH ₂ AsO ₄ ⁺						-860.42		-860.62	-860.62
FeHAsO ₄ ⁰						-825.43		-824.08	-824.08
FeAsO ₄ ⁻						-778.16		-781.02	-781.02
FeH ₂ AsO ₃ ²⁺								-645.98	-645.98
BaH ₂ AsO ₃ ⁺								-1156.10	-1156.10
Solids									
AsS (α, realgar)	-35.167 ⁽³⁾	-35.146 ⁽⁶⁾	-35.146 ⁽⁶⁾	-33.2 ⁽⁹⁾	-31.3				-31.3
As ₂ S ₃ (α, orpiment)	-168.406 ⁽³⁾	-168.615 ⁽⁴⁾	-168.615 ⁽⁴⁾	-86 ⁽⁹⁾	-84.9				-84.9
As ₂ O ₃	-589.107 ⁽¹⁾	-575.969 ⁽⁶⁾	-576.555 ⁽⁴⁾		-576.34				-576.34
As ₂ O ₅	-781.99 ⁽¹⁾				-774.96				-774.96
FeAsS (arsenopyrite)			-109.621 ⁽⁷⁾	-141.6 ⁽¹¹⁾					-141.6
FeAsO ₄ ·2H ₂ O (Scorodite)			-1307.5 ⁽⁸⁾	-1307.5 ⁽⁸⁾		-1287.08 ⁽¹²⁾			-1287.08
FeAsO ₄ ·2H ₂ O (am)						-1270.98 ⁽¹²⁾			-1270.98
Fe(OH) ₃ (a)				-693.3 ⁽⁴⁾	-699				-699
Ba ₃ (AsO ₄) ₂							-3113.40		-3095.11 ⁽¹⁴⁾
BaHAsO ₄ ·H ₂ O							-1544.47		-1538.65 ⁽¹⁴⁾

(1) Sergeyeva and Khodakovsky (1969); (2) Sillen and Martell (1964); (3) Robie and Waldbaum (1968); (4) Wagman et al. (1982); (5) Dove and Rimstidt (1985); (6) Robie et al. (1978); (7) Naumov et al. (1974); (8) Vink (1996); (9) Pokrovski et al. (1996); (10) Shock and Helgeson (1988); (11) Ball and Nordstrom (1991); (12) Recalculated values based on the solubility product of crystalline scorodite (Langmuir et al., 2006); (13) Shock et al. (1997); (14) Recalculated values based on Zhu et al. (2005)'s experiments.

3. Eh-pH DIAGRAMS

3.1. As-O-H

Figure 1 shows the predominance of arsenic species in the system As-O-H at 25 °C and 0.1 MPa. While the predominance fields for arsenate species under oxidizing conditions are similar in all Eh-pH diagrams published, the field boundaries for arsenite species are significantly different. The predominance fields of arsenite in Figure 1 are the same as Figure 2 of Nordstrom and Archer (2002) because the same thermodynamic data for arsenite species were used. The values of the Gibbs free energy of formation for species $HAsO_3^{2-}$ and AsO_3^{3-} adopted by Nordstrom and Archer (2002) are 16.9 kJ/mol and 25.9 kJ/mol higher, respectively, than those of Dove and Rimstidt (1985), which were used by Brookins (1986; 1988) and Vink (1996) (Table 3). Due to these large uncertainties, the species $HAsO_3^{2-}$ and AsO_3^{3-} were omitted from Fig. 1, although they are present in the diagrams of Brookins (1986; 1988) and Vink (1996). Using the thermodynamic data from Nordstrom and Archer (2002), $H_3AsO_3^o$ is the predominant species from pH 0 to 9.17, and $H_2AsO_3^-$ from pH 9.17 to 14.

Arsenic is fairly mobile under oxidizing and mildly reducing conditions. Under strongly reducing conditions, near the lower limit of the stability field of water, native arsenic is stable within the H_2O stability field and limits the mobility of the arsenic. As pointed out by Vink (1996), arsenolite (As_2O_3) or claudetite (As_2O_3) only occur at extremely high activities of aqueous arsenic species (diagrams not shown).

Figure 1 was constructed for the As-O-H system with $\sum As = 10^{-6}$ M. The symbol “ $\sum As$ ” represents the sum of the concentrations of all aqueous As species present in the system.

3.2. As-O-H-S

The Eh-pH diagrams for the system As-O-H-S are shown in Fig. 2, which are different from those of Brookins (1986; 1988) and Vink (1996), but similar to that of Plant et al. (2003) at low arsenic concentrations. The revisions result from the inclusion in our diagrams of two aqueous thioarsenite species $As_3S_4(HS)_2^-$ and $AsS(OH)SH^-$ from Nordstrom and Archer (2002) and also in that of Plant et al. (2003). Thioarsenite species were not included by Brookins (1986; 1988) and Vink (1996), but Ferguson and Gavis (1972) included the species $HAsS_2^o$ and AsS_2^- . These species, however, are regarded as unstable with respect to solid As_2S_3 by Wagemann (1978). With the inclusion of thioarsenite species, the stability fields for orpiment (As_2S_3) and realgar (AsS) shrink appreciably in comparison to those in the previous studies that did not include the thioarsenite species (Brookins, 1988; Vink, 1996). As shown in Fig. 2, the decrease of $\sum As$ increases the predominance field of $AsS(OH)SH^-$. The predominance field of the thioarsenite species $As_3S_4(HS)_2^-$ does not appear in the Eh-pH diagrams.

In addition, the standard state Gibbs free energy of formation for the arsenic sulfide mineral orpiment (Table 3) is given with a range of values (varying by approximately 80 kJ/mol) in the literature (Ferguson and Gavis, 1972; Brookins, 1986; 1988; Vink, 1996; Nordstrom and Archer, 2002). This results in large differences among the Eh-pH diagrams that adopt these different values.

In Fig. 2, the higher $\sum As$, the wider the stability field of orpiment and realgar. When $\sum S$ (representing the sum of the concentrations of all aqueous sulfur species) decreases to $10^{-4.5}$ M, the stability field of orpiment disappears from the diagram at $\sum As$

= 10^{-6} M (data not shown). Decreasing ΣS further to 10^{-5} results in the disappearance of the stability field of realgar (data not shown).

In comparison with As-O-H system, arsenic mobility is limited under mildly reducing and low pH conditions. In contrast to Brookins (1986; 1988), arsenic partitions significantly into aqueous phases under mild-reducing and neutral pH conditions due to the inclusion of the species $AsS(OH)SH^{-}$.

3.3. As-O-H-S-Fe

The effects of mineral stability and aqueous species predominance by addition of Fe to the system As-O-H-S are shown in Fig. 3 at $\Sigma S = 10^{-3}$ M and for a range of ΣAs . Our Fig. 3 is characterized by a large stability field for scorodite ($FeAsO_4 \cdot 2H_2O$) in acidic and neutral pH, under oxidizing conditions with $\Sigma As \geq 10^{-6}$ M. The thermodynamic properties for scorodite are the subject of considerable debate and studies (Dove and Rimstidt, 1985; Robins, 1987; Krause and Ettel, 1988; Robins, 1990; Zhu and Merkel, 2001; Langmuir et al., 2006). Langmuir et al. (2006) recently evaluated the solubility products of scorodite by geochemical modeling, taking into account aqueous ferric hydroxide, ferric sulfate, and ferric arsenate complexes. Their derived solubility product of $10^{-26.12}$ for crystalline scorodite is approximately 6 orders of magnitude lower than the previously estimated value of $10^{-20.24}$ (Chukhlantsev, 1956). Vink (1996) estimated an even smaller solubility product for crystalline scorodite ($10^{-31.2}$). The stability field of scorodite in Fig. 3 reflects the log K value of Langmuir et al. (2006) (being recalculated in this study). Use of this value results in a scorodite stability field existing under a considerably narrower range of pH and Eh conditions in oxidizing environments than was previously predicted (Vink, 1996; Craw et al., 2003).

Addition of Fe to the system As-O-H-S shrinks the stability fields of orpiment and realgar appreciably because of the formation of arsenopyrite ($FeAsS$). Decreasing ΣAs further decreases the stability fields of orpiment and realgar, and increases the dominance field of the thioarsenite species $AsS(OH)SH^-$. Arsenopyrite is stable under acidic to basic, reducing conditions. The arsenopyrite stability field replaces part of the thioarsenite species and arsenous acid fields in the As-O-H-S system (Fig. 2). The stability field of arsenopyrite in Vink's (1996) Eh-pH diagram is much smaller and restricted to basic pH. The difference between the arsenopyrite stability field in Fig. 3 and Craw et al. (2003)'s Eh-pH diagram is minor because the difference is caused by thermodynamic data for other arsenic species while identical thermodynamic data were used for arsenopyrite.

Decrease of ΣS results in a shrinking stability field for orpiment and, to varying degrees, enlarging the stability field of realgar and native arsenic. The stability field of both orpiment and realgar disappears when ΣS decreases to 10^{-7} M, when $\Sigma As = 10^{-3}$ and $\Sigma Fe = 10^{-6}$ M. Note that the boundary between native arsenic and arsenopyrite shifts with ΣS values, given constant ΣAs (1.0×10^{-3} M) and ΣFe (10^{-6} M). At $\Sigma As = \Sigma Fe = \Sigma S = 10^{-6}$ M, both orpiment and realgar are not stable, which is in marked contrast with the large stability field of these phases under acidic pH in previously published Eh-pH diagrams (Vink, 1996).

Increase of ΣFe leads to a significant expansion of the stability fields for scorodite and arsenopyrite, shrinking the realgar field, and absence of the native arsenic field. The stability field of arsenopyrite encroaches on the field of orpiment with increasing ΣFe at a fixed ΣAs (10^{-3} M) and ΣS (10^{-3} M).

The aqueous species predominance fields in Fig. 3 also result from the inclusion of ferric and ferrous arsenate species from Marini and Accornero (2007). As a result, $FeHAsO_4^+$, $FeH_2AsO_4^+$, and $FeH_2AsO_4^{2+}$ species reduce the predominance fields of H_3AsO_4 and $H_2AsO_4^-$ under extremely acidic pH with a fixed ΣAs (10^{-6} M) and ΣS (10^{-3} M) when the ΣFe is $\geq 10^{-3}$ M.

The addition of Fe into the As-O-H-S system results in decreased arsenic mobility under extremely oxidizing and low pH conditions and mild reducing and neutral pH conditions.

3.4. As-O-H-Ba and As-O-H-S-Fe-Ba

An Eh-pH diagram for the system As-O-H-Ba is presented in Fig. 4 (ΣBa^{2+} is 10^{-3} M). Using new solubility data based on Zhu et al. (2005), barium arsenate is only stable at high pH conditions (pH > 10.3). In contrast, if the log K values of -7.89 or -8.91 for reaction $Ba_3(AsO_4)_2(c) + 6H^+ = 2H_3AsO_3^0 + 3Ba^{2+}$ (reported in the databases of WATEQ4f or MINTEQ, see Table 2) were used, the stability field of barium arsenate (pH > 2.1) would not only encroach on the fields of AsO_4^{3-} but also on $HAsO_4^{2-}$ and $H_2AsO_4^-$ (diagram not shown). The new solubility data suggest that barium arsenate is significantly less stable than previously thought (Zhu et al., 2005). The barium arsenate stability field disappears when Ba^{2+} is less than 10^{-4} M (diagram not shown). The stability field of barium hydrogen arsenate does not appear in the diagram.

Calculations were also made to construct Eh-pH diagrams for the system As-O-H-S-Fe-Ba. Figure 5 shows the predominance and stability fields at $\Sigma Fe = 10^{-6}$ M and $\Sigma Ba^{2+} = \Sigma S = 10^{-3}$ M, and ΣAs from 10^{-3} to 10^{-8} M. At higher ΣAs , for example, 10^{-3} M,

scorodite and barium arsenate are the dominant solid phases under oxidizing conditions, and arsenopyrite, orpiment, realgar, and native arsenic are dominant under reducing conditions. When $\sum \text{As}$ decreases, the stability fields of scorodite and barium arsenate are replaced by arsenate aqueous species. In addition, the stability fields for orpiment, barium arsenate, and arsenopyrite significantly shrink. Note that the thioarsenic species $\text{AsS}(\text{OH})\text{SH}^-$ is present between the orpiment and arsenopyrite fields. With a low value of As ($\sum \text{As} = 10^{-8} \text{ M}$), arsenic aqueous species prevail at oxidizing and slightly reducing conditions. The diagram looks the same as Fig. 3d. The addition of Ba into the As-O-H-S-Fe system results in decreased arsenic mobility under oxidizing and mild reducing and high pH conditions.

4. CONCLUDING REMARKS

We compiled thermodynamic properties for aqueous and solid arsenic species from the literature, recalculated those properties to ensure internal consistency, and used these data to construct Eh-pH diagrams. These diagrams provide ready references for scientists working on arsenic geochemistry. As pointed out by Garrels and Christ (1965), Eh-pH diagrams are only as accurate as the accuracy of the free energy data used in constructing them and valid only for those species specifically considered. Significant discrepancies exist in the Gibbs free energy of formation data for arsenic solids in the literature, which casts uncertainty over the Eh-pH diagrams using these data. It is also well known that natural waters lack internal redox equilibrium (Cherry et al., 1979; Lindberg and Runnells, 1984; Stumm and Morgan, 1996). However, these diagrams are nevertheless useful as we need to study disequilibrium as a deviation from equilibrium.

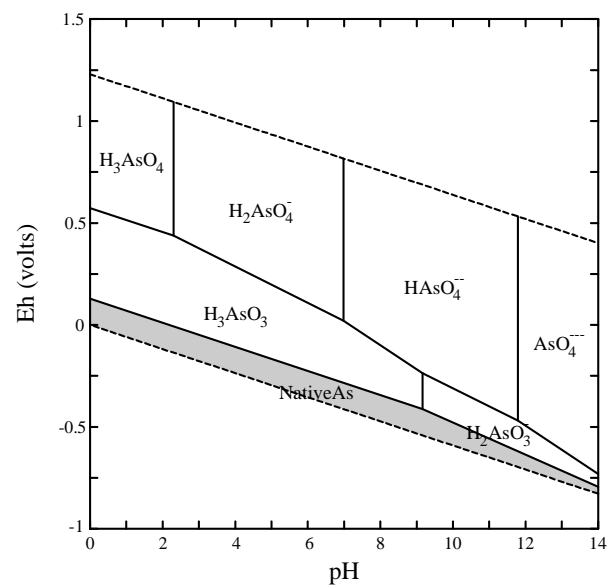


Figure 1. Eh-pH diagram for the system As-O-H at 25 °C and 0.1 MPa. ΣAs is set at 10^{-6} M. Gray shaded area denotes the solid phase.

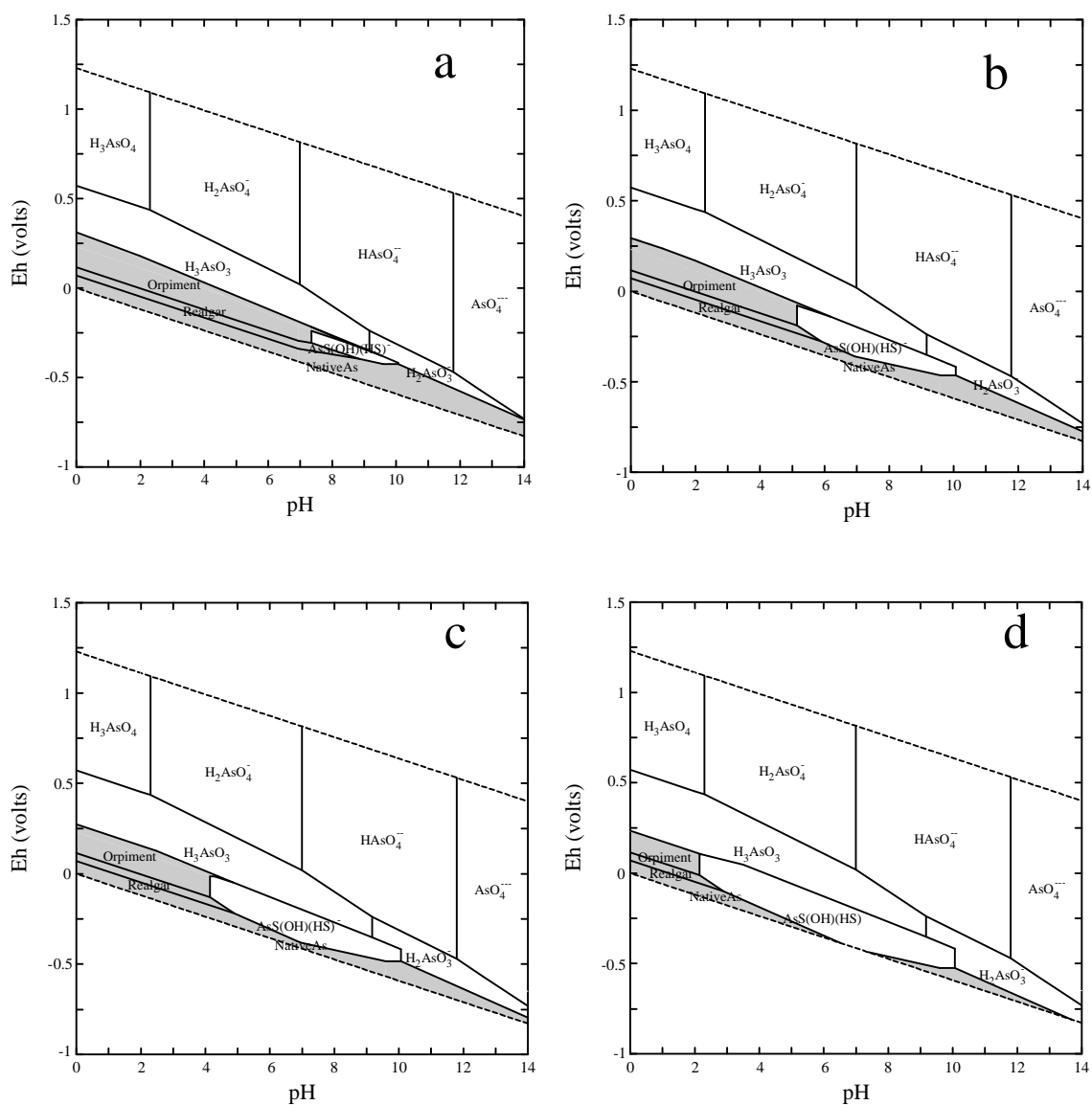


Figure 2. Eh-pH diagrams for the system As-O-H-S at 25 °C and 0.1 MPa. ΣS is set at 10^{-3} M for the above diagrams. ΣAs is (a) 1.0×10^{-3} M, (b) 1.0×10^{-5} M, (c) 1.0×10^{-6} M, and (d) 1.0×10^{-8} M, respectively. Gray shaded areas denote the solid phases.

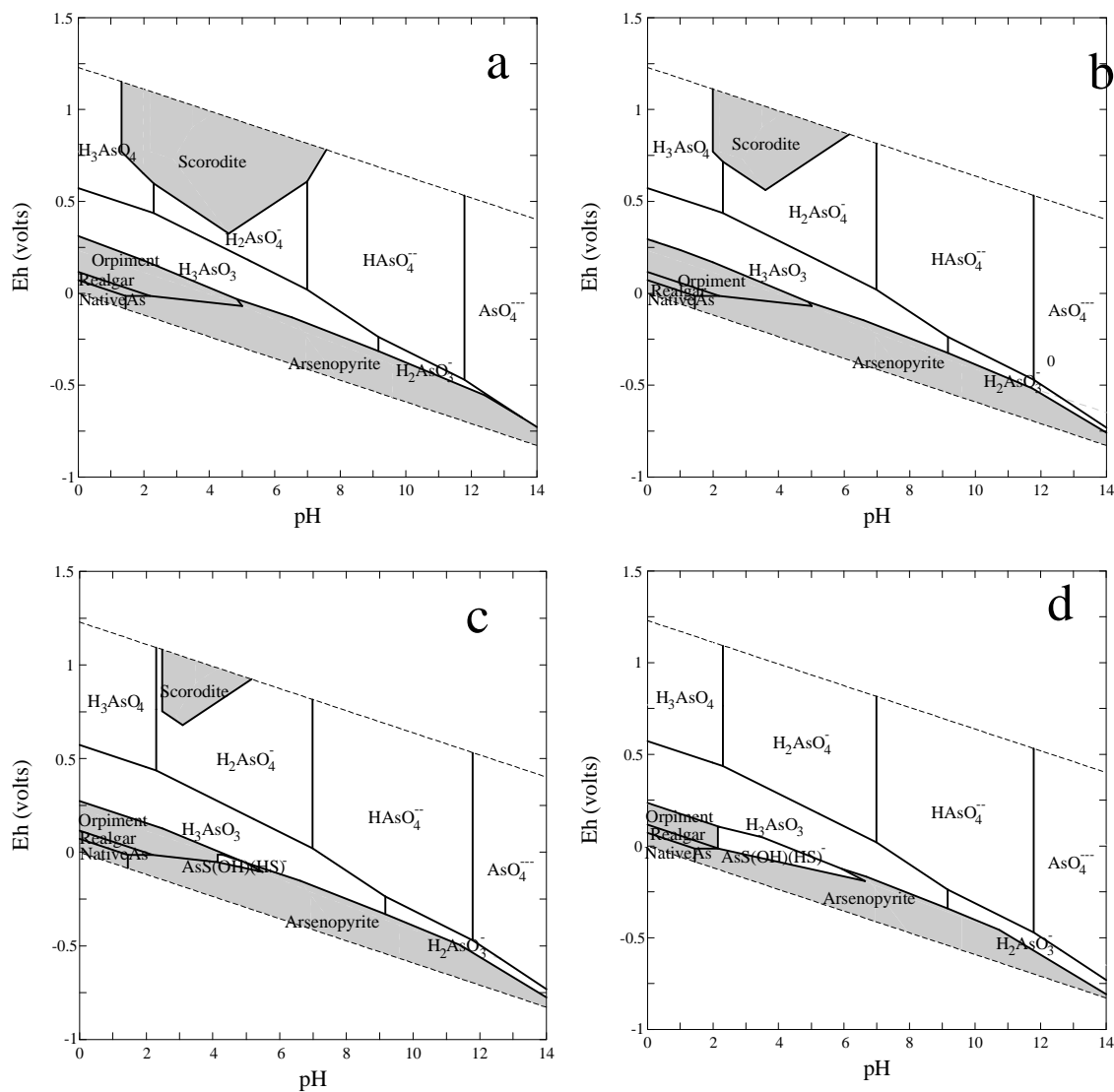


Figure 3. Eh-pH diagrams for the system As-O-H-S-Fe at 25 °C and 0.1 MPa. ΣS and ΣFe are set at 10^{-3} and 10^{-6} M, respectively. ΣAs is set at (a) 10^{-3} M, (b) 10^{-5} M, (c) 10^{-6} M, and (d) 10^{-8} M, respectively. Gray shaded areas denote the solid phases.

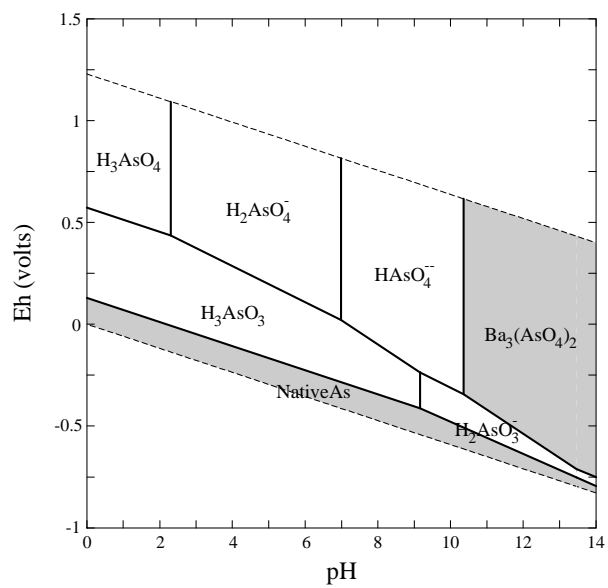


Figure 4. Eh-pH diagrams for the system As-O-H-Ba at 25 °C and 0.1 MPa. $\Sigma\text{As} = 10^{-6}$ and $\Sigma\text{Ba} = 10^{-3}$ M. Gray shaded areas denote the solid phases.

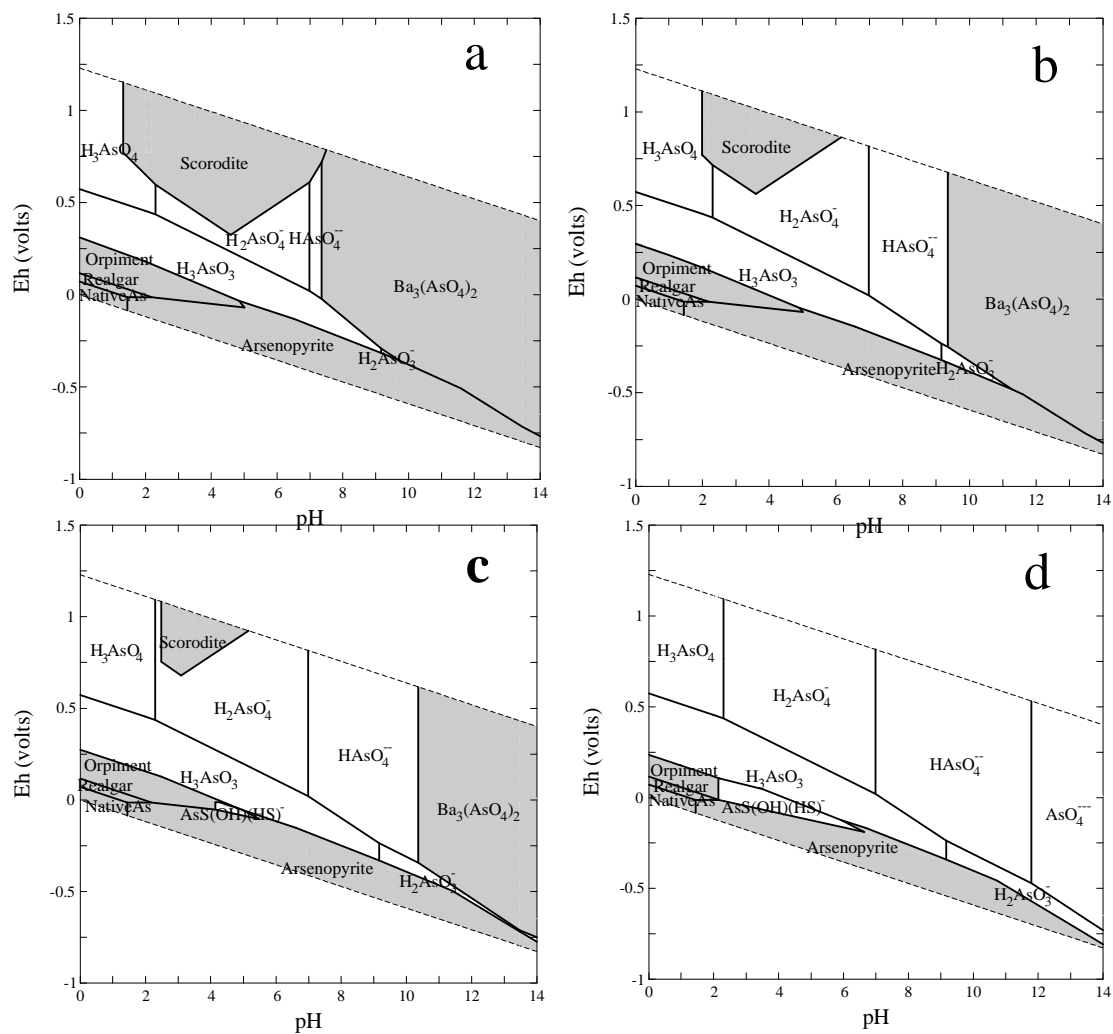


Figure 5. Eh-pH diagrams for the system As-O-H-S-Fe-Ba at 25 °C and 0.1 MPa. $\Sigma\text{Fe} = 10^{-6}$ M, ΣBa and $\Sigma\text{S} = 10^{-3}$ M. ΣAs is set at (a) 10^{-3} M; (b) 10^{-5} M; (c) 10^{-6} M; and (d) 10^{-8} M, respectively.

REFERENCES

- Allison, J. D., Brown, D. S., and Novo-Gradac, K. J., 1991. *MINTEQA2/PRODEFA2, a geochemical assessment model for environmental systems, version 3.0 user's manual*. U.S. Environmental Protection Agency Report EPA/600/3-91/021.
- Amirbahman, A., Kent, D. B., Curtis, G. P., and Davis, J. A., 2006. Kinetics of sorption and abiotic oxidation of arsenic(III) by aquifer materials. *Geochim. Cosmochim. Acta* **70**, 533-547
- Ball, J. W. and Nordstrom, D. K., 1991. *User's manual for WATEQ4F, with revised thermodynamic data base and test cases for calculating speciation of major, trace, and redox elements in natural waters*. U.S. Geological Survey Open-File Report 91-183.
- Bethke, C. M., 2004. *The Geochemist's Workbench, version 5.0, GWB Reference Manual*. Hydrogeology Program, University of Illinois.
- Brookins, D. G., 1986. Geochemical behavior of antimony, arsenic, cadmium and thallium: Eh-pH diagrams for 25 °C, 1 bar pressure. *Chem. Geol.* **54**, 271-278.
- Brookins, D. G., 1988. *Eh-pH diagrams for geochemistry*. Springer-Verlag, Berlin.
- Cherry, J. A., Shaikh, A. U., Tallman, D. E., and Nicholson, R. V., 1979. Arsenic species as an indicator of redox conditions in groundwater. *J. Hydrol.* **43**, 373-392.
- Christensen, J. J., Eatough, D. J., and Izatt, R. M., 1975. *Handbook of metal ligand heats and related thermodynamic quantities (2nd ed.)*. Marcel Dekker, New York.
- Chukhlantsev, V. G., 1956. Solubility products of a series of arsenates. *J. Inorganic Chem. (USSR)* **1**, 1975-1982.
- Craw, D., Falconer, D., and Yongson, J. H., 2003. Environmental arsenopyrite stability and dissolution: theory, experiment, and field observations. *Chem. Geol.* **179**, 71-82.
- Dove, P. M. and Rimstidt, J. D., 1985. The solubility and stability of scorodite, $\text{FeAsO}_4 \cdot 2\text{H}_2\text{O}$. *Am. Miner.* **70**, 838-844.
- Essington, M. E., 1988. Solubility of barium arsenate. *Soil Sci. Soc. Am. J.* **52**, 1566-1570.
- Ferguson, J. F. and Gavis, J., 1972. A review of the arsenic cycle in natural waters. *Water Res.* **6**, 1259-1274.
- Fukushi, K. and Sverjensky, D. A., 2007. A predictive model (ETLM) for arsenate adsorption and surface speciation on oxides consistent with spectroscopic and theoretical molecular evidence. *Geochim. Cosmochim. Acta* **71**, 3717-3745.

- Garrels, R. M. and Christ, C. L., 1965. *Minerals, solutions, and equilibria*. Harper and Rowley, New York.
- Hollibaugh, J. T., Carini, S., Gurleyuk, H., Jellison, R., Joye, S. B., Lecleir, G., Meile, C., Vasquez, L., and Wallschlager, D., 2005. Arsenic speciation in Mono Lake, California: Response to seasonal stratification and anoxia. *Geochim. Cosmochim. Acta* **69**, 1925-1937.
- Keimowitz, A. R., Zheng, Y., Chillrud, S. N., Mailloux, B., Jung, H. B., Stute, M., and Simpson, H. J., 2005. Arsenic redistribution between sediments and water near a highly contaminated source. *Environ. Sci. Technol.* **39**, 8606-8613.
- Krause, E. and Ettel, V. A., 1988. Solubility and stability of scorodite, $\text{FeAsO}_4 \cdot 2\text{H}_2\text{O}$: New data and further discussion. *Am. Miner.* **73**, 850-854.
- Krauskopf, K. B. and Bird, D. K., 1995. *Introduction to Geochemistry*. McGraw-Hill, New York.
- Langmuir, D., 1979. Techniques of estimating thermodynamic properties for some aqueous complexes of geochemical interest. In: Jenne, E. A. (Ed.), *Chemical modeling in aqueous systems: speciation, sorption, solubility, and kinetics*. ACS Symp. Ser. 93. American Chemical Society, Washington, 353-387.
- Langmuir, D., Mahoney, J., and Rowson, J., 2006. Solubility products of amorphous ferric arsenate and crystalline scorodite ($\text{FeAsO}_4 \cdot 2\text{H}_2\text{O}$) and their application to arsenic behavior in buried mine tailings. *Geochim. Cosmochim. Acta* **70**, 2942-2956.
- Lindberg, R. D. and Runnells, D. D., 1984. Ground water redox reactions: An analysis of equilibrium state applied to Eh measurements and geochemical modeling. *Science* **225**, 925-927.
- Marini, L. and Accornero, M., 2007. Prediction of the thermodynamic properties of metal-arsenate and metal-arsenite aqueous complexes to high temperatures and pressures and some geological consequences. *Environ. Geol.* **52**, 1343-1363.
- Naumov, G. B., Ryzhenko, B. N., and Khodakovsky, I. L., 1974. *Handbook of thermodynamic data*. U.S. Geological Survey, Reston, VA.
- Nordstrom, D. K. and Archer, D. G., 2002. Arsenic thermodynamic data and environmental geochemistry. In: Welch, A. H. and Stollenwerk, K. G. (Eds.), *Arsenic in ground water*. Springer.
- Oremland, R. S. and Stolz, J. F., 2003. The Ecology of Arsenic. *Science* **300**, 939-944.

- Plant, J. A., Kinniburgh, D. G., Smedley, P. L., Fordyce, F. M., and Klinck, B. A., 2003. Arsenic and selenium. In: Lollar, B. S. (Ed.), *Environmental Geochemistry*. Elsevier, Amsterdam.
- Pokrovski, G. S., Gout, R., Zotov, A., Schott, J., and Harrichoury, J. C., 1996. Thermodynamic properties and stoichiometry of the arsenic (III) hydroxide complexes at hydrothermal conditions. *Geochim. Cosmochim. Acta* **60**, 737-749.
- Pokrovski, G. S., Kara, S., and Roux, J., 2002. Stability and solubility of arsenopyrite, FeAsS, in crustal fluids. *Geochim. Cosmochim. Acta* **66**, 2361-2378.
- Pourbaix, M., 1966. *Atlas of electrochemical equilibria*. Pergamon Press, Oxford.
- Robie, R. A., Hemingway, B. S., and Fisher, J. R., 1978. *Thermodynamic properties of minerals and related substances at 298.15 K and 1 bar (105 pascals) pressure and at higher temperatures*. U.S. Geological Survey Bulletin 1452.
- Robie, R. A. and Waldbaum, D. R., 1968. *Thermodynamic properties of minerals and related substances at 298.15 K and one atmosphere pressure and at higher temperatures*. Geological Survey Bulletin No. 1259. U.S. Department of the Interior.
- Robins, R. G., 1987. Solubility and stability of scorodite, FeAsO₄·2H₂O: Discussion. *Am. Miner.* **72**, 842-844.
- Robins, R. G., 1990. The stability and solubility of ferric arsenate-an update. In: Gaskell, D. R. (Ed.), *EPD Congress '90*, TMS Annual Meeting.
- Root, R. A., Vlassopoulos, D., Rivera, N. A., Rafferty, M. T., Andrews, C., and O'day, P. A., 2009. Speciation and natural attenuation of arsenic and iron in a tidally influenced shallow aquifer. *Geochim. Cosmochim. Acta* **73**, 5528-5553.
- Sergeyeva, E. I. and Khodakovskiy, I. L., 1969. Physicochemical conditions of formation of native arsenic in hydrothermal deposits. *Geochem. Int.* **7**, 846-859.
- Shock, E. L. and Helgeson, H. C., 1988. Calculation of the thermodynamic and transport properties of aqueous species at high pressure and temperature: correlation algorithm for ionic species and equation of state predictions to 5kb and 1000 °C. *Geochim. Cosmochim. Acta* **52**, 2009-2036.
- Shock, E. L., Sassani, D. C., Willis, M., and Sverjensky, D. A., 1997. Inorganic species in geologic fluids: Correlations among standard molal thermodynamic properties of aqueous ions and hydroxide complexes. *Geochim. Cosmochim. Acta* **61**, 907-950.
- Sillen, L. G. and Martell, A. E., 1964. *Stability constants*. Spec. Publ. No. 17. The chemical society, London.

- Smedley, P. L. and Kinniburgh, D. G., 2002. A review of the source, behaviour and distribution of arsenic in natural waters. *Appl. Geochem.* **17**, 517-568
- Stumm, W. and Morgan, J. J., 1996. *Aquatic Chemistry, Chemical Equilibria and Rates in Natural Waters*, 3rd ed. John Wiley & Sons, Inc., New York, 1022p.
- Sverjensky, D. A. and Fukushi, K., 2006. A predictive model (ETLM) for As(III) adsorption and surface speciation on oxides consistent with spectroscopic data. *Geochim. Cosmochim. Acta* **70**, 3778-3802.
- Swartz, C. H., Blute, N. K., Badruzzman, B., Ali, A., Brabander, D., Jay, J., Besancon, J., Islam, S., Hemond, H. F., and Harvey, C. F., 2004. Mobility of arsenic in a Bangladesh aquifer: Inferences from geochemical profiles, leaching data, and mineralogical characterization. *Geochim. Cosmochim. Acta* **68**, 4539-4557
- Takeno, N., 2005. *Atlas of Eh-pH diagrams. Intercomparison of thermodynamic databases*. Geological Survey of Japan Open File Report No.419.
- Tamaki, S. and Frankenberger, W. T. J., 1992. Environmental biochemistry of arsenic. *Reviews Environ. Contam. Toxicol.* **124**, 79-110.
- Turner, R. R., 1981. Oxidation state of arsenic in coal ash leachate. *Environ. Sci. Technol.* **15**, 1062-1066.
- Vink, B. W., 1996. Stability relations of antimony and arsenic compounds in the light of revised and extended Eh-pH diagrams. *Chem. Geol.* **130**, 21-30.
- Wagemann, R., 1978. Some theoretical aspects of stability and solubility of inorganic arsenic in the freshwater environment. *Water Res.* **12**, 139-145.
- Wagman, D. D., Evans, W. H., Parker, V. B., Schumm, R. H., Halow, I., Bailey, S. M., Churney, K. L., and Nuttall, R. L., 1982. The NBS tables of chemical thermodynamic properties - selected values for inorganic and C-1 and C-2 organic substances in SI units. *J. Phys. Chem. Ref. Data* **11**, 1-390.
- Whiting, K. S., 1992. *The thermodynamics and geochemistry of arsenic, with application to subsurface waters at the Sharon Steel Superfund Site at Midvale, Utah*. MS Thesis, Colorado School of Mines, Golden, CO.
- Who, 2001. *Environmental Health Criteria 224: Arsenic and Arsenic Compounds*. World Health Organization, Geneva.
- Wilson, F. H. and Hawkins, D. B., 1978. Arsenic in streams, stream sediments, and ground water, Fairbanks Area, Alaska. *Environ. Geol.* **2**, 195-202.

- Wolery, T. J., 1992. *EQ3/6, A software package for geochemical modeling of aqueous systems: Package overview and installation guide (version 7.0)*. URCL-MA-110662-PT-I, Livermore, Calif., Univ. California, Lawrence Livermore Laboratory.
- Zhu, Y. and Merkel, B. J., 2001. The dissolution and solubility of scorodite, $\text{FeAsO}_4 \cdot 2\text{H}_2\text{O}$ evaluation and simulation with PHREEQC2. *Wiss.Mitt. Inst. für Geologie, TU Bergakademie Freiberg, Germany* **18**, 1-12.
- Zhu, Y. N., Zhang, X. H., Xie, Q. L., Chen, Y. D., Wang, D. Q., Liang, Y. P., and Lu, J., 2005. Solubility and stability of barium arsenate and barium hydrogen arsenate at 25 °C. *J. Hazard. Mater.* **120**, 37-44.

CHAPTER 8

LEAD COPRECIPITATION WITH IRON OXYHYDROXIDE NANO-PARTICLES ⁷

⁷ This chapter is currently in preparation for publication: Lu, P., Nuhfer, N. T., Kelly, S., Li., Q., Elswick, E., and Zhu, C. Lead coprecipitation with iron oxyhydroxide nano-particles. *Geochimica et Cosmochimica Acta*, in preparation.

1. INTRODUCTION

The bioavailability, mobility, transport, distribution, and cycling of trace metals in subsurface and surficial geological systems are often regulated by iron cycling (Davis and Kent, 1990; Jenne, 1968; Krauskopf, 1956). Iron oxyhydroxides occur widely in surficial and subsurface geological environments, and even though they may constitute a minor fraction of the bulk rock, soil, or sediment, they are efficient scavengers of trace metals and radionuclides (Jambor and Dutrizac, 1998). However, the mechanisms by which trace elements are sorbed onto iron oxyhydroxides in pristine and anthropogenically impacted geological systems are not well known. Knowledge of sorption mechanisms is nevertheless central to both developing quantitative partitioning models that serve as a theoretical basis for the applications of trace elements as signatures of fluid flow and chemical reactions, and to predicting contaminant transport and stability in geological media.

Presence of lead (Pb^{2+}) in the environment has severe adverse effects on human health, particularly for infants and young children (Nriagu, 1992). Also, the study of lead isotopes is of great interest to geologists, and hence the quantitative partitioning of Pb^{2+} between aqueous solutions and geological solid matrix bears significance to isotope geochemistry. Possible mechanisms in controlling lead concentrations in aqueous solutions include solubility, surface adsorption, surface precipitation, and coprecipitation. Coprecipitation (CPT) is often referred to as the simultaneous removal of a trace constituent, together with a carrier constituent from a homogeneous aqueous solution. However, the mechanism of coprecipitation is poorly understood. The term coprecipitation is loosely used in a phenomenological sense, alluding to the century-old

observation that trace constituents, often metals, are efficiently removed together with a major constituent from a homogeneous aqueous solution.

In the following discussion, “coprecipitation experiments” refer to the design in which the tracer (e.g., Pb^{2+}) is present in the solution when the carrier ion (e.g., Fe^{3+}) hydrolyzes and precipitates to form hydrous oxides. In “adsorption experiments” (ADS), the tracer is added to a suspension of already precipitated and aged (typically for a period of a few hours to a few days) hydrous oxides of the carrier ion (e.g., ferrihydrite). The term “sorption” refers to all processes that transfer an ion from the aqueous phase to the solid phase (Sposito, 1984), without reference to specific processes (e.g., CPT or ADS).

Many geological, environmental, and industrial systems resemble base titration as in our CPT experiments described below. For example, when acid mine drainage loaded with ferric iron and metals is mixed with neutral surface and ground water or reacted with calcite in soils, sediments, and aquifers, Fe^{3+} and trace metals are co-precipitated simultaneously. Iron oxidation/precipitation may prevail in natural aquatic environments, and thus trace metals are likely coprecipitated.

Although numerous Pb^{2+} adsorption experiments have already been conducted (e.g., Balistrieri and Murray, 1982; Gadde and Laitinen, 1973; Hayes and Leckie, 1986; Kinniburgh et al., 1976; Lutzenkirchen, 1997; Rose and Bianchimosquera, 1993; Swallow et al., 1980; Trivedi et al., 2003), studies of coprecipitation are scarce and sporadic (e.g, Ford et al., 1997; Ford et al., 1999; Martinez and McBride, 1998; Martinez and McBride, 2001). Direct comparison of Pb ADS and CPT contact methods are even scarcer (Schultz et al., 1987). However, it is important to compare the CPT and ADS methods.

First, sorption behaviors for some metals are different when they are prepared using the CPT or ADS “contact method”. Previous work shows that sorption isotherms and sorption pH edges prepared with ADS and CPT experimental procedures are appreciably different for Cu^{2+} sorption onto hydrous iron and aluminum oxides (Karthikeyan et al., 1997; Karthikeyan et al., 1999), As^{5+} sorption onto ferrihydrite, and Ni^{2+} and Cr^{3+} sorption onto hydrous iron oxides (Crawford et al., 1993), with coprecipitation being the more efficient process for metal removal from aqueous solutions. CPT sorption edges are located up to 2.6 pH units lower on the uptake-pH diagrams, and at the same sorbate/sorbent ratio, metal uptake is enhanced in CPT systems as compared to the ADS system (Charlet and Manceau, 1992; Karthikeyan et al., 1997; Waychunas et al., 1993). However, to illustrate the complexity of the metastable system and metal specific nature, CPT and ADS sorption edges with Zn^{2+} on iron oxyhydroxide (Crawford et al., 1993) and Cu^{2+} on hydrous aluminum hydroxide (Karthikeyan et al., 1997) show no appreciable differences, and contradictory experimental results for CPT-ADS have been found for Cu^{2+} onto iron-oxyhydroxide sorption edges (Karthikeyan et al., 1997; Swallow et al., 1980).

Second, whether or not CPT may represent more permanent sequestration of toxic metals in iron oxyhydroxide from the environment is an important question. The first iron oxyhydroxide to be precipitated from aqueous solution is commonly ferrihydrite, a poorly ordered and metastable phase, which will subsequently transform to highly ordered phases (e.g., goethite and hematite) over time (Cornell and Schwertmann, 1996). The transformation of metal-ferrihydrite coprecipitates to more ordered phases may lead to

structural incorporation of sorbed metals (see summary in Cornell and Schwertmann, 1996), resulting in apparent irreversible sorption or desorption hysteresis.

This paper follows our earlier report on the EXAFS study of the structure of the coprecipitated Pb onto nano-particles of iron oxyhydroxides (Kelly et al., 2008), and presents companion laboratory experiments of sorption and desorption of Pb²⁺ onto iron nano-particles with CPT and ADS contact methods, High-Resolution Transmission and Analytical Electron Microscopy (HR TEM-AEM), and geochemical modeling study of coprecipitation of Pb²⁺ with ferric iron. EDTA extraction experiments permit comparison of the strength of Pb association with nano-particles of iron oxyhydroxides from the ADS and CPT experiments. To investigate the relative stability of sorbed Pb in the environment, sorbents from both ADS and CPT experiments were aged at 60 °C for 14 days and at 90 °C for 24 h. Desorption experiments were conducted again on these aged solids. Finally, we attempt to integrate sorption edge measurements with advanced electron microscopy. The macroscopic chemistry data covering a wide range of conditions supplement the molecular scale EXAFS and HRTEM data for elucidating the Pb-Fe coprecipitation mechanism and developing a quantitative model for the partitioning of Pb²⁺ between aqueous solution and iron oxyhydroxides.

2. MATERIALS AND METHODS

2.1. Reagents

All reagents were from Fisher Scientific, and were of analytical grade. Fe-Pb solutions were made from ferric nitrate ($\text{Fe}(\text{NO}_3)_3 \cdot 9\text{H}_2\text{O}$, purity 99.1%) and lead nitrate. All solutions were prepared in a 10 mM KNO_3 background electrolyte solution.

Laboratory plastic-ware was washed with nitric acid solution and then with deionized water.

2.2. Synthesis of 2-line Ferrihydrite

Two-line Ferrihydrite was prepared using the modified procedure of Schwertmann and Cornell (1996). One gram $\text{Fe}(\text{NO}_3)_3 \cdot 9\text{H}_2\text{O}$ was dissolved in 12.5 mL deionized water. A Teflon capillary of N_2 bubbling was used to prevent the possible influence of atmospheric CO_2 and to agitate the solution. The pH of the solution was measured using an Accumet AB15 plus pH meter, calibrated with buffers (pH 4, 7, and 10). 1 M KOH was added cumulatively into the vessel until pH was 7~8. The gel produced was repeatedly centrifuged and washed with deionized water for five times. The gel was then resuspended in the media of 250 mL deionized water by ultrasonification for 10 minutes and magnetic stirring for 20 minutes. The suspended ferrihydrite was aged for 48 hours in closed vessels on an orbital shaker. The fresh prepared gel was used within 2 days for ADS studies. Synthetic 2-line ferrihydrite has been confirmed with X-ray diffraction (XRD) analysis as shown in XRD results section.

2.3. ADS Experiments

An aliquot of 500 mL suspended ferrihydrite was used to prepare 2 batches of solution with different concentrations of Pb, i.e., Batch A (5.25 mmol/L Fe, 0.37 mmol/L Pb, and 10 mmol/L KNO_3) and Batch B (5.43 mmol/L Fe, 0.70 mmol/L Pb, and 10 mmol/L KNO_3). The Fe and Pb concentrations of initial solutions were confirmed with

a Perkins Elmer 5000 flame and graphite furnace Atomic Adsorption Spectrometer (AAS).

A 50-mL aliquot of the solution (ferrihydrite suspension with the presence of Pb) was transferred into a 150-mL high-density polypropylene jar. While stirring the solution vigorously (using Teflon coated magnetic stir bar), 1M KOH was injected into the vessel with the rate of ~ 0.1 mL/min while pH values were continuous monitored. The relatively slow titration rate and vigorously stirring are used to avoid artifacts due to localized high alkalinity during titration as noted by Martinez and McBride (1998b). When the pH approached the target value, a few drops of 0.1M KOH were used to reach the desired pH. The samples were placed on an orbital shaker for 24 hours after which time the pH was re-measured. Measurements at every subsequent hour, up to 100 hours, showed that solution pH had stabilized after 24 hours.

2.4. CPT Experiments

Three batches of solution with different concentrations of Pb were prepared. They are Batch C (6.27 mmol/L Fe, 0.10 mmol/L Pb, and 10 mmol/L KNO_3), Batch D (5.77 mmol/L Fe, 0.37 mmol/L Pb, and 10mmol/L KNO_3) and Batch E (6.77 mmol/L Fe, 0.73 mmol/L Pb, and 10mmol/L KNO_3). The Fe and Pb concentrations of initial solutions were confirmed with AAS analysis.

A 50-mL aliquot of the solution was transferred into a 150-mL high-density polypropylene jar. While stirring the solution vigorously (using a Teflon coated magnetic stir bar), 1M NaOH solution was injected into the vessel with the rate of ~ 0.1 mL/min while constant recording the pH. When the pH approached the target value, a few drops

of 0.1M NaOH were added to reach the desired pH. The samples were put on an orbital shaker for 24 hours after which time the pH was re-measured.

2.5. Solid-liquid Separation

The solids were separated by centrifugation at a maximum relative centrifugal force of 4000 (RCF, g-force) for 45 minutes and the liquid supernatant decanted. Precipitates were immediately transferred into capped vials in ethyl alcohol to prevent further reaction before XRD and TEM measurements, which were performed within 1-3 weeks. All supernatants were filtered through a 0.22 micron cellulose membrane filter connected to a 20 ml polypropylene syringe. The receiving vessel was an air-tight polyethylene centrifugation tube connected to a vacuum pump.

2.6. Extraction (desorption) Experiments

Room temperature ($\sim 22^{\circ}\text{C}$) and high temperature (60°C) extraction experiments were conducted using ethylenediamine tetraacetic acid (EDTA) to assess the fraction of Pb sorbed onto the external surfaces of hydrous iron oxides of both ADS and CPT experiments (pH 6, aged 24 h) after solid-liquid separation (following the methods described in § 2.5). Pb remained in supernatant was measured and subtracted. The difference between initial Pb and Pb in supernatant was regarded as total Pb in extraction experiments. The containers with solids for high temperature extraction experiments were immersed in a water bath (60°C) and aged for 14 days.

An aliquot of 80 mL EDTA solution (with different EDTA concentration) was added to the solids in the bottles. The suspension was agitated with an orbital shaker for

the designated time. After the extraction or desorption experiments, solid and liquid were separated according to procedures described in § 2.5.

2.7. Analytical Methods

The liquid supernatant was measured for its pH, and was acidified using concentrated ultrapure HCl. These solutions were analyzed for Fe and Pb using a Perkins Elmer 5000 flame and graphite furnace AAS (following EPA method 200.7) or a Thermo Jarrell Ash ICAP 61E ICP-MS (following EPA method 200.8). All supernatants were stored at 4° C until analysis.

The solid specimens were prepared for examination by High-Resolution Transmission Electron Microscopy (HRTEM) first by ultra-sonication in ethyl alcohol to re-suspend the particles. Then the suspension was pipetted onto a holey-carbon film supported by a copper-mesh TEM grid, and air-dried. To prevent transformation during ultrasonication, the vessel with the suspension of coprecipitates and ethyl alcohol was cooled in water.

The specimens coprecipitated at pH 5.2 and 6.0 were observed with a Philips FEI Tecnai F20 TEM/STEM with a point-to-point resolution of 0.24 nm, and equipped with a Gatan Imaging Filter (GIF) and Energy Dispersive X-ray (EDX) detector, and a JEOL 4000EX with a point-to-point resolution of 0.17 nm, with a Gatan Imaging Filter. The Philips FEI Tecani F20 TEM/STEM was used for energy-filtered imaging and microanalysis. The JEOL 4000EX HRTEM was used to obtain the highest possible lattice imaging resolution.

XRD analysis of the Pb-Fe coprecipitates was carried out using a Bruker D8 Advance X-ray powder diffractometers (Cu K α radiation), equipped with a solid-state

energy-discriminating detector. The scan parameters used were 10.010 to 80° 2 θ , with a step size of 0.02° 2 θ . The samples were prepared for analysis by dispersing the precipitates in acetone to form a thick suspension. This suspension was deposited on a zero background quartz plate and air dried at room temperature before collecting the XRD scans.

Samples after ADS and CPT, and synthetic 2-line ferrihydrite (as a base line) were particularly prepared to evaluate the phase changes in the products with ADS or CPT aged at elevated temperature. Samples were aged 24 hours at 95° C and 14 d at 60 °C in a water bath before XRD analysis.

3. EXPERIMENTAL RESULTS

3.1. Sorption Edges in Coprecipitation and Adsorption Experiments

The bioavailability, mobility, transport, distribution, and cycling of trace metals in subsurface and surficial geological systems are often regulated by iron cycling (Davis and Kent, 1990; Jenne, 1968; Krauskopf, 1956). Iron oxyhydroxides occur widely in surficial and subsurface geological environments, and even though they may constitute a minor fraction of the bulk rock, soil, or sediment, they are efficient scavengers of trace metals and radionuclides (Jambor and Dutrizac, 1998). However, the mechanisms by which trace elements are sorbed onto iron oxyhydroxides in pristine and anthropogenically impacted geological systems are not well known. Knowledge of sorption mechanisms is nevertheless central to both developing quantitative partitioning models that serve as a theoretical basis for the applications of trace elements as signatures of fluid flow and

chemical reactions, and to predicting contaminant transport and stability in geological media.

Presence of lead (Pb^{2+}) in the environment has severe adverse effects on human health, particularly for infants and young children (Nriagu, 1992). Also, the study of lead isotopes is of great interest to geologists, and hence the quantitative partitioning of Pb^{2+} between aqueous solutions and geological solid matrix bears significance to isotope geochemistry. Possible mechanisms in controlling lead concentrations in aqueous solutions include solubility, surface adsorption, surface precipitation, and coprecipitation. Coprecipitation (CPT) is often referred to as the simultaneous removal of a trace constituent, together with a carrier constituent from a homogeneous aqueous solution. However, the mechanism of coprecipitation is poorly understood. The term *coprecipitation* is loosely used in a phenomenological sense, alluding to the century-old observation that trace constituents, often metals, are efficiently removed together with a major constituent from a homogeneous aqueous solution.

In the following discussion, “coprecipitation experiments” refer to the design in which the tracer (e.g., Pb^{2+}) is present in the solution when the carrier ion (e.g., Fe^{3+}) hydrolyzes and precipitates to form hydrous oxides. In “adsorption experiments” (ADS), the tracer is added to a suspension of already precipitated and aged (typically for a period of a few hours to a few days) hydrous oxides of the carrier ion (e.g., ferrihydrite). The term “sorption” refers to all processes that transfer an ion from the aqueous phase to the solid phase (Sposito, 1984), without reference to specific processes (e.g., CPT or ADS).

Many geological, environmental, and industrial systems resemble base titration as in our CPT experiments described below. For example, when acid mine drainage loaded

with ferric iron and metals is mixed with neutral surface and ground water or reacted with calcite in soils, sediments, and aquifers, Fe^{3+} and trace metals are co-precipitated simultaneously. Iron oxidation/precipitation may prevail in natural aquatic environments, and thus trace metals are likely coprecipitated.

Although numerous Pb^{2+} adsorption experiments have already been conducted (e.g., Balistrieri and Murray, 1982; Gadde and Laitinen, 1973; Hayes and Leckie, 1986; Kinniburgh et al., 1976; Lutzenkirchen, 1997; Rose and Bianchimosquera, 1993; Swallow et al., 1980; Trivedi et al., 2003), studies of coprecipitation are scarce and sporadic (e.g., Ford et al., 1997; Ford et al., 1999; Martinez and McBride, 1998; Martinez and McBride, 2001). Direct comparison of Pb ADS and CPT contact methods are even scarcer (Schultz et al., 1987). However, it is important to compare the CPT and ADS methods.

First, sorption behaviors for some metals are different when they are prepared using the CPT or ADS “contact method”. Previous work shows that sorption isotherms and sorption pH edges prepared with ADS and CPT experimental procedures are appreciably different for Cu^{2+} sorption onto hydrous iron and aluminum oxides (Karthikeyan et al., 1997; Karthikeyan et al., 1999), As^{5+} sorption onto ferrihydrite, and Ni^{2+} and Cr^{3+} sorption onto hydrous iron oxides (Crawford et al., 1993), with coprecipitation being the more efficient process for metal removal from aqueous solutions. CPT sorption edges are located up to 2.6 pH units lower on the uptake-pH diagrams, and at the same sorbate/sorbent ratio, metal uptake is enhanced in CPT systems as compared to the ADS system (Charlet and Manceau, 1992; Karthikeyan et al., 1997; Waychunas et al., 1993). However, to illustrate the complexity of the metastable system

and metal specific nature, CPT and ADS sorption edges with Zn^{2+} on iron oxyhydroxide (Crawford et al., 1993) and Cu^{2+} on hydrous aluminum hydroxide (Karthikeyan et al., 1997) show no appreciable differences, and contradictory experimental results for CPT-ADS have been found for Cu^{2+} onto iron-oxyhydroxide sorption edges (Karthikeyan et al., 1997; Swallow et al., 1980).

Second, whether or not CPT may represent more permanent sequestration of toxic metals in iron oxyhydroxide from the environment is an important question. The first iron oxyhydroxide to be precipitated from aqueous solution is commonly ferrihydrite, a poorly ordered and metastable phase, which will subsequently transform to highly ordered phases (e.g., goethite and hematite) over time (Cornell and Schwertmann, 1996). The transformation of metal-ferrihydrite coprecipitates to more ordered phases may lead to structural incorporation of sorbed metals (see summary in Cornell and Schwertmann, 1996), resulting in apparent irreversible sorption or desorption hysteresis.

This paper follows our earlier report on the EXAFS study of the structure of the coprecipitated Pb onto nano-particles of iron oxyhydroxides (Kelly et al., 2008), and presents companion laboratory experiments of sorption and desorption of Pb^{2+} onto iron nano-particles with CPT and ADS contact methods, High-Resolution Transmission and Analytical Electron Microscopy (HR TEM-AEM), and geochemical modeling study of coprecipitation of Pb^{2+} with ferric iron. EDTA extraction experiments permit comparison of the strength of Pb association with nano-particles of iron oxyhydroxides from the ADS and CPT experiments. To investigate the relative stability of sorbed Pb in the environment, sorbents from both ADS and CPT experiments were aged at 60 °C for 14 days and at 90 °C for 24 h. Desorption experiments were conducted again on these aged

solids. Finally, we attempt to integrate sorption edge measurements with advanced electron microscopy. The macroscopic chemistry data covering a wide range of conditions supplement the molecular scale EXAFS and HRTEM data for elucidating the Pb-Fe coprecipitation mechanism and developing a quantitative model for the partitioning of Pb^{2+} between aqueous solution and iron oxyhydroxides.

Table 1. Titration Experimental Conditions

	HFOFe (g/L)	Pb (mM)	Fe:Pb total	Total strong sites (moles) ¹	Total weak sites (moles) ²	Surface loading (%) ³	Pb/Pb+Fe in precipitates	pH	Eq Time (hr)	Background solutions (mM)
Batch A [†]	0.47	5.25	0.37	1:0.07	2.62×10^{-5}	1.05×10^{-3}	35%		24	10 KNO ₃
Batch B [†]	0.48	5.43	0.70	1:0.13	2.72×10^{-5}	1.09×10^{-3}	65%		24	10 KNO ₃
Batch C	0.56	6.27	0.10	1:0.02	3.14×10^{-5}	1.25×10^{-3}	8%	0.02 [§]	24	10 KNO ₃
Batch D	0.51	5.77	0.37	1:0.06	2.89×10^{-5}	1.15×10^{-3}	31%		24	10 KNO ₃
Batch E	0.6	6.77	0.73	1:0.11	3.39×10^{-5}	1.35×10^{-3}	53%	0.10 [†]	6 [†] /5.25* 30	10 KNO ₃

[§]values if 100% precipitated, [†]Used for TEM and * for EXAFS study. All studies used Fe(NO₃)₃ and Pb(NO₃)₂. [‡]Ferrihydrite gel aged for 48 hours subsequently used for adsorption studies within a further 48 hours. ¹Total strong sites were calculated with 0.005 sites/mol (Dzombak and Morel, 1990). ²Total weak sites were calculated with 0.2 sites/mol (Dzombak and Morel, 1990). ³Surface loading = (Total Pb concentration)/(Total strong sites + Total weak sites).

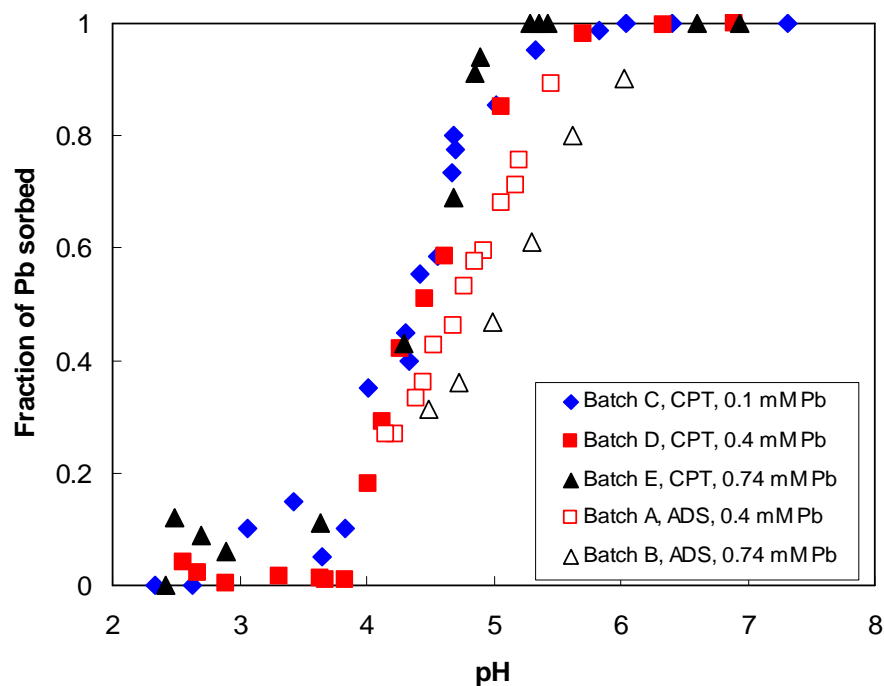


Figure 1. Comparison of adsorption (Batch A and B) with coprecipitation experiments (Batch C, D and E). 10 mM KNO_3 as background solution. Total Fe concentration varies from 5.25-6.77 mM).

3.2. Desorption Experiments at Room Temperature

The amount of Pb^{2+} extracted from the Pb-loaded sorbents increase rapidly with increasing strength of EDTA at low EDTA concentrations for 1 h contact time, but leveled off at EDTA concentration of $> \sim 0.003$ M. Significantly more Pb was extracted from the sorbents from the adsorption experiments than the sorbents from coprecipitation experiments when the concentrations of EDTA are less than 0.002 M (Fig. 5). Caution must be exercised that the reported fraction of Pb or Fe extracted/dissolved in extraction experiments may be underestimated because of possible loss of solid during separation.

Pb^{2+} may be desorbed from the sorbents by both forming EDTA-Pb^{2+} aqueous complexes and by dissolving the iron oxyhydroxides substrate (sorbents) on which Pb^{2+}

was adsorbed or with which Pb^{2+} was coprecipitated. Therefore, the relationship between dissolved Fe^{3+} and Pb^{2+} is indicative to incorporation mechanisms of Pb^{2+} in the sorbents. Figure 6 shows a linear relationship between the Pb extracted and Fe dissolved for CPT solids with EDTA concentrations from 0.0003 to 0.01 M and contact time of 1 h, but a parabolic relationship for ADS solids. The different patterns of Pb versus Fe relationships for ADS and CPT suggest that ADS and CPT are controlled by different mechanisms. About 90% of Pb was extracted when only about 15% of Fe was dissolved for sorbents from ADS experiments, but it took 30% to 40% of Fe dissolution to release ~ 90% of Pb from the sorbents in the coprecipitation experiments (Fig. 6). If enhanced Pb removal for CPT method is simply attributable to an increase in surface area or site density, more Pb should be released in the CPT system compared to the solids from the ADS system.

If we assume that the sorbents in both CPT and ADS experiments are spherical (see the TEM section below) and Fe is uniformly distributed in the sphere, a 5-nm ferrihydrite sphere is reduced to 4.82, 4.64, and 4.44 nm if 10%, 20%, and 30% of volume is reduced or 10, 20, and 30% of total Fe in the sphere is dissolved, respectively. This calculation suggests that Pb presents mainly in top 0.27 nm layer of a 5 nm diameter domain (~15% of the bulk) in the sorbents from the ADS experiments. 0.27 nm is roughly the length of the Fe(III)-O- bonds (Manceau and Drits, 1993). This indicates that Pb is mainly surface bound in ADS solids.

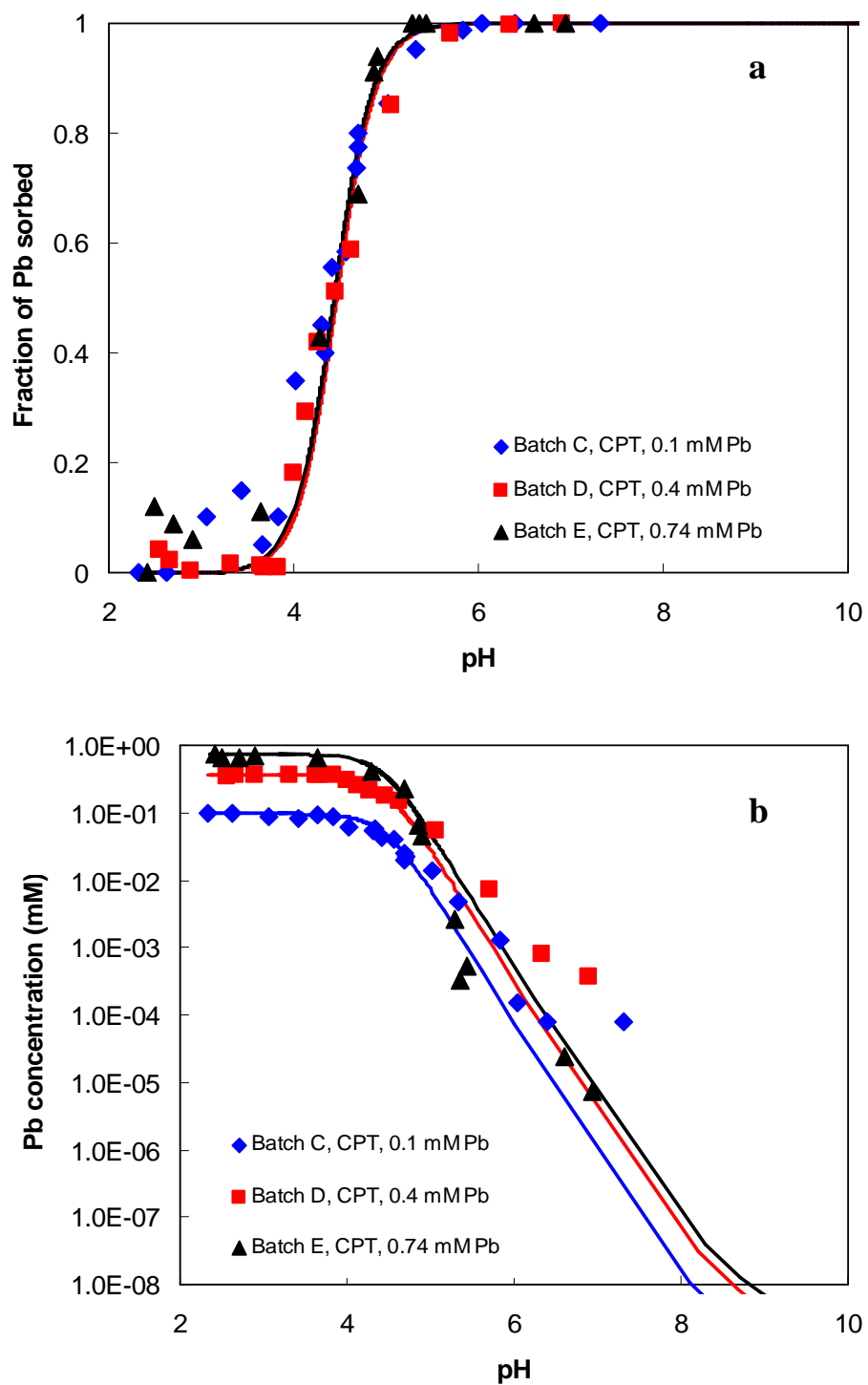


Figure 2. Comparison of model calculations with experimental results. Solid symbols are results from CPT experiments. Experimental conditions are listed in Table 1. The lines were calculated with solid solution models.

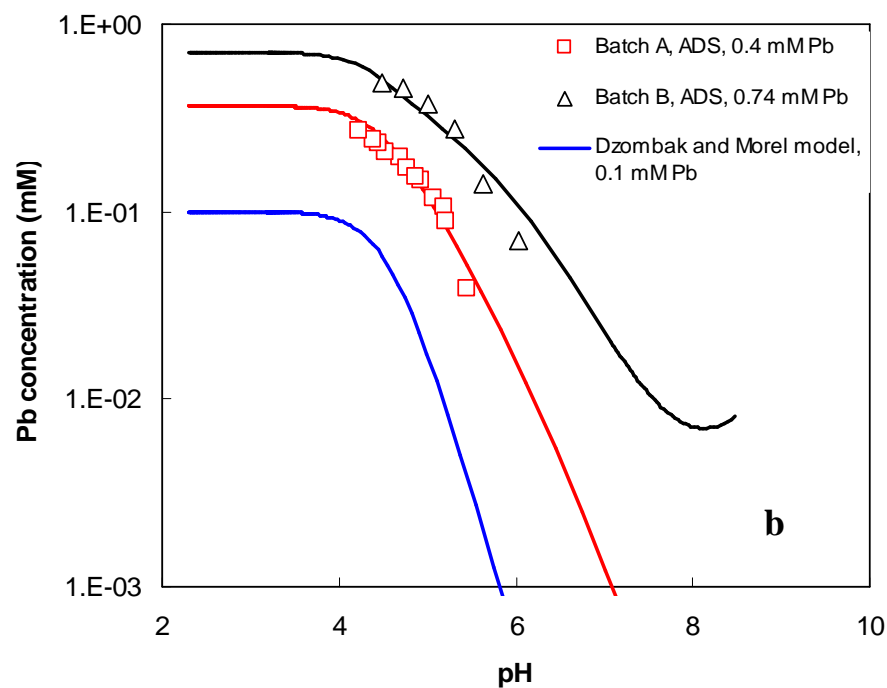
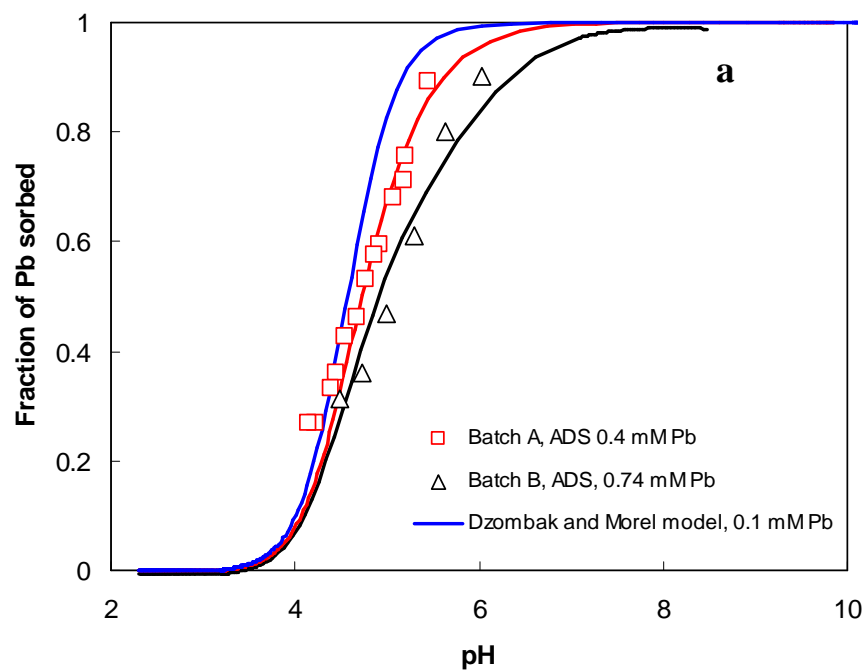


Figure 3. Comparison of model calculations with experimental results. Solid symbols are results from ADS experiments. Experimental conditions are listed in Table 1. The lines were calculated with the model parameters by Dzombak and Morel (1990).

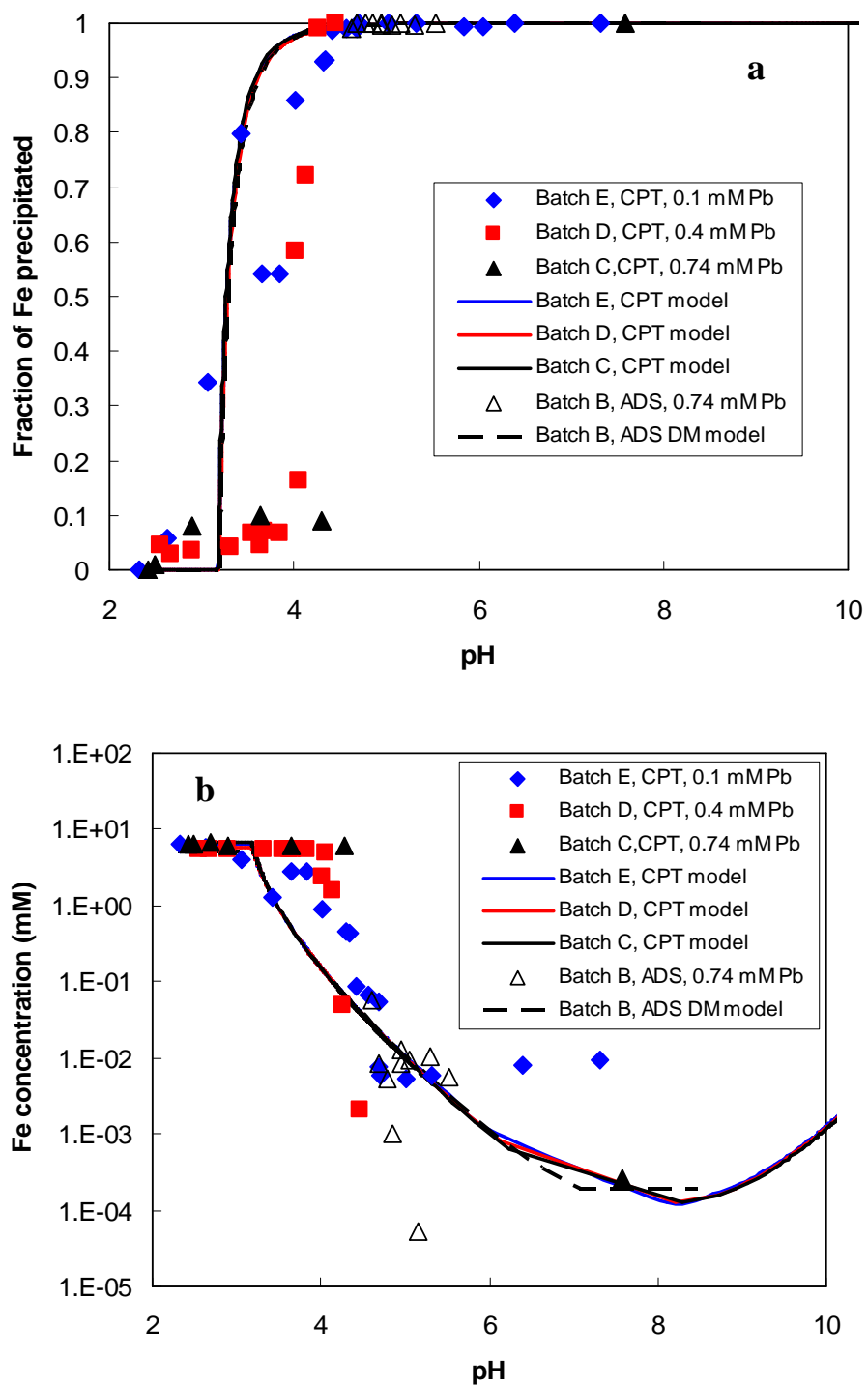


Figure 4. Comparison of Fe^{3+} solubility data (symbols) with modeling calculations (line). The solubility constant for amorphous $\text{Fe}(\text{OH})_3$ was from Wagman et al. (1982). Equilibrium constants of Fe^{3+} hydrolysis were from Nordstrom et al. (1990). Speciation calculation show that $\text{Fe}^{3+}\text{-NO}_3^-$ complexes were not significant during all experiments (equilibrium constant of $\text{Fe}(\text{NO}_3)_2$ from Wagman et al., 1982).

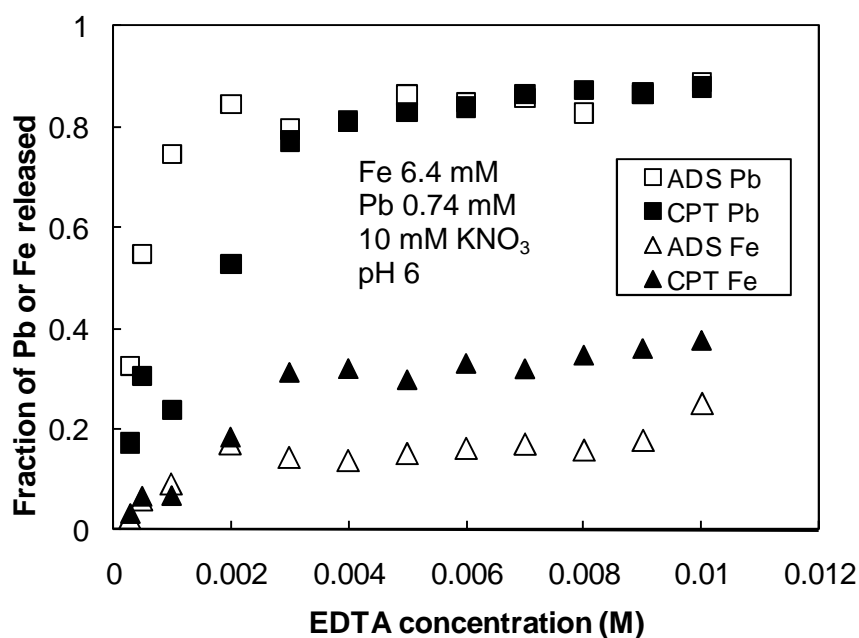


Figure 5. Fraction of Pb extracted after ADS and CPT experiments as a function of different EDTA concentration (room temperature, ~ 22 °C). The contact time is 1 h.

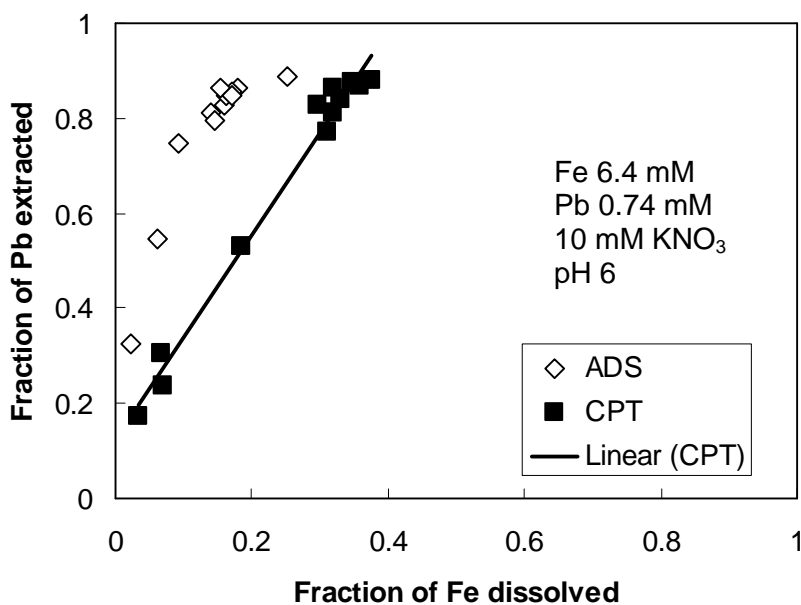


Figure 6. Fraction of Pb extracted as a function of fraction of Fe dissolved contacting with different concentration of EDTA for 1 h (at room temperature, ~ 22 °C). Pb extracted vs. Fe dissolved of coprecipitation precipitates showed a linear relationship, but extraction from adsorption precipitates did not.

3.3. Extraction Experiments after the Sorbents were Aged at High Temperature (60 °C)

Figure 7 shows the results of extraction experiments after the sorbents were aged at 60 °C for 14 days. As shown in the next section, XRD patterns show that the aged sorbents are a mixture of goethite, hematite, and 2LFh. The fractions of Pb desorbed in the ADS case increase parabolically with increasing EDTA concentrations and leveled off at fractions ~0.6. The desorbed Pb^{2+} also increase parabolically with the increasing Fe concentrations (Fig. 7b). These results indicate that Pb^{2+} was mainly associated with the outer layer in the aged solids of ADS.

For aged sorbents from CPT experiments, there are a much weaker correlations between Pb^{2+} concentrations and EDTA or Fe concentrations. One could argue that there is a linear correlation between Pb^{2+} and Fe (Fig. 7b).

Even with increasing EDTA concentrations, about 40-50% of Pb was retained with the CPT solids (residual) after the extraction experiments. This coincides with the level off of dissolved Fe concentrations—crystalline goethite and hematite do not dissolve more in increasingly concentrated EDTA solutions (Fig. 7a). This correlation between Pb and Fe indicates that Pb is incorporated into the hematite and goethite structure (see XRD section below). In the processes of transformation to more ordered structures (e.g., hematite or goethite), part of Pb may be expelled from the inside of the Fe structure and become mobile again. This explains ~50% of Pb was easily to be extracted even at low EDTA concentration (0.0003 M).

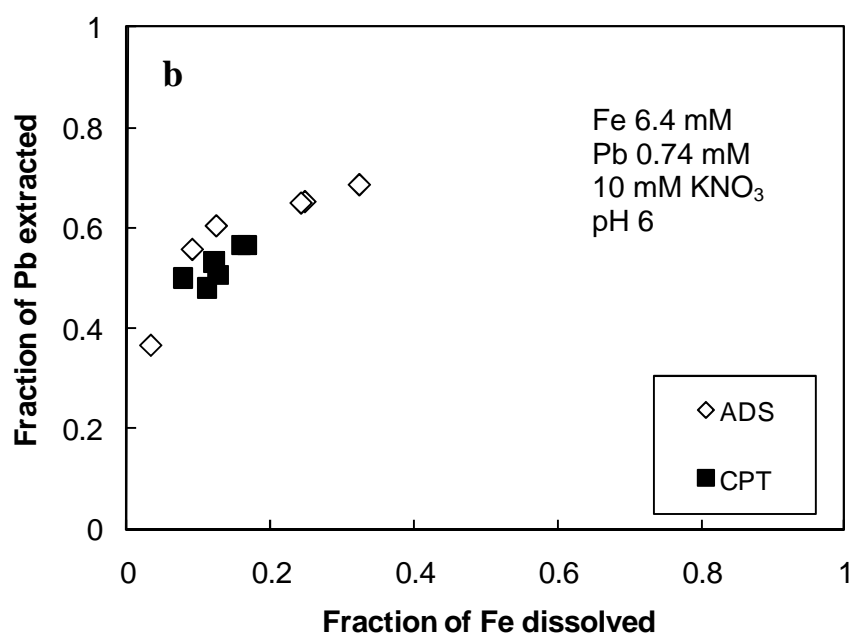
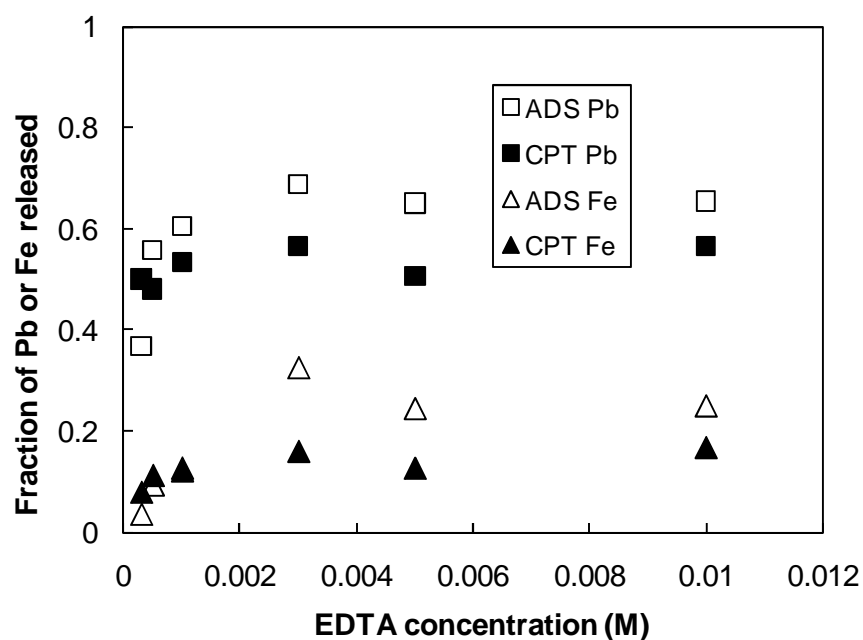


Figure 7. (a) Dissolved Pb and Fe concentrations as a function of EDTA concentrations. The contact time is 1 h. The solids were aged at 60 °C for 14 days before the extraction experiments. XRD patterns show a mixture of 2LFh, hematite, and goethite. (b) Fraction of Pb vs. Fe ifrom the same experiments.

3.4. X-ray Diffraction Data

XRD patterns of precipitates from CPT experiments show a mixture of lepidocrocite and two additional broad peaks at a d -spacing of 0.154 and 0.27 nm, respectively (Fig. 8). These two broad peaks are similar to those of synthetic and natural 2-line ferrihydrite (2LFh, Schwertmann and Cornell, 1996). The formation of lepidocrocite is likely due to the exclusion of CO₂. Lepidocrocite is favored to form in the absence of carbonate. In the presence, however, goethite will form over lepidocrocite (Schwertmann and Taylor, 1972a; Schwertmann and Taylor, 1972b; Schwertmann and Fitzpatrick, 1977; Schwertmann and Cornell, 1991; Cornell and Schwertmann, 1996). Lepidocrocite is relatively metastable with respect to its polymorphous, goethite but the transformation to goethite is extremely slow at ambient temperature (2LFh, Schwertmann and Cornell, 1996). The XRD identifications are consistent with TEM observations (see below).

Ferrihydrite, a common iron oxyhydroxides in waters, sediments, soils, mine wastes and acid mine drainage (Jambor and Dutrizac, 1998), acts as an efficient scavenger for trace metals (including Pb²⁺) and radionuclides (Jambor and Dutrizac, 1998) due to its high specific surface area and reactivity (Dzombak and Morel, 1990; Cornell and Schwertmann, 1996). Ferrihydrite is commonly designed as “two-line” or “six-line” on the basis of the number of poorly defined, broadened maxima observed in X-ray diffraction (XRD) pattern (Cornell and Schwertmann, 1996). However, latest literature suggests the single phase and nanocrystallinity nature of ferrihydrite (Michel et al., 2007a; 2007b). The domain sizes ranged from 2 to 6 nm (Michel et al., 2007a; 2007b), which is consistent with the TEM results of this study (see below).

XRD patterns of precipitates after CPT and ADS experiments aged at 60 °C for 14 d and 95 °C for 24 h were compared with synthesized 2-line ferrihydrite aged at both 95 °C and 22 °C for 24 h (Fig. 9), to investigate the phase transformation of precipitates during aging at hydrothermal conditions. Synthesized 2-line ferrihydrite aged 24 h at 22 °C is shown as a base line. Synthesized 2-line ferrihydrite aged at 95 °C for 24 h shows a significant phase transformation from nano-crystalline ferrihydrite to crystalline goethite and hematite (Figure 9). For solids after CPT and ADS experiments, the transformation from lepidocrocite and/or nano-crystalline ferrihydrite (Figure 8) to goethite and hematite seems to be largely retarded compared with synthesized 2-line ferrihydrite aged at 95 °C (Fig. 9). Goethite formation seems to be suppressed in solids after ADS experiments aged at 60 °C for 14 d and 95 °C for 24 h. The retardation of phase transformation due to the presence of impurity foreign ions at the crystal growth site was also noted in (Walton, 1967). Waychunas et al. (1993) found that the presence of arsenate ions poisoned the surface of precipitating HFO, disrupting the normal crystallization process. Significant amount of nano-crystalline 2-line ferrihydrite remained in precipitates after CPT experiments aged at 60 °C for 14 d (Figure 9) and even more was remained in that of ADS experiments. This may explain the phenomenon that Pb and Fe are easier to be extracted in solids after ADS experiments than in CPT experiments after aging for 14 d at 60 °C (Fig. 7).

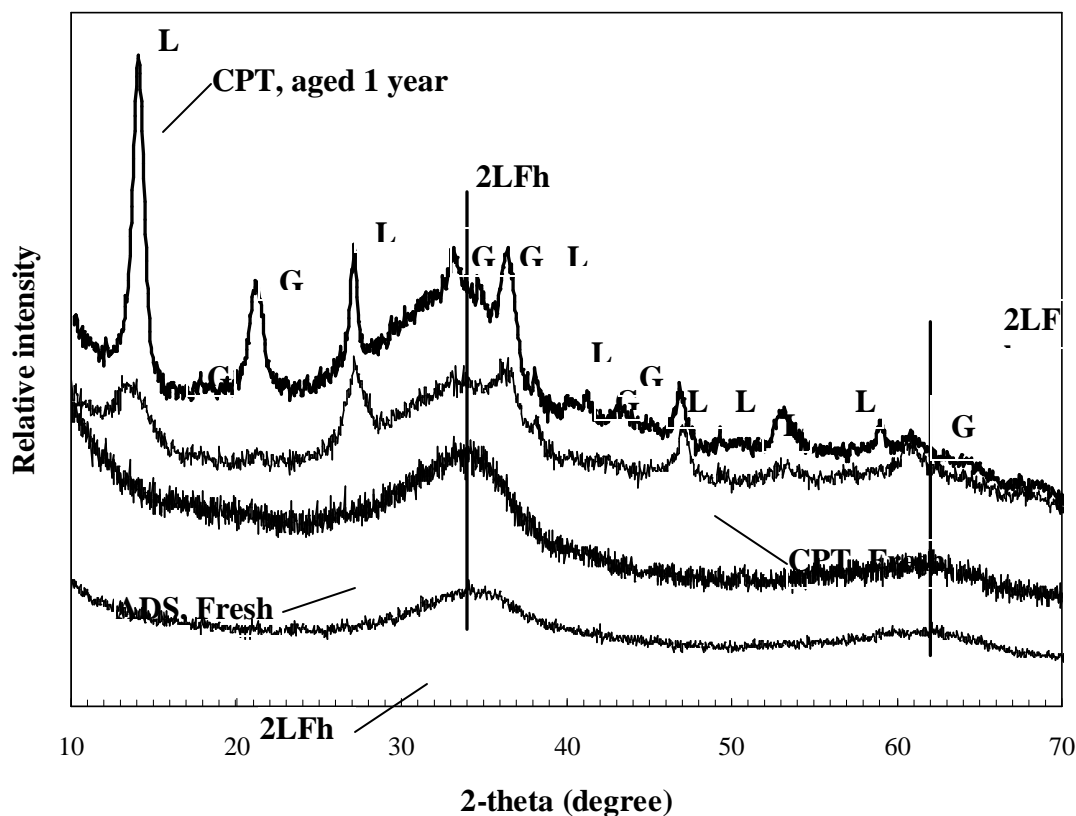


Figure 8. X-ray diffraction spectrum for precipitates after CPT experiments with precipitates after ADS experiments (at 22 °C). Precipitates aged 1 year after CPT experiments were more ordered than freshly precipitated ones. Lepidocrocite (ICDD: 44-1415) and goethite (ICDD: 28-0713) are identified as Fe phases in addition to 2-line ferrihydrite in precipitates after CPT experiments. The XRD pattern of precipitates after ADS experiments are almost entirely amorphous and look similar to that of synthesized 2-line ferrihydrite; no crystalline Fe or Pb phases were observed.

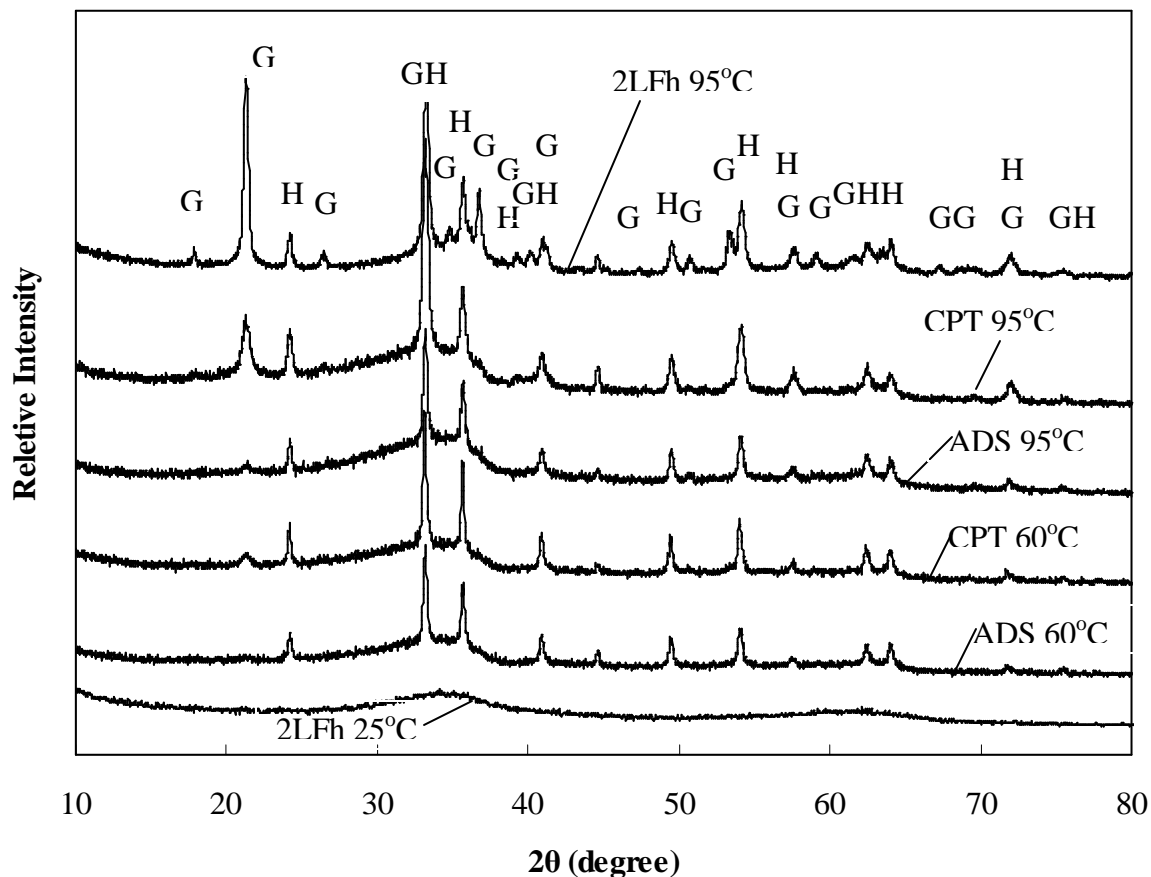


Figure 9. Comparison of precipitates of ADS (aged 24 h at 95 °C or 14 d at 60 °C), CPT (aged 24 h at 95 °C or 14 d at 60 °C), and synthesized 2-line ferrihydrite (aged 24 h at 95 °C). Goethite ($\text{FeO}(\text{OH})$, ICDD 28-0713) and hematite (Fe_2O_3 , ICDD 89-0599) were identified as the main Fe crystalline phases. XRD pattern of synthesized 2-line ferrihydrite aged 24 h at 22 °C was shown as a reference for the position and intensity of amorphous phases.

3.5. High Resolution Transmission and Analytical Electron Microscopy

High-resolution electron microscopy of the solids from CPT experiments (22 °C) shows two types of particles. The first type of particles is spherical, with diameters ranging from 2 to 6 nm; the majority of spheres being about 5 nm in diameter (Figs. 10 and 11). Fast Fourier Transformation (FFT) of the images (inset in Fig. 13) shows several d -spacings, whereas two-line ferrihydrites (2LFh) have mainly two intense rings

(Janney et al., 2000). These TEM results argue for a different structure from 2LFh, or a distorted 2LFh as compared to pure iron 2LFh. Janney et al. (2000) point out that the commonly referred 2LFh include a variety of structures and the structures vary from particle to particle in a sample.

In addition to the small, spherical particles, dendrites or needles are also present. The needles are 8-20 nm across by 200-300 nm long, and are crystalline. High-resolution images show that the needles are composed of multiple domains 2-3 nm across (Fig. 12). FFT analysis of the image shows that the lattice images of these small domains are parallel but slightly offset, suggesting that alignment is the mechanism of aggregation during crystal growth (Banfield et al., 2000; Penn et al., 2001).

No additional phases other than the iron oxyhydroxides mentioned above were found even though we examined many view fields and hundreds of particles. From this, we conclude that mechanical occlusion of fine particles (e.g., PbO , Pb(OH)_2 , PbCO_3) is unlikely a dominant mechanism of coprecipitation in our CPT experiments. It has been suspected that lead hydroxide may form as an artifact of localized high pH in the reactor during titration (Martinez and McBride, 1998b), but TEM data show that this does not occur in our experiments. Theoretical modeling predicted, at high surface coverage, e.g., $> 10\%$, that Pb^{2+} may form a surface precipitate, which resembles to a solid solution (Farley et al., 1985). In our Batch E experiments, the Fe:Pb molar ratio is 1:0.11. When all the Pb^{2+} is sorbed, about 53% of the surface sites are covered with Pb^{2+} , according to the surface site densities recommended by Dzombak and Morel (1990). However, high-resolution lattice images of our samples do not show a distinctly different phase at the edges of the particles (Figs. 11, 12).

STEM/EDX analysis shows that the clusters contain Fe, O, and Pb, with a ratio of Pb to Fe close to that from the mass balance of solution chemistry in the samples examined (Fig. 13a). Over fifty EDX spectrums also showed no Pb-concentrated areas, indicating that the Pb is homogeneously distributed (Fig. 13b). The probe size for the analysis was 0.5 nm at 1 nanoampere of beam current, but the specimen preparation did not completely separate the individual grains and therefore most analyses sampled overlapped particles.

4. GEOCHEMICAL MODELING

We evaluated whether surface complexation models and solid solution models can fit the experimentally measured sorption edges. The geochemical modeling code PHREEQC (Parkhurst and Appello, 1999) was used for the simulation. The standard states for the solids are defined as unit activity for pure solids at the temperature and pressure of interest. The standard state for water is the unit activity of pure water. For aqueous species other than H₂O, the standard state is the unit activity of the species in a hypothetical one molal ideal solution referenced to infinite dilution at the temperature and pressure of interest. Standard states for the surface sites are the unit activity of a completely unsaturated surface at the pressure and temperature of interest and for surface species the unit activity on a completely saturated surface with zero potential with reference to infinite dilution at the P , T of interest (Sverjensky, 2003). The thermodynamic properties used in the simulations are listed in Table 2.

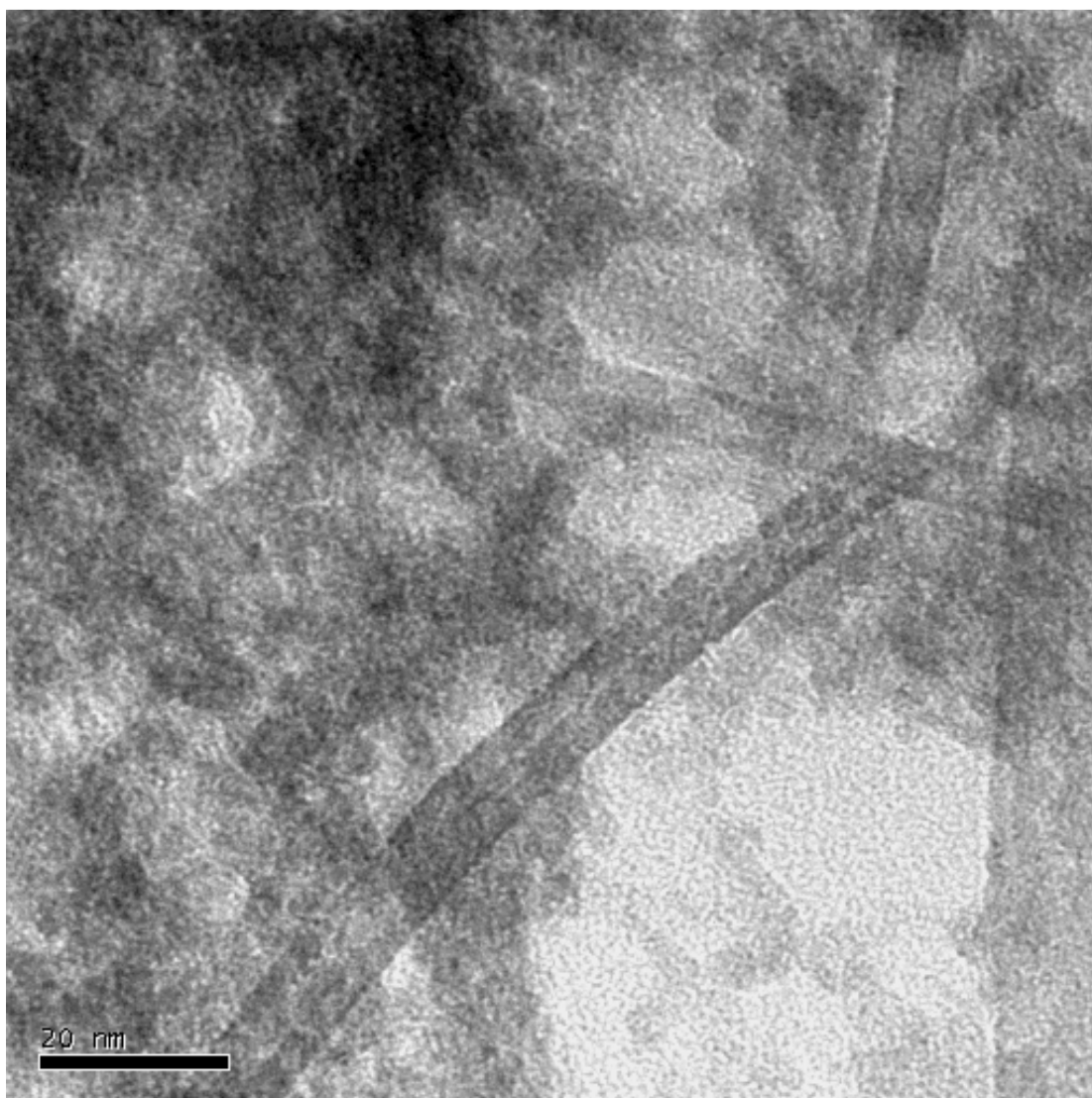


Figure 10. TEM image of Fe^{3+} and Pb^{2+} coprecipitates on holey carbon support. Two types of particles are shown: spherical and needle like.

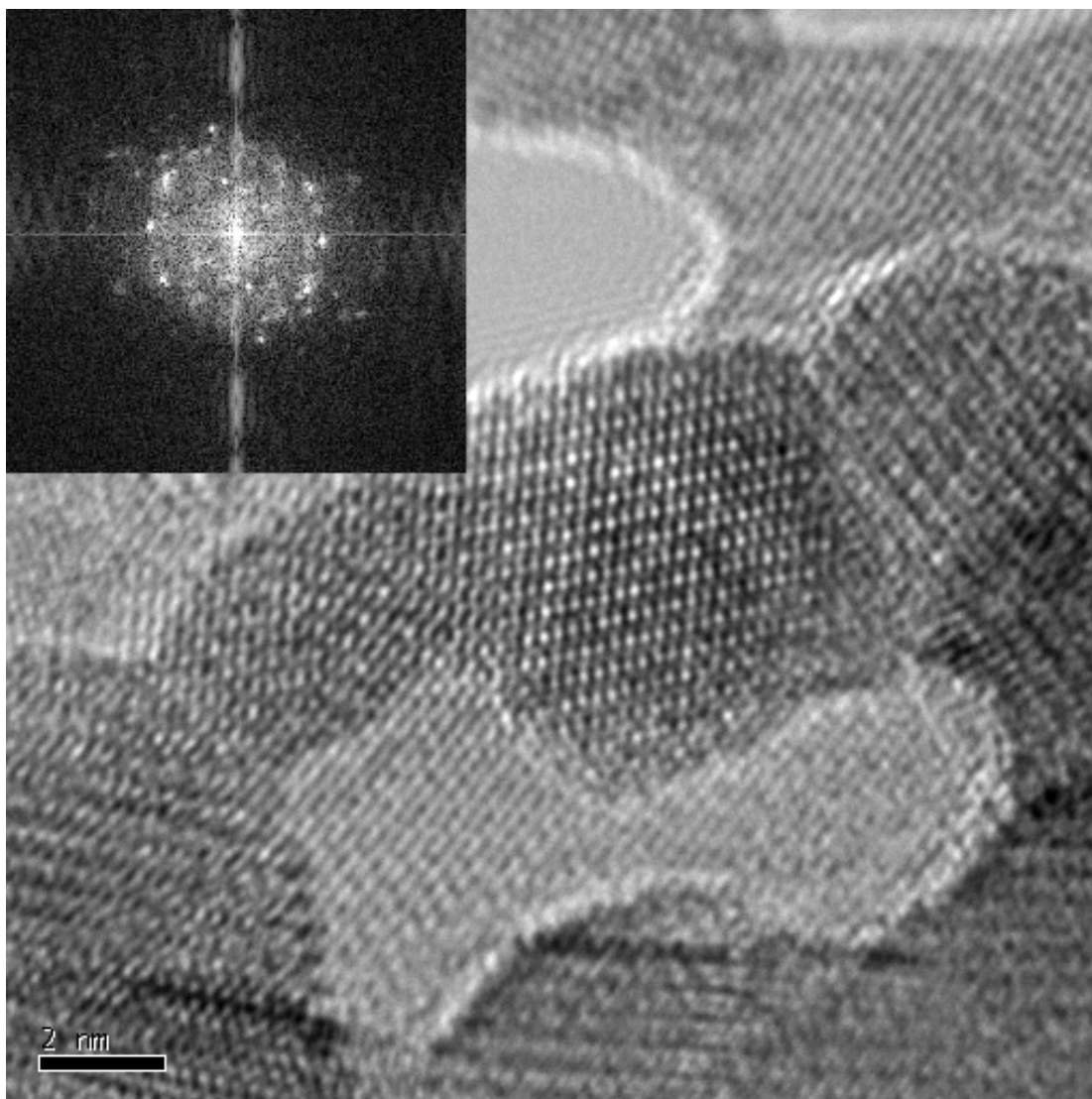


Figure 11a. HRTEM image of Fe^{3+} and Pb^{2+} coprecipitates with spherical shape. Each particle is a well single crystallite. Patterns are lattice images.

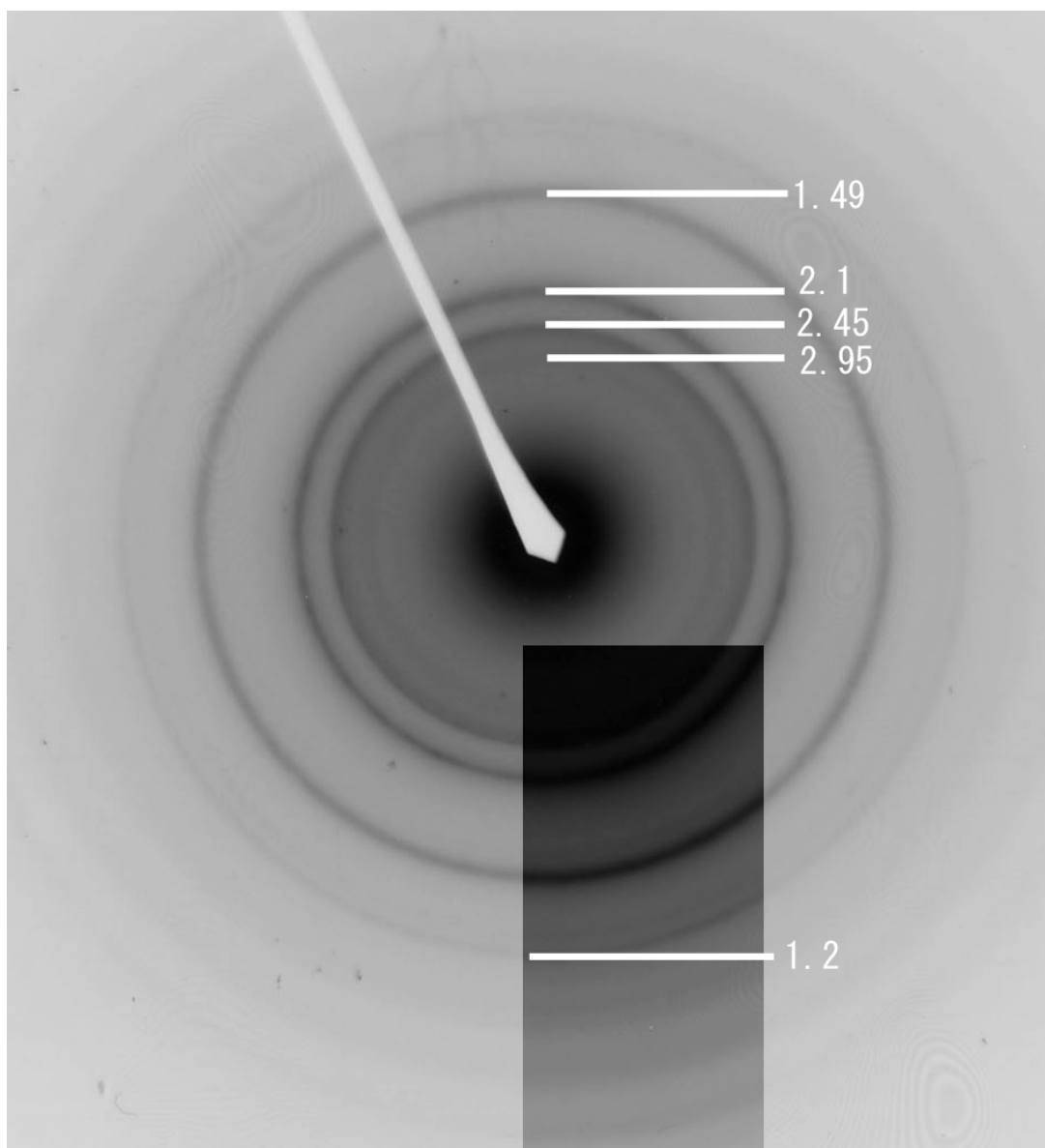


Figure 11b. Selected Area Electron Diffraction (SAED) from iron oxide particles that coprecipitated with Pb.

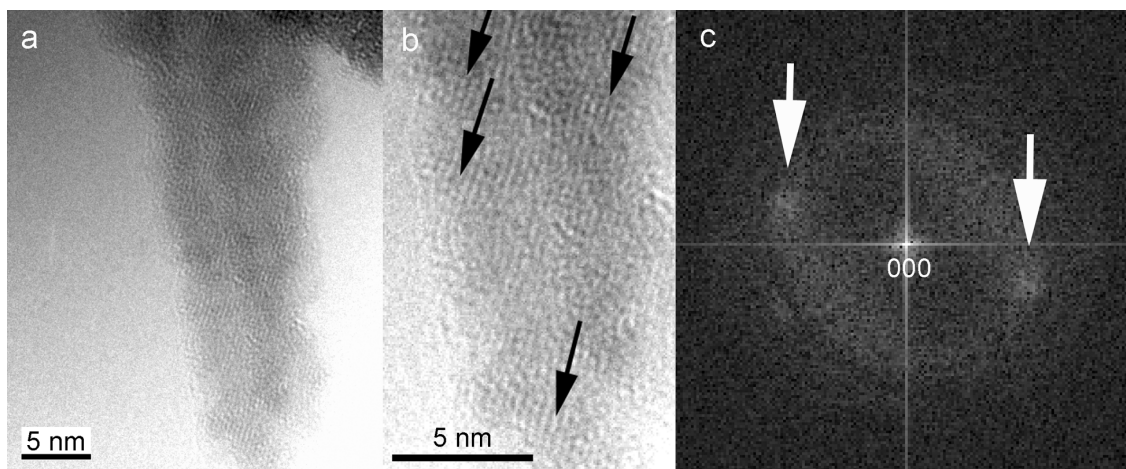
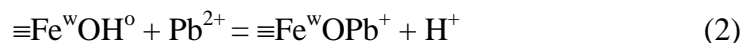
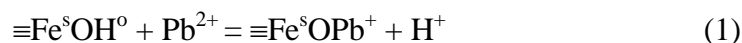


Figure 12. HRTEM image of Fe^{3+} and Pb^{2+} coprecipitates with needle like shape. (a) and (b) HRTEM images. The tip of the needle is composed of domains with a slightly different orientations. Black arrows indicate the orientation of lattice images; and (c) fast Fourier transform (FFT) images of the tip of a Pb-bearing iron-oxyhydroxide needle. The FFT image shows two broad spots (white arrows), suggesting that each small domain has a similar but slightly different orientations.

4.1. Surface Complexation Models

The generalized diffuse layer model (Dzombak and Morel, 1990) were used for modeling surface adsorption in the proposed study. Other electrostatic surface adsorption models have been proposed, e.g., constant capacitance and triple layer models, but all electrostatic models can describe limited experimental sorption data sets (Venema et al., 1996; Westall and Hohl, 1980). Models that use one site type generally require more than one complex species (e.g., Dyer et al., 2003). Dzombak and Morel (1990), in their treatise that provides a consistent theory and a large database of self-consistent surface complexation constants for adsorption on hydrous ferric oxides, reviewed Pb^{2+} adsorption experimental (ADS) data and developed a two-site model for Pb^{2+} adsorption, a "weak" site and a "strong" site, through the reactions:



where the symbol “ \equiv ” denotes the surface site or functional group. Intrinsic surface complexation constants for reactions (1) and (2), derived from systematic evaluation of the ADS data by Dzombak and Morel (1990), and Pb^{2+} hydrolysis constants are listed in Table 2. Other surface properties are listed in Table 3. The generalized diffuse two-layer model fit well our ADS experiment data (Fig. 3). As expected, the SCM predicts shifts of pH sorption edges with different Pb:Fe ratios.

However, the same Dzombak and Morel’s (1990) SCM model grossly underestimated sorption edges measured in the CPT experiments (Fig. 14). Some workers found the need for different, actually stronger binding constants to fit their own adsorption experimental data (Ainsworth et al., 1994; Dyer et al., 2003). Dyer et al. (2003) also developed a triple layer model, in which they used bidentate Pb^{2+} complexes. The increase of the complexation constant values sharpens the sorption edge and lower the concentrations of Pb^{2+} , which will move the sorption edge to a lower pH. As shown below, one hypothesis to explain CPT from ADS is that CPT represents greater binding strength because of multiple surface sites. We tested this hypothesis by increasing the complexation constants for the weak site to the values proposed by Ainsworth et al. (1994) and Dyer et al. (2003). However, the SCM still cannot fit the CPT data.

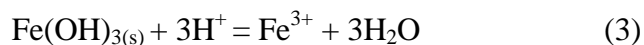
We then increased the site density while keeping a high complexation constant for the weak site. With a higher site density N_{s} (0.9 mol sites/mol Fe versus 0.2 mol sites/mol Fe in the Dzombak and Morel model for weak site and 0.0225 mol sites/mol Fe versus 0.005 mol sites/mol Fe for strong site), the model matches well with our lower

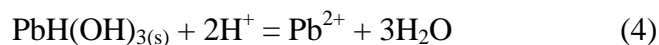
Pb:Fe ratio experiments (batch C and D), but not with the high Pb:Fe ratio experiment (Batch E) (Fig. 14). Dyer et al. (2003) found, from isotherms at pH 5.5 and 6.5, the maximum Pb surface loading is approximately 0.35 – 0.4 mol Pb/mol Fe. Additionally, the assumption of a higher site density in CPT experiment is not consistent with our desorption experimental data, which show less desorption than from CPT sorbents than ADS sorbents at low EDTA concentrations. Therefore, we can conclude that surface complexation alone cannot fit the experimental data well.

4.2. Solid Solution Models

Modeling the coprecipitation as solid solution formation faces the challenge of the lack of knowledge on stoichiometry of the solid solution. The stoichiometry of 2LFh is controversial. Recently, Michel et al. (2007a) proposed a structural formulae of $\text{Fe}_{10}\text{O}_{14}(\text{OH})_2$ and the ideal form contains 20% tetrahedrally and 80% octahedrally coordinated Fe. Our EXFAS work shows that incorporated Pb is mostly octahedrally coordinated. The EXFAS data also show that the much larger ionic radius of Pb^{2+} as compared to that of Fe^{3+} shift the Pb^{2+} octahedra from the Fe octahedra sheet. Amid the lack of solid solution stoichiometry and non-ideality data, it is difficult to fit the experimental data to a solid solution model. Rather, it is more prudent to use solid solution models to examine the characteristics of pH sorption edges if the incorporation mechanism is dominantly solid solution.

For solid solution modeling, it is assumed that the precipitated iron oxyhydroxide has a nominal formula of $\text{Fe}(\text{OH})_{3(\text{am})}$ (Dzombak and Morel, 1990). CPT was modeled as an ideal solid solution. A solid solution model takes the stoichiometry of





Here, we assume that the one-for-one substitution of Pb^{2+} for Fe^{3+} is compensated by an addition of H^+ into the crystalline structure or a replacement of OH^- for O^{2-} (e.g., Waychunas et al., 2002). When a Henrian standard state is defined as hypothetical pure $\text{PbH}(\text{OH})_{3(s)}$ end members of the solid solution with an $\text{Fe}(\text{OH})_{3(\text{am})}$ structure, extrapolated from the infinitely dilute solution regions where Henry's law is obeyed, and a Raoultian standard state remains for the $\text{Fe}(\text{OH})_3$ end member, the activity coefficients for both $\text{Fe}(\text{OH})_3$ and $\text{PbH}(\text{OH})_{3(s)}$ are unity in the dilute solution regions where Henry's law is obeyed for the tracer (Ganguly and Saxena, 1987).

The above solid solution model was used to model our Fe-Pb CPT experiments. The solid solution models successfully predict the Pb^{2+} concentrations in the low pH range ($\text{pH} < 5$) on the concentration – pH diagram (Fig. 2b) but predict more Pb^{2+} partitioned into the solid solution than experimental data at higher pH values (Fig. 2b). The mismatches probably result from above mentioned simplistic assumptions about the solid solution. The real benefit of solid solution modeling is theoretical prediction of invariant pH sorption edges in experiments with different Pb:Fe ratios, regardless of the specific solid solution models.

4.3. Solid Solution versus Surface Complexation Models

The markedly different sorption edges for coprecipitation and adsorption experiments (Fig. 1) call for different mechanisms for interpreting the CPT from that for ADS experiments. We used both surface complexation models and solid solution models to simulate the CPT experiments. Theoretically, the surface complexation models predict that sorption edges for higher Pb:Fe ratios will move to higher pH and the sorption edge

will become flatter; the solid solution model, however, predicts that the sorption edges are invariant with regard to Pb:Fe ratios. Hence, modeling results add macroscopic evidence that the dominant mechanism for Pb^{2+} uptake in the CPT experiments is the formation of Pb-Fe solid solution. However, the two sorption mechanisms—solid solution and surface adsorption—may not be mutually exclusive in CPT experiments. A combination of surface complexation and solid solution models to fit the CPT data has been tried, but the results are almost identical to those of solid solution only that suggests the influence of surface complexation is insignificant.

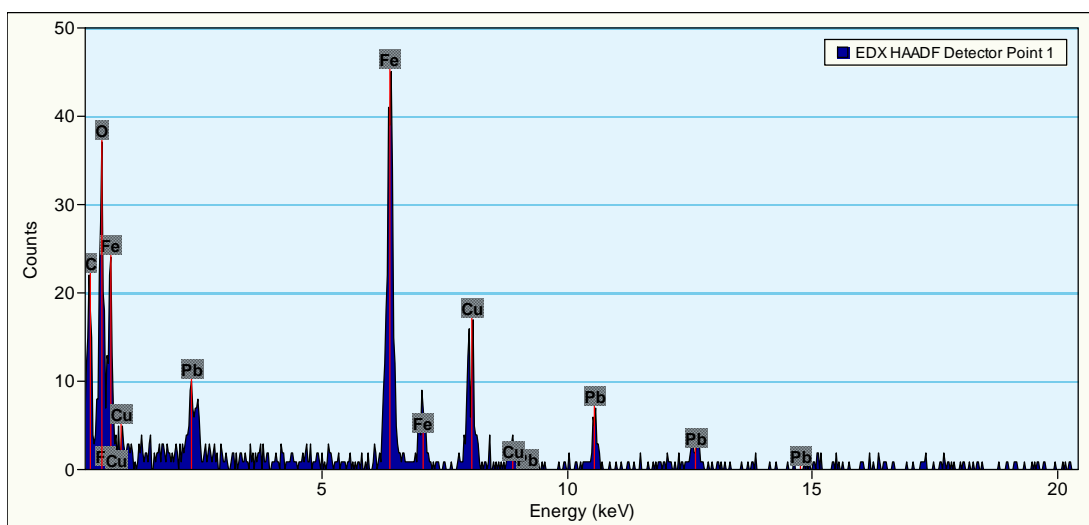


Figure 13a. EDS Spectrum data show that Pb^{2+} is associated in the freshly co-precipitated solids. Cu is from TEM grid, and carbon is used in coating. The spectrum data also show no other chemical constituents in the co-precipitates.

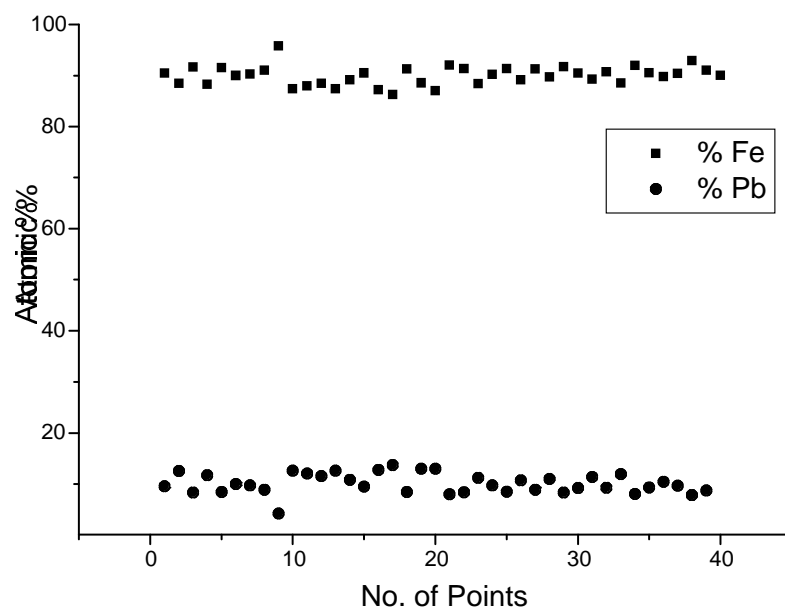


Figure 13b. Fifty measurements for composition analysis by Energy Dispersive X-ray for the ratio of Fe and Pb in atomic %.

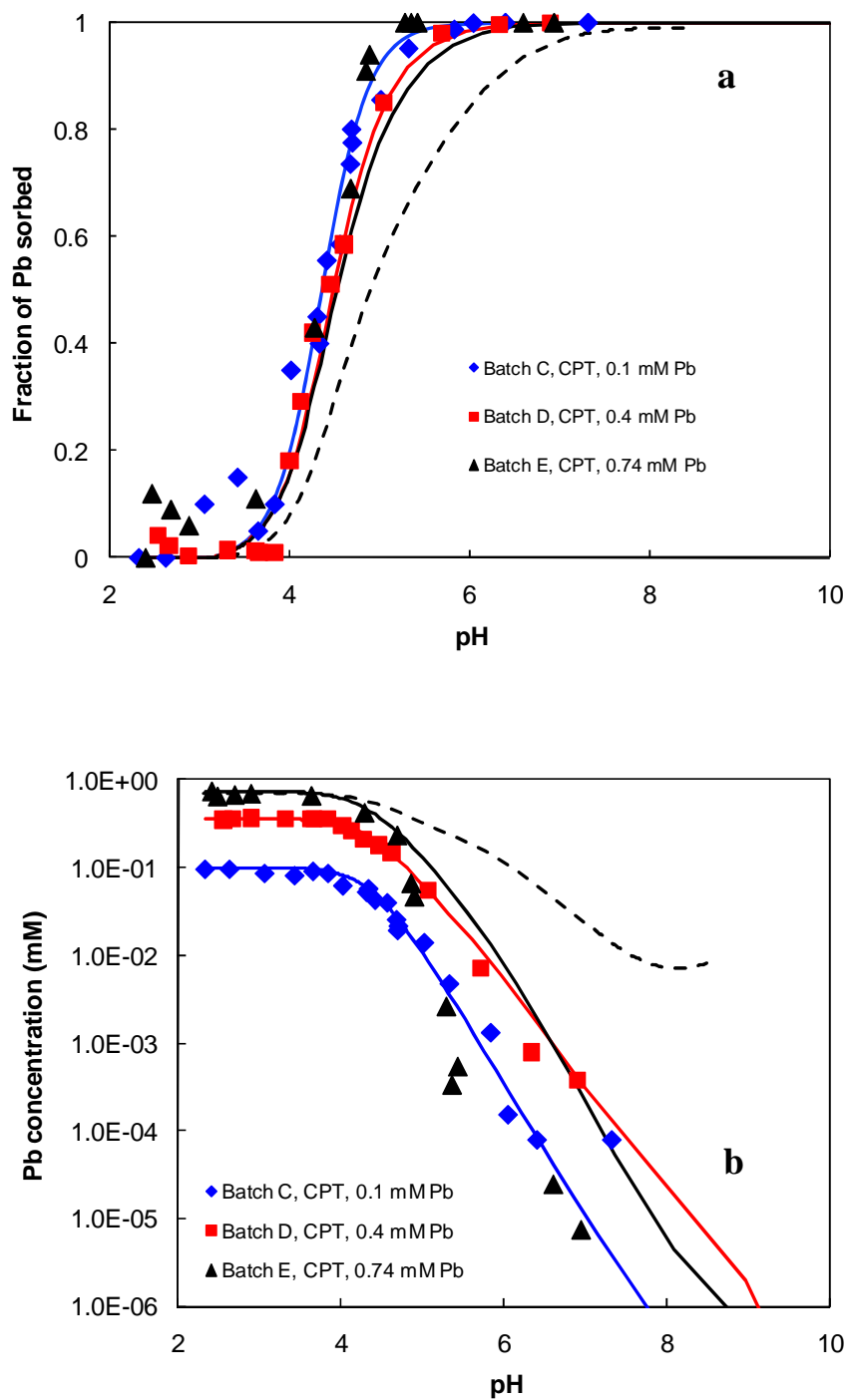


Figure 14. Modeling coprecipitation experiments with surface complexation models. Solid lines are models with site density values of 0.9 mol/mol Fe for weak sites and 0.0225 for strong sites. Dashed lines are model for 0.74 mM Pb for comparison with HFO surface properties from Dzombak and Morel (1990) (0.2 mol/mol Fe for weak sites and 0.005 for strong sites).

Table 2. Equilibrium constants used in modeling

Species	Reactions	Log <i>K</i>	Ref
Aqueous species			
FeOH ⁺⁺	Fe ³⁺ + H ₂ O = FeOH ²⁺ + H ⁺	-2.19	a
Fe(OH) ₂ ⁺	Fe ³⁺ + 2H ₂ O = Fe(OH) ₂ ⁺ + 2H ⁺	-5.67	a
Fe(OH) ₃ [°]	Fe ³⁺ + 3H ₂ O = Fe(OH) ₃ [°] + 3H ⁺	-12.56	a
Fe(OH) ₄ ⁻	Fe ³⁺ + 4H ₂ O = Fe(OH) ₄ ⁻ + 4H ⁺	-21.6	a
Fe ₃ (OH) ₄ ⁵⁺	3Fe ³⁺ + 4H ₂ O = Fe ₃ (OH) ₄ ⁵⁺ + 4H ⁺	-6.3	a
Fe ₂ (OH) ₂ ⁴⁺	2Fe ³⁺ + 2H ₂ O = Fe ₂ (OH) ₂ ⁴⁺ + 2H ⁺	-2.95	a
PbNO ₃ ⁺	Pb ²⁺ + NO ₃ ⁻ = PbNO ₃ ⁺	1.17	d
PbOH ⁺	Pb ²⁺ + H ₂ O = PbOH ⁺ + H ⁺	-7.71	d
Pb ₂ OH ³⁺	2Pb ²⁺ + H ₂ O = Pb ₂ OH ³⁺ + H ⁺	-6.36	d
Pb(OH) ₂ [°]	Pb ²⁺ + 2H ₂ O = Pb(OH) ₂ [°] + 2H ⁺	-17.12	d
Pb(OH) ₃ ⁻	Pb ²⁺ + 3H ₂ O = Pb(OH) ₃ ⁻ + 3H ⁺	-28.06	d
Pb(OH) ₄ ²⁻	Pb ²⁺ + 4H ₂ O = Pb(OH) ₄ ²⁻ + 4H ⁺	-39.70	d
Surface species			
Hfo_wOH ₂ ⁺	Hfo_wOH + H ⁺ = Hfo_wOH ₂ ⁺	7.29	b
Hfo_wO ⁻	Hfo_wOH = Hfo_wO ⁻ + H ⁺	-8.93	b
Hfo_sOPb ⁺	Hfo_sOH + Pb ²⁺ = Hfo_sOPb ⁺ + H ⁺	4.65	b
Hfo_wOPb ⁺	Hfo_wOH + Pb ²⁺ = Hfo_wOPb ⁺ + H ⁺	0.3/1.23 [†]	b
Hfo_wOH ₂ ⁺	Hfo_wOH + H ⁺ = Hfo_wOH ₂ ⁺	6.43	g
Hfo_wO ⁻	Hfo_wOH = Hfo_wO ⁻ + H ⁺	-9.75	g
Hfo_sOPb ⁺	Hfo_sOH + Pb ²⁺ = Hfo_sOPb ⁺ + H ⁺	2.5	g
Hfo_wOPb ⁺	Hfo_wOH + Pb ²⁺ = Hfo_wOPb ⁺ + H ⁺	1.0	g
Solid species			
Pb(OH) _{2(c)}	Pb(OH) ₂ + 2H ⁺ = Pb ²⁺ + 2H ₂ O	8.15	d
Fe(OH) _{3(a)}	Fe(OH) _{3(a)} + 3H ⁺ = Fe ³⁺ + 3H ₂ O	5.6	c
[§] PbH(OH) _{3(s)}	PbH(OH) ₂ + 2H ⁺ = Pb ²⁺ + 3H ₂ O	6.33	e

a: Nordstrom et al. (1990); b: Dzombak and Morel (1990); c: Wagman et al. (1982). d: Ball and Nordstrom (1991); e: retrieved from experimental data in this study. g: Dyer et al. (2003). [§] Solid solution components. [†] Ainsworth et al. (1994)

Table 3. Surface properties for HFO used in this study

Properties		Values		
Site density (mol/mol Fe)				
N_s	weak (w)	0.2 ^a	0.9 ^b	0.2 ^c
	strong (s)	0.005 ^a	0.005 ^b	0.005 ^c
Surface area (m ² /g)		600 ^a	600 ^b	600 ^c
Mol wt (g/mol)		89 ^a	89 ^b	89 ^c

^aDzombak and Morel (1990); ^bDyer et al. (2003); ^cThis study.

5. DISCUSSION AND CONCLUSIONS

5.1. Hypotheses of Coprecipitation

Laboratory studies have shown that for some systems macroscopic sorption behaviors (including pH-dependent sorption edges and extent of uptake) differ if the contact method is CPT versus ADS (Charlet and Manceau, 1992; Crawford et al., 1993; Karthikeyan et al., 1997; Karthikeyan and elloitt, 1999; Waychunas et al., 1993). The differences or similarities are often assumed to be caused by the atomic environment of the trace metal upon sorption to the host material. Different mechanistic explanations have been offered:

(1) CPT represents enhanced surface area or site availability (Corey, 1981; Crawford et al., 1993; Karthikeyan et al., 1997). The nature of the sorbed metal-(O,OH)-Fe bonds appear to be the same on the two substrates prepared with ADS and CPT methods;

(2) CPT represents a greater binding strength (having multiple surface site types) over a simple precipitate surface (ADS having a single surface type) (Crawford et al., 1993; Taylor, 1973); and

(3) CPT represents solid solution formation by heavy metals incorporation into the hydrous oxide lattice (Karthikeyan et al., 1997; Martinez and McBride, 1998).

In our companion study of EXAFS on solids collected from the same experiments, Kelly et al. (2008) showed that Pb formed a solid solution in the Pb-Fe coprecipitate. Our conclusion was based on the co-refinement of the Pb L_{III}-edge and the Fe K-edge EXAFS spectra with the same local atomic environment. The larger atomic size of Pb as compared to Fe was accounted for in the model of the FeO₆ sheet structure by displacing the PbO₆ unit perpendicular to the sheet by 0.30 ± 0.02 Å from the FeO₆ unit position.

In previous studies, Crawford et al. (1993) showed with their calculation (their Figure 8) that the increase in effective surface area would need to be at least one order of magnitude larger to account for the increase removal profile by CPT method. Their calculations weakened the assumption of enhanced surface area or site availability to be the mechanism of the difference between CPT and ADS. Laxen (1985) and Waychunas et al. (1993) suggested CPT increased adsorption site density of that of ADS. However, our desorption experiments contradict to this hypothesis in explaining our experiments.

Recent studies favored the third explanation (solid solution formation) as the CPT mechanism. Charlet and Manceau (1992) employed extended X-ray adsorption fine-structure spectroscopy (EXAFS) to demonstrate that in CPT Cr(III) atoms are incorporated into the HFO matrix so that a solid solution, Fe_{0.99}Cr_{0.01}OOH(s), forms with different structure and solubility than either pure Cr(OH)₃(s) or Cr ADS with HFO. Spadini et al. (1994) proposed the formation of a mixed phase [α -(Cd_{0.005}Fe_{0.995})OOH] using EXAFS when Cd²⁺ was CPT with goethite. Karthikeyan et al. (1997) suggested

some Cu substituted into the HFO lattice because more Cu was incorporated internal to HFO flocs during CPT than during ADS.

Whether or not CPT and ADS may represent more permanent sequestration of toxic metals in from the environment is an important question. Commonly, ferrihydrite is the first phase to be precipitated from an aqueous Fe^{3+} solution. Ferrihydrite is poorly ordered and metastable. Over time, ferrihydrite is transformed to more ordered phases (e.g., goethite and hematite) (Cornell and Schwertmann, 1996). This transformation can lead to structural incorporation of the trace metals, resulting in irreversible sorption also called desorption hysteresis (Cornell, 1988; Cornell, 1991; Cornell et al., 1992; Ebinger and Schulze, 1990; Kumar et al., 1990). A study by Ainsworth et al. (1994) suggested Cd^{2+} incorporation into the recrystallizing HFO structure after long reaction times and transformation to goethite.

5.2. A Hypothesis for Pb-Fe Coprecipitation Mechanism

There is little ambiguity that coprecipitation and adsorption contact methods have produced different Pb^{2+} uptake mechanisms by nano-particles of iron oxyhydroxides. Multiple lines of evidence provided above point to that the predominant mechanism for Pb-Fe coprecipitation is solid solution formation. Our HRTEM observations have conclusively ruled out the presence of segregated high Pb concentration phases either inside the iron oxyhydroxide phases or at the edges or surfaces of these phases at the time of examination. HRTEM observations also show that Fe^{3+} first precipitated out as nano-particles of 2 – 3 nm in diameter at pH around 3-4. At one pH unit higher (~4), Pb^{2+} started to be adsorbed onto these nano-particles. The initial adsorption explains the pH

lag for Fe^{3+} (Fig. 4) and Pb^{2+} (Fig. 1 and 2) removal from the aqueous solution, and the coincidence of sorption pH around 4 for both CPT and ADS experiments. The access to the smaller incipient particles during the CPT experiments explain the more efficient removal of Pb^{2+} in CPT experiments than the ADS contact methods.

HRTEM shows that a coalescence process occurred shortly after, and the 2-3 nm domains assembled to form larger particles of lepidocrocite and 2-line ferrihydrite. During the coalescence process, Pb^{2+} was trapped within the iron oxyhydroxide structures and formed Pb-Fe solid solutions. The formation of solid solutions must have occurred < 24 h because the CPT pH sorption edges measured after 24 h show invariance regarding sorbate/sorbent ratios, a characteristics of solid solution as the sorption mechanism but not surface complexation mechanisms from the theoretical point of view. Desorption experiment data on the Pb-loaded precipitates from CPT and ADS showed most sorbed Pb^{2+} onto ADS sorbents was desorbed in dilute EDTA solutions while only a small percentage was desorbed from CPT sorbents. All these macroscopic chemistry data—and they are far more abundant and cover a wide range of conditions than molecular information obtained with HRTEM and EXFAS—conform to the EXFAS data that Pb-Fe formed a solid solution in Pb-Fe CPT experiments. EXAFS data show that the much larger Pb^{2+} ionic radius result in PbO_6 octahedra protruding 0.30 Å perpendicular to the FeO_6 sheet.

After Pb^{2+} -loaded sorbents from CPT and ADS experiments were aged for 14 days at 60 °C and 24 h at 90 °C, the sorbents from both ADS and CPT were transformed into goethite and hematite. Compared with control experiments on Pb-free 2LFh, the transformation was retarded. Desorption experiments show that more loaded Pb^{2+} was

permanently incorporated into goethite and hematite structures in CPT sorbents than ADS sorbents, although both solids sequestered about 30-50% loaded Pb^{2+} . These results are generally consistent with previous aging studies of Pb^{2+} adsorption onto hydrous ferric oxides (HFO) (Ainsworth et al., 1994) and co-precipitated with HFO (Ford et al., 1997). Previous work attributed these retained metals to either structural incorporation in the more crystalline phases or formation of aggregate phase (Ford et al., 1997; Karthikeyan et al., 1997). Our TEM conclusively show that there are no segregated phases. Our data suggest that CPT contact methods result in more permanent removal of Pb^{2+} by iron oxyhydroxides in the environment.

REFERENCES

- Ainsworth, C. C., Pilon, J. L., Gassman, P. L., and Van Der Sluys, W. G., 1994. Cobalt, cadmium, and lead sorption to hydrous iron oxides: Residence time effect. *Soil Sci. Soc. Am.* **58**, 1615-1623.
- Anderson, G. M. and Crerar, D. A., 1993. Thermodynamics in Geochemistry--The Equilibrium Model. Oxford University Press, New York.
- Balistrieri, L. S. and Murray, J. W., 1982. The adsorption of Cu, Pb, Zn, and Cd on goethite from major ion seawater. *Geochim. Cosmochim. Acta* **46**, 1253-1265.
- Ball, J. W. and Nordstrom, D. K., 1991. User's manual for WATEQ4F, with revised thermodynamic data base and test cases for calculating speciation of major, trace, and redox elements in natural waters. U.S. Geological Survey Open File Report 91-183.
- Banfield, J. F., Welch, S. A., Zhang, H., Ebert, T. T., and Penn, R. L., 2000. Aggregation-based crystal growth and microstructure development in natural iron oxyhydroxide biomineralization products. *Science* **289**, 751-754.
- Cederberg, G. A., Leckie, J. O., and Street, R. L., 1985. A groundwater mass transport and equilibrium chemistry model for multicomponent systems. *Water Resour. Res.* **21**, 1095-1104.

- Charlet, L. and Manceau, A., 1992. X-ray absorption spectroscopic study of the sorption of Cr(III) at the oxide water interface .2. Adsorption, coprecipitation, and surface precipitation on hydrous ferric-oxide. *J. Colloid Interf. Sci.* **148**, 443-470.
- Corey, R. B., 1981. Adsorption vs. precipitation. In: Anderson, M. A. and Rubin, A. J. Eds.), *Adsorption of inorganics at solid-liquid interfaces*. Ann Arbor, MI: Annals of Arbor Science Publisher. pp. 161-182.
- Cornell, R. M., 1988. The influence of some divalent cations on the transformation of ferrihydrite to more crystalline products. *Clay Miner.* **23**, 329-332.
- Cornell, R. M., 1991. Simultaneous incorporation of Mn, Ni and Co in the goethite (alpha-FeOOH) structure. *Clay Miner.* **26**, 427-430.
- Cornell, R. M., Schneider, W., and Giovanoli, R., 1992. The effect of nickel on the conversion of amorphous iron(III) hydroxide into more crystalline iron oxides in alkaline media. *J. Chem. Technol. Biot.* **53**, 73-79.
- Cornell, R. M. and Schwertmann, U., 1996. The Iron Oxides: Structures, Properties, Reactions, Occurrence and Uses. VCH, Inc., New York.
- Crawford, R. J., Harding, I. H., and Mainwaring, D. E., 1993. Adsorption and coprecipitation of single heavy metal ions onto the hydrated oxides of iron and chromium. *Langmuir* **9**, 3035-3056.
- Davis, J. A. and Kent, D. B., 1990. Surface complexation modeling in aqueous geochemistry In: Hochella, M.F., White, A.F. (Eds.) *Mineral-Water Interface Geochemistry* **23**, 177-260.
- Dyer, J. A., Triverdi, P., Scrivner, N. C., and Sparks, D. L., 2003. Lead sorption onto ferrihydrite. 2. Surface complexation modeling. *Environ. Sci. Technol.* **37**, 915-922.
- Dzombak, D. A. and Morel, F. M. M., 1990. *Surface Complexation Modeling: Hydrous Ferric Oxide*. John Wiley & Sons, New York.
- Ebinger, M. H. and Schulze, D. G., 1990. The influence of pH on the synthesis of mixed Fe-Mn oxide minerals. *Clay Miner.* **25**, 507-518.
- Farley, K. J., Dzombak, D. A., and Morel, F. M. M., 1985. A surface precipitation model for the sorption of cations on metal oxides. *J. Colloid Interf. Sci.* **106**, 226-242.
- Ford, R., Bertsch, P. M., and Farley, K. J., 1997. Changes in transition and heavy metal partitioning during hydrous iron oxide aging. *Environ. Sci. Technol.* **31**, 2028-2033.

- Ford, R. T., Kemner, K. M., and Bertsch, P. M., 1999. Influence of sorbate-sorbent interactions on the crystallization kinetics of nickel- and lead-ferrihydrite coprecipitates. *Geochim. Cosmochim. Acta* **63**, 39-48.
- Gadde, R. R. and Laitinen, H. A., 1973. Study of the sorption of lead by hydrous ferric oxide. *Environ. Lett.* **5**, 223-235.
- Ganguly, J. and Saxena, S. K., 1987. *Mixtures and Mineral Reactions*. Springer-Verlag.
- Hayes, K. F. and Leckie, J. O., 1986. Mechanism of lead ion adsorption at the goethite-water interface. In: Davis, J. A. and Hayes, K. F. (Eds.), *Geochemical Processes at Mineral Surfaces*. Proc. Am. Chem. Soc. Symp. Ser. 323, ACS, Washington, DC, pp. 114-141.
- Jambor, J. L. and Dutrizac, J. E., 1998. Occurrence and constitution of natural and synthetic ferrihydrite, a widespread iron oxyhydroxide. *Chem. Rev.* **98**, 2549-2586.
- Janney, D. E., Cowley, J. M., and Buseck, P. R., 2000. Structure of synthetic 2-line ferrihydrite by electron nanodiffraction. *Am. Mineral.* **85**, 1180-1187.
- Jenne, E. A., 1968. Controls on Mn, Co, Ni, Cu, and Zn concentrations in soils and water: the significant role of hydrous Mn and Fe oxides. In: Baker, R. A. (Ed.), *Trace Inorganic in Water*. American Chemical Society, Washington DC.
- Karthikeyan, K. G., Elliott, H. A., and Cannon, F. S., 1997. Adsorption and coprecipitation of copper with the hydrous oxides of iron and aluminum. *Environ. Sci. Technol.* **31**, 2721-2725.
- Karthikeyan, K. G. and Elloitt, H. A., 1999. Surface complexation modeling of copper sorption by hydrous oxides of iron and aluminum. *J. Colloid Interf. Sci.* **220**, 88-95.
- Karthikeyan, K. G., Elloitt, H. A., and Chorover, J., 1999. Role of surface precipitation in copper sorption by the hydrous oxides of iron and aluminum. *J. Colloid Interf. Sci.* **209**, 72-78.
- Kelly, S., Lu, P., Bolin, T., Chattopadhyay, S., Newville, M. G., Shibata, T., and Zhu, C. (2008) Molecular structure of lead(II) coprecipitated with iron(III) oxyhydroxide, in: Barnett, M. and Kent D. (Eds.) *Adsorption of Metals by Geomedia II: Variables, Mechanisms, and Model Applications* Elsevier Science, pp. 67-94.
- Kinniburgh, D. G., Jackson, M. L., and Syers, J. K., 1976. Adsorption of Alkaline Earth, Transition, and Heavy Metal Cations by Hydrous Oxide Gels of Iron and Aluminum. *Soil Sci. Soc. Am.* **40**, 796-799.
- Krauskopf, K. B., 1956. Factors controlling the concentrations of thirteen rare metals in seawater. *Geochim. Cosmochim. Acta* **9**, 1-32.

- Kumar, R., Ray, R. K., and Biswas, A. K., 1990. Physico-chemical nature and leaching behaviour of goethites containing Ni, Co and Cu in the sorption and coprecipitation mode. *Hydrometallurgy* **25**, 61-83.
- Lützenkirchen, J., 1997. Ionic strength effects on cation sorption to oxides: Macroscopic observations and their significance in microscopic interpretation. *J. Colloid Interf. Sci.* **195**, 149-155.
- Manceau, A. and Drits, V. A., 1993. Local structure of ferrihydrite and ferroxhyte by EXAFS spectroscopy. *Clay Clay Miner.* **28**, 165-184.
- Martinez, C. E. and McBride, M. B., 1998. Solubility of Cd^{2+} , Cu^{2+} , Pb^{2+} , and Zn^{2+} in aged coprecipitates with amorphous iron hydroxides. *Environ. Sci. Technol.* **32**, 743-748.
- Martinez, C. E. and McBride, M. B., 2001. Cd, Cu, Pb, and Zn coprecipitation in Fe oxide formed at different pH: Aging effects on metal solubility and extractability by citrate. *Environ. Toxicol. Chem.* **20**, 122-126.
- Michel, F. M., Ehm, L., Antao, S. M., Lee, P. L., Chupas, P. J., Liu, G., Strongin, D. R., Schoonen, M. A. A., Phillips, B. L., and Parise, J. B., 2007a. The structure of ferrihydrite, a nanocrystalline material. *Science* **316**, 1726-1729.
- Michel, F. M., Ehm, L., Liu, G., Han, W. Q., Antao, S. M., Chupas, P. J., Lee, P. L., Knorr, K., Eulert, H., Kim, J., Grey, C. P., Celestian, A. J., Gillow, J., Schoonen, M. A. A., Strongin, D. R., and Parise, J. B., 2007b. Similarities in 2- and 6-line ferrihydrite based on pair distribution function analysis of X-ray total scattering. *Chem. Mater.* **19**, 1489-1496.
- Nordstrom, D. K., Plummer, L. N., Langmuir, D., Busenberg, E., May, H. M., Jones, B., and Parkhurst, D. L., 1990. Revised chemical equilibrium data for major water-mineral reactions and their limitations. In: Melchior, D. C. and Bassett, R. L. (Eds.), *Chemical Modeling of Aqueous Systems II*. American Chemical Society.
- Lin-Fu, J. 1992. Modern history of lead poisoning: a century of discovery and rediscovery. In: Needleman, H. (Ed.), *Human Lead Exposure*. CRC Press, Boca Raton.
- Parkhurst, D. L. and Appello, A. A. J., 1999. User's Guide to PHREEQC (version 2) -- A Computer Program for Speciation, Batch-Reaction, One-Dimensional Transport, and Inverse Geochemical Calculations. U.S. Geological Survey, Water-resource investigation report, pp. 99-4259.
- Penn, R. L., Zhu, C., Xu, H., and Veblen, D. R., 2001. Iron oxide coatings on sand grains from the Atlantic coastal plain: High-resolution transmission electron microscopy characterization. *Geology* **29**, 843-846.

- Rose, A. W. and Bianchi-Mosquera, G. C., 1993. Adsorption of Cu, Pb, Zn, Co, Ni, and Ag on goethite and hematite; a control on metal mobilization from red beds into stratiform copper deposits. *Econ. Geol.* **88**, 1226-1236.
- Schroth, J., 1994. Unipure technology removes heavy-metals from waste-water. *Hazardous Waste Cons.* **12**, A33-34.
- Schultz, M. F., Benjamin, M. M., and Ferguson, J. F., 1987. Adsorption and desorption of metals on ferrihydrite: Reversibility of the reaction and sorption properties of the regenerated solid. *Environ. Sci. Technol.* **21**, 863-869.
- Schwertmann, U. and Cornell, R. M., 1991. Iron oxides in the laboratory: preparation and characterization. VCH, New York.
- Schwertmann, U. and Fitzpatrick, R. W., 1977. Occurrence of lepidocrocite and its association with goethite in Natal soils. *Soil Sci. Soc. Am. J.* **41**, 1013-1018.
- Schwertmann, U. and Taylor, R. M., 1972a. The influence of silicate on the transformation of lepidocrocite to goethite. *Clay Clay Miner.* **20**, 159-164.
- Schwertmann, U. and Taylor, R. M., 1972b. Transformation of lepidocrocite to goethite. *Clay Clay Miner.* **20**, 151-158.
- Sposito, G., 1984. The Surface Chemistry of Soils. Oxford University Press, New York.
- Sverjensky, D. A., 2003. Standard states for the activities of mineral surface sites and species. *Geochim. Cosmochim. Acta* **67**, 17-28.
- Swallow, K. C., Hume, D. N., and Morel, F. M. M., 1980. Sorption of copper and lead by hydrous ferric oxides. *Environ. Sci. Technol.* **14**, 1326-1331.
- Taylor, H. F. W., 1973. Crystal structure of some double hydroxide minerals. *Miner. Mag.* **39**, 377-389.
- Trivedi, P., Dyer, J. A., and Sparks, D. L., 2003. Lead sorption onto ferrihydrite. 1. A macroscopic and spectroscopic assessment. *Environ. Sci. Technol.* **37**, 908-914.
- Venema, P., Hiemstra, T., and van Riemsdijk, W. H., 1996. Comparison of different site binding models for cation sorption: Description of pH dependency, salt dependency, and cation-proton exchange. *J. Colloid Interf. Sci.* **181**, 45-59.
- Wagman, D. D., Evans, W. H., Parker, V. B., Schumm, R. H., Halow, I., Bailey, S. M., Churney, K. L., and Nuttall, R. L., 1982. The NBS tables of chemical thermodynamic properties: Selected values for inorganic and Cl and C2 substances in SI units. *J. Phys. Chem. Ref. Data* **11**, Supplement No. 2.

- Walton, A. G., 1967. *The Formation and Properties of Precipitates*. Wiley, New York, 44 p.
- Waychunas, G. A., Fuller, C. C., and Davis, J. A., 2002. Surface complexation and precipitation geometry for aqueous Zn(II) sorption on ferrihydrite I: X-ray absorption extended fine structure spectroscopy analysis. *Geochim. Cosmochim. Acta* **66**, 1119-1137.
- Waychunas, G. A., Rea, B. A., Fuller, C. C., and Davis, J. A., 1993. Surface chemistry of ferrihydrite: Part 1. EXAFS studies of the geometry of coprecipitated and adsorbed arsenate. *Geochim. Cosmochim. Acta* **57**, 2251-2269.
- Westall, J. C. and Hohl, H., 1980. A comparison of electrostatic models for the oxide/solution interface. *Adv. Colloid Interface Sci* **12**, 265-294.

CHAPTER 9

FUTURE WORK

COUPLED PLAGIOCLASE DISSOLUTION AND SECONDARY MINERAL PRECIPITATION IN SUPERCRITICAL CO₂ SATURATED SOLUTIONS

1. Introduction

Injection of CO₂ into deep geological formations is presently envisaged as one means of sequestering CO₂ released from the burning of fossil fuels in power generation facilities (IPCC, 2007a; 2007b). Candidates for the suitable formations include deep saline aquifers in sedimentary basins, depleted oil and gas fields, and unmineable coal seams (IPCC, 2005). Deep saline aquifers currently receive a great deal of attention because of their common occurrence, large volume of pore space available, and potential for long-term hydrodynamic trapping of CO₂ (DOE-NETL, 2008). Injected CO₂ will dissolve into the native formation water, making the brine corrosive and therefore aggressively reactive toward the native minerals.

Feldspars are abundant in both sandstone (reservoir rock) and shale (caprock). For example, the Mt. Simon Sandstone, a potential target for carbon sequestration in the Midwest of the U.S., contains about 22% feldspars (Eliasson et al., 1998). Eau Claire Shale, the caprock for Mt. Simon Sandstone, contains an average of ~ 20 % feldspars (Becker et al., 1978). Although feldspar dissolution rates are usually slow (in the order of 10^{-8} to 10^{-12} mol m⁻² s⁻¹) in the temperature range relevant to geological carbon sequestration (Blum and Stillings, 1995), the extent of water-feldspar reaction will be significant because (1) the brine will be acidic, (2) the time scale for successful, safe storage of CO₂ in a sequestration site is in the orders of 1,000 to 100,000 years, and (3) feldspars are abundant. In general, the dissolution of feldspars is likely to increase porosity and thus enhance CO₂ mobility and accelerate further geochemical reactions, but the formation and mobility of clay minerals may inversely affect permeability (Emery

and Robinson, 1993; Rogen and Fabricius, 2002; Strazisar et al., 2006; Worden and Morad, 2003).

Numerous laboratory experiments have been performed to measure the dissolution rates of feldspars (Blum and Stillings, 1995; Brantley, 2008). As a result, a significant amount of experimental data is available on the dissolution of feldspars at far from equilibrium conditions or with specific aqueous concentrations and the free energy of reactions (Blum and Stillings, 1995; Brantley, 2008). However, dissolution of feldspars will increase the solution concentration and lead to the precipitation of secondary minerals. The dissolution of primary minerals and precipitation of secondary minerals can be coupled together through the free energy term and through the evolution of surface areas (Zhu, 2009; Zhu et al., Submitted).

While dissolution rates are best measured with mixed flow reactors (Brantley, 2005; Oelkers et al., 2001), batch experiments are more suitable for studying the precipitation of secondary minerals, temporal evolution of the solution, and reaction extent (Alekseyev et al., 1997; Fu et al., 2009; Zhu and Lu, 2009). The coupling between silicate dissolution and secondary precipitation can be deciphered even though it is much more difficult to decipher reaction mechanisms. While many batch reactor experiments have been performed for olivine and serpentine (Giammar et al., 2005; Golubev et al., 2005; Mcgrail et al., 2006; O'connor et al., 2002; Pokrovsky and Schott, 2000; Wogelius and Walther, 1991) and wollastonite (Daval et al., 2009; Golubev et al., 2005; Huijgen et al., 2006), data are still lacking for feldspars—the most abundant minerals in the earth's crust. In addition, the majority of experiments reported in the literature did not collect the secondary mineralogy data, and some did not collect the solution chemistry data.

Acquiring both solution chemistry and secondary mineral information are critical to the value of an experiment.

In the past a few years, this data gap is partially filled by the new experiments and modeling studies by Zhu and collaborators (Indiana University, University of Minnesota, and NETL). These authors have conducted batch experiments of alkali feldspar hydrolysis and have collected both solution chemistry and secondary mineral data (Fu et al., 2009; Lu et al., To be submitted; Zhu and Lu, 2009). With both solution chemistry and mineralogical data, Zhu and co-workers were able to make conclusions that the partial equilibrium assumption does not hold in the feldspar hydrolysis experiments, and the coupling of dissolution of feldspar and secondary mineral precipitation result in a negative feedback and slow down further dissolution of the feldspars (Zhu, 2009; Zhu and Lu, 2009; Zhu et al., Submitted). These results point out that it is likely that the predicted feldspar-CO₂-brine reactions in the current reactive mass transport models for carbon sequestration without the consideration of how reactions are coupled have over-predicted the extent of reactions (e.g., extent of feldspar dissolution, clay precipitation, and mineral trapping, acid buffering capacity, and porosity/permeability variations).

However, the new experimental data are only for alkali feldspars, and the CO₂ partial pressure used in their experiments are low compared to CO₂ injection and reservoir conditions. The dissolution and precipitation reactions involving plagioclase feldspars, which contain calcium (Ca²⁺) present another challenge: not only secondary minerals like boehmite (AlO(OH)), kaolinite, and paragonite, would precipitate, calcite and dawsonite may also precipitate under high *p*CO₂ conditions. The relationship among plagioclase dissolution, clay precipitation, and carbonate precipitation would be complex.

For example, where precipitated carbonate minerals will be located? Will the carbonate mineral precipitation affect overall feldspar dissolution rates? What are the effects of carbonate formation on the coupling of feldspar dissolution -- aluminosilicate secondary minerals precipitation? These relationships have never been examined before, but nevertheless important for the performance assessment of the CCS projects. In addition, as the concentrations of NaCl solutions (0.5-4 M) and $p\text{CO}_2$ are high, dawsonite is expected to form. However, dawsonite precipitation kinetics needs to be investigated as this is one of the most common product phases of numerical simulations for geological carbon sequestration and yet is not a common phase observed in experiments or in geological systems (IEA, 2008).

Therefore, I propose to conduct a series of laboratory batch experiments that will dissolve plagioclase (e.g., labradorite), precipitate calcite, dawsonite, and secondary aluminosilicate minerals. These experiments will be built upon our work in the past five years, and will be integrated to the modeling work that we have been pursuing.

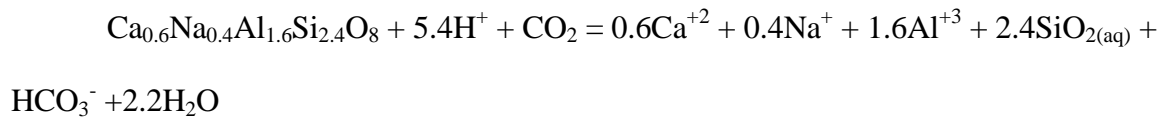
2. Background and Rationale

When CO_2 is injected into geological formations, CO_2 will be dissolved into native brines and the pH of brine will be lowered to about 3. The acidic brine then aggressively dissolves the minerals that are already in the aquifer (termed primary here) and precipitate secondary minerals.

In the example of labradorite dissolution, we can view it as two processes:

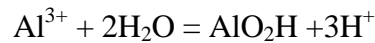
Dissolution reaction:

Plagioclase

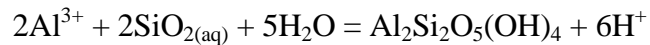


Precipitation reactions:

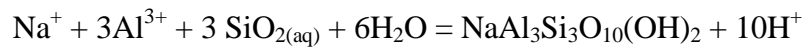
Boehmite



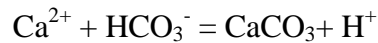
Kaolinite



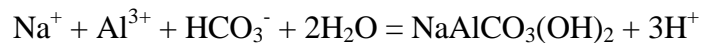
Paragonite



Calcite



Dawsonite



The dissolution – precipitation processes can alter the reservoir's porosity and permeability, and injectivity if it happens near the well bore, which can either enhance or compromise the integrity of the caprocks. Although no clear guidance as how long the performance assessment period is from federal agencies, the likely period is in thousands to hundreds of thousands of years. This long performance period make the chemical reactions with minerals that are not very reactive also important for carbon sequestration.

Feldspars are the most abundant silicate minerals and comprise over 50% of the volume of the earth's crust. Dissolution of feldspars can also release Ca^{2+} , which can form carbonate precipitates. This is the most desired consequence of CO_2 injection because carbonate solids are immobile and are permanently stored in deep geological

formations without the risk of seeping back to the surface. As pointed out by the NRC workshop report (NRC, 2003), this is a natural process of weathering. However, the key to the carbon sequestration program is an understanding of the reaction kinetics and how to accelerate the process.

Another consequence of silicate reaction after CO₂ injection is the change of porosities in the geological formation, which can alter the patterns of fluid flow and cause formation damage. Strazisar et al. (2006) demonstrated that the magnitudes of porosity changes are closely related to the kinetic parameters used in the model.

However, evaluation of the effects of these reactions is a challenge. It runs into one of the fundamental problems in modern geochemistry, the persistent two to five orders of magnitude discrepancy between laboratory-measured and field-derived feldspar dissolution rates (see reviews by Blum and Stillings, 1995; Drever and Clow, 1995; White, 1995; Zhu, 2003). As shown by Strazisar et al. (2006) in their assessment of the possible reactions of injection in the Alberta basin, Canada, the use of laboratory and field based rates result in drastically different model predictions. Thus, the lack of proper values of the kinetic parameters is one of the major road blocks for evaluation of geological sequestration.

A number of experimental designs have been used for measuring silicate dissolution rates, including batch, continuously stirred, plug flow, and fluidized bed (see review by Brantley and Chen, 1995). However, the primary focus has been to derive the dissolution rates from steady state chemical compositions. In such experimental designs, feldspars are dissolved far from equilibrium and secondary mineral precipitation is avoided.

However, if secondary mineral precipitation is the rate-limiting step in geological systems (Zhu et al., 2004), a different experimental design is necessary to test this hypothesis, which will traverse to the opposite direction of the prevailing practice. Our experiments are therefore designed to allow the precipitation of secondary minerals and to allow the solution to approach equilibrium with respect to the dissolving mineral being tested. *Our working hypothesis is, thus, that the rate constants from numerous previous experimental measurements are valid; and experimental data can be modeled using these rate constants, together with the information of how reactions are coupled revealed from these experimental data* (Ganor et al., 2007; Zhu et al., submitted).

Recently, Daval et al. (2009) conducted batch experiments of wollastonite carbonation at 90 °C and 150 bars $p\text{CO}_2$. They observed alternative layers of calcite and amorphous silica coating on the wollastonite surface. Whether such coating layers are porous and permeable or acting as diffusion barriers depend on solution chemistry conditions. Mineral carbonation experiments performed at NETL (Fauth et al., 2001), Los Alamos (Carey et al., 2003), and the Albany Research Center indicated that the precipitation of carbonate, which rings around the surface of dissolving silicate, may slow or stop the carbonation reactions (NRC, 2003). The dissolution and precipitation processes are thus coupled, through either chemical processes (the slowest reaction controls the overall reaction) or physical processes (diffusion through the precipitate rinds).

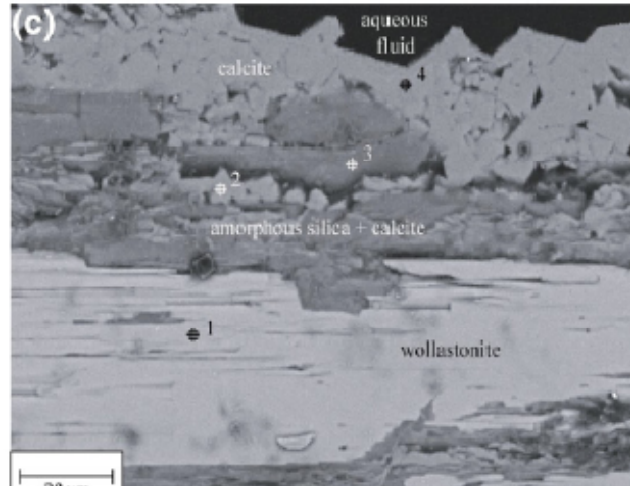


Figure 1. Backscattered SEM images of cross-section of Wollastonite grain after 2 days of reaction in circum-neutral pH conditions (sample C6). Note the succession of the inner intact core of reacting wollastonite, a fractured layer composed with calcite and silica, and the compact continuous and poorly permeable coating of calcite (from Daval et al., 2009).

Our proposed research is thus a significant departure from the state-of-the-practice approaches to the kinetics problem. The novelty of our approach lies in both experimental design and use of sophisticated geochemical models to interpret the experimental data. The results from our approach are more realistic representations of chemical kinetics for reactions that will occur in deep geological formation upon injections of CO₂.

In addition to the long-term controversy between field and laboratory rates, there is a general lack of experimental data at conditions pertinent to the geological carbon sequestration program (Fig. 2). The reactions pertinent to geological carbon sequestration occur in about 50 to 150 °C, high CO₂ pressure, and in saline brines. Although high CO₂ concentrations might suggest pH lowering and more rapid dissolution of primary aluminosilicates, these conditions may enhance further the stability of clay minerals and

carbonate minerals, with attendant effects on the overall reaction rate schemes.

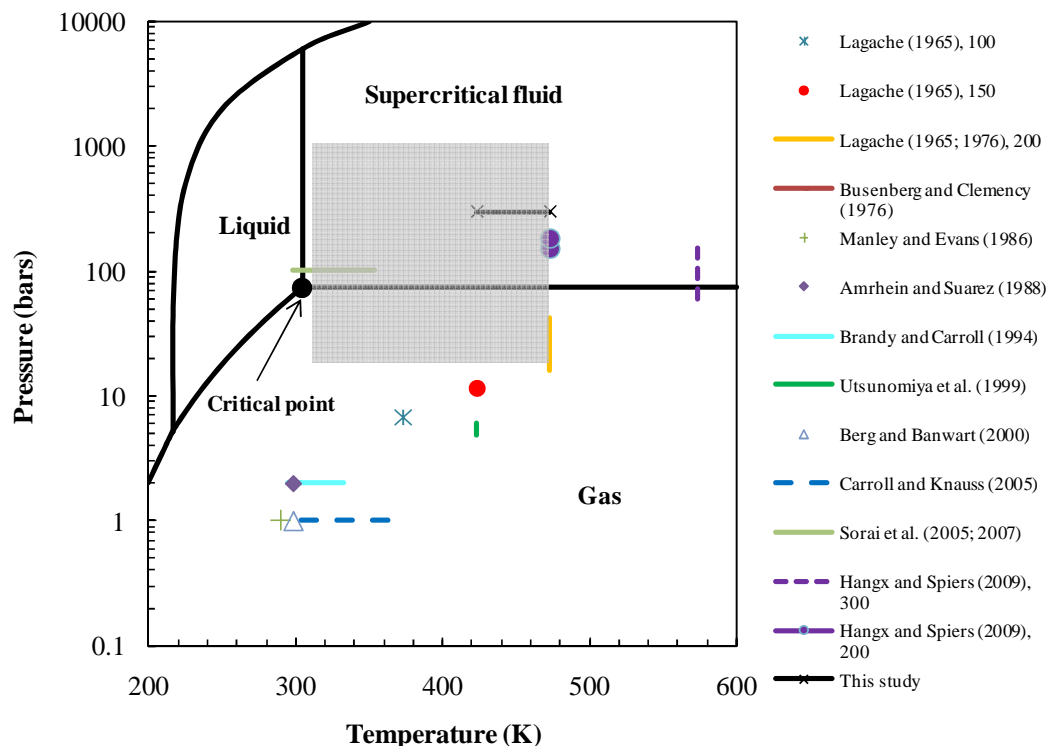


Figure 2. Experimental T - P conditions compared with T , P ranges relevant to geological sequestration (40-200 °C, 20-1000 bars, or 2-100 MPa, gray shaded area) superimposed on carbon dioxide phase diagram (data from Brubacher, 2006). Total pressure in the system instead of $p\text{CO}_2$ is used for representing experimental data.

There is still a dearth of kinetic data relevant to geological carbon sequestration, and hence the need for experimental measurements.

With these goals in mind, we have devised an innovative experimental and theoretical interpretation program to address these urgent and significant outstanding scientific issues facing the carbon sequestration program.

3. Project Description

Different aspects of this study are designed to address all of these issues, and they are organized as three tasks below:

Task 1: To conduct a time series of experiments of feldspar dissolution – secondary mineral precipitation under reservoir conditions;

Task 2: To conduct detailed mineralogical analysis of reaction products, textures, and micro-chemistry at a detailed level using new X-ray diffraction, Field Emission Gun-(FEG)-Scanning Electron Microscopy (SEM) and FEG-Transmission Electron Microscopy (TEM) techniques;

Task 3: To use reaction path models to simulate reaction, rates, and processes in the batch reactor to understand the coupling between dissolution and precipitation reactions.

3.1 Task 1: Experiments

Labradorite (Lake County, Oregon) will be purchased from WARD'S Natural Sciences Establishments, Inc. The feldspar crystals will be handpicked, ground with an agate mortar and pestle, and subsequently dry sieved to retain the fraction between 50 and 100 μm in size. For the freshly ground material, there will be a large number of submicron-to-micron particles that adhered to the surface of large grains. Dissolution of these ultra-fine particles will result in initially non-linear rates of reaction or parabolic kinetics (Holdren and Berner, 1979). To remove these particles, the sample will be first ultrasonically cleansed using analytical grade acetone. This will be performed eight times on each aliquot for about 20 min per treatment. The cleaned labradorite grains will be finally rinsed with deionized water and then freeze-dried. Before experiments, feldspar

sample will be kept in an oven at 105 °C overnight to exclude possible organic contamination (Fu et al., 2009).

The key feature of the batch experiments is the capability to continually monitor the fluid chemistry co-existing with the mineral reactants. These experimental data are generally superior to those derived from samples collected after the reactors are cooled down because backward reactions may occur during cooling.

The batch experiments will be performed using flexible cell hydrothermal equipment (Seyfried et al., 1987). In brief, the central element of this experimental approach involves a gold reaction cell with detachable Ti-closure. This arrangement allows easy access to the reactants at the end of an experiment. More importantly, the flexible cell permits on-line sampling of the aqueous phase at constant temperature and pressure simply by adding water, in an amount equivalent to the sampled fluid, to the region surrounding the reaction cell (Fig. 3).

A Beckman Coulter SA-3100 surface area analyzer will be used for BET surface area analysis of feldspar sample before experiments. The samples will be degassed at 250 °C overnight prior to measurements. The instrument will be calibrated before and during measurements periodically, using National Institute of Standards and Technology reference material 1900, a silicon nitrite powder with surface area of 2.85 m²/g. Multipoint N₂ gas adsorption isotherms will be measured to obtain the specific surface area (from experience it will be around 0.13 m²/g).

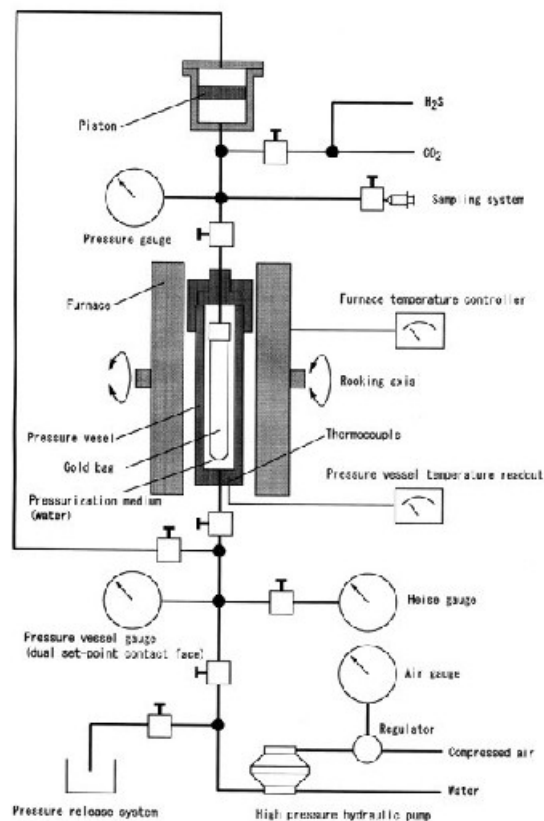


Figure 3. Schematic illustration of the flexible cell reaction system (SEYFRIED et al., 1987), which will be used for the proposed mineral dissolution/precipitation rate study.

The chemical compositions of feldspar will be determined by wavelength dispersive electron microprobe using a CAMECA SX50 instrument. Operation accelerating voltage will be 15 kV while beam current and beam size will be 15 nA and ~1 μm , respectively.

Fluid samples taken from the reactor will be analyzed for major and some minor dissolved constituents. Dissolved cations will be analyzed with inductively coupled plasma mass spectrometry (ICP-MS). Anions will be analyzed by ion chromatography. Experimental run products will be retrieved and characterized with a

variety of microscopic and analytical techniques (See below). The feldspar and aqueous solutions will be loaded into a flexible Au/Ti reaction cell, which will be placed in a steel-alloy autoclave, following procedures described in Seyfried et al. (1987). Thus, internally filtered fluid samples could be recovered from the reaction cell contents any time during an experiment.

The experiments will be conducted at 100 °C, 20 MPa, with 0.5-4 M NaCl solution to mimic prevailing reservoir conditions. The solubility of CO₂ under such conditions is close to 0.56-1 M (Duan et al., 2006), and the pH is near 3. A series of identical experiments will be carried out with excess CO₂ to buffer the pH and the sampling interval will be at 1 h, 3 h, 6 h, 12 h, 1 d, 10 d, 30 d, 60 d, and 120 d.

3.2 Task 2: Mineralogical and Electron Microscopic Characterization of Reaction Products and Mineral-clay Interfaces

Reaction products from batch reactors will be investigated by an array of sophisticated techniques for mineral analysis. In fact, mineral separates will be investigated using SEM (phase relationships and surface morphology), electron microprobe, and XPS (surface chemistry), as well as High-resolution TEM (structure and chemistry).

Overall, we anticipate a total of 10 to 15 intensively studied samples. In a progression from lower magnification to high-resolution microscopic techniques, standard petrography using thin sections, XRD, SEM, and electron microprobe will be used to determine the size, composition, and abundance of minerals. FEG-SEM and HRTEM will be used to examine the micro-texture, micro-structures, and compositional gradients at the phase boundaries at a nanometer-scale resolution, with an emphasis on

the feldspar-clay-carbonate interfaces (Hochella and Banfield, 1995; Veblen, 1991). The interfaces are not necessarily confined to the grain edges, as extensive internal porosity and micro-channels often develop (Hochella and Banfield, 1995).

3.2.1. X-ray diffraction

X-ray diffraction gives the definitive identification of secondary mineral products. Powder X-ray diffraction analyses will be carried out using a Bruker D8 Advance diffractometers, equipped with a Cu anode at 20 kV and 5 mA, and with a SolX energy-dispersive detector. The scan parameters used will be 2 to 70° 2 θ , with a step size of 0.02° 2 θ . Two different sample preparation methods will be employed: “cavity mount” and “slurry mount”. For the cavity mount, starting samples will be ground by hand in an agate mortar and pestle to get sufficient small particles. These particles will be subsequently filled into the cavity of a titanium sample holder for XRD analysis. For the slurry mount, reaction products will be immersed in 20 ml DI water in a plastic vessel (25 ml volume) and ultrasonicated three times for 15 minutes per treatment with 15 minutes interval. After the final ultrasonication, the samples will be allowed to settle overnight. Then, a pipette (0.5 ml volume) will be used to carefully suck out the suspension and a syringe filter unit with silver filter membrane will be employed to collect the clay minerals. The filter unit will be aided with a vacuum system. After filtering, the silver membrane (with the slurry) will be carefully removed from the filter unit. The slurry (clay with water) on the silver membrane will be air-dried. Finally, the membrane with clays and carbonates will be mounted onto zero-background quartz plate for XRD characterization.

3.2.2. FEG-SEM

Reaction products will be examined using a new Field Emission Gun (FEG)-Scanning Electron Microscope (SEM) at the Indiana University. The SEM offers fewer sample preparation artifacts, a wide field of view (from low to high resolution), and ease of operation. However, SEM cannot provide structural information. In the proposed study, we will first use the SEM to select areas of interest and then prepare TEM samples from these areas to obtain structural information.

Thus, our primary goals for FEG-SEM study are to answer the following questions:

- Are there clay or carbonate rinds on feldspars (see Fig. 4)?
- What are the clay minerals? Are they boehmite and/or kaolinite? How much?
- Where is calcite (and dawsonite) precipitated?
- What are the morphologies of feldspar grain surfaces?

Indiana University's SEM is a Quanta 400 Field Emission Gun (FEG). The Energy Dispersive X-ray Spectrometer (EDS) system has an EDAX thin window and CDU LEAP detector. The low energy X-ray detection with FEG provided high spatial resolution for microanalysis down to $\sim 0.1 \mu\text{m}^2$ under optimum conditions. SEM samples will be prepared with double sided conductive tape and the reaction products will be sprinkled on an aluminum sample holder.

3.2.1. FEG-TEM, HRTEM, STEM

Transmission Electron Microscopy (TEM) observations will be performed with the new Indiana University JEOL JEM 3200FS. The electron microscope is a 300kV FEG TEM designed for HRTEM and equipped with an in-column energy filter for EELS

and EFTEM, an EDS detector for elemental analysis and scanning coils that allow the instrument to perform as a scanning transmission electron microscope (STEM) as well. STEM imaging using the high angle, annular dark-field detector (HAADF-STEM) produces Z-contrast images, where the image intensity is directly proportional to Z^2 (the atomic number, Z, squared), such Z-contrast images directly map compositional changes across nanoscale interfaces. HAADF-STEM can also be combined with either EDS or EELS, providing high spatial resolution images that also provide direct information on elemental composition as well as chemical state (*e.g.*, oxidation state). The rapid acquisition of EELS data (full spectra can be recorded in less than a second) and application of low dose imaging techniques whenever possible will help minimize electron beam-induced radiation damage. This combination of HRTEM, STEM, EDS, and EELS can, therefore, provide a wide range of information regarding microstructure and micro-chemistry of mineral reactions at the nanometer scale.

The TEM samples will be prepared with ultrasonic method. A fraction of the reaction products will be immersed into absolute ethanol and ultrasonicated for several minutes to disengage the secondary minerals from feldspar surfaces. A drop of the resulting suspension (with grains of feldspar as well as secondary minerals) will be mounted onto a holey-carbon film supported by a standard Cu TEM grid and air-dried for ~ 10 min.

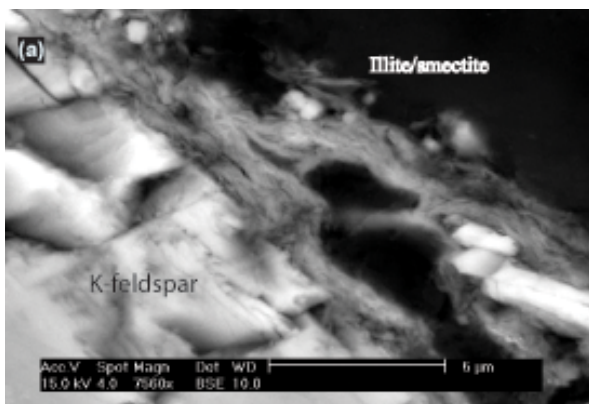


Figure 4. SEM micrograph of K-feldspar grain enveloped by a clay rind in the Navajo sandstone. Feldspar “remnants” of variable sizes are embedded in the clay layer.

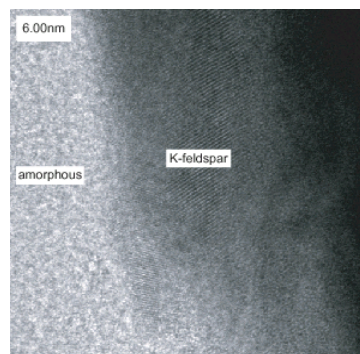


Figure 5. High-resolution TEM images showing K-feldspar with lattice fringes at atomic resolution and a K^+ deficient amorphous layer on the feldspar surface on the left.

Geochemists have argued for nearly a century about the existence and role of a residual and/or product surface layer(s) on laboratory and naturally dissolved feldspars (Berner and Holdren, 1979; Brantley and Stillings, 1996; Casey et al., 1988; Chou and Wollast, 1985; Helgeson, 1971; Hellmann et al., 1990; Nesbitt and Muir, 1988; Nesbitt and Skinner, 2001). We examined the Navajo sandstone samples with High-Resolution Transmission Electron Microscopy (HRTEM) with an imaging information limit of 0.12 nm, a resolution only recently available to earth scientists, and with FEG-SEM. The electron microscopy study revealed two distinctly different surface coatings. First, we observed a highly K^+ deficient, amorphous layer (no lattice fringes in electron diffraction, Fig. 5), which continuously covers all feldspar surfaces. The amorphous layer remains thin, having a thickness less than 10 nm, even after reacting for hundreds of thousands to millions of years.

A much thicker leached layer has been observed on feldspars after dissolution at

acidic pH in the laboratory (Casey et al., 1989; Nesbitt and Skinner, 2001) and in acidic soils (Nesbitt and Muir, 1988), but it has never been observed on naturally weathered feldspars from neutral to slightly alkaline environments. Instead, previous research had suggested that a leached layer does not exist in circumneutral pH solutions, and that this indicates there is different reaction mechanism at acidic or basic pH conditions. Our observations, however, suggest a similar dissolution mechanism throughout a wide pH range.

Questions remain whether the amorphous layer is present ubiquitously under different conditions. The proposed experiments will produce feldspars that have reacted with solutions of different pH, for different time periods, and temperature and are ideal for discerning the presence of the amorphous layer.

Additionally, although our study of the natural samples shows a “leached” origin, Hellmann et al. (2003) recently argued for a dissolution-precipitation origin of the amorphous layer they found on feldspars leached in acid solutions in the lab. The distinction between a leached layer and a precipitation layer is difficult to make from the morphology alone, although our samples show feldspar islands in the amorphous layer and argue for a leached origin. In the proposed study, we will (1) study more samples; (2) prepare samples with microtome method; and (3) use EFTEM to characterize the chemical compositions and chemical ratios of the leached zone.

3.3. Task 3: Geochemical Modeling

Task 1 and 2 produce experimental data on both solution chemistry and secondary mineral identities and phase relationships. These data will allow us to use reaction path

models to quantitatively evaluate the coupling between dissolution and precipitation reactions. We will utilize the rate constants and rate laws derived from flow-through reactions, in which the precipitation of secondary minerals were largely suppressed (Carroll and Knauss, 2005; Taylor et al., 2000). Therefore, in our modeling work, we will not attempt to use our experimental data to derive rate constants or rate laws as it is well known that rates measured from batch reactor is complicated by precipitation of secondary minerals (e.g., Harouiya and Oelkers, 2004; Hellmann, 1994). Rather, we will build on flow through reactor results and interpret the time series experimental data.

We will first compile an internally consistent thermodynamic database relevant to the experimental systems. The standard states for the solids are defined as unit activity for pure end-member solids at the temperature and pressure of interest. The standard state for water is the unit activity of pure water. For aqueous species other than H₂O, the standard state is the unit activity of the species in a hypothetical one molal solution referenced to infinite dilution at the temperature and pressure of interest. Standard state thermodynamic properties for mineral end-members will be taken from Holland and Powell (1998) except for boehmite (see Zhu and Lu, 2009) and dawsonite (calculated from Eqn. 15 of Bénézeth et al., 2007), for water from Haar et al. (1984), for Al-bearing aqueous species from Tagirov and Schott (2001), and all other aqueous species from Shock and Helgeson (1988), Shock et al. (1989), Shock et al. (1997), and Sverjensky et al. (1997). The temperature and pressure dependences of thermodynamic properties for aqueous species, when applicable, will be predicted using the parameters of the revised HKF equations of state (Helgeson et al., 1981; Shock et al., 1992; Tanger and Helgeson, 1988). Calculations of equilibrium constants will be facilitated with a modified version of

SUPCRT92 (Johnson et al., 1992) with the heat capacity function of Holland and Powell (1998) for minerals.

Second, we will conduct speciation solubility calculation. We will use the pH and total analytical concentrations of the constituents measured at ambient conditions (e.g., 22 °C and 0.1 MPa) as input into the modeling codes and then “re-heat” the solution to experimental T and P. This method calculates the “*in situ*” pH at the experimental conditions by taking account of the effects of T and P on the distribution of aqueous species (Reed and Spycher, 1984). Saturation indices (SI) for relevant minerals were calculated from the measured temperatures, pressures, and chemical compositions of experimental aqueous solutions. SI is defined as $\log(Q/K)$, where Q denotes the activity quotient and K the equilibrium constant (Zhu and Anderson, 2002, p. 45). Equilibrium activity-activity diagrams for mineral stability and phase relations were constructed to trace the evolution of the aqueous chemistry during the batch experiments (Fig. 6). Speciation and solubility calculations were aided with the computer code PHREEQC (Parkhurst and Appello, 1999) and EQ3/6 (Wolery, 1992) together with our own equilibrium constant databases for the programs with thermodynamic properties noted above. Activity coefficients for the charged aqueous species were calculated from the extended Debye-Hückel equation or B-dot equation fitted to mean salt NaCl activity coefficients (Helgeson et al., 1978; Oelkers and Helgeson, 1990).

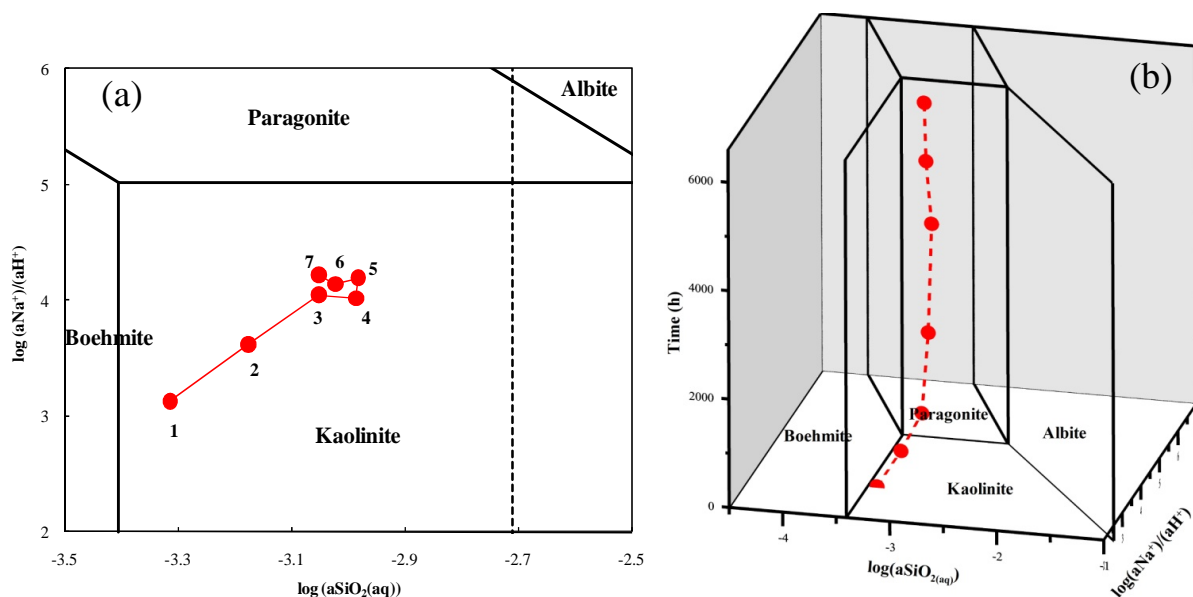


Fig. 6. Activity – activity diagrams showing the phase relations in the system Na_2O -(Al_2O_3)- SiO_2 - H_2O - HCl at 200 °C and 300 bars (30 MPa). The dashed line in (a) denotes quartz saturation. Symbols represent experimental results of albite dissolution in 200 mmol/kg KCl solution and 13.3 mmol/kg $\text{CO}_{2(\text{aq})}$ at 150 °C and 300 bars. The activity and activity ratios were obtained from speciation modeling of the experimental system Na_2O - K_2O - Al_2O_3 - SiO_2 - H_2O - HCl , based on the experimental solution chemistry data. Points 1 through 7 represent experiment solutions at reaction time of 24, 456, 960, 2472, 4392, 5568, and 6600 h, respectively. The red line in (a) and red dashed line in (b) connecting experimental data is for visualization of fluid chemical evolution.

Reaction path models calculate a sequence of states involving incremental or step-wise mass transfer between the phases within a system, or incremental addition or subtraction of a reactant from the system (Helgeson, 1968; Helgeson, 1969). Feldspar hydrolysis is the system in which Helgeson (1968) developed the reaction-path modeling approach. Although the original example is based on local and partial equilibrium (Helgeson, 1968; Helgeson, 1969; Helgeson, 1979), Helgeson and Murphy (1983) added feldspar dissolution kinetics into the model. Lasaga (1998) further showed that different reaction paths will result from different relative rates of feldspar dissolution and secondary mineral precipitation.

Reaction path modeling is different from the speciation and solubility modeling. Speciation and solubility modeling simulates a snapshot of a chemical system while the reaction path modeling simulates processes. To simulate the experimental processes, reaction path models use the initial experimental solutions as the starting point. The course of the chemical evolution in the system is set by the rate laws for primary mineral dissolution and secondary mineral precipitation. In reaction path modeling, it is therefore necessary to make assumptions regarding reactive surface areas and the appropriate forms that the rate laws should take. Both topics are controversial and undergoing intense research.

However, the reaction path models give rich quantitative information of the reaction processes during experiments. For example, the speciation – solubility modeling does not tell how the dissolution and precipitation reactions are coupled quantitatively, but reaction path modeling does (Fig. 7), as shown in Zhu et al. (Submitted). We should emphasize that the batch systems are simple model systems to test ideas of reaction kinetics before kinetic theories can be applied to complex natural systems, e.g., without further assumptions of flow and transport properties (Zhu, 2009). It is a necessary step in the process of going from laboratory dissolution rate experiments at far-from-equilibrium (e.g., mixed flow reactor with fixed solution chemistry) to natural systems.

Reaction path model will be constructed using PHREEQC with customized rate laws and a modified database. A general form of rate laws for heterogeneous reactions may be written as (Lasaga et al., 1994)

$$r_j = \frac{dN_j}{dt} = k_j S_j a_{H^+}^{n_{H^+}} g(I) \prod_a a_i^{n_i} f(\Delta G_r) \quad (1)$$

where r_j is the dissolution rate of the j th mineral ($\text{mol s}^{-1} \text{kgw}^{-1}$), N_j denotes the moles of mineral j , k_j is the respective rate constant ($\text{mol s}^{-1} \text{m}^{-2}$), and S_j is the reactive surface area of the j th mineral ($\text{m}^2 \text{kgw}^{-1}$). a_{H^+} stands for the activity of hydrogen in the aqueous solution, and hence this term accounts for the well-noted pH dependence of dissolution rates. The term $g(I)$ accounts for possible ionic strength dependence of the rates. The term $\prod_a a_i^{n_i}$ incorporates possible catalytic and inhibitory effects of aqueous species. ΔG_r (J/mol) denotes the Gibbs free energy of reaction.

The term $f(\Delta G_r)$ describes the effect of deviation from equilibrium on the rate and represents the thermodynamic driving force for chemical reactions (Aagaard and Helgeson, 1982; Prigogine and Defay, 1965). A simple form for the r_j - ΔG_r relationship is proposed based on the Transition State Theory (TST) (Aagaard and Helgeson, 1982; Lasaga, 1981a; Lasaga, 1981b),

$$f(\Delta G_r) = \left(1 - \exp\left(\frac{\Delta G_r}{RT}\right) \right) \quad (2)$$

This formulation of the free energy term has also been termed the “linear TST rate law” because the relationship between r_j and ΔG_r becomes linear near equilibrium.

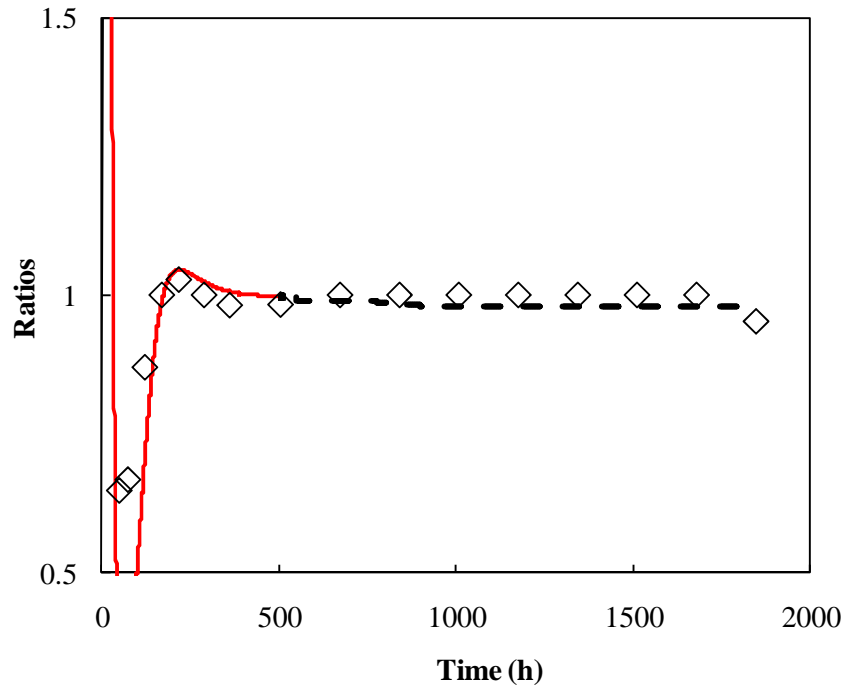


Figure 7. Albite dissolution and sanidine precipitation are strongly coupled (Zhu et al., Submitted). Ratios of albite dissolution rates vs. sanidine precipitation rates when expressed in unit of $\text{mol kgw}^{-1} \text{s}^{-1}$. Symbols denote experimental data; lines denote the results of numerical reaction path model simulation. Dotted line shows portion of 672-1848 h.

However, a number of experiments near equilibrium have shown that the actual relationship between r_j and ΔG_r deviates from this so-called linear kinetics (Aleseyev et al., 1997; Beig and Lüttge, 2006; Burch et al., 1993; Cama et al., 2000; Gautier et al., 1994; Hellmann and Tisserand, 2006; Nagy et al., 1991; Nagy and Lasaga, 1992; Nagy and Lasaga, 1993; Schramke et al., 1987; Taylor et al., 2000). Alekseyev et al. (1997) introduced a non-linear rate law in the form of

$$r / S = \pm k \left| 1 - (Q / K)^p \right|^q \quad (3)$$

where Q is the activity quotient, K is the equilibrium constant, p and q are fitting parameters.

Therefore, in our reaction path modeling, plagioclase dissolution reactions will be modeled using the empirical parallel rate law of Burch et al. (1993) in the form of,

$$r / S = k_1[1 - \exp(-ng^{m_1})] + k_2[1 - \exp(-g)]^{m_2} \quad (4)$$

where k_1 and k_2 denote the rate constants in units of $\text{mol s}^{-1} \text{m}^{-2}$, $g \equiv |\Delta G_r| / RT$, and n , m_1 , and m_2 are empirical parameters fitted from experimental data. Note that the first term is equivalent to Eqn (3) if $n = p$, $m_1 = 1$, and $q = 1$. The second term is equivalent if $p = 1$ and $m_2 = q$. The involved parameters n , m_1 , m_2 , and k_1/k_2 of this rate expression will be taken from Hellmann and Tisserand (2006), which are 7.98×10^{-5} , 3.81, 1.17, and 56.65, respectively.

For boehmite precipitation, we will follow Bénézech et al. (2008) and use the rate law,

$$r_{Bhm} = -k_-^* (H^+)^{1.7} \left(e^{\frac{\Delta G_r}{RT}} - 1 \right) \quad (5)$$

Bénézech et al. (2008) conducted boehmite precipitation experiments for pH 6 – 9 at 103 °C. They found that the TST $f(\Delta G_r)$ function fit to their data and the precipitation rate is a function of pH. However, boehmite precipitation in our experiments will occur in the pH range of 3 to 5, slightly acidic than the experimental condition of Bénézech et al. (2008). Nagy (1995) documented V-shaped pH dependence of aluminum oxyhydroxides

dissolution rates and proposed an exponent of 1.7 for hydrogen concentrations for acid solutions, which we will adopt.

For kaolinite, calcite, paragonite, and dawsonite precipitation, we will use the classic BCF (Burton-Cabreera-Frank) theory for crystal growth (Burton et al., 1951). The BCF theory makes another prediction for the form of the $f(\Delta G_r)$ function. In its simplest case,

$$f(\Delta G) = 1 - \exp\left(-\frac{\Delta G_r}{RT}\right)^n \quad (6)$$

where n signifies a coefficient that depends on the growth mechanism, where $n = 1$ for transport or adsorption controlled growth and $n = 2$ for spiral growth (cf. Blum and Lasaga, 1987; Shiraki and Brantley, 1995).

The concept of “reactive surface area (RSA)” (Helgeson et al., 1984) is rooted in the theories of surface controlled reaction kinetics. The rates of heterogeneous reactions are proportional to the “concentrations” of reactive surface sites. The RSA thus substitutes for site concentrations in lieu of reactant concentrations in a first order rate law (Zhu and Anderson, 2002). Apparently, RSA represents the key scaling parameter for extrapolating from atomic to laboratory and field scales. However, this concept is difficult to implement in practice. Different crystal faces have different types of surface sites and site concentrations. Surface topography (e.g., kinks, edges, and adatoms) and types and densities of defects on mineral surfaces are difficult to quantify. The “reactive site concentrations” would also depend on whether and how deep a “leached layer” is developed near the mineral surfaces (Oelkers, 2001; Stillings et al., 1995).

The common practice in geochemistry is to use BET (Brunauer-Emmett-Teller) surface area (Braunauer et al., 1938) of the dry powder as a proxy for the RSA. However, there are several challenges in substituting BET SA for RSA in Eqn (1). From a theoretical point of view, we are using a single parameter to represent a variety of surface sites with different reactivity and concentrations. The BET SA is more physically based (gas adsorption and surface roughness) than chemical in nature. From a practical point of view, it is difficult to measure BET SA for a mineral within a mixture and for secondary minerals with miniature quantities. Often, the reactive surface areas are significantly less than the BET surface area (Helgeson et al., 1984).

In an experiment, reactive surface area may vary due to the growth or reduction of crystal sizes. In such cases, S during dissolution or precipitation may be empirically related to the initial total surface area (S^o) by (Christoffersen and Christoffersen, 1976; He et al., 1994; Witkamp et al., 1990; Zhang and Nancollas, 1992)

$$S / S^o = (N^t / N^o)^P \quad (7)$$

where P is a coefficient that depends on the shape of the crystal and the relative rates of dissolution (or growth) on different surfaces. P equates to 2/3 if the shape of the crystals remains unchanged and rates on all faces are equal. P values of 0.5 indicates that dissolution or growth occur predominantly in two directions while P values of 0 indicates one direction (e.g., Witkamp et al., 1990).

The reactive surface areas may also vary during experiments as a result of the extinction of highly reactive fine particles (Helgeson et al., 1984), change of the ratios of reactive and nonreactive sites (Gautier et al., 2001), mechanical disaggregation of

particles (Ganor et al., 1999; Nagy and Lasaga, 1992), and formation of surface coating (Cubillas et al., 2005; Ganor et al., 1995; Metz et al., 2005; Nugent et al., 1998).

It is even more difficult to estimate the reactive surface areas for precipitating secondary phases. Precipitation of new mineral phase requires nucleation and crystal growth. Currently, the lack of parameters prevents the application to the experiments that we examined in this study (see review by Fritz and Noguera, 2009). For modeling, it also presents a dilemma: precipitation cannot proceed without surface area first; and without precipitates at first, there are no surface areas for the secondary phases.

In the proposed study, we will follow the common practice in geochemistry and used the BET surface areas for starting reactants in the reaction path modeling as the initial conditions. Then, we will assess the possible temporal variation of reactive surface areas from experimental data. When it is difficult to separate the effects of rate constant and reactive surface area from batch reactor data, we introduced an effective rate constant, k^*

$$k^* = k \times S \quad (8)$$

where S_A stands for reactive surface area. k^* has a unit of $\text{mol s}^{-1}\text{kgw}^{-1}$ if S has the unit of $\text{m}^2 \text{kgw}^{-1}$. Note that k^* , as a fitting parameter, in effect, could represent all terms in the empirical rate law (Eqn. 4) except for the Gibbs free energy term and other effects explicitly noted.

Thus, the only fitting parameters are essentially the effective rates of secondary minerals. These parameters will be constrained with multiple lines of evidences from the hydrothermal experiments: solution chemistry evolution as a function of time (Fig. 8), mineral dissolution and precipitation rates (Fig. 9), saturation indices evolution as a

function of time (Fig. 10), mineral abundance data (Fig. 11), and reaction path evolution in activity-activity diagrams (Fig. 12). Then, the abundant information acquired from modeling will be used to decipher the complex interplay and a reaction network among feldspar dissolution, clay precipitation, and carbonate precipitation.

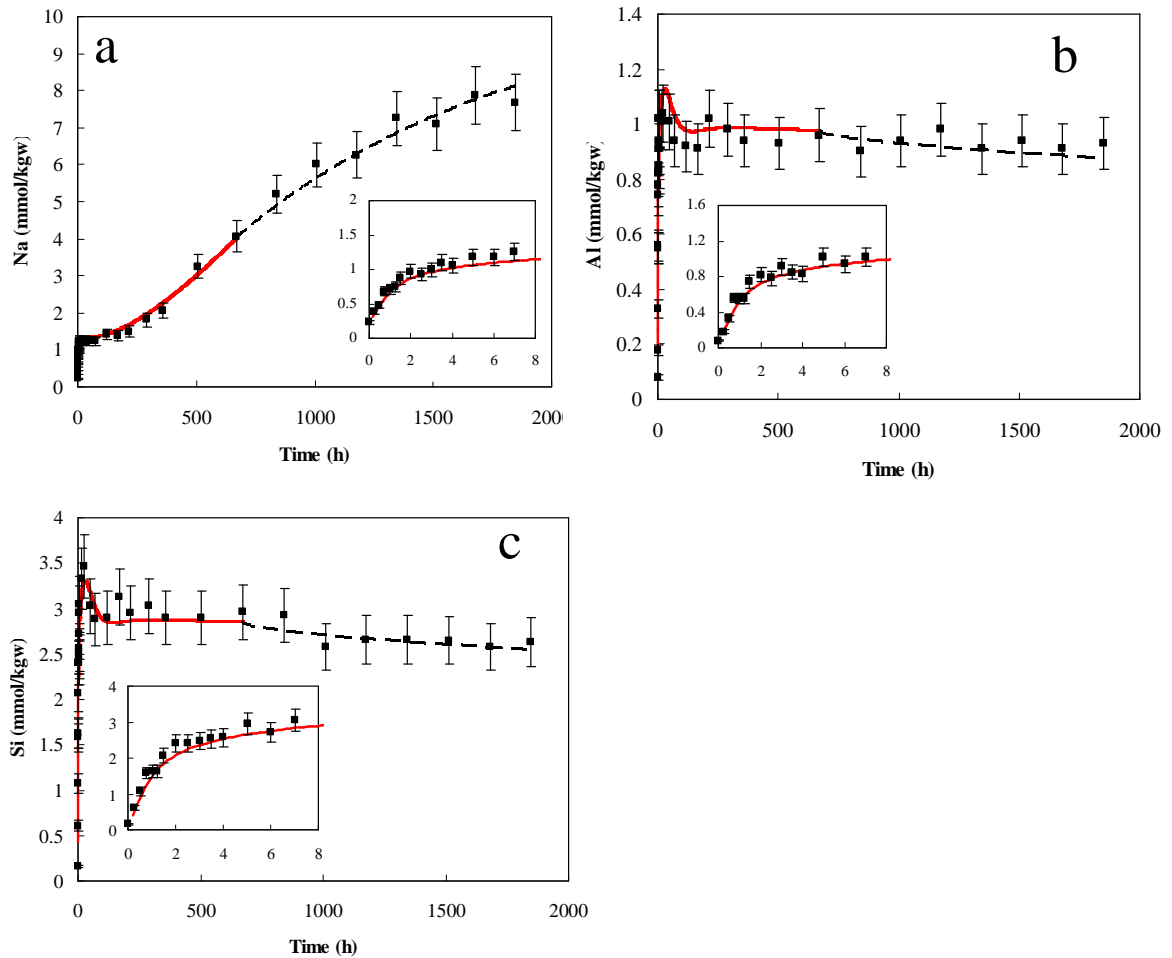


Figure 8. Temporal evolution of dissolved constituent concentrations: (a) Na; (b) Al, and (c) Si. Symbols denote experimental data; lines results from numerical reaction path model simulation. The portion of dotted line shows the simulation results during 672-1848 h. Error bars indicate 10% uncertainty in analytical measurements (from Zhu et al., Submitted).

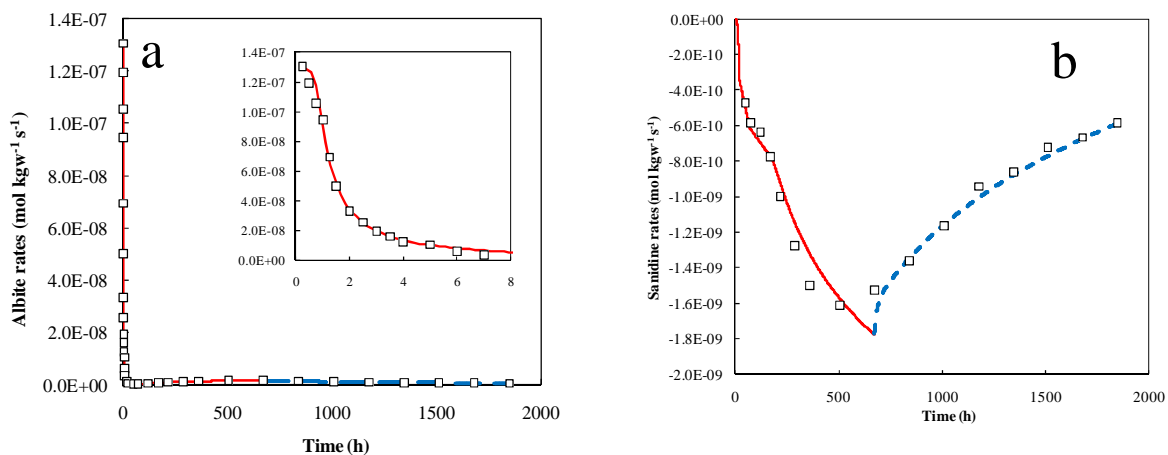


Figure 9. Albite dissolution (a) and sanidine precipitation (b) rates over time. Symbols denote experimental data (Alek97); lines result from numerical reaction path model simulation. Note that the unit of the rates is expressed in $\text{mol L}^{-1} \text{s}^{-1}$. A Y function was introduced to take account for the evolution of r_{Ab} as reaction progressed. Rates are a function of both S_A and ΔG_r (from Zhu et al., Submitted).

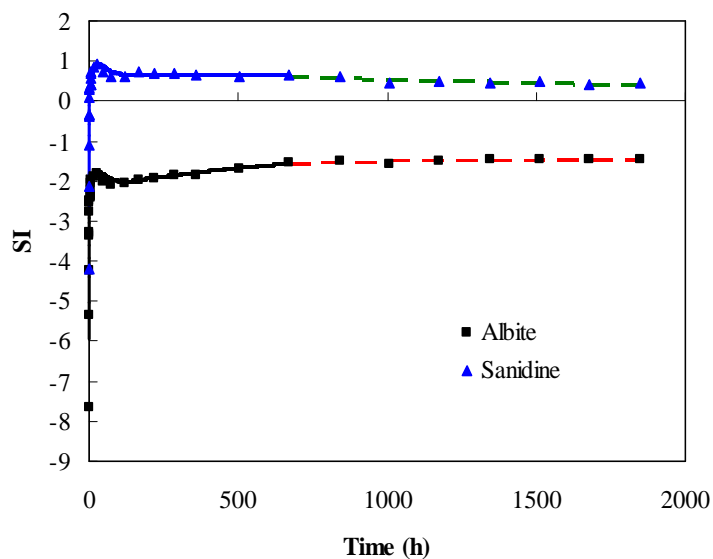


Figure 10. Saturation indices (SI) over time. Symbols represent SI calculated from speciation – solubility modeling for samples independently from each other (as snapshots) (Zhu and Lu, 2009). Lines from reaction path modeling that simulate the processes (from Zhu et al., Submitted).

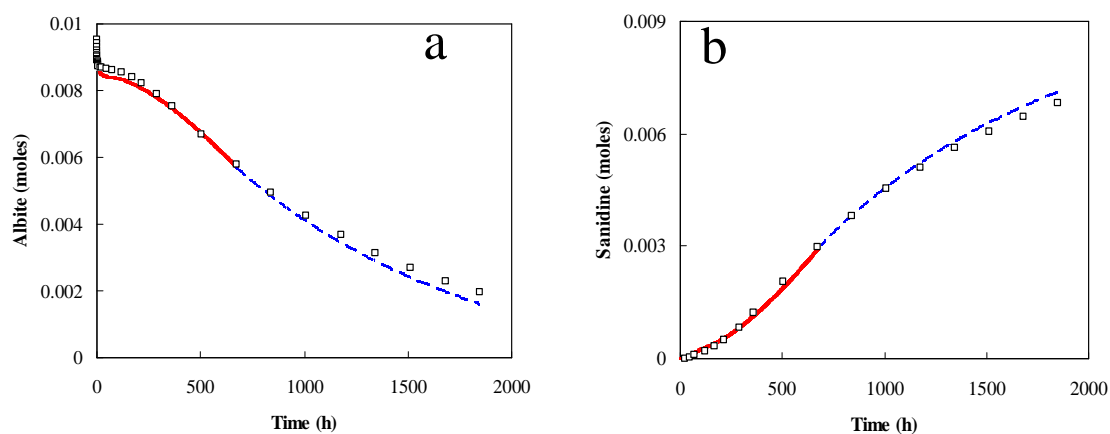


Figure 11. Comparison of the mass of albite (a) and sanidine (b) in the reactor (mol L^{-1}) predicted from the reaction path simulation (line) with rough estimation from rates and reaction intervals (symbols) (from Zhu et al., Submitted).

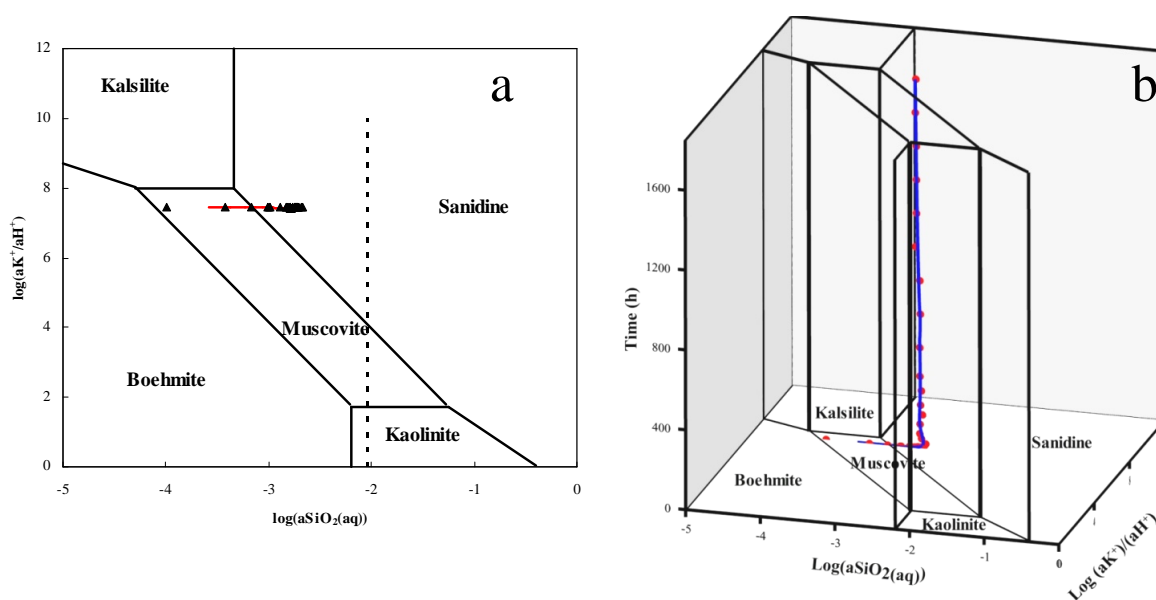


Figure 12. Activity diagram in the $K_2O-Al_2O_3-SiO_2-H_2O-(CO_2)-HCl$ system at 300 °C and 88 bars (8.8 MPa) for albite dissolution (from Zhu et al., Submitted). The dashed line is quartz saturation. Symbols denote experimental results, and the solid line the reaction path simulation results. (b) shows the evolution of reaction path as a function of time.

Therefore, an essential feature of this proposal is the tightly integrated hydrothermal experiments, electron microscopic characterization, and geochemical modeling. We believe this will give us a more complete picture of the chemical reaction kinetics.

4. Anticipated Results and Significance

The proposed research addresses some critical and urgent needs of the carbon sequestration program. The proposed research program is built upon our substantial previous work in the field of water-gas-rock interactions, including the work by the carbon sequestration program. Hence, the proposed work can be easily integrated with the NETL in-house research, and NETL-sponsored programs of field tests of injecting CO₂ into deep geological formations (Frio sandstone, Sleipner, and Weyburn projects), and mineral carbonation and brine sequestration programs (NETL, Los Alamos, Albany Research Center). Specially, we anticipate the following results:

- 1) Experimental measurements of plagioclase feldspar dissolution, at conditions pertinent to the geological carbon sequestration program;
- 2) Electron microscopy of the reactants and products to discern the reaction mechanisms;
- 3) Theoretical and modeling studies to interpret and synthesize experimental data, and development of a strategy to simulate *in situ* reaction kinetics in geological formation.

Overall, our results will help to resolve one of the major outstanding scientific issues facing the carbon sequestration program: the rates of chemical reactions in geological formations. The results will benefit the program by introducing the development of numerical performance assessment models, which will reduce the costs

of monitoring and design.

References

- Aagaard, P. and Helgeson, H. C., 1982. Thermodynamic and kinetic constraints on reaction rates among minerals and aqueous solutions. I. Theoretical considerations. *Am. J. of Sci.* **282**, 237-285.
- Alekseyev, V. A., Medvedeva, L. S., Prisyagina, N. I., Meshalkin, S. S., and Balabin, A. I., 1997. Change in the dissolution rates of alkali feldspars as a result of secondary mineral precipitation and approach to equilibrium. *Geochim. Cosmochim. Acta* **61**, 1125-1142.
- Becker, L. E., Hreha, A. J., and Dawson, T. A., 1978. *Pre-knox (Cambrian) Stratigraphy in Indiana*. Department of Natural Resources, Geological Survey Bulletin 57.
- Beig, M. S. and Lüttge, A., 2006. Albite dissolution kinetics as a function of distance from equilibrium: Implications for natural feldspar weathering. *Geochim. Cosmochim. Acta* **70**, 1402-1420.
- Bénézech, P., Palmer, D. A., Anovitz, L. M., and Horita, J., 2007. Dawsonite synthesis and reevaluation of its thermodynamic properties from solubility measurements: Implications for mineral trapping of CO₂. *Geochim. Cosmochim. Acta* **71**, 4438-4455.
- Bénézech, P., Palmer, D. A., and Wesolowski, D. J., 2008. Dissolution/precipitation kinetics of boehmite and gibbsite: Application of a pH-relaxation technique to study near-equilibrium rates. *Geochim. Cosmochim. Acta* **72**, 2429-2453.
- Berner, R. A. and Holdren, G. R., 1979. Mechanism of feldspar weathering-II. Observations of feldspars from soils. *Geochim. Cosmochim. Acta* **43**, 1173-1186.
- Blum, A. and Stillings, L., 1995. Feldspar dissolution kinetics. In: Brantley, S. L. and White, A. F. (Eds.), *Chemical Weathering Rates of Silicate Minerals*. Mineralogical Society of America, Washington DC. pp. 291-351.
- Blum, A. E. and Lasaga, A. C., 1987. Monte Carlo simulations of surface reaction rate laws. In: Stumm, W. (Ed.), *Aquatic Surface Chemistry*, 255-292. Wiley, New York.
- Brantley, S. L., 2005. Reaction kinetics of primary rock-forming minerals under ambient conditions. In: Holland, H. D. and Turekian, K. K. (Eds.), *Treatise on Geochemistry*. Volume 5, Elsevier, 73-117.
- Brantley, S. L., 2008. Kinetics of Mineral Dissolution. In: Brantley, S. L., Kubicki, J. D., and White, A. F. (Eds.), *Kinetics of Water-Rock Interaction*. Springer, New York.

- Brantley, S. L. and Chen, Y., 1995. Chemical weathering rates of pyroxenes and amphiboles. In: White, A. F. and Brantley, S. L. (Eds.), *Chemical Weathering Rates of Silicate Minerals*. Mineralogical Society of America, Washington DC.
- Brantley, S. L. and Stillings, L., 1996. Feldspar dissolution at 25 °C and low pH. *Am. J. Sci.* **296**, 101-127.
- Braunauer, S., Emmett, P. H., and Teller, E., 1938. Adsorption of gases in multimolecular layers. *J. Am. Chem. Soc.* **60**, 309-319.
- Brubacher, L., 2006. Obtaining reliable data online — Phase diagram for carbon dioxide. http://www.chem13news.uwaterloo.ca/issues/342/342_nov_06.html.
- Burch, T. E., Nagy, K. L., and Lasaga, A. C., 1993. Free energy dependence of albite dissolution kinetics at 80 °C and pH 8.8. *Chem. Geol.* **105**, 137-162.
- Burton, W. K., Cabrera, N., and Frank, F. C., 1951. The growth of crystals and the equilibrium structure of their surfaces. *Royal Soc. London Philos. Trans.* **243**, 299-358.
- Cama, J., Ganor, J., Ayora, C., and Lasaga, C. A., 2000. Smetite dissolution kinetics at 80 °C and pH 8.8. *Geochim. Cosmochim. Acta* **64**, 2701-2717.
- Carey, J. W., Lichtner, P. C., Rosen, E. P., Ziock, H. J., and Guthrie, G. D. J., 2003. Geochemical mechanisms of serpentine and olivine carbonation. Second annual conference on carbon sequestration, Alexandria, Virginia, Alexandria, Virginia.
- Carroll, S. A. and Knauss, K. G., 2005. Dependence of labradorite dissolution kinetics on CO₂(aq), Al(aq), and temperature. *Chem. Geol.* **217**, 213-225.
- Casey, W. H., Westrich, H. R., and Arnold, G. W., 1988. Surface chemistry of Labradorite Feldspar Reacted with Aqueous Solutions at pH - 2, 3, and 12. *Geochim. Cosmochim. Acta* **52**, 2795-2807.
- Casey, W. H., Westrich, H. R., Arnold, G. W., and Banfield, J. F., 1989. The surface chemistry of dissolving labradorite feldspar. *Geochim. Cosmochim. Acta* **58**, 821-832.
- Chou, L. and Wollast, R., 1985. Steady-state kinetics and dissolution mechanisms of albite. *Am. J. Sci.* **285**, 963-993.
- Christoffersen, J. and Christoffersen, M. R., 1976. The kinetics of dissolution of calcium sulphate dihydrate in water. *J. Cryst. Growth* **35**, 79-88.
- Cubillas, P., Kohler, S., Prieto, M., Causserand, C., and Oelkers, E. H., 2005. How do mineral coating affect dissolution rates? An experimental study of coupled CdCO₃ dissolution -- CdCO₃ precipitation. *Geochim. Cosmochim. Acta* **69**, 5459-5476.

- Daval, D., Martinez, I., Corvisier, J., Findling, N., Goffe, B., and Guyot, F., 2009. Carbonation of Ca-bearing silicates, the case of wollastonite: Experimental investigations and kinetic modeling. *Chem. Geol.* **265**, 63-78.
- DOE-NETL, 2008. Carbon Sequestration Atlas of the United States and Canada, 2nd ed., U.S. Dept. of Energy, www.netl.doe.gov/technologies/carbonseq/refshelf/atlas/ATLAS.pdf.
- Drever, J. I. and Clow, D. W., 1995. Weathering rates in catchments. In: White, A. F. and Brantley, S. L. (Eds.), *Chemical Weathering Rates of Silicate Minerals*. Mineralogical Society of America.
- Duan, Z., Sun, R., Zhu, C., and Chou, I., 2006. An improved model for the calculation of CO₂ solubility in aqueous solutions containing Na⁺, K⁺, Ca²⁺, Mg²⁺, Cl⁻, and SO₄²⁻. *Mar. Chem.* **98**, 131-139.
- Eliasson, B., Riemer, P.W.F., and Wokaun, A., 1998. *Greenhouse Gas Control Technologies: Proceedings of the 4th International Conference on Greenhouse Gas Control Technologies*. Elsevier.
- Emery, D. and Robinson, A. D., 1993. *Inorganic Geochemistry: Application to Petroleum Geology*. Blackwell Scientific Publication.
- Fauth, D. J., Baltrus, J. P., Knoer, J. P., Soong, Y., Howard, B. H., Graham, W. J., Maroto-Valer, M. M., and Andresen, J. M., 2001. Conversion of silicate minerals with carbon dioxide producing environmentally benign and stable carbonates. *Prepr. Am. Chem. Soc. Div. Fuel Chem.* **46**, 278-279.
- Fritz, B. and Noguera, C., 2009. Mineral precipitation kinetics. In: Oelkers, E. H. and Schott, J. (Eds.), *Thermodynamics and kinetics of water-rock interaction*. Mineralogical Society of America.
- Fu, Q., Lu, P., Konishi, H., Dilmore, R., Xu, H., Seyfried, W. E., Jr., and Zhu, C., 2009. Coupled alkali-feldspar dissolution and secondary mineral precipitation in batch systems: 1. New experiments at 200 °C and 300 bars. *Chem. Geol.* **258**, 125-135.
- Ganor, J., Lu, P., Zheng, Z., and Zhu, C., 2007. Bridging the gap between laboratory measurements and field estimations of silicate weathering using simple calculations. *Environ. Geol.* **53**, 599-610.
- Ganor, J., Mogollon, J. L., and Lasaga, A. C., 1995. The effect of pH on kaolinite dissolution rates and on activation energy. *Geochim. Cosmochim. Acta* **59**, 1037-1052.
- Ganor, J., Mogollon, J. L., and Lasaga, A. C., 1999. Kinetics of gibbsite dissolution under low ionic strength conditions. *Geochim. Cosmochim. Acta* **63**, 1635-1651.

- Gautier, J.-M., Oelkers, E. H., and Schott, J., 1994. Experimental study of K-feldspar dissolution rates as a function of chemical affinity at 150 °C and pH 9. *Geochim. Cosmochim. Acta* **58**, 4549-4560.
- Gautier, J. M., Oelkers, E. H., and Schott, J., 2001. Are quartz dissolution rates proportional to B.E.T. surface areas? *Geochim. Cosmochim. Acta* **65**, 1059-1070.
- Giammar, D. E., Bruant, R. G., and Peters, C. A., 2005. Forsterite dissolution and magnesite precipitation at conditions relevant for deep saline aquifer storage and sequestration of carbon dioxide. *Chem. Geol.* **217**, 257-276.
- Golubev, S. V., Pokrovsky, O. S., and Schott, J., 2005. Experimental determination of the effect of dissolved CO₂ on the dissolution kinetics of Mg and Ca silicates at 25 °C. *Chem. Geol.* **217**, 227-238.
- Haar, L., Gallagher, J. S., and Kell, G. S., 1984. *NBS/NRC Steam Tables: Thermodynamic and Transport Properties and Computer Programs for Vapor and Liquid States of Water in SI Units*. Hemisphere Publishing Corporation, New York, 320p.
- Harouiya, N. and Oelkers, E. H., 2004. An experimental study of the effect of aqueous fluoride on quartz and alkali-feldspar dissolution rates. *Chem. Geol.* **205**, 155-167.
- He, S., Oddo, J. E., and Tomson, M. B., 1994. The Seeded Growth of Calcium Sulfate Dihydrate Crystals in NaCl Solutions up to 6 m and 90 °C. *J. Colloid Interf. Sci.* **163**, 372-378.
- Helgeson, H. C., 1968. Evaluation of irreversible reactions in geochemical processes involving minerals and aqueous solutions-1. Thermodynamic relations. *Geochim. Cosmochim. Acta* **32**, 853-877.
- Helgeson, H. C., 1969. Thermodynamics of hydrothermal systems at elevated temperatures and pressures. *Am. J. Sci.* **267**, 729-804.
- Helgeson, H. C., 1971. Kinetics of mass transfer among silicates and aqueous solutions. *Geochim. Cosmochim. Acta* **35**, 421-469.
- Helgeson, H. C., 1979. Mass transfer among minerals and hydrothermal solutions. In: Barnes, H. L. (Ed.), *Geochemistry of Hydrothermal Ore Deposits*. John Wiley & Sons, New York.
- Helgeson, H. C., Delany, J. M., Nesbitt, H. W., and Bird, D. K., 1978. Summary and critique of the thermodynamic properties of rock-forming minerals. *Am. J. Sci.* **278A**, 1-229.

- Helgeson, H. C., Kirkham, D. H., and Flowers, G. C., 1981. Theoretical prediction of the thermodynamic behavior of aqueous electrolytes by high pressures and temperatures. IV. Calculation of activity coefficients, osmotic coefficients, and apparent molal and standard and relative partial molal properties to 600 °C and 5 kb. *Am. J. Sci.* **281**, 1249-1516.
- Helgeson, H. C. and Murphy, W. M., 1983. Calculation of mass transfer among minerals and aqueous solutions as a function of times and surface area in geochemical processes, I. Computational approach. *Math. Geol.* **15**, 109-130.
- Helgeson, H. C., Murphy, W. M., and Aagaard, P., 1984. Thermodynamic and kinetic constraints on reaction rates among minerals and aqueous solutions II. Rate constants, effective surface area, and the hydrolysis of feldspar. *Geochim. Cosmochim. Acta* **48**, 2405-2432.
- Hellmann, R., 1994. The albite-water system; Part I, The kinetics of dissolution as a function of pH at 100, 200, and 300 °C. *Geochim. Cosmochim. Acta* **58**, 595-611.
- Hellmann, R., Eggleston, C. R., Hochella, M. F., and Crerar, D. A., 1990. The formation of leached layers on albite surfaces during dissolution under hydrothermal conditions. *Geochim. Cosmochim. Acta* **54**, 1267-1281.
- Hellmann, R., Penisson, J. M., Hervig, R. L., Thomassin, J. H., and Abrioux, M. F., 2003. An EFTEM/HRTEM high-resolution study of the near surface of labradorite feldspar altered at acid pH: evidence for interfacial dissolution-reprecipitation. *Phys. Chem. Miner.* **30**, 192-197.
- Hellmann, R. and Tisserand, D., 2006. Dissolution kinetics as a function of the Gibbs free energy of reaction: An experimental study based on albite feldspar. *Geochim. Cosmochim. Acta* **70**, 364-383.
- Hochella, M. F. J. and Banfield, J. F., 1995. Chemical weathering of silicates in nature: A microscopic perspective with theoretical considerations. In: White, A. F. and Brantley, S. L. (Eds.), *Chemical Weathering Rates of Silicate Minerals*. Mineralogical Society of America.
- Holdren, G. R. and Berner, R. A., 1979. Mechanism of feldspar weathering. I. Experimental studies. *Geochim. Cosmochim. Acta* **43**, 1161-1171.
- Holland, T. J. B. and Powell, R., 1998. An internally consistent thermodynamic data set for phases of petrological interest. *J. Metamor. Geol.* **16**, 309-343.
- Huijgen, W. J. J., Witkamp, G. J., and Comans, R. N. J., 2006. Mechanisms of aqueous wollastonite carbonation as a possible CO₂ sequestration process. *Chem. Eng. Sci.* **61**, 4242-4251.

- IEA, 2008. Aquifer Storage - Development Issues, 2008/12, RPT08-1257. IEA Greenhouse Gas R&D Programme (IEA GHG).
<http://www.co2crc.com.au/publications/>.
- IPCC, 2005. Special Report on carbon Dioxide Capture and Storage.
<http://www.unep.ch/ipcc/activity/srccs/>.
- IPCC, 2007a. Climate Change 2007: Climate Changes Impacts, Adaptions, and Vulnerability. www.ipcc-wg2.org/index.html.
- IPCC, 2007b. Climate Change 2007: The Physical Science Basis. Cambridge University Press.
- Johnson, J. W., Oelkers, E. H., and Helgeson, H. C., 1992. SUPCRT92 - A software package for calculating the standard molal thermodynamic properties of minerals, gases, aqueous species, and reactions from 1-bar to 5000-bar and 0 °C to 1000 °C. *Comput. Geosci.* **18**, 899-947.
- Lasaga, A. C., 1981a. Rate laws of chemical reactions. In: Lasaga, A. C., Kirkpatrick, R.J. (Ed.), *Kinetics of Geochemical Processes*. Mineralogical Society of America, Washington DC.
- Lasaga, A. C., 1981b. Transition State Theory. In: Lasaga, A. C. and Kirkpatrick, R. J. (Eds.), *Kinetics of Geochemical Processes*. Mineralogical Society of America, Washington DC.
- Lasaga, A. C., 1998. *Kinetic Theory in the Earth Sciences*. Princeton University Press, New York.
- Lasaga, A. C., Soler, J. M., Ganor, J., Burch, T. E., and Nagy, K. L., 1994. Chemical weathering rate laws and global geochemical cycles. *Geochim. Cosmochim. Acta* **58**, 2361-2386.
- Lu, P., Fu, Q., Seyfried, W. E., Jr., Hedges, S., Jones, K., and Zhu, C., To be submitted. Coupled alkali feldspar dissolution and secondary mineral precipitation in batch systems: 2. New experiments with CO₂ and implications for carbon sequestration. *Int. J. Greenh. Gas Con.*
- McGrail, B. P., Schaef, H. T., Ho, A. M., Chien, Y. J., Dooley, J. J., and Davidson, C. L., 2006. Potential for carbon dioxide sequestration in flood basalts. *J. Geophys. Res.-Sol. Ea.* 111 B12201.
- Metz, V., Raanan, H., Pieper, H., Bosbach, D., and Ganor, J., 2005. Towards the establishment of a reliable proxy for the reactive surface area of smectite. *Geochim. Cosmochim. Acta* **69**, 2581-2591.

- Nagy, K. L., 1995. Dissolution and precipitation kinetics of sheet silicates. In: White, A. F. and Brantley, S. L. (Eds.), Chemical Weathering Rates of Silicate Minerals. Mineralogical Society of America.
- Nagy, K. L., Blum, A. E., and Lasaga, A. C., 1991. Dissolution and precipitation kinetics of kaolinite at 80° C and pH 3: The dependence on solution saturation state. *Am. J. Sci.* **291**, 649-686.
- Nagy, K. L. and Lasaga, A. C., 1992. Dissolution and precipitation kinetics of gibbsite at 80°C and pH 3: The dependence on solution saturation state. *Geochim. Cosmochim. Acta* **56**, 3093-3111.
- Nagy, K. L. and Lasaga, A. C., 1993. Simultaneous precipitation kinetics of kaolinite and gibbsite at 80°C and pH 3. *Geochim. Cosmochim. Acta* **57**, 4329-4335.
- Nesbitt, H. W. and Muir, I., 1988. SIMS depth profiles of weathered plagioclase and processes affecting dissolved Al and Si in some acidic soil solutions. *Nature* **334**, 336-338.
- Nesbitt, H. W. and Skinner, W. M., 2001. Early development of Al, Ca, and Na compositional gradients in labradorite leached in pH 2 HCl solutions. *Geochim. Cosmochim. Acta* **65**, 715-727.
- NRC, 2003. Novel approaches to carbon management separation, capture, sequestration, and conversion to useful products workshop report. National Research council, Washington, DC.
- Nugent, M. A., Brantley, S. L., Pantano, C. G., and Maurice, P. A., 1998. The influence of natural mineral coatings on feldspar weathering. *Nature* **395**, 588-591.
- O'Connor, W. K., Dahlin, D. C., Rush, G. E., Dahlin, C. L., and Collins, W. K., 2002. Carbon dioxide sequestration by direct mineral carbonation: process mineralogy of feed and products. *Miner. Metall. Proc.* **19**, 95-101.
- Oelkers, E. H., 2001. General kinetic description of multioxide silicate mineral and glass dissolution. *Geochim. Cosmochim. Acta* **65**, 3703-3719.
- Oelkers, E. H. and Helgeson, H. C., 1990. Triple-ion anions and polynuclear complexing in supercritical electrolyte solutions. *Geochim. Cosmochim. Acta* **54**, 727-738.
- Oelkers, E. H., Schott, J., and Devidal, J. L., 2001. On the interpretation of closed system mineral dissolution experiments: Comment on "Mechanism of kaolinite dissolution at room temperature and pressure Part II: Kinetic study" by Huertas et al. (1999). *Geochim. Cosmochim. Acta* **65**, 4429-4432.

- Parkhurst, D. L. and Appello, A. A. J., 1999. *User's guide to PHREEQC (version 2)-a computer program for speciation, batch-reaction, one dimensional transport, and inverse geochemical calculations*. Water-Resource Investigation Report. U.S. Geological Survey.
- Pokrovsky, O. S. and Schott, J., 2000. Kinetics and mechanism of forsterite dissolution at 25 °C and pH from 1 to 12. *Geochim. Cosmochim. Acta* **64**, 3313-3325.
- Prigogine, I. and Defay, R., 1965. *Chemical Thermodynamics*. Longmans Green, London.
- Reed, M. H. and Spycher, N. F., 1984. Calculation of pH and mineral equilibria in hydrothermal waters with application to geothermometry and studies of boiling and dilution. *Geochim. Cosmochim. Acta* **48**, 1479-1492.
- Rogen, B. and Fabricius, I. L., 2002. Influence of clay and silica on permeability and capillary entry pressure of chalk reservoirs in the North Sea. *Petrol. Geosci.* **8**, 287-293.
- Schramke, J. A., Kerrick, D. M., and Lasaga, A. C., 1987. The reaction muscovite + quartz \rightleftharpoons andalusite + K-feldspar + water. Part I. Growth kinetics and mechanism. *Am. J. Sci.* **287**, 517-559.
- Seyfried, W. E., Jr., Janecky, D. R., and Berndt, M. E., 1987. Rocking autoclaves for hydrothermal experiments; II, The flexible reaction-cell system. In: Barnes, H. L. (Ed.), *Hydrothermal Experimental Techniques*. Wiley-Interscience, 216-239.
- Shiraki, R. and Brantley, S. L., 1995. Kinetics of near-equilibrium calcite precipitation at 100°C: An evaluation of elementary reaction-based and affinity based rate laws. *Geochim. Cosmochim. Acta* **59**, 1457-1471.
- Shock, E. L. and Helgeson, H. C., 1988. Calculation of the thermodynamic and transport properties of aqueous species at high pressures and temperatures: Correlation algorithms for ionic species and equation of state predictions to 5 kb and 1000 °C. *Geochim. Cosmochim. Acta* **52**, 2009-2036.
- Shock, E. L., Helgeson, H. C., and Sverjensky, D. A., 1989. Calculations of the thermodynamic and transport properties of aqueous species at high pressures and temperatures: Standard partial molal properties of inorganic neutral species. *Geochim. Cosmochim. Acta* **53**, 2157-2183.
- Shock, E. L., Oelkers, E. H., Sverjensky, D. A., Johnson, J. W., and Helgeson, H. C., 1992. Calculation of thermodynamic and transport properties of aqueous species at high pressures and temperatures. Effective electrostatic radii, dissociation constants and standard partial molal properties to 1000° C and 5 kb. *J. Chem. Soc. London, Faraday Transactions* **88**, 803-826.

- Shock, E. L., Sassani, D. C., Willis, M., and Sverjensky, D. A., 1997. Inorganic species in geologic fluids: Correlations among standard molal thermodynamic properties of aqueous ions and hydroxide complexes. *Geochim. Cosmochim. Acta* **61**, 907-950.
- Stillings, L. L., Brantley, S. L., and Machesky, M. L., 1995. Proton adsorption at an adularia feldspar surface. *Geochim. Cosmochim. Acta* **59**, 1473-1482.
- Strazisar, B. R., Zhu, C., and Hedges, S. W., 2006. Preliminary modeling of the long-term fate of CO₂ following injection into deep geological formations. *Environ. Geosci.* **13**, 1-15.
- Sverjensky, D. A., 1987. Calculation of the thermodynamic properties of aqueous species and the solubilities of minerals in supercritical electrolyte-solutions. *Reviews in Mineralogy and Geochemistry* **17**, 177-209.
- Sverjensky, D. A., Shock, E. L., and Helgeson, H. C., 1997. Prediction of the thermodynamic properties of aqueous metal complexes to 5 Kb and 1000 °C. *Geochim. Cosmochim. Acta* **61**, 1359-1412.
- Tagirov, B. and Schott, J., 2001. Aluminum speciation in crustal fluids revisited. *Geochim. Cosmochim. Acta* **65**, 3965-3992.
- Tanger, J. C. and Helgeson, H. C., 1988. Calculations of the thermodynamic and transport properties of aqueous species at high pressures and temperatures: Revised equation of state for the standard partial molal properties of ions and electrolytes. *Am. J. Sci.* **288**, 19-98.
- Taylor, A. S., Blum, J. D., and Lasaga, A. C., 2000. The dependence of labradorite dissolution and Sr isotope release rates on solution saturation state. *Geochim. Cosmochim. Acta* **64**, 2389-2400.
- Veblen, D. R., 1991. Polysomatism and polysomatic series: A review and applications. *Am. Mineral.* **76**, 801-826.
- White, A. F., 1995. Chemical weathering of silicate minerals in soils. In: White, A. F. and Brantley, S. L. (Eds.), *Chemical Weathering Rates of Silicate Minerals*. Mineralogical Society of America.
- Witkamp, G. J., Van der Eerden, J. P., and Van Rosmalen, G. M., 1990. Growth of gypsum : I. Kinetics. *J. Cryst. Growth* **102**, 281-289.
- Wogelius, R. A. and Walther, J. V., 1991. Olivine dissolution at 25 °C: Effects of pH, CO₂, and organic acids. *Geochim. Cosmochim. Acta* **55**, 943-954.

- Wolery, T. J., 1992. EQ3/6, *A software package for geochemical modeling of aqueous systems: Package overview and installation guide (version 7.0)*. URCL-MA-110662-PT-I, Livermore, Calif., Univ. California, Lawrence Livermore Laboratory.
- Worden, R. and Morad, S., 2003. *Clay Mineral Cements in Sandstones: Special Publication 34 of the IAS*. Wiley-Blackwell. 520 p.
- Zhang, J. and Nancollas, G. H., 1992. Influence of calcium/sulfate molar ratio on the growth rate of calcium sulfate dihydrate at constant supersaturation. *J. Cryst. Growth* **118**, 287-294.
- Zhu, C., 2003. A case against Kd-based transport model: Natural attenuation at a mill tailings site. *Comput. Geosci.* **29**, 351-359.
- Zhu, C., 2009. Geochemical modeling of reaction paths and geochemical reaction networks. In: Oelkers, E. H. and Schott, J. (Eds.), *Thermodynamics and kinetics of water-rock interaction*. Mineralogical Society of America.
- Zhu, C. and Anderson, G. M., 2002. *Environmental Applications of Geochemical Modeling*. Cambridge University Press, London.
- Zhu, C., Blum, A. E., and Veblen, D. R., 2004. Feldspar dissolution rates and clay precipitation in the Navajo aquifer at Black Mesa, Arizona, USA. In: Wanty, R. B. and Seal, R. R. I. (Eds.), *Water-Rock Interaction*. A.A. Balkema, Saratoga Springs, New York.
- Zhu, C. and Lu, P., 2009. Coupled alkali feldspar dissolution and secondary mineral precipitation in batch systems: 3. Saturation Indices of Product Minerals and Reaction Paths. *Geochim. Cosmochim. Acta* **73**, 3171-3200.
- Zhu, C., Lu, P., Zheng, Z., and Ganor, J., Submitted. Alkali feldspar dissolution and secondary mineral precipitation in batch systems: 4. Numerical modeling of kinetic reaction paths. *Geochim. Cosmochim. Acta*.

CHAPTER 10

CONCLUSIONS

Feldspars comprise over 50% of the volume of the earth's crust. Establishing reliable rates for low-temperature feldspar dissolution is essential to quantify many basic geological and environmental processes.

The pioneering work by Helgeson and co-workers (Garrels and Mackenzie, 1967; Helgeson, 1968; Helgeson et al., 1969, 1984; Aagaard and Helgeson, 1982; Helgeson and Murphy, 1983) to model feldspar hydrolysis as a process of coupled dissolution and precipitation reactions transformed the study of water-rock interactions into a quantitative science and opened up vast new fields of geochemistry in the following decades. The early model, however, assumed partial equilibria between the aqueous solution and the secondary phases. Although the assumption of partial equilibrium has been questioned in the intervening years (Steefel and Van Cappellen, 1990; Nagy and Lasaga, 1993; Small, 1993; Lasaga et al., 1994; Alekseyev et al., 1997; Lasaga, 1998; Zhu et al., 2004; Price et al., 2005; Zhu, 2006; Ganor et al., 2007), until now there has never been a rigorous examination of this hypothesis. Here, we systematically analyzed this assumption by conducting new hydrothermal experiments and performing speciation-solubility and reaction path modeling.

(1) Alkali-feldspar hydrolysis experiments were conducted using a well-mixed batch reactor at 150-200 °C and 300 bars with or without the presence of CO₂. SEM, HRTEM and XRD analyses of the surface of alkali-feldspars provide clear evidence for the dissolution of feldspars and coexistence of secondary mineralization (boehmite, kaolinite, and paragonite). These secondary minerals persisted metastably during the entire durations of experiments as indicated by both mineralogical characterizations and speciation-solubility calculations.

- (2) We find three lines of experimental evidence that contradicts the partial equilibrium hypothesis in the experimental feldspar–water system: saturation indices, reaction paths, and secondary mineral paragenesis.
- (3) The primary mineral dissolution and secondary mineral precipitation are strongly coupled, forming a reaction network. The reconciliation of the apparent discrepancy between laboratory measured and field derived dissolution rates needs to be achieved by regarding primary mineral dissolution as part of the reaction network.
- (4) The precipitation of secondary minerals is the limiting step in the system, which caps the dissolution rate of the primary mineral.
- (5) Modeling results show that a quasi-steady state was reached. At the quasi-steady state, dissolution reactions proceeded at rates that are orders of magnitude slower than the rates measured at far-from-equilibrium. The quasi-steady state is determined by the relative rate constants, and strongly influenced by the function of Gibbs free energy of reaction (ΔG_r) in the rate laws.
- (6) The experimental and geochemical modeling results lend support to the Zhu-Blum-Veblen hypothesis for explaining the apparent field – lab discrepancy (Zhu et al., 2004).

The injection of CO₂ into deep saline aquifers is being considered as an option for greenhouse gas mitigation. However, the response of an aquifer to the injected CO₂ is largely unknown. Experiments involving the reaction of Navajo Sandstone with acidic brine were conducted at 200 °C and 25 or 30 MPa to evaluate the extent of fluid-rock interactions. The solution chemistry data indicate that the SiO₂(aq) increases gradually and pH increases slowly with reaction progress. Silicate minerals in the sandstone display textures (dissolution features, secondary mineralization), indicating that these phases are

reacting strongly with the fluid. Dissolved CO₂ is likely to acidify the brine and to provide a source of carbon for the precipitation of carbonate minerals. The chemical reactions likely increase the bulk porosity of the sandstone due to dissolution of silicate minerals. However, allophane and illite/smectite fill voids in sandstone grains. There is no evidence for the removal of clay coatings due to chemical reactions. It is uncertain whether the mechanical forces near an injection well would mobilize the smectite and allophane and clog pore throats. Trace amounts of metals, including Cu, Zn, and Ba, were mobilized.

We compiled thermodynamic properties for aqueous and solid arsenic species from the literature, recalculated those properties to ensure internal consistency, and used these data to construct Eh-pH diagrams. These diagrams provide ready references for scientists working on arsenic geochemistry.

The differences of adsorption and coprecipitation of Pb with iron oxyhydroxide are studied with sorption edge measurements, High Resolution Transmission and Analytical Electron Microscopy (HR TEM-AEM), and geochemical modeling. Coprecipitation of Pb²⁺ with ferric oxyhydroxides occurred at ~ pH 4, about 0.5-1.0 pH unit higher than Fe³⁺ precipitation. Coprecipitation is more efficient than adsorption in removing Pb²⁺ from aqueous solutions at similar sorbate/sorbent ratios. X-ray Diffraction (XRD) shows peaks of lepidocrocite and two additional broad peaks similar to fine particles of 2-line ferrihydrite (2LFh). HRTEM of the Pb-Fe coprecipitates shows a mixture of 2 to 6 nm diameter spheres and 8-20 by 200-300 nm needles, both uniformly distributed with Pb²⁺. Geochemical modeling shows that surface complexation model explains adsorption experimental data well. In contrast, solid solution model or combined

solid solution formation and surface complexation can fit coprecipitation experimental data sets well and explain the overlap between sorption edges with different Pb:Fe ratios, but surface complexation alone cannot account for all the Pb^{2+} bound to the solids.

Based on these results, we hypothesize that after coprecipitation experiment Pb^{2+} was first adsorbed onto the nanometer-sized, metastable, iron oxyhydroxide polymers of 2LFh. As the iron oxyhydroxides grew and transformed into more stable phases, Pb^{2+} was trapped in the iron oxyhydroxide structure. Hence, coprecipitation and adsorption experiments resulted in different Pb^{2+} incorporation mechanisms, which could result in different mobility, bioavailability, and long-term stability of Pb^{2+} in the environment.

REFERENCES

- Aagaard P. and Helgeson H. C. (1982) Thermodynamic and kinetic constraints on reaction rates among minerals and aqueous solutions. I. Theoretical considerations. *Am. J. Sci.* **282**, 237–285.
- Alekseyev V. A., Medvedeva L. S., Prisyagina N. I., Meshalkin S. S. and Balabin A. I. (1997) Change in the dissolution rates of alkali feldspars as a result of secondary mineral precipitation and approach to equilibrium. *Geochim. Cosmochim. Acta* **61**, 1125–1142.
- Ganor J., Lu P., Zheng Z. and Zhu C. (2007) Bridging the gap between laboratory measurements and field estimations of weathering using simple calculations. *Environ. Geol.* **53**, 599–610.
- Garrels R. M. and Mackenzie F. T. (1967) Origin of the chemical composition of some springs and lakes. In *Equilibrium Concepts in Natural Water Systems*, vol. 67 (ed. R. F. Gould). American Chemical Society, Washington, DC, pp. 222–242.
- Helgeson H. C. (1968) Evaluation of irreversible reactions in geochemical processes involving minerals and aqueous solutions-1. Thermodynamic relations. *Geochim. Cosmochim. Acta* **32**, 853–877.
- Helgeson H. C., Garrels R. M. and Mackenzie F. T. (1969) Evaluation of irreversible reactions in geochemical processing involving minerals and aqueous solutions-II. Applications. *Geochim. Cosmochim. Acta* **33**, 455–481.

- Helgeson H. C. and Murphy W. M. (1983) Calculation of mass transfer among minerals and aqueous solutions as a function of times and surface area in geochemical processes, I. Computational approach. *Math. Geol.* **15**, 109–130.
- Helgeson H. C., Murphy W. M. and Aagaard P. (1984) Thermodynamic and kinetic constraints on reaction rates among minerals and aqueous solutions II. Rate constants, effective surface area, and the hydrolysis of feldspar. *Geochim. Cosmochim. Acta* **48**, 2405–2432.
- Lasaga A. C. (1998) *Kinetic Theory in the Earth Sciences*. Princeton University Press, New York.
- Lasaga A. C., Soler J. M., Ganor J., Burch T. E. and Nagy K. L. (1994) Chemical weathering rate laws and global geochemical cycles. *Geochim. Cosmochim. Acta* **58**, 2361–2386.
- Nagy K. L. and Lasaga A. C. (1993) Kinetics of simultaneous kaolinite and gibbsite precipitation. *Geochim. Cosmochim. Acta* **57**, 4329–4337.
- Price J. R., Velbel M. A. and Patino L. C. (2005) Rates and time scales of clay-mineral formation by weathering in saprolitic regoliths of the southern Appalachians from geochemical mass balance. *Geol. Soc. Am. Bull.* **117**, 783–794.
- Small J. S. (1993) Experimental determination of the rates of precipitation of authigenic illite and kaolinite in the presence of aqueous oxalate and comparison to the K/Ar ages of authigenic illite in reservoir sandstones. *Clays Clay Miner.* **41**, 191–208.
- Steefel, C. I. and van Cappellen, P., 1990. A new kinetic approach to modeling water-rock interaction: The role of nucleation, precursors, and Ostwald ripening. *Geochim. Cosmochim. Acta* **54**, 2657–2677.
- Zhu C. (2006) In situ silicate reaction rates in sandy aquifers. *Geochim. Cosmochim. Acta* **70**, A753.
- Zhu C., Blum A. E. and Veblen D. R. (2004) Feldspar dissolution rates and clay precipitation in the Navajo aquifer at Black Mesa, Arizona, USA. In *Water–Rock Interaction* (eds. R. B. Wanty and R. R. I. Seal). A.A. Balkema, Saratoga Springs, New York, pp. 895–899.

Vita

Peng Lu

Department of Geological Sciences, Indiana University
1001 East 10th Street
Bloomington, IN 47405

pelu@indiana.edu
Office: (812) 856-3170

Education

- **Ph.D., Hydrogeochemistry**, May. 2010, Indiana University, Bloomington, Indiana
Advisor: Dr. Chen Zhu
- **M.S., Geosciences**, Jun. 2003, Nanjing University, Nanjing, China
Advisor: Dr. Jianping Zhai
- **B.S., Geology**, Jun. 2000, Nanjing University, Nanjing, China
Advisor: Dr. Xiangning Yang

Professional Activities

- **08/2004-Present**, Research Assistant, Geochemical Modeling and Wet Chemistry labs, Indiana University, Bloomington, IN
- **Fall 2007-Fall 2009**, Associate Instructor, Department of Geological Sciences, Indiana University, Bloomington, IN
- **09/2000-05/2004**, Research Assistant, Green Building Materials Group, Nanjing University, Nanjing, China

Refereed Publications

- **Lu, P.** and Zhu, C. Arsenic Eh-pH and solubility diagrams at 25 °C and 1 bar (0.1 MPa). *Environ. Earth. Sci.* submitted.
- **Lu, P.**, Fu, Q., Seyfried, W. E., Hereford, A., and Zhu, C. (2010) Navajo sandstone-brine-CO₂ interaction: implications for geological carbon sequestration. *Environ. Earth. Sci.* in press, DOI: 10.1007/s12665-010-0501-y.
- Zhu, C., **Lu, P.**, Zheng, Z., and Ganor, J. (2010) Alkali feldspar dissolution and secondary mineral precipitation in batch systems: 4. Numerical modeling of kinetic reaction paths. *Geochim. Cosmochim. Acta* in press.
- Zhu, C. and **Lu, P.** (2009) Alkali feldspar dissolution and secondary mineral precipitation in batch systems: 3. Saturation states of product minerals and reaction paths. *Geochim. Cosmochim. Acta* **73** (11): 3171-3200.
- Fu, Q., **Lu, P.**, Konishi, H., Dillmore, R., Xu, H., Seyfried, W. E. and Zhu, C. (2009) Coupled alkali-feldspar dissolution and secondary mineral precipitation in batch systems: 1. New experiments at 200 °C and 300 bars (30 MPa). *Chem. Geol.* **258** (3-4): 125-135.

- **Lu, P.**, Li, Q., and Zhai, J. (2008) Mineralogical characterizations and reaction path modeling of the pozzolanic reaction of fly ash-lime systems. *J. Am. Ceram. Soc.* **91**(3): 955-964.
- Huang, L., Zhai, j., **Lu, P.** Nutrient removal ability and resistance of five hydrophytes under low-temperature conditions. *Int. J. Environ. Pollut.* in press.
- Dillmore, R., **Lu, P.**, Allen, D., Soong, Y., Hedges, S., Fu, J.K., Dobbs, C.L., Degalbo, A., and Zhu, C. (2008) Sequestration of CO₂ in mixtures of bauxite residue and saline waste water. *Energ. Fuel* **22**: 343-353.
- Kelly, S., **Lu, P.**, Bolin, T., Chattopadhyay, S., Newville, M. G., Shibata, T., and Zhu, C. (2008) Molecular structure of lead(II) coprecipitated with iron(III) oxyhydroxide, in: Barnett, M. and Kent D. (Eds.) *Adsorption of Metals by Geomedia II: Variables, Mechanisms, and Model Applications* Elsevier Science, pp. 67-94.
- Ganor, J., **Lu, P.**, Zheng, Z., and Zhu, C. (2007) Bridging the gap between laboratory measurements and field estimations of silicate weathering using simple calculations. *Environ. Geol.* **53**(3): 599-610.
- **Lu, P.**, Zhai, J., Lu, H., et. al. (2005) Morphological and compositional characteristics of fly ash residues of pozzolanic reaction. *Journal of the Chinese Ceramic Society.* **33**(5): 627-631 (in Chinese with English abstract)
- **Lu, P.**, Zhai, J., Lu, H., et. al., et. al. (2005) Study on the pozzolanic activities of mineral additives. *Journal of Building Materials.* **8**(3): 289-293 (in Chinese with English abstract)
- **Lu, P.**, Zhai, J., and Nie, R. (2004) Study on the early stage hydration of Portland cement with environmental SEM. *Journal of the Chinese Ceramic Society.* **32**(4): 530-536 (in Chinese with English abstract)
- **Lu, P.**, Xu, H., and Lu, H. (2003) Methods of selecting residual carbon from fly ash: present and future. *Environmental Protection Science.* **29**(3):1-3. (in Chinese with English abstract)
- **Lu, P.**, Zhai, J., Fu, X., and Nie, R. (2003) Using fly ash to treat leachate from a waste disposal site. *Fly Ash Comprehensive Utilization.* No.1:14-16. (in Chinese with English abstract)
- Huang, L., Shen, M., Nie, R., **Lu, P.**, Xu, H. (2003) Properties of fly ash discharged from Yuntianhua Group Co., Ltd. *Environmental Protection Science.* **29**(1):1-4. (in Chinese with English abstract)
- Xu, H., Shen, M., Huang, L., **Lu, P.** (2003) Comprehensive evaluation and utilization of fly ash discharged from Yuntianhua Group Co., Ltd. *Environmental Protection Science.* No. 2:1-3. (in Chinese with English abstract)
- Shen, M., Zhai, J., **Lu, P.**, Fu, X. (2003) Classifying ground fly ash discharged from Huaneng Power Plant. *Fly Ash Comprehensive Utilization.* No.6:6-9. (in Chinese with English abstract)

- Fu, X., Zhai, J., **Lu, P.**, and Huang, L. (2002) Compressive strength of the cenospheres of fly ash. *Fly Ash Comprehensive Utilization*. No. 4: 27-30. (in Chinese with English abstract)
- Zhai, J., Tan, Q., Fu, X., **Lu, P.** (2002) Fly ash as an agricultural soil amendment/fertilizer. *Fly Ash Comprehensive Utilization*. No. 2: 3-6. (in Chinese with English abstract)
- Zhai, J., Li, W., Fu, X., **Lu, P.**, (2002) Effects of Na-salt on strength of fly ash-lime system. *Fly Ash Comprehensive Utilization*. No. 5: 13-15. (in Chinese with English abstract)

Conference Abstract

- **Lu, P.**, Fu, Q., Seyfried, W.E., Griffith, C., Hedges, S., Soong, Y. and Zhu, C. (2009) Sandstone/Shale-Brine-CO₂ Interactions: Implications for Geological Carbon Sequestration. American Geophysical Union Fall Meeting, December 14-18, San Francisco, California
- Liu, F., **Lu, P.**, Zhu, C., and Xiao, Y. (2009) Reactive transport modeling of the injection and CO₂ fate in the Mt. Simon sandstone formation. American Geophysical Union Fall Meeting, December 14-18, San Francisco, California
- **Lu, P.**, Fu, Q., Seyfried, W.E., Griffith, C., Hedges, S., Soong, Y. and Zhu, C. (2009) Sandstone/Shale-Brine-CO₂ Interactions: Implications for Geological Carbon Sequestration. Eastern Section AAPG Annual Meeting, September 20-22, 2009, Evansville, Indiana
- Liu, F., **Lu, P.**, Zhu, C., and Xiao, Y. (2009) Reactive transport modeling of the injection and CO₂ fate in the Mt. Simon sandstone formation. Eastern Section AAPG Annual Meeting, September 20-22, 2009, Evansville, Indiana
- **Lu, P.** and Zhu, C. (2009) Coprecipitation in the Barite Isostructural Family. 237th American Chemical Society National Meeting, Salt Lake City, UT, March 22-26.
- **Lu, P.**, Zhu, C., Kelly, S., and Nuhfer, T. (2009) Pb and Zn Coprecipitation with Iron Oxyhydroxide Nano-Particles. 237th American Chemical Society National Meeting, Salt Lake City, UT, March 22-26.
- **Lu, P.**, Fu, Q., Seyfried, W.E., and Zhu, C. (2008) Navajo sandstone-brine-CO₂ interactions: implications for geological carbon sequestration. GSA annual meeting, October 5-9, Houston, TX.
- **Lu, P.**, Zhu, C., Hedges, S. (2008) Geochemical modeling as an effective tool for monitoring, measuring, verification of CO₂ sequestration in deep geological formations, 7th Carbon Sequestration Meeting, May 5-8, Pittsburgh, PA.
- **Lu, P.**, Dillmore, R., Soong, Y., Zhu, C. (2008) Novel beneficial use of oil field brine and bauxite residue for carbon sequestration. AAPG Annual Convention and Exhibition, April 20-23, San Antonio, TX.
- **Lu, P.**, Fu, Q., Seyfried, W.E., Strazisar, B.R., Hedges, S.W., Zheng, Z., Zhu, C. (2007) Experimental determination of reaction rates and modeling of the long-term fate of CO₂ in deep geological formations. AAPG Annual Convention and Exhibition, April 1-4, Long

Beach, CA.

- Zhu, C., **Lu, P.**, Kelly, S., Nuhfer, N. (2006) Pb-Fe coprecipitation Part II: chemical modeling. Abstracts of Papers of the American Chemical Society 231: - 101-GEOC MAR 26, 2006.
- Kelly, S., Zhu, C., **Lu, P.**, Nuhfer, N. (2006) Pb-Fe coprecipitation Part I: Pb and Fe EXAFS characterization of the coprecipitates. Abstracts of Papers of the American Chemical Society 231: - 101-GEOC MAR 26 2006.
- **Lu, P.**, Zhu, C., Kelly, S., et. al (2005) A high resolution TEM-AEM, EXAFS, sorption edge measurement, and modeling study of Pb²⁺ coprecipitation with ferrihydrite. Geological Society of America Abstracts with Programs, 37(7): 324.

Service

- Manuscript Reviewed for: *Geochimica et Cosmochimica Acta*, *Journal of the American Ceramic Society*, *SPE International*, and *Environmental and Engineering Geoscience*
- 2008-2009 Academic Year, Graduate Moderator, Student Advisory Committee, Department of Geological Sciences, Indiana University